NASA Technical Memorandum 86246

Reports of Planetary Geology Program - 1983

APRIL 1984

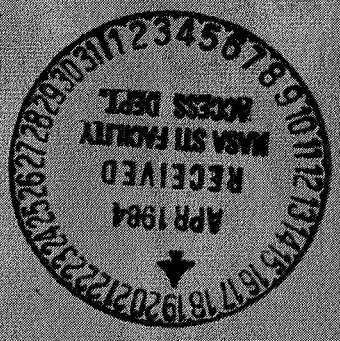

NASA

NASA Technical Memorandum 86246

Reports of Planetary Geology Program - 1983

Compiled by
Henry E. Holt
NASA Office of Space Science and Applications
Washington, D.C.

National Aeronautics
and Space Administration

**Scientific and Technical
Information Office**

1984

Foreword

This is a compilation of abstracts of reports from Principal Investigators of NASA's Office of Space Science and Applications, Solar System Exploration Division, Planetary Geology Program.

The purpose is to provide a document which succinctly summarizes work conducted in this program. Each report reflects significant accomplishments within the area of the author's funded grant or contract.

No attempt has been made to introduce editorial or stylistic uniformity; on the contrary, the style of each report is that of the Principal Investigator and may best portray his research.

Joseph M. Boyce
Discipline Scientist
Planetary Geology Program

TABLE OF CONTENTS

Page

CHAPTER 3 - VENUS

CHAPTER 4 - CRATERING PROCESSES AND LANDFORM DEVELOPMENT

Chapter 1

OUTER SOLAR SYSTEM SATELLITES

D1

ICE-COVERED VOLCANIC WATER FLOWS ON GANYMEDE

M. Lee Allison, Dept. of Geology & Geography, and Stephen M. Clifford, Dept. of Physics & Astronomy, Univ. of Massachusetts, Amherst, MA. 01003.

The most geologically reasonable model for the origin of grooved terrain on Ganymede involves flooding of a planetary graben system by water or water-ice magmas that rose to the surface along normal faults in the rift zones (Allison et al., 1980; Parmentier et al., 1982). To investigate this process further, we have examined the thermal evolution of a water flow on Ganymede's surface. The model is a variation of earlier work on ice-covered water flows by Lingenfelter et al. (1968), Wallace and Sagan (1979), and Carr (1982). It is based on the simplifying assumptions that laminar flow and a concomitant solid ice cover are achieved relatively soon after eruption; and that the amount of energy lost to the substratum is negligible (D. L. Stevenson, unpublished manuscript).

We begin our analysis by considering the heat balance at the surface of an ice-covered water flow (Fig. 1; variables are defined in Table 1). The two primary sources of heat at the ice surface are the fraction of solar radiation absorbed within the ice ($(1-f)q_i$, where $q_i = I(1-A)$), and the conductive heat flux from the underlying water flow ($q_c = k(273.15 - T)/x$). These heat inputs are balanced by radiative cooling ($4\sigma T^4$) and by the heat lost through sublimation of the ice cover ($L_s\ dm_u/dt$). Thus, the total surface heat balance is given by the equation:

$$(1-f)q_i + q_c = 4\sigma T^4 + L_s\ dm_u/dt \qquad (1)$$

where f, the fraction of incident solar radiation which is transmitted through the ice, is (after Carr, 1982) given by:

$$f = \exp(-Kx). \qquad (2)$$

K, the bulk extinction coefficient (=.01 cm^{-1}), was selected on the basis of several studies on the optical properties of terrestrial sea and glacial ice (Grenfell and Maykut, 1977; Grenfell, 1979). The variation of f with depth is illustrated in Fig. 2.

The equilibrium surface temperature required to solve the surface energy balance in Equation 1 was found using Newton's method. In the same manner as Carr (1982) this temperature was then used to determine the conductive heat loss (q_c) from the underlying water flow. Consideration of the heat balance at the base of the ice layer shows that q_c equals the sum of the fraction of the solar flux absorbed in the water (fq_i) and the latent heat released by freezing ($L_f\ dm_l/dt$) as the ice cover thickens with time. More simply:

$$q_c = fq_i + L_f\ dm_l/dt \qquad (3)$$

The increase in ice thickness dx which occurs in the time interval dt was calculated by noting that $dm_l/dt = \rho\, dx/dt$. Equation 3 was then solved for dx, yielding:

$$dx = dt(q_c - fq_i)/L_f \qquad (4)$$

where we have assumed $\rho = 1$ g cm^{-3}. With each time step the series of

calculations (Equations 1-4) were repeated based on the increase in ice thickness determined in the previous time step. The net effect of the increase in ice thickness is to reduce both the conductive heat loss from the water (q_c) and the fraction of solar radiation absorbed in the water (f).

The results of our calculations are summarized in Figures 3 and 4. During the first few minutes following the eruption of the water-magma, the surface temperature of the ice cover drops from 273 K to ~170 K. In the next several hours the temperature falls to 160 K; eventually the surface cools to below 150 K on a time scale of several tens of days (Fig. 3). These surface temperatures assume a magma flow which is sufficiently deep that a portion remains unfrozen beneath its protective ice cover over the given time period. The rate of increase in ice cover thickness is illustrated in Figure 4. During the first hour, the ice cover thickens to more than 10 cm - after which the growth rate begins to slow significantly. Thus a 5 m thick water flow, for example, would take about 75-80 days to freeze to its base.

The above results appear to be independent of reasonable changes in the assumed value of the bulk extinction coefficient or the albedo of the ice surface. The most sensitive parameter is the thermal conductivity of the ice cover; for example, decreasing it by 20% from our assumed value of .013 cal cm^{-1} s^{-1} K^{-1} means that a 5 m thick flow would take about 10 more days to freeze to its base than illustrated in Figure 4.

Our results suggest that water, under a protective and thickening ice cover, can exist on the surface of Ganymede for significant periods of time. For a typical Columbia River Plateau basalt flow on Earth the average discharge from a 1 km length of active fissure was approximately .1 km^3 per day (Swanson et al., 1975). Given a similar rate of discharge for water volcanism on Ganymede (per kilometer length of active fissure), a 5 m thick flow could flood an area of 20 km^2 in a single day - and nearly 1600 km^2 in the time required to freeze the flow to its base. Based on these calculations, we conclude that it would not be difficult for a series of water flows to fill Ganymede's planetary rift system and create the high albedo grooved terrain in a geologically reasonable interval of time.

Acknowledgement: This work was supported in part by NASA Grant NSG 7405.

REFERENCES

Allison, M.L., J.W. Head, & E.M. Parmentier, 1980, IAU Colloq. 57, The Satellites of Jupiter, #6-7.
Carr, M., 1982, NASA TM-85127, p203-205.
Grenfell, T.G., and G.A. Maykut, 1977, J. Glac., v18, p445-463.
Grenfell, T.G., 1979, J. Glac., v22, p305-320.
Lingenfelter, R.E., S.J. Peale, & G. Schubert, 1968, Science, 161, p266-269.
Parmentier, E.M., S.W. Squyres, J.W. Head, & M.L. Allison, 1982, Nature, 295, 290-293.
Swanson, D.A., T.L. Wright, & R.T. Helz, 1975, Am. J. Sci., 275, p877-905.
Wallace, D., and C. Sagan, 1979, Icarus, 39, p385-400.

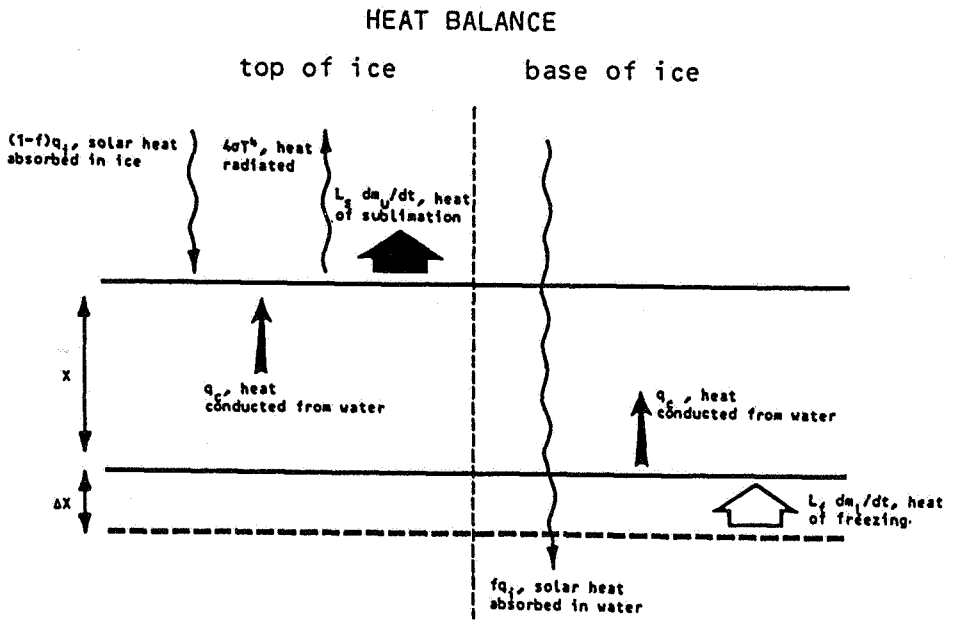

Fig. 1 Energy balance of thickening ice layer over water

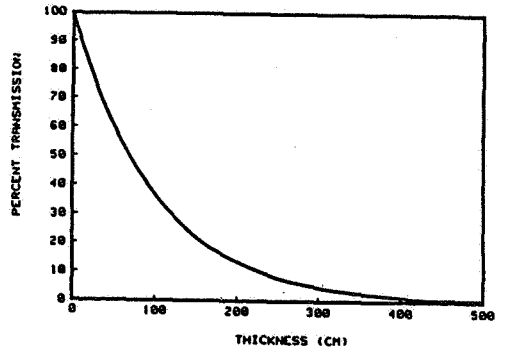

Fig. 2 Percentage of solar radiation penetrating pure ice with an extinction coefficient of .01

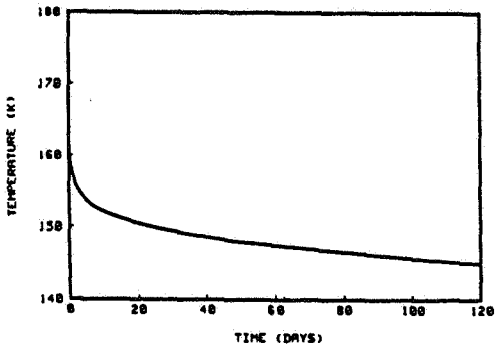

Fig. 3 Surface temperature of ice as a function of time after eruption

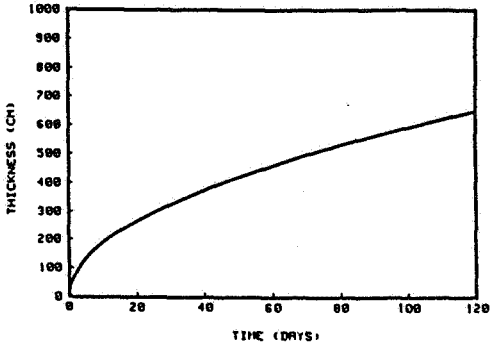

Fig. 4 Thickness of ice layer as a function of time after eruption

Table 1. Definition of symbols

f	fraction of q_i absorbed in water
q_i	solar heat absorbed at or below ice surface
q_c	heat conducted to surface
L_f	latent heat of freezing
L_s	latent heat of sublimation
k	thermal conductivity
K	bulk extinction coefficient
dt	incremental time change
x	ice thickness
dx	increase in ice thickness
σ	Stefan-Boltzmann constant
dm_l/dt	mass gain at ice base - freezing
dm_u/dt	mass loss at ice top - sublimation
T	surface temperature of ice
A	mean surface bond albedo
I	solar insolation

D2 N84 23433

ORIGIN AND EVOLUTION OF THE SATURN SYSTEM. James B. Pollack, Space Science Division, NASA Ames Research Center, Moffett Field, CA 94035 and Guy Consolmagno, Dept. of Earth and Planetary Sciences, MIT, Cambridge, MA 02138

As was the case for Jupiter, Saturn formed either as a result of a gas instability within the solar nebula or the accretion of a solid core that induced an instability within the surrounding solar nebula. In either case, the proto-planet's history can be divided into three major stages: early, quasi-hydrostatic evolution (stage 1); hydrodynamical collapse (stage 2); and late, quasi-hydrostatic contraction (stage 3). During stage 1, Saturn had a radius of several hundred times that of its present radius, R_S, while stage 3 began when Saturn had a radius of 3.5 R_S. Stages 1 and 2 lasted 10^6-10^7 years and 1 year, respectively, while stage 3 is continuing through the present epoch.

Saturn's current excess luminosity is due, in part, to the loss of thermal energy built up by a faster contraction that marked the earliest phases of stage 3. But, in contrast to the situation for Jupiter, this internal energy source fails by a factor of several in producing the observed excess luminosity. The remainder is most likely due to the gravitational separation of helium from hydrogen due to its partial immiscibility in the outer region of the metallic hydrogen zone.

The irregular satellite Phoebe was most likely captured by gas drag experienced in its passage through a bloated Saturn, just prior to the onset of stage 2. During stage 2, a nebular disk formed from the outermost portions of Saturn, due to a progressive increase in their rotational velocity as the planet contracted. This increase may have been enhanced significantly by a transfer of angular momentum from the inner to the outer regions of the planet. The nebular disk served as the birthplace of Saturn's regular satellites and probably the ring material. Viscous dissipation within the nebula caused an inward transfer of mass, and thus may have determined the nebula's lifetime, and an outward transfer of angular momentum. It is not clear what the relative roles of Saturn's luminosity and viscous dissipation were in determining the nebula's radial temperature structure and its evolution with time.

As Saturn's excess luminosity declined or less viscous dissipation in the nebula occurred during the early portion of stage 3, water was able to condense at progressively closer distances to the center of the system and water clathrates and hydrates were able to form throughout much of the nebula, especially in its outer regions. It is the likely presence of ices other than pure water ice in at least some of the regular moons of Saturn that make them chemically distinct from the large icy moons of Jupiter. If Saturn's nebula had a high enough pressure (greater than several tens of bars) in its inner region, a liquid solution of water and ammonia, rather than water ice, would have been the first "icy" condensate to form.

Despite the comparatively small size (hundreds to about a thousand kilometers) of the inner moons of Saturn, a number, especially Dione and Rhea, may have experienced significant expansion and melting during the first 1×10^9 years due to the presence of substantial quantities of ammonia monohydrate (10-20% by weight). The occurrence of the youngest known surfaces in the Saturn system on the comparatively small sized Enceladus is most readily attributed to strong tidal heating created by its forced orbital eccentricity. But a significantly larger eccentricity is required at some time in its past for tidal heating to be quantitatively capable of initiating melting, with the current eccentricity being perhaps large enough to maintain a molten interior.

During the early history of the Saturn system, giant impact events may have catastrophically disrupted most of the original satellites of Saturn. Such disruption, followed by reaccretion, may be responsible, in part, for the occurrence of "Trojans" and "co-orbital" moons in the Saturn system, the apparent presence of a stochastic component in the trend of satellite density with radial distance, and the present population of ring particles.

Titan's atmosphere formed from the hydrates and clathrates - especially ammonia monohydrate and/or nitrogen clathrate and methane clathrate - that constituted the satellite. Over the age of the solar system, a nontrivial amount of atmospheric nitrogen (about several tens of percent of the current atmospheric inventory) and much more methane than is presently in the atmosphere have been lost, through a combination of N and H escape to space and the irreversible formation of organic compounds. These considerations imply quasi-real time buffering of atmospheric methane by a near-surface methane reservoir and the existence of a layer of 0.1-1 km thickness of organic compounds close to or on Titan's surface.

D3

N84 23434

The Laplacian Resonance and Tidal Dissipation

A.F. Cook, Herzberg Institute of Astrophysics, National Research Council of Canada, Ottawa (on leave from the Smithsonian Astrophysical Observatory, Cambridge, Massachusetts)

The Laplacian resonance amongst Io, Europa and Ganymede has been examined by several authors (e.g., Yoder 1979, Greenberg 1982, Casen, Peal and Reynolds 1982) who took tidal dissipation in Jupiter, Io and Europa into account in various ways. The author and F.A. Franklin (Smithsonian Astrophysical Observatory) are completing a discussion in which it is shown that, in equilibrium, it is not permissible to neglect dissipation in Europa nor the torques of Jupiter on Europa and Ganymede. A formal calculation has been made on the assumption that the tidal torques and the torques in orbit-orbit resonance have reached an equilibrium such that the rates of decrease of the mean motions of the satellites are in the ratios 4:2:1. The results are

$$Q_J/K_J = 167\ Q_1/K_1,\ Q_2/K_2 = 0.44\ Q_1/K_1,$$

where Q denotes the quality at the body's frequency of rotation, K its second degree Love number and the subscripts J, 1 and 2 denote Jupiter, Io and Europa, respectively. The actual Q_J is taken to be inversely proportional to the synodic mean motion of each satellite, as expected at frequencies well below any resonant frequencies (Stevenson 1983). The Q_J found above is at Jupiter's frequency of rotation. The rate of tidal dissipation in Europa comes to one fifth that of Io. Such a low value of

Q_2/K_2 can be plausible if dissipation in both Io and Europa is due to tidal friction in fluid against underlying and overlying solid layers.

We can eliminate by inspection the possibility that Europa is emitting energy at such a high rate through hot spots and suffering negligible thermal leakage through its crust as Io appears to do. There is evidence for a low level of venting through the surface (Cook et al. 1982). An additional process is required to open such vents: Perhaps the process of generation of cracks proposed by Helfenstein and Parmentier (1983) is still active.

The nominal value of Q_1/K_1 in current use is about 100, matching a rate of dissipation of 2×10^{20} ergs 5^{-1} in Io. The corresponding value of Q_J/K_J is 17,000, that of Q_2/K_2 is 45. Such a low value of Q_J cannot have been in effect for long because the corresponding rate of evolution of the three satellite orbits is incredibly fast. Also the only mechanism currently available to account for such a low Q_J/K_J is that of "helium rain" (for references see the discussion of Stevenson 1983). The rate of depletion of helium from Jupiter's atmosphere becomes so rapid that a short limit is placed on the total duration of "helium rain".

If there has been a recent drop in Q_J/K_J, then, as discussed by Yoder (1979) and Greenberg (1982), Io and Europa may be in equilibrium together with tidal torques from Jupiter and just now overtaking Ganymede or they may merely appear to be doing so due to a recent quasi-periodic drop in Q_J/K_J, a distinct possibility, as pointed out by Stevenson (1983). In all of these cases, the value of Q_2/K_2 found above becomes a lower limit and that of Q_J/K_J is to be slightly reduced.

References

Cassen, P.M., Peale, S.N., and Reynolds, R.T., 1982. Structure and thermal evolution of the Galilean satellites, in Satellites of Jupiter, ed. by D. Morrison and M.S. Matthews, Tucson, U. of Arizona Press, pp. 93-128.

Cook, A.F., Shoemaker, E.M., Soderblom, L.A., Mullins, K.F., and Fiedler, R., 1982. Volcanism in ice on Europa, in Reports of Planetary Geology 1982, NASA TM 85127.

Greenberg, R., 1982. Orbital evolution of the Galilean satellites, in Satellites of Jupiter, ed. by D. Morrison and M.S. Matthews, Tucson, U. of Arizona Press, pp. 65-92.

Helfenstein, P., and Parmentier, E.M., 1983. Patterns of fracture and tidal stresses on Europa, Icarus 53, 415-430.

Stevenson, D.J., 1983. Anomalous bulk viscosity of two-phase fluids and implications for planetary interiors, Journ. Geophys. Res. 88, 2445-2455.

Yoder, C.F., 1979. How tidal heating in Io drives the Galilean orbital resonance locks, Nature 279, 767-770.

N84 23435

THE STRUCTURE OF THE IONIAN LITHOSPHERE

Michael H. Carr and Gary D. Clow. U.S. Geological Survey, Menlo Park, CA

This is a report on some exploratory work on the structure of the Ionian lithosphere. The approach is to examine temperature profiles within the lithosphere that result from different distributions of sulfur and silicates and different conductive heat fluxes, then compare such profiles with observations in the expectation that only a limited set of the profiles are possible. In this preliminary work some rather simplistic assumptions have been taken and the report should be viewed more as a demonstration of a method rather than a presentation of results.

Temperature profiles were calculated as follows. Sulfur was assumed to decrease exponentially with depth and the thermal conductivity within the lithosphere was varied as though it changed linearly with the proportions of silicates and sulfur. Thermal conductivities of 4×10^5 and 2.5×10^4 erg/cm-sec °K were taken for silicates and sulfur respectively. Tidal dissipation energy was assumed to be generated uniformly thoughout the rigid lithosphere, and the base of the lithosphere was defined as the depth at which the temperature reaches 0.75 times the melting temperature of silicates, at which point silicates generally undergo ductile rather than elastic deformation.

The temperature profile was computed by an iterative numerical procedure. The profile was first divided into small elements. The upper surface of the topmost element was set at 130°K, the thermal conductivity of the element was computed from the mix of silicates and sulfur as indicated above, and a conductive heat flux was assumed. The temperature at the base of the element could then be readily calculated. For the second element the flux is decreased to account for that fraction of the total flux that was generated higher in the profile by tidal dissipation. The other parameters were changed appropriately then the temperature at the base of that element was calculated. This process was repeated until the limiting temperature for elastic behavior was reached, which defines the base of the lithosphere. Initially the heat generated per unit volume of the lithosphere was computed on the basis of a 50-km thick lithosphere. Once a profile had been computed a revised value for the heat generated per unit volume based on the calculated lithosphere thickness was used, and the profile recalculated until consistency was achieved.

The results can be displayed on a plot of the assumed scale depth for sulfur and the assumed conductive heat flux (figure 1). Parts of such a plot can be excluded on the basis of observational evidence. The depth of melting of sulfur cannot be shallower than 2 km (Clow and Carr, 1980) and significant amounts of sulfur must be present at depths where the melting temperature of sulfur is reached otherwise there would be no sulfur volcanism. For purposes of illustration, 5% was chosen as significant,

but other values could clearly be used. It is immediately apparent from the diagram that only a small fraction of the total heat lost by the satellite is lost through conduction. The total heat flux is close to 2 W m^{-2} (Matson et al. 1980; Sinton, 1980; Cassen et al. , 1982). If the assumptions taken here are close to valid then no more than 0.3 W m^{-2} can be lost by conduction. The rest must be lost through transport of materials upward through the profile. Reynolds et al. (1980) showed that resurfacing by silicates at a rate of 0.1 cm yr^{-1} causes heat loss at a rate of 0.18 W m^{-2}. The corresponding number for sulfur is 0.016 W m^{-2}. Since the total amount of heat lost through transport of material to the surface, and the ratio of sulfur to silicates in the upper parts of the profile are defined by the model, the resurfacing rates for different conditions can be computed, and these are shown on figure 1. The resurfacing rates are high, in the order of a cm yr^{-1}, because such a large fraction of the 2 W m^{-2} lost is effected by resurfacing.

REFERENCES.

Cassen, P. M., Peale, S.J., and Reynolds, R.T., 1982, Structure and thermal evolution of the Galilean satellites: in The Satellites of Jupiter (D. Morrison, ed.) University of Arizona Press, Tucson, Ariz.

Clow, G.D., and Carr, M.H., 1980, Stability of sulfur slopes on Io: Icarus, v. 44, p. 268-279.

Matson, D.L., Ransford, G.A., and Johnson, T.V., 1980, Heat flow from Io (J1): J. Geophys. Res., v. 86, p. 1664-1672.

Reynolds, R.T., Peale, S.J., and Cassen, P., 1981, Io: Energy constraints and plume volcanism: Icarus, v. 44, p. 234-239.

Sinton, W.M., 1981, The thermal emission spectrum of Io and a determination of its heat flux from its hot spots: J. Geophys. Res., v. 86, 3122-3128.

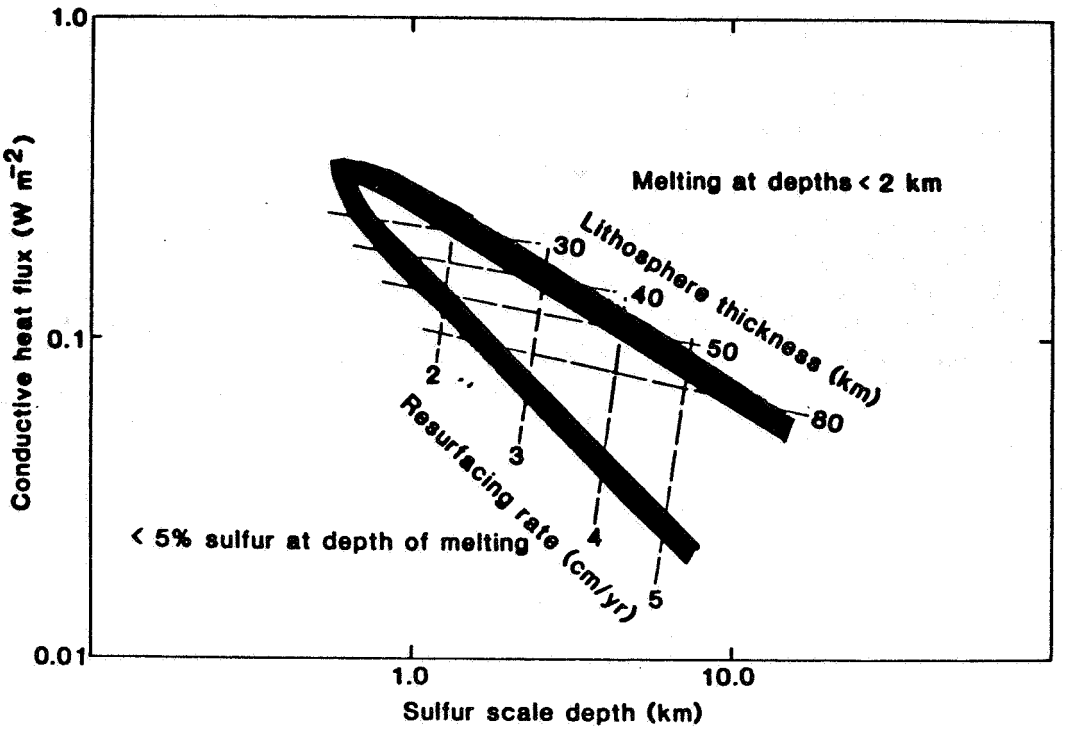

Figure 1. Constraints on the structure of the Ionian lithosphere. Possible conditions are all enclosed within the shaded area. For example, if the conductive heat fluxe is 0.1 W m^{-2} the sulfur scale depth can range from 2-4 km, the lithosphere thickness is 50-80 km, and the resurfacing rate is 2.5-4.0 cm yr^{-1}.

P5 N84 23436

MODELING IO VOLCANISM: MAXIMUM VOLCANIC TEMPERATURES, DEPTHS OF MELTING AND MAGMA COMPOSITION

Larry S. Crumpler and Robert G. Strom, Lunar and Planetary Laboratory, University of Arizona, Tucson, AZ 85721

Interim results of thermal and structural modeling of volcanism on Io have been presented by Crumpler and Strom (1). This abstract summarizes the final results of the modeling. The basic analysis is an evaluation of the "magma trigger" mechanism for initiating and maintaining eruptions. Secondary aspects include models of the mechanical mode of magma emplacement, interactions with a sulphur-rich upper crust, and more speculative implications for Io's volcanism.

In simplest finite element form, the initial temperature (Tm) of the contact between sulphur in the upper crust of Io and a freshly intruded silicate magma is given by:

$$Tm^{t} = T_{m-1}^{t-1} + \left(2\Delta t\alpha_{m+1}\right)^{0.5}\left[\left(T_{m+1}^{t-1} - T_{m-1}^{t-1}\right) \Big/ \left(\left(2\Delta t\alpha_{m+1}\right)^{0.5} + \left(2\Delta t\alpha_{m-1}\right)^{0.5}\right)\right] \quad (1)$$

Here m-1 is a finite plane within the sulphur layer, m + 1 is a plane within the silicate intrusion, α_{m+1} and α_{m-1} are the thermal diffusivities of the sulpher and silicate magma respectively, and t is time. The results for a reasonable temperature range of magma (1200-1500K) and sulphur (130-400K) are about 700K 100K, or approximately the vapor temperature of elemental sulphur. A silicate sill or laccolith 10m thick will yield energetic vapor for a period of several weeks to several months depending on the precise vapor temperature and the amount of advective cooling of the sulphur-silicate interface. This model can account for the origin of plumes and sulphur flows, as well as for their observed temperatures (2) and lifetimes (3). If sulphur vapor temperatures at the contact are exceeded by no more than 40°K at the equator, then no sulphur vapor will be generated above about 50° latitude because the initial sulphur temperatures above these latitudes will not yield contact temperatures of the required temperature. This would explain the lack of large plumes in the polar areas.

The darkest deposits on the floor of the average dark caldera cover 10% of the floor area. If these are hot areas (475-600°K), then the area of all dark calderas on Io covered by similar proportions of hot surfaces yields a heat flow from 0.8 - 2.9 Wm^{-2}, in agreement with the observed flux.

proportions of hot surfaces ranges from 0.8 - 2.9 Wm^{-2}, in agreement with the observed flux.

Estimates of the probable depth to the silicate magma source (h_c) can be derived from laccolith hydraulics (4) in which:

$$h_c = \left(16\delta_{max} E h^2 / [3g\Delta\rho(1-\nu^2)r^4 + \rho_s h / D\rho] \right)^{0.5} \quad (2)$$

where δ_{max} is the laccolith thickness, E in Young's modulus, Δp is the magma-crust density contrast, h is the overburden thickness, ν is Poisson's ratio, r is the laccolith radius, and ρ_s is the sulphur crust density. Calculations indicate depths of 40 to 200km to magma sources, with a most probable depth near ~ 100km. Any magma capable of forming a laccolith has the necessary magma driving pressure to create surface silicate volcanism as well. A 40km thick crust is the minimum required to support the highest mountains of Io. For most viable mechanisms of building the observed mountains, however, a lithospheric thickness of 140km is required.

The amount of melt that must make its way to the surface to carry the nominal tidal heat input depends on the average temperature of the melt and its heat capacity. In order for silicate melts between 1200-1500°K to move 1 Wm^{-2} — the average of the tidal input and observed radiant output of Io — 10 to 4 average laccoliths (r=20 km) need to be erupted at the sulphur crust-silicate crust interface per year. This is within the range of probable frequency of thermal outbursts estimated at 10 per year (5). This is also within the volume limits of silicate magma necessary to mobilize the volume of sulphur inferred to be cycled from resurfacing rates.

Temperatures much above the melting point of sulphur at the base of a sulphur crust would result in rapid overturn, or advection. Thus, the temperature at the base of the sulphur crust may be buffered at ~ 400°K. For this reason the existence of a "sulphur ocean" is unlikely. Similarly, the base of the silicate lithosphere may be maintained at the silicate melting temperature. The depth to melting is constrained either by the depth to which stressing and fracturing penetrates the lithosphere and initiates advective heat transfer, or the depth to which melting first occurs from a given conducted thermal gradient. On Io, there is no lack of heat for melting at any depth, and therefore, the depth to silicate melting may be buffered by the depth of tidal fracturing.

Equation (1) sets a lower limit of 1200K for the silicate magma temperature if the base of the sulphur crust does not exceed 400K as implied above. Such a temperature is characteristic of silicic and alkalic magmas on the Earth (rhyolite or trachyte). The High K and Na in the Io torus may reflect high abundances of these elements in

the silicate crust and magma, both elements being abundant in terrestrial silicic magmas. For all other elements of the thermal model of advection to work coherently, all magmas shallower than about 100km will have temperatures of about 1200°K. Active silicate volcanism on Io of silicic composition intruded in a sulphur-rich crust best explains the observed characteristics of its overall thermal budget and volcanic style.

References

(1) Crumpler, L.S., and Strom, R.G., 1982, Active Volcanism on Io: A Unified Model and Mechanism. Reports of the Planetary Geology Program. NASA Tech. Mem. 85127, p. 409.

(2) McEwen, A.S., and L.A. Soderblom, 1983, Two Classes of Volcanic Plumes on Io. Icarus, 55, 191-217.

(3) Pearl, T.C., and N.M. Sinton, 1982, Hot Spots of Io. in D. Morrison, ed., The Satellites of Jupiter, Tucson, University of Arizona Press, 724-755.

(4) Pollard, D.D., 1969, Deformation of Host Rocks During Sill and Laccolith Formation. Stanford University, Ph. D., 134p.

(5) Sinton, N.M., 1980, Io: Are Vapor Explosions Responsible for the 5mm Outbursts? Icarus 43, 56-64.

VOLCANIC FORMS IN THE KANE PATERA REGION, IO

Frank R. Karner, Geology Department, University of North Dakota, Grand Forks, ND 58202

Four morphologically distinct major volcanic forms occur within and adjacent to the Kane Patera, high resolution map quadrangle Ji2B (lat 15° to 50° S., long 355° to 20°W.) Volcanic vents and flows form four types of features: low-relief shield volcanoes, domical shield volcanoes, large calderas and isolated groups of flows not obviously associated with a central vent.

Low-relief shield volcanoes typically consist of a central vent region 15-30 km in diameter and sulfur flows extending typically assymmetrically from the vents for 150-250 km. Mbali Patera (Figure 1) with major recent flows bilaterally extending to the south and north is an example. Initial study of the central vent region suggests a pair of rounded vents linked by elongate trough all within a shallow depression at the top of the low broad shield. Talos Patera (Figure 2) with recent flows to the southwest and northeast is another example.

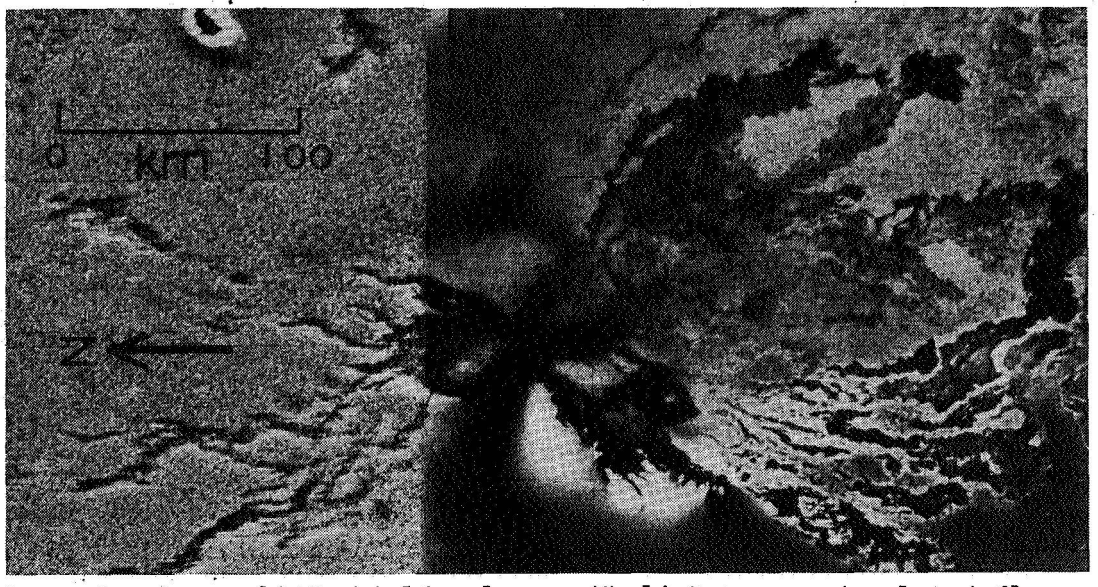

Figure 1. Low-relief shield volcano, Mbali Patera and related flows, centered at lat 33° S., long 8° W. Recent sulfur flows to the S are darkest (dark reddish-brown to dark gray) and have light (yellow to yellow orange) margins or haloes. Older flows are intermediate tones (orange to brown). The central vent region appears to consist of two dark (reddish brown to gray to black) irregular to rounded depressions consisting of elongate darkest (grey to black) regions which may be rifts and/or flows.

Domical shield volcanoes consist of a central vent 10-20 km in diameter surrounded symmetrically by sulfur-silicate (?) flows extending 50-150 km from the vent to a marginal scarp. Taw Patera (Figure 2) is an example with nearly rounded form while Inachus Tholus just northeast of Ji2b is an example with almost perfectly rounded form.

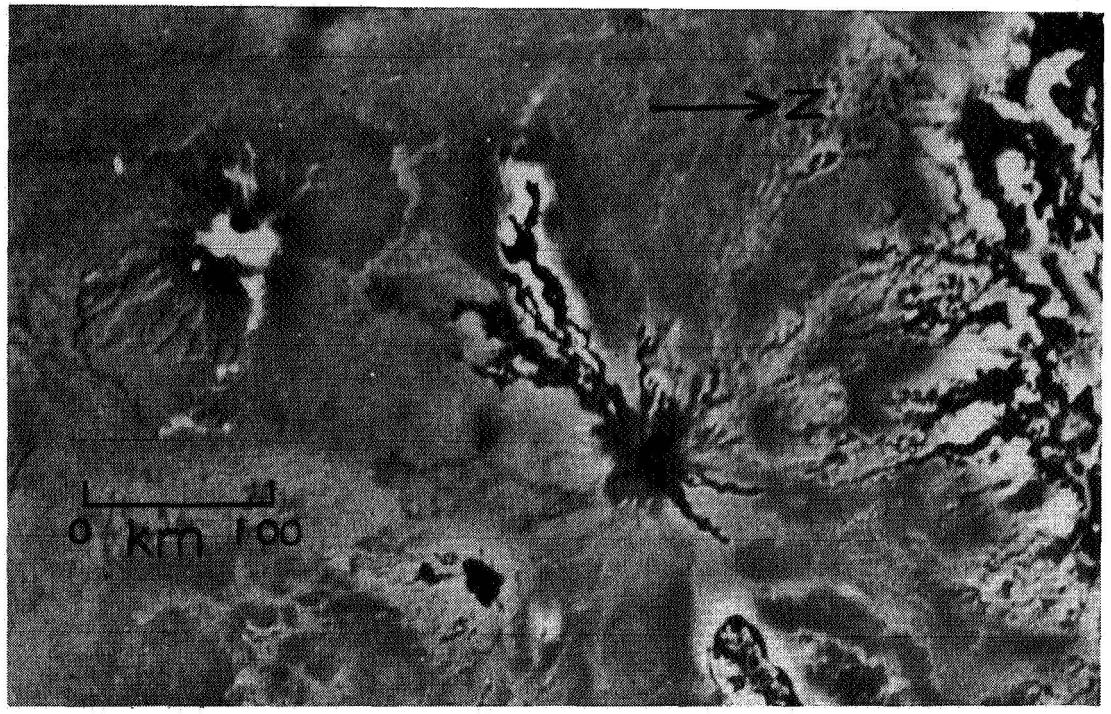

Figure 2. Domical shield volcano, Taw Patera and related flows, centered at lat 33° S., long 359° W and low-relief shield volcano, Talos Patera and related flows, to the northeast centered at lat 26° S., long 356° W. The sulfur-silicate flows from Taw Patera have intermediate tone (orangish tan), and appear to have steeper dips and higher relief than those of low-relief shields with sulfur flows. A scarp partly outlines the outer margins of the uppermost sulfur-silicate flows. The vent appears to be a small black crater with an assymmetrical bright (yellow to orange) halo.

Calderas consist of large depressions 50-200 km in diameter typically developed on low-relief plains and surrounded by thin surface deposits and/or low-relief flows. Kane Patera (Figure 3) is an example with several apparent subsidence levels within the crater. Siun Patera and Paive Patera along with two unnamed depressions in the northwest part of Ji2b are other examples.

Isolated groups of flows are fresh-appearing elliptical regions of sulfur flow complexes about 350 km long and 150 km wide. Flows in the western part of Ji2b (Figure 3) are an example. These flows are between Uta Patera and Mbali Patera but do not appear to be derived from either. They may have a fissure source (W. Elston, September, 1983; personal communication) or may have small or covered central vents. Another example is present at the northeastern border of Ji2b.

Further study is being directed toward: (1) detailed study of individual examples of the four major types of volcanic forms in Ji2b; (2) comparison with features in other regions of Io; and (3) evaluation of the interrelationships and processes of formation of the four types.

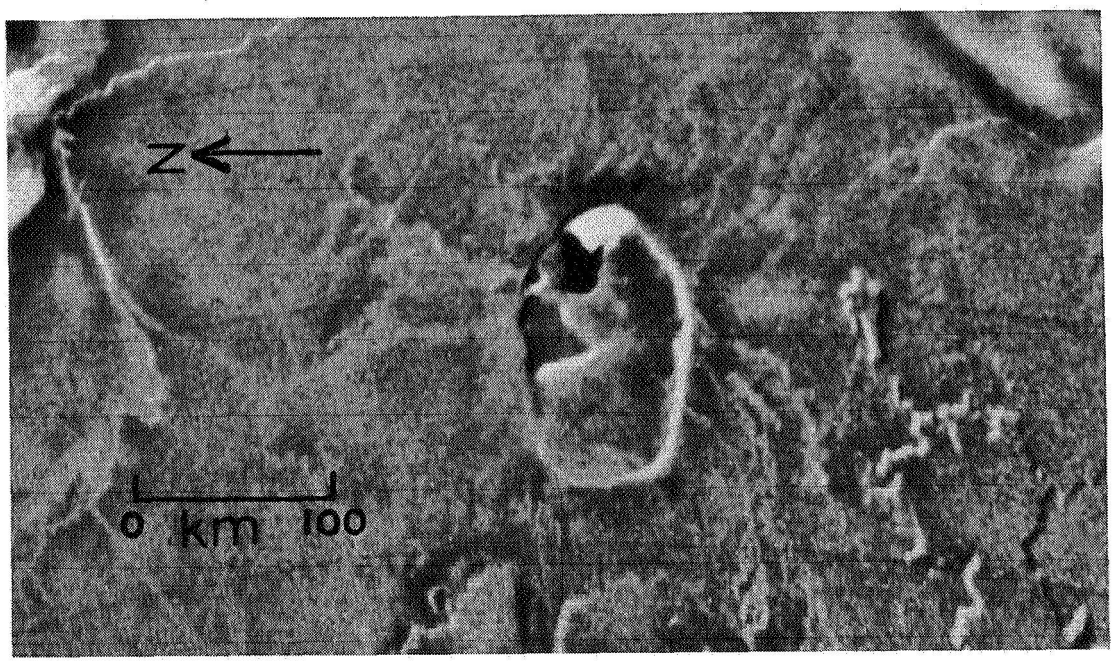

Figure 3. Large caldera, Kane Patera, centered at lat 48° S., long 14° W. The caldera floor in its lowest level is black with bright (orange) intermediate levels and a grey (greyish brown) extensive upper level. Faint dark grey (orangish brown) flows surround the caldera.

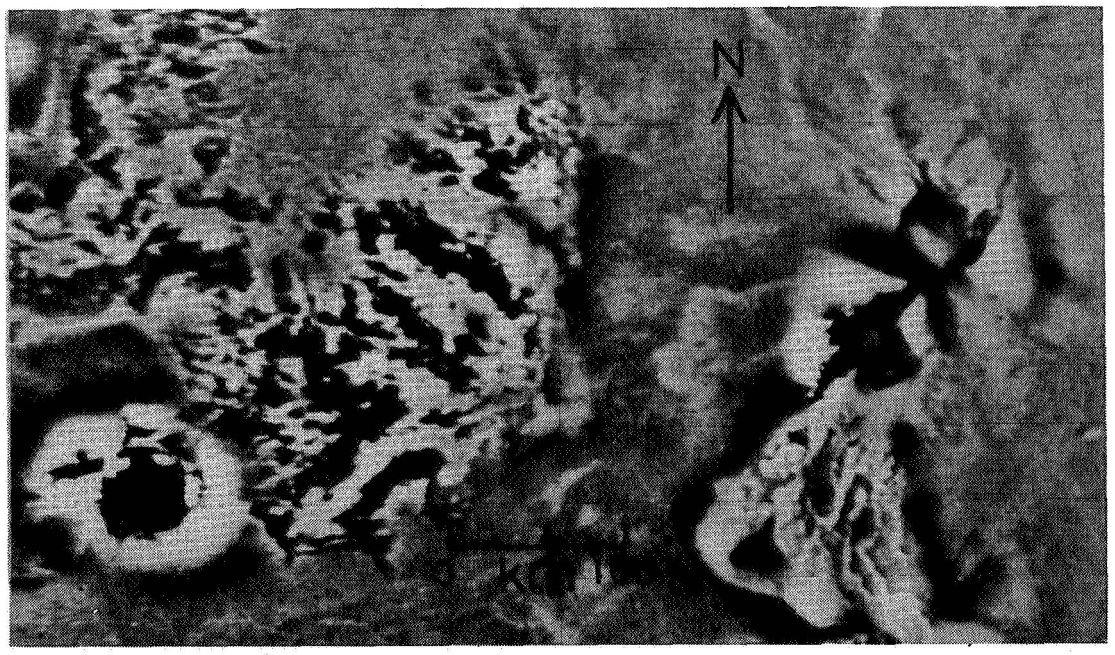

Figure 4. Unnamed isolated group of flows centered at lat 33° S., long 19° W between Mbali Patera to the E and Uta Patera to the SW. Young-appearing dark (dark grey to dark reddish brown) have broad light (light grey to yellow) margins. They appear to extend to the W from small or covered vents on the E margin of the flow group.

D7 N84 23438

PHOTOMETRY OF ICY SATELLITES: HOW IMPORTANT IS MULTIPLE SCATTERING IN DILUTING SHADOWS?

B. Buratti* and J. Veverka, Cornell University

Voyager observations have shown that the photometric properties of icy satellites are influenced significantly by large-scale roughness elements on the surfaces (Buratti and Veverka, 1983; Buratti, 1983). While recent progress has been made in treating the photometric effects of macroscopic roughness, it is still the case that even the most complete models (e.g., Hapke, 1983) do not account for the effects of multiple scattering fully. It is clear that multiple scattering will dilute shadows caused by large-scale features, yet for any specific model it is difficult to calculate the amount of dilution as a function of albedo. Accordingly, laboratory measurements were undertaken using the Cornell Goniometer to evaluate the magnitude of the effect. A pair of dark samples (reflectance = 0.02) was prepared; one flat, the other with a paraboloidal crater (depth/diameter = 0.40) near the center covering 25% of the sample area viewed by the detector (Figure 1). A similar pair of bright samples (reflectance = 0.95) was also constructed. For each pair (flat and cratered) we held the emission angle at 0°, and varied the incidence and phase angles. For the dark samples, the measured difference (flat minus cratered) of scattered light agreed well with model calculations in which the dilution of shadows within the model crater (by multiple scattering) is neglected. (For details see Veverka and Wasserman, 1972; Buratti, 1983). For the bright samples, the measured difference was significantly less (by about 50%) than predicted by the model, and much less dependent on phase angle than for the dark surfaces where the difference increases strongly with phase angle.

The results are shown in Figure 2. Specific conclusions include:

a) For dark surfaces (which scatter according to a lunar-like law) the photometric effects of shadowing increase rapidly with increasing phase angle α. These effects can be modeled adequately by theoretical calculations which neglect the dilution of large-scale shadows by multiple scattering (solid curve, bottom of Figure 2).

b) For bright surfaces, especially those which scatter approximately according to Lambert's law, the photometric effects of shadowing remain approximately constant with increasing phase angle up to at least α = 70°. This constancy is qualitatively consistent with the approximately isotropic nature of such scattering. In such cases, model calculations overestimate the magnitude of the effect, evidently because the theoretical calculations do not allow for the destruction of large-scale shadows by multiple scattering.

c) Our measurements suggest that for bright icy satellites (Europa, Enceladus, etc.) the effects of macroscopic roughness are overestimated in currently available models and that the importance of such effects is less dependent on phase angle than is the case for dark surfaces.

This research was supported by NASA Grant NSG 7156.

---

*Now at Jet Propulsion Laboratory.

REFERENCES:
Buratti, B. (1983). Photometric Properties of Europa and the Icy Satellites of Saturn. Ph.D. Dissertation, Cornell University.
Buratti, B., and Veverka, J. (1983). Voyager photometry of Rhea, Dione, Tethys, Enceladus, and Mimas. Submitted to Icarus.
Hapke, B. W. (1983). Bidirectional reflectance spectroscopy. 3. Correction for macroscopic roughness. Submitted to Icarus.
Veverka, J., and Wasserman, L. (1972). Effects of surface roughness on the photometric properties of Mars. Icarus 16, 281-290.

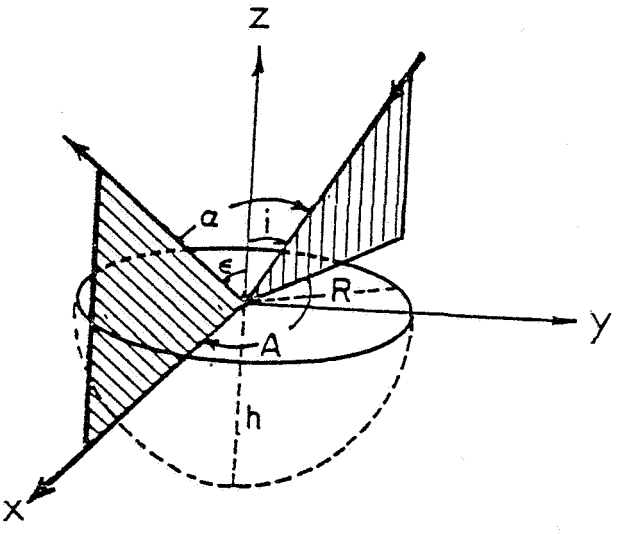

FIGURE 1. Sketch of model crater and definition of scattering geometry. The incidence angle is represented by i; ε is the scattering angle and α is the phase angle. In our experiment h/R was equal to 0.4.

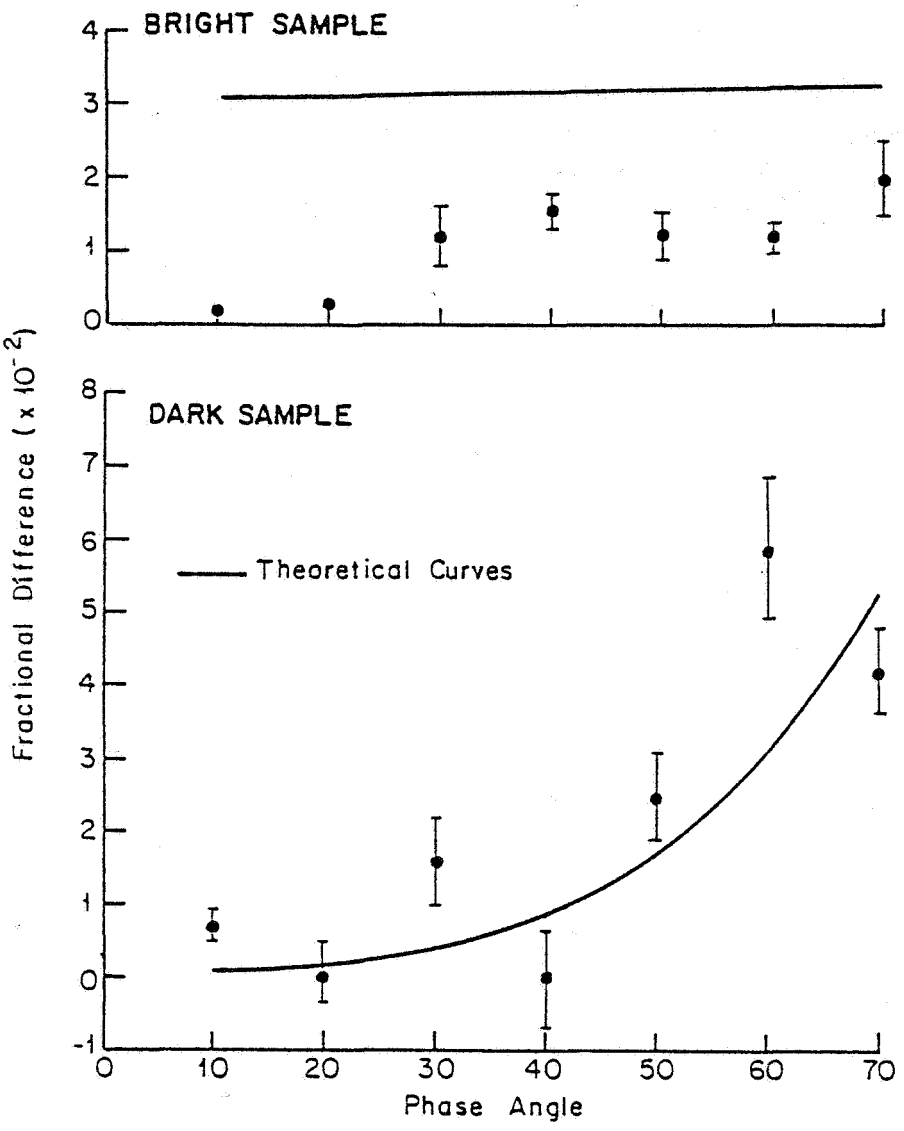

FIGURE 2. Goniometer I/F measurements as a function of phase angle for bright (r_n = 0.95) and dark (r_n = 0.02) samples. The data are shown as fractional differences between the I/F values for the flat and cratered samples ([Flat-Cratered]/[Flat]). The central 25% by area of the "cratered" samples consists of a crater having a depth-to-diameter ratio of 0.4 (Figure 1). Solid lines are theoretical curves; measurements are shown by points. The error bars are larger in the lower graph due to the lower intensity of scattered light from the darker sample. Here I is the intensity of scattered light and πF is the incident plane parallel flux at i = 0°.

COMPARISON OF HAPKE'S PHOTOMETRIC THEORY WITH VOYAGER OBSERVATIONS OF EUROPA, ENCELADUS, RHEA, AND MIMAS

B. Buratti* and J. Veverka, Cornell University

Voyager imaging observations of the satellites of Jupiter and Saturn provide an excellent test for various photometric theories that have been proposed to describe the scattering properties of planetary and satellite surfaces (Lumme and Bowell, 1981; Goguen, 1981; Hapke, 1981, 1983). Not only does the Voyager data set include observations of surfaces ranging widely in albedo, but it provides measurements (in both disc-integrated and disc-resolved forms) over a wide range of phase angles. We report on a detailed comparison of the above models with Voyager data for Europa, Enceladus, Rhea, and Mimas. These satellites were selected because they cover a range of reflectances from 0.65 to 1.0 (Buratti and Veverka, 1983) and because for them the Voyager photometric data sets are most complete.

Our main result is that Hapke's theory (Hapke, 1981, 1983) fits the Voyager observations not only well, but consistently: a consistent set of parameters can be derived for each satellite from the observations of disc-integrated brightness as a function of phase angle, and from measurements of the brightness distribution across a satellite's disc at individual phase angles (ranging from near opposition to well beyond 90° in some cases). The results are summarized in Table 1 and in Figure 1. The parameter g (the Henyey-Greenstein asymmetry factor) describes the directionality of scattering by individual scattering elements ("particles") within the surface (negative values indicate backscattering; for isotropic scattering g = 0). ω_0 is the single scattering albedo of the particles and h is the compaction parameter of the surface, defined most simply by $h \simeq k(\rho/\rho_0)$ where ρ is the bulk density of the optically active surface layer, ρ_0 the density of individual particles and k a constant approximately equal to 2 (Hapke and Wells, 1981). θ is the model mean slope angle used by Hapke (1983) to describe large-scale surface roughness. We stress that θ is a model parameter, useful in comparisons among different satellites, but difficult to relate reliably to actual surface slopes measured on some specified scale. Only for Europa and Mimas are the Voyager data sets complete enough at large phase angles to derive values of θ.

Except in the case of Europa, our results show that icy objects such as Mimas, Enceladus and Rhea have compaction parameters closely similar to that of the lunar surface. This observation suggests that at least the optically active outer layers of icy regoliths have textures similar to that of the rocky regolith on the Moon. Europa appears to have a distinctly more compact regolith than any of the satellites in Table 1.

Since Goguen's theory (Goguen, 1981) is conceptually similar to that of Hapke (1983) we expect that it too would also fit the Voyager data adequately, although we have not carried out the test in any detail. We have, however, tested the Lumme-Bowell model, and find that at least in its published form (Lumme and Bowell, 1981) the model does not fit the

*Now at Jet Propulsion Laboratory.

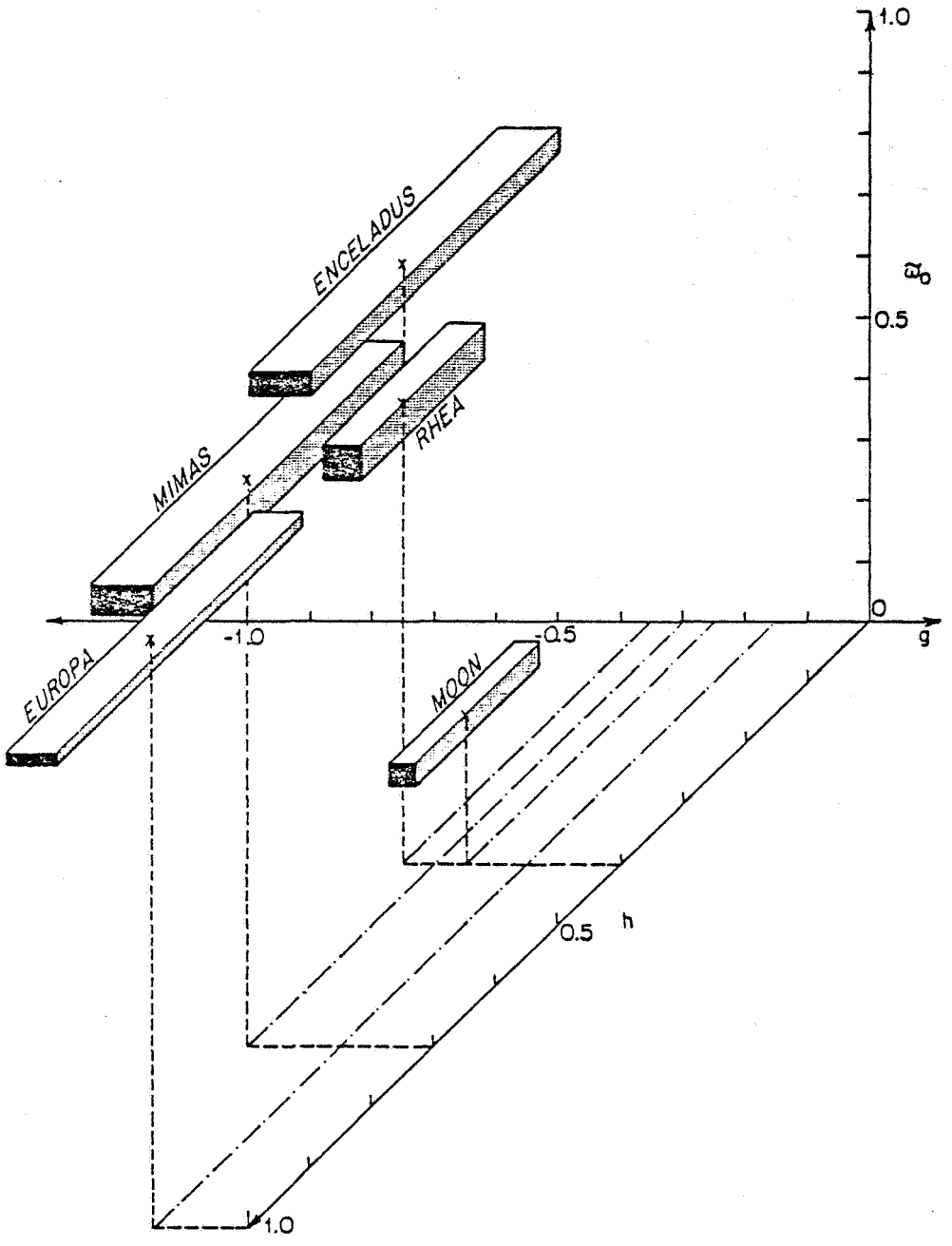

FIGURE 1. Values of the parameters $\tilde{\omega}_0$, h and g derived by filtering Hapke's theory to Voyager observations of Europa, Mimas, Enceladus, and Rhea. Values for the Moon, derived from the observations of Lane and Irvine (1973), are shown for comparison.

Voyager observations of the icy satellites adequately. A particularly troublesome feature of the Lumme-Bowell model is that different model parameters must be used at small and large phase angles. We suspect that the failure of the Lumme-Bowell model to fit observations of icy satellites over a wide range of phase angles is in part due to simplifying assumptions that are involved--for instance, that the single scattered light component can be approximated in all cases by the behavior observed in the case of asteroids near opposition.

This research was supported by NASA Grant NSG-7156.

REFERENCES

Buratti, B., and Veverka, J. (1983). Voyager photometry of Rhea, Dione, Tethys, Enceladus, and Mimas. Submitted to Icarus.

Goguen, J. D. (1981). A theoretical and experimental investigation of the photometric functions of particulate surfaces. Ph.D. Thesis, Cornell University.

Hapke, B. W. (1981). Bidirectional reflectance spectroscopy. 1. Theory. J. Geophys. Res. 86, 3039-3054.

Hapke, B. W. (1983). Bidirectional reflectance spectroscopy. 3. Correction for macroscopic roughness. Submitted to Icarus.

Hapke, B. W., and Wells, E. (1981). Bidirectional reflectance spectroscopy. II. Experiments and observations. J. Geophys. Res. 86, 3055-3060.

Lane, A. P., and Irvine, W. M. (1973). Monochromatic phase curves and albedos for the lunar disk. Astron. J. 78, 267-277.

Lumme, K., and Bowell, E. (1981). Radiative transfer in the surfaces of airless bodies. I. Theory. Astron. J. 86, 1694-1704.

TABLE 1. Values of $\tilde{\omega}_0$, h, g, and Mean Slope Angle Derived by Fitting Hapke's Theory to Voyager Clear Filter Observations

Satellite	Single particle Scattering Albedo $\tilde{\omega}_0$	Hapke Compaction Parameter h	Asymmetry Factor g	Model Slope Angle θ
Moon*	0.25 ± 0.02	0.4 ± 0.1	-0.25 ± 0.02	
Europa	0.97 ± 0.01	1.0 ± 0.2	-0.15 ± 0.04	23°
Mimas	0.93 ± 0.03	0.7 ± 0.2	-0.30 ± 0.05	30°
Enceladus	0.99 ± 0.02	0.4 ± 0.2	-0.35 ± 0.03	
Rhea	0.76 ± 0.03	0.4 ± 0.1	-0.35 ± 0.05	

*Derived from observations by Lane and Irvine (1973).

D9 ABSTRACT

N84 23440

VOYAGER FEATURE-FIXED PHOTOMETRY OF IAPETUS

J. Goguen, D. Morrison, and M. Tripicco, Institute for Astronomy, University of Hawaii, Honolulu, HI 96822

Iapetus is one of the most mysterious objects in the Solar System. As indicated by previous ground-based studies and dramatically confirmed by the Voyager images, the surface of this satellite has a strikingly bimodal distribution of albedo and color. While the underlying object seems to be a largely icy satellite similar to Rhea, the leading hemisphere of Iapetus is dominated by a very dark patch of hemispheric scale. The symmetry of this dark material with respect to the orbital motion of the satellite strongly suggests an external control, if not necessarily an external origin, for the dark material.

We are using quantitative photometric techniques to map the photometric function of the surface material over Iapetus. The approach is to study clearly defined surface areas that appear on a number of Voyager images obtained under different spacecraft and lighting geometries. The pixels within each area are then identified on each frame, and the reflectance as a function of phase angle determined for each spot. The areas studied appear to follow the standard relationships of brightness to angles of incidence and emission, permitting a determination for each area of a two-parameter characterization of the photometric function: r (normal reflectance); and β (linear phase coefficient).

We have derived the values of r and β for 23 fixed circular regions 200 km in diameter using Voyager 1 and Voyager 2 frames at phase angles from 10° to 90°. This quantitative analysis confirms the bimodal character of the surface. For the bright areas, $\bar{r} = 0.38$ and $\bar{\beta} = 0.009$; for the dark areas, $\bar{r} = 0.03$ and $\bar{\beta} = 0.016$. On the scale of 200-km-diameter areas, there are no spots with $0.06 < r < 0.25$ except where the images clearly include a mixture of distinct light and dark pixels. The darkest area is at the apex of motion, but the brightest area is near 210° W, 60° N, rather than at the antapex.

Additional analysis of higher-resolution Voyager 2 frames that include the boundary between light and dark areas indicate that the width of the transition zone is of the order of 200 km. We are continuing the higher-resolution studies with emphasis on the nature of this boundary. We expect that these results will place important limits on the mixing of the light and dark material, and may thus constrain models for the hemispheric dichotomy on this satellite.

D16

THEORETICAL ASPECTS OF PHOTOCLINOMETRIC TERRAIN PROFILING ON THE GALILEAN SATELLITES

Lionel Wilson and Marion A. Brown, Dept. of Environmental Sciences, Univ. of Lancaster, Lancaster LA1 4YQ, U.K.; E.M. Parmentier and J.W. Head, Dept. of Geological Sciences, Brown Univ., Providence, RI 02912

For large parts of the surfaces of the Galilean satellites there is no stereoscopic high-resolution imagery, and so for shadow-free regions far from the terminator, the only method of obtaining topographic information is photoclinometry, the technique of converting brightness variations into local surface tilts and hence into topographic profiles and contour maps {1-3}.

The conversion from brightness changes to slopes requires knowledge of the angular photometric function for the type of planetary surface terrain being analyzed, i.e. the relationship describing the brightness of the surface as a function of the angles of incidence (I) and emergence (E) of light at a surface element. Theoretical analyses {e.g. ref. 4} show that the expected form of the function is approximately

$$B = B_0 \left(\frac{\cos I}{\cos I + \cos E} \right) F(G)$$

where B_0 essentially represents the normal albedo of the surface and F(G) is a function of the phase angle (G, the angle measured at the surface element between the incident and emergent light rays). Within any one spacecraft image of a planetary surface, G (and hence F(G)) is very nearly constant and so brightness variations are almost entirely dictated by the middle term in the equation, the so-called Lommel-Seeliger function. This approximation has been used by Squyres {5} to produce some terrain profiles on Ganymede.

Recently, Hapke {6,7} has developed a more detailed theoretical model of planetary light-scattering which shows that, even when G remains constant within the area of interest, the above equation in general requires considerable modification. The angles I and E are replaced by (I+I') and (E+E'), respectively, where I' and E' are functions of the mean macroscopic slope, S, caused by the roughness of the terrain. F(G) is modified to include an explicit dependence on (I+I') and (E+E') as well as G and there are also other multiplicative terms in the equation.

In order to investigate the effects of these changes on the shapes of topographic profiles deduced from the functions, we have analyzed an area of grooved terrain (lines 500-505, samples 550-650 on frame 20640.27 0060J2) using wide ranges of values of all the adjustable parameters in Hapke's new photometric function {7}. As expected, the dependence is mainly on the macroscopic slope S; very wide variations in the other parameters yield only up to 5% variation in the heights and depths deduced for surface features. Table 1 illustrates the relationships between deduced topography and the value assumed for S: the reference "height" in the Table is the height of an isolated hill or the depth of an isolated crater which would have been deduced using the simple Lommel-Seeliger function. The spread of height values as S varies shows that it

is unlikely that errors in relative heights and local slopes will be greater than 15% no matter what value is adopted for S.

The above remarks apply to the frame analyzed and also to other frames in which the illumination and viewing geometry are fairly simple. However, when areas are illuminated and viewed very obliquely, and when the planes containing the incident and emergent rays are far apart, the deduced topography becomes more sensitive to the correct choice of S and, indeed, to the functional form of the photometric equation. We are currently investigating these effects on other Voyager frames in an attempt to identify the best-fit set of parameters of the equations which apply to each terrain type on the Galilean satellites.

References: {1} K. Watson, U.S.G.S. Prof. Paper 599-B, 10 pp, 1968; {2} B. Hapke et al., JGR, 80, 2431, 1975; {3} P.J. Mouginis-Mark and L. Wilson, Computers & Geosci., 7, 35, 1981; {4} B. Hapke, Astron. J., 71, 333, 1966; {5} S. Squyres, NASA TM-84412, 365, 1981; {6} B. Hapke, JGR 86, 3039, 1981; {7} B. Hapke, JGR, 87, in press, 1982.

Table 1.

Mean macroscopic slope, S (degrees)	Height of feature (arbitrary units)	Comments
7.5	100	Value which would be found using simple Lommel-Seeliger function
0	116	As S increases, deduced height decreases at first
10	93	
20	86	
40	92	For (improbably large?) values of S >about 25° height increases again as S increases

Topography on Ganymede Derived from Photoclinometry

Michael C. Malin, Department of Geology, Arizona State University, Tempe, AZ 85287
G. E. Danielson, Division of Geological and Planetary Sciences, California Institute of Technology, Pasadena, CA 91125

Introduction

A fundamental limitation in the quantitative analysis of planetary geomorphology and structural geology results from the absense of topographic data. Among the studies that might be addressed, were such data available, are volumetric and slope relationships of ionian volcanics, fracture and annealing processes in icy crusts on Europa and Ganymede, and evaluation of viscous relaxation as a means of degrading landforms on Europa, Ganymede, and Callisto. The intent of this work has been to develop and apply a technique for acquiring topographic data on the galilean satellites using photoclinometry.

Technique

Photoclinometry is a technique for determing slopes on the basis of brightness variations that result from changes in declivity, illumination, and viewing angles. It has had a long and checkered application to planetary problems, applied with less than total confidence owing to poor camera calibration and the stong interference effects of albedo (see e.g., 1, 2, 3). The Voyager cameras are photometrically well behaved and understood, with conservative estimates of relative precision (that measure used in photoclinometric studies) of better than 3%. By selecting areas of relatively uniform albedo, photoclinometry can, in theory, be used with modest potential for success (4).

One failing of topographic analysis by photoclinometric techniques is the uncertainty of slope azimuth, which prevents true, analytical, planimetric solutions. All photometric techniques integrate the along-sun component of slope. The cross-sun component cannot be computed directly, but must be estimated by statistical (5) or heursitic averaging techniques.

Our procedure uses C-matrices (6) for specific Voyager frames to compute viewing and illumination geometry values and planetocentric coordinates for every pixel in the frame (referenced to an oblate spheroid or tri-axial ellipsoid, depending on body). The frame is then geometrically transformed to a solar illumination coordinate system. After a reference slope is specified, the transformed image is integrated line by line, each line compared with its adjacent neighbors for deviations from systematic, topographic trends. If such deviations exceed a specified tolerance, a more complicated neighbor search determines if the trend has changed, or if there is an anomaly in the given line. If the latter, the line is forced to match its neighbors. Thus, a two dimensional portrayal of relief is developed by a heuristic averaging technique. The spacial and vertical resolution of these data will be somewhat less than the ori-

ginal (<<10%). After integration, the relief image is transformed back to planetary spacial coordinates.

Results

Figures 1 and 2 show several examples of landforms on Ganymede, including craters of different sizes and morphology, and grooves. Horizontal resolution in these 'wire-mesh' presentations is about 1 km per grid, and they are shown without vertical exaggeration. Shaded relief presentations of the topographic data have been compared to actual images of the same features in order to determine the accuracy of the topography. The results of these comparisons are extremely encouraging—the correlation is high and suggests that the derived topography is truely representative of the actual relief.

The topographic data now in hand is being used to develop, among other things, an improved picture of depth/diameter relationships on Ganymede as a function of terrain type, crater 'age', etc. They are also acting as input and test constraints in numerical models of geophysical processes. Although presently limited to areas of uniform albedo, we are attempting to incorporate color/albdeo discrimination into our software (e.g., 7). This will open even larger applications of photoclinometry to planetary surfaces.

References

1) Leighton, R. B. (1966) Sci. Amer. 214, 54-66.
2) Watson, K. L. (1968) U. S, Geol. Survey Prof. Paper 599B, B1-B10.
3) Wildey, R. L. (1975) Icarus 75, 613-626.
4) Passey, Q. (1982) Ph.D. dissertation, California Institute of Technology, Pasadena, CA 91126.
5) Wildey, R. L. (1983) Science (in press).
6) Davies, M. L. and F. Y. Katayama (1981) J. Geophys. Res. 86, 8635-8657.
7) Eliason, P. T., L. A. Soderblom, and P. S. Chavez (1981) Photogramm. Eng. Rem. Sensing 48, 1571-1579.

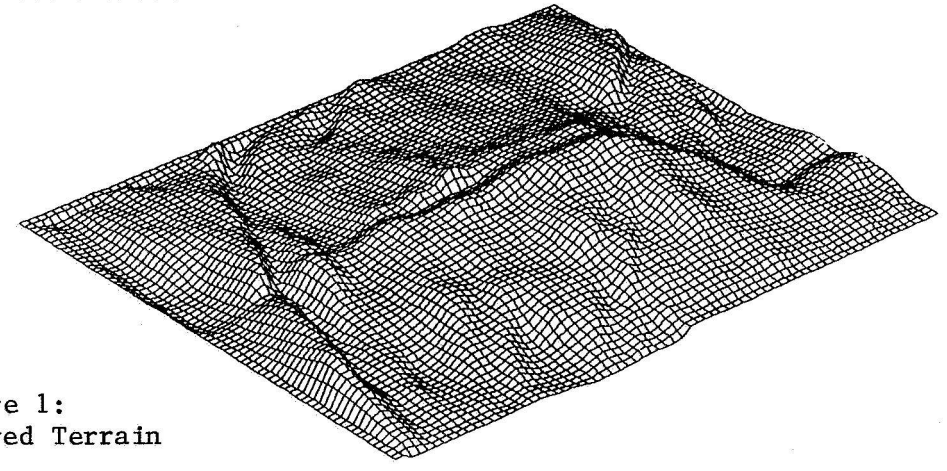

Figure 1:
Grooved Terrain

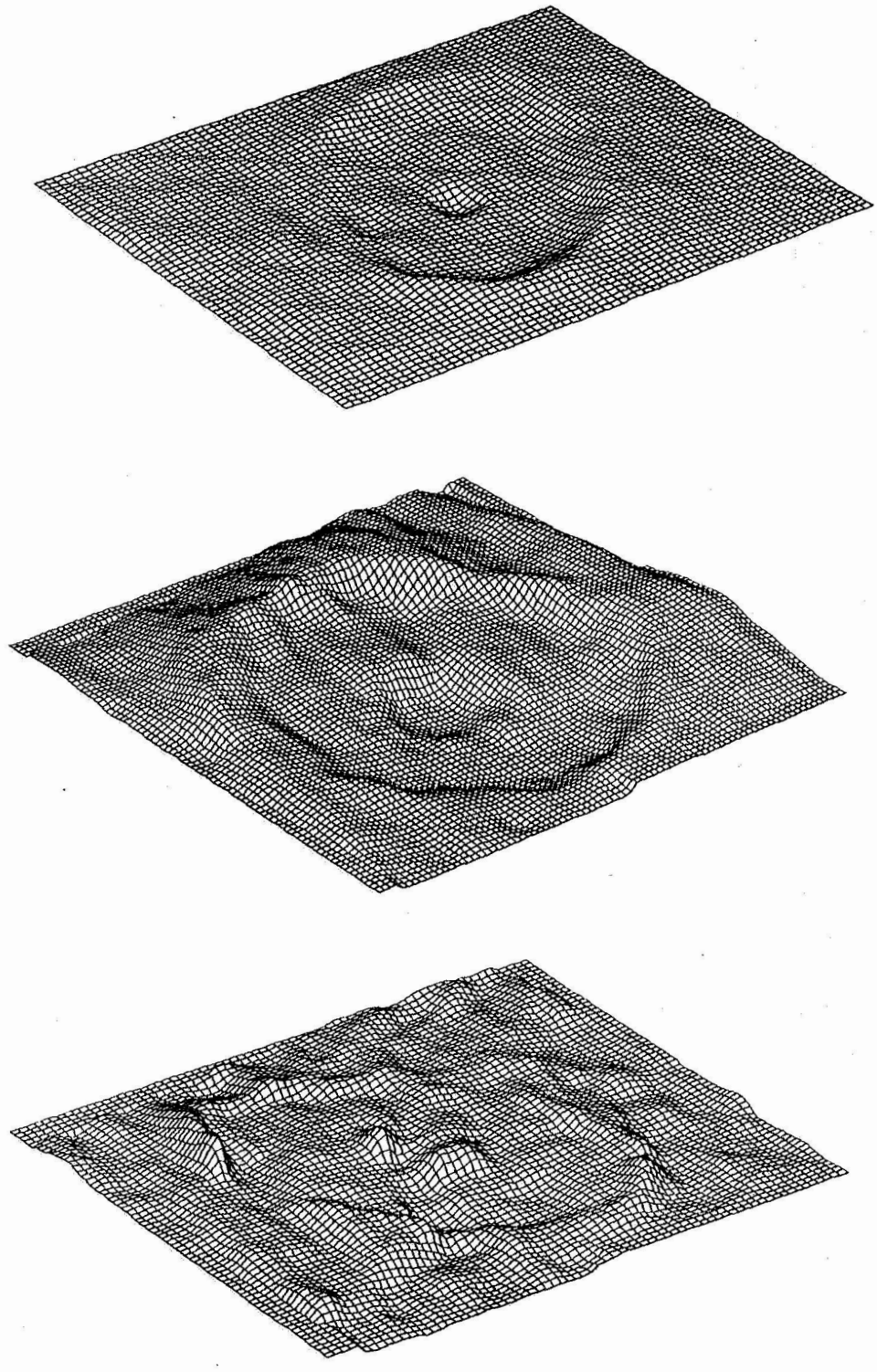

Figure 2: Impact Craters

D12

N84 23443

NEW MODELS FOR LANDFORM EVOLUTION ON IO

Peter J. Mouginis-Mark[1], James L. Whitford-Stark[2] and James W. Head[3].
1. Planetary Geosciences Division, Hawaii Institute of Geophysics, Univ. of Hawaii, Honolulu HI 96822. 2. Geology Department, Sul Ross State Univ., Alpine TX 79832. 3. Department of Geological Sciences, Brown Univ., Providence RI 02912.

As part of the Galilean Satellites Mappers Program, we have been studying the South Polar region of Io. Our examination of the Voyager images has led us to reassess the possible mechanisms by which certain units were created or modified in this area. Specifically, our analyses have focused on determining the relative age of the mountain material and on the process by which the layered plains material was eroded.

Both the mountain material and the eroded plains material appear to be preferentially located toward higher southern latitudes, but some examples of mountains can be found in equatorial regions[1]. Schaber[1] interpreted the mountain material to be the oldest recognizable unit on Io, and characterized it as a tectonically-disrupted, rugged surface with about 9 km of relief. The mechanism by which the layered plains are eroded has been attributed to the collapse of this unit due to the removal of volatile materials from the upper layers [1,2]. Bright fumarole deposits along the boundary scarps of the layered plains unit are thought to be associated with pit craters that are formed during this volatile outgassing.

The age of mountain material: Mountain material is frequently associated with plains units, particularly the layered plains. Although previous interpretations assign an old relative age to the mountain material[1], it is extremely difficult to distinguish between overlap and superposition relationships on the basis of photogeologic criteria. This difficulty appears to be particularly evident where downslope movement has caused topographically higher mountain material to overlie the plains unit[3]. Our mapping has identified several attributes of the mountain material which suggest that it is younger than the surrounding plains:

1) There is little, if any, apparent change in scarp height where layered plains intersect mountain material. In certain cases, one part of the mountain has been removed by erosion to show that parts of the layered plains continue beneath the mountain (e.g. FDS 16391.18 and 16391.28).
2) Mountain material is morphologically similar to the material around active source regions of large plumes such as Pele (FDS 16391.30). It is therefore possible that mountain material could have been seen by Voyager to be in the process of formation.
3) A close association between mountain material and recent volcanism is suggested by bright haloes around several massifs; craters or crater chains are sometimes well preserved in these massifs (FDS 16391.18).
4) The edges of mountain material are frequently lobate in outline and give the appearance of emplacement by surface flow. This hypothesis is further supported by the absence of any scarp between the mountains and the adjacent plains; in nearly all cases the edge of the mountain is a shallow slope, rather than an escarpment (FDS 16391.28).

On the basis of these observations, we feel that the mountain material on Io could be much younger than previously believed, and that rather than being either nunataks or kipukas of older material rising through the younger

plains, mountains may actually be young volcanic constructs built upon the layered plains[3].

An erosion mechanism for the layered plains: Although we agree with previous investigators who feel that scarp retreat due to volatile loss is probably taking place at some localities on Io, we offer an alternative explanation for the mode of formation of the eroded layered plains. We prefer a model involving thermal erosion of the layered plains' surface by subsequent lava flows, rather than the devolatilization model currently in favor[1,2]. We base this new model on the following observations:

1) Erosion of the layered plains seems to remove only discrete layers. A comparison of layer thicknesses in eroded areas and adjacent non-eroded sections shows that individual layers are never only partially removed (FDS 16391.50). Were collapse to be due to the withdrawal of subsurface materials, we would expect to see parts of individual layers preserved rather than always complete layers.

2) Active venting at the base of escarpments bordering layered plains occurs at localities where no subsidence is recognizable in the images, suggesting that venting and erosion (or sapping) are not always linked.

3) The areas of eroded layered plains are quite limited in their extent. Morphologically similar material can be found on either side of such an eroded area, but this adjacent material has been totally unaffected by erosion.

4) Remnants of the eroded layered plains are frequently aligned (FDS 16391.50). The long axis of each remnant is often several times larger than the short axis, and several such remnants superficially resemble martian streamlined islands that have then been modified by scarp retreat.

5) If scarp retreat and/or sapping were the dominant erosional mechanism responsible for altering the layered plains, we would expect to find talus or unconsolidated intra-plains debris at the foot of some escarpments. No such material is observed.

We feel that these observations necessitate the consideration of an alternative mechanism for the erosion of the layered plains on Io. In our view, the alignment of the remnants of the eroded plains and their streamlined outlines suggest that the layered plains have been eroded by surface flow rather than by sapping and collapse. The spatially-restricted distribution of this material, the lack of talus, and the lack of down-cutting of the plains to a common base level could all be consistent with a form of thermal erosion due to lava flows. Such flows may have crossed the layered plains, eroded down to the local base level, and then drained away into nearby lowlands. The eroded segments of the layered plains would have been removed from the area along with these lava flows. Circumstantial evidence to support this model also exists in that no lava flows have been found that are preserved on layered plains material; in all areas the flows appear to have cut escarpments at the edge of a layered plains sequence.

References:

1) G.G.Schaber (1982) In: Satellites of Jupiter, Ed. David Morrison, Univ. of Arizona Press, p. 556-597.
2) J.F.McCauley, B.A.Smith and L.A.Soderblom (1979) Nature 280, 736-738.
3) J.L.Whitford-Stark (1982) Lunar Plan. Sci. XIII, 859-860.

D13

N84 23444

GEOLOGY OF DIONE J.B. Plescia, Jet Propulsion Laboratory, California Institute of Technology, Pasadena, CA 91109.

Dione is one of the most geologically complex of the saturnian satellites. Crater counts and surface morphology indicates the geologic units observed are of variable age and origin. In an attempt to understand the processes which have affected Dione, a geologic map was prepared (figure 1). Several geologic units have been identified; ancient heavily cratered terrain, two plains units: cratered plains and lightly cratered plains, lobate deposits, crater rim deposits and bright wispy material.

Craters were observed ranging in diameter from 200 km down to the limits of resolution (3 km/lp). All craters are simple in form and relatively well preserved. There are no large complex multiring structures as observed on Ganymede and Callisto or the terrestrial planets. Two populations of craters have been recognized on Dione. Population I is characterized by numerous large craters with a size-frequency distribution slope of -1.7. Population II is dominated by small craters, none larger than 30 km and a steep distribution slope, -2.5 to -3.0. While interiors were not well resolved several of the larger craters contain bright concentric rings within the rim suggestive of terraced walls. Craters whose interiors were well resolved all have central peaks, simple concial hills. Neither craters with central pits nor flat or bowl shaped interiors were observed. Craters with central peaks on Dione occur over the diameter range of $\leq$ 15 km to 175 km, while on Ganymede such crater occur in the size range of 5 - 30 km. The larger size range on Dione can be attributed to the lower surface gravity which produces lower stresses from central peaks thereby allowing the crust to support larger peak sizes relative to Ganymede. Only 1 bright rayed crater (Cassandra) and no dark rayed craters were observed. Several craters appear to have bright ejecta deposits surrounding their rims.

Structural features appear to be limited to the "chasma" and a subtle series of lineaments associated with the bright wispy material. The chasma range in width from 5-20 km. Some are straight and simple while others are complex sinuous features.

The heavily cratered terrain covers the largest fraction of the satellite. While mapped as a single unit it most likely is much more complex and heterogeneous than currently recognized. Crater frequencies are very high indicating that this surface dates to the period of heavy bombardment. This is the oldest unit on Dione.

Cratered plains and lightly cratered plains occur on the leading hemisphere between 30° and 60° longitude. Contacts between the plains units and with the heavily cratered terrain are sharp indicating that each is a distinct unit and that the plains overly the heavily cratered terrain. The plains are

characterized by smooth surfaces with topography being associated only with craters and the chasma. Albedo of the plains units is distinctly higher than for the cratered terrain. Additionally there is an albedo contrast between the plains units, the lightly crater plains (the younger of the two) being brighter. Crater frequencies suggest the two plains units are slightly different in age and that both are younger than the heavily cratered terrain.

A unit with a surface morphology suggestive of fluidized origin occurs near 45° S, 60° W has been termed the lobate deposits. The surface of this unit is mottled with a series of northeast trending low ridges and shallow troughs. Parallel to and along the intricate margin of the deposit is a low ridge. Morphologic aspects of this unit resemble those of the ejecta deposits of the Martian rampart craters. Orientation of surface features suggests flowage from southwest to northeast. The suspected source region to the southwest was not imaged and so the unit's origin remains obscure. Crater frequencies on the unit are the lowest of any, making the lobate deposits the youngest surface.

Deposits of bright wispy material form the largest scale features on the satellite. Lane of the material radiate from a bright region on the trailing hemisphere and extend > 1000 km into the leading hemisphere. No topography or subduing of surface features is observed which suggests that deposit is relatively thin. Chasma or subtle lineaments occur with the bright wisphy material where it is observed in high resolution images. It is suggested that the bright material represents a volcanic deposit explosively erupted from the chasma or lineaments.

Crater rim deposits are associated with only a few craters. Generally these deposits are brighter than the unit on which they lie. Following an impact the low surface gravity of Dione apparently allows the ejected debris to be dispersed over a wide area rather than in a coherent blanket around the crater.

Dione has evolved to some extent behond its accretionary form. Wide areas of smooth plains with variable crater frequency indicate the resurfacing activity was prolonged and widespread. The morphology of the young units suggest they were formed by some type of volcanic process. The material may have been erupted in a fluidized state and then flowed across the surface or it may have been explosively erupted falling back to the surface in a snow-like form. From the indications of prolonged endogenic activity it can be infered that the composition of Dione is more complicated that water ice and silicates Additionally the presence of low melting temperature clathrates is strongly indicated.

This research was carried out at J.P.L. and sponsored by N.A.S.A.

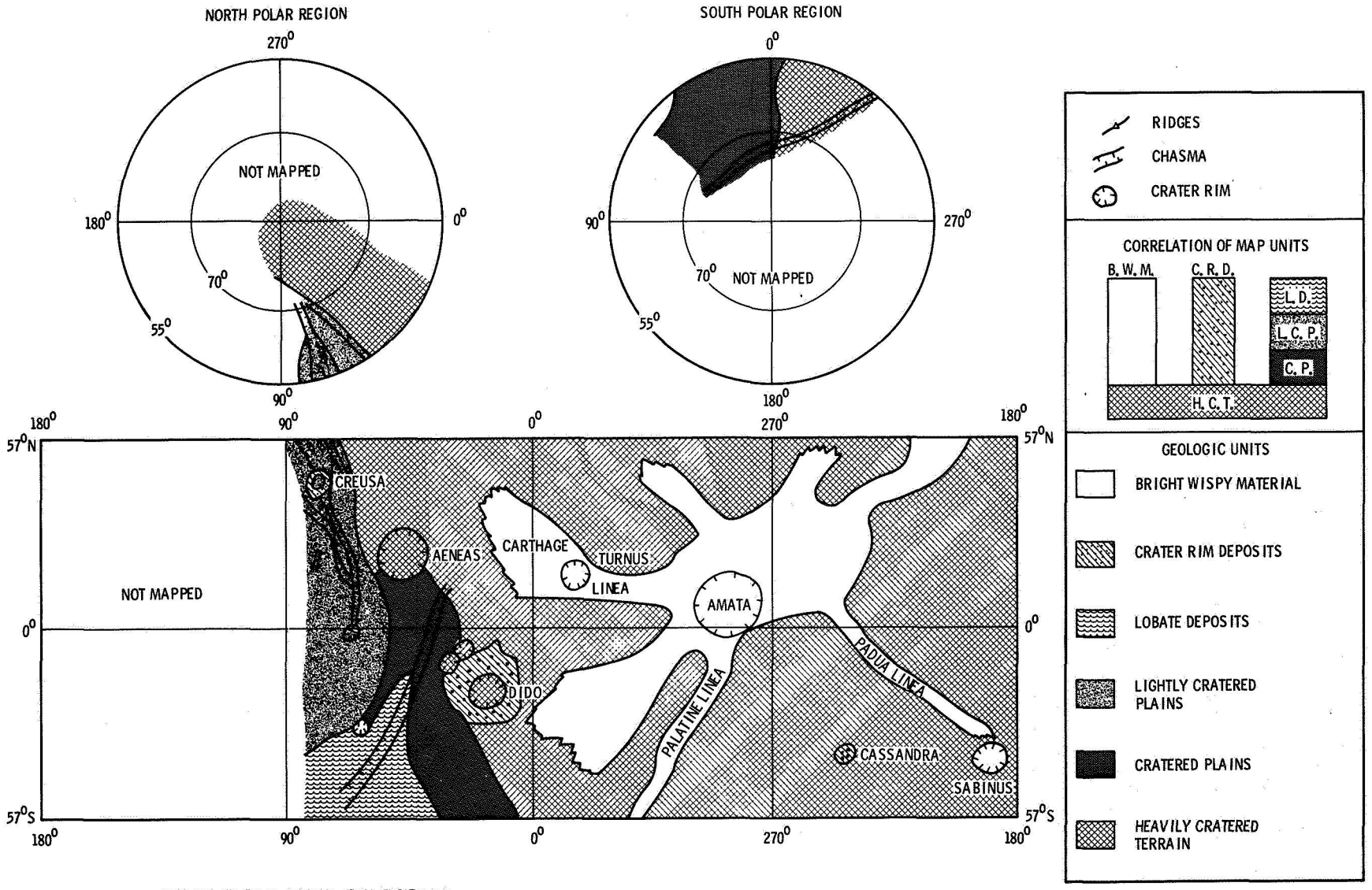

GEOLOGIC MAP OF DIONE

N84 23445

D14 ABSTRACT ONLY

EVOLUTION OF THE URANUS-NEPTUNE PLANETESIMAL SWARM: CONSEQUENCES FOR THE EARTH

Eugene M. Shoemaker and Ruth F. Wolfe, U.S. Geological Survey,Flagstaff, Arizona 86001

In our new Monte Carlo study undertaken to evaluate the evolution of planetesimals in the outer Solar System, both stellar and planetary encounters have been considered from the outset. About 20% of the Uranus-Neptune planetesimals (UNP's) enter the comet cloud and are stored primarily in the region inside the observational limits of the Oort cloud. Half of the comets have survived to the present time; the cloud now has a mass of the order of Jupiter's mass. Most UNP's are ejected from the Solar System, and about half of the planetesimal swarm is passed to the control of Jupiter prior to ejection. Jupiter's perturbations drive a large flux of these planetesimals into Earth-crossing orbits, and it now appears highly probable that UNP's account for most of the late heavy bombardment of the Moon and Earth. Assuming that only water bound in clay minerals (~10% by weight of the solid objects) survives ablation by solar heating, the amount of water delivered to the Earth on ablated UNP's accounts for the oceans. If the rocky fraction of UNP's is similar to Type I carbonaceous chondrites, the carbon budget of the Earth's crust also appears to be approximately accounted for. Many and probably most UNP's perturbed to Earth-crossing orbits disintegrated into meteor streams. A significant fraction of organic chemicals of probable interstellar origin in UNP meteoroids may have survived encounter with the Earth and been delivered to the UNP-derived primordial ocean.

D15

N84 23446

HIGH-RESOLUTION COLOR IMAGES OF IO Alfred S. McEwen and Laurence A. Soderblom, U. S. Geological Survey, Flagstaff, AZ.

Color versions of the highest resolution Voyager images of Io have been produced by combining the low-resolution color images with the high-resolution, clear-filter images. High-resolution versions of the orange-, blue-, and violet-filter images are produced by:

orange = high-res clear * [low-res orange / low-res clear]
blue = high-res clear * [low-res blue / low-res clear]
violet = high-res clear * [low-res violet / low-res clear]

The spectral responses of the high- and low-resolution clear filter images cancel, leaving the color, while the spatial frequencies of the two low resolution images cancel, leaving the high resolution.

Two sets of resolution-enhanced color mosaics have been produced. The first set consists of point-perspective images, without geometric transformation into a map projection. High-resolution, clear-filter images from the narrow-angle camera were combined with the low-resolution, wide-angle camera images which were shuttered nearly simultaneously with the narrow-angle camera. Some of the wide-angle images are partly saturated from overexposure, but when images in three of the four filters needed are good, the fourth has been approximated from the others using the relation: 3 * clear = orange + blue + violet.

A second set of enhanced-resolution color mosaics has been produced in Mercator projection. A photometric normalization has been applied using the limb-darkening corrections described in [1], and a phase correction consisting of the measured-disk integrated phase function of Io [2] divided by the integration of the limb-darkening function. The resulting phase corrections (C), as a function of phase angle (α), are closely approximated by:

$$C(\alpha\ 3°\text{-}10°) = 1.00 + 0.047\alpha - 0.00198\alpha^2$$
$$C(\alpha\ 10°\text{-}50°) = 1.09 + 0.02\alpha - 0.00018\alpha^2$$

These mosaics cover the entire region of Io from latitudes -60° to 60°N and longitudes 240° to 45°W.

Each image combines the best resolution with the color data into a single image, resulting in greater geologic interpretability. All of the final images will be distributed to the regional planetary data facilities, where they will be available to the planetary science community.

References

[1] McEwen, A.S., and Soderblom, L.A., Multi-image photometric solutions for the Galilean satellites (abs): Reports of Planetary Geology Program, this volume, 1983.
[2] Simonelli, D., and Veverka, J., Voyager surface and disk-integrated photometry of Io (abs): Reports of Planetary Geology Program, 9-11, 1982.

D16

SHORT TIME-SCALE SURFACE CHANGES ON IO

Richard J. Terrile, Jet Propulsion Laboratory, California Institute of Technology, Pasadena, CA 91109.

Imaging data from the Voyager 1 and 2 encounters with the Jupiter system provide a data set for the examination of short time-scale variations of surface features on Io. Clear evidence exists for variations near the known eruption sites (Strom et al. 1982) and for other areas which appeared to have erupted between the encounters (McEwen and Soderblom, 1983). In this study we examine regions outside the known active eruption sites in order to look for variations in the surface scattering properties which may be due to undetected small-scale volcanic activity. The phase functions of many areas are intercompared in order to look for regions with phase functions outside the normal range for satellite surface properties. Areas with unusual scattering properties may be related to small-scale eruptions of gas or particles. Determination of the distribution of these areas will have strong implications for the resurfacing rates for Io.

For this analysis we used the region just south-east of the edge of the ejecta deposit surrounding Mafuike Patera (plume Pele). This area was choosen because it was imaged in four colors and at several times over a 10 hour period by Voyager 1. These images show areas where relative contrast changes occur in data recorded close together in time and at similar resolutions. These photometric effects must be due to local effects and not by material ejected from Pele. These areas are located well outside the ejecta envelopes of any known eruption sites. Images were geometrically scaled and photometrically calibrated in order to allow a pixel by pixel comparison of features. Photometric measurements were made of several terrain types and for features with and without relative contrast changes. In general, most features show a phase function in which brightness increases with decreasing phase angle and have uniform slopes in the orange, blue and violet filters. These slopes are similar to those measured by Clancy and Danielson (1982) for generalized colored regions on Io. However, several regions were found with opposite slopes (limb brightening) and with a strong color dependence to the phase function. This kind of photometric behavior falls outside the envelope of scattering phase functions observed on the other Galilean satellite surfaces and for any reasonable model for surface scattering. Scattering from locally erupted gas or dust in one or more of the images may account for these peculiar photometric properties. Further work on modeling the observed phase functions will be done in order to better characterize the scattering and to estimate the amounts of locally erupted materials needed.

References:

Clancy, T. R. and Danielson, G. E. (1982) "High Resolution Albebo Measurements of Io From Voyager 1." J. Geophys. Res., 86, 8627.

McEwen, A. S. and Soderblom, L. A. (1983) "Two Classes of Volcanic Plumes on Io." Icarus, 55, 191.

Strom, R. G., Schneider, N. M., Terrile, R. J., Cook, A. F. and Hansen, C. (1982) "Volcanic Eruptions on Io" J. Geophys. Res., 86, 8593.

D17

N84 23448

GEOLOGIC STUDIES OF OUTER SOLAR SYSTEM SATELLITES: IAPETUS AND EUROPA

S.W. Squyres and R.T. Reynolds, NASA Ames Research Center, Moffett Field, CA 94035

A number of models have been formulated to describe regolith evolution on airless bodies (1,2). Such models have to date not included the effects of a strongly asymmetric impact flux across the body, as exists for many synchronously rotating satellites. We are developing a model of regolith evolution on bodies subjected to an asymmetric impact flux. The general effect of an asymmetric impact flux is ballistic diffusion of regolith from areas of high impact flux to areas of lower flux. The effect is most pronounced on low gravity bodies where ejecta travel distances are large, and on bodies with strong flux asymmetries. It may be especially important on Iapetus, where retrograde debris from Phoebe striking the leading hemisphere may produce a flux asymmetry as large as 100:1 from apex to antapex (3).

Consider a point on a synchronously rotating satellite with latitude Θ and longitude Φ. Let J be a function that gives the mass flux of meteoritic material striking the surface at any point. In the simplest case, J will be largest at the apex of orbital motion, and smallest at the antapex. Call f the ratio of the mass of ejecta generated during an impact event to the mass of the projectile. The rate of removal of material from a surface element at (Θ,Φ) by impact ejection is therefore $fJ(\Theta,\Phi)$. Now, call α the angular distance along the surface from an impact point. There is a function $F(\alpha)$ that describes the mass distribution of ejecta produced by an impact. It is largest immediately adjacent to the point of impact, and decreases with increasing angular distance away from the impact point (i.e., with imcreasing α). The net erosion or deposition rate at any point on the satellite's surface may then be calculated by summing the removal rate due to ejection with the rate at which material is deposited from impacts on all other parts of the satellite:

$$dM/dt(\Theta,\Phi) = -fJ(\Theta,\Phi) + fR^2\int_0^{\pi}\int_0^{2\pi}F(\alpha)J(\alpha,\xi)\sin\alpha\, d\xi\, d\alpha. \quad (1)$$

In this expression, R is the radius of the satellite, and ξ is the azimuth from the point under consideration. If $J(\Theta,\Phi)$ and $F(\alpha)$ are known, then the erosion and deposition rates can be calculated as a function of position on any object.

To date, we have performed solutions of equation (1) for axisymmetric impact flux distributions, using a very simple form of $F(\alpha)$ based on the experimental work of Gault and Heitowit (4). We find that the net amount of material transported by ballistic diffusion is inversely proportional to satellite density, but that the dependence on radius is more complex. For very large satellites the effect is small, because the large gravity results in most ejecta travelling only small angular distances. With decreasing radius, the effect becomes more pronounced. For very small satellites

($R < 25$ km), however, there is net erosion over the entire body, as significant quantities of ejecta reach escape velocity. (We neglect capture of ejecta in planetary orbit and later sweeping-up by the satellite, although this process may be important on bodies such as Phobos and Deimos.) The amount of transport of course increases with increasing flux asymmetry. Preliminary calculations for some of the saturnian satellites suggest that erosion of a few meters to tens of meters over geologic time could be expected on the leading hemispheres of these bodies. Over the next year we will derive a more sophisticated expression for $F(\alpha)$ based on both theoretical and experimental considerations, and expand the calculation technique to consider more realistic non-axisymmetric impact flux variations.

We have recently begun to examine some of the consequences of our model for the interior of Europa (5) - that is, a thin ice crust underlain by a substantial ocean of liquid water. Theoretical calculations and Voyager observations support the view that tidal heating has been sufficient to maintain a liquid layer throughout the history of the satellite. First, we have evaluated the habitability of a europan ocean for terrestrial-type organisms, based on the assumption that the availability of biologically useful energy is the limiting factor. Photosynthetic, thermal, electrical, and chemical energy sources have been considered. The calculations suggest that there may be regions on Europa, very limited in space and time, with physical conditions that are within the range of adaptation of life on Earth (6).

Second, we have quantitatively explored the electrical currents within Europa that could be set up by motion through Jupiter's magnetic field. The possibilities for electrical effects on Europa are much higher than for Io due to Europa's higher electrical surface conductivity and lack of an appreciable conducting ionosphere. Calculations show, however, that for a thick ice crust the currents produced are still very small (less than 10^{-2} A m^{-2} for a few km of ice). For the time varying eddy current mode, even a substantial liquid subsurface layer will not yield significant electrical effects. For the transverse magnetic mode (unipolar generator), however, a very thin ice crust or a transient liquid surface could produce locally significant currents and electrical heating under certain special conditions (7).

We will continue to study the consequences of a liquid water ocean on Europa over the coming year. While there is some fairly convincing evidence that Europa has been recently resurfaced by eruptions of water vapor and condensation of frost on the surface (5), an actual eruption has not yet been definitely observed. We will construct a detailed hydrodynamic model of such an eruption to investigate its detectability by either Earth-based infrared observation or by the Galileo spacecraft.

REFERENCES

(1) Shoemaker, E.M., et al. (1970). Proc. Apollo 11 Lunar Sci. Conf., 2399.

(2) Housen, K.R., et al. (1981). Icarus 39, 317.

(3) Squyres, S.W., and Sagan, C. (1983). Nature 303, 782.

(4) Gault, D.E., and Heitowit, E.D. (1963). Proc. 6th Hypervel. Impact Symp., 419.

(5) Squyres, S.W., et al. (1983). Nature 301, 255.

(6) Reynolds, R.T., et al., Icarus, in press.

(7) Colburn, D.S., and Reynolds, R.T., Icarus, submitted.

Chapter 2

ASTEROIDS AND COMETS

D18

THE PLANET CROSSING ASTEROID SURVEY -- PROGRESS IN THE ANALYSIS OF POPULATIONS AND TERRESTRIAL-PLANET CRATERING RATES

Eleanor F. Helin and R. Scott Dunbar,
Jet Propulsion Laboratory

The Planet-Crossing Asteroid Survey (PCAS), now in its eleventh year, was initiated with the aim of expanding the database of known near-Earth asteroids for the purposes of a statistical evaluation of their total population and their relation to the lunar and terrestrial cratering record. The discoveries from this continuing photographic survey have refined the estimates of the populations of crater-forming bodies which have impacted the Earth and Moon and also the other terrestrial planets over geologic time. Studies of the dynamics of these bodies show that their orbits change significantly over time, causing some objects not presently in planet-crossing orbits to become so periodically, and thus subject to collisions. Hence we must consider not only those asteroids which intersect the orbits of the terrestrial planets, but also those which are in pre-crossing states, in those regions of the asteroid belt which may be sources of planet-crossing asteroids and meteorites. The Hungaria, Phocaea, and Flora regions of the proper orbit element phase space are of particular interest, as they lie in the neighborhood of three important secular resonances. The resonances, first studied in detail by Williams (1969), drive large oscillations in the orbital eccentricity and inclination, and are viewed as a plausible dynamical mechanism for the transport of main-belt asteroidal material to the inner solar system. These source regions are particularly important, as the planet-crossing asteroid population is necesssarily short-lived; the population must be replenished continually to maintain the observed numbers of existing objects.

At present, 4 Atens, 32 Apollos, 36 Amors, and over 100 Mars-crossing asteroids are known, with about half of the Amors considered to be periodically Earth-crossing under the influence of secular perturbations. More than half of the planet-crossers of these types discovered in the last ten years are due to our systematic survey program. Population estimates derived from these observed numbers remain consistent with those previously published [Helin and Shoemaker (1979), Wetherill and Shoemaker (1982), Helin (1982)]. In the last five years the number of planet-crossing and pre-crossing objects discovered by the PCAS program has tripled overall, with higher increases in the numbers of Amors, Mars-crossing, Phocaea, Hungaria, and Flora-type objects. This leads naturally to a refinement of the uncertainties in the populations, though by the very nature of this work the build-up of statistics sufficient to significantly improve the population estimates and related uncertainties is a continuous and long-term effort. There have been a number of independent rediscoveries of known objects in the past five years, and simultaneously a somewhat higher discovery rate of new objects. These

offsetting effects, while probably purely due to the statistics of small numbers, are presently under study to determine what net effect, if any, they have on the estimated populations and the corresponding crater rates.

The survey program is fundamental to the entire process of calculating the asteroid populations and terrestrial planet cratering rates, for without a broader knowledge of the numbers and orbits of planet-crossing asteroids no meaningful conclusions can be reached. While the present data base is still small, it has been greatly expanded over its status ten years ago. However, though the numbers and orbits of these asteroids, analyzed in the context of a controlled systematic search, are essential at the outset of any attempt to characterize populations and collision probabilities, the refinement of the estimates depends on other types of observations as well. Precise definition of the magnitude-frequency distribution for each class of planet-crossing and pre-crossing objects, a necessary element in the calculation of cratering rates, awaits a more comprehensive set of statistics on the surface spectral reflectances and albedos, obtainable from photoelectric photometry and radiometry, from which the diameters of the asteroids may be calculated and their bulk compositions may be inferred. These physical observations necessarily lag the survey and discovery work by a few years, mainly because of the need for astrometric observations to determine well-defined orbits. In lieu of these observations, we are beginning a program of photographic photometry of the asteroids discovered in the course of the UK-Caltech Asteroid Survey (UCAS). From this data we hope to infer rough albedo statistics from the study of the phase functions of the nearly 1000 asteroids from that program, thus improving the magnitude-frequency distributions significantly. This program is to be carried out over the next six to eight months.

The discoveries of new asteroids from the PCAS have added to the knowledge of the distribution of orbits of planet-crossing and pre-crossing objects, occasionally offering tantalizing evidence as to the dynamical mechanisms which transport these objects into the neighborhood of the terrestrial planets. Among the recent discoveries from the PCAS, which include an Apollo, three Amors, and a Hungaria (see table below), the deep Mars-crosser 1983 PA is a very interesting object. Its orbit has characteristics of both Phocaea-type and Hungaria-type asteroids, and yet it has the fourth smallest perihelion distance (1.45 AU) among the known Mars-crossing asteroids. This is strongly suggestive of an asteroid in the process of orbital evolution under the influence of nearby secular resonances, caught between the main-belt source region and the initial planet-crossing state.

RECENT PLANET-CROSSING ASTEROID DISCOVERIES

	a (AU)	e	i (deg)	q (AU)	Type
1983 LC	2.63	0.71	1.5	0.77	Apollo
1983 LB	2.31	0.48	25.0	1.19	Amor
1983 RB	2.14	0.49	18.0	1.09	Amor
1983 RD	2.04	0.47	9.3	1.07	Amor
1983 PA	2.23	0.35	19.1	1.45	Mars-crosser
1983 LD	1.95	0.04	19.1	1.75	Hungaria

In summary, the Planet-Crossing Asteroid Survey is making steady progress toward the accumulation of the data required to make improved estimates of the populations and cratering rates which can be compared with the existing record of impact events. The PCAS has been the chief source of new objects on which to base these calculations over the past decade, and as such is an integral part of the continuing refinement of the estimates used in planetological applications. An adjunct effort to determine albedo statistics from photometry of UCAS plates is being pursued as well, to better define the magnitude-frequency distributions of asteroids. This will improve the quality of the population and collision probability calculations. Finally, the survey effort continues to discover new asteroids whose orbital characteristics may reveal the origin and evolution mechanisms reponsible for the transport of the planet-crossing asteroids to the inner solar system, which underlies the whole problem we have attempted to address.

REFERENCES

Williams, J. G. (1969) "Secular Resonances in the Solar System", Ph.D. dissertation, UCLA.

Helin, E. F. and Shoemaker, E. M. (1979) "The Palomar Planet-Crossing Asteroid Survey, 1973-1978", Icarus, V. 40, pp. 321-328.

Wetherill, G. W. and Shoemaker, E. M. (1982) "Collision of astronomically observable bodies with the Earth", Geological Society of America, Special Paper 190.

Helin, E. F. (1982) "Earth-Crossing Asteroids: New Discoveries", Sun and Planetary System, ed. W. Fricke and G. Teleki, D. Reidel Pub. Co.

D19 N84 23450

SURVEY FOR MARS-CROSSING ASTEROIDS, 1983

Shoemaker, E. M., U. S. Geological Survey, Flagstaff, AZ, and
Shoemaker, C. S., California Institute of Technology, Pasadena, CA

More than 35 asteroids and one long period comet were discovered in the past year, in the course of a survey for Mars-crossing asteroids conducted by us with the Palomar 46-cm Schmidt camera. Among these objects, at least six are Mars-crossing asteroids: 1982 RA and 1983 RB are Earth-approaching Amor asteroids that pass deep inside the orbit of Mars; 1982 VB, 1983 AF2, 1983 AG2 and 1983 EA1 are also fairly strong Mars crossers with osculating perihelion distances in the range 1.538 to 1.686 AU. These latter Mars crossers all have orbits with relatively high inclinations and occupy the Hungaria or Phocaea regions of orbital element phase space. One object, 1982 VB, has been linked with 1981 KE, initially discovered by A. Mrkos at Kleť. The new Mars crossers range in diameter from about one to ten kilometers.

A very unusual ~60 km diameter asteroid, discovered by C. S. Shoemaker in January 1983, has now been assigned number 2906 and has been named Caltech. This object, which probably is among the 300 largest minor planets, has a semimajor axis of 3.156 AU and an inclination of 30°.74. It has only one known relatively near neighbor in orbital element phase space. Instead of precessing under the influence of planetary perturbations in normal fashion, the argument of perihelion of 2906 Caltech librates around a fixed value in the same manner as the highly inclined distant asteroid 1373 Cincinnati [1]. Discovery of this relatively large body so late in the history of asteroid search can be attributed to the fact that it is seldom observed near the ecliptic.

Comet Shoemaker (1983p) is a long period comet on a retrograde orbit, with a perihelion distance of about 3.3 AU. It is relatively bright, for a comet of large heliocentric distance, and has an estimated absolute visual magnitude of about 4.

Reference

[1] Kozai, Yoshihide, Astron. J., 67, 591-598, 1962.

N84 23451

D20

COMETARY NUCLEUS AND ACTIVE REGIONS

Fred L. Whipple - Smithsonian Astrophysical Observatory,
60 Garden Street, Cambridge, MA 02138

On the basis of the icy conglomerate model of cometary nuclei various observations demonstrate the "spotted" nature of many or most nuclei, i.e., regions of unusual activity, either high or low. Rotation periods, spin axes and even precession of the axes have been determined. The observational evidence for variations in activity over the surfaces of cometary nuclei includes at least five different effects:

a) Periodic "parabolic" envelopes in the coma (C/Donati, for example);
b) Activity centers that move on P/Schwassmann-Wachmann I, observed as asymmetric comas;
c) Periodicity in halo diameters of the coma in many comets;
d) Unusual light curves (P/Encke, for example);
e) Jets, rays, fans, streams, etc., of the inner coma, sometimes associated with effects in both the dust and ion tails.

SUMMARY OF EVIDENCE CONCERNING FINE-DUST EJECTION

1) The narrowness of many jets for P/Swift-Tuttle, 1862 III (P/ST), requires both that the dust emission areas be small and that they be imbedded in larger areas of equal or greater activity. Occasional wide fans and halos demonstrate the phenomena when the latter condition is not satisfied.
2) Sekanina's gas production rate derived from the jets to raise the fine dust is much less than the average expected for a comet in P/ST's brightness class, suggesting that the average production rate around the dust sources is greater than that within the sources.
3) The dust production rate calculated by Sekanina from the dust sources is smaller than expected from areas of average dust/gas ratios for other similar comets. This may imply an overload of dust to ices in the dusty zones.
4) The gas production rate in 2) above appears inadequate to raise the larger Perseid meteoroids.
5) The variation of activity of the dust sources with zenith distance of the noon-day Sun, as $(\cos)^{2.4}$, is larger than expected for ordinary active areas on comets.
6) Dusty comets show smaller NG accelerations than less dusty comets of comparable intrinsic brightness.
7) Dusty comets tend to fade more rapidly at great solar distances than less dusty comets.

The general behavior of the micron dust jet emissions as described above suggests that they arise from localized regions of somewhat less volatile materials than broader active regions around them. If this is true I visualize them as resembling exposed geological dikes, tilted strata exposed above the surrounding areas. Sublimation of non-uniform materials would produce grotesque formations with overhanging ledges, mushroom tops and extremely slender towers. The irregular wasting of such features would expose surfaces for sublimation on successive comets days.

The totality of this evidence suggests that during the formation of comets there was a considerable period of time over a considerable region of space during which micron-sized dust accreted in relatively thick layers on many comets of all sizes. The thickness of the layers was the order of at least tens of meters, the dust being accumulated along with ices of only moderate volatility. The expected volatility depends directly upon the unknown loading factor of the dust/gas ratio, which may be high.

The author is indebted to the National Aeronautics and Space Administration's division of Planetary Geology for support of this research and to the Smithsonian Institution for travel support to the Budapest conference. Discussions with Zdenek Sekanina have been extremely valuable.

COMET IRAS-ARAKI-ALCOCK (1983d) - An Intimate Study

F.L. Whipple and R.E. Schild - Smithsonian Astrophysical Observatory, 60 Garden Street, Cambridge, MA 02138

On June 11 this comet approached the Earth to a distance of 0.031 AU, the nearest since C/Lexell, 1770 I, providing a unique opportunity for near-nucleus observations. Numerous images with a resolving power down to $\sim$ 20 km were obtained with the CCD photometer on the 24-inch reflector at the Whipple Observatory. Preliminary analysis of these images establishes the spin axis of the nucleus, with an obliquity to the orbit plane of approximately 50°, and a lag angle of sublimation approximately 35° from the solar meridian on the nucleus. The rotation is retrograde. The large lag angle suggests a moderately short spin period, confirmed provisionally as $8^{h}\ 42^{m}.5$ from visual observations of diameters by J.E. Bortle, D.W.E. Green and C.S. Morris. Asymmetries of the inner coma suggests a "crazy-quilt" distribution of ices with differing volatility over the surface of the nucleus. Further interpretations of the CCD data requires knowledge of the spectra as a function of radial distance from the nucleus and measures of asymmetries over a larger field. This research is partially funded by NASA Grant NSG 7082.

D21 ABSTRACT ONLY

COMET P/HOLMES, 1892 III - A Case of Duplicity?

Fred L. Whipple - Smithsonian Astrophysical Observatory,
60 Garden Street, Cambridge, MA 02138

The observations of Comet P/Holmes 1892 III, exhibiting two 8-10 magnitude bursts, have been carefully analyzed. The phenomena are consistent with the grazing encounter of a small satellite with the nucleus on November 4.6, 1892 and the final encounter on January 16.0, 1893. The grazing encounter produced, besides the first great burst, an active area on the nucleus, which was rotating retrograde with a period of 16.3hr and inclination nearly 180°. After the final encounter, the spin period was essentially unchanged, but two areas became active, separated some 164° in longitude on the nucleus. After the first burst the total magnitude fell less than two magnitudes from November 7 to November 30 (barely naked eye) while the nuclear region remained diffuse or complex, rarely if ever showing a stellar appearance. The fading was much more rapid after the second burst (barely naked eye at maximum), while the nucleus frequently appeared stellar after the first day. It seems reasonable to conclude that the grazing encounter distributed a volume of large chunks in the neighborhood of the nucleus, maintaining activity for weeks. The final encounter only activated a new area on the nucleus, the shock and fall back disturbing the area already exposed by the grazing encounter. More quantitative material is being prepared for publication. This research is funded by NASA Grant NSG 7082.

D22 N84 23453

A GENERALIZED BEHAVIORAL MODEL FOR ROTATING SHORT PERIOD COMETS WITH SPECTRAL ORBITAL ELEMENTS AND AXIAL ORIENTATION.

F.P. Fanale and J. R. Salvail, Planetary Geosciences Div., Hawaii Inst. of Geophysics, Univ. of Hawaii, Honolulu, HI.

A generalized model for short period comets is developed which integrates in a fairly rigorous manner the isolation history of regions on rotating comets with specified axial orientation and the complex feedback processes involving heat, gas and dust transport, dust mantle development and coma opacity. Attention is focused on development, reconfiguration and partial or complete launching of dust mantles and the reciprocal effects of these three processes on ice surface temperature and gas and dust production. In this model the dust mantle controls the H_2O flux not only by its effect on the temperature at the ice interface but (dominantly) by its dynamic stability which strongly influences vapor diffusivity. The model includes the effects of latitude, rotation and spin axis orientation, and is applied to an initially "homogeneous" sphere of H_2O ice and silicate using the orbital parameters of comet Encke. Numerous variations of the model, using combinations of grain size distribution, dust-to-ice ratio, latitude and spin axis orientation, are presented and discussed. Included also, for purposes of comparison with earlier studies, are some results for a similar nonrotating, constant sun orientation model.

It is found that initially homogeneous comets in typical short period orbits tend strongly to be cyclical, dust mantles tend to be very thin (< 1cm) at all orbital positions and all points on the comet for the range of "cannonical" grain size distributions and dust-to-ice ratios. Nevertheless, these thin mantles can exert a significant influence on cometary activity. We find that complex behavior, including gas and dust flux discontinuities or "flareups" can result for even a simple homogeneous comet because of episodic regional changes in the qualitative mode of vapor transport through the ice poor mantle especially the transition from a quiescent mantle where flow is controlled by Knudsen diffusion, to a disrupted mantle. These changes do not necessarily involve full mantle blow off and can precede the latter. Rotation is shown to be the key factor in limiting the thickness of dust mantles and in preventing the growth of thick, permanent mantles. Thus rotation and obliquity must be included in any valid global cometary model.

Comparison to the observations has been so far limited to inferred H_2O flux histories because in this case there is enough reliable data to test a generalized model. We find that the H_2O flux histories of most short period comets are suprisingly coherent with each other and with the generalized model considering the simplifying assumptions still retained in the latter and the observational errors associated with the former. A clear exception is comet Encke: Though we used realistic values for Encke's axial orientation, orbital parameters and rotation, the model predicted that Encke should be capable of freely stripping mantle during perihelion passage; in fact it is easy to show that most of Encke is persistently mantled. Nonetheless we were able to use the model to analyze

Encke's behavior: The radar data on Encke combined with the fluxes may be used to show that only a tiny portion of Enckes surface can consist of exposed H_2O ice. Therefore we examined the output of the model for Encke on a regional basis. The model suggests that two of the most anomalous behavioral features of Encke (a precipitous drop in H_2O flux at ~0.75 coupled with a model-anomalous low flux for a comet with Encke's radar cross section) can best be simultaneously fit if, during the incoming leg, Encke were 98% covered by a thick mantle but that an active area or latitudinal band existed which represented ~2 % of the comet's area and was located at ~65°N.

These results indicate that thick, permanent mantles, which can change a comet into an asteroid like body, are very difficult to instigate for an idealized comet with an initially homogeneous nucleus, in an Encke orbit and with "canonical" values of grain size parameters and dust-to-ice ratios. Specifically, it is not possible to form permanent mantles on such idealized short period comets simply by giving them Encke's current axial orientation and orbit (although for an imagined extreme case of constant sun orientation the model did predict irreversible asymptotic mantle thickening.) On Encke the persistent mantle development process must have been abetted by factors not quantitatively treated in our model. The more likely factors include: 1) internal compositional inhomogeneities involving inherent or initial gross departures from the dust:ice ratio used in the model, 2) agglomeration of grains which can lead to a discrepancy between the actual sail area-mass ratio of silicates and that currently suggested by the observations and therefore input to the model, and 3) three dimensional effects such as transfer of dust from one area of a comet to another.

Although spontaneous origination of a permanent mantle on an idealized homogeneous short period comet is contraindicated, the model also indicates that only ~3 cm of mantle is needed to instigate irreversible asymptotic thickening and evolution to an asteroid-like body. Because of this, because at least one largely mantled body exists, and because of general interest in any possible genetic link between cometary and asteroidal objects, we used the model to trace the long term evolution of a postulated transitional object. This object, in orbit, had an initial mantle growth of ~1 cm on the first cycle, and ~0.1 cm on the second. On the third, mantle disruption ceased and flow subsequently occurred by Knudsen diffusion alone. From then on, until the end of its lifetime (now presumably limited by celestial mechanics -not evaporation- to 10^8 years) the constantly decreasing H_2O flux averaged only 3×10^{-13} g cm^{-2} sec^{-1}. Therefore, if any cometary objects have evolved to Apollo objects, H_2O ice should still be available within a few meters (or even centimeters) of the surface despite innumerable close perihelion passages.

D23 N84 23454

PROPERTIES OF SIMULATED COMET MANTLE

Dr. Frazer Fanale, University of Hawaii, Dr. R. Stephen Saunders, Dr. Bruce Banerdt, James Stephens and Eric Laue, Jet Propulsion Laboratory, Pasadena, CA, and Steve Sutton, University of Michigan

The properties of freeze-dried dilute dispersions of dust in water ice are of considerable interest in studies of comet nucleus mantles. The formation of a "rind" residue produced by the sublimation of water ice containing various amounts of fine clay particles may be an important process.

We have attempted to simulate the development of the dry dust rind on the surface of comets. This rind is the result of preferential ice sublimation.

We have studied the development and disruption of this rind and its subsequent levitation by water vapor flow. These simulations were achieved by a variety of experimental approaches. The most interesting rind simulant is produced by dispersing 0.1 micron particles of montmorillonite in water in concentrations of 10%, 1%, and 0.1%. These dispersions are then sprayed into liquid nitrogen in the form of 100 micron droplets. The frozen droplets are then "freeze-dried" in a vacuum which prevents the ice temperature from rising above -30°C. Sublimation of the nitrogen and the water produced dry rinds. In those experiments which we believe to be the closest to a realistic simulation of cometary conditions, the most striking result was the development of large cohesive matrices of individual clay particles, and in some cases a continuous cohesive crust. Scanning electron microscope observations reveal that the material formed by freeze-drying the 0.1% dispersion does not retain the original spherical shape of the sprayed 100 micron droplets; instead it consists of a continuous filamentary network, as shown in the SEM stereo micrographs.

The results of the control experiments show that formation of these rinds does not require the occurrence of cementation processes involving the leaching of salt and their subsequent redeposition between clay particles. Instead, strongly cohesive and even elastic structures can apparently be made simply as the result of the flow of cold water vapor around individual clay grains during their release from the ice and contact with the growing filaments that form tough, fibrous structures. One, as yet unproven, hypothesis is that the flow of water vapor can cause enough electrical charging to cause the clay particles to assemble into such filamentary structures. Once assembled, however, retention the of charge or the water does not appear necessary to the survival of these agglomerates. These filamentary structures were examined at length under the electron microscope without a conductive coating (gold or carbon) and yet persisted as tough and pliable structures.

These processes could play a major role in creating the grain size distribution of silicates launched from the comets and observed in their tails. Thus, an understanding of the processes involved in the formation and cohesion of these aggregates may be necessary to fully interpret telescopic observations in terms of the intrinsic properties of the silicate component as it exists in cometary nuclei, its state as a residual rind on cometary surfaces, and its condition as it populates cometary dust tails.

A mantle composed of this type of material should provide a unique combination of low thermal conductivity and high vapor diffusivity. These properties combine to produce a nearly optimal vapor counter-flow/vacuum-radiation insulation. The quality of such insulation may impact our thermodynamic models for comets and their possible evolution into asteroids.

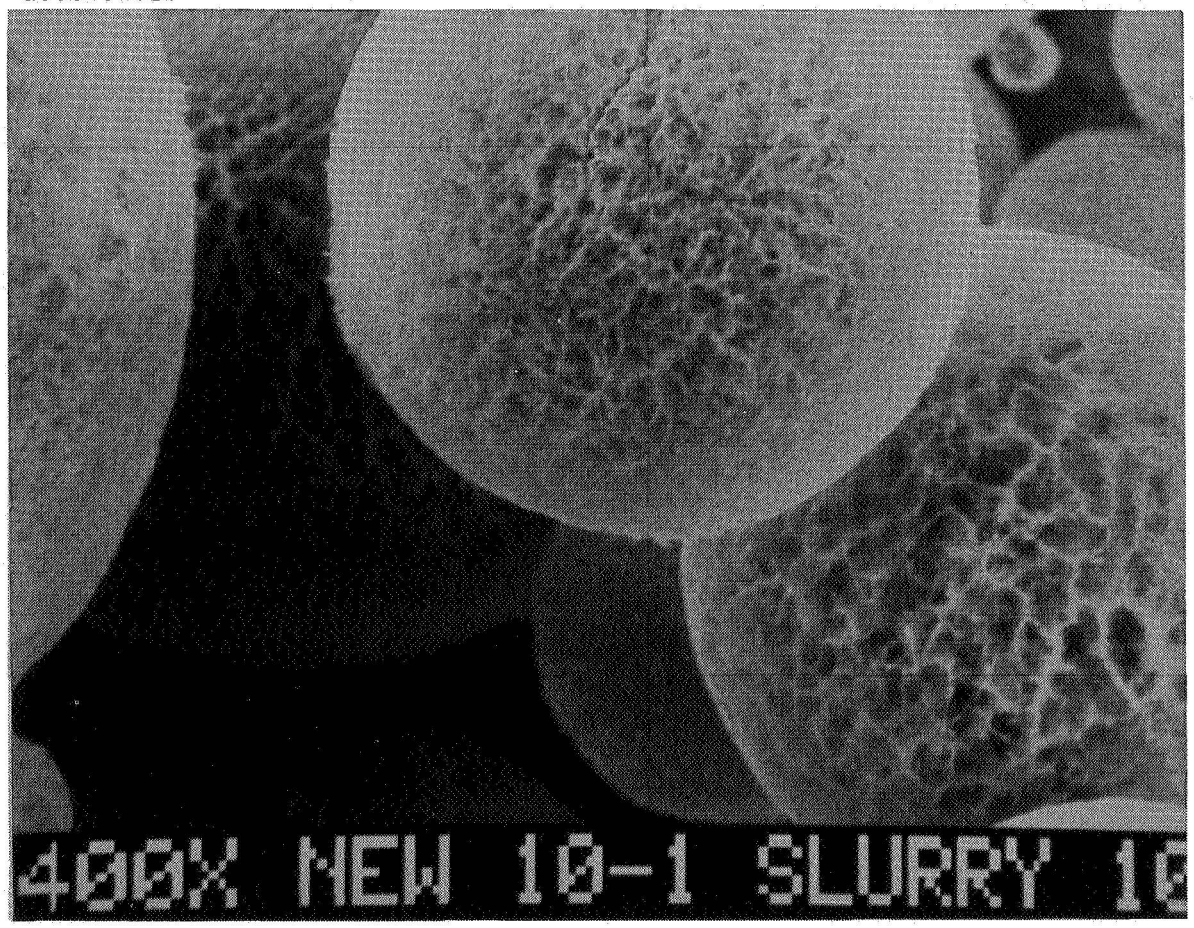

Figure 1: SEM photomicrograph of freeze-dried 100 micron droplets of 10% dispersion of montmorillonite in water ice. Note that the clay particles in the 10% clay dispersion were in contact with one another and that the droplet surfaces are maintained because the particles were not free to move during sublimation.

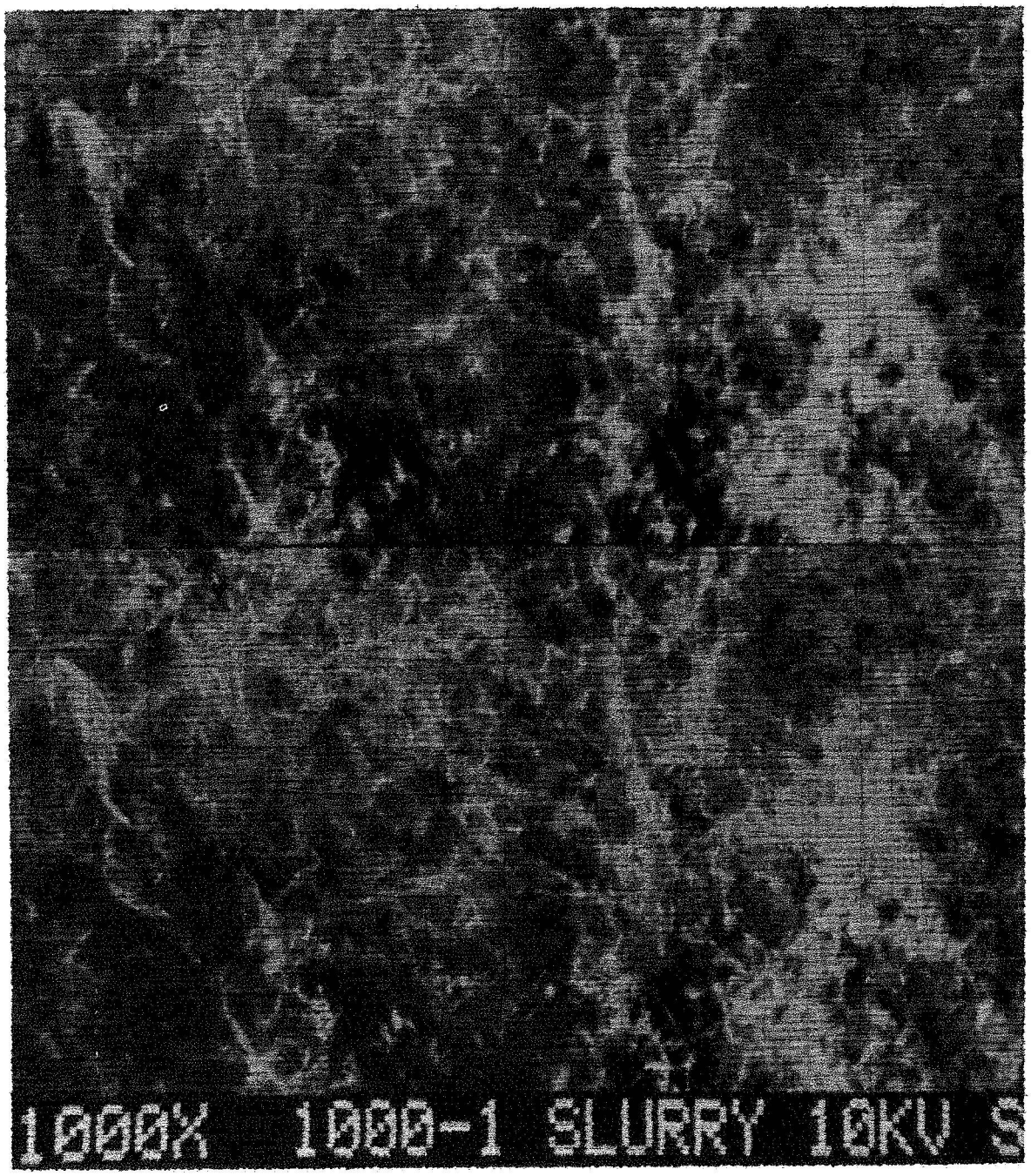

FIGURE 2: SEM stereo photo showing photomicrograph of the filamentary network resulting from the freeze drying of 0.1% dispersion of montmorillonite in water ice. Note that the clay particles were not in contact with one another in the ice and were free to form the filamentary structure during sublimation.

D24

RECENT COMET IMPACTS ON THE MOON: THE EVIDENCE FROM SPECTRAL REFLECTANCE STUDIES

B. R. Hawke and J.F. Bell, Planetary Geosciences Division, Hawaii Institute of Geophysics, Univ. of Hawaii, Honolulu, HI 96822

Introduction: The Reiner Gamma Formation, an albedo and magnetic anomaly in western Oceanus Procellarum, is the only easily observable nearside example of the enigmatic lunar swirl belts. Swirls are much more abundant on the farside where concentrations exist north and east of Mare Marginis, in and near Mare Ingenii, near Gerasimovich crater, and northwest of the Apollo basin[1,2]. Early interest in lunar swirls centered around the unusual geometry of the albedo patterns which is markedly different from common crater rays[2,3]. Renewed interest in these unusual features has followed the determination that Reiner Gamma and other swirl concentrations are associated with major lunar magnetic anomalies[2,4,5]. Recently, major controversies have developed concerning the origin of swirls and their associated magnetic anomalies. Hood and co-workers[4,5,6] have proposed that the Reiner Gamma Formation consists of unusually magnetic secondary crater ejecta associated with the nearby crater, Cavalerius, or much less likely, with Olbers A. According to this model, the formation's magnetism was created when shocked and/or heated ejecta fragments with abundant Fe^0 cooled in the presence of a strong magnetic field. Reiner Gamma's high albedo was attributed to the lack of surface darkening because of the deflection of the solar wind by the magnetic anomaly[6].

An alternative hypothesis suggests that Reiner Gamma and other swirls are the imprints of one or more recent cometary impacts[1,7]. According to this model, streamers of gas and/or dust in the inner coma struck the lunar surface at high velocity and produced major changes in the upper regolith. Schultz and co-workers[1,7,8] proposed that swirls are relatively young and that the magnetism of Reiner Gamma was induced by the cometary field during impact.

In a recent paper[9], we presented the results of analyses of near-infrared spectra obtained for various portions of Reiner Gamma and surrounding units. It was determined that spectra for bright portions could be matched by mixtures of 90-95% fresh mare basalt and 5-10% fresh highlands material. These spectra are very different from those obtained for the mature highlands material exposed in the Cavalerius ejecta blanket and fresh highlands material on the interior of Olbers A. No evidence was found for the presence of "exotic" components such as magnetite, free iron, or cometary material.

Although these results placed major constraints on the dominant hypotheses for the origin of Reiner Gamma, it was clear that additional spectral data were necessary. The needed data were recently obtained and the results of their analysis are presented here.

Method: Higher-resolution vidicon images of the Reiner Gamma region were obtained using a silicon vidicon camera and processed using the

procedure and techniques described by McCord et al.[10]. Multispectral ratio images and spectral units maps were prepared[10,11]. New near-infrared spectra (0.6-2.5 μm) were acquired for very small areas (1-2 km in diameter) associated with Reiner Gamma using the UH 2.2m telescope at the Mauna Kea Observatory. All spectra were processed using the techniques presented by McCord et al.[12].

Results and Discussion: The new high-resolution multispectral images are generally very similar to the lower resolution 0.45/0.56 μm images previously presented[9]. Hence none of the features discussed are due to instrumental or processing artifacts. Of particular interest is the "red halo" which surrounds Reiner Gamma and is clearly seen in the 0.40/0.56 μm image. The region exhibits low 0.40/0.56 μm values and has an intermediate albedo. Since this "red halo" appears to correlate closely with the magnetic anomaly presented by Hood et al.[4,5,13], it is possible that the halo, rather than the bright swirls, may contain magnetized material.

Near-infrared spectra were obtained for two portions of the halo. One area was north of the swirl and the other was to the south. Analyses of these spectra indicate that the halo material is very similar to local, mature mare deposits. Abundant agglutinitic glass is present. No "exotic" material was indicated but may be present in amounts to less than those which we can detect by reflection spectroscopy.

High spatial resolution spectra were obtained for the brightest portions of the Reiner Gamma Formation. These spectra are for areas <3 km in diameter whereas our previous spectra were for areas about 5 by 10 km in extent. Inclusion of small patches of darker terrain in the areas for which the previous spectra were obtained was a major concern. Analysis of the new spectra fully confirm our previous results. The brightest portion of Reiner Gamma consists of major amounts of fresh mare basalt fragments similar to those excavated by the nearby crater Reiner K. Very minor amounts of highlands material (~5%) are present. The presence of small amounts of highlands debris is not surprising since even larger proportions of highlands material were reported for regolith samples returned from the Appollo 11 and 12 sites[14]. All of the materials in the bright areas are extremely fresh. No agglutinate-rich surface layer is present, hence Reiner Gamma must have been formed in relatively recent times.

Previous suggestions that Reiner Gamma was somehow related to Cavalerius[4,5] prompted us to collect additional spectra for this crater. Spectra obtained for the interior of Cavalerius are almost identical to those of exterior ejecta deposits. Apparently Cavalerius excavated and deposited highlands material which has weathered to maturity. Since the composition and maturity level of Cavalerius-related deposits are quite different from those of the bright portion of the Reiner Gamma Formation, (mature highlands vs. fresh mare) a related origin seems unlikely.

The similarity in albedo of Olbers A ray deposits to that of Reiner Gamma has been noted[5] and an association between Olbes A crater and Reiner Gamma has been suggested[3]. Olbers A is a very fresh, bright-rayed, late

Copernican impact crater which is located in the highlands about 400 km west-northwest of Reiner Gamma.

To further investigate this question, spectra were obtained for several areas along the well-developed NE-trending Olbers A ray system in western Oceanus Procellarum as well as for nearby fresh mare craters and mature mare surfaces. The ray spectra are different from those of both the parent crater and the Reiner Gamma Formation. This result suggests that Reiner Gamma is not a product of the Olbers A impact event.

A previously unidentified swirl-like feature in the central highlands was pointed out to us by Dr. P. Schultz. This feature is located just west of Airy crater at 3°E, 18°S and exhibits bright areas as well as a dark lane. Spectra were obtained for the brightest portion of the swirl-like feature and the nearby crater Argelander D. The spectra are identical and their characteristics indicate that immature, feldspar-rich highlands material are present in each area.

Conclusions: The results of analyses of near-infrared reflectance spectra are inconsistent with numerous previous interpretations of the Reiner Gamma Formation. These include: 1) nuée ardente or volcanic ash deposits[16], 2) volcanically derived sublimates[15,17], 3) high albedo volcanic deposits[15], and 4) highlands debris emplaced as impact ejecta. These results, as well as those of Schultz and co-workers[1,7,8], strongly suggest that the selective preservation of high albedo features (formed by secondaries) by a local magnetic field enhancement is not a viable hypothesis. Our results are generally consistent with, but place constraints on, the cometary impact hypothesis of Schultz and co-workers[1,7,8]. While the presence of a magnetized component was not detected in either the bright or dark portions of the Reiner Gamma Formation, this material may be present in amounts under our current detection limits.

References: 1) P. Schultz and L. Srnka (1980) Nature 284, 22; P. Schultz and L. Srnka (1980) Nature 287, 86. 2) L. Hood (1981) PLPSC 12B, 817. 3) P. Schultz (1976) Moon Morphology. 4) L. Hood et al. (1979) Science 204, 53. 5) L. Hood et al. (1979) PLPSC 10, 2235. 6) L. Hood and G. Schubert (1980) Science 208, 49. 7) L. Srnka and P. Schultz (1980) LPS XI, 1076. 8) P. Schultz et al. (1980) LPS XI, 1009. 9) J. Bell and B.R. Hawke (1981) PLPSC 12B, 679. 10) T. McCord et al. (1976) Icarus 29, 1. 11) T. McCord et al. (1982) JGR 87, 10,129. 12) T. McCord et al. (1981) JGR 86, 10,883. 13) L. Hood et al. (1979) Physics of the Earth and Planetary Int. 20, 291. 14) J. Papike et al. (1982) Rev. Geophys and Space Physics 20, 761. 15) F. El-Baz (1972) NASA SP-315, 29-32. 16) J. McCauley (1967) USGS Misc. Inv. Map I-491. 17) E. Whitaker (1969) NASA SP-201.

THE PERIHELION BRIGHTNESS SURGE OF SHORT-PERIOD COMETS

Wolfe, R. F., U.S. Geological Survey, Flagstaff, AZ; Degewij, J., Technical College for Computer Sciences, The Netherlands; Shoemaker, E. M., U.S. Geological Survey, Flagstaff, AZ

Within 0.5 U of their perihelia, the reduced nuclear magnitudes of relatively active short-period comets observed by E. Roemer show similar curves of relative brightness when plotted against the parameter *distance from the sun minus perihelion distance*. The shapes of these curves are independent of perihelion distance, which indicates that the response of periodic comets to insolation is closely adjusted to their present orbits. Apparently a lag deposit with a volatile content equilibrated to the insolation maximum is formed on the surface of each comet.

Chapter 3

VENUS

N84 23456

D25

CHARACTERIZATION OF SURFICIAL GEOLOGIC UNITS ON VENUS FROM PIONEER VENUS RADAR DATA: A PROGRESS REPORT

P.A. Davis, G.G. Schaber, and H. Masursky, U.S. Geological Survey, Flagstaff, AZ 86001

Our previous research efforts on Venus have concentrated on statisical classification of Venus' surficial units by linear discriminant cluster analysis of the Pioneer Venus radar data [1,2]. Four databases have been used in the classification process: altimetry, rms slope (surface roughness), topographic slope derived from the altimetry data [2], and reflectivity either derived from the altimetry data or obtained from the 8X8 side-looking imaging mode. Both reflectivity databases were not used in the same classification because their mutual inclusion would give double weighting to reflectivity. As many as four radar databases were used in the classification in order to provide as much discrimination as possible between surficial units; however, the results from this number of data sets proved to be difficult to interpret in terms of each database's relative contribution to the resultant cluster units. The absence of a clear understanding, beyond theoretical considerations, of the geologic significance of each radar database and their interrelations in nature added to the ambiguity of the classification results.

In order to simplify the interpretation of the classification results, by reducing to three the number of variables for the classification process, but still retaining the discriminatory power of the results, principal-component analysis was performed on each pair of Pioneer Venus databases. The principal component that retains the most variance of a pair of databases was deemed a suitable substitute database for the classification procedure. Of the four databases listed above (disregarding 8X8 reflectivity because of its smaller coverage), the first principal component of altimetry and topographic slope resulted in the highest retention of variance (80 percent) among the pairs of databases, 6 to 14 percent higher than that for the other database pairs. This result is expected because the topographic slope database was produced from the altimetry data. Even though the topographic slope data are a byproduct of the altimetry data, the topographic slope data show more variation or detail in the higher elevations than the altimetry data, but the altimetry data show more detail in the lower elevations than the topographic slope data. The first principal component of these two databases retains the detailed variations at higher elevations displayed by the topographic slope data, and also the detailed variation in the lower elevations displayed by the altimetry data.

With the reduction of the radar databases to three, we now plan to produce a classification database using the reflectivity (derived from the altimetry data), rms slope, and the first principal component of altimetry and topographic slope. We will then examine the resultant clustered data qualitatively as well as quantitatively, to establish the statistical integrity of each cluster by use of an interactive, ternary plotting algorithm. This algorithm plots, for a cluster, the position of each of

its pixels within a ternary diagram whose apices represent reflectivity, rms slope, and the first principal component. The digital values in these three databases have been normalized such that unity is represented by a value of 255 in each database. The frequencies of each plotted point within the ternary diagram are recorded in order to establish the mode of each cluster. The pixels of each cluster are displayed as one separate color; their ternary plot will show not only the interrelations between clusters, but also the presence of any anomalous points within a cluster.

Once the pixels of each cluster are displayed within the ternary diagram, the cursor can be used to designate individual points or to draw a polygonal area around a group of points for further qualitative and quantitative examination. Qualitatively, the indicated point or polygonal area is highlighted on the displayed databases to determine its spatial relation to the other pixels within the cluster and the possible geologic significance of either its separation from or inclusion in an existing cluster. Quantitatively, the digital values in the three databases for the indicated point are listed, or the frequency, mean and standard deviation of a polygonal area are listed, in order to determine the statistical significance of the points in relation to their predetermined cluster unit and the other cluster units in the classification database.

At this same time, we will be using existing lunar and terrestrial analog radar data to establish fields within this ternary diagram that are indicative of as many different geologic materials and tectonic settings as possible. We will then use the resultant fields to determine empirically the geologic significance of the clusters resulting from the cluster analysis. We will check the results of this empirical examination for internal consistancy as well as for their consistancy with existing radar theory. This entire process should result in a better understanding of the Venus radar data, as well as the geologic and tectonic environments on Venus.

REFERENCES:

[1] Schaber, G.G., Kozak, R.C., Davis, P.A., and Eliason, E.M. (1982) Venus Pioneer: Ratios and composite maps of altimetry, RMS slopes and the Fresnel reflection coefficient (abs.): Lunar and Planetary Science XIII, Lunar and Planetary Institute, Houston, p. 683-684.

[2] Schaber, G.G., Davis, P.A., Kozak, R.C., and Eliason, E.M. (1982) The tectonics and surface roughness of Venus: A progress report (abs.): National Aeronautics and Space Administration Technical Memorandum 85127, Reports of Planetary Geology Programs 1982, p. 75-76.

D26

WIND ABRASION ON VENUS: A MEANS FOR EXPERIMENTAL INVESTIGATIONS

Ronald Greeley, *Department of Geology, Arizona State University, Tempe, AZ 85287, and* **John R. Marshall**, *Department of Physics, University of Santa Clara, CA 95053*

Aeolian activity probably occurs on Venus and may be one of the few—if not the sole—surface-modifying process. We have completed a study to determine the feasibility of conducting experiments to simulate the aeolian environment on Venus as related to wind abrasion. Ideally, such experiments should involve complete investigation of weathering, in which mechanical, thermal, and chemical parameters are taken into account. This is particularly important for Venus, where atmospheric temperatures and pressures at the surface produce an environment which is equivalent to low or medium grade metamorphic conditions on Earth. In this report, we present some details of the *Venus Aeolian Abrasion Device* (VAAD; Fig. 1)—an apparatus presently under consideration to study the weathering and erosion of rocks on Venus which are subject to aeolian processes. VAAD would enable experiments to be conducted with the same chemistry, temperature, pressure, and other physical properties of the Venus atmosphere near the surface.

The proposed device enables the important aeolian parameters to be controlled and monitored, including particle size, velocity, impact-angle and flux, atmospheric pressure, temperature, and gas composition. Particles are directed toward rock targets as they would be in nature. There are no sources of atmospheric contamination other than potential reactions with the chamber materials; these reactions are minimized by the use of high-grade stainless steel and titanium- and gold-coated components where applicable. Figure 2 shows details of the abrasion chamber where rock targets are bombarded with particles. The particles are fired downwards at a target from position A by a gas flow which enters through a mesh at M_1 and exhausts through a mesh at M_2. After impact, the particles fall to the bottom of the chamber at B and are then recycled to position A by a reverse gas flow from M_2 to M_1. Controlled flow rates in both directions enabled flux and impact velocity to be varied systematically. Access to the abrasion chamber is obtained by removal of the pressure vessel end plate, followed by actuation of a pneumatic cylinder built into the main "push-pull" shaft. This ejects the bellows/abrasion chamber unit from the pressure vessel while maintaining a rigid mounting for the unit during chamber inspection. Atmospheric composition in the abrasion chamber can be monitored during an experiment either by remote wavelength-analysis techniques or by direct sampling methods. Gas flow is generated by two linked, reciprocating bellows (one on each side of the abrasion chamber) which are driven by a pneumatically-controlled shaft. To one of the bellows is attached a gas reservoir containing a high concentration of the minor, potentially reactive constituents of the Venus atmosphere: HCl, HF, H_2SO_4, H_2O. These gases can be released in controlled quantities into the abrasion chamber/bellows system at any time during an experiment.

The abrasion chamber, bellows and reservoir comprise one sealed unit which is contained within a pressure vessel. Venus temperature (730 K) is achieved by heating elements wrapped around the pressure vessel. The latter also contains CO_2 reservoir tubes which are maintained at a pressure somewhat greater than 95 bar; they are linked externally through a regulator to the pressure vessel to maintain a constant pressure in the system. The shaft operating the bellows passes through a bearing at the end of the pressure vessel and connects directly to a pneumatic cylinder. Continuous action of the cylinder is achieved by an automatically-actuated, pneumatic spool-valve. The pneumatics incorporate a counter which registers the number of particle-impact cycles. It also incorporates a reciprocating-piston delay system which enables "relaxation" time between cycles for particle settling in the abrasion chamber. Calibration of particle velocity and flux are obtained via high-speed motion pictures taken through a glass port. During filming, the chemically-resistant metal front of the abrasion chamber is replaced by a glass plate.

VAAD can produce gas flows of any speed up to 20 m/s and these are highly reproducible

for each impact cycle because the gas volume is confined by the bellows and the bellows are operated by an essentially invariable mechanism. The large velocity range enables tests to be conducted at 1 bar with particle speeds typical of terrestrial environments to serve as experimental controls.

Measurements of target abrasion would be accomplished in two ways: 1) the target would be weighed before and after each run; however, this technique may require extremely long runs because of the low particle speeds on Venus; weight loss also may be affected by the high temperatures through dehydration and chemical alteration of minerals, or thermally-induced mechanical damage; 2) The second method involves the use of a stylus-profiling technique which provides topographic profiles of surface damage at a resolution of one micron. In addition, both targets and particles will be examined with the scanning electron microscope to discern the nature of any mechanical, thermal, and chemical damage.

It is also planned to conduct atmospheric chemistry experiments as part of the investigation. By continuously monitoring gas chemistry, it should be possible to determine gases released into the atmosphere or extracted from the atmosphere by rocks and particles in the chamber. Such experiments would provide insight into the origin of atmospheric constituents on Venus by determining, for example, the atmospheric/lithospheric interactions for a quiescent environment (no aeolian action) and comparing them with interactions for a mobile surface (wind-blown particles) where fresh material is continuously exposed to the reactive environment.

FIGURE 2. ABRASION CHAMBER

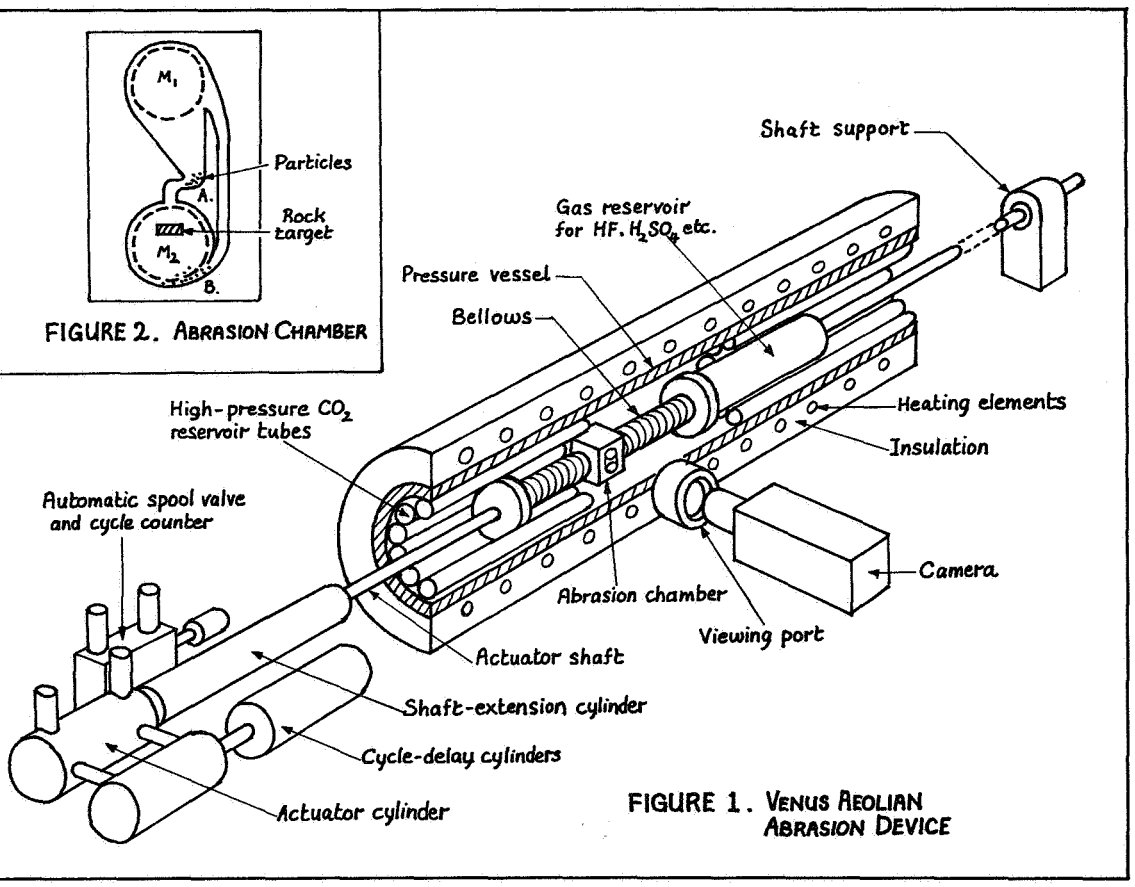

FIGURE 1. VENUS AEOLIAN ABRASION DEVICE

D27

AEOLIAN PROCESSES ON VENUS

Ronald Greeley, *Department of Geology and Center for Meteorite Studies, Arizona State University, Tempe, AZ 85287*

Aeolian processes were predicted for Venus by Ronca and Green (1970) from considerations of the surface environment. Subsequently, Sagan (1975), Hess (1975), Iversen et al. (1976), and Iversen and White (1982) predicted the minimum wind friction speeds required to entrain particles on Venus based principally on extrapolation from experiments performed under terrestrial conditions. In 1975 the Soviet landers, Veneras 9 and 10, measured venusian wind speeds of 0.5 to 1 m/s at the height of the wind sensors (~1 m above the surface). More recent measurements of wind speeds obtained by the Pioneer-Venus atmospheric probe imply a surface wind speed of 1 to 2 m/s (Counselman et al., 1979). Although it is difficult to convert these measurements to surface wind friction speeds (u_*) without detailed knowledge of the wind speed profile and surface roughness, these values are well within the range predicted as necessary for particle movement. Venera images of the surface show rock slabs, rock fragments several cm across, and fines (<1 cm), which could all contribute material in the size range appropriate for aeolian activity. Further evidence of fine particles on the venusian surface is discussed by Garvin (1981) based on Venera and Pioneer Venus data which suggest that particles 18 to 30 μm in diameter were raised as dust clouds by the landers and the probe. Thus, both requirements for aeolian processes–small particles and winds of sufficient strength to move them–appear to be met on Venus. Given the possibility of aeolian transportation of surface materials, several questions may be asked:

1. What is the nature of particle movement on Venus? For example, what are the velocities and trajectories of entrained particles? Are the particles sufficiently energetic to cause abrasion of rocks and concommitant particle attrition and comminution?
2. What is the sedimentary "budget" on Venus if materials are transported by wind? Do certain regions act predominantly as source areas while others act as regions of deposition?
3. Does the transport of material give rise to familiar aeolian bedforms such as ripples and dunes? If so, what are the characteristics of these sedimentary features?
4. Is the transported material in sufficient quantity to cause significant chemical changes of surface deposits and of the composition of the atmosphere?

Many of the questions regarding aeolian processes on Venus and the subsequent implications for surface history involve understanding the physics of particle motion in the venusian environment. The approach in this investigation is to simulate the surface environment of Venus as closely as practicable using the *Venus Wind Tunnel* (Greeley et al., 1981) and to determine threshold wind speeds, particle flux, particle velocities, and the characteristics of various aeolian bedforms.

Results from experiments run thus far have implications for several aspects of the surface evolution of Venus, as related to the questions posed above. On Earth and Mars, aeolian processes play a significant role in surface modification by erosion and deposition. It has been suggested that aeolian processes on Venus may transport weathered material from the highlands into low regions to form the extensive lowland plains observed via radar (Warner, 1980; McGill et al., 1983). The experiments show that despite the relatively low wind speeds on Venus, the flux of windblown material on Venus is potentially high and that a high fraction of material is transported as surface creep by rolling; estimates yield rates up to 100 kg per cm lane width per year depending upon the availability of material and wind frequency, suggesting that the formation of lowland plains by aeolian processes and the burial of various landforms such as impact craters could occur on short geological time-scales. This result also has bearing on the atmosphere. Aeolian activity has been suggested by Nozette and Lewis (1982) as the mechanism for geochemical "buffering" of the venusian atmosphere. They suggest that calcium- and magnesium-rich weathering products are generated from igneous rocks and are transported by surface winds. During entrainment, the fine-grained, windblown weathering products react with the atmosphere to produce the observed abundances of CO_2, H_2O, SO_2, and HF. Thus, given the potentially high flux of aeolian particles, this model of atmospheric buffering may well account for the observed composition of the venusian atmosphere.

Ripple marks have been reported from analysis of Venera 13 and 14 images (Florensky et al., 1983). Wind tunnel studies have also been conducted to assess the characteristics of various bedforms which might form in

the venusian environment. Because of the dense atmosphere on Venus, the morphologies of some aeolian erosional and depositional features may be different from those found on Earth. For example, the geometry of ripples is at least partly related to the trajectory path of grains in saltation (Bagnold, 1941; Sharp, 1963). Estimates by Greeley et al. (1980) and White (1981) suggest that the saltation path lengths of grains on Venus are relatively short, which in turn implies that the wavelength of ripples may also be relatively short–perhaps a few centimeters–in contrast to ripples on Earth which have typical wavelengths of 10-15 cm. Wave-like structures of various configurations have been observed to form in the venusian experiments. They have approximately the same height and wavelength as terrestrial ripples although their geometry is somewhat different. Because of the very short saltation path lengths at venusian atmospheric density, these wave-like structures may, in fact, be small dunes, rather than ripples. It is yet to be determined whether or not these particular features are indeed venusian analogues of terrestrial bedforms.

In summary, aeolian processes appear to be active on Venus at present and are likely to have been active in the past. Wind tunnel simulations demonstrate that aeolian processes may be very effective in modifying the surface through erosion and deposition and may have an important influence on the composition of the atmosphere.

REFERENCES

Bagnold, R.A., 1941. The Physics of Blown Sand and Desert Dunes, Methuen, London.

Counselman, C.C., S.A. Gourevitch, R.W. King, G.B. Loriot, and R.G. Prinn, 1979. Venus winds are zonal and retrograde below the clouds, Science 205, 85-87.

Florensky, C.P., A.T. Basilevsky, V.P. Kryuchkov, R.O. Kusmin, O.V. Nikolaeva, A.A. Pronin, I.M. Chernaya, Yu.S. Tyuflin, A.S. Selivanov, M.K. Naraeva and L.B. Ronca, 1983. Venera 13 and Venera 14: Sedimentary rocks on Venus? Science 221, 57-59.

Garvin, J.B., 1981. Landing induced dust clouds on Venus and Mars, Proc. Lunar Planet. Sci. Conf. 12B, 1493-1505.

Greeley, R., B.R. White, R. Leach, R. Leonard, J. Pollack, and J.D. Iversen, 1980. Venus aeolian processes: saltation studies and the venusian wind tunnel, Repts. Planet. Geol. Prog. NASA Tech. Mem. 82385, 275-277.

Greeley, R., J. Iversen, B. White, R. Leach, and S. Williams, 1981. Venusian surface wind tunnel, Rept. Planet. Geol. Proc., NASA Tech. Mem. 84211, 200.

Hess, S.C., 1975. Dust on Venus, J. Atmos. Sci. 32, 1076-1078.

Iversen, J.D., R. Greeley, and J.B. Pollack, 1976. Windblown dust on Earth, Mars, and Venus, J. Atmos. Sci. 33, 2425-2429.

Iversen, J.D. and B.R. White, 1982. Saltation threshold in Earth, Mars, and Venus, Sedimentology 29, 111-119.

McGill, G.E., J.L. Warner, M.C. Malin, E. Eliason, S. Nozette, and R.D. Reasenberg, 1983. Topography, surface properties, and tectonic evolution, in Venus, Hunton, D. and L. Colin, eds., Univ. Ariz. Press, 69-130.

Nozette, S. and J.S. Lewis, 1982. Venus: Chemical weathering of igneous rocks and buffering of atmospheric composition, Science 216, 181-183.

Ronca, L.B. and R.R. Green, 1970. Aeolian regime of the surface of Venus, Astrophys. and Space Sci. 8, 59-65.

Sagan, C., 1975. Windblown dust on Venus, J. Atmos. Sci. 32, 1079-1083.

Sharp, R.P., 1963. Wind ripples, J. Geol. 71, 617-636.

Warner, J.L., 1980. Venus: Do sediments cover lowlands? (abs.), Div. Planet. Sci. Amer. Astron. Soc. 12, 691.

White, B.R., 1981. Venusian saltation, Icarus 46, 226-232.

D28

N84 23459

NEW MAPS OF LAKSHMI PLANUM AND EASTERN APHRODITE, VENUS

George E. McGill, Department of Geology and Geography,
University of Massachusetts, Amherst, MA 01003

All current models for the thermal structure of Venus predict a hot and thin lithosphere; this implies a positive buoyancy for the lithosphere (1) and thus the absence of slab pull, one of the favorite driving forces for plate tectonics on Earth. Furthermore, neither Pioneer Venus altimetry nor radar images from Earth and from Pioneer Venus support the presence of an Earth-like system of plate-tectonic landforms (2) even though the data are capable of resolving many of these landforms if they were present (3).

Two opposing viewpoints have developed regarding Venus tectonics: 1) Venus is a one-plate planet, and its tectonic style is dominated by heat loss through hot spots (4), or 2) Venus is characterized by many small lithospheric plates, and its tectonic style is dominated by heat loss along fast-spreading divergent boundaries (5). Neither of these would produce global-scale landforms like those due to modern-Earth plate tectonics. It is interesting to note that the same two hypotheses have been proposed by various persons to explain the tectonic style of Earth during the Archean when radioactive heat generation was several times greater than now.

Interest on Venus has centered on three regions: 1) Aphrodite Terra, especially east of the main upland portion, 2) Ishtar Terra, especially Lakshmi Planum and its bounding scarp and massifs, and 3) Beta Regio-Phoebe Regio. The last region is topographically similar to the East African rift system, and has been inferred to have a similar tectonic origin (6). The Aphrodite region is part of a 21,000 km long tectonic zone (7) that seems best explained as due to extension, and that may represent hot spots clustered along an incipient divergent plate boundary. The most interesting and complex portion of this tectonic zone is that part of eastern Aphrodite between Thetis Regio and Atla Regio. In contrast, the Lakshmi Planum region has many topographic characteristics suggesting that it is a true continent, and thus indicative of convergence and a thick crust (4, 8).

Figures 1 and 2 are new, detailed topographic contour maps of eastern Aphrodite Terra and of Lakshmi Planum. They are published here in order to make them available to those interested in the tectonic style of Venus.

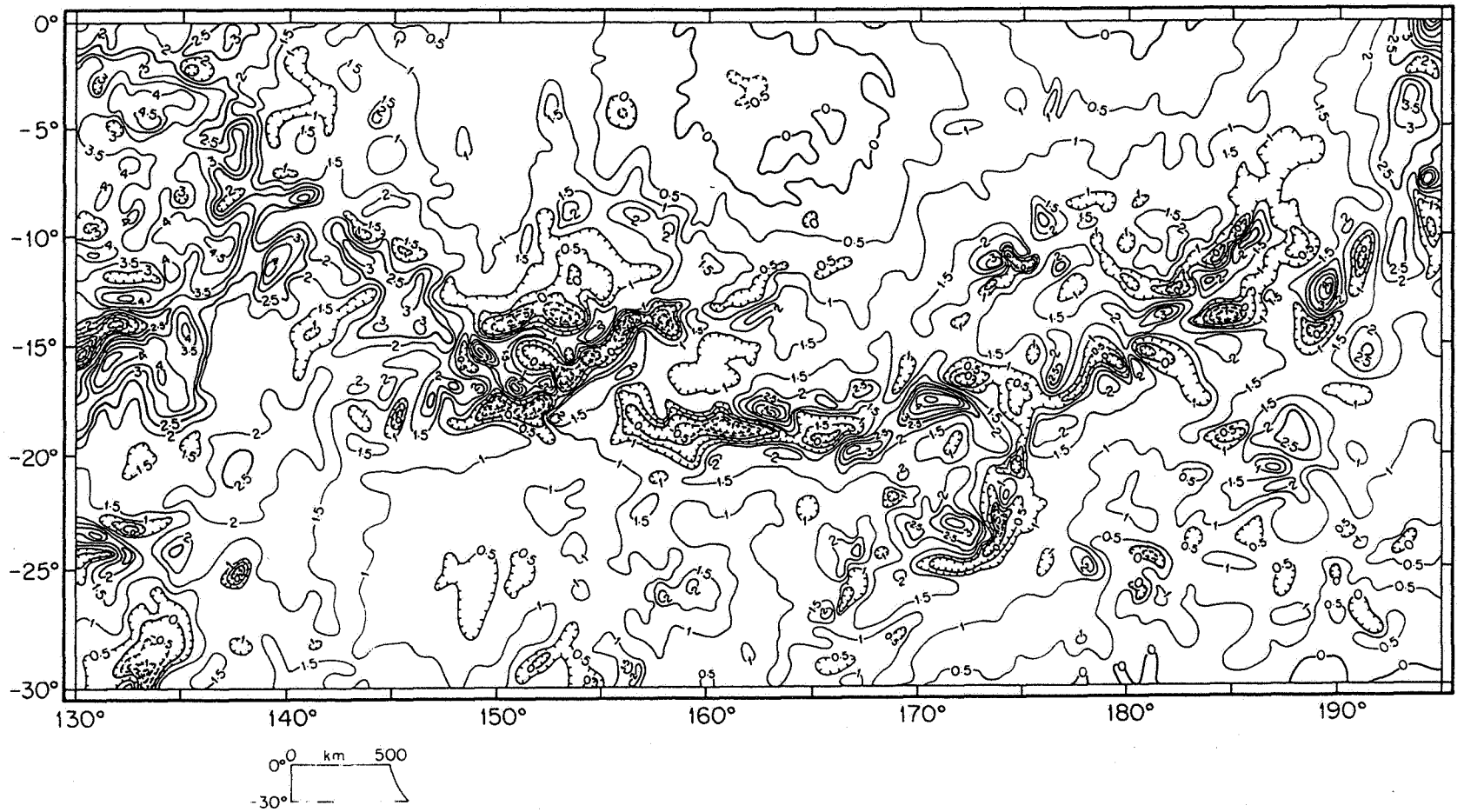

Fig. 1. Eastern Aphrodite Terra. CI = 0.5 km, datum = median radius (6051.6 km).

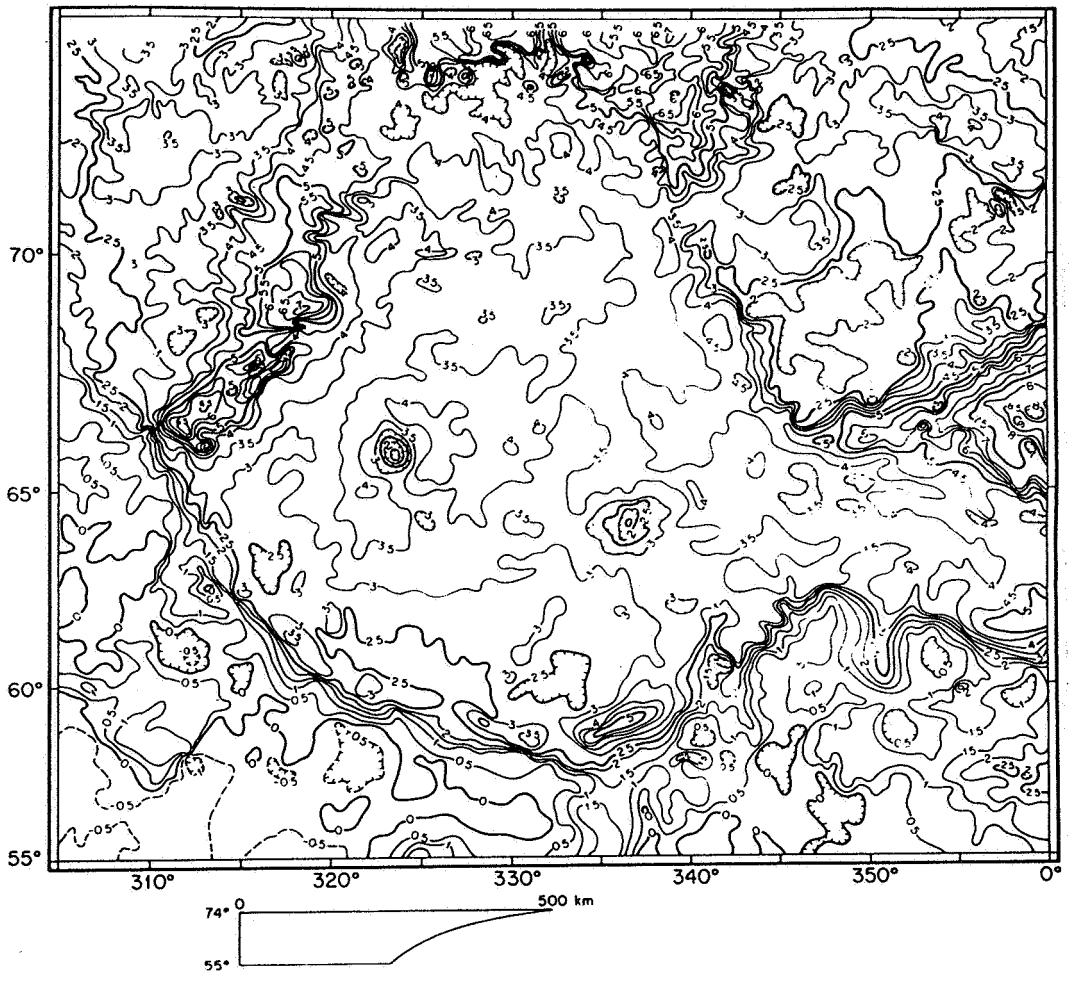

Fig. 2. Lakshmi Planum. CI = 0.5 km, datum = median radius.

****

References Cited

1. Anderson, D.L. Geophys. Res. Letts., 8, 309-311, 1981.
2. McGill, G.E., et al. Venus, Univ. Ariz. Press, p. 69-130, 1983.
3. Arvidson, R.E., and Davies, G.F. Geophys. Res. Letts., 8, 741-744, 1981.
4. Phillips, R.J., and Malin, M.C. Venus, Univ. Ariz. Press, p. 159-214, 1983.
5. Solomon, S.C., and Head, J.W. Jour. Geophys. Res., 87, 9236-9246, 1982.
6. McGill, G.E. et al. Geophys. Res. Letts., 8, 737-740, 1981.
7. Schaber, G.G. Geophys. Res. Letts., 9, 499-502, 1982.
8. Campbell, D.B. et al. Science, 221, 644-647, 1983.

D29 N84 23460

VENUS BANDED TERRAIN: EVALUATION OF TECTONIC MODELS FOR THE ORIGIN OF BANDING. Sean C. Solomon, Dept. of Earth and Space Sciences and Institute of Geophysics and Planetary Physics, U.C.L.A., Los Angeles, CA 90024 (Permanent address: Dept. of Earth and Planetary Sciences, M.I.T., Cambridge, MA 02139); and James W. Head, Dept. of Geological Sciences, Brown University, Providence, RI 02912.

Introduction. Two major unsolved problems for Venus, the most Earth-like of the terrestrial planets, are the dominant mechanism of lithospheric heat loss [1] and the origin of highland and mountainous terrain [2]. Available topographic [3] and imaging [4] data for Venus are at too coarse a resolution to decide unequivocally whether Venus displays features diagnostic of large-scale horizontal motions and plate recycling as on Earth, or is more like the smaller one-plate planets with more limited histories of volcanism and primarily vertical tectonics. The highland regions of Venus, and in particular the mountain belts of Ishtar Terra [2], are unlike terrain on the one-plate planets and at least superficially resemble most closely the continents and mountain ranges of the Earth.

Recent images of Ishtar Terra obtained at 3 km radar resolution by the Arecibo Observatory [5] show that the mountain belts of Ishtar are characterized by a series of linear bands of alternating greater and lesser reflectivity. The bands are generally aligned with the long axis of the mountain ranges, and the outlines of the brightest banded terrain generally coincide with the topographic contour defining the mountain units. Spacing between adjacent bands is somewhat variable, but 15 to 20 km is a typical value [5].

A number of hypotheses have been considered for the origin of these bands, including wind activity, mass wasting, volcanism, and tectonism; the detailed geometry of the bands and the relationship of banded terrain to topography suggest that a tectonic origin is most likely [5]. In this paper, we consider two types of quantitative tectonic models for the formation of band structure: folding models and extensional models. Our goals are to test the viability of each type of model, to determine the implications of each model for the mechanical properties of the Venus crust, and to assess whether additional insight may be gained into the coupled issues of the mechanism of Venus heat loss and the origin of Venus mountain belts.

Folding Models. If the bands are folds in the underlying rock units, analogous to folds in terrestrial mountain belts, then the band spacing may be used to infer both the thickness of the layer that underwent folding and the magnitude of the compressive stress that acted to induce the folds [6]. For a single elastic layer of thickness T, Young's modulus E, and Poisson's ratio ν overlying an inviscid fluid of density ρ in a gravitational field of acceleration g, the wavelength λ of fold growth at the least value of horizontal compressive stress σ is related to T by [6]

$$T = A \left(\frac{\gamma}{B}\right)^{1/3} \left(\frac{\lambda}{2\pi}\right)^{4/3} , \qquad (1)$$

and the critical compressive stress is

$$\sigma = \frac{2}{A} \gamma^{2/3} B^{1/3} \left(\frac{\lambda}{2\pi}\right)^{2/3} \qquad (2)$$

where $\gamma = \rho g$, $B = E/12(1-\nu^2)$, and $A = 1$. For Venus, we take $g = 887$ cm/s^2, $\nu = 0.25$, $\rho = 3$ g/cm^3, and E in the range 10^{11} to 10^{12} dyne/cm^2. Using λ = 15-20 km from the observed band spacing gives T = 0.5 - 1.5 km and σ = 1.5 - 4 kbar.

The large, and perhaps excessive, value of compressive stress required to induce folding of a single layer at the observed wavelength of the bands may be reduced if the folded member consists of a stack of layers between which the friction is zero. In terrestrial mountain belts, such layering occurs through a sequence of sedimentary units of differing mechanical properties; on Venus such layering might be at least partly of volcanic origin. For n layers of total thickness T folded together, (1) and (2) still hold except $A = n^{2/3}$. For n = 10 (100), σ is reduced by a factor of 4.6 (21.5), and T is increased by the same factor. We conclude that folding is an acceptable explanation for the bands, and that the required stresses are reasonable as long as the folded unit has some internal layering.

Extensional Models. We next evaluate the hypothesis that the banded terrain arises by lithospheric extension, i.e., that the banded regions have a basin-and-range type structure. Such extension may also arise from the spreading of mountain units under the influence of gravity; because of the high surface temperature of Venus, such spreading may occur by viscous creep at much more rapid rates than on Earth [7]. By this explanation, the bands are not primary features associated with the origin of the mountain belts, but rather secondary features produced during their later modification.

As a basis for several extensional models we begin with the hypothesis of Vening-Meinesz [8] that once an elastic-brittle layer under extension fails along a through-going normal fault, slip on that fault will induce bending stresses in the plate on either side. If extension continues, the next fault will form where the horizontal bending stress is most extensional. This theory has been used successfully to predict the widths of continental rifts [8,9]. As applied to Venus, we consider three alternatives: (i) the half-wavelength of Venusian bands equals the graben width; (ii) once a graben forms, the next adjacent graben forms in a position of favorable bending stress; (iii) extension occurs by imbricate normal faulting rather than by horst-and-graben formation. These alternatives yield slightly different relations between the thickness T of the elastic/brittle layer and the band wavelength λ: All follow equation (1), with A = 4 for case (i), A = 1.18 for case (ii), and A = 10.1 for case (iii). For λ = 15-20 km, these alternatives give T = 0.5-7 km.

A different model for basin-and-range structure has been proposed [10] based on the extensional necking of a plastic surface layer overlying a substrate that deforms by power-law creep. By this model, the ratio of the wavelength of necking to the thickness of the surface layer is in the range 3.4 to 4 [10]; λ = 15-20 km corresponds to T = 4-6 km.

Conclusions. A tectonic origin for Venus banded terrain is consistent with band spacing. Both compressional (folding) and extensional models for band formation can fit present observations. Band spacing cannot therefore distinguish among scenarios for global heat loss and for the origin of highland terrain [1]. The principal new result is that tectonic models for band formation indicate that the surficial brittle layer in the Venus highlands is no more than a few kilometers thick.

References: S.C. Solomon and J.W. Head, JGR, 87, 9236, 1982; [2] H. Masursky et al., JGR, 85, 8232, 1980; [3] G. H. Pettengill et al., JGR, 85, 8261, 1980; [4] D.B. Campbell and B.A. Burns, JGR, 85, 8271, 1980; [5] D.B. Campbell et al., Science, submitted, 1982; [6] A.M. Johnson, Physical Processes in Geology, Freeman Cooper, 1970; [7] J. Weertman, PEPI, 19, 197, 1979; [8] W.A. Heiskanen and F.A. Vening Meinesz, The Earth and Its Gravity Field, McGraw-Hill, 1978; [9] M.H.P. Bott, Tectonophysics, 36, 77, 1976; [10] R.C. Fletcher and B. Hallet, JGR, in press, 1982.

D30 N84 23461

VENUS: THE NATURE OF THE SURFACE FROM VENERA PANORAMAS

J.B. Garvin, J.W. Head, M.T. Zuber and P. Helfenstein, Dept. of Geological Sciences, Brown Univ., Providence, RI 02912

Images of the surface of Venus obtained by the Soviet Venera 9, 10, 13 and 14 landers have been analyzed to provide a basis for understanding the nature of geologic processes operating there. The four spacecraft landed in the Beta-Phoebe region at median elevations in the upland rolling plains province. The landing points are each separated by distances of more than a thousand kilometers. The Venera panoramas were digitized and transformed into various perspectives in order to facilitate analysis and comparison with other planetary surfaces. Bedrock is exposed at the Venera 10, 13 and 14 sites and is characterized by semi-continuous, flat polygonal to subrounded patches up to several meters in width. The bedrock surface is often dominated by sub-horizontal to horizontal layered plates with thicknesses of several cm and abundant linear and polygonal vertical fractures. Angular to subangular layered to platy blocks in the 5 to 70 cm range dominate the Venera 9 site and occur much less frequently at the other sites. Blocks appear to share many characteristics with the exposed bedrock and are interpreted to be largely derived from it. Soils (particles <1 cm) are abundant at the Venera 9, 10 and 13 sites, but are uncommon at Venera 14. Features indicative of a strong eolian influence (moats, dunes, wind tails) are not observed. A striking aspect of the Venera landing sites is their extreme similarity despite separation distances of thousands of kilometers. Several hypotheses are considered for the origin of the bedrock surfaces, and it is concluded that bedrock originated from surface lava flows. In this interpretation, the broadly platy nature of the surface is analogous to the rolling and undulating nature of terrestrial pahoehoe flows caused by the formation and deformation of a semi-solid crust. The layering is interpreted to be formed by a combination of upper thermal boundary layer formation and horizontal sheets formed by cooling and shearing during flow emplacement. Vertical fractures are attributed largely to joint patterns formed during cooling. This interpretation made on the basis of surface morphology is consistent with Venera 13 and 14 geochemical results which reported high potassium basalt and tholeiitic basalt compositions, respectively. If this interpretation is correct large re ions of the Beta-Phoebe area are likely to be characterized by lava flows. The relative freshness of features observed by the Veneras suggests that erosion rates are very low or that some bedrock surfaces are geologically young.
(This paper has been submitted for publication.)

TABLE II

Observed Characteristics of Venera Lander Sites

Site	Bedrock	Fragments (>1 cm)	Fines/Soil (<1 cm)
Venera 9	• No unambiguous evidence for bedrock exposure.	• Abundance of angular to subangular layered and platy blocks in the 5-70 cm range. • Several blocks have elongate, rounded ridges and other undulatory surfaces. • Some blocks polygonal in outline; some are steeply inclined relative to horizon. • Finer fraction (1-5 cm) distributed in interblock areas	• Apparent bimodal distribution (fines below limits of resolution, coarse, ~1 cm). • Few intermediate fragments between fines and 10 cm blocks. • Distributed between blocks, little evidence of fillets around blocks.
Venera 10	• Covers 40-60% of surface. • Exposed as semi-continuous, generally flat, subrounded to polygonal patches up to several meters in width. • Surface rough; in nearfield, 5-10 cm of topography, up to a meter in background. • Surface texture is pitted, and also contains a cuspate scarp. • Linear and orthogonal fractures.	• Only a few discrete fragments >5 cm. • Located in areas dominated by fines, not on bedrock. • Visible fragments in soil grade into roughness at the scale of resolution in intermediate and far field.	• Fines distributed in extensive patches in low areas and in small patches on bedrock surfaces. • Fines lower albedo than bedrock. • Fines grade into small fragments in size.
Venera 13	• Covers 20-50% of surface. • Exposed as semi-continuous, generally flat polygonal to subrounded patches. • Surface rough in nearfield, bedrock plate edges and surface shows 5-10 cm of topography; pits and shallow linear depressions. • Several rounded, elongate, and cuspate scarps. • Linear fractures. • Surface has a somewhat layered appearance.	• Larger fragments are angular to subangular, layered and platy; locally distributed in patches associated primarily with bedrock. Many fragment boundaries can be related to adjacent bedrock fractures. • Smaller fragments are located on and within soil/fines patches and only occasionally on bedrock. Occur in two modes: 1) in an annulus surrounding the lander ring. The most rounded particles occur here; fragments lie on top of soil layer; 2) in soil patches between bedrock exposures. Particles mostly partly buried.	• Fines distributed in extensive patches between bedrock exposures and in local small patches in bedrock pits and depressions. • Fines lower albedo than bedrock. • Bimodal distribution? • Soil occurs on surface of lander ring on both sides of spacecraft and on lens cover.

Table II, continued

Site	Bedrock	Fragments (>1 cm)	Fines/Soil (<1 cm)
Venera 14	•Covers almost 100% of surface. •Exposed as continuous areas of interlocking, generally flat, polygonal plates. •Surface is rough at scale of centimeters. •Surface structure dominated by subhorizontal to horizontal layered plates with thicknesses of several centimeters. Some layers show different albedo, with uppermost layers darkest. Uppermost plate in nearfield has hole or window revealing underlying layer. Some surface sublayers show tongue-like overlaps. •Surface textures include pitting, waviness and elongate, cuspate scarps. •Abundant linear and polygonal fractures.	•Only a few discrete blocks >10 cm. •One 50 cm block with layered/striated texture. •Fragments are angular to subangular; several can be geometrically fitted into adjacent bedrock. •In farfield, fragments appear in local patches between extensive flat platy bedrock exposures. •In nearfield, smaller fragments have two modes of occurrence: 1) in depressions and fractures in bedrock; 2) distributed around lander ring on arm side of spacecraft.	•Distinct paucity of fines compared to other sites. •Some local accumulations in fractures in bedrock and in front of spacecraft on arm side. •Soil occurs on surface of lander ring only on arm side of spacecraft.

N84 23462

D31

GEOLOGY OF MAXWELL MONTES, VENUS

J.W. Head, Dept. of Geological Sciences, Brown University, Providence, RI 02912, D.B. Campbell, Arecibo Observatory, P.O. Box 995, Arecibo, PR 00612, A.R. Peterfreund, Brown University, and S.A. Zisk, MIT/Haystack Observatory, Westford, MA 01886

Maxwell Montes represent the most distinctive topography on the surface of Venus, rising some 11 km above mean planetary radius. The mountainous structure superposed on Ishtar Terra has been attributed to numerous geological processes, including a fault-bounded massif of volcanic origin (1) and a domed or folded uplift (2). The nature of major mountain ranges on the planets is important evidence concerning the types of surface process and the major modes of lithospheric heat transfer (3). The purpose of this contribution is to analyze the multiple data sets of the Pioneer mission and Earth-based radar observations to characterize Maxwell Montes.

Maxwell Montes is a pork-chop-shaped feature (Fig. 1a) located at the eastern end of Lakshmi Planum. The main massif trends about N20W for approximately 1000 km and the narrow "handle" extends several hundred km WSW from the north end of the main massif, descending down toward Lakshmi Planum. The main massif is rectilinear and approximately 500 km wide. The southern and northern edges of Maxwell Montes coincide with major topographic boundaries defining the edge of Ishtar Terra. The eastern and western boundaries separate two distinct subprovinces within Ishtar Terra (4). Maxwell Montes is the most prominent of several linear mountain belts on Ishtar Terra (1,5). The central part of the massif rises over 11 km above mean planetary radius and over 7 km above Lakshmi Planum. The topography is markedly asymmetric, with the steepest slopes toward the west (Fig. 1b). At the existing 100 km resolution, most slopes average less than 3^{o} but locally exceed $5\text{-}7^{o}$ along the western flanks. Radar images from Arecibo (5) at 3-6 km resolution reveal more detailed characteristics of Maxwell (Fig. 1c). The radar image can be subdivided into several units (Fig. 1d) including: 1) Banded - a distinctive set of linear to curvilinear bands with an average separation of 10-20 km. These bands parallel the long axis of the massif and are best developed on the central high plateau. Bands are seen on other mountain ranges on Ishtar. 2) Mottled areas developed primarily on the southern and northern slopes of the main massif. 3) Patchy areas of low backscatter less than about 80 km in diameter. The banded terrain terminates at the edges of these irregularly outlined patches. 4) A circular region which consists of three superposed circular features of differing backscatter; the intermediate structure is approximately 105 km in diameter, the outermost is about 200 km diameter, and the innermost feature is of low backscatter, about 40-50 km diameter and offset to the NW. Topographic data suggest that this 100-200 km circular feature may be a depression but the resolution is insufficient to define its detailed structure.

Radar data show that the slopes of Maxwell Montes are extremely rough at the centimeter to meter scale (6,7,8,9). At 12.6 cm wavelengths the signal scattered back from Maxwell is about 50 times the intensity of

that received from the surrounding terrain and is heavily depolarized. RMS slopes often exceed 4.5° (1,6). However, the highest backscatter is not correlated with the highest elevations on Maxwell. Rather, highest backscatter appears correlated with the mottled units occurring on the steep slopes at the northern, southern, and western flanks of Maxwell. Maxwell Montes is also a region of very high reflectivity (10). The high reflectivity has been interpreted to indicate the presence of significant amounts of a conducting mineral (such as pyrite) as inclusions in rock exposed at the surface (10).

References: 1) H. Masursky et al. (1980) J.G.R., 85, 8232. 2) McGill et al. (1983) Chapter 6, Venus, in press. 3) S. Solomon and J. Head (1982) J.G.R., 87, 9236. 4) J. Head et al. (1983) LPSC XIV. 5) D. Campbell et al. (1983) Science, in review. 6) G. Pettengill et al. (1980) J.G.R., 85, 8261. 7) D. Campbell and B. Burns (1980) J.G.R., 85, 8271. 8) R. Jurgens (1970) Radio Sci., 5, 435. 9) A. Basilevsky et al. (1982) Moon and Planets, 27, 89. 10) G. Pettengill et al. (1982) Science 217, 640.

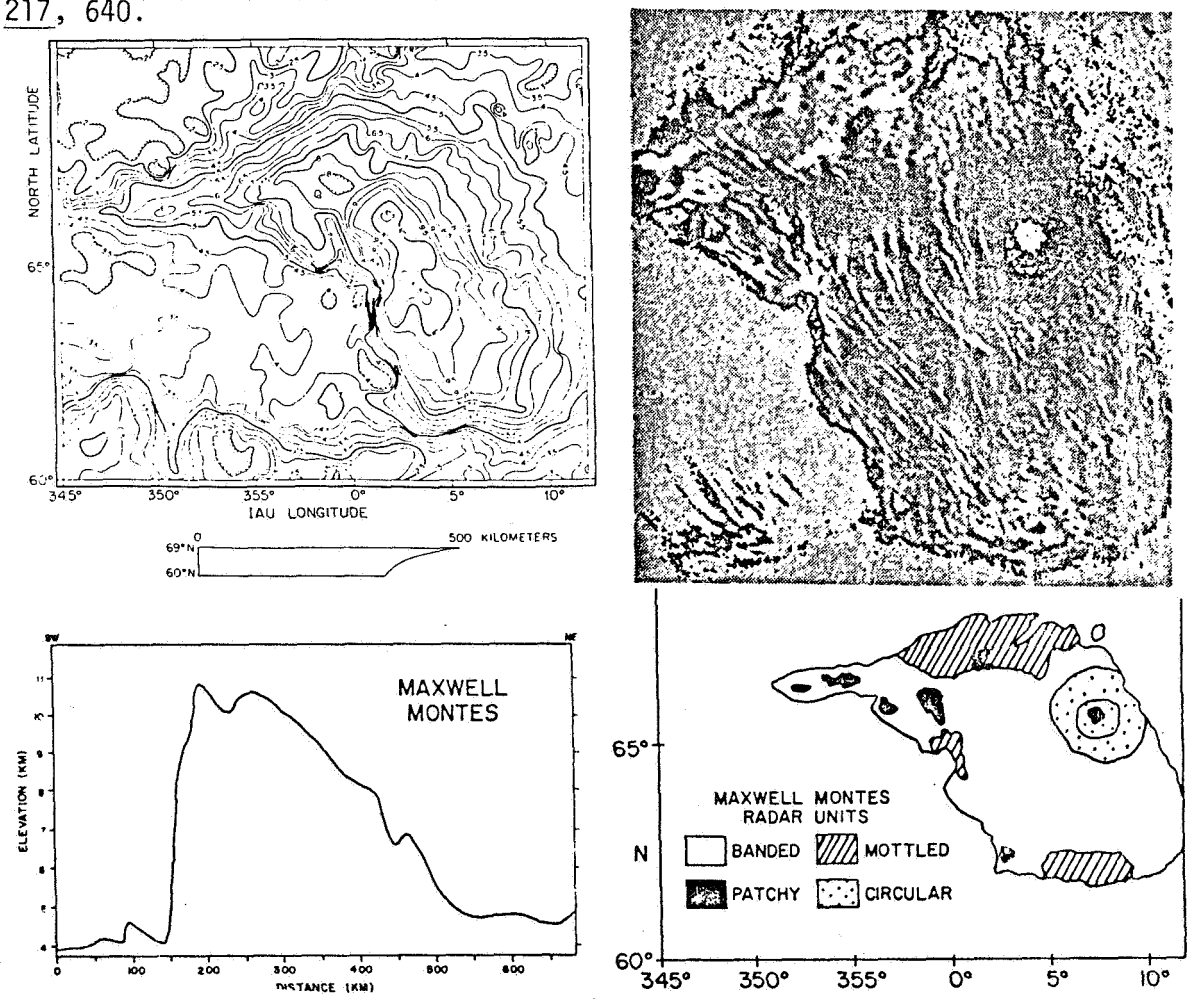

Figure 1. a. Topography of Maxwell Montes (1,2,6). Contour interval 500 m. b. Topographic profile of Maxwell Montes. c. Radar image of Maxwell Montes with a two-tier stretch (black is a higher backscatter than the gray background). d. Radar reflectivity unit map.

VENUS: GLOBAL DISTRIBUTION OF PIONEER-VENUS RADAR ROUGHNESS AND REFLECTIVITY AND GLOBAL CORRELATION OF ALTIMETRY, ROUGHNESS AND REFLECTIVITY OBSERVATIONS

J.W. Head, J.B. Garvin and A.R. Peterfreund, Dept. of Geological Sci., Brown University, Providence, RI 02912, S.A. Zisk, MIT/Haystack Observatory, Westford, MA 01886, G. Pettengill, Dept. Earth and Planetary Sciences, MIT, Cambridge, MA 02139, and V.S. Sharpton, Brown Univ.

An improved version of the Pioneer-Venus orbital data {Nov. 82} was used for a statistical analysis of global radar roughness (α^0) and reflectivity (ρ). The distribution of α^0 in terms of RMS slopes on scales of 0.10-10 m as a function of area is skewed heavily toward the "smooth" end of the spectrum; only 7% of the planet approaches the α^0 of the lunar highlands or martian fresh volcanic plains. The mean α^0 is $2.59^0 \pm 1.4^0$. Correlation of α^0 with altimetry (z) demonstrates a trend of increasing α^0 with z. This increase is non-monotonic and the mean α^0vs. z distribution shows a series of discrete plateaus (constant α^0), transitions (increasing α^0) and peaks. The boundary between the upland rolling plains (URP) and the highlands (6053 km) coincides with a change in the α^0 distribution, with the least elevated highlands having a fairly constant α^0 compared to the highest plains. Highest altitude regions (>4.5 km) who highest α^0 values (>5.0). No correlation between the plains-lowlands boundary (6051 km) and changes in the α^0 distribution is observed. The pattern of Fresnel ρ follows a slightly skewed Gaussian distribution with a mean of 0.13±0.03. Over 48% of the surface falls within the range 0.10-0.16 (vs. 49% within 1σ of the α^0 mean). There is no correlation between ρ and z, as observed with α^0. The widest range of ρ occurs in the URP, and the highest concentration of values >0.30 occurs near mean planetary radius (6051.5 km). The distribution of ρ vs. z is non-monotonic; regions above 4.5 km elevation show the highest ρ values. A general decrease in ρ with z occurs in the lowlands and plains provinces. A change in the distribution occurs at the plains-highlands boundary (6053 km), as with α^0. The least elevated highlands (<3.5 km) have almost constant ρ, but ρ increases with z in regions at 3.5-5.0 km. Chasmata have variable α^0 and ρ values, possibly due to compositional/textural differences between their walls and floors.

Classification maps of the venusian surface have been produced in a supervised manner on the basis of statistical and empirical studies of the individual data sets. The primary objective is to assess the degree of homogeneity of surface radar properties within topographic provinces in order to map possible geologic boundaries. Maps were produced by correlating two data sets at a time. Altimetry divisions (radius km) were chosen to be similar to those defined in Masursky et al. (1980 JGR 85, 8232): 1) <6051.0, lowlands; 2) 6051-6053.0, rolling uplands; 3) 6053.0-6055.5, highlands; and 4) >6055.5, mountainous regions. Roughness (degrees RMS) and reflectivity divisions were based on statistical distributions (~mean ±s.d.) as well as an interpretive scheme. Roughness divisions used were: 1) $<2.0^0$, smooth; 2) 2.0^0-4.0^0, transitional; and 3) $>4.0^0$, blocky and/or hummocky. Reflectivity divisions were: 1)

<0.1, low bulk density (<2.0 g/cm^3) and absence of high dielectrics; 2) 0.1-0.2, bulk density (2.0-3.2 g/cm^3) and minor amounts of high dielectrics (<1%); and 3) 0.2-0.5, high bulk density (>3.2 g/cm^3) and/or high concentration of dielectrics. Lowlands and rolling uplands are mostly composed of materials with low to moderate reflectivity, and are smooth to moderately rough. Anomalous regions include a rough region east of Beta Regio, and high reflectivity regions east of Tethus Regio, southwest of Ishtar and southeast of Aino Planitia. Highland regions have a broad range of radar characteristics indicating a diversity of formational/modificational processes. Mountainous regions are radar rough, but do not display a high reflectivity. Classification of specific regions, such as Ishtar, has demonstrated that distinct geologic units can be identified.

Chapter 4

CRATERING PROCESSES AND LANDFORM DEVELOPMENT

MARTIAN CRATER SIZE/FREQUENCY DISTRIBUTIONS AND TERRAIN AGES

Nadine G. Barlow and Robert G. Strom, Lunar and Planetary Laboratory, University of Arizona, Tucson, AZ 85721

The crater size/frequency distributions of large (> 8 km) craters on the moon and terrestrial planets display two very different curves representing two crater populations. The heavily cratered regions of the Moon, Mercury, and Mars show the same highly structured curve which cannot be represented by a single-slope distribution function. This crater population was emplaced during the period of late heavy bombardment by a family of impacting objects which became extinct about 4 B. Y. ago on the Moon. In contrast, the lunar post-mare crater population has a size/frequency distribution which differs significantly from that in the highlands over the same diameter range, and can be represented by a single-slope distribution function of -2.8 differential. A Chi-square statistical test indicates that this crater population is different from that in the highlands at the 99% confidence level. On areas of martian lightly cratered northern plains, the crater population is essentially identical to that of the post-mare population. This indicates that the same two families of impacting objects were responsible for the cratering records on both the Moon and Mars.

The origin of the objects responsible for the period of late heavy bombardment is uncertain. They may have been long lived remnants left over from the accretion of the terrestrial planets (Ref. 1), a gravitationally disrupted planetesimal perturbed into the inner Solar System (Ref. 2), or comets as suggested by Shoemaker. Any of these origins have orbital dynamics that lead to a termination of heavy bombardment which is essentially contemporaneous on the Moon and Mars, i.e. ~ 4 B. Y. ago. Consequently, Martian surfaces which have a highly structured crater size/frequency distribution (the highlands signature) are older than about 4 B. Y., and surfaces with a single slope (-2.8) size/frequency distribution are younger than about 4 B. Y. Furthermore, the relative ages of various terrains within the major time divisions can be determined from differences in the crater densities. Determining absolute ages from crater densities within these time divisions requires a knowledge of the impact rate and how it varies with time (Refs 3, 4, 5). This, in turn, depends on the origin of the impacting objects which is still uncertain.

The Martian surface has been divided into about 20 major geologic units based mostly on published Mariner geologic maps and extensive remapping of certain areas from Viking data. Craters within the geologic units have been mapped over most of the surface from available U.S.G.S. Viking 1:2 M photomosaics. Only MC-1, MC-30

and MC-26 SW & SE have not been mapped because they are not yet available. The craters are classified according to whether they pre-date (are partially buried) or post-date the surface on which they occur. It was also noted whether the craters pre-date or post-date tectonic structures. At present the craters are being measured.

Preliminary results for various lightly cratered northern plains units in MC 2-7 show they all have a size/frequency distribution for post-plains craters similar to the lunar maria and are therefore younger than 4 B. Y. In contrast, the pre-plains (partially buried) craters have a size/frequency distribution that shows a severe paucity of small craters relative to the post-plains curve. At larger diameters the curve is the same as the post-plains curve, but the diameter at which the pancity begins varies from unit to unit. This shows that the thickness of mantling material (probable lava) varies among the various plains units, and can be calculated from the depth/diameter scaling relations for martian craters (Ref. 6).

References

(1) Wetherill, G.W., (1977) Proc. Lunar Planet. Sci. Conf. 8, p.1-15.
(2) Wetherill, G.W., (1975) Proc. Lunar Sci. Conf. G, p.1539-1561.
(3) Hartmann, W.K., (1973) J.G.R. v. 78, p.4096-4116.
(4) Soderblom, L.A., Condit, C.D., West, R.A., Herman, B.M., and Kreidler, T.J., (1974) Icarus v. 22, p.239-263.
(5) Neukum, G. and Wise, D.U., (1976) Science v. 194, p.1381-1387
(6) Pike, R.J., (1980), Proc. Lunar Planet. Sci. Conf. 11, p.2159-2189.

D34

MERCURY: NEW IDENTIFICATION OF ANCIENT MULTI-RING BASINS AND IMPLICATIONS FOR GEOLOGIC EVOLUTION

Paul D. Spudis, U.S. Geological Survey, Flagstaff, AZ 86001 and Dept. of Geology, Arizona State Univ., Tempe, AZ 85287

Initial examination of photographs of Mercury provided by Mariner 10 almost a decade ago revealed the presence of numerous impact features including large basin-sized structures [1]. In subsequent studies of these photographs, many workers have attempted to make a systematic inventory of the large basin population of Mercury [2-7]. Recent geologic mapping of the Michelangelo (H-12) quadrangle [8] indicates that the regional geology is strongly controlled by the presence of four large, nearly obliterated multi-ring basins [9]. Under this impetus, a systematic survey of the entire Mariner 10 coverage of Mercury was performed to determine the number, distribution and dimensions of additional ancient basins on the planet (Table 1).

Ancient multi-ringed basins on Mercury can be recognized by the following criteria: 1) arcs of massif chains and isolated massifs that protrude through younger units; 2) arcuate segments of lobate ridges (rupes) that align with massifs in circular patterns; 3) arcuate scarps that are aligned with ridges and massifs; and 4) isolated regions of anomalously high topography within the intercrater regions of heavily cratered terrain. All of the newly identified basins predate the mercurian intercrater plains, previously held to be the oldest geologic unit on the planet [10]. The degradational state of these features is comparable to ancient lunar basins such as Al-Khwarizmi-King [11, 12] and some nearly obliterated martian multi-ring basins [13]. Thus, the current inventory (Table 1) is probably an underestimate due to the relatively poor Mariner 10 photographic coverage of Mercury. These multi-ring basins are here named for unrelated, superposed craters and named plains regions, following a similar practice developed for naming degraded lunar basins [12].

Subsequent structural evolution of various regions has been influenced by the presence of these basins. A global network of lobate ridges (rupes), interpreted as thrust faults, had been previously recognized [14]. In many cases, the arcuate trend of these ridges outlines an ancient basin ring (e.g., Hero Rupes, part of ring 2 of Vincente-Yakovlev). In other instances, a more-or- less continuous ridge network may encounter a pre-existing basin ring obliquely, follow the outline of that ring, deflect in towards the next ring and re-establish the circular outline of an inlying ring (e.g., Adventure-Discovery Rupes and rings 3-5 of Andal-Coleridge). These relations suggest that although the ridge system is probably related to global compression, local trends are controlled by pre-existing structural patterns provided by ancient multi-ring basins.

Extensive smooth plains deposits were recognized in the initial geologic mapping effort of [10], but controversy over the origin of this unit continues [14, 15]. The distribution of smooth plains materials on Mercury has been remapped for this effort. Smooth plains units appear to be more extensive than mapped by [10] and more than 90 percent of them appear to be basin contained or basin related. As none of these ancient basins has preserved ejecta deposits, it is unlikely that the smooth plains units are an ejecta facies from the basins. Moreover, a paucity of large fresh basins within the study region of Mercury precludes a Cayley-type origin for the majority of these deposits. A typical occurrence is the expanse of smooth plains at lat -25°, long 100° where the rings of adjacent basins Bartok-Ives and Matisse-Repin intersect. The concentration of extensive smooth plains material within and associated with basin structural and depositional environments suggests a volcanic origin for most of this unit, analogous to the lunar maria.

The new identifications of mercurian basins may change concepts of cratering histories for the terrestrial planets. Previous studies of mercurian basins have all emphasized the apparent deficiency of basins on Mercury relative to the Moon [2-4, 7]. Cumulative basin density on Mercury ($D \geq 200$ km) is reported by [7] to be only 37 percent of that of the Moon. The Moon has at least 62 basins ($D \geq 200$ km; [4]) resulting in a average density of 1.72 ± 0.13 per 10^6 km^2.

Only about 35 percent of Mercury's surface was photographed with lighting conditions adequate [16] to recognize ancient basin structures. The newly identified basins suggest that Mercury has at least 50 basins ($D \geq 200$ km) within this area. Thus, the average density of mercurian basins is 1.92 ± 0.14 per 10^6 km^2. This value suggests that Mercury is not deficient in multi-ring basins and may possibly have more per unit area than the Moon. The presence of a large population of multi-ring basins that pre-date the mercurian intercrater plains suggests that basin production was a more- or- less continuous process during the early history of planets, and lends support to hypotheses of continually declining cratering rates [17] rather than to a late "cataclysm" model of basin production.

The recognition of a large number of previously unrecognized ancient multi-ring basins on Mercury has several implications concerning the geologic evolution of terrestrial planet crusts. It now appears that all terrestrial bodies with preserved ancient surfaces (Moon, Mercury, Mars) have a large population of multi-ringed impact structures. All of the newly discovered mercurian basins pre-date the intercrater plains on a planetwide basis. This relation suggests a distinct epoch of intercrater plains formation that at least partly erased the pre-existing crater population, leaving remnants of only the largest structures. Thus, the process responsible for formation of the intercrater plains units must have been a planetwide phenomenon. The hypothesis that the intercrater plains material is a primordial crust [10] appears untenable; if it were, a spectrum of multi-ring basin preservation states would be evident. The mercurian intercrater plains material may be at least partly volcanic [18], its surface morphology having been disrupted by the last phases of heavy bombardment. The tendancy of global tectonic patterns to be locally influenced by multi-ring basin structure appears analogous to similar patterns on the Moon [19] and Mars [13]. Thus, basins appear to provide the basic structural pattern of early terrestrial planetary crusts. The concentration of regional smooth plains deposits within and associated with ancient basins argues for a dominantly volcanic origin for this material, analogous to the lunar maria and martian highlands plains (e.g., Sinai Planum [13]).

REFERENCES [1] Murray, B. et al.(1974) Science 185, 169 [2] Wood, C. and Head, J. (1976) PLSC 7, 3629 [3] Malin, M. (1976) PLSC 7, 3589 [4] Schaber, G. et al. (1977) PEPI 15, 189 [5] DeHon, R. (1978) NASA TM 79729, 150 [6] Croft, S. (1979) Ph.D. Thesis, UCLA [7] Frey, H. and Lowry, B. (1979) PLPSC 10, 2669 [8] Spudis, P. and Prosser, J. (in press) USGS Map, H-12 quadrangle [9] Spudis, P. (1983) GSA Ann. Mtg. 16 [10] Trask, N. and Guest, J. (1975) JGR 80, 2461 [11] El-Baz, F. (1973) Science 180, 1173 [12] Wilhelms, D. and El-Baz, F. (1977) USGS Map I-948 [13] Schultz, P. et al. (1982) JGR 87, 9803 [14] Strom, R. et al. (1975) JGR 80, 2478 [15] Wilhelms, D (1976) Icarus 28, 551 [16] Strom, R. (1979) Space Sci. Rev. 24, 3 [17] Hartmann, W. (1975) Icarus 24, 181 [18] Strom, R. (1977) PEPI 15, 156 [19] Wilhelms, D. (in prep) Geologic history of the Moon, USGS Prof. Paper.

TABLE 1. ANCIENT MERCURIAN MULTI-RING BASINS

Basin[1]	Confid.[2]	Center	Ring Diameters[3] (km) 1st	2nd	3rd	4th	5th	Comments[4]
Borealis	2	73°, 53°	-	-	860	1530	(2230)	Partially mapped by [16]
Gluck-Holbein	3	35°, 19°	240	500	950	-	-	
Derzhavin-Sor Juana	2	51°, 27°	-	560	740	890	-	Partially mapped by [4]
Sobkou	1	34°, 132°	-	490	850	1420	-	Partial arcs: 810, 1010, 1280; partially mapped by [6]
Chong-Gauguin	3	57°, 106°	220	350	580	940	-	
Brahams-Zola	1	59°, 172°	340	620	840	(1080)	-	Partial arcs: 500, 740, 940
Donne-Moliere	3	4°, 10°	375	700	(825)	1060	1500	
Hiroshige-Mahler	1	-16°, 23°	150	355	(700)	-	-	
Mena-Theophanes	1	-1°, 129°	260	475	770	1200	-	Partially mapped by [4]
Tir	1	6°, 168°	380	660	950	1250	-	
Budh	2	17°, 151°	-	580	850	1140	-	
Ibsen-Petrarch	2	-31°, 30°	425	640	930	1175	-	
Andal-Coleridge	1	-43°, 49°	(420)	700	1030	1300	1750	
Matisse-Repin	1	-24°, 75°	410	850	1250	(1550)	(1900)	"Haydn-Raphael" of [6]
Bartok-Ives	3	-33°, 115°	480	790	1175	(1500)	-	
Hawthorne-Riemenschneider	2	-56°, 105°	270	500	780	1050	-	
Vincente-Yakovlev	1	-52°, 162°	360	725	950	1250	(1700)	
Eitoku-Milton	1	-23°, 171°	280	590	850	1180	-	
Boccaccio-Scopas	3	-82.5°, 44°	360	600	930	(1310)	-	

1 Basin nomenclature after system developed for ancient lunar basins [12]

2 Confidence level of identification: 1 - definite; 2 - probable; 3 - possible.

3 Numbers in parentheses reflect uncertain ring continuity; assignment to the five ring rankings is arbitrary.

4 Partial arcs are concentric structures confined to one side of basin; previous studies that are referenced mapped portions of larger, multi-ring structures recognized here.

D35

N84 23466

RING SPACING OF MERCURIAN MULTI-RING BASINS AND BASIN RING FORMATION

R. J. Pike, U. S. Geological Survey, Menlo Park, CA 94025, and P. D. Spudis, U.S. Geological Survey, Flagstaff, AZ 86001 and Dept. of Geology, Arizona State Univ., AZ 85287.

Introduction: Recent systematic mapping of Mercury has revealed many ancient and previously unrecognized multi-ring basins [1]. The population of these basins now stands at 20, possibly is as large as 25, and includes at least 76 measurable rings. From the new data base, we present some systematics of basin ring spacing on Mercury, compare them with similar data for the Moon, and draw some preliminary conclusions on conditions of ring formation for basins on the terrestrial planets.

Observations: The rings of basins on Mercury are spaced at an interval that increases incrementally outward by approximately $2^{-2}D$, the multiplier first recognized to best describe rings of the fresh lunar multi-ring basin, Orientale [2]. The incremental spacing of basin rings is evident from graphical analysis. Plotting ring diameters against that of the physiographically strongest ring [3] for each basin in the $\log_{10}$ domain [4] separates most of the 76 mercurian rings into five linear clusters (Figure 1), which are subparallel, slope at about unity, and are spaced at roughly 2^{-2}. Rings are not evenly distributed, but vary from six to 14 per cluster. Some rings fall between the better-defined trends, and in four cases, two closely-spaced rings from the same basin occupy a position normally filled by only one. These five distributions, plus a sixth formed by plotting the strongest ring against itself, constitute an empirical statistical model for ring spacing on Mercury. If the six groups are numbered I through VI, in order of increasing ring size, the strongest and most frequently occurring ring, the topographic rim, ranks as IV. Provisional taxonomy followed here for the other ring groups is: (I) Inner, (II) Peak, (III) Intermediate, (V) Outer-1, and (VI) Outer-2. The equivalent ring diameters are $D_{I...VI}$.

The six groups in Figure 1 have familiar lunar equivalents. Mercury groups II through VI are essentially the five clusters of lunar rings evident in Figure 27 of [3]. The same five groups also seem to be the classes of lunar rings identified by [4], their "inner" ring group being equivalent to Mercury groups II and III. Ring groups II, III, and IV correspond, respectively, to the lunar central-peak ring, intermediate ring, and outer ring of [5]. Mercury ring groups I through V also correspond to the six lunar classes of [6], his two types of "intermediate" rings being equivalent to Mercury group III. The sixth ring on Mercury is an outer arc whose lunar counterpart may be represented by the Imbrium "outer ring" [7], but is rare [6].

Ring intervals on Mercury correspond well to the $2^{-2}D$ model, although variance within the five groups in Figure 1 (see also [8]) precludes treating the $2^{-2}D$ spacing as a deterministic "law." Departures of observed from theoretical spacings, which are attributed to sample size, statistical scatter, and the degraded state of many of the ancient mercurian basins [1], are evaluated by fitting each ring group with a least-squares expression and calculating $D_{I...VI}/D_{IV}$ for the geometric mean of D_{IV}. Differences between this ratio and the closest fractions or multiples of D^{-2} range from 0.011 (D_I) to 0.046 (D_{VI}) (Table 1). Analogous values of percentage deviations for rings of multi-ring basins on the Moon are similar. However, lunar values of r are higher than those of Mercury, slopes of the lunar equations are much closer to unity, and an inverse dependence of ring-ratio deviation upon sample size that is evident for the 56 lunar rings is tenuous for the 76 mercurian rings (Table 1). These differences likely reflect the much better preservation of basin rings on the Moon.

Of the five equations relating D_{IV} to other ring diameters on Mercury, that describing D_{II}/D_{IV}, for the peak ring,

$$D_{II} = 0.251\ D_{IV}^{1.106} \qquad (1)$$

ring spacing include: 1) pre-existing target structure and topography associated with older basins [17,18]; 2) lithospheric thickness at the time of basin impact [19,20]; and 3) subsequent endogenic modification of basin topography [3,15,16,21]. This scheme differs critically from other "wave" models [13,22]: basin ring topography is not the result of a "frozen" traveling wave in rock, but rather derives from structural failure at discrete zones of weakness induced by concentrations of standing-wave stress. Such a model appears to accommodate most geologic and physical observations of basin rings on the terrestrial planets [6,11,15,16].

REFERENCES: [1] Spudis, P. (1983) this volume; [2] Fielder, G. (1963) Nature 198, 1256; [3] Hartmann, W. and Wood, C. (1971) Moon 3, 3; [4] Wilhelms, D. et al. (1977) Impact Expl. Cratering, 539; [5] Head, J. (1977) Impact Expl. Cratering 563; [6] Croft, S. (1981) PLPSC 12A, 227; [7] Wilhelms, D. and McCauley, J. (1971) USGS Map I-703; [8] Clow, G. and Pike, R. (1982) LPS XIII, 123; [9] Pike, R. (1983) LPS XIV, 610; [10] Pike, R. (1982) NASA TM 85127, 117; [11] McCauley, J. (1977) PEPI 15, 220; [12] Head, J. (1974) Moon 11, 327; [13] Baldwin, R. (1981) PLPSC 12A, 275; [14] Chadderton, L. et al., (1969) Nature 223, 259; [15] Schultz, P. (1976) Moon Morph., 626 p.; [16] Spudis, P. (1982) Ph.D. thesis, Ariz. State Univ., 292 p.; [17] Spudis, P. and Head, J. (1977) PLSC 8, 2785; [18] Schultz, P. and Spudis, P. (1978) LPS IX, 1033; [19] Melosh, H. and McKinnon, W. (1978) GRL 5, 985; [20] McGetchin, T. et al. (1979) NASA TM 80339, 168; [21] Schultz, P. (1979) Conf. Lunar Highlands Crust, 141; [22] Murray, J. (1980) Moon and Planets 22, 269.

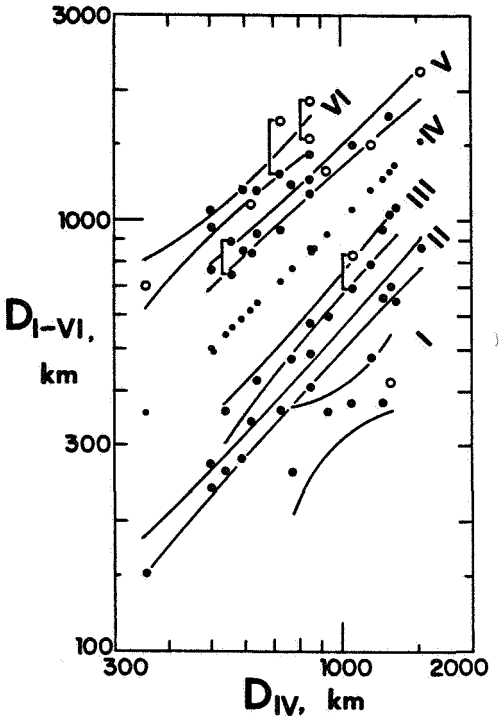

Figure 1. Ring diameter, $D_{I...VI}$, (n=76) as a function of Topographic rim diameter, D_{IV}, for 20 multi-ring basins on Mercury [1]. Lines are 95% confidence intervals for five resulting clusters of rings. Accompanying linear least-squares fits, spaced at roughly $2^{-2}D$ increments, are given in Table 1. Open circles are partial arcs only [1]; bracketed points (see text) averaged for fits.

Table 1. Theoretical and Observed Ring Spacing for the Moon and Mercury

Ring	n	Slope	$D_{I...VI}$ at D_{IV}=1.0 km	Ring Ratio* $D_{I...VI}/D_{IV}$ (Theor.)	(Obs.)	Deviation ((T-O)/T)	r	1-Slope
				MERCURY				
I	6	0.87	0.85	0.354	0.35	+0.01	0.85	+0.13
II	13	1.106	0.251	0.500	0.507	-0.014	0.990	-0.11
III	10	1.201	0.176	0.707	0.698	+0.013	0.988	-0.20
IV	20	--	--	1.000	--	--	--	--
V	14	0.934	2.198	1.414	1.362	+0.037	0.985	+0.07
VI	9	0.917	3.248	2.000	1.908	+0.046	0.964	+0.08
				MOON				
I	4	0.92	0.35	0.354	0.33	+0.06	0.99	+0.08
II	15	1.028	0.415	0.500	0.505	-0.010	0.989	-0.03
III	11	1.010	0.669	0.707	0.721	-0.020	0.996	-0.01
IV	15	--	--	1.000	--	--	--	--
V	9	1.022	1.178	1.414	1.364	+0.035	0.992	-0.02
VI	2	1.0	1.8	2.000	1.8	+0.1	--	--

* Geometric mean

is of special interest. Average D_{II}/D_{IV} is 0.51, almost identical to 0.50 D_i/D for the 34 two-ring basins on Mercury described by

$$D_i = 0.338\ D^{1.071}, \qquad (2)$$

where D is the outer ring and D_i the inner ring. The two distributions thus are sufficiently similar for their combined 47 data points to be represented by a single expression,

$$D_{II} = 0.406\ D_{IV}^{1.036}, \qquad (3)$$

for which average D_{II}/D_{IV} is 0.50. The lunar case is similar [9]. Protobasins, where on Mercury (n=20)

$$D_i = 0.394\ D^{0.998}, \qquad (4)$$

are omitted from the fit because their inner rings differ so obviously in geometry from those of two-ring and multi-ring basins [10]. Equation (3) slopes slightly more than 1.0. Slopes of each of the two original equations (1,2) exceed unity by more than this, but not enough for peak rings of two-ring basins (eq. 2) to align with intermediate rings of multi-ring basins, the next-highest group of rings in Figure 1:

$$D_{III} = 0.18\ D_{IV}^{1.20}. \qquad (5)$$

Moreover, average D_{III}/D_{IV} for the 10 intermediate rings is 0.70, far in excess of the 0.50-0.51 ratio of all D_{II}/D_{IV} distributions on Mercury.

Adjacent rings observed for a basin on Mercury do not always occupy adjacent groups in Figure 1. For example, the four rings of the Eitoku-Milton basin [1] fall into groups II, IV, V, and VI, but not III. However, the $2^{-2}D$ spacing still applies to this basin, because all its other rings belong to $2^{-2}D$ groups; the D_{III} position simply is unoccupied. Thus not all adjacent observed rings, e.g., rings II and IV of Eitoku-Milton, are necessarily spaced at the $2^{-2}D$ interval. Instead, some are spaced at multiples or fractions of it, such as 2.0 or 0.5 [3]. The "missing" ring III of Eitoku-Milton basin may have formed but is now buried, or it may not have formed initially. It follows further that the 0.5 D_i/D spacing frequently documented for two-ring basins (e.g., eq. 2) could be a variant on the $2^{-2}D$ spacing wherein a potential ring position always remains unfilled in small basins. The 0.5 interval of two-ring basins thus could have arisen from the same fundamental mechanism(s) that formed the multiple rings of larger basins.

Discussion: The striking regularity of ring spacing on both the Moon and Mercury (Table 1) strongly suggests physical control by some periodic function. Numerous models have been proposed for basin ring origin, including active megaterracing [11], passive megaterracing [12], "nested" craters due to crustal layering [4], and "tsunami-like" deformation in fluidized rock [13]. The constancy of ring spacing for multi-ring structures on the Moon and Mercury suggests that standing [14], not traveling [13], waves are involved in ring formation. The physics of standing wave patterns on solid planetary bodies was discussed in detail by [14], who demonstrated that both concentric and radial stress patterns result from a point-source release of energy. Standing stress waves from a large impact could have created concentric patterns of rock failure, resulting in multiple rings of predominently structural origin [3]. Numerous geologic studies have marshalled evidence for structural deformation associated with basin rings [3,11,15,16].

We suggest that basin rings form by complex brittle failure of rocks along annular zones of stress induced by standing waves. Secondary effects that modulate the basic pattern of constant

IMPACT ORIGIN OF UPHEAVAL DOME, UTAH

E. M. SHOEMAKER, U.S. Geological Survey, Flagstaff, AZ and
K. E. Herkenhoff, California Institute of Technology, Pasadena, CA

Reexamination of Upheaval Dome in the Canyonlands National Park, Utah, has shown that the structure of this remarkable feature conforms with that expected for a deeply eroded astrobleme. The structure is definitely not compatible with an origin due simply to plastic flowage of salt and other rocks in the underlying Paradox Formation, as suggested by McKnight [1]. The most strongly deformed rocks at Upheaval Dome are bounded by a series of circumferential listric faults. Beds of the Wingate Sandstone, Kayenta Formation, and Navajo Sandstone are displaced toward the center of the dome. Near the center, these same beds have been deformed by convergent flow into tight to open folds that plunge away from the apex of the dome. Thinning of the Wingate Sandstone reported by McKnight [1] is due entirely to faulting. At the center of the dome, beds of the Moenkopi Formation are duplicated by displacement along numerous small thrust faults. Sand from the underlying White Rim Sandstone Member of the Cutler Formation has been mobilized and injected into the Moenkopi as large massive clastic dikes.

The convergent displacement of the rocks at Upheaval Dome corresponds to the deformation that results from collapse of a transient cavity produced by high-speed impact. Beneath the listric faults, beds are deformed in a broad structural dimple that is bounded, at least on the north, by a partial circumferential anticline. This type of structure is produced by plastic flow of rocks at great depth beneath large impact craters. Asymmetry of the development of the deep anticline suggests that impact may have been from the south. Growth of a central dome probably was due partly to early convergent flow during opening of the initial cavity, as well as to late stage collapse. It is likely that the presence of plastic beds in the Paradox Formation at depth facilitated early growth of the dome.

From considerations of the probable depth of exposure of the impact structure and upward extrapolation of the listric faults, the final collapsed crater is estimated to have been about 8 to 10 km in diameter; the impacting body probably was on the order of 0.5 km in diameter. As much as 2 km of beds appear to have been removed by erosion since the impact structure was formed. Restoration of this thickness of rocks suggests that the impact occurred in latest Cretaceous or Paleogene time.

Reference

[1] McKnight, E. T., Geology of area between Green and Colorado Rivers, Grand and San Juan Counties, Utah, U.S. Geol. Survey Bull. 908, 147 p., 1940.

D37 N84 23468

MORPHOLOGY OF FRESH CRATERS ON GANYMEDE AND THE ORIGIN OF PEDESTAL CRATERS

Vicki M. Horner and Ronald Greeley, *Department of Geology, Arizona State University, Tempe, AZ 85287*

Properties of the planetary surface and subsurface can affect the morphology of impact craters (1). We propose a mechanism to explain pedestal craters and domed floors within fresh craters on Ganymede. Voyager 1 and 2 images with resolutions ≤3.2 km/lp were examined and 523 fresh craters have been identified. For each crater, the rim and ejecta diameters were measured, and the crater was characterized by ejecta class(es), interior features, floor morphology and target terrain. Of the craters examined, 97 show moderate to prominent doming of the crater floor; 340 craters have continuous ejecta which terminates in a scarp ["pedestal craters", (2)], of which 86 (25%) have a high-albedo diffuse deposit beyond the pedestal.

Even before Voyager spacecraft reached the Jovian system some researchers predicted that the high proportion of ice (detected spectroscopically) on the surfaces of the outer Galilean satellites would result in subdued and/or obliterated topography by slow, viscous relaxation (3,4). With the return of Voyager images, the domed floors seen within many craters have been cited as proof of a slow viscous relaxation effect (5,6). We observe, however, that 97 fresh craters show a moderate to prominent convexity, and within this group, 17 craters have ray systems (fig. 1), indicative of their relative youth. Most of the fresh craters with domed floors are larger than 40 km; the smallest fresh craters with domed floors are about 15 km in diameter. There appears to be no correlation between terrain type and fresh craters having domed floors. If we assume that crisp craters and ray systems are characteristic of relatively young craters (6), then floor doming either occurs immediately after impact or at times much less than those required for ray removal [~0.5–~2 b.y. (6)]. Recent work indicates that ice viscosity may be underestimated by several orders of magnitude–from earlier values of 10^{25} -10^{26} poise to ~10^{30} poise at $\overline{T}_{Ganymede}$ = 115 K (7). This increased "stiffness" would greatly inhibit a slow viscous relaxation of topography for essentially any fresh crater on Ganymede (7).

Pedestal crater ejecta are sometimes truncated in a given direction at terrain boundaries, or ridge-groove sets. Twenty-seven pedestal craters with truncated ejecta have been identified, suggesting that either: (1) some ridge/groove systems may have formed after the impact and pedestal emplacement, and thus transected the pedestal ejecta, or (2) as the ejecta flowed across the boundary, it was disrupted (possibly by turbulent flows) and was not preserved as a coherent blanket and pedestal.

Hypothesis 1 could explain some craters with truncated ejecta. However, for many craters in which the pedestal ejecta is truncated at a ridge/groove boundary, the crater is superimposed on the boundary and postdates it. In some cases material crosses terrain boundaries (fig. 2), and therefore hypothesis 2 may explain pedestal ejecta truncation. Presently, (2) seems to be the more acceptable explanation for most truncated pedestals. This would imply that the emplacement of pedestal ejecta can be affected by changes in surface topography, and therefore during part of the emplacement process the ejecta must travel along the surface.

As discussed above, 25% of all pedestal craters have an outer, generally high-albedo, diffuse annulus beyond the pedestal. Hypotheses for the origin of pedestals, which may reflect impacts into volatile-rich targets (2), must also include an explanation for this diffuse deposit. As the temperature difference between fusion and vaporization of H_2O is only 100 K at 1 bar, most ejected products from impact into ice will be steam and ice fragments. Kieffer and Simonds (8) show that at the 100 kb isobar within an icy target during impact, solid H_2O should begin to melt or vaporize, and that approximately five times as much melt and gas should be generated as would be expected for a granite target. They predict that the melt would be in the form of steam which would condense to snow (or rain) and disperse over a wide area. This may explain the bright outer ejecta deposits.

At surface temperatures ~115 K, ice should behave similar to silicate rock so that some of the target undergoes brittle deformation during impact. Previous work (e.g., 9) shows that for craters in silicates, a range of fragment sizes is ejected. If the ice fragments are ejected in sufficient quantities they could trap some of the escaping steam, so that the mass behaves as a lubricated flow. The mass would cease to flow when the gradual escape and/or condensation of the steam increases the density of the flow past some threshold value. This is similar to models proposed for martian flow ejecta crater emplacement. In particular, Carr et al. (10) hypothesize that after the ballistic emplacement of martian crater ejecta, the ejecta was sufficiently fluidized to continue flowing outward along the surface. A more recent hypothesis (11) includes martian crater ejecta in the form of rock fragments, ice, steam, and a small amount of water. The steam nucleates on the dust-sized ejecta, forming droplets with freezing times greater than the ballistic flight time, thus enhancing flow.

The effect of shockwave passage through ice may also explain the presence of convex floors within relatively fresh craters. Peak pressures occur closest to impact: for a 1 km diabase meteorite with an initial velocity of 17 km/sec, initial pressures at the impact site within an ice target have been calculated (8) to exceed 1900 kb, with 44% of the initial energy of the impact transferred to the ground. The distance to the 100 kb isobar from the impact site is calculated as 1.54 km; the distance to the 1 kb isobar from the origin is calculated as 5.20 km (8). Therefore, beyond the 100 kb isobar limit for ice phase transition (8), some energy is still imparted to the icy surface via the shockwave. Several researchers have indicated the possible importance for impacts into silicate rocks of the loss of material strength with the passing of the shockwave, and have tried to calculate the effects of a shockwave which reduces cohesive strength as the peak pressure is increased for given ranges from the impact (12,13). It was found that for a Mohr-Coulomb material with a von Mises limit, there is an increase in the final radius-to-depth ratio compared to calculations for craters where loss of cohesiveness was not considered (12,13). This loss of cohesiveness could correspond to a decrease in viscosity for icy target materials and thus facilitate topographic relaxation shortly after an impact. Impact cratering experiments (14) indicate that at high impact energies and low target viscosities, viscous topographic deformation does occur immediately after the impact event. Thus, much of the viscous relaxation of the crater floor could occur shortly after the impact event, before the site cools to its equilibrium temperature. We emphasize that this hypothesis does not preclude viscous relaxation resulting from higher surface heat flows early in the history of Ganymede (15).

REFERENCES

1) Wood, C.A., et al., 1978. Proc. Lunar Planet. Sci. Conf. 9th, 3691-3709.
2) Horner, V.M. and R. Greeley, 1982. Icarus 51, 549-562.
3) Johnson, T.V. and T.R. McGetchin, 1973. Icarus 18, 612-620.
4) Parmentier, E.M. and J.W. Head, 1979. J. Geophys. Res. 84, 6263-6276.
5) Smith, B.A., et al., 1979. Science 204, 951-972.
6) Passey, Q. and E. Shoemaker, 1977. in Satellites of Jupiter, 379-434.
7) Croft, S.K., 1982. Lunar Planet. Sci. Conf. XIV, 136-137.
8) Kieffer, S.W. and C.H. Simonds, 1980. Rev. Geophys. Space Phys. 18, 143-181.
9) Oberbeck, V.R., 1975. Rev. Geophys. Space Phys. 13, 337-362.
10) Carr, M.H., et al., 1977. J. Geophys. Res. 82, 4055-4065.
11) Malin, M.C., 1982. NASA TM 85127, 103-104.
12) Swift, R.P., 1977. in Impact and Explosion Cratering, 1025-1042.
13) O'Keefe, J.D. and T.J. Ahrens, 1981. Rev. Geophys. and Space Phys. 19, 1-12.
14) Greeley, R., et al., 1982. in Satellites of Jupiter, 340-378.
15) Cassen, P.M., et al., 1982. in Satellites of Jupiter, 93-128.

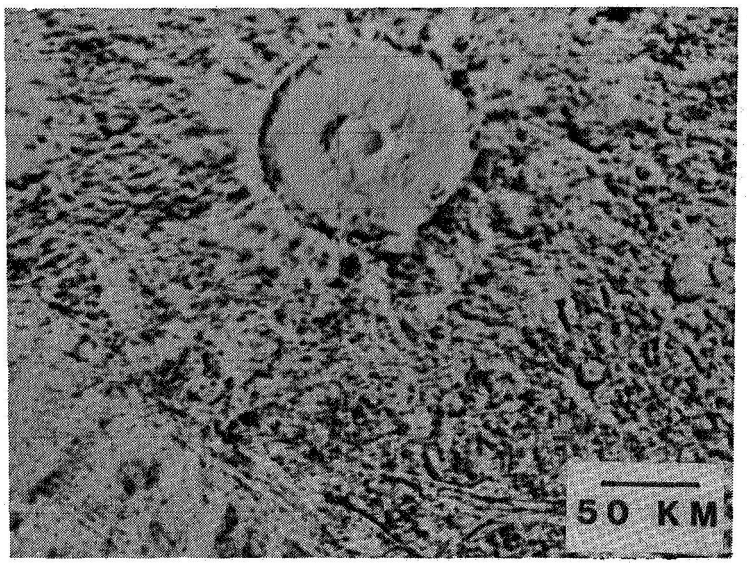

Figure 1. The crater Osiris, shown above, has the most prominent ray system on Ganymede yet the crater floor is convex. FDS 20637.59.

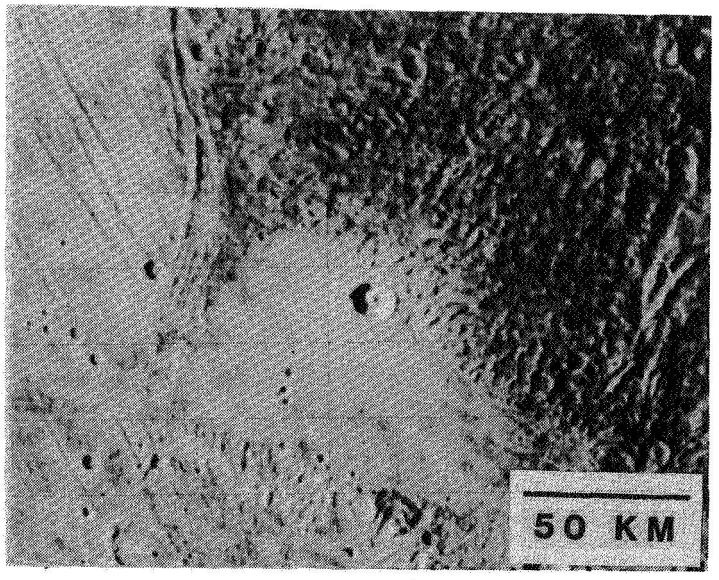

Figure 2. Although this impact occurred in the smooth plains, the ejecta crossed into the dark cratered terrain to the NE during emplacement. Compare the pedestal ejecta form represented on the smooth plain with the bright diffuse ejecta form on the ancient terrain. FDS 20640.25.

D38

N84 23469

Does "Saturation" Cratering exist in the Solar System?

William K. Hartmann, Planetary Science Institute, Tucson, Arizona 86719

A number of researchers, such as Strom, Woronow, and co-workers, have concluded that saturation equilibrium cratering exists nowhere in the solar system, and therefore that diameter distributions in even the most heavily cratered provinces reveal initial production functions related to impacting bodies. Based on this premise, they identify different populations of impactors in different epochs and regions of the solar system. These hypotheses are clearly crucial to interpreting planetary history and need further independent examination.

I have assembled my own crater counts on heavily cratered surfaces throughout the solar system. As shown in Figures 1 and 2, I found that the most heavily cratered regions of the lunar highlands, the lunar maria at small crater diameters, Mercury, Mars, Phobos, Deimos, Callisto, Mimas, Tethys, and Rhea all cluster around (within a factor 2) the same -1.83 power law for crater densities ($0.06<D<1448$ km). This envelope is well below the theoretically proposed saturation equilibrium values of Woronow, Strom, and Gurnis (1982, in Satellites of Jupiter, ed. D. Morrision), by a factor of about 2 to 6. A striking coincidence would be needed if all these surfaces were unsaturated but all had about the same crater density. Instead, I propose that the data points in Figures 1 and 2 define an empirical saturation level reached on some surfaces in different parts of the solar system.

The crater counts on frontside lunar uplands, used by Strom and coworkers as a basic reference curve identified with one of their populations of early impactors, are confirmed by my counts. However, this area is contaminated with ancient, ejecta-masked basalts (Hawke, Bell, and Clark, 1983, Natural Satellites Colloquium abstracts, Cornell). The crater population is deficient in 1 - 16 km craters, which may be obliterated by the lavas. Thus this curve is not representative of heavily cratered highlands, and is of questionable value as a standard comparison curve. The "pure" highlands show a "flatter", less structured curve, as shown in Fig. 1.

There is evidence of a turndown at large diameters in these populations. The production function in the outer solar system may differ from that in the inner solar system, as proposed by Woronow, Strom, and Gurnis (1982), but it is also possible that viscous relaxation of ice craters or immediate flooding of craters that penetrate through an ice lithosphere into watery substrate may explain the greater deficiency of large craters on icy moons. This problem is controversial and needs more study.

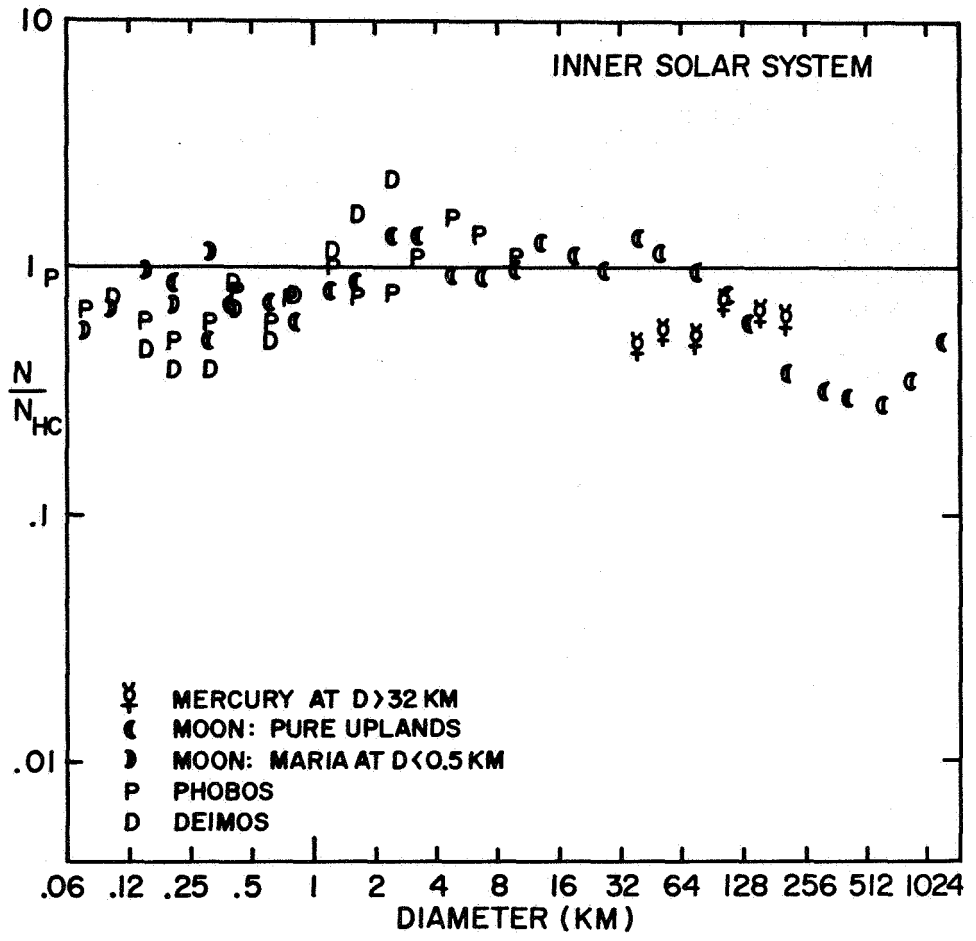

Fig. 1. Crater densities on the most heavily cratered surfaces in the inner solar system, including regions on Mercury, Moon, Phobos, and Deimos. The graph is a relative plot, showing observed number of craters/km^2 in each $\sqrt{2}$ diameter bin (N), relative to an estimated best fit for heavily cratered regions (N_{HC}). The solid horizontal line represents N_{HC}, which is a power law with exponent -1.83. Observed clustering of most counts from heavily cratered regions within a factor of 2 of this line suggests an empirical identification of saturation equilibrium cratering.

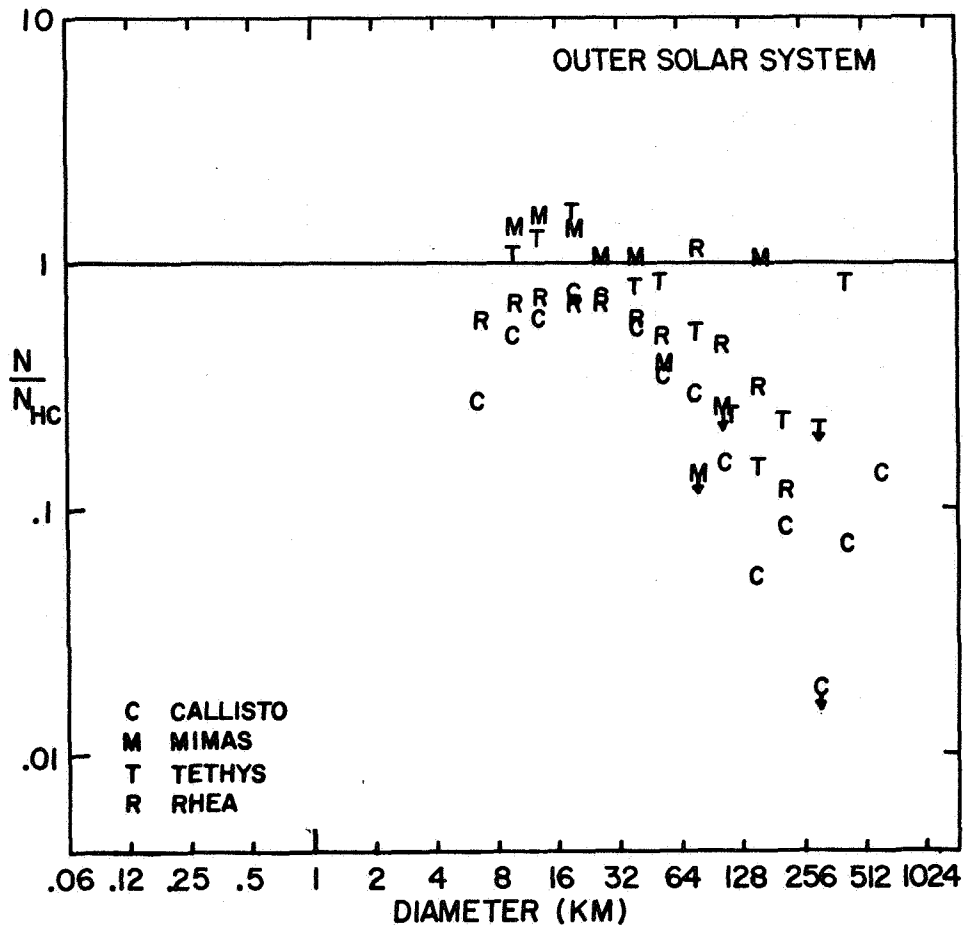

Fig. 2. Same as Figure 1, for four heavily cratered moons in the outer solar system. Coincidence of the maximum crater densities within factor 2 of values in inner solar system reinforces the suggestion of an empirical saturation equilibrium crater density, shown by the horizontal line. This line is well below the saturation equilibrium densities proposed theoretically by Woronow and co-workers, with consequent important implications about planetary surface evolution.

D39

N84 23470

DIFFERENTIAL DEGRADATION OF MARTIAN IMPACT BASINS

Marianne Stam, Department of Geology and Geography, University of Massachusetts, Amherst, MA 01003

Among the major problems of martian geologic history are the cause of the highland-lowland dichotomy, and of the scarp separating these two global-scale provinces. These features were formed after much of the early bombardment was completed (Wise et al., 1979); consequently, many of the surviving impact basins very likely were present during the creation of the dichotomy, and it is possible that differences in their present morphologies as a function of location and of relative age may provide clues to the tectonic and geomorphic processes responsible for the dichotomy and the scarp.

As an approach to the understanding of the geomorphic and tectonic processes active early in martian history, I am systematically mapping 5 basins with respect to the morphology of associated landforms, tectonic features, and materials. Tectonic and landform maps have been completed for three of the basins cited by Schultz et al. (1982): Ladon (-18°, 29°), Sirenum (-43.5°, 167°), and Al Qahira (-15.5°, 190°). These were chosen for their similar diameters (~1000 km) and for their wide geographic distribution. The tectonic maps portray features that are believed to be dominantly of endogenic or endogenic plus impact origin: ridges and scarps, massifs, knobs and platforms, grabens, and floor-fractured craters. The landform maps portray features dominantly of exogenic origin: narrow valley networks, outflow channels and associated chaotic terrain, longitudinal valley systems (Baker, 1982), furrowed crater walls, and zones of heavy to light furrowing. The areal distributions of some of the mapped landforms and structures contribute to the definition of the basin shape on photographs and maps, and the relative importance of different features for basin discrimination has been rank ordered for each basin. Other landforms and structures, although not contributing to our ability to discriminate the basin, do exhibit distributions suggesting some sort of control by the basin structure on their formation.

Preliminary results suggest that the inner rings of all three basins are best defined by concentric arrangements of massifs, knobs, and platforms. The outermost rings, however, seem best defined by scarps. In addition to these similarities, there are some interesting differences.

Ladon has a well developed radial system of narrow valley networks that clearly defines the innermost basin ring. Floor-fractured craters and furrowed craters appear to be abnormally abundant between the second and fourth definable rings (counting from the basin center). Large outflow channels and chaotic terrain also are associated with Ladon, and some segments of the scarp bounding the chaotic terrain have trends and positions suggesting structural control by the basin. Of particular interest is the absence of narrow valley networks associated with the younger and slightly overlapping basin to the SW (Holden). This rather

remarkable difference in two immediately adjacent basins is of potential significance for the histories of regolith volatiles and valley network formation, but more such data will be needed to develop a model.

In contrast to Ladon, the Sirenum basin shows poorly developed narrow valley networks, few floor-fractured craters, and no outflow or longitudinal valley systems. However, a well developed regional ridge system is deflected around the innermost and second rings (Chicarro et al., 1983), thus helping to define the basin form. Zones of lightly furrowed terrain also help define the basin form, particularly around the second ring. The trend and locations of grabens, on the other hand, seem unrelated to the basin structure.

Al Qahira is the most cryptic of the three basins. The most important features for basin definition (other than massifs, knobs, and platforms) are the approximately concentric arrangements of zones of furrowing, changes in the density of ridges, and changes in the width, depth, and trend of the longitudinal valley systems found east of the basin center. Narrow valley networks east of the basin center also seem to have a vague (but not very convincing) distribution concentric to the center of Al Qahira. These valley networks are much less well developed than those associated with Ladon, but better developed than those in the Sirenum area.

These preliminary results are encouraging because they demonstrate that there are, in fact, second-order differences in the present morphologies of impact basins that can be related to relative age or to location of the basins. These morphologic differences presumably reflect differences in the tectonic or geomorphic processes that have been active. Additional mapping of these and of other basins is needed to provide a larger data base for analysis. This work is in progress.

References Cited

Baker, V. R. (1982) The Channels of Mars. University of Texas Press, Austin.

Chicarro, A. et al. (1983) Basin Control of Ridge Patterns on Mars. Lunar and Planetary Science XIV, p. 105-106.

Schultz, P. H. et al. (1982) The Structure and Evolution of Ancient Impact Basins on Mars. JGR 87 (B12): 9803-9820.

Wise, D. U. et al. (1979) Tectonic Evolution of Mars. JGR 84 (B14): 7934-7939.

D40

N84 23471

PROGRESSIVE IMPACT CRATERING

R. A. De Hon, Department of Geosciences, Northeast Louisiana University, Monroe, LA 71209.

Most cratering experiments are designed to study the effects of a single hypervelocity impact into a target of uniform properties (1). Experiments involving multiple impacts are usually limited to low velocity projectiles and unconsolidated target materials. Gault (2) described saturation cratering in an unconsolidated target. Quaide and Oberbeck (3) studied crater forms produced by hypervelocity impact into layered targets. Several investigators (4, 5, 6) have modeled the generation of either a regolith or megaregolith by repeated impact on planetary surfaces.

Studies now in progress examine changes in crater morphology and target properties by repeated impact into an initially consolidated target. Current studies employ low velocity projectiles (2 g at 0.5 km/sec) and consolidated salt targets. Records of crater size, morphology, and accumulated ejecta thickness are maintained as impacts collect on the surface.

Initial impacts into the target block produce simple, bowl-shaped craters (approximately 3.2 cm diam. and 1.5 cm deep) with minor structural rims. During this early stage of cratering, while impacts are essentially in unaltered target material, all ejecta is fine-grained. Once crater saturation is reached and impacts begin to impinge on previously formed craters, large blocks of ejecta begin to dominate the growing ejecta mantle. At this later stage, craters tend to be 2 to 5 times larger than the initial craters and exhibit irregular morphologies. The overall morphology is largely controlled by the irregular thickness of the ejecta mantle, the irregular boundary between solid substrate and concomitant mantle, and the distribution of large blocks within the ejecta mantle.

Continued impact comminution of the surficial materials by repeated impact reduces the population of large blocks and increases the thickness of the surficial mantle by bulking of ejecta and continued quarrying of the substrate. In this late stage of cratering, craters acquire classic bowl-shaped morphologies with well-defined ejecta rims. The overall crater dimensions increase to greater than 10 times the size of the initial craters in an unmodified target material.

Current studies are obviously constrained by experimental conditions to strength craters formed by a single impact energy at terrestrial gravity and atmospheric pressure. Nevertheless, these experiments shed light on the interaction between crater-forming processes and alteration of the target as impacts accumulate on the surface. At this scale, crater morphology is strongly controlled by irregular development of the surficial layer. The non-uniform nature of surface topography, mantle thickness, and substrate boundary layer precludes the development of a characteristic progression of crater forms as a simple function of increasing mantle thickness with time.

References

(1) Gault D. E. et al. 1968, in Shock Metamorphism of Natural Materials, Mono Book Corp., p. 8799.
(2) Gault D. E. 1970, Radio Sci., 5, 273-291.
(3) Quaide V. L. and Oberbeck V. 1968, Journ. Geophys. Res., 73, 5247-5270.
(4) Hartmann W. K. 1973, Icarus, 18, 634-639.
(5) Head J. W. 1976, Proc. Lunar Sci. Conf. 7th, 2913-2927.
(6) Housen K. R. et al. 1979, Icarus, 39, 317-351.

D41 N84 23472

ODE TO GRAVITY: DEPTH/DIAMETER FOR FRESH CRATERS ON MERCURY.

R. J. Pike and G. D. Clow, U. S. Geological Survey, Menlo Park, CA 94025.

Opinions conflict over the role of surface gravity in shaping impact craters on Mercury. One view holds that the effects of g are evident in measurable aspects of crater form; other investigators find little or no evidence for g's geomorphic importance (see review by Strom [1]). We believe that ambiguity in the role of g and other variables in cratering on Mercury stems largely from uncertainty in identifying major geomorphic contrasts and the crater sizes at which they occur. One of these, depth/diameter (d/D), undergoes a major change at the transition from simple (bowl shaped) to complex (peaks and terraces) crater interiors [2].

Four least-squares d/D fits for fresh craters on Mercury have been attempted [3-6]. The results are inconsistent. Here we present d/D data that should resolve previous shortcomings. The revised d/D distributions for simple and complex craters, which intersect at a diameter of about 5 km, support the initial thesis [3] that g substantially influences the form of Mercury's craters.

We calculated depth and diameter for 316 fresh craters 225 m to 160 km across. The selected craters have a crisp overall morphology, continuous rims, and where resolution permitts, some indication of textured ejecta or satellitic craters. The shadow-length technique used to calculate depth further limited the sample to craters close to the terminator, mostly in the Northwest quadrant of the imaged hemisphere. The craters were divided into two subsets on the basis of terrain type: "cratered terrain" (CT) and "smooth plains" (SP) [7], mostly by interpretation of photomosaics [8].

Mean rim-to-rim diameters and maximum (bowl-shaped interior) or mean (complex interior) shadow lengths were measured directly on Mariner-10 images with an optical comparator. Repeatability of measurements was judged very good. Shadow tips were identified without photometric analysis [9], but visual discrimination of shadow umbra from penumbra introduced no detectable error into the depths. Positional data from the latest Mercury control net eliminate errors in the published SEDR parameters that resulted from camera-pointing uncertainties. Depths and diameters were obtained by calculations that accommodate virtually any spacecraft altitude or look angle, location on the planet, or degree of foreshortening. Bowl-shaped craters wherein the shadow tip lay more than 5% D from the crater center were rejected.

We recognized four morphologic classes among the 250 remaining craters: Simple (deep, bowl shaped); Modified Simple (less deep, bowl shape but very small, usually unidentifiable, central feature); Immature Complex (wall failure but no terrace (s), maybe a central peak; similar to lunar Class TRI [10]; Mature Complex (terraces and peaks; like lunar Class TYC [10]).

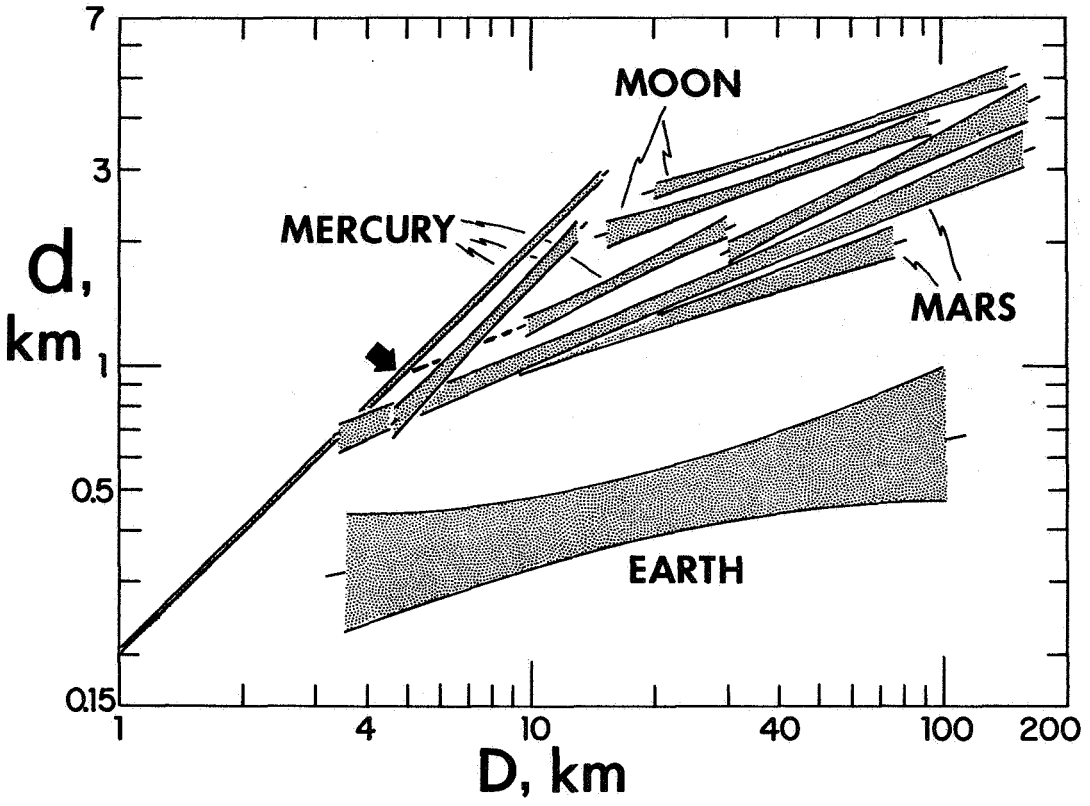

Figure 1. Least-squares fits, with 95% confidence interval, to depth/diameter (d/D) data for Mercury (Table 1) and three other silicate planets (Pike, 1980). For Mercury, the crater distributions from left to right are Simple, Modified Simple, Immature Complex, and Mature Complex (confidence envelope not given for combined complex-crater fit, only partly shown by heavy dashes). Curves for other planets describe complex craters only. Upper curve for the Moon is upland (n=37), lower curve mare (n=20). For Mars, upper curve is cratered terrain (n=54), lower curve plains (n=51). The curve for Earth represents 12 craters. Arrow indicates intersection of simple and complex d/D curves for Mercury at 0.95 $\pm$ 0.11 km/ 4.8 $\pm$ 0.6 km

Linear least-squares fits to the d/D distributions at the 95% confidence level (Figure 1, Table 1) differ from previous results. The equation for Mercury's simple craters, whose d/D remains a high 1/5 throughout, resembles those for simple craters on the Moon and Mars [2]. Earth's craters are shallower. The expression for all complex craters (immature plus mature), is steep and falls between those for lunar and Martian complex craters, but lies closer to the Martian curves. It intersects the simple-crater equation at a diameter of 4.8 $\pm$ 0.6 km, about half the value reported from prior analyses of d/D [3-6]. The CT/SP contrasts in d/D for each class of crater are too small to show up in Figure 1, thus supporting the thesis [7,11] that contrasts in the Mercurian substrate have little effect on crater shape.

The 4.8 km intersection diameter, $D_{d/D}$, for Mercury is consistent with the direct gravity-scaling of depth for complex impact craters on silicate bodies. The inverse monotonic relation between $D_{d/D}$, in km, and g, in cm/sec^2, roughly $D_{d/D} = 3 \times 10^3\ g^{-1}$, for craters on Mercury, Earth, the Moon, and Mars [2, Table 3], applies primarily to the first three bodies. The $D_{d/D}$ value for Mars, 3.1 $\pm$ ca. 0.5 km, is lower than expected, an anomaly that could well reflect the volatile-laden Martian crust. Evidence for a non-1.0 inverse g-scaling of crater depth, probably about -0.25, for non-silicate bodies [12] awaits reliable d/D data for fresh craters on the outer satellites.

REFERENCES: [1] Strom, R. G., 1975, Space Sci. Revs., 24, 3-70; [2] Pike, R. J., 1980, Proc. Lunar Planet. Sci. Conf. 11th, 2159-2189; [3] Gault, D. E., et al., 1975, J. Geophys. Res., 80, 2444-2460; [4] Malin, M. C., and Dzurisin, D., 1977, J. Geophys. Res., 82, 376-388; [5] Mouginis-Mark, P. J., and Wilson, L., 1979, Lunar Planet. Sci. X, 873-875; [6] Pike, R. J., and Clow, G. D., 1982, NASA Tech. Memo. 85127, 120-122; [7] Cintala, M. J., Wood, C. A., and Head, J. W., 1977, Proc. Lunar Sci. Conf. 8th, 3409-3425; [8] Davies, M. E., Dwornik, S. E., Gault, D. E., and Strom, R. G., 1976, Atlas of Mercury; [9] Pike, R. J., and Arthur, D. W. G., 1979, NASA Tech. Memo. 80339, 132-134; [10] Wood, C. A., and Andersson, L., 1978, Proc. Lunar Planet. Sci. Conf. 9th, 3669-3689; [11] Smith, E. I., and Hartnell, J. A., 1978, Moon and Planets, 19, 479-511; [12] Basilevsky, A. T., 1981, Dokl. USSR Acad. Sci., 258, 323-325.

TABLE 1. LEAST-SQUARES FITS TO DEPTH/DIAMETER FOR MERCURIAN CRATERS

Class	n	r	Slope	95% C.I. for Slope	d at D= 1 km	95% C.I. for d at D=1km
SIMPLE	104	0.997	0.995	0.981-1.010	0.199	0.194-0.204
MODIFIED SIMPLE	19	0.975	1.029	0.908-1.150	0.151	0.116-0.197
IMMATURE COMPLEX	69	0.766	0.490	0.389-0.590	0.410	0.309-0.544
MATURE COMPLEX	58	0.823	0.496	0.408-0.589	0.353	0.244-0.503
COMPLEX (ALL)	127	0.898	0.418	0.382-0.454	0.492	0.435-0.557

D42

MORPHOMETRY OF BURIED CRATERS: LAVA THICKNESS ESTIMATES BY SIMULATED FLOODING.

Ted A. Maxwell and Victoria F. Avery, Center for Earth and Planetary Studies, National Air and Space Museum, Smithsonian Institution, Washington, D.C. 20560

Partially and completely buried craters on planetary surfaces are used as probes to determine the thickness and extent of the overlying material as well as the composition of underlying terrain units. Rims of craters protruding through mare basalts on the Moon have been used extensively by DeHon (1977, 1979) to develop isopach maps of both the circular and irregular maria. Such estimates are possible because of Apollo topographic data and the extensive coverage by Lunar Orbiter photographs at various sun angles. On planetary surfaces without such data, however, shadow measurements can only be made by pixel listings with appropriate assumptions concerning support data. In addition, high resolution geochemical data is not available to determine whether the exposed crater rim is composed of material dissimilar from the lavas. Because of the need for lava thickness data, we have simulated flooding of lunar mare and highland craters for which topographic data is available in order to determine empirical relationships between dimensions observed in orbital images and the thickness of the "lava". The method is similar to that proposed by Baldwin (1970), but differs in that detailed Apollo topography is used for the analysis.

For the simulated flooding, the percent of rim height flooded above the surrounding terrain (beyond the ejecta) was measured for crater exterior thickness estimates (Re), and the percent of crater depth flooded was measured for interior estimates (Ri; using rim height to the bottom of the crater). In the case of exterior estimates, the percent of rim height flooded was compared to the diameter of the exposed crater (De), ratioed to rim crest diameter (D). Five highland craters were used in the study, ranging in diameter from 13 to 140 km, as well as six mare craters with a smaller diameter range of 10 to 23 km. Because of the extreme variations in topography surrounding the highland craters, the relationship between Re and exposed diameter (De) is particularly dependent on an arbitrary determination of De. In contrast, craters on level terrain such as the lunar maria would be circled symmetrically by lava and exhibit a logarithmic relationship between the geographic extent of the remaining crater and the percent of rim elevation flooded (Fig. 1). For the 6 mare craters studied, a relationship of:

$$Re = 0.66e^{5.11\ D/De}$$

provides a good fit ($r = 0.93$) to the simulated flooding.

In order to use observed crater morphology to estimate the thickness of interior crater fill, the simulation of lava flooding was continued after the rim was breached. Using the same set of lunar craters, the percent of crater depth flooded has been plotted as a function of the extent of observed original crater rim (Ri/D). External flooding of the ejecta blanket was held at a constant level as the crater filled. As

would be expected from hummocky and flat-floored craters, initial flooding rapidly obscures floor relief, yet contributes little to the thickness. As lava rises to the steeper slopes of the interior walls, the thickness increases rapidly with the corresponding decrease in exposed rim. Finally, when the lava level within the crater equals that outside, obscuration of the rim occurs more rapidly until the entire crater is buried. Based on these observations of the simulation, the relationship between exposed rim and lava thickness is divided into three sections, and each was fit with a linear regression (Fig. 2).

In previous estimates of lava thicknesses on the Moon, DeHon and Waskom (1976) noted that a wide range in error was introduced by using the rim width/diameter measurements to determine depth of burial. However, since no detailed topographic data are available for Mars (unless resorting to pixel counts or image modeling), estimates of lava thickness based on flooded crater morphometry provide an independent check on pixel measurements and the ability to study areas not covered by images with suitable sun angles. The method proposed here is applicable to studies of volcanic flood volumes as well as load-induced tectonism. The use of these relationships is dependent on the topographic characteristics of the pre-lava terrain, the degradation state of the flooded crater, and for applications to other planets, the assumption of similar crater morphometry. We are presently applying this method to 260 craters in the western hemisphere of Mars which have been classified according to degradation and type of flooding. The resulting thickness estimates will be compared with previous estimates of thicknesses for the Tharsis region (Plescia and Saunders, 1980), and will be used for further stratigraphic and structural studies.

References

Baldwin, R.B., 1970, A new method of determining the depth of the lava in lunar maria. Pub. Astron. Soc. Pacific, v. 82, p. 857-864.

DeHon, R.A., 1977, Mare Humorum and Mare Nubium: Basalt thickness and basin-forming history. Proc. LSC, 8th, p. 633-641.

DeHon, R.A., 1979, Thickness of the western mare basalts. Proc. LPSC, 10th, p. 2935-2955.

DeHon, R.A. and Waskom, J.D., 1976, Geologic structure of the eastern mare basins. Proc. LSC, 7th, p. 2729-2746.

Plescia, J.B. and Saunders, R.S., 1980, Estimation of the thickness of the Tharsis lava flows and implications for the nature of the topography of the Tharsis plateau. Proc. LPSC, 11th, p. 2423-2436.

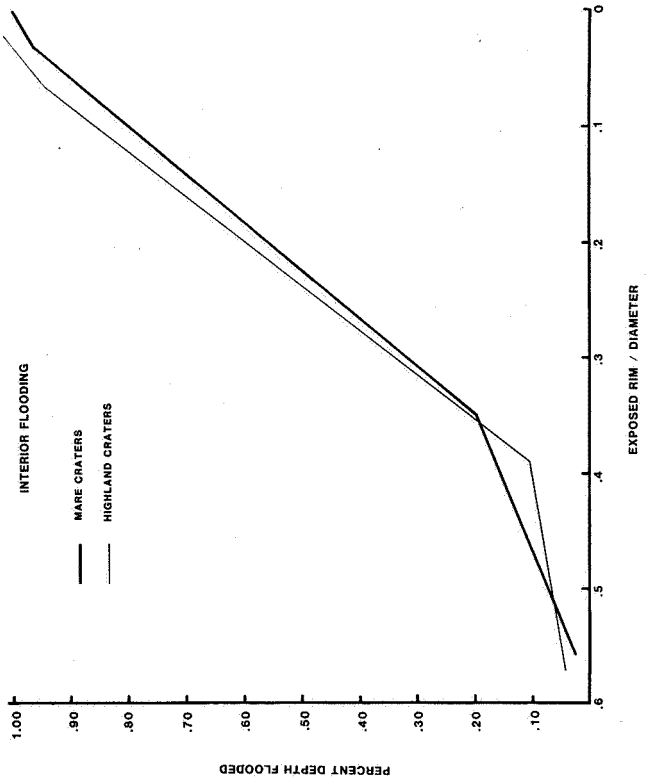

Figure 2

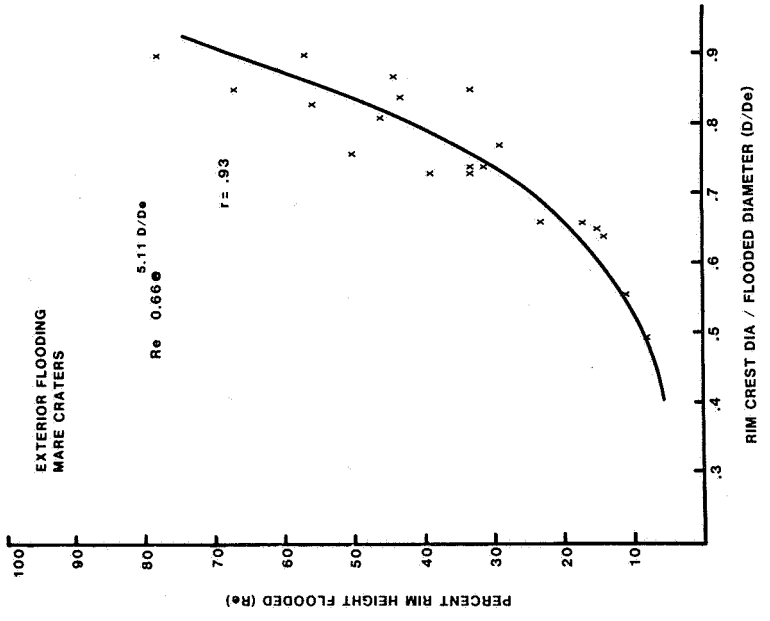

Figure 1

D43

N84 23474

THE BOREALIS BASIN OF MARS

Don E. Wilhelms, U.S. Geological Survey (MS 46), Menlo Park, CA 94025 and Steven W. Squyres, NASA Ames Research Center (MS 245-3), Moffett Field, CA 94035 [1].

Why the lowlands of Mars are concentrated in the northern hemisphere and the highlands in the southern hemisphere is probably the most fundamental unsolved problem in martian geology [2]. No explanation that accounts both for this asymmetric distribution and for the isostatic equilibrium across the scarp or sloping transition zone dividing the two provinces [3] has been generally accepted; thinning of the lithosphere in the northern hemisphere by internal processes has been suggested [4]. Because other lowland-highland distributions on Mars [5], Moon, and Mercury are controlled by impact basins, we propose that a giant basin formed early in Mars' history has caused the martian hemispheric dichotomy as well.

We found that many massifs and narrow plateaus that are not parts of a previously known basin lie along a small circle which coincides with the largest contiguous parts of the highland-lowland province boundary (fig. 1). The circle is about 7,700 km (130° of latitude) in diameter (measured along the surface curvature) and is centered at 50° N., 190° W. The area south of the circle contains almost all of the cratered highland province, including lowlands concentrated in previously known basins. Most of the terrain north of the circle is lowland, including Vastitatis Borealis and Amazonis, Arcadia, Elysium, and Utopia Planitiae. We propose that the circular alignment of mountains and scarps defines a 7,700-km basin, which we call Borealis because it encloses Vastitatis Borealis and because of its northern location [1].

The Borealis basin readily accounts for (a) the largest otherwise unexplained topographic depression on Mars, (b) the corresponding restriction of heavily cratered highlands to outside the basin rim, that is, to terrane probably underlain by basin ejecta or to prebasin terrane, (c) existence and concentric orientation of massifs and narrow plateaus not related to other basins, (d) isolated highland tracts surrounded by lowland plains but lying along the circle (for example, the Mareotis-Tempe terra), (e) redistribution of mass from the lowlands to the highlands followed by isostatic compensation, (f) abrupt scarps between highlands and lowlands, most of which are readily explained as parts of the inward scarp of the basin's rim, and (g) the annular transition zone of highland breakup, localized by the rim and inner wall of the basin. Locally the breakup zone has retreated outside the trace of the basin rim, as in Acidalia Planitia.

A possible objection to the proposed basin, that such a large impact might destroy the planet, is answered by the fact that the 2,500-km South Pole-Aitken basin and the 3,200-km Procellarum basin did not destroy the smaller Moon [6]. The radius of Procellarum is 0.92 times that of the Moon and the radius of the Borealis basin is 1.1 times that of Mars (3,394 km). Basins penetrate less deeply in proportion to their diameters than do small, simple craters [7], and therefore inflict less damage than their

great diameters might suggest. Judging from the lack of mantle material in the samples returned from the Moon [8] even the giant Procellarum basin did not substantially penetrate the 74±12-km-thick lunar crust [6,9]. If the depth/diameter ratios of the Borealis and Procellarum basins were the same, Borealis did little damage below 175 km, only 5 percent of Mars' radius.

The energy required to form a basin as large as Borealis is readily attained by a large impact. Calculations based on scaling relations for small craters suggest that a body 600 km in diameter, having a density of 3.0 g/cm^3, and impacting at 24 km/s (the orbital velocity of Mars), would generate the requisite energy [1]. Moreover, a significantly smaller body would suffice for a proportionally shallower excavation.

The probability that such a large impact occurred on Mars is supported by estimates based on ancient impact rates on the Moon. Basins cover the lunar terra [10,11]. At least 39 basins $\geq$300 km in diameter were formed before emplacement of the visible mare basalts began about 3.8 aeons ago [11]. Stabilization of the lunar crust by about 4.2 aeons [12] sets an approximate maximum age for the oldest observed basins. Therefore, during this 400-million-year interval a population of large projectiles created lunar basins at a minimum rate of 98 per aeon. Extrapolation of the basins' size-frequency distribution [based on data from 11] shows that the same population impacting at the same rate would theoretically contain projectiles capable of producing a 7,700-km basin once every 3.5 aeons on the Moon or once every 0.9 aeon on the 3.8-times larger area of Mars. The odds of such a large basin forming on Mars are even more favorable if the basin-production rate was greater than the lunar rate or if the impact rate was greater before 4.2 aeons ago, both of which are likely [13]. Creation of a basin the size of Borealis on Mars is therefore consistent with the distribution of highlands and lowlands on Mars and with the early impact history of the terrestrial planets.

---

[1] This is a condensation of a paper submitted in August 1983 for publication in Nature. The research was funded by the Planetary Geology Program, NASA (DEW) and by a National Research Council postdoctoral fellowship (SWS). [2] Mutch T. A., Arvidson R. E., Head J. W., Jones K. L. & Saunders R. S. (1976) The Geology of Mars: Princeton, 56; Carr M. H. (1981) The Surface of Mars: Yale, 65, 73. [3] Janle P. (1983) The Moon and the Planets **28**, 55-67. [4] Wise D. U., Golombek M. P. & McGill G. E. (1979) JGR **84**, 7934-7939. [5] Wilhelms D. E. (1973) JGR **78**, 4084-4095; Schultz H. & Glicken H. (1979) JGR **84**, 8033-8047; Schultz H., Schultz R. A. & Rogers J. (1982) JGR **87**, 9803-9820. [6] Whitaker E. A. (1981) Multi-ring basins: Geochim. Cosmochim Acta suppl. 15, 105-111; Wilhelms D. E. (1982) NASA TM 85127, 111-113; Wilhelms D. E. (1983) Lunar & Planetary Sci. XIV, 845-846. [7] Baldwin R. B. (1963) The Measure of the Moon: Chicago, 166; Head J. W., Settle M. & Stein R. S. (1975) Proc. Lunar Sci. Conf. 6, 2805-2829. [8] Herzberg C. T. & Baker M. B. (1980) Proc. Conf. on Lunar Highlands Crust: Geochim. Cosmochim. Acta suppl. 12, 113-132. [9] Basaltic Volcanism Study Project (1981) Basaltic Volcanism on the Terrestrial Plan-

ets: Lunar & Planet. Inst., 671. [10] Howard K. A., Wilhelms D. E. & Scott D. H. (1974) Rev. Geophys. Space Phys. **12**, 309-327. [11] Wilhelms D. E. (in press) The Geologic History of the Moon: U.S. Geol. Survey Prof. Paper. [12] Taylor S. R. (1982) Planetary Science: A Lunar Perspective: Lunar and Planet. Inst., 246. [13] Soderblom L. A., Condit C. D., West R. A., Herman B. M. & Kreidler T. J. (1974) Icarus **22**, 239-263; Neukum G. & Wise D. U. (1976) Science **194**, 1381-1387; Hartmann W. K. (1976) Icarus **31**, 260-276; ref. 9, 1075-1081.

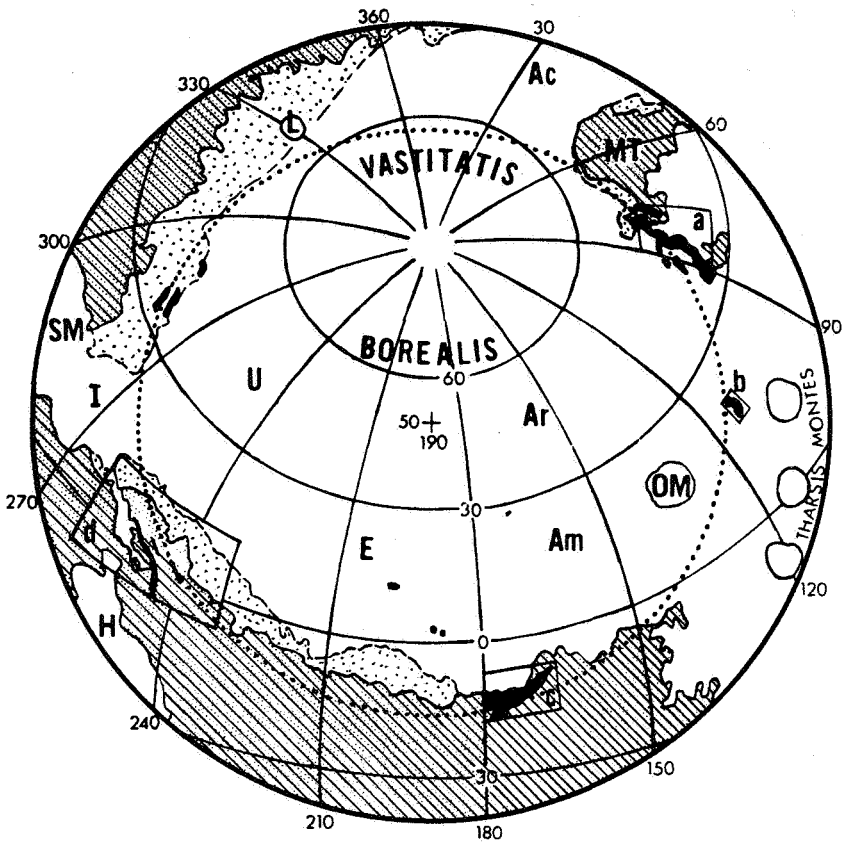

Fig. 1. Polar stereographic projection of part of Mars centered about 50° N., 190° W. Dotted circle indicates inferred rim of Borealis basin. Ac, Am, Ar, E, H, I, SM, U = Acidalia, Amazonis, Arcadia, Elysium, Hesperia, Isidis, Syrtis Major, and Utopia Planitiae, respectively; L = Lyot, 215-km ringed basin; MT = Mareotis-Tempe terra; OM = Olympus Mons. Black = massifs and narrow plateaus believed part of Borealis basin (including 3 near E that may be part of inner ring); shaded = other highland terrain; stippled = modified highland terrain in the highland-lowland transition zone (frets, chaos, knobs, channels, etc.); blank = young terrain (including OM and three Tharsis Montes shown separately). (The numbered boxes refer to figures in [1]).

N84 23475 D44

CRATERING HISTORY OF THE SATURNIAN SATELLITES J.B. Plescia, Jet Propulsion Laboratory, California Institute of Technology, Pasadena, CA 91109 and J.M. Boyce, EL-4, NASA Headqauters, Washington, D.C. 20546.

In an attempt to relate the observed crater frequencies on the saturnian satellites (Plescia and Boyce, 1982,1983) with absolute time, we have modeled the cratering history of the Saturn system. The model is based upon several assumptions. First, the cumulative flux history at saturn resembles that of the inner solar system. That is to say, a high cratering rate which rapidly (exponentially) decayed over the first few hundred million years followed by a significantly lower but more constant flux to the present (Wetherill, 1975; Shoemaker, personal communication). Second, the end of the heavy bombardment occured about 3.7-3.8 b.y. ago. Third, Population I craters, dominated by large diameters and having a shallow size-freqeucny distribution slope (Smith et al., 1981,1982), were formed during the period of heavy bombardment. Population II craters, characterized by small craters and a steep distribution slope, have formed since the heavy bombardment ended.

Before the observed crater frequencies can be intercompared between satellites a correction must be made for the gravitational focusing of projectiles by Saturn. The focusing results in an increase in the cratering rate with decreasing orbital radii, i.e. rates are lowest at Iapetus and highest at Mimas. To correct for this effect the observed crater frequencies for Iapetus have been held constant and those of the other satellites reduced by factors (based on data from Smith et al., 1982) ranging from 1.9 for Rhea to 20 for Mimas.

The model uses the distribution of 20 km craters. This diameter was choosen because it balances statistics with resolution. Maximum resolution on the saturnian satellites ranged from 1 km/lp to 17 km/lp hence crater counts could not be consistently made at diameters < 20km. The frequency of craters observed on the satellites varies by an order of magnitude between the least and most cratered surfaces. On some of the least cratered surfaces, such as the plains of Dione and all of Enceladus, crater > 20 km are either few or completely lacking. Hence use of a larger size would have required extrapolating from smaller diameters.

Under the assumption that the differing populations of craters reflect syn- and post- heavy bombardment, the crater frequency corresponding to the end of the heavy bombardment was estimated. Most of the cumulative size-frequency distributions obtained could be assigned to either Population I or II based on the slope of the distribution and the largest crater size observed. The crater freequency which seperated the two groups was assumed to represent the freqquency at which the heavy bombardment ended.

The projectiles which produced Populaion I craters were from a variety of sources. Shoemaker and Wolfe (1981) have estimated the contribution from several sources; Jupiter family, Saturn family and long period comets and concluded that the Saturn family comets dominate. They and Smith et al. have interpreted the Population II craters to be the result of either material ejected from the satellites during large impacts events (i.e. Hershcel or Odysseus) and from the destruction of small co-orbiting bodies (i.e. Dione B). Finally they propose a third population of objects which is responsible for the current cratering with a flux so low that it is reflected only the in micrometeor size range.

We disagree with the proposed origin of the objects which produced population II craters. Blocks of material ejected from the satellites would be of relatively small mass and have low velocity, as escape velocties are only a few hundred meters per second. Ultimately the ejected debris would return with approximately the original velocity. It seems highly unlikely that craters 20-30 km in diameter could be formed by small low velocity impacts. Such a process would also predict that the highest density of such "secondary" craters would occur on the trailing hemisphere contrary to what is observed. Using the the observed crater frequencies to estimate the local flux rate at each satellite at various times it appears statistically unlikely that co-orbiting bodies like Dione B would be destroyed after the end of the heavy bombardment to produce debris to form Population II craters.

We therefore interpret Population II craters to be the result of projectiles from outside the saturn system, i.e material in solar orbit or in orbit around Saturn with high inclinations, eccentricities and periods. The source population of the projectiles appears to have evolved over time as reflected in the slopes of the size-frequency distributions. The less cratered the surface is (i.e. the younger it is) the steeper the slope of the distribution. This suggests that the larger projectiles were being removed from the parent population by some process with time.

The modeled flux predicts a "normalized" cratering rate approximately equal to that of the Moon at 3.5 b.y. and about an order of magnitude lower since then. This is consistent with estimates of the cratering rate at Saturn by others (e.g. Hartmann, 1977).

Crater frequencies thus indicate that the majority of surfaces on the satellites are > 3.5 b.y old. Activity on Tethys, Rhea and Mimas occured > 3.5. b.y. ago. Dione appears to have had a more prolonged history with activity extending to < 3.0 b.y. with the formation of the plains and lobate deposits. Enceladus displays surfaces which range in age from 3.7 b.y. to perhaps the present. The age ranges appear to indicate that a correlation exists between the length of endogenic activity and the bulk

density of the satellite. The higher the bulk density the longer the body appears to have been active.

This research was carried out at J.P.L. under contract with N.A.S.A.

References:

Hartmann, W.K., (1977) Icarus 31, 260-276.
Plescia, J.B. and Boyce, J.M., (1982) Nature 295, 285-290.
Plescia, J.B. and Boyce, J.M., (1983) Nature 301, 666-670.
Shoemaker, E. M. and Wolfe, R. F., (1981) Abst. Lunar Planet. Sci. Conf. Suppl. A. 1-3.
Smith B.A. et al., (1981) Science 212, 163-191.
Smith B.A. et al., (1982) Science 215, 504-537.
Wetherill, G.W., (1975) Proc. Lunar Sci.Conf. 6th, 1539-1561.

D45

N84 23476

GEOMORPHIC CLUES TO THE MARTIAN VOLATILE INVENTORY; I. FLOW EJECTA BLANKETS

David Pieri, Jet Propulsion Laboratory, Pasadena, CA
Stephen Baloga, U. S. Department of Energy, Washington, D. C.
Mary Norris*, Virginia Polytechnical Institute, Blacksburg, VA.
*NASA Summer Intern

The apparent role of volatiles is perhaps one of the most pervasive themes in martian geomorphology, and important in this context is the history and distribution of volatiles on Mars and related implications for climatic history. There are classes of landforms whose presence on Mars is strongly suggestive, if not confirmatory, of the participation of volatiles, presumably water, in its geomorphic development: (1) valley networks, (2) outflow channels, (3) landslides, and (4) flow-ejecta blankets. The first two may represent landforms generated by the movement of volatiles from sources, while the latter two probably represent the dissipation of energy generated by forcing inputs (e.g., kinetic energy and gravity) modulated by volatiles. In many areas on Mars, all four processes have acted on the same lithologic materials and were influenced by the composition of those units, and possibly by the climatic regime at the time of their formation. Inevitably, in any discussion of either valley networks (Ref. 1) or outflow channels (Ref. 2), the question of the amount and distribution of the generative volatiles (presumably groundwater) is raised, but has not yet been conclusively addressed for either landform. One of our approaches to this specific problem of landform genesis, and to the general problem of the present and past states of martian volatiles, is to attempt to constrain the distribution, amount, and history of available volatiles by using possible evidence of volatile participation expressed in the morphology of other related landforms (e.g., flow-ejecta blankets and landslides) coupled with physical models for landform genesis.

Previous work on flow-ejecta blankets has involved surveys of their distribution and morphology, as well as classification (Refs. 3, 4, 5, 6, 7, 8, 9, 10, 11, 12). Laboratory studies (Refs. 13, 14, 15) have shown that some of the full-scale martian ejecta morphology can be duplicated in miniature. Theoretical work has addressed the role of impact melt and volatiles (Ref. 16), ejecta as low-angle landslides (Ref. 17), and the possibility of atmospheric interaction (Ref. 18). While interesting work on landslides ("acoustic fluidization") suggests the possibility of emplacement of flow-ejecta without volatiles present (Refs. 19, 20), the prevailing opinion holds that flow-ejecta blankets probably result from optimally-sized impacts into volatile-rich layered substrate.

In an attempt to create a high-quality high-resolution data base of flow-ejecta morphology, we compiled a series of 16 morphologic maps and 4 stratigraphic/geologic unit maps from the best examples, with extensive use of stereo images where available. From these data, we have begun to develop our own preliminary classification scheme on the basis of primary morphologic characteristics (e.g., (1) single or multiple blankets, (2) squat or elongated lobes, (3) the presence or absence of radial stria-

tions) and secondary characteristics (e.g., (1) extent of blanket, (2) terrain of emplacement, (3) thickness of the blanket, (4) edge morphology, (5) albedo, and (6) extent of zone of ballistic ejecta). We have also begun a more quantitative assessment of volume of ejecta and the presence or absence of pre-existing craters, as well as detailed examinations of flow past obstacles in order to develop a constraint between the flow velocity and the blanket viscosity (or its analog) (Ref. 21).

We have begun to investigate the topographic profile of the flow-ejecta blanket as a constraint on the emplacement process, where ultimately we want to compare theoretically derived profiles to photogrammetric and/ or photoclinometric data. We have approached it as a "free-boundary" problem where the height of the flow is free to vary according to the details of the flow characteristics with local and total ejecta volume constraints. The location of the free boundary condition, namely the vanishing of the shear stress of its analog at the surface of the flow, must be determined as part of the solution. During the emplacement of the ejecta blanket, local mass conservation is guaranteed by the equation

$$\frac{dh}{dt} + \frac{1}{r} \cdot \frac{d}{dr} (r \cdot h \cdot J) = 0, \qquad (1)$$

where $h=h(r,t)$ is the location of the free boundary surface of the flow, r is the radial coordinate, and $J=J(h)$ is the local volume flux (volume per unit cross-sectional area per unit time) in the flow. Subject to appropriate boundary conditions, this equation governs the profile of the ejecta blanket. We also have the total ejection volume conservation law,

$$r_o \cdot h_o \cdot \int_o^t J(r_o, t)\, dt = \int_{r_o}^{r_f(t)} h(r,t)\, r\, dr, \qquad (2)$$

where the zero subscript indicates values at the ballistic to flow transition and r_f is the location of the flow front. This equation simply accounts for volume additions to the flow by modifying the integrated profile and delineates the region of validity of equation (1) by virtue of the explicit appearance of r_f. Although we cannot witness the dynamic evolution of an ejecta blanket, equation (2) provides the relation,

$$V_o = \int_{r_o}^{r_\infty} h(r, t \to \infty)\, r\, dr, \qquad (3)$$

where V_o is the total volume ejected and r_∞ is the observable terminal location of the blanket flow front. Whether we obtain V_o from estimates of the crater excavation or directly from photogrammetric and/or photoclinometric observations, this relation establishes an important constraint on any predictive free surface ejecta blanket model. Equations (1) through (3) must be supplemented with another physical law such as the Navier-Stokes

equation as a model for the dissipation of momentum in the layers of the ejecta blanket. This equation for the dissipation of momentum in a region limited by a free boundary location and equation (2) is the crucial link in determining the dependence of J on h. The heart of the analysis is to find reasonable theoretical models which yield a J(h) dependence consistent with the measured profiles and equation (3).

1. Pieri, D. C., 1980, Martian valleys: morphology, distribution, age, and origin, Science, 210, pp. 895-897.
2. Baker, V. R., 1982, The Channels of Mars, Univ. of Texas Press, 198 pgs.
3. Carr, M. H. et al., 1977, Martian impact craters and emplacement of ejecta by surface flow, J. Geophys. Res. 82, pp. 4055-4065.
4. Mouginis-Mark, P. J., 1978, Morphology of martian rampart craters, Nature 272, pp. 870-872.
5. Mouginis-Mark, P.J., 1979, Martian fluidized crater morphology: variations with crater size, latitude, and target material, J. Geophys. Res. 84, pp. 8011-8022.
6. Mouginis-Mark, P. J., 1981, Ejecta emplacement and modes of formation of martian fluidized ejecta craters, Icarus 45, pp. 60-76.
7. Allen, C. C., 1979, Areal distribution of martian rampart craters, Icarus 39, pp. 111-123.
8. Johansen, L. A., 1979, The latitude dependence of martian splosh cratering and its relationship to water, NASA Tech. Memo. 80339, pp. 247-249.
9. Boyce, J. M. and N. E. Witbeck, 1980, Distribution of thermal gradient values in the equatorial region of Mars based on impact crater morphology, NASA Tech. Memo. 82385, pp. 140-143.
10. Blausius, K. A. and J. A. Cutts, 1980, NASA Tech. Memo. 82385, p. 147.
11. Mutch, P. and A. Woronow, 1980, Martian rampart and pedestal craters' ejecta-emplacement: Coprates quadrangle, Icarus 41, pp. 259-268.
12. Horner, V. M. and R. Greeley, 1981, Martian ejecta flow craters, NASA Tech. Memo. 84211, pp. 75-76.
13. Greeley, R. et al., 1980, Impact cratering in viscous targets: laboratory experiments, Proc. Lunar. Planet. Sci. Conf. 11th, pp. 2075-2097.
14. Wohletz, K. H. and M. F. Sheridan, 1980, Rampart crater ejecta: Experiments and analysis of melt-water interactions, NASA Tech. Memo. 82385, pp. 134-136.
15. Fink, J. H. et al., 1981, Experimental impact craters formed in viscous fluids, NASA Tech. Memo. 84211, p. 81.
16. Kieffer, S. W. and C. H. Simonds, 1980, The role of volatiles and lithology in the impact cratering process, Rev. Geophys. Space Phys. 18, pp. 143-181.
17. Woronow, A., 1981, Preflow stresses in martian rampart ejecta blankets: a means of estimating water content, Icarus 45, pp. 320-330.
18. Schultz, P. H. and D. E. Gault, 1979, Atmospheric effects on martian ejecta emplacement, J.Geophys. Res. 84, pp. 7669-7687.
19. Melosh, H. J., 1983, Acoustic fluidization, Amer. Sci. 74, pp. 158-165.
20. Hsu, K. J., 1975, Catastrophic debris streams (sturtzstroms) generated by rockfalls, Geol. Soc. Am. Bull. 86, pp. 129-140.
21. Burgers, J. M., 1948, Advan. Appl. Mech. 1, p. 171.

Chapter 5

VOLCANIC PROCESSES AND LANDFORMS

N84 23477

D46

EAST BUTTE - A VOLCANIC DOME OF THE EASTERN SNAKE RIVER PLAIN, IDAHO

John E. Bretches and John S. King, Department of Geological Sciences, State University of New York at Buffalo, Amherst, N.Y. 14226

East Butte is one of three prominent domes (Big Southern, Middle, and East Buttes) located on the Eastern Snake River Plain. East Butte rises an average 350 m above the basalt flows which encircle its 2.4 km diameter base (fig. 1). It is located 51 km west of Idaho Falls, in the southeast corner

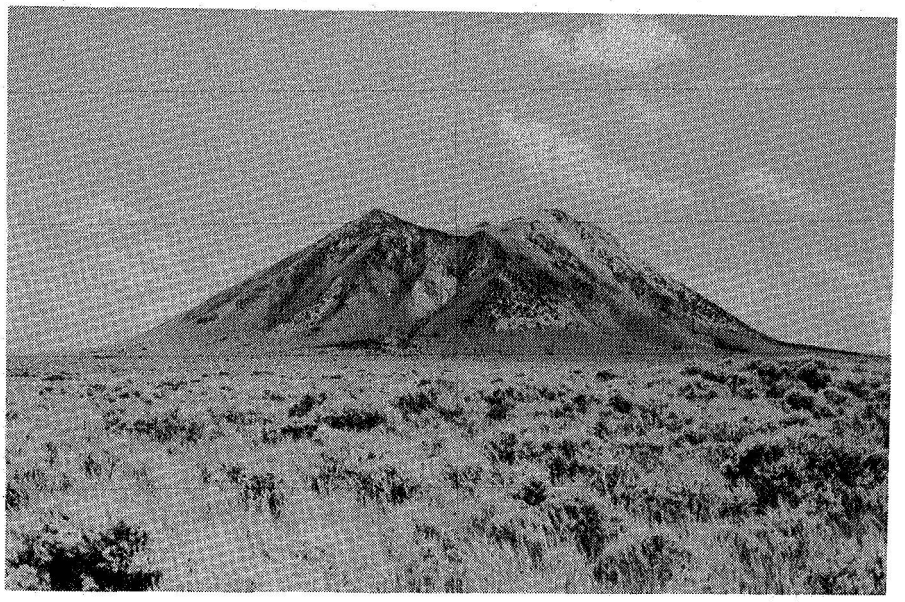

Figure 1. View of East Butte to the east-southeast from 2.5 km away.

of the Idaho National Engineering Laboratory facility. East Butte is composed nearly entirely of rhyolite, which can be placed into several groups based on megascopic appearance.

Previous investigations dealing with the Buttes of the Eastern Snake River Plain have yielded various interpretations for their origin. East Butte and Big Southern Butte were first thought to have been steptoes - ancient rhyolitic volcanoes surrounded by a sea of basalt (Russell, 1902). Stearns and others (1938) proposed that faulting was the key in the development of East and Middle Buttes. Faulting generated a mountain range which was later differentially eroded because of the existence of both silicic and mafic lavas. Two prominent highs (East and Middle Buttes) were the result of these processes. Only in the last 20 years were the Buttes identified as rhyolitic domes, and even more recent speculation suggests that the parent magma developed due to remobilization of a rhyolitic basement beneath the basalts (Spear and King, 1977).

Armstrong and others (1975) determined a K-Ar age of 0.6 $\pm$ 0.01 m.y. B.P. for the rhyolite of East Butte compared to 0.30 $\pm$ 0.02 m.y. B.P. for the rhyolite of Big Southern Butte, located 31 km to the southwest.

In this study, preliminary mapping has shown East Butte to be a single, large cumulo-dome composed dominantly of rhyolite. This rhyolite can be classified into three main groups based on color and structure. The first group, which makes up the largest volume of East Butte, consists of a massive, light to moderate gray rhyolite. The second group is also massive, but is reddish to pinkish gray in color. The third group is flow-layered with pinkish gray bands (fig. 2).

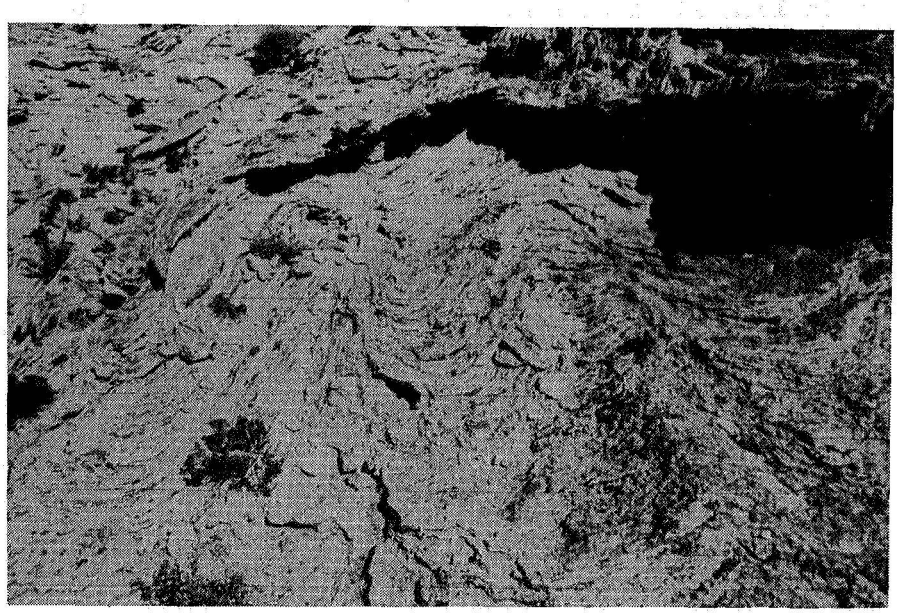

Figure 2. Flow-layered rhyolite on the south slope of East Butte. Width of photograph is approximately 5 meters.

In a reconnaissance petrographic study, Spear (1977) suggested that observed variations in the rhyolites of East Butte were due to the percentage of glass in the matrix. In this study, geochemical analyses of numerous samples will be carried out to determine if the color variations of the rhyolites are compositionally unique.

The rhyolite of East Butte is aphanitic with phenocrysts of sanidine and quartz which vary from 1 to 5 mm in length.

Vesicular reddish black inclusions of basalt up to 10 cm in length are found in all varieties of the East Butte rhyolites. These basalt inclusions are believed to have originated from fragmentation of the basalt walls of the conduit by rhyolitic magma as it was emplaced. Most of the inclusions contain plagioclase phenocrysts. These phenocrysts measure up to 1 to 2 cm in length and have a typical euhedral, tabular habit.

Figure 3 shows an example of one of the basalt inclusions in a flow-layered rhyolite on the south slope of East Butte. Rhyolite flow bands surround the inclusion indicating that it was carried up during the growth of the dome and followed flow patterns of the rhyolite until the silicic magma solidified.

Dips taken from various outcrops of flow-layered rhyolite observed on East Butte indicate that they are generally inclined away from the center,

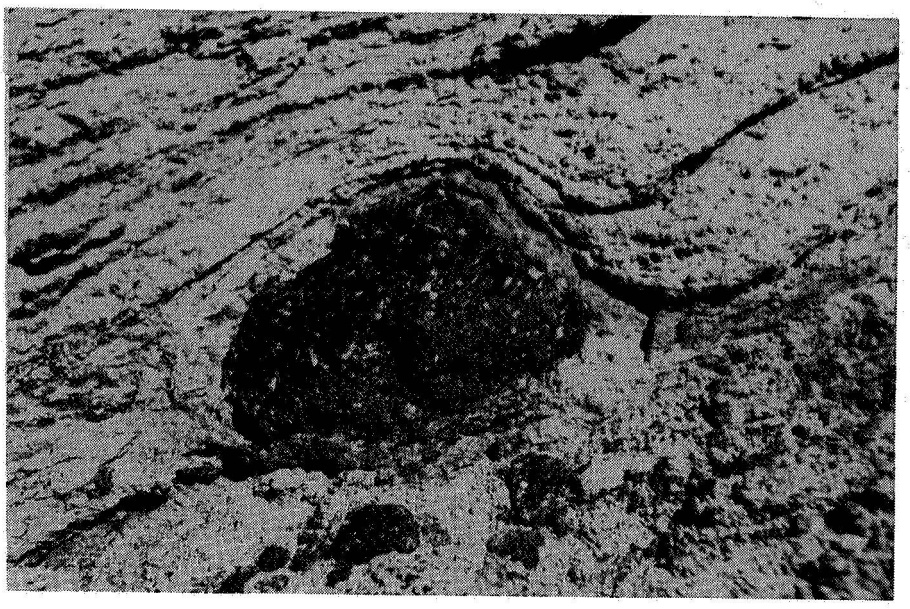

Figure 3. Basalt inclusion in flow-layered rhyolite of East Butte. Flow bands surround the inclusion. Size of the inclusion is about 10 cm.

although variations in the degree of dip readings around the Butte were observed.

A 250 m diameter depression which has the appearance of a crater is located at the top of East Butte. Evidence supporting the fact that the depression is a crater is displayed by three small (3 to 5 m in height) mounds of massive rhyolite which border the depression (fig. 4). These

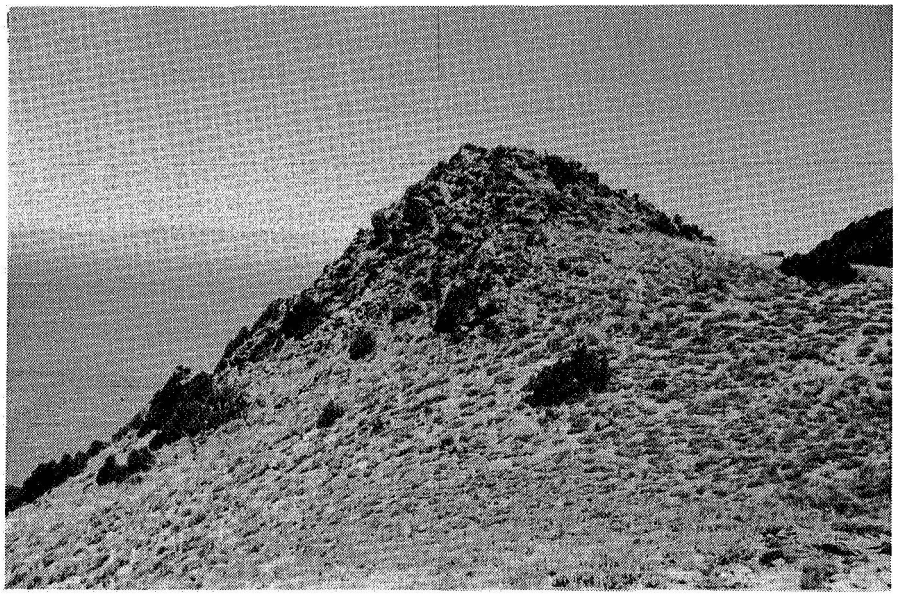

Figure 4. Rhyolite mound bordering the depression at the top of East Butte. Height of mound is approximately 4 meters.

mounds are believed to have been formed when viscous rhyolite magma was extruded from fractures which bounded the crater. These fractures may have resulted when a portion of the rhyolitic magma within the conduit leading to the top of East Butte withdrew. No other evidence was observed.

Volcanic morphologic features such as domes are not unique to the earth. The Gruithuisen dome region at the northwest edge of Mare Imbrium and the Rumker Hills in the northern Oceanus Procellarum are two such analogs found on the Moon. Although larger, these domes are morphologically similar to East Butte and other Buttes like it on the Eastern Snake River Plain. These lunar domes may have been created by processes similar to those which occur on the Snake River Plain and other terresrial volcanic provinces. A theory explaining the existence of lunar domes is a more viscous mafic lava, with possibly a slightly higher silica content, being extruded to form a steep-sided volcanic construct.

References:

Armstrong, R.L., W.P. Leeman, and H.E. Malde, 1975. K-Ar dating, Quaternary and Neogene volcanic rocks of the Snake River Plain, Idaho: Amer. Jour. Sci., v. 275, p. 225-251.

Russell, I.C., 1902. Geology and water resources of the Snake River Plains of Idaho: U.S. Geol. Survey Bull. 199, 192 p.

Spear, D.B., 1977. Big Southern, Middle, and East Buttes: in Greeley, R.C. and J.S. King, eds., Volcanism of the Eastern Snake River Plain, Idaho: A Comparative Planetology Guidebook, National Aeronautics and Space Administration, no. CR-154621, p. 114-120.

_____ and J.S. King, 1977. Big Southern and East Buttes, rhyolitic domes on the Snake River Plain in Idaho: in Arvidson, R. and R. Wahmann, eds., Reports of Planetary Geology Program, 1976-1977, National Aeronautics and Space Administration Technical Memorandum X-3511, p. 136.

Stearns, H.T., L. Crandall, and W.G. Steward, 1938. Geology and groundwater resources of the Snake River Plains in southeastern Idaho: U.S. Geol. Survey Water Supply Paper 774, 268 p.

CHRONOLOGY, MORPHOLOGY AND STRATIGRAPHY OF PUMICEOUS PYROCLASTIC- FLOW (IGNIMBRITE) DEPOSITS FROM THE ERUPTION OF MOUNT ST. HELENS ON 5/18/83

C. William Criswell and Wolfgang E. Elston, Department of Geology
University of New Mexico, Albuquerque, NM 87131

Between 1217 and 1620 hours (PDT), on May 18, 1980, the magmatic eruption column of Mount St. Helens formed an ash fountain (1) and pyroclastic flows dominated the eruption process over tephra ejection. Eruption-rate pulsations generally increased to a maximum at 1600 to 1700 hrs. After 1620 hrs, the eruption assumed an open-vent discharge (2) with strong, vertical ejection of tephra (3). Relative eruption rates (relative mass flux rates) of the pyroclastic flows have been determined by correlating sequential photographs and SLAR images (4), obtained during the eruption, with stratigraphy and surface morphology of the deposits.

The pyroclastic flows formed unwelded ignimbrite and cover approximately 15 km^2; the volume is estimated to be less than 0.5 km^3 (5). A preliminary stratigraphic column consists of pyroclastic units Pa, Pb, Pc, Pd and the ash-cloud deposit, unit Pe. Components of pyroclastic flows are poorly sorted dacitic ash and pumice clasts, crystals and variable amounts of lithic fragments. Flow deposits are enriched in crystals with respect to vitric ash, compared to pumice compositions. Finely comminuted vitric ash was reconcentrated in ash-cloud (nuee ardente) deposits northeast and downwind of the ignimbrite. Ash clouds did not form primary flows.

Unit Pa is a lower sequence (10 m exposed by erosion) of poorly stratified to locally well-bedded and graded ash-flow deposits, each about 10 cm to 1 m thick, containing several percent lithic lapilli. Unit Pb (6-10 m thick) is unstratified and contains several percent small lithic blocks and pumice lapilli. Its surface is relatively flat, consisting of low, ridged plains, locally mantled by lithic ash and lapilli, producing a smooth, dark-toned, modified plain (6). Surficial unit Pc (3-20 m thick) is graded block-and-ash flow containing disseminated and locally concentrated lithic blocks; it has a surface of ridged plains and marginal ridged channels (6), consisting of light-toned, fines-depleted pumice clasts. Unit Pd is a thin (2-4 m), local, poorly graded upper unit having abundant lithic and pumice lapilli; its surface is characterized by furrowed channels, incised into unit Pc. The furrowed channels are characterized by longitudinal erosional channels with inward dipping, low-angle scarps that truncate primary flow structures. In contrast, ridged plains and channels on surfaces of unit Pc are depositional landforms (6). Unit Pe consists of vitric ash (5), with a few percent lithic and pumice lapilli. Its discontinuous flat surfaces are generally duned, but locally grade into small secondary flow lobes on steep slopes.

Times of emplacement and changes in rates of eruption were determined by correlating clock times, registered on photographs, with positions of pyroclastic-flow margins and azimuths of nuee ardente clouds. Marginal lobes of units Pc and Pd are traceable up the northwest flank of the volcano, where they have been correlated with strandline positions. The strandlines consist of light-toned pumice clasts and migrated outward from the crater breach during the eruption,

indicating an increasing mass flux during the latter stages of pyroclastic flow.

Estimates of mass flux were determined by measuring the cross-sectional area of the breach (from topographic data) occupied by the pyroclastic flows, over specified time periods. Because it was assumed that flow velocities remained constant, results are minimum values. Actually, velocities may have increased with increasing eruption rates. Mass-flux rates during the emplacement of unit Pb and Pc are estimated to be 2 and 5 times greater than that during emplacement of unit Pa. Calibration of absolute rates requires volumetric data and correlation of the ash-fall stratigraphy (7); this work is still in progress.

An eruption sequence, interpreted from these data, includes: start of pyroclastic flow at 1217 hrs (unit Pa); increase in volume, beginning about 1430 hrs (unit Pb); peak flow from 1530 to 1610 hrs (unit Pc); and, markedly reduced flow (unit Pd) and transition to strictly tephra ejection by 1630 hrs. Volume increase and timing of pyroclastic flows is consistent with changes in amplitudes of harmonic tremors (8) and heights of the eruption column (9), as depicted in Figure 1. The striking correlation between mass flux (pyroclastic flow) and seismic tremor amplitude suggests that the signals recorded were triggered by pumiceous masses, moving in the conduit.

References cited

(1) Sparks, R.S.J. et al., 1978, J. Geophys. Res., 83, p.1727. (2) Wilson, L., et al., 1978, J. Geophys. Res., 83, p.1829. (3) Walker, G.P.L., 1981, Bull. Volcanol., 44-2, p.223. (4) Rosenfeld, C.L., 1980, Am. Sci., 68, p.509. (5) Rowley, P.D. et al., 1981, U.S.G.S. PP 1250, p.489. (6) Criswell, C.W. and Elston, W.E., 1982, NASA TM 85127, p.143. (7) Waitt, R.B.Jr. and Dzurisin, D., 1981, U.S.G.S. PP 1250, p.601. (8) Scandone, R. and Malone, S.D., in prep., J. Volcanol. Geotherm. Res. (9) Harris, D.M., et al., 1981, U.S.G.S. PP 1250, p.323.

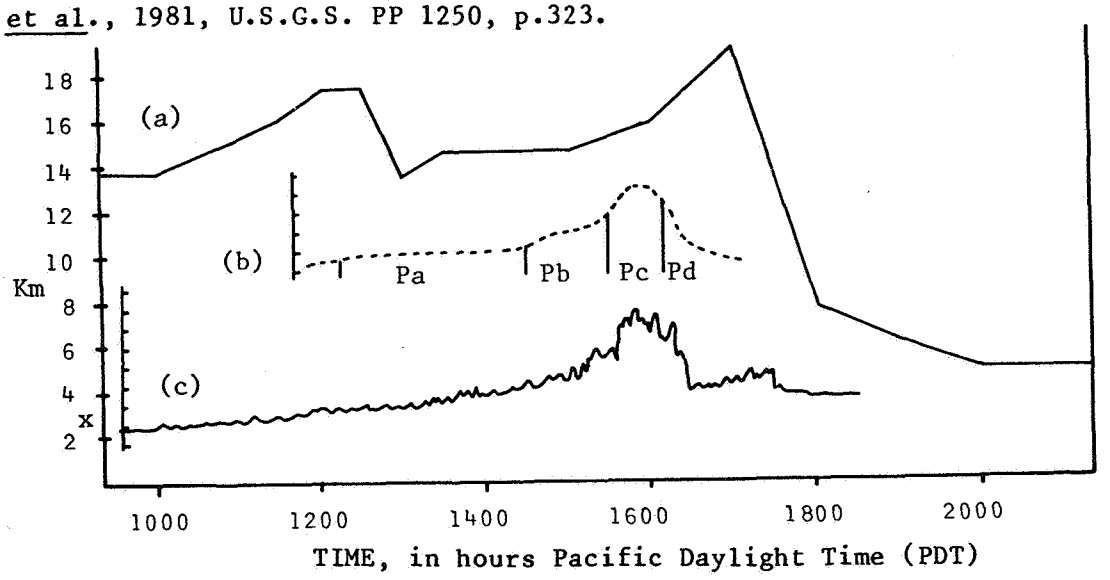

Figure 1. Relationships between (a) height of the eruption column in km above sea level (x-vent)(9); (b) relative mass flux rate and stratigraphy of pyroclastic flows discussed in text, the abscissa represents an approximation of volume/time; and (c) relative amplitude of seismic harmonic tremor, the abscissa is an empirical scale based on the amplitude of the trace of a particular seismogram (8).

 D48

CLASSIFICATION OF VOLCANOES OF THE KANE PATERA QUADRANGLE OF IO: PROPORTIONS OF LAVA FLOWS AND PYROCLASTIC FLOWS

Wolfgang E. Elston, Department of Geology, University of New Mexico, Albuquerque, NM 87131

Voyager 1 images shows 14 volcanic centers wholly or partly within the Kane Patera quadrangle of Io (lat. -15 to -50°, long. 20 to 355°), which can be divided into four major classes:

Class 1: Shield with parallel flows, length/width of flows > 3 (example: unnamed feature, lat. -33°, long. 18°; Fig. 1, B).

Class 2: Shield with early radial fan-shaped flows with length/width < 2, late radial flows with length/width > 5 (examples: Mbali Patera, lat. -35°, long. 3°; Fig. 1, A; Talos Patera, lat. -26°, long. 356°; Fig. 1, E).

Class 3: Shield with radial fan shaped flows, surfaces of flows textured with longitudinal ridges, length/width ≈1. (example: Taw Patera, lat. -33°, long. 0°; Fig. 1, C).

Class 4: Depression surrounded by plateau-forming scarp-bounded, untextured deposits, length/width ≈1 (example: Kane Patera, lat. -48°, long. 14°; Fig. 1, E).

The term flow is here used without genetic connotation, to include both lava and pyroclastic flows, regardless of silicate and/or sulfur composition. Any genetic interpretation of volcanoes on Io is risky, considering the incomplete state of knowledge on their topography, composition, driving mechanisms, and heat sources (1, 2, 3). However, limited analogies with terrestrial volcanoes are possible, under the following simplifying assumptions:

1. Magmas on both Earth and Io are capable of evolving a volatile phase in low-pressure regimes.
2. Magmas on both Earth and Io span a wide range of viscosities, depending on both temperatures and compositions.
3. Low-viscosity high-volatile magmas tend to have the greatest proportion of pyroclastic deposits relative to lavas.

In this light, the four classes can be interpreted as arranged in order of increasing volatile content of magmas. Consequently, pyroclastic eruptions play an increasingly important role, relative to lavas, in the progression from classes 1 to 4.

Class 1 consists predominantly of lavas; parallel flows can be explained by interpreting their vents as fissures. Terrestrial Iceland-style basalt fissure eruption or flank eruptions of Mauna Loa are possible analogs. The early fan-shaped deposits of Class 2 can be interpretd as pyroclastic flows from a volatile-rich source, later flows of high width/length as lavas. The freshest lava flows of both classes 1 and 2 have low albedos and high-albedo fringes, the "auras" of Baloga and others (4). The fringes can be interpreted as sublimates, or ash-cloud, or surge deposits; sublimates of sulfur or sulfur compounds are the most probable explanation. The albedo contrasts fade progressively with time.

The deposits of Class 3 are interpreted as dominantly pyroclastic, from a volatile-rich magma. The textured surfaces of fan shaped deposits may be formed by small late-stage pyroclastic flows; alternatively they are small lava flows of devolatilized residues. Class 4 deposits are interpreted as overlapping widespread pyroclastic flows, analogous to terrestrial ignimbrite plateaus; the source pits resemble large

non-resurgent collapse calderas. Lavas are confined to small patches of low-albedo material within calderas.

The interpretation attempted here hinges largely on the ability to distinguish lava flows from pyroclastic flows by remote sensing. Pyroclastic deposits are highly complex and difficult to characterize, even for well-observed terrestrial eruptions as at Mount St. Helens in 1980 (5, 6, 7). There are obvious limitations in extrapolating terrestrial conditions to Io but the interpretations given here are permitted by the present state of knowledge.

References

(1) Carr, M.H., Masursky, H., Strom, R.G., and Terrile, R.J., 1979, Volcanic features on Io: Nature, v. 280, p. 729-733.

(2) Smith, B.A., Shoemaker, E.M., Kieffer, S.W., and Cook, A.F., II, 1979, The role of SO_2 in volcanism on Io: Nature, v. 280, p. 738-743.

(3) Sagan, Carl, 1979, Sulphur flows on Io: Nature, v. 280, p. 750-753.

(4) Baloga, S.M., Pieri, D.C., and Matson, D.L., 1982, Regolith outgassing by sulphur flows on Io, in Reports of Planetary Geology Program - 1982 (H.E. Holt, editor), NASA Adm. Tech. Mem. 85127, p. 5-7.

(5) Criswell, C.W., and Elston, W.E., 1981, Morphological characteristics of terrestrial ash-flow tuff (ignimbrite) and related pyroclastic deposits, in Report of Planetary Geology Program - 1981 (H.E. Holt, editor): Nat. Aeronautics and Space Adm. Tech. Mem. 84211, p. 174-176.

(6) Criswell, C.W., and Elston, W.E., 1982, Criteria for identifying pyroclastic flows on high- and low-resolution images: The Mount St. Helens pumice plain, in Report of Planetary Geology Program - 1982 (H.E. Holt, editor): Nat. Aeronautics and Space Admin. Tech. Mem. 85127, p. 143-145.

(7) Criswell, C.W. and Elston, 1983, Chronology, morphology, and stratigraphy of pumiceous pyroclastic-flow (ignimbrite) deposits from the eruption of Mount St. Helens on 5/18/80: this volume.

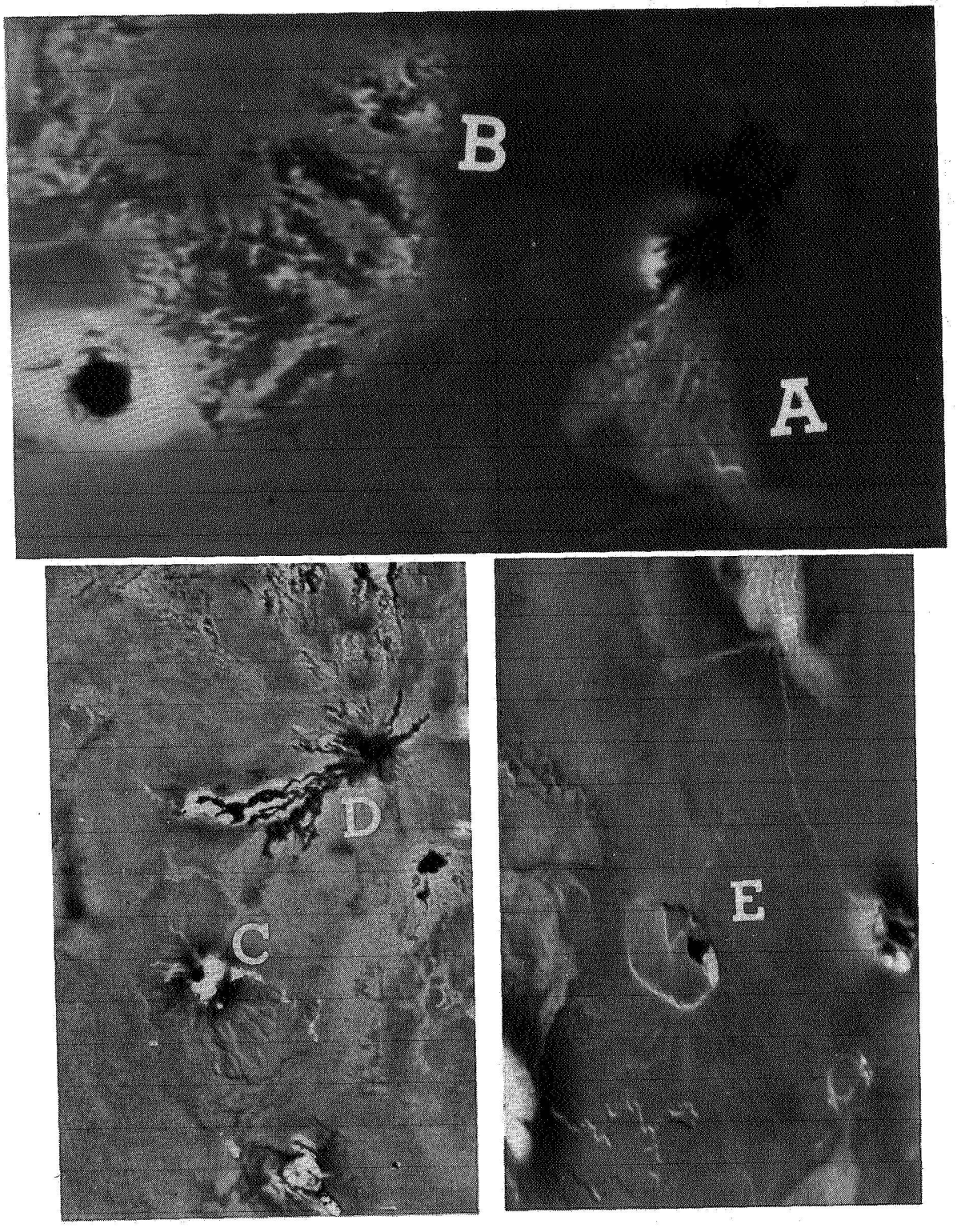

Figure 1. Examples of volcanoes from the Kane Patera quadrangle of Io: A - Mbali Patera (class 2), B - Unnamed (class 1), C - Taw Patera (class 3), D - Talos Patera (class 2), E - Kane Patera (class 4).

D49

N84 23480

DISTRIBUTION AND PROPERTIES OF SMALL VOLCANOES IN ACIDALIA PLANITIA

Herbert Frey and Ann Semeniuk, Geophysics Branch, Goddard Space Flight Center, Greenbelt, MD 20771

Eastern Acidalia Planitia contains a wide variety of terrain types on which are thousands of subkilometer volcanoes(1). We previously reported apparent morphometric variation as a function of terrain type for the cones in the Cydonia area(2)and here extend our study to the rest of Acidalia for which high resolution Viking imagery exist. The present study includes crater counts for the six types of plains identified, density distributions of subkilometer cones found on each type of terrain, and morphometric data by morphological subclass as a function of terrain for more than 1400 cones.

The plains-forming units in Acidalia are of two major types: fractured and smooth. The fractured plains consist of two subclasses which are often but not always contiguous, and which differ principally in that subdued fractured plains (pfs) have fewer, less well-defined fractures lacking sharp edges and deep bottoms than the fractured plains (pf) proper. Interfracture plains are generally smooth and impact craters, small cones and occasional mesas are widely scattered. Smooth plains have been subdivided into four units. Uniform smooth plains (psu) are restricted in extent and have uniform albedo and texture. Small craters are rare. Uniform smooth plains/fractured (psu/f) designates a single unusual occurance of smooth plains surrounding a steep ridge-like feature from which fractures appear to originate(2,3). Patterned smooth plains (psp) have a blotchy appearance and higher crater density than psu. Mottled smooth plains (psm) show albedo variations like psp but also greater textural variation, due to small scale topographic irregularities and a high density of very small craters, perhaps secondaries from the Bamberg impact(4).

In the 420,000 km^2 which we have mapped in detail, pfs and psp are the most abundant plains-forming units, each occupying 35-40% of the sampled area. As shown in Figure 1a the number of subkilometer cones for which we have high quality measurements varies roughly as the distribution of plains. When separated by morphological subclass, the distribution of cones by terrain is as shown in Figure 1b. Mound-like forms dominate everywhere, generally comprising more than 50% of the sample on each type of terrain. Elliptical and cone-like forms generally make up less than 20%. "Others" refers to mixed types or cones whose unusual structure does not permit simple classification. Note the anti-correlation between "others" and "mound-like" as a function of terrain. Where mound-like forms are most common (psu, psu/f), "others" are least common.

Density distributions were calculated in two ways. Average densities on an image-by-image basis were found for cones on each type of terrain. Minimum values were obtained by counting only those cones for which high quality measurements were available. Maximum values were found by adding similar small cones which also appeared on the images but which were generally too small for accurate cone and crater diameter measurements. Average cluster densities were found by restricting the counting area to that immediately around discrete groups of cones. Minimum and maximum values were found as above. The actual density (number/1000 km^2 probably lies somewhere between these extremes. Note that in Figure 1c both image density and cluster density show the same pattern of variation with terrain: cones

are densely grouped on psu and psu/f, thinly distributed on pf and pfs, and have intermediate densities on psp and psm. The variation in cluster density is more than a factor of two. The extremely high maximum cluster density for psm is due to 2 clusters (of a total of 6 in a small area) with very high densities of more than 450/1000 km^2. Note by comparison of Figures 1a and 1c that the plains with the smallest sample size (psu, psu/f, psm) have the largest average densities.

We counted impact craters larger than 0.5, 1, 2, and 4 km diameter, but due to the small areal extent of some plains, the largest diameter cutoff available for all terrain units is 2 km. Shown in Figure 1d are the cumulative number of craters larger than 2 km per 1000 km^2, divided by the average crater density for the entire study area. psu and psu/f have fewer craters per unit area than the other terrains and are probably the youngest plains. The fractured plains are clearly older. Note that Figure 1d and 1c are in general anti-correlated: high crater density corresponds to lower cone density and plains with the fewest craters have the highest density of volcanic cones. Also shown in Figure 1d are direct counts for craters with diameters $\geq$ 0.5 km, normalized by the average for the entire area. Significant enhancements in the density of small craters are obvious for psu and psm, perhaps due to secondary impacts.

We previously reported for the Cydonia area alone a difference in the distribution of crater/cone diameter ratios for psu and psu/f compared to other types of terrain(2). Figure 2 shows histograms of this parameter for 1200 well-measured cones throughout Acidalia. Only psu and psu/f lack the single sharp peak in the 0.45-0.54 bin. As shown in Figure 1e the ratio of number of crater/cone values in the 0.45-0.54 bin to those in the 0.35-0.44 bin (the bin distribution ratio) is nearly 1.0 for psu and psu/f. pfs has a ratio of 2.3 and intermediate values are found for pf, psp and psm. In genreal the variation in the bin distribution ratio follows that for the crater counts, although the ratio for pfs is somewhat large.

The somewhat systematic variations of properties for both cones and terrain units may be explicable in terms of natural erosional evolution and aeolian deposition in the area. In general the density of small volcanic cones increases with decreasing terrain crater density: younger plains have denser cone distributions. The increase in the bin distribution ratio (the sharpening of the peak in the 0.45-0.54 bin in Figure 2) could be due to gradual widening of the crater diameter with time due to erosion. Blanketing of what is now pfs terrain by dust would further enhance this ratio by decreasing cone diameters (Figure 1e). Such blanketing would also decrease small crater densities somewhat and might also decrease cone densities by covering over the smallest cones. Combined erosion of old cones and blanketing could also produce more unusual morphological types, leading to more "others" as seen on pfs in Figure 1b. Likewise, a high flux of small impacts on psm (Figure 1d) could also cause enough damage to cone structure to increase "others" (Figure 1b).

References: (1) Frey, H. and M. Jarosewich (1982) J. Geophys. Res. 87, 9867.
(2) Frey, H., A.M. Semeniuk and M. Jarosewich (1983) Lunar. Planet. Sci. XIV, 215 (abstract).
(3) Allen, C.C. (1979) J. Geophs. Res. 84, 8048.
(4) Mouginis-Mark, P. (1979) Proc. Lunar Planet. Sci. Conf. 10th, 2651.

FIGURE 1

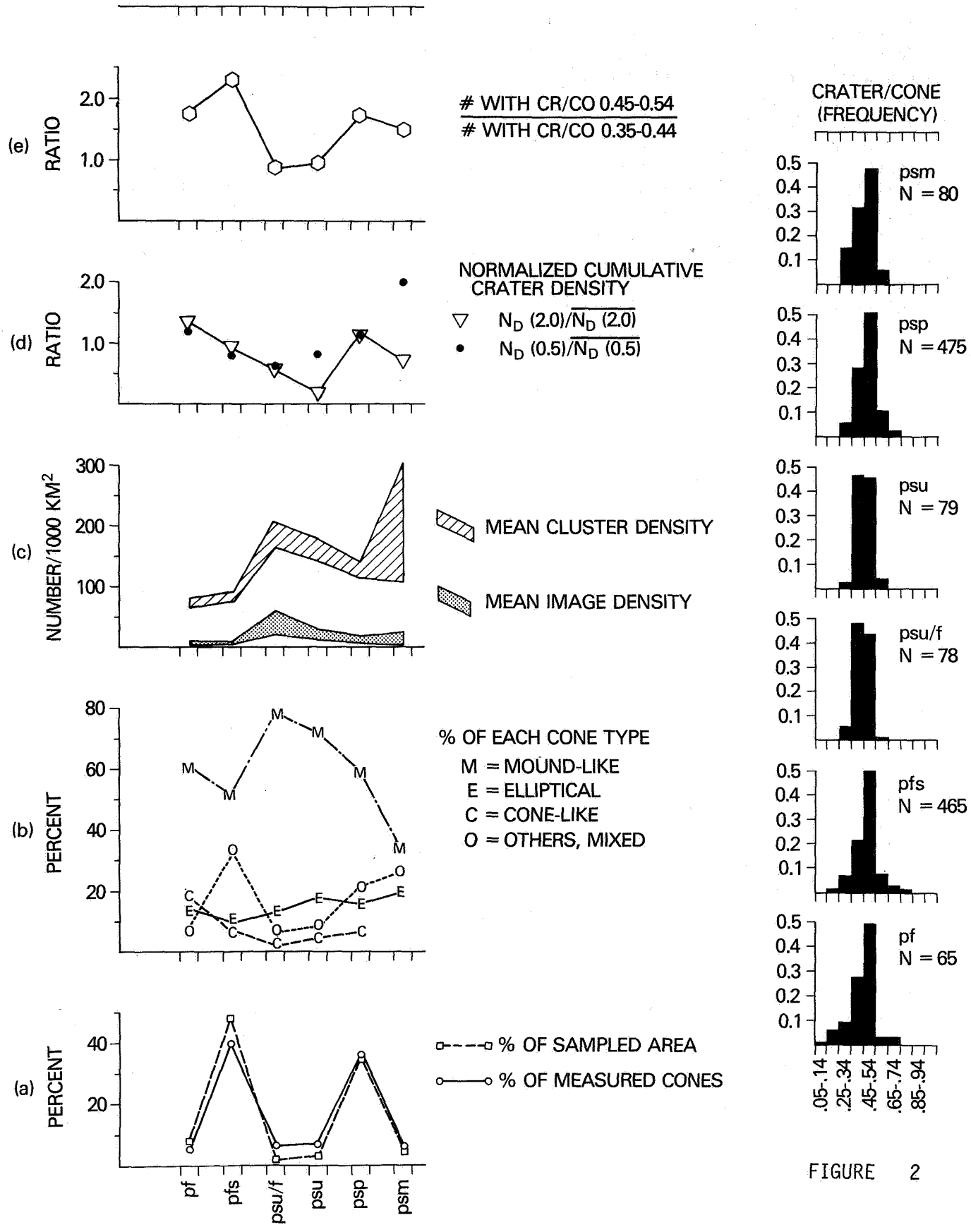

FIGURE 2

THE 1950 SULFUR FLOW OF MAUNA LOA: CONSIDERATIONS FOR IO

Ronald Greeley, Eilene Theilig, and Philip Christensen, *Department of Geology, Arizona State University, Tempe, AZ 85287*

Lava flows on Io exhibit features that are typical of terrestrial flows of silicate compositions. Estimates by Clow and Carr (1980) of the material properties of the ionian flows near their source vents also suggest silicate compositions. On the other hand, spectral properties of the surface indicate the presence of sulfur and/or sulfur-rich compounds, although the spectral properties apply only to the upper few millimeters and the sulfur may be only a "sprinkling" of material over silicate flows. Thus, the composition of flows on Io remains in question. One approach to address the question is through the study of flow morphology; because of the unusual rheological properties of sulfur (it becomes less viscous as it cools through the range of 200° to 160°C), it has been suggested that distinctive landforms may develop in sulfur flows. Because little is known about sulfur flow morphology, we have conducted laboratory experiments to simulate sulfur eruptions (Greeley et al., 1981), carried out numerical modelling of sulfur flows (Fink et al., 1983), and initiated study of full-scale natural and manmade sulfur flows on Earth (the subject of this report).

Natural sulfur flows are rare on Earth (see review by Theilig, 1982); however, the 1950 sulfur flow of Mauna Loa, Hawaii, is well-preserved and relatively accessible. In August, 1983, a field excursion was completed to examine this flow. First described by Skinner (1970), the flow occurs on the western side of Sulphur Cone, a cinder-and-spatter-cone located at the 11,200 ft level on the southwest rift of Mauna Loa. The flow is about 27 m long, 14 m wide and ranges in thickness from 10 to 45 cm, and was derived from secondary (fumarolic) sulfur deposits which were presumably mobilized by heating related to the 1950 Mauna Loa eruption. Fumarolic sulfur deposits are common throughout this part of the rift zone, and the loose rubble comprising the talus deposits on the flank of Sulphur Cone, from which the sulfur flow originated, would be ideal for fumarolic accumulation. Sulfur becomes relatively fluid at its melting point (~115°C) and given typical basalt flow temperatures of >1000°C, it is reasonable to expect mobilization of the sulfur, even if it is not in direct contact with the molten lava. Moreover, several segments of the rift pass directly through the cone, thus increasing the likelihood of heating above the sulfur liquidus during the 1950 eruption.

The Mauna Loa sulfur flow is fan-shaped with the apex pointing toward the apparent source which is buried beneath the talus. The distal end is marked by a 1 to 1.5 m fault scarp which Skinner cites as having truncated the sulfur flow. However, we noted that in one area sulfur has flowed over the scarp. Thus, either new sulfur flows have occurred since Skinner's visit in 1967, or the overflow was not apparent at that time. Flow surface features include sheet flows, a leveed channel, and numerous flow lobes ranging in size from 1 to 10 cm wide, a few cm to 50 cm long, and up to 2 cm thick. The flow lobes are overlapping and anastomosing in a pattern suggesting repeated outflow from the source area. Most of the flow lobes occur in the upper (near-source) 1/3 of the flow; in the lower part of the flow, the lobes grade into a knobby texture which also appears to be a primary flow texture. Many of the lobes have small pits along the axis, suggestive of small, partly collapsed "lava" tubes. Parts of the southern (lateral) margin of the flow appear to have been ablated; the margin is very smooth, forming an overhang of ~8 cm, and follows the contours of some rocks, but is separated from the rocks by several cm. In addition, a small lava tube having a diameter of ~30 cm and a roof thickness of about 5 cm is exposed along this margin; unfortunately, a talus block has broken the roof and the full extent of the tube cannot be determined. The tube appears to have fed a small flow lobe measuring 4 m long by 2.5 m wide.

In addition, patches of sulfur occur as "splashes" on the surrounding basalt flows; these "splashes" are as large as 25 cm across and are found as far as 5 m from the flow. Evidently, turbulence in the flow was sufficiently vigorous to eject blobs of very fluid sulfur away from the flow.

Despite the fact that the entire Mauna Loa sulfur flow is smaller than a single Voyager image resolution element (pixel) on Io, some of the geological relationships observed in the flow may apply in considering volcanic processes on Io:

1. Given the presence of sulfur/sulfur compounds in the eruption plumes and on the surface of Io, it is likely that extensive secondary deposits of sulfur exist, some of which may be of fumarolic origin and analogous to the Mauna Loa deposit.
2. Given the likelihood of silicate volcanism of Io based on the inferred material properties of some flows, and the attendant high temperatures for silicate volcanism, it is likely that the secondary surface deposits of sulfur would have been mobilized without being heated to the high viscosity stage.
3. Mobilized sulfur flows on Io may flow long distances as a result of: a) low viscosities in the melting range, b) sustained effusion resulting from continued heating of source area, c) continued remobilization within the flow as a consequence of surges from the source, and d) extension via lava tubes, or similar conduits through which there is little heat loss.
4. Sulfur flows may form a relatively thin veneer over silicate flows and other surface units, given their fluidity and low mobilization temperature; furthermore, active splashing and splattering may spread sulfur over a wider area than the flow itself, contributing the bright "blooms" observed in association with some ionian flows.

REFERENCES

Clow, G.D. and M.H. Carr, 1980. Stability of sulfur slopes on Io, Icarus 44, 268-279.

Fink, J.H., S.O. Park, and R. Greeley, 1983. Cooling and deformation of sulfur flows, Icarus (in press).

Greeley, R., J.H. Fink, and S.O. Park, 1981. Sulfur flows on Io: laboratory and theoretical modelling, EOS 62, 1080.

Skinner, B.J., 1970. A sulfur lava flow on Mauna Loa, Pacific Science 24, 144-145.

Theilig, E., 1982. A primer on sulfur for the planetary geologist, NASA CR 3595, 34 pp.

Watanabe, T., 1940. Eruptions of molten sulphur from the Siretoko-Iosan Volcano, Hokkaido, Japan, Japanese Jour. of Geology and Geography 17, 289-310.

D51

N84 23482

VOLCANISM IN THE VALLES MARINERIS

Baerbel K. Lucchitta, U.S. Geological Survey, Flagstaff, Arizona 86001

The Valles Marineris have a long history of tectonism that is partly contemporaneous with large-scale volcanism in the Tharsis area nearby. Was this tectonism accompanied by volcanic activity inside the troughs? A careful examination of Viking stereoscopic images reveals several features best explained as of volcanic origin, and circumstantial evidence also suggests that volcanic activity occurred. This report discusses some of these features and evidence.

Mafic Volcanism

The deposits inside the troughs, here called basin beds, are interlayered with beds of low albedo, one of which appears on Viking images as dark as shadows. This bed forms a resistant ledge exposed in a steep hillside, and sheds dark talus. The exposure resembles that of basaltic layers in basin beds in Nevada. The albedo and morphology of the martian bed indicate that it is most likely a resistant ledge of mafic volcanic rock that is being exposed by erosion. It could be a sill, but, by analogy with the Nevada exposures, it is more likely a buried lava layer.

Stereoscopic images show an elongate trough on the western part of the floor of Candor Chasma. This trough is filled with level, very dark material that embays adjacent gullies, a configuration suggesting that the material was a liquid which flooded subjacent terrain. The low albedo suggests mafic rock. This probable volcanic flow appears to be relatively young, because it is not buried by windblown material, although it could also be an older flow that has been exhumed.

In several places in the Valles Marineris, dark knobs protrude from valley floors or from steep slopes on eroded basin beds. Commonly these knobs are surrounded by deposits of dark materials. The knobs measure about 0.5 to 2 km in diameter and resemble vents surrounded by ash. However, the knobs could also be necks of former volcanic feeders to intra-basin bed flows; the surrounding dark material would then be eroded neck material dispersed by the wind. These necks, also, could have fed the ancient lavas of the Lunae Planum plateau, although lavas probably were erupted through fissures along faults rather than from circular vents. This interpretation is supported by the presence of resistant spurs projecting into the troughs along fault traces; these spurs could be remnants of ancient dikes.

Dark patches on the Moon have been attributed to explosive volcanism [1]. This hypothesis was confirmed when returned samples showed the dark deposits to be composed of volcanic glass [2]. Dark patches on Mars are generally interpreted as having been deposited by the wind and being derived from some distant, unknown source. Wind-deposited dark materials commonly occur where trapped by physiographic obstacles, such as crater rims or scarps. In the Valles Marineris, some dark patches fan outward from point sources without obvious traps nearby. These patches may well be volcanic material spread from small vents or necks.

In the Valles Marineris, few features occur that, by shape alone, suggest volcanic flows. The floors of the valles, however, are buried in most places by eolian material that would cover such flows. Therefore, the absence of obvious flows may not be significant. The evidence of at least two dark flowlike features and of several possible vents suggests that mafic activity did take place.

Felsic Volcanism

Evidence for felsic volcanism is difficult to obtain because vent structures may be silicic domes that appear on satellite images as small the undiagnostic hummocks. Although such hummocks are visible on the floors of the Valles Marineris, they could be attributed to various causes.

Circumstantial evidence, however, suggests that felsic volcanism occurred. The basin beds locally have a higher albedo than most other units on Mars except the polar caps and beds exposed in the Memnonia quadrangle, which are interpreted as ignimbrite [3]. The beds in the Valles Marineris are soft and easily eroded by the wind. Similarily eroded are the beds in the Memnonia quadrangle and some deposits on the Earth [4].

The volume of the basin beds suggests addition of extraneous material. The volume of the interior beds is larger than that eroded from the trough walls, many of which are steep faultline scarps. Even though some of the material in the basin beds may have come from the walls and been deposited in lakes and playas [5], a contribution of material from elsewhere is also required. Because the surrounding plateau surface is little dissected, this contribution probably came from the trough interior by volcanism. An alternative source might be deposition by wind, although the bedding is too even for this mechanism. Wind deposition associated with polar layered beds [6], assuming that the pole was situated over the Valles Marineris, is unlikely because no equivalent layered deposits occur on the adjacent plateaus. If the basin beds do, indeed, contain volcanic material, it is more likely felsic than mafic because of the high albedo of most of the beds.

Silicic volcanism on the Earth is associated with vents that have formed domes or large calderas where massive ignimbrite flows were erupted. In the Valles Marineris, only one structure was identified that forms a crater of the dimensions of terrestrial calderas: It is a circular crater about 10 km across, nested inside a more elongate crater. This circular crater is situated on basin beds in east-central Candor Chasma. The two craters have no obvious rims. Dark material has streamed into the smaller crater from an exposure on the north side of its rim. The structure could be of impact origin, and its peculiar morphology could be due to impact into unusually soft material; however, the nested shape more nearly resembles that of volcanic craters. Nonetheless, no collapse structures common to calderas are visible, and it is difficult to ascertain whether the crater, if volcanic, is a caldera or an explosion pit. Overall, the evidence for felsic volcanism in the Valles Marineris is less convincing than that for mafic volcanism, but the possibility remains, nevertheless.

In summary, tectonism in the Valles Marineris appears to have been accompanied by volcanism. The proposed volcanic features, though probably contemporaneous with the gigantic ones in the Tharsis area, are composed of small, mafic and, possibly, somewhat larger felsic flows. The size of these features is similar to that of volcanic flows on the Earth.

References

[1] Wilhelms, D. E., and McCauley, J. F., 1971, Geologic map of the near side of the Moon: U.S. Geol. Surv. Misc. Geol. Invest. Map I-703.

[2] Heiken, G. H., McKay, D. S., and Brown, R. W., 1974, Lunar deposits of possible pyroclastic origin: Geochim. Cosmochim. Acta, v. 38, p. 1703-1718.

[3] Scott, D. H., 1982, Volcanoes and volcanic provinces: Martian western hemisphere: J. Geophys. Res., v. 87, no. B12, p. 9839-9851.

[4] Francis, P. W., and Wood, C. A., 1982, Absence of silicic volcanism on Mars: Implications for crustal composition and volatile abundance: J. Geophys. Res., v. 87, no. B12, p. 9881-9889.

[5] Lucchitta, B. K., 1982, Lakes and playas in the Valles Marineris: In Reports of Planetary Geology Program 1982, NASA Tech. Memo. 85127, p. 233-234.

[6] Schultz, P. H., and Lutz-Garihan, A. B., 1981, Equatorial paleo-poles on Mars: In Lunar and Planetary Science XII, Lunar and Planetary Institute, Houston, TX, p. 946-948.

D52

N84 23483

VOLCANISM IN ELYSIUM PLANITIA, MARS

Peter J. Mouginis-Mark, Planetary Geosciences Division, Hawaii Institute of Geophysics, Univ. Hawaii, Honolulu, HI 96822

With the continued analysis of the Viking Orbiter image data set, it is increasingly apparent that Mars possesses a wide diversity of volcanic landforms, many of which are not represented by the volcanoes in the Tharsis Region[1]. In particular, several volcanic features within Elysium Planitia have no direct equivalents within Tharsis, thereby offering the opportunity to conduct comparative investigations of relatively young[2], constructional volcanic provinces[1,3] on Mars.

Recently, geomorphic mapping has revealed that the three volcanic constructs within Elysium Planitia (Hecates Tholus, Elysium Mons and Albor Tholus) are very different in their overall morphology and represent three distinct types of martian volcano. Hecates Tholus has been found to possess the most likely possible example of a young, explosively-generated, air-fall deposit[4], while the volume of magma erupted from Elysium Mons appears to have been orders of magnitude larger than that erupted from Albor Tholus[5]. A fourth volcanic center, which lacks any associated constructional feature, has also been recognized in the Elysium Fossae area[5].

A primary aim of the present regional geological analysis of Elysium Planitia is to further understand the volcanic and tectonic evolution of the area by the identification and interpretation of individual lava flows and their source vents. Lava flow size, spatial distribution, flow direction and the stratigraphic relationships of these lava flows to adjacent structural features have all been measured. A comparable study of the Tharsis Region[6] demonstrated the value of such an approach, in that the vents on Arsia Mons (and on a parasitic cone to the south of the Arsia Caldera) were seen to contribute major amounts of lava during the formation of the Tharsis Plains, and that few of the preserved vents are located beyond the perimeters of the four largest shield volcanoes. An analysis of the lava flows and vent distribution within Elysium Planitia (Figure 1) shows a markedly different style of regional volcanism compared to Tharsis. Effusive activity has been the dominant way inwhich the surrounding plains in both regions have been resurfaced, but the topographic form of Elysium Mons has totally controlled the flow direction of lava flows within Elysium Planitia. Both Hecates Tholus and Albor Tholus are seen to have been partially buried by Elysium Mons lavas, which all appear to postdate effusive activity on the tholi. Lava flows from Elysium Mons can be traced for distances of 150 - 250 km in a radial direction from the volcano but, unlike Tharsis, parasitic vents located beyond the recognizable volcanic construct also conform to this radial pattern. These parasitic vents have been located by this study to lie more than 400 km from the summit of Elysium Mons in some instances.

A second unusual characteristic of the Elysium Planitia region is the high frequency of occurrence of sinuous channels that are morphologically similar to lunar sinuous rilles[7,8]. Over 40 such channels within Elysium Planitia have been identified in this study: this number represents over half the total number of such features so far found on Mars. Currently, two

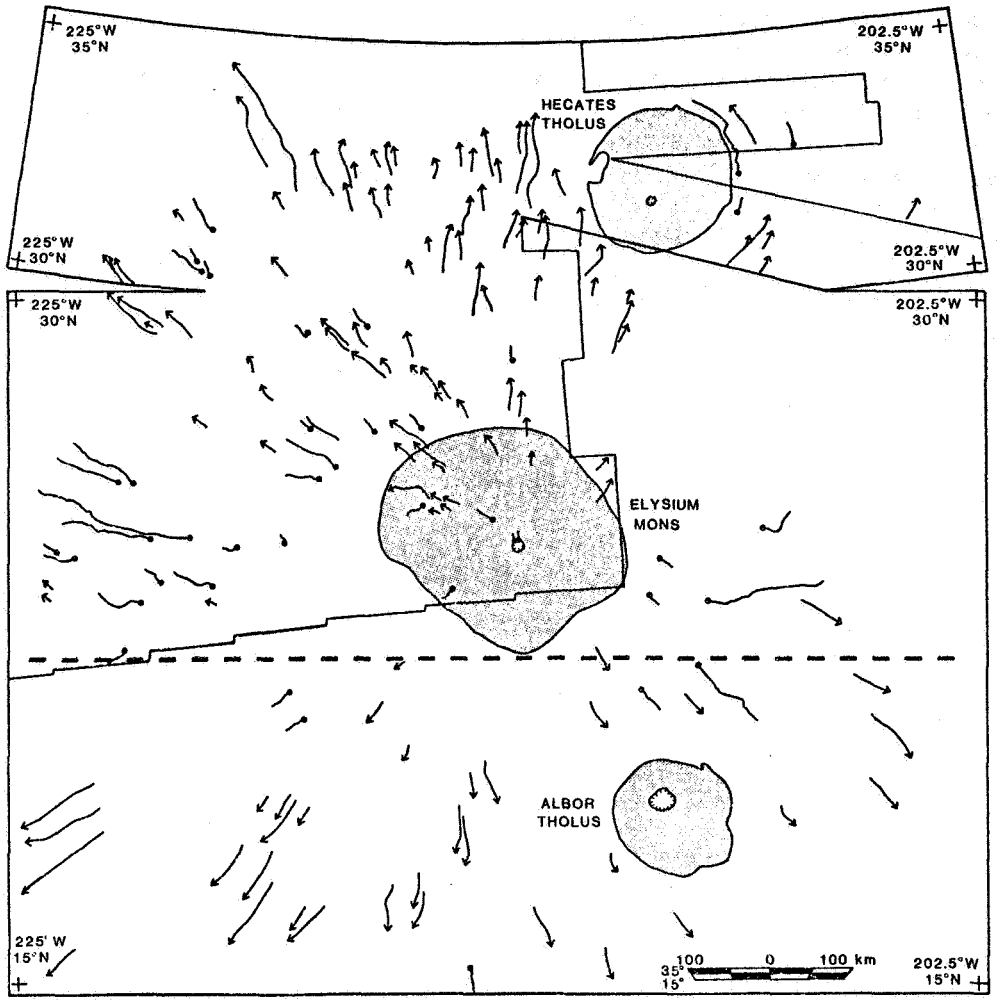

Figure 1: Distribution map of all lava flows (arrows) and sinuous channels within Elysium Planitia; length of each line shows the distance for which the flow lobes can be traced. Map prepared using medium and high resolution Viking Orbiter images, with the outlined area at top left showing the coverage at a resolution of 150 meters per pixel or higher. Dashed line to the south of Elysium Mons shows the location of the radar groundtrack along which the topographic data were acquired (Figure 2). Note that the outlines of the volcanic constructs are only approximate, particularly in the case of Elysium Mons where many lava flows extend across this boundary to the north and west.

alternative models by which lava channels may have preferentially formed at this locality are being investigated. The first model involves the eruption of unusually fluid and/or large volumes of magma; the second model considers the effects of unusually steep regional slopes which may have promoted the formation of turbulent lava flows and, hence, more lava channels due to excessive thermal erosion[7]. Some indirect information is available to support this second model, because Earth-based radar measurements of local topography[9] show that the steepest regional slopes (on a scale of 100 - 300 km) yet measured on Mars occur to the south of Elysium Mons and Elysium Fossae (Figure 2). However, in order to further constrain such an interpretation, more detailed measurements of channel dimensions are currently being made. Future work will also be directed toward placing the time of eruption of the lava flows into the sequence of tectonic events responsible for the formation of the circumferential graben around Elysium Mons[10]. In this way, it is hoped to more fully contrast the volcanological and structural evolution of Elysium Planitia with the more frequently studied Tharsis Region.

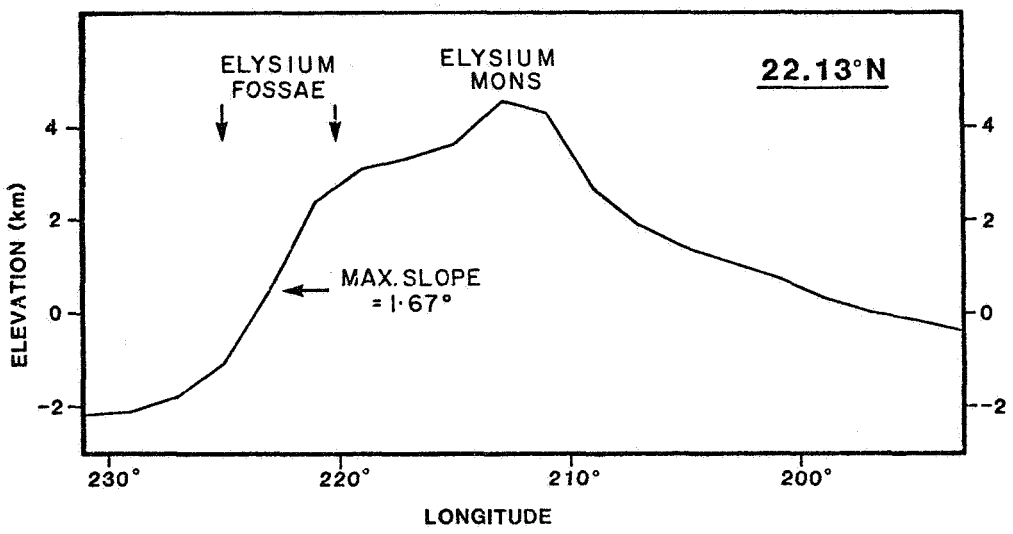

Figure 2: Topography of southern Elysium Planitia at 22.13°N, as measured by Earth-based radar[9]. Groundtrack of radar is shown in Figure 1.

References:
1) R. Greeley and P. D. Spudis (1981) Revs. Geophys. Space Phys. 19, 13-41.
2) G. Neukum and K. Hiller (1981) JGR 86, 3097-3121.
3) M. Malin (1977) Geol. Soc. Amer. Bull. 88, 908-919.
4) P. J. Mouginis-Mark, L. Wilson and J. W. Head (1982) JGR 87, 9890-9904.
5) P. J. Mouginis-Mark, L. Wilson, J. W. Head, J. L. Hall, S. C. Solomon and K. D. Sullivan (1983) Elysium Planitia, Mars: Regional Geology, Volcanology and Evidence for Volcano/Ground Ice Interactions. To be submitted to The Moon and Planets.
6) P. J. Mouginis-Mark, S. H. Zisk and G. S. Downs (1982) Nature 297, 546-550.
7) G. Hulme (1973) Modern Geology 4, 107-117.
8) J. W. Head and L. Wilson (1981) Lunar Plan. Sci. XII, 427-429.
9) G. S. Downs, P. J. Mouginis-Mark, S. H. Zisk and T. W. Thompson (1982) JGR 87, 9747-9754.
10) J. L. Hall, S. C. Solomon, J. W. Head and P. J. Mouginis-Mark (1983) Lunar Plan. Sci. XIV, 275-276.

N84 23484

EFFUSION RATE, LENGTH, AND AREA RELATIONSHIPS FOR SOME LAVA FLOWS ON HAWAII AND MOUNT ETNA WITH PLANETARY IMPLICATIONS.

David Pieri, Jet Propulsion Laboratory, Pasadena, CA 91109
Stephen Baloga, Department of Energy, Washington, D. C. 20545

Much of the work on the correspondence of morphological and process parameters has been qualitative and/or empirical (Refs. 1, 2) and few theoretical treatments have been attempted (Refs. 3, 4, 5, 6). We have outlined a model for the cooling by radiation of thermally well-mixed lava flows and have applied that model to a remote sensing study of extraterrestrial lavas (Ref. 7). Other work on the relationship between effusion rate and length and area is summarized here.

We start with a simple one-dimensional heat transport equation (Ref. 7)

$$\rho c_p(\delta/\delta t + u\ \delta/\delta x)TYW = -\varepsilon\sigma T^4 W \qquad (1)$$

where $T=T(x,t)$, $W=W(x)$, and $Y=Y(x)$ respectively denote flow temperature, width and depth for a constant effusion rate and mean flow velocity u, ρ is the density, c_p is the specific heat capacity at constant pressure, ε is the emissivity, σ is the Stefan-Boltzmann radiation constant, t is time, and x is the distance down the flow.

If the flow width (W) is known, remembering that $Q=uWY$, and knowing the time dependency of the source temperature, $T_o(t)$ at $x=0$, we arrive at the following solution for equation (1)

$$T(x,t) = \{T_o^{-3}[t-(x/u)] + (3\varepsilon\sigma/\rho c_p Q)\int_o^x W(y)dy\}^{-1/3} \quad . \qquad (2)$$

If we assume a constant source temperature, then from (2) we arrive at

$$Q = [3\varepsilon\sigma(x_2-x_1)W]/[\rho c_p(T_2^{-3}-T_1^{-3})] \quad . \qquad (3)$$

If we allow the distance x_2-x_1 to equal the flow length, L, and T_1 and T_2 to be equal to the initial eruption temperature, T_o, and the solidification temperature of the flow, T_s, respectively, equation (3) yields

$$Q = \{[3\varepsilon\sigma]/[\rho c_p(T_s^{-3}/T_o^{-3})]\} \quad . \quad A \qquad (4)$$

where A is the plan area of the flow.

We can address here simply the formation of a solidified cover or lava tube and derive bounding values for the length of a given flow either under a solidified insulating cover or freely radiating.

Equation (4) can be rearranged to

$$L_m = [(\rho c_p Q/W)/(3\varepsilon\sigma T_o^3)][(T_o^3/T_s^3)-1] \qquad (5)$$

where L_m is the length of the flow if it is well-mixed thermally. If it is not thermally well-mixed and is crusted, the surface of the flow is always below the solidus, i.e.,

$$dT/dx \geq -\varepsilon\sigma T_s^4/\rho c_p(Q/W) \qquad \text{yielding} \qquad (6)$$

$$L_u \geq (T_o - T_s)(\rho c_p Q/W)/(\varepsilon\sigma T_s^4) \qquad (7)$$

where L_u is the length of the same flow with an insulating cover. Thus $L_u \geq L_m$.

We can interpret T_s as follows. If the length of a lava flow and parameters other than the solidification temperature are known, we can solve for T_s. Assuming the slowest possible heat loss for that flow, that is, radiation through an insulating cover, T_s becomes the effective radiation temperature (T_{eff}) of the insulating cover. For freely radiating, rapidly cooling flows (relatively short with high effusion rates) we calculate effective temperatures of about 1000-1100°K. For relatively well-insulated tubed flows (long with low effusion rates) we calculate effective radiation temperatures of about 400-500°K.

If radiative cooling is the prime mode of heat loss for a lava flow, we should expect to see a stronger correlation between the effusion rate (Q) and the plan area ($A=W\cdot L$) of the flow, than between effusion rate and just flow length. Different flows on a single volcano with differing initial temperatures, volatile content, and gross compositions should yield different areas for a given effusion rate and thus plot with different slopes on a graph of effusion rate versus area. Likewise, a range of slopes for the relationship between effusion rate and flow area should result from comparisons between different volcanoes.

As a test of these ideas, we surveyed available data on the effusion rates, lengths, and areas of volcanic flows. We utilized compilations kindly provided by M. Malin (Hawaiian flows) and by R. Lopez and J. Guest (Ref. 8) (Etnean flows), as well as data extracted from excellent monographs on Hawaiian and Etnean flows (Refs. 9, 10, 11). We examined the statistics of effusion-rate/area and effusion-rate/length relationships for individual flows during a given eruption, for individual flows in different eruptions on the same volcano, and for flows on different volcanoes.

We found (1) that the effusion-rate/area correlation was statistically more significant than the correlation between effusion rate and length for four out of the five eruption episodes which met the necessary criteria of more than three individual flows with area, length, and effusion rate independently measured; (2) that there exists a minimum length and area for a given effusion rate, reflecting competition between the rate of heat loss and the mass flux; and (3) that each volcano has an overall characteristic proportionality between effusion rate and flow length, width, and area.

The statistics of effusion rate versus plan variables and insight gained from the radiative cooling model indicate that combining the measurements of many flows is a randomizing process, but that for individual flows analyzed here, the correlations are statistically more meaningful. Roth and Saunders (Ref. 12) analysis generally supports the idea that grouping flows by some criteria (e.g., composition) enhances the correlation. Small variations in initial eruption temperature and solidification temperature will have a marked effect on the extent of the flow. Such variations will occur as a function of change in volatile

content and general flow composition. In addition, the linear dependencies on the other indicated parameters will at times also be significant. Where lava tubes form, a drastic alteration of the thermal regime occurs and low effective radiation temperatures allow flows to enlarge greatly at only modest effusion rates.

An important application of these ideas is found in planetary lava flows (Refs. 5, 12) where dimensional data are far more abundant than compositional data and where time histories may be only vaguely known. The literature on planetary volcanism is extensive (Ref. 13). We have applied the radiative cooling model to lava flows at Ra Patera on Io (Ref. 7) and have concluded that they are primarily of sulfur composition, erupting at effusion rates characteristic of large terrestrial basaltic eruptions ($\sim 10^{11}$ cm^3/sec). Further applications exist for lava flows on Mars where high resolution Viking Orbiter data have spatial resolution of less than 50 meters and where stereo coverage exists. For instance, if a suite of flow dimensions (e.g., length, width, area, thickness) can be measured for a given volcano, bounding estimates can be made for effusion rates for well-mixed flows (with lava channels) and unmixed flows (with lava tubes) for various eruption temperatures.

1. Walker, G. P. L., 1973, Lengths of lava flows, Phil. Trans. R. Soc. Lond. A274, p. 107-118.
2. Malin, M. C., 1980, Lengths of Hawaiian lava flows, Geology, 8, p. 306-308.
3. Danes, Z. F., 1972, Dynamics of lava flows, Jour. Geophys. Res., 77, p. 1430-1432.
4. Harrison, C. G. A. and C. Rooth, 1976, The dynamics of flowing lavas, Volcanoes and Tectonospheres, Tokai University Press, Japan, p. 103-113.
5. Hulme, G., 1974, The interpretation of lava flow morphology, Geophys. J. R. Astr. Soc., 39, p. 361-383.
6. Shaw, H. R. and D. A. Swanson, 1974, Eruption flow rates of flood basalts, Proc. 2nd Columbia River Basalt Symposium, p. 271-299, East Washington State College Press.
7. Pieri, D. C. and S. M. Baloga, 1983, Effusion rate, length, and area relationships for some lava flows on Mauna Loa, Kilauea, and Mount Etna, in preparation for submittal to Geology.
8. Lopez, Rosaly and J. E. Guest, 1981, Lava flows on Etna, a morphometric study, Comparative Study of the Planets, NATO Advanced Institute presentation, Vulcano, Eolie, Sept. 1981.
9. Swanson, D. A. et al., 1979, Chronological narrative of the 1969-1971 Mauna Ulu eruption of Kilauea Volcano, Hawaii, USGS Prof. Paper 1056, pp. 55.
10. Romano, R. and J. E. Guest, 1979, Volcanic geology of the summit and northern flank of Mount Etna, Sicily, Boll. Soc. Geol. It., 98, p. 189-215.
11. Romano, R. and C. Sturiale, 1975, Geologia della tavoletta "Monte Etna Sud", Boll. Soc. Geol. It., 94, p. 1109-1148.
12. Roth, L. E. and R. S. Saunders, 1983, Rheology of the Arsia Mons lava flows, Lunar and Planet. Sci. XIV, abst., p. 652-653.
13. Basaltic Volcanism Study Project, 1981, Basaltic Volcanism on the Terrestrial Planets, 1286 pgs., Pergamon Press, New York.

D54

N84 23485

EXPERIMENTS ON WATER/MELT EXPLOSIONS, NATURE OF PRODUCTS, AND MODELS OF DISPERSAL

Michael F.Sheridan[1] and Kenneth H. Wohletz[2]. 1) Department of Geology, Arizona State University, Tempe, AZ 85287. 2) ESS1, Los Alamos National Laboratory, Los Alamos, NM 87545

Experiments were carried out in a steel pressure device using controlled amounts of water and thermite melt to examine the mechanical energy released on explosive mixing following the initial contact of the two materials. An experimental design was used to allow the direct calculation of the mechanical energy by the dynamic lift of the device as recorded both optically and physically. A large number of experiments were run to accurately determine the optimum mixture of water and melt for the conversion of thermal to mechanical energy. The maximum efficiency observed was about 12% at a water/thermite mass ratio of 0.50. Very little mechanical energy is developed for water/melt ratios less than 0.2. Experiments were not conducted at water/melt ratios higher than 1.0. However, it appears that there would be very little mechanical energy released for water/melt ratios greater than 2.0.

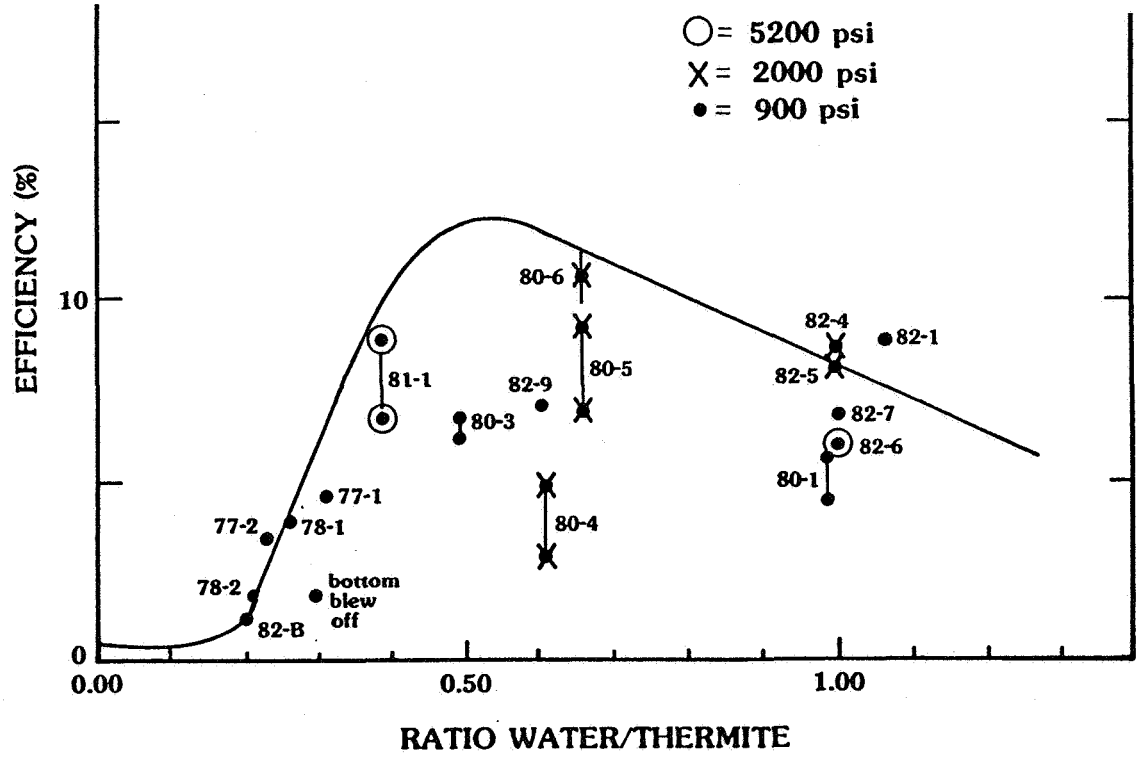

Fig. 1. The relationship of efficiency of conversion of thermal energy to mechanical energy vs. the mass ratio of water/thermite in the system. The line shows the energy envelope.

These experiments (Wohletz and McQueen, 1983) are the basis for the development of models of hydroexplosions (Sheridan and Wohletz, 1983) and melt fragmentation. Particles collected from the experimental products are smilar in size and shape to pyroclasts produced by much larger hydrovolcanic explosions (Wohletz, 1983). Melt rupture at optimum ratios produces very fine particles (less than 50 um), whereas rupture at high or low water/melt ratios produces large melt fragments. Grain surface textures in the experimental products are also related to the water/melt ratio and the mechanism of explosive mixing. It is thus possible to have qualtiative information about the nature of the explosion from the sizes and shapes of the fragments produced.

Volcanic hydroexplosions produce particles with the same general sizes and shapes as those from the experiments. Because natural explosions are much larger than those possible in the laboratory, the products from hydrovolcanic explosions might be useful for interpretation of materials on the surfaces of planets with significant water. To this end a scanning electron microscope was used to characterize the various surface textures on pyroclasts that relate to melt rupture and the transport, deposition, and diagenesis of the particles (Sheridan and Marshall, 1983).

The first conclusion of this work is that particles resulting from hydroexplosions are very fine grained. The second conclusion is that particles produced by strong water/melt interaction are generally hydrated. Thus, hydroexplosions could be a possible source for the presence of palagonite (hydrated basaltic glass) on the surface of Mars.

The lateral dispersal of fine-grained particles from large explosions has recieved a great deal of attention and many models have been proposed. A general computer-assisted model based on the energy line concept was tested for the products of the 1980 Mount St. Helens blast (Malin and Sheridan,1982) and several explosive volcanic eruptions in Italy (Sheridan and Malin, 1983). The model only assumes that the bulk of the particles lifted by the explosion disperse laterally under the effect of a gravitational field to a distance controlled by the internal friction of the cloud of dust and gases. Although the details of the rheology of the flows is not considred in the present model, it produces a good first-order approximation to the distribution of gravity-driven particulate flows on Earth and may be an appropiate means to test the empalcement of similar types of deposits on other planets.

References Cited

Malin, M.C. and Sheridan, M.F., 1982. Computer-assisted mapping of pyroclastic surges. Science, 217: 637-639.

Sheridan, M.F. and Malin, M.C., 1983a. Application of computer-assisted mapping to volcanic hazard evaluation of surge eruptions: Vulcano, Lipari, Vesuvius. In: M.F. Sheridan and F. Barberi (Editors), Explosive Volcanism. J. Volcanol. Geotherm. Res., 17: 187-202.

Sheridan, M.F. and Wohletz, K.H., 1983. Explosive hydrovolcanism: Basic considerations and review. In: M.F. Sheridan and F. Barberi (Editors), Explosive Volcanism. J. Volcanol. Geotherm. Res., 17: 1-29.

Sheridan, M.F. and Marshall, J.R., 1983. Interpretation of pyroclast surface features using SEM images. J. Volcanol. Geotherm. Res., 16: 153-159.

Wohletz, K.H., 1983. Mechanisms of hydrovolcanic pyroclast formation: Size, scanning electron microscopy, and experimental studies. In: M.F. Sheridan and F. Barberi (Editors), Explosive Volcanism. J. Volcanol. Geotherm. Res., 17: 31-66.

Wohletz, K.H. and McQueen, R.G., 1983. Experimental Hydromagmatic volcanism. In: F.R. Boyd (Editor), Explosive volcanism: inception, evolution, and hazards. Studies in Geophysics, National Academy of Science.

D55

RIDGES ON BASALT FLOWS

Eilene Theilig, *Department of Geology, Arizona State University, Tempe, Arizona 85287*

Pressure ridges are surface features on basaltic lava flows and, as with other surface features, they may be related to the emplacement of a flow and the rheological properties of the lava. Ridges are common but not ubiquitous on basaltic flows and may reflect differences between flow emplacement which are not yet understood. Several mechanisms of formation have been proposed for pressure ridges but none can explain all types of pressure ridges and usually have been applied to explain only the ridges within a certain flow. Of these, the two most favored are: 1) inflation by continued addition of material either locally (Wentworth and Macdonald, 1953) or behind a slowly advancing flow front (Holcomb, 1980); and 2) buckling or crumpling of the crust associated with withdrawal of molten lava from a flow and subsequent loss of support (Skeats and James, 1937; Nichols, 1946; Parker, 1963; Champion, 1973). Field work has been initiated to determine ridge morphology on a variety of lava flows (Wapi flow, Idaho; McCartys flow, New Mexico; Schonchin Butte flow, California; and various flows on Kilauea, Hawaii) in order to define ridge types and to place constraints on mechanisms of formation. By understanding the factors important in the formation of pressure ridges it may be possible to place constraints on the method of emplacement, the eruptive rate, and the rheological properties of basaltic lava flows which contain them. Since many ridges are of sufficient size (as much as 20 m high, 50 m wide, and hundreds of meters long) to be detected on high resolution orbital images, an understanding of pressure ridges could provide a means for interpreting volcanic flows on other terrestrial planets.

Three different types of pressure ridges have been identified, so far, on the basis of morphology. Type I ridges are the most common and are associated with multiple flow unit pahoehoe in which the ridges are embayed by secondary toe-fed lava. They tend to be restricted to wider sections or margins of the flow and to be oriented longitudinal to flow direction; however, oblique or transverse orientation is not uncommon.

Profiles and crack locations are both related to the size of the ridge. Wide ridges tend to form domed arches with major cracks located near the margins and with minor medial cracks. Smaller, narrower ridges are usually gable-shaped with one major medial crack. Most type I ridges are intermediate between these two extremes. Preliminary analysis suggests that total crack width is also related to ridge size. Many of the cracks are asymmetric, with vertical offset of the surface or one wall at a much shallower angle than the other. This suggests a nonequal amount of rotation for each block. Very little lateral offset is exhibited. One feature which may be a unique characteristic of this ridge type is collapse areas along the ridge margin.

Bulbous squeeze-ups are common within cracks and may reflect relative timing of crack formation. This secondary material can completely fill a crack (in a few cases it flowed onto the surface of a ridge); but more commonly, the squeeze-up is attached to one wall suggesting continued crack separation after the source of the squeeze-up material had been cut off. In several cases, a series of squeeze-ups have been identified indicating alternate periods of crack formation and injection of material or slow crack separation and squeeze out of lava after a critical width was reached. Squeeze-up material attached to one wall generally grades downward into the ridge material and could be used to estimate depth to liquid lava.

The interior structure of type I ridges, as revealed by the large cracks and roadcuts, consists of an upper slab section which generally contains columnar joints and a lower massive section with an irregular surface. *This basic distinction may mark the thickness of the surface crust when ridge formation was initiated.*

Type II ridges occur in association with type I and are very similar with the exception of the secondary squeeze-out material. Instead of only filling cracks, the secondary material on these ridges originated from underneath a thin crust and flowed as toes or channels from the top and sides of the ridge. Medial cracks are smaller on these ridges.

Type III ridges are present on the Schonchin Butte block lava flow and have much steeper sides (almost vertical at the top) than the other types. Medial cracks are very wide and the crack walls are convex upward. No squeeze-ups are present. The main difference between type III and the others may be reflection of viscosity. Morphometric analyses are being done to determine other possible distinctions.

Evidence of the collapse mechanism for ridge formation as proposed by Skeats and James (1937) and Nichols (1946) includes: 1) definition of a plane by the relative ridge crest heights and 2) presence of a lower flow adjacent to and originating from the primary flow containing the ridges. Relative ridge crest heights have been determined on the Wapi, McCartys, and Schonchin Butte flows and no consistent pattern can be established. On only one of a sequence of profiles across the McCartys flow can a plane be defined by ignoring smaller ridges and using only the major ridges in the interior of the flow. On the Schonchin Butte flow a general pattern of higher ridge crests upstream and toward the center of the flow can be identified, but ridge crest heights vary and do not define a plane. Secondary material can be identified on the Wapi and McCartys lava flows. A field map was produced of a section of the McCartys flow to determine the relationship of the primary and secondary material. The ridges predominantly consist of primary material and the secondary material forms a series of flow units filling the depressions between ridges, with only one unit located on the outer edge of the flow. If the secondary material originated by draining from the primary flow and initiating collapse, then one would expect this material to be predominantly located outside or downstream of the main flow. However this is not the case. No secondary material was identified on the Schonchin Butte flow. Based on this evidence it seems unlikely for the pressure ridges studied so far to have formed by collapse.

REFERENCES

Champion, D.E., 1973. The relationship of large scale surface morphology to lava flow direction, Wapi lava field, SE Idaho, unpublished Master's thesis, State University of New York at Buffalo, 44 p.

Holcomb, R.T., 1980. Kilauea Volcano, Hawaii: Chronology and morphology of the surficial lava flows, unpublished report.

Nichols, R.L., 1946. McCartys basalt flow, Valencia County, New Mexico, Geol. Soc. Amer. Bull. 57, 1049-1086.

Parker, R.B., 1963. Recent volcanism at Amboy Crater, San Bernardino County, California, Calif. Div. Mines and Geology Sp. Rept. 76, 22 p.

Skeats, E.W. and A.V.G. James, 1937. Basaltic Barriers and other surface features of the newer basalts of western Victoria, Royal Soc. Victoria Proc. 49, 247-278.

Wentworth, C.K. and G.A. MacDonald, 1953. Structures and forms of basaltic rocks in Hawaii, U.S. Geol. Surv. Bull. 994, 98 p.

D56

N84 23487

Calderas in the Solar System

C. A. Wood, SN4/NASA Johnson Space Center, Houston, TX 77058

Caldera-topped volcanoes are the largest volcanic edifices on a planet, and represent relatively long term development of near surface magma chambers. In this report I compare the types, geometries, numbers, and distributions of calderas on the Earth, Mars, Venus, and Io. No calderas (as distinct from gravitationally enlarged craters on small shield volcanoes, see Wood (1984)) are known from the Moon, Mercury, or satellites other than Io.

Terrestrial Calderas. Following Williams (1941), terrestrial calderas are commonly defined as large, more or less circular, volcanic collapse depressions, with diameters considerably larger than any included vent. Somewhat arbitrarily calderas have been defined as having diameters >1 mile or sometimes >1 km; smaller depressions are termed craters. In actual practice these diameters do separate nearly all craters on cinder cones, maars, tuff rings, and summit pits on stratovolcanoes - most of which are simple eruption vents - from depressions resulting from partial emptying of near surface magma chambers. Only three general classes of calderas are numerically important on Earth: shield calderas (e.g., Mauna Loa), stratocone calderas (Crater Lake), and ashflow calderas (Valles). Shield calderas occur on broad, tall basaltic shield volcanoes when tumescent summits subside along near vertical ring fractures following partial drainage of magma from near surface chambers into rift zones. Evidence that basaltic ash was associated with caldera formation at Kilauea (Holcomb, 1981), Fernandina (Simkin and Howard, 1970), and Masaya (Bice, 1980) suggest that while collapse into a partially drained chamber is the main mechanism of caldera formation on shields, explosive activity may also play a significant role. Stratocone calderas truncate the summits of 2-3 km high stratovolcanoes (Frances and Abbott, 1973) following eruptions of 0.1 to 100 km^3 of silicic ash and pumice. Caldera formation occurs 2-3 times in many stratovolcanoes (e.g., Etna, Fuji), and most extinct stratovolcanoes have a caldera or a dome filled one. Ashflow calderas result from similar eruption processes but the eruptive volume is huge (100-1000 km^3), and commonly no single pre-existing cone existed.

The diameter distribution of terrestrial calderas (Fig. 1), based on data for 220 calderas compiled by Pike (1978) and Pike and Clow (1981), shows that each caldera class is dominant for a particular diameter (D) interval: shield calderas, D<2 Km, stratocone calderas D = 2-13 km, ashflow calderas D>13 km.

To aid in the interpretation of possible calderas on other planets additional topographic data, averaged from values listed in Pike (1978) and Pike and Clow (1981) are given in Table 1. The relation of caldera classes to tectonic environments is summarized in Figure 2.

Martian Calderas. About 2 dozen calderas have been recognized on Mars and these have been classified into a multitude of distinct morphological types. However, Alba Patera, domes, and shields all appear to be shield caldera variants. Highland paterae and amphitrites calderas are clearly different from the martian shields (and each other) and are unlike any terrestrial caldera classes. Thus only 3 classes of caldera are relatively

common on Mars, but the mechanisms of formation of the non-shields are not understood.

Ioian Calderas. One hundred percent of Io is covered by volcanic deposits, and calderas and pit craters abound. The distinction between calderas and pit craters is apparently the presence of radiating flows from the former (Schaber, 1980), but both types of depressions are calderas morphologically. Ioian calderas, however, are not formed on mountain summits but appear to lie on flat plains (Carr et al., 1979). The large diameters (ave. = 54 km) and low relief of calderas on Io suggested to Carr et al. (1979) and Schaber (1980) that ashflow calderas are the best terrestrial analog. This is unlikely based on the shield like morphology of the calderas themselves, and the lack of evidence of resurgence or ring extrusions in the ionian calderas.

Venusian Calderas. The evidence for calderas on Venus is inconclusive but suggestive. Theia Mons is the best candidate on Venus for an Olympus Mons-like shield volcano and caldera (Saunders and Malin, 1977). Other low relief calderas may exist on Venus, but the limitations of radar data currently available makes difficult deciding between impact and volcanic origins (e.g., Burns and Campbell, 1983).

Caldera Comparisons on Different Worlds. The number of calderas on a planet is roughly proportional to the planet's mass (Fig. 3), which is a major factor in regulating planetary thermal evolution. Based upon the relation shown in Figure 3, Mercury may have a few calderas (none have been found on the 46% of the planet photographed by Mariner 10), Venus should have a few hundred, and Titan and smaller satellites should have none. Io is a clear anomaly, but its volcanism is tidally produced, not the result of internal thermal evolution.

Only 4-5 caldera classes (eruption mechanisms) are common in the solar system. Shields are the most common type of calderas on the observed planets, attesting to the prevalence of similar thermal and tectonic mechanisms (hot spots). It is remarkable that the total volume of individual large shields (or shield lines - e.g., Hawaii-Emperor Chain - on Earth) is nearly the same (1-3 x 10^6 km^3) on Earth, Mars, and Venus, perhaps implying relatively similar compositions (including radioactivity contents).

The average diameters for calderas on Earth, Mars, Venus, and Io are 5, 85, $\sim$75, and 54 km, respectively. If, as at Kilauea, caldera diameter approximately equals magma chamber diameter and depth, terrestrial magma chambers are significantly smaller and shallower than are their counterparts on other planets. However, since shield caldera diameters are about 10% of shield edifice diameter on Earth, Mars, and Venus, the smallness of terrestrial magma chambers probably reflects simply the small size of the Earth's shield volcanoes.

References

D.C. BICE (1980) Absts/Programs GSA 12, 98; B.A. BURNS and D.B. CAMPBELL (1983) "Radar evidence for cratering on Venus", in press; M.H. CARR et al. (1979) Nature 280, 729; P. FRANCIS and B. ABBOTT (1973) Nature 244, 22; R. HOLCOMB (1980) USGS Open File Rpt. 81/354; R.J. PIKE (1978) Proc. Lunar Planet. Sci. Conf 9th, 3239; R. J. PIKE and G.D. CLOW (1981) USGS Open File Rpt. 81/1038; R.S. SAUNDERS and M.C. MALIN (1977) Geol. Romana 15, 507; G.G. SCHABER (1980) Icarus 43, 302; T. SIMKIN and K.A. HOWARD (1970) Science 169, 429; H. WILLIAMS (1941) Univ. Calif. Pubs. Dept. Geol. Sci.

25, 239; C.A. WOOD (1984) "Calderas: A planetary perspective", in press.

TABLE 1: Average Topographic Data for Planetary Caldera Classes

Class	D	W	H	D/W	H/W	Volume	#
Earth							
Shield	3.7 km	41 km	1.7 km	0.09	0.04	$7x10^3 km^3$	32
Stratocone	5.1	26	1.0	0.20	0.04	$2x10^3$	142
Ashflow	17.7	46	0.5	0.38	0.01	$3x10^3$	38
Mars							
Shield	78	600	18	0.13	0.03	$2x10^6$	4
Domes	31	115	3.8	0.27	0.03	$1x10^4$	4
Patera	58	245	?	0.23	?	?	3
Amphitrite	87	?	?	?	?	?	5
Stratocone	6	19	?	0.31	?	?	1
Venus							
Shield	~75	~700	~10	~0.11	~0.01	$\sim 1x10^6$	1
Io							
Shield	54	?	?	?	?	?	93

Data Sources:

Earth and Mars: Pike, 1979 and Pike and Clow, 1981.
Venus: Malin and Saunders, 1977.
Io: Schaber, 1982.
D = average caldera diameter. W = average diameter of volcano. H = average height of volcano. # = number of volcanoes used to determine averages.

DIAMETER DISTRIBUTION: TERRESTRIAL CALDERAS

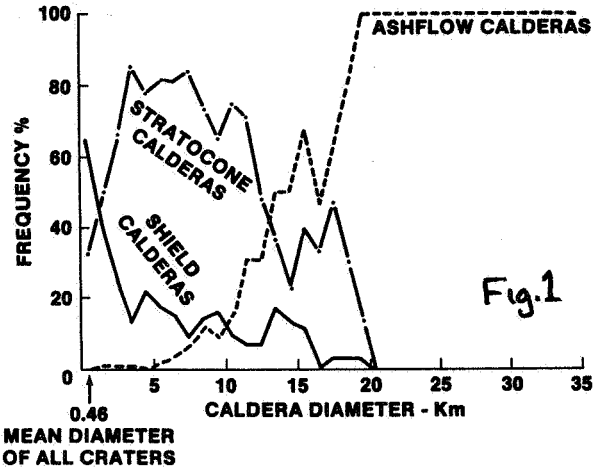

Fig.1

Fig.2

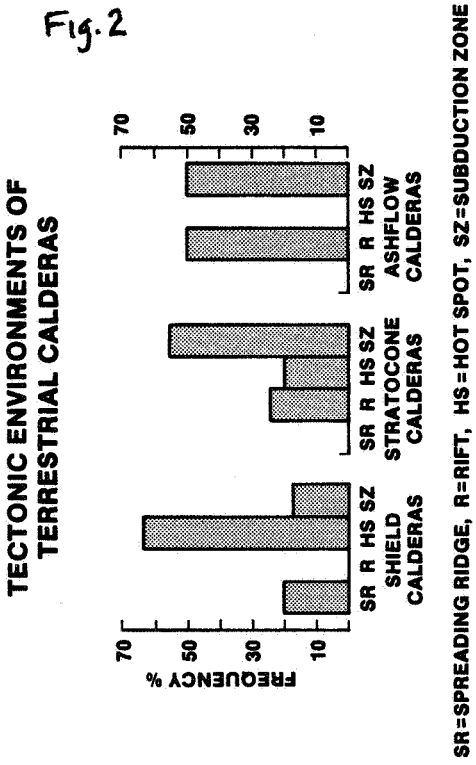

Fig.3

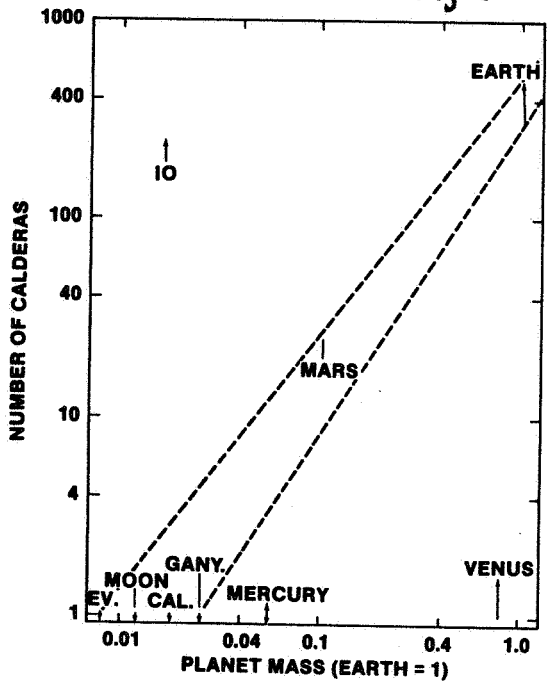

Chapter 6

AEOLIAN PROCESSES AND LANDFORMS

WIND STREAKS ON MARS: COMPARISONS OF PRODUCTION MODELS WITH OBSERVATIONS OF BRIGHT STREAKS

Steven W. Lee, Cornell University

To investigate the influence of crater size on martian wind streaks, the characteristics of bright streaks associated with craters ranging from ~ 100 m to ~ 80 km in diameter have been analyzed in several regions (Lee, 1983). The ratio of streak length to obstacle height (L/h) could be diagnostic of the relative effectiveness of different sized obstacles in disturbing near-surface atmospheric flow; since the crater rim height to diameter relationship has not previously been determined for Mars, the rim heights of numerous craters have been estimated from shadow measurements (Fig. 1). In all areas studied, bright streak L/h values decrease with increasing h, indicating that smaller obstacles produce longer streaks relative to their height than do larger obstacles. Several models of bright streak production have been considered to explain this behavior.

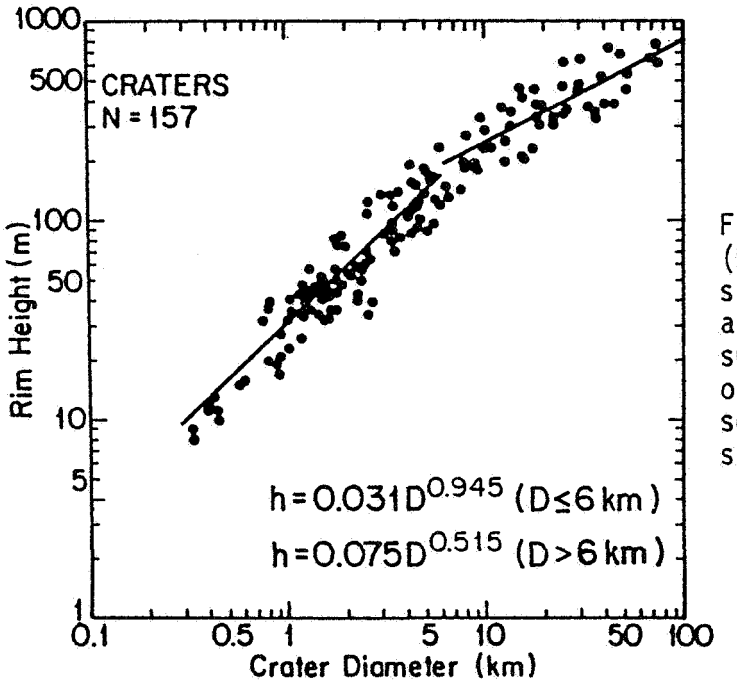

FIGURE 1. Crater rim height (h) to diameter (D) relationship for Mars. Rim heights are derived from shadow measurements. N is the number of craters included. Least-squares fits to the data are shown.

A. Blocking model: Veverka et al. (1981) proposed that bright streaks result when atmospheric flow is blocked downwind of an obstacle during times of high static stability and significant dust loading (such as the late stages of global dust storms). Dust settles out of the sheltered zone and is deposited on the surface, forming a bright streak. In this model, streak length is proportional to $h/C_d^{\frac{1}{2}}$ where C_d is a drag coefficient related to the surface roughness. Least-squares fits of this model to the L/h data for bright streaks have been made using C_d as the free parameter (Fig. 2). For the areas considered, the match between

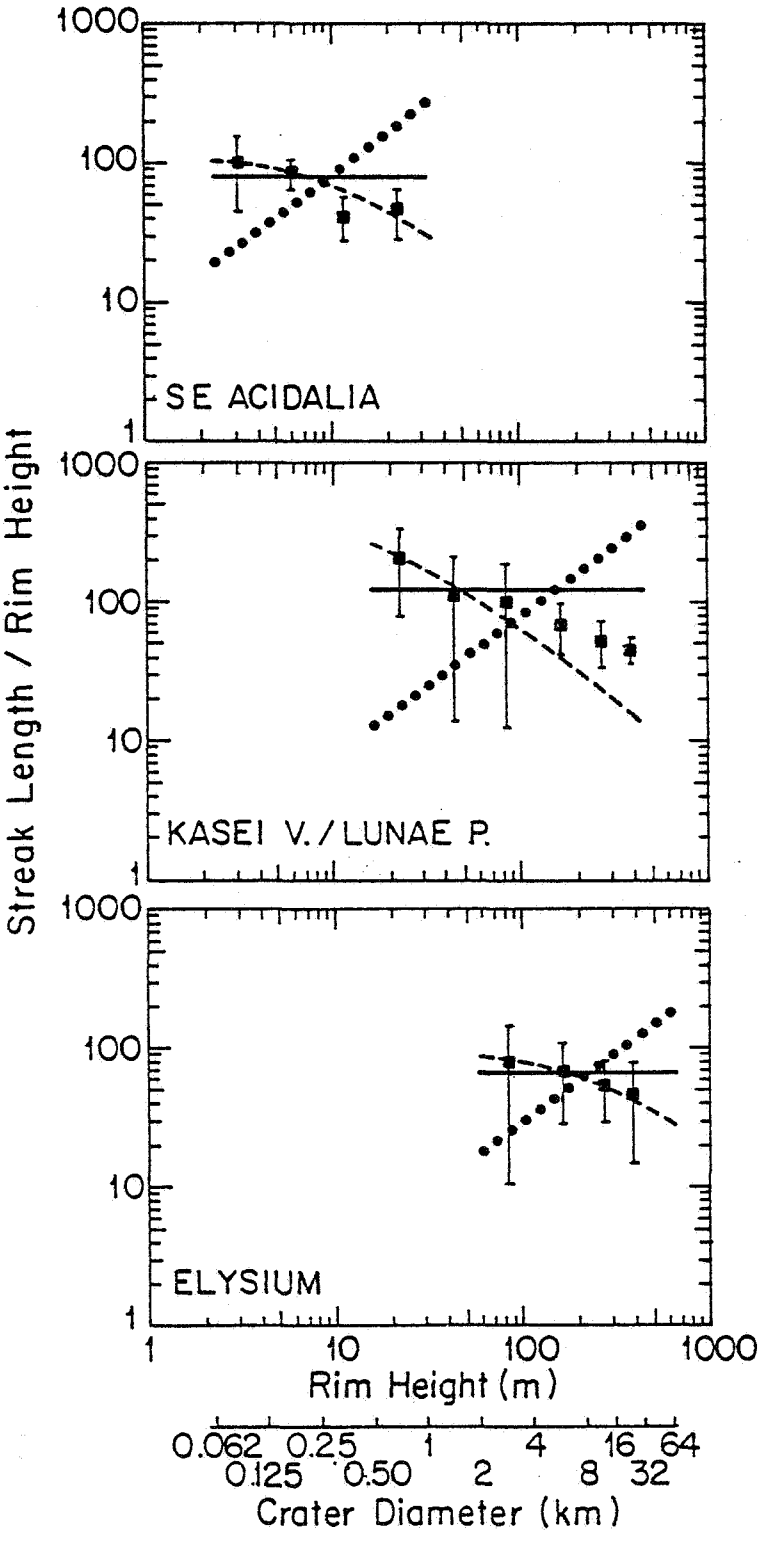

FIGURE 2. Models of bright streak production compared to streak occurrence data for several regions. Mean L/H values (squares) represent the observed streak behavior; error bars denote one standard deviation in L/h. Least-squares fits of the blocking model (solid line), the constant eddy diffusion model (dotted line), and the height-dependent dust loading model (dashed line) are shown for each area.

model and observed lengths is good for smaller craters; however, larger obstacles generally produce shorter streaks than would be expected from this model. It may well be that as crater diameter, and hence complexity of crater and ejecta morphology (Pike, 1980) increases, so does C_d, effectively producing the observed negative slope in L/h vs. h.

B. Constant eddy diffusion model: R. Kahn (personal communication, 1983) has suggested that dust diffusion into the lee of an obstacle is due to eddies induced by the surrounding rather than by the obstacle itself. In this case, streak length is proportional to $(U/\nu)h^2$ where U is the free-stream wind speed and ν is an isotropic eddy diffusion coefficient. Using U/ν as the free parameter for least-squares fits, the trend predicted by this model is clearly contrary to the observations (Fig. 2).

C. Height-dependent dust loading: If most of the suspended dust at the time of streak formation is concentrated near the surface, increasing the height of a blocking obstacle may yield little increase in the amount of dust available for deposition. The simple blocking model described above can be modified to account for the dust scale height (H) so that $L \sim H(1-e^{-h/H})/(C_d^{-\frac{1}{2}})$. Least-squares fits using H and C_d as free parameters agree with the observations reasonably well (Fig. 2). However, the estimated dust scale heights, ranging from a few tens to a few hundred meters, are difficult to accept as realistic; observations of martian dust storm clouds suggest uniform dust loading within the lower km or more of the atmosphere (Conrath, 1975; Pollack et al., 1979).

We conclude that Model A is the most satisfactory. It can be made consistent with the observations by assuming that C_d is a function of crater diameter and does not make any unreasonable assumptions about martian conditions. Model B is clearly incompatible with the observations. Model C can be made to fit the data very well, but involves an assumption (dust loading strongly concentrated near the surface) which is inconsistent with generally accepted interpretations of conditions on Mars.

This study was supported by NASA Grant NSG-7546.

REFERENCES:

Conrath, B. Thermal structure of the martian atmosphere during dissipation of the dust storm of 1971. Icarus 24, 36-46, 1975.

Lee, S. W. Mars: Wind streak production as related to obstacle type and size. Submitted to Icarus, 1983.

Pike, R. J. Control of crater morphology by gravity and target type: Mars, Earth, Moon. Proc. Lunar Planet. Sci. Conf. 11th, 2159-2189, 1980.

Pollack, J. B., D. S. Colburn, F. M. Flasar, R. Kahn, C. E. Carlston, and D. Padek. Properties and effects of dust particles suspended in the martian atmosphere. J. Geophys. Res. 84, 2929-2945, 1979.

Veverka, J., P. Gierasch, and P. Thomas. Wind streaks on Mars: Meteorological control of occurrence and mode of formation. Icarus 45, 154-166, 1981.

D58

N84 23489

MARTIAN DUST STORM WITNESSED BY VIKING LANDER 1

Henry J. Moore (U.S. Geological Survey, Menlo Park, CA., 94025). E. A. Guinness, R. E. Arvidson (Department of Earth and Planetary Sciences, Washington University, St. Louis, MO., 63130).

Viking Lander 1 (Mutch Memorial Station) observations on Mars were punctuated by a strong local dust storm after two martian years of mild wind conditions (1, 2, 3). Tens of micrometers of dust settled to the surface during global dust storms of the first two falls and winters; some of this dust was locally removed during the second year (4). A late-winter local dust storm of the first year (5) caused little or no erosion of the surface materials (6) despite wind speeds of 25-30 m/s (5).

The strong local dust storm occurred during late winter of the third martian year (3). Winds of this storm altered and demolished small conical piles of surface materials constructed at the onset the first winter, removed 4-5 mm-size fragments, displaced centimeter-size fragments, destroyed clods in areas disrupted by the sampler and footpad, eroded impact pits, and darkened the sky. Most of the erosion occurred where cohesions of the surface materials were destroyed by the sampler; otherwise the surface materials appeared to be quite stable.

Movement of erosional products and tiny wind tails indicate easterly to northeasterly winds. If the 4-5 mm size fragments were entrained and removed by the wind, threshold friction speeds (7) near 3 to 5 m/s would have been required for the atmospheric temperatures and pressures that prevailed during the late-winter of the third year. Using the Von Karman relationship, surface roughness values of 0.1 to 1.0 cm (8), and these friction speeds, we would expect wind speeds of 40-90 m/s at the height of the meteorology wind sensor (1.6m).

A global dust storm was in progress early in the fourth fall season (2,3).

References:

[1] Moore, H. J., 1982, Erosion of surface materials at the Mutch Memorial Station (Lander 1), Mars: Repts Planet. Geology Prog.-1982, p. 180-181.

[2] Wall, S. D., 1982, Viking Lander monitor mission imaging investigtion status report: Repts. Planet. Geology Prog. 1982, p. 379-381.

[3] Arvidson, R. E., Guinness, E. A., Moore, H. J., Tillman, J., and Wall, S. D., 1983, Three Mars years: Mutch Memorial Station (Viking Lander 1) imaging observations: accepted by Science.

[4] Guinness, E. A., Leff, C. E. and Arvidson, R. E., 1982, Two Mars years of surface changes seen at the Viking landing sites: Jour. Geophys. Res. v. 87, p. 10,051-10,058.
[5] Ryan, J. A., Sharman, R.D., and Lucich, R. D., 1981, Local Mars dust storm generation mechanism: Geophys. Res. Lttrs., v. 8, p. 899-901.
[6] Moore, H. J., Spitzer, C. R., Bradford, K. Z., Cates, P. M., Hutton, R. E. and Shorthill, R. W., 1979, Samplefields of the Viking Landers, physical properties, and aeolian processes: Jour. Geophys. Res., v. 84, p. 8365-8377.
[7] Iversen, J. D., Greeley, R., and Pollack, J. B., 1976, Windblown dust on Earth, Mars and Venus: Jour. Atmos. Sciences, v. 33, p. 2425-2429.
[8] Sutton, J. L, Leovy, C. B., and Tillman, J. E., 1978, Diurnal variations of the martian surface layer meteorological parameters during the first 45 sols at the two Viking Lander sites: Jour. Atmos. Sciences, v. 35, p. 2346-2355.

D59

N84 23490

LONG RANGE TRANSPORT OF FINE GRAINED SEDIMENTS ON MARS: ATMOSPHERIC DUST LOADING, AS INFERRED FROM VIKING LANDER IMAGING DATA. James B. Pollack and David S. Colburn, Space Science Division, NASA Ames Research Center, Moffett Field, CA 94035.

During a typical Martian year, hundreds of local dust storms and one or several global dust storms occur. In addition to involving saltation by 100 micron-sized sand grains, these storms also result in the emplacement of micro-sized dust particles into suspension. Once in suspension, the dust is carried long distance by the prevailing winds before being deposited. Studies of the amount of dust loading in the atmosphere over the course of a Martian year and its interannual variation help to define the rate at which aeolian erosion and deposition are occurring over large distance scales.

We are analyzing Viking lander imaging data in order to obtain quantitative estimates of atmospheric dust loading. During the first 900 SOLS at both landing sites, optical depths for the dust can be obtained in a straightforward manner by applying Beer's law to pictures taken of the sun with the sun diode. At later times, no sun diode data is available, but the brightness of the sky and ground can be modelled with a radiative transfer code to derive somewhat less accurate values of the dust optical depth. This approach makes use of microphysical properties of the dust and the photometric function of the surface derived from earlier parts of the mission when the optical depth was found from sun diode images. In applying this technique, we have carefully selected several patches at the lander 1 site that show little change in contrast over the mission. Optical depths are derived independently for both several ground patches and several portions of the sky to provide a check on the accuracy of this technique.

Results to date are as follows: During the first Viking year, two global dust storms occurred and they contributed about 90% of the dust suspended in the Martian atmosphere on a global average, over the course of this year. The remainder was due to the cumulative effect of local dust storms. When globally distributed, the amount of suspended dust introduced into the atmosphere this Martian year was about 5×10^{-3} g/cm^2. This mass loading was derived from the incremental optical depths measured over this year and estimates of the mean size of the dust particles (2.5 microns). During the second Martian year, global dust storms were far more muted than during the first year. No near-perihelion dust storm occurred, and a somewhat weaker dust storm may have occurred near the start of the spring season in the southern hemisphere, at about the same time that the first global dust storm of the first year occurred. Thus, the dust loading derived for the first Martian year may be somewhat higher than the average over many Martian years, a conclusion that appears to be supported by our preliminary studies of Martian years beyond the second Viking year on Mars.

DUST STREAKS ON MARS: COLORS AND PHOTOMETRY

P. Thomas, Laboratory for Planetary Studies, Cornell University
Ithaca, New York 14853

Photometric studies of crater-related bright and dark streaks have strongly supported the hypothesis that the bright streaks are excess dust deposits and dark streaks are erosional windows in a partial dust cover. The findings include:

1. Colors of streaks. Red-blue (and red-violet) plots such as Fig. 1 show that bright streaks are consistent with mosaics of bright red dust (taken to be similar to brighter parts of Arabia) and background material. Here the plains are also consistent with a partial cust cover; the dark streak is the least covered area.

2. Phase effects. Bright and dark streaks both reverse contrast relative to surrounding plains at phase angles over 100°, in violet filter (λ_{eff} ~ 0.45 μm) images (Fig. 2a). Laboratory simulations of dust deposition can crudely simulate this behavior with either optically thick or optically thin dust deposits (Fig. 2b). The similar phase behavior of both bright and dark streaks supports the idea that they are both changes in the amount of dust cover.

3. Red-violet plots of bright streaks are most easily explained by mosaics of optically thick dust and plains material. Optically thin coatings of dust give mixing lines on red-violet plots that project above the violet reflectance of dust; the bright streak data project at or below the dust value. This behavior can be matched by mosaics of optically thick dust, in some cases preferentially deposited on the parts of background brighter in the violet (on soil between boulders?).

4. Lengths of bright streaks are independent of their contrasts. This suggests the streak deposition, if in the mosaic patterns indicated above, is a function of available sites of deposition, rather than atmospheric dust loading. Differences in wind shear may control the percentage of the ground available for dust deposition and thereby control the average brightness of the ground.

5. Contrasts of dark streaks with plains indicate the plains have fractional dust covers nearly as great as the maximum additional cover in bright streaks. The bright streaks thus store very little of the global supply of dust. The amounts of dust in streaks may be much less than 10^{-3} gm/cm^2 (Wells et al., 1983). The total amount of dust in all bright streaks on Mars might be only ~ 10^5 tons. Partial dust coverage of the plains can easily accommodate dust raised in martian global dust storms (Pollack et al., 1979).

REFERENCES:

Pollack, J. B., D. G. Colburn, F. M. Flasar, R. Kahn, C. E. Carlston, and D. Pidek, 1979. Properties and effects of dust particles suspended in the martian atmosphere. J. Geophys. Res. 84, 2929-2945

Wells, E. N., J. Veverka, and P. Thomas (1983). "Mars: Albedo changes caused by dust fallout." Submitted to Icarus.

FIG. 1. Red and blue reflectance of bright streaks, dark streaks, and plains in Amazonis Planitia. V.O. images 41B53,55. Color of "dust" is obtained from images taken at similar geometry in Arabia. The straight trend is consistent with, but does not prove, a mosaic of the dust and a darker background. Here the background is the dark streak; the plains and bright streak could be mosaics of progressively greater coverage by dust.

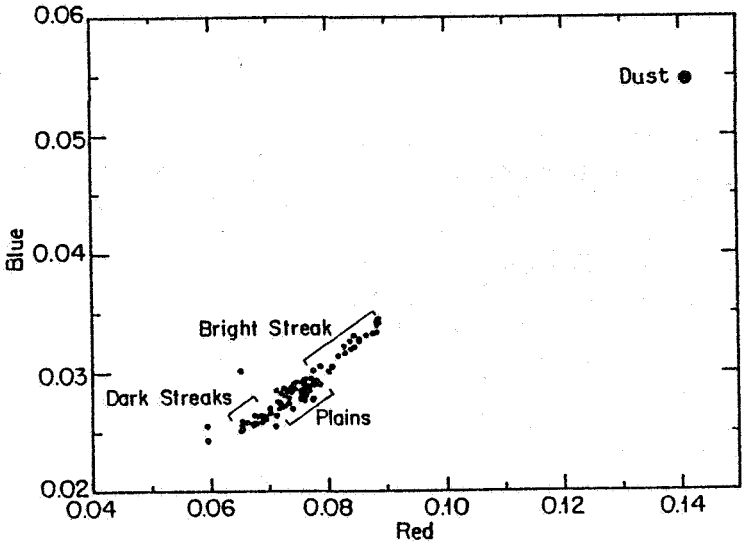

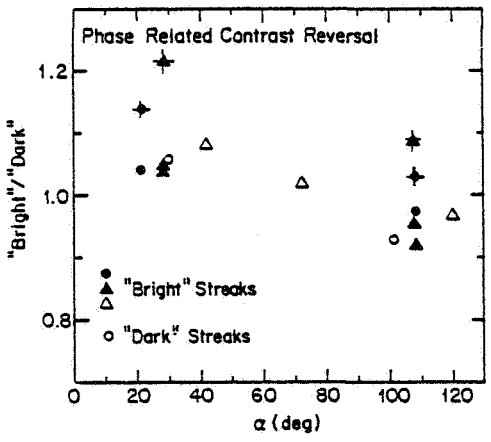

2a.

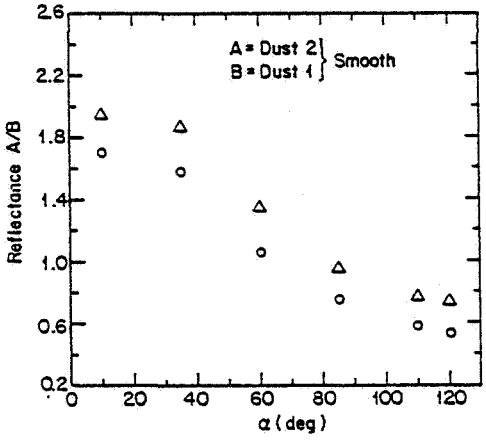

2b.

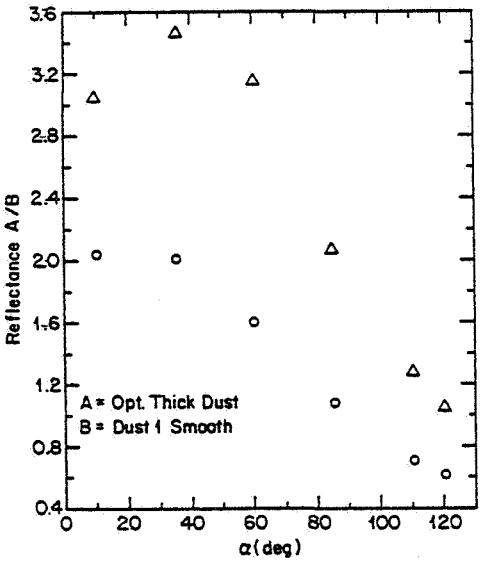

2c.

FIG. 2. Phase behavior of bright and dark streaks compared to laboratory simulation of dust streaks.
a. Phase behavior of bright and dark streaks from Viking Orbiter data, violet filter (λ = 0.45 μm), and red ($\lambda \sim 0.59$ μm; crosses indicate red filter data). Values plotted are the brightness ratios of streak/plains for "bright" streaks and plains/streaks for dark streaks.
b,c. Contrast reversal in laboratory dust deposits. Triangles are data at 0.59 μm; circles are at 0.45 μm. Layer 1 is 9×10^{-5} gm/cm^2, layer 2 is 2.1×10^{-4} gm/cm^2. Optically thick layer is 3.5×10^{-3} gm/cm^2. In both instances the greater deposit of dust becomes darker in the violet at high phase angles.

N84 23492

D61

A POSSIBLE SOURCE FOR THE MARTIAN CIRCUMPOLAR DUNE MATERIAL

R. Stephen Saunders, Bruce Banerdt, Jet Propulsion Laboratory, Pasadena, CA.; Steve Sutton, University of Michigan; Frazer Fanale, University of Hawaii; Eric Laue, James Stephens, Jet Propulsion Laboratory, Pasadena, CA.

The properties of freeze-dried dilute dispersions of dust in water are of considerable interest in studies of sedimentary processes in the polar regions of Mars. The formation of a "rind" residue due to the sublimation of water ice containing various amounts of clay may be an important step in these processes. Such phenomena may occur as the result of seasonal or long term (climatic) sublimation of dirty ice caps on Mars.

We have attempted to simulate the development and disruption of dust residues on the surface of ice-dust mixtures as a result of preferential ice sublimation. These simulations were achieved by a variety of experimental approaches, including the simultaneous spraying of 100 micron water droplets and 0.1 micron montmorillonite grains into liquid nitrogen and the fine spraying of various concentrations (10%, 1%, and 0.1%) of the same silicate in liquid water into liquid nitrogen. Sublimation of the nitrogen and the water produced ice-free rinds in the form of large cohesive agglomerates of individual clay particles, and in some cases a continuous cohesive crust. Scanning electron microscope observations reveal that the material formed by freeze-drying the 0.1% suspension does not retain the original spherical shape of the sprayed droplets; instead it consists of a uniform, open, filamentary network.

When this material is placed in a tumbler, it breaks up into smaller particles with a distribution of sizes which are still considerably larger than the original submicron clay particles (about 2 mm) and have an extremely low density (<0.1 gm/cm^3) (see figure). These aggregates differ from those discussed by Greeley (1979) in several respects. They have a very open, porous structure resulting in low density, as opposed to Greeley's "popcorn ball" structure. Also, electrostatic charging does not appear to be important as a binding force, since the particles were studied at length in an SEM without detectable disruption or charge build-up.

We suggest that the martian circumpolar dune fields may have been formed by deposits of this type of material transported from the polar deposits. We propose the following scenario. Fine dust particles are deposited in the polar cap. Primarily by acting as nucleation centers for condensation of water and carbon dioxide and precipitating out of the atmosphere in the form of "dirty snow". This results in an intimate mixture of fine particles and ice. When the cap later sublimes, these

particles form a fluffy rind on top of the receding ice surface. The rind is disrupted by wind and comminuted into roughly sand-sized particles. These particles have a high sail area to mass ratio, and can be easily moved and formed into dunes by the relatively sluggish polar winds. The material may later become immobilized by collapse of the particles due to the burial.

While the strength of the inter-particle bonds appears to be only moderate, the survivability of the aggregates is enhanced both by their low density (hence low impact momentum) and the shock absorbing characteristics of the filamentary structure. We are currently investigating the strength of these particles via compressibility and long-term comminution experiments, as well as refining our production methods in order to more closely simulate martian conditions.

Figure: Particle formed by freezing a 1% suspension of montmorillonite, subliming it in a vacuum, and tumbling the residue for 1/2 hour. Particle diameter is about 5mm and its density is 0.03 gm/cm^3.

D62

N84 23493

VELOCITIES OF WINDBLOWN PARTICLES IN SALTATION: VENUS, EARTH, AND MARS

Ronald Greeley, *Department of Geology, Arizona State University, Tempe, AZ 85287*

Aeolian (wind) processes occur on all terrestrial planets except Mercury and to varying degrees are responsible for surface modification through erosion and deposition. In order to assess such factors as rates of transportation and erosion by windblown grains, knowledge of particle velocities as functions of such factors as wind speed is required for the diverse environments found on the planets subject to aeolian processes (Table 1).

Particle velocities have been determined in environmental wind tunnels capable of simulating aeolian processes on Earth, Mars, and Venus (Greeley et al., 1981, 1982). Particles of a given composition and size were placed in the tunnels and subjected to various wind speeds above threshold. For Earth and Mars simulations, particle velocities were measured directly using a velocimeter (Greeley et al., 1983) positioned at specific heights above the surface; approximately 200 velocities were determined at each height. The particles used were in a narrow size range and were subjected to a steady wind. Figure 1a shows a typical distribution of velocities measured at a single height; the wide range in speeds is a reflection of grains in different parts of their saltation trajectory. White (1979) has demonstrated that particle velocity should increase throughout the trajectory on Earth and Mars, reaching a maximum upon impact with the surface. In some experiments, however, some particles travel at speeds in excess of the wind speed, which is attributed to acceleration resulting from intergrain collisions and elastic rebound. Figure 1b shows the general increase in particle speed with height which reflects the general increase in wind speed through the boundary layer above the surface. In addition, grains reaching greater heights in their saltation trajectory are in flight longer and can be accelerated to a greater speed than grains on short trajectories.

Figure 1c shows velocities at a single height for two sizes of particles as functions of wind speed. Smaller particles travel at higher velocities than larger particles, which may be attributed to a better "coupling" between the wind and the smaller particles owing to their larger cross-sectional area-to-mass ratio. However, despite a wide range in freestream wind speeds, the average particle velocity remains remarkably constant.

Velocities of windblown grains were also determined using high-speed motion pictures in a field experiment on Earth and in wind tunnel simulations for terrestrial and venusian environments. Using filming rates up to 10,000 frames per second enabled individual grains to be photographed to determine their velocities and trajectories. Although few experiments have been run using this technique, results from the field experiment are closely matched by results obtained from the wind tunnel and give confidence in the simulations. The filming technique has also been applied to the analyses of particle velocities from experiments run in the Venus Wind Tunnel. Although the absolute velocities are very low (a reflection of the low threshold wind speeds on Venus), it was found that the particles achieve very nearly the same velocity as freestream wind speed.

Comparisons of results for Earth, Mars, and Venus reveal some remarkable differences. As shown in Figure 2, most particles achieve speeds nearly equal to freestream wind speed on Venus, but seldom achieve half the wind speed on Mars; Earth cases are of intermediate values. This is attributed to the differences in atmospheric density and to the threshold wind speeds among the three planetary environments (Table 1). Particles are more easily moved in the dense venusian atmosphere than on Mars; consequently, threshold speeds are very low, and for the range of wind speeds in which most movement is presumed to occur (just above threshold speeds), the grains need not be moving very fast to achieve 100% of the wind speed. Conversely, particles on Mars must accelerate very rapidly to achieve the speed of the high winds required for threshold, and despite the fact that saltation path lengths are long on Mars (White, 1979), most grains fall to the surface before achieving even 50-60% of freestream wind speed.

These results imply that aeolian abrasion should be most effective on Mars, least effective on Venus, and would be intermediate on Earth, all other factors such as supply of windblown materials, being equal. However, as has been demonstrated for Mars (Greeley et al., 1982), analyses of wind abrasion and erosion is a complex phenomenon which involves many parameters, each of which must be assessed individually and in the context of the whole system.

REFERENCES

Greeley, R., B.R. White, J.B. Pollack, J.D. Iversen, and R.N. Leach, 1981. Dust storms on Mars: Considerations and simulations: NASA Technical Memo. TM 78423, 29.

Greeley, R., R.N. Leach, S.H. Williams, B.R. White, J.B. Pollack, D.H. Krinsley, and J.R. Marshall, 1982. Rate of wind abrasion on Mars: J. Geophys. Res. 87, 10009-10024.

Greeley, R., S.H. Williams, and J.R. Marshall, 1983. Velocities of windblown particles in saltation: Preliminary laboratory and field measurements: Proc. International Assoc. Sedimentologists, Symposium on Aeolian Processes, Hamilton, Ont., 1982 (in press).

White, B.R., 1979. Soil transport by winds on Mars: J. Geophys. Res. 84, 4643-4651.

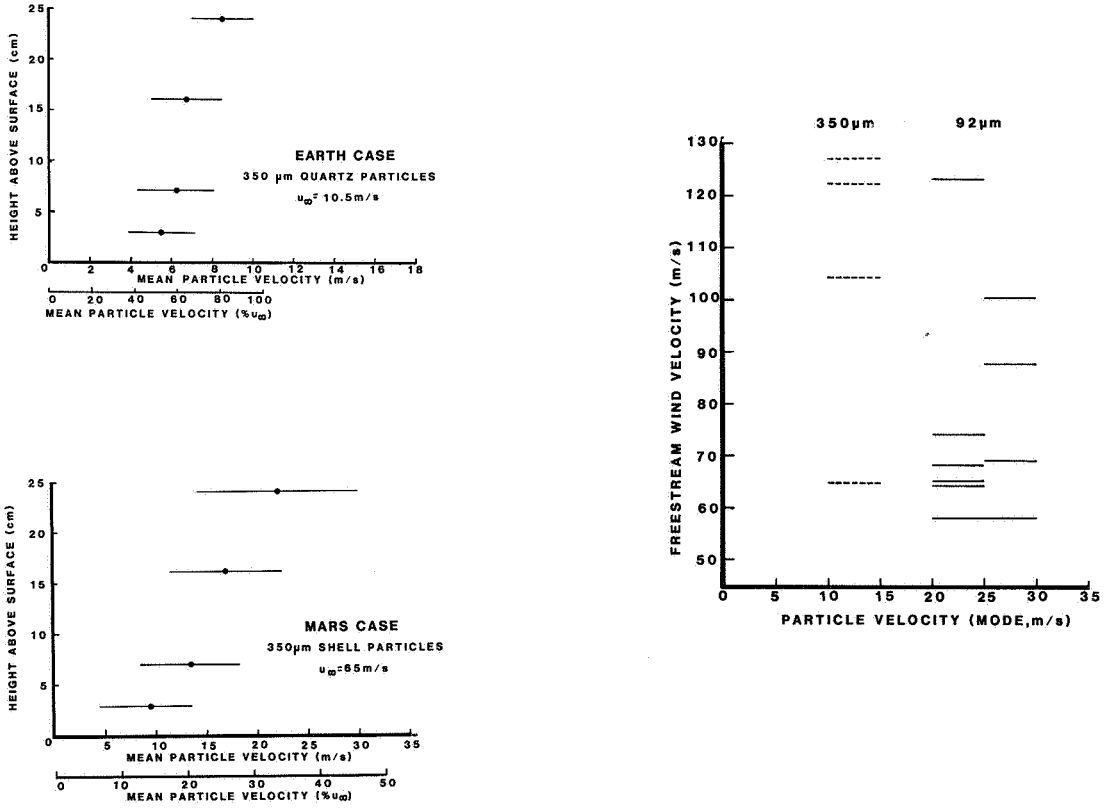

Figure 1. a) Distribution of particle velocities for 350 μm quartz grains subjected to a freestream wind speed of 10.22 m/s, measured at a height of 16.1 cm (Earth simulation); b) velocities of 350 μm particles subjected to a freestream wind speed of 16.5 m/s in a martian simulation; c) particle velocities for two particle sizes as a function of freestream wind speed.

Table 1. Aeolian Parameters, Earth, Mars, and Venus

	VENUS	*EARTH*	*MARS*
Atmospheric surface pressure (millibars)	90,000	1,000	6
Atmospheric composition (principal)	CO_2	N_2,O_2	CO_2
Surface temperature (average)	480°C	22°C	-23°C
Surface gravity (Earth = 1)	.88	1	.38
Minimum threshold wind speed (cm/sec)	2.2	20.5	250
Optimum particle size (μm)	115	75	75

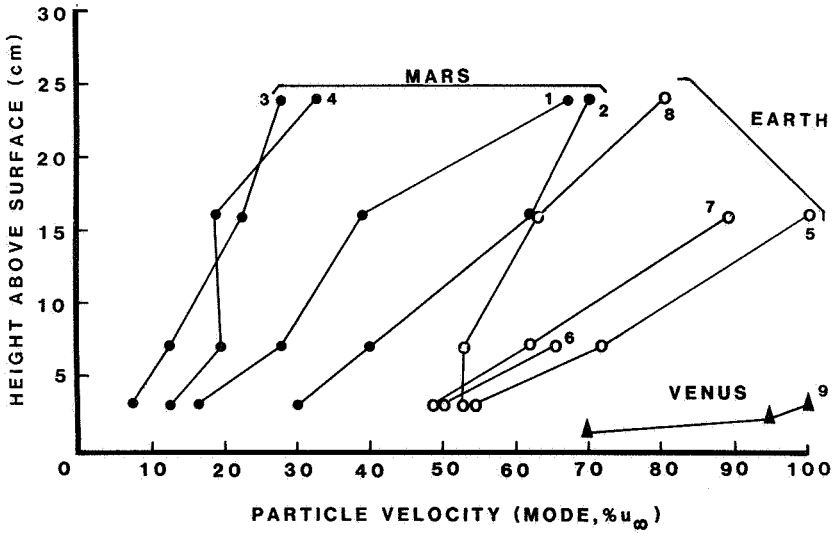

Figure 2. Particle velocities in Earth, Mars, and Venus simulations normalized to freestream wind speed.

DESERT PAVEMENT STUDY AT AMBOY, CALIFORNIA

Steven Williams and Ronald Greeley, *Department of Geology, Arizona State University, Tempe, AZ 85287*

Desert pavement is a general term describing a surface that typically consists of a thin layer of cm-sized rock fragments set on top of a layer of finer material in which no fragments are found (Cooke and Warren, 1973). The concentration of fragments can be very high, sometimes with the fragment edges interlocking. Desert pavements are common and are often known by local names, including gibber plains (Australia), hammada (Middle East), reg (Middle East), and sai (central Asia). Three mechanisms for desert pavement formation have been suggested (see Cooke and Warren, 1973, for summary). The first is purely aeolian in which fine particles are deflated by wind from a surface, leaving fragments which form an armored surface (Blake, 1904; Gilbert, 1875; Symmons and Hemming, 1968). The second mechanism requires the upward migration of rock fragments from within the soil layer, driven by cycles of freezing and thawing or cycles of wetting and drying (Springer, 1958; Inglis, 1965; Cooke, 1970). The third mechanism of pavement formation is the removal of fine particles from a surface by sheet wash (Sharon, 1962).

An understanding of desert pavement is important to planetary geology because they may play a major role in the formation and visibility of various aeolian features such as wind streaks, which are important on Mars (Thomas et al., 1981; Veverka et al., 1981; and others) and may be important on Venus. As a part of this study, an experiment has been underway since 1978 in the Mojave Desert near Amboy, California. The Amboy site was selected because it has well developed pavement surfaces, is the site of a wind streak, and has been used for martian planetary studies (Greeley et al., 1978). Two sites were selected for analysis, one inside the wind streak and one upwind of the streak. In each site, two 3 m^2 plots were prepared, one in which the desert pavement surface was removed by gentle raking and one in which the rock fragments were trampled into the subsurface layer. The sites have been monitored about five times each year to determine the rate of reestablishment of the pavement surface. It was found that the trampled surfaces were restored very quickly—on the order of months— but the raked surfaces have had no restoration of fragments except near the margin of the plot where a few fragments were transported into the raked area by sheet wash. There was no observed difference in the rate of reestablishment of the pavement between the site in the streak and the site upwind of it.

Results of the field studies enable assessment of the three methods of desert pavement formation. It was observed that aeolian activity can restore a pavement in a few weeks if the rock fragments are near the surface. However, two observations argue against aeolian activity as the sole agent of pavement formation: 1) an aeolian origin does not explain the presence of a fragment-depleted subsurface zone and 2) the concentration of fragments observed on the surface is greater than that required for the surface to be armored. Chepil (1950) showed that an inter-fragment spacing of ~5 times the fragment diameter was sufficient to prevent material in saltation from striking between the fragments, yet spacings observed on pavements are much smaller. These two objections do not apply to the fragment migration model of pavement formation. However, this process operates much more slowly—if at all—having brought no fragments to the surface of the raked plot in four years. Furthermore, neither mechanism can explain the interlocking of fragment edges, although some interlocks could possibly be formed as new fragments emerge among fragments already on the surface. The sheet wash mechanism could explain how the fragments move relative to one another, forming interlocks, but it fails to account for the fragment depleted layer. Sheet wash probably does

remove very fine particles from the surface, as there are a few well developed small playas in depressions in the wind streak zone. It must be concluded that, in general, no one mechanism is exclusively responsible for the formation of desert pavement; rather it is probably a combination of the three mechanisms acting together which produces a pavement surface, with the relative importance of each mechanism being controlled by the specific environment involved.

The probable sequence of events for the formation and evolution of a typical desert pavement surface, based on this experiment and the work of others, is as follows. Starting with a layer of surface material consisting of both fine particles and rock fragments, aeolian deflation will rapidly erode the surface until an armored lag is developed, after which aeolian processes become less important. The concentration of fragments then slowly increases as new fragments are brought to the surface from the subsurface and as fragments move downslope by sheet wash. Sheet wash would be responsible for removing very fine particles from the surface and for moving the fragments relative to one another, forming interlocks.

REFERENCES

Blake, W.P., 1904. Origin of pebble-covered plains in desert regions, Trans. Am. Inst. Min. Eng. 34, 161-162.

Chepil, W.S., 1950. Properties of soil which influence wind erosion: I. The governing principle of surface roughness, Soil Sci. 69, 149-162.

Cooke, R.U., 1970. Stone pavements in deserts, Ann. Assoc. Am. Geog. 60, 560-577.

Cooke, R.U. and A. Warren, 1973. Geomorphology in Deserts, Univ. Cal. Press, Los Angeles, 120-121.

Gilbert, G.K., 1875. Report on the geology of portions of Nevada, Utah, California, and Arizona, part I of Geographical and Geological Explorations and Surveys west of the 100th Meridian (Engineers Dept., U.S. Army), 3, 21-187.

Greeley, R., M. Womer, R. Papson, and P. Spudis, eds., 1978. Aeolian features of southern California: A comparative planetary geology guidebook, NASA Field Guide Series.

Inglis, D.R., 1965. Particle sorting and stone migration by freezing and thawing, Science 148, 1616-1617.

Sharon, D., 1962. On the nature of hammadas in Israel, Zeit fur Geom. 6, 129-147.

Springer, M.E., 1958. Desert pavement and vesicular layer of some desert soils in the desert of the Lahontan Basin, Nevada, Proc. Soil Sci. Soc. Am. 22, 63-66.

Symmons, P.M. and D.F. Hemming, 1968. A note on wind-stable stone mantles in the southern Sahara, Geog. Jour. 134, 60-64.

Thomas, P., J. Veverka, S. Lee, and A. Bloom, 1981. Classification of wind streaks on Mars, Icarus 45, 124-153.

Veverka, J., P. Gierasch, and P. Thomas, 1981. Wind streaks on Mars: Meteorological control of occurrence and mode of formation, Icarus 45, 154-166.

D64
ABS. ONLY

N84 23495

Wind Erosion and Dune Formation on High Frozen Bluffs

W. M. Marsh, Research and Community Science Department, University of Michigan, Flint, MI 48503
B. D. Marsh, Department of Earth and Planetary Sciences, Johns Hopkins University, Baltimore, MD 21218

Frost penetration increases upslope on barren, windswept bluffs in cold environments. Along the south shore of Lake Superior, near the brow of 100 m high bluffs it typically exceeds 5 m. Frost increases the shear strength of damp sand to a level comparable to that of concrete, making winter slopes highly stable despite undercutting by waves and ground-water sapping along the footslope. Sublimation of interparticle ice in the slope face increases with wind speed and lower vapor pressures. The cold and dry winter winds of Lake Superior ablate these slopes through loss of binding ice. Bowen and Lindley (1977) show that wind speed on such slopes increases three-fold from the toe to crest. Wind erosion on Lake Superior bluffs is focused along the brow and appears to increase linearly with slope height. Most wind erosion occurs in the cold season, November through March. Wind erosion rates, based on measurements of sand accumulation on the forest floor downwind of the brow, show most airborne sand falls out within several meters of the brow, forming a berm 1-3 m high after many years. The spatial pattern of sand deposition, however, varies considerably over distances of several hundred meters along the top bluffs in response to frost conditions and the build-up of gravel lag on the slope face, sand exposure from mass movements, and local aerodynamics of the crest slope. The formation of perched sand dunes in the Great Lakes region is clearly related to wind erosion of sand from high bluffs in winter. The nourishment of dune fields such as the Grand Sable and Sleeping Bear are directly dependent on maintenance of devegetated fluff faces and thus in turn to wave action, sapping, mass movements, and high levels of aerodynamic and thermal stress. Based on measurments at several sites, over the past 10 years, a 7 km stretch of bluff at the Grand Sable Dunes annually yields about 7,000 m^3 of sand to the dune system. Broadly similar processes may operate on Mars.

Chapter 7

FLUVIAL PROCESSES AND LANDFORM DEVELOPMENT

D65

N84 23496

FLUVIAL EROSION OF IMPACT CRATERS: EARTH AND MARS

Victor R. Baker, Department of Geosciences and Department of Planetary Sciences, University of Arizona, Tucson, Arizona 85721

Geomorphic studies of impact structures in central Australia are being used to understand the complexities of fluvial dissection in the heavily cratered terrains of Mars (Figure 1). At Henbury, Northern Territory, approximately 12 small meteorite craters have interacted with a semiarid drainage system (Figure 2). The detailed mapping of the geologic and structural features at Henbury (Milton, 1968) allowed this study to concentrate on degradational landforms. The breaching of crater rims by gullies (craters 3 and 4) was facilitated by the northward movement of sheetwash along an extensive pediment surface extending from the Bacon Range (Figure 2). South-facing crater rims have been preferentially breached because gullies on those sides were able to tap the largest amounts of runoff. At crater 6 a probable rim-gully system has captured the headward reaches of a pre-impact stream channel. The interactive history of impacts and drainage development is critical to understanding the relationships in the heavily cratered uplands of Mars (Mars Channel Working Group, 1983).

Whereas Henbury craters are younger than 4700 yrs. B.P. (Milton, 1968), the Gosses Bluff structure formed about 130 million years ago (Milton et al., 1972). The bluff is essentially an etched central peak composed of resistant sandstone units. Post-impact erosion has removed much of the less resistant brecciated sandstone and siltstone associated with the original crater form. An erosion surface was cut across the bluff in Cretaceous time, and a long history of degradation followed in the Tertiary. Elements of a mid-Tertiary erosional level, common throughout the region, are also preserved on the structure. The phased exposure of resistant rock units comprising this impact structure seems to be a useful analog to the degradation of Martian craters.

References

Mars Channel Working Group, 1983, Channels and valleys on Mars: Geol. Soc. America Bull., v. 94, p. 1035-1054.

Milton, D.J., 1968, Structural geology of the Henbury meteorite craters, Northern Territory, Australia: U.S. Geol. Survey Prof. Paper 499-C, 17 p.

Milton, D.J. and others, 1972, Gosses Bluff impact structure, Australia: Science, v. 175, p. 1199-1207.

Scott, D.H., Morris, E.C., and West, M.N., 1978, Geologic map of the Aeolis Quadrangle of Mars: U.S. Geol. Survey Misc. Inv. Map I-1111.

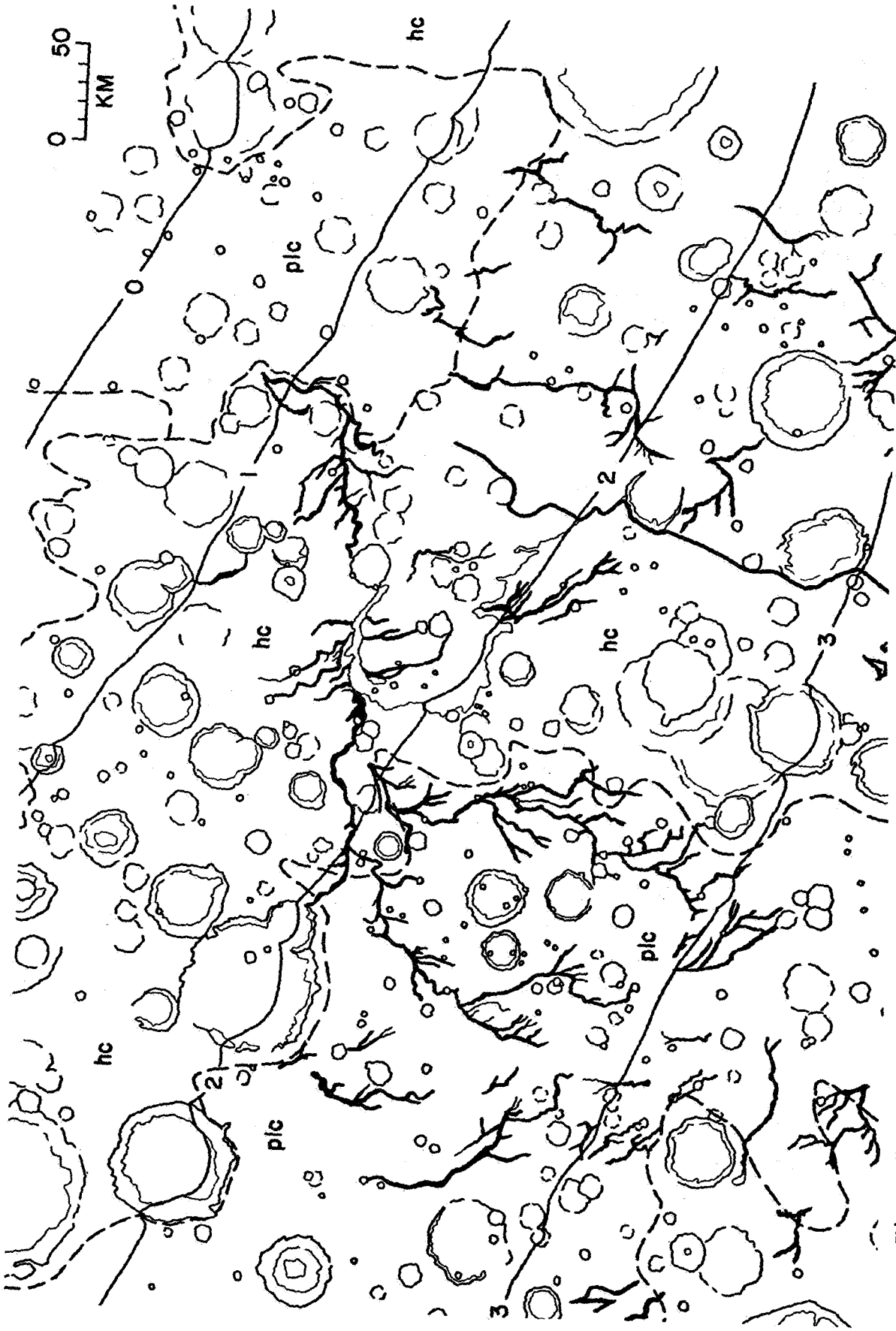

Figure 1. Drainage map of valley networks in the Aeolis region of Mars (14°S, 206°W). Networks are developed in hilly/cratered terrain (hc) and cratered plateau (plc) materials (Scott et al., 1978).

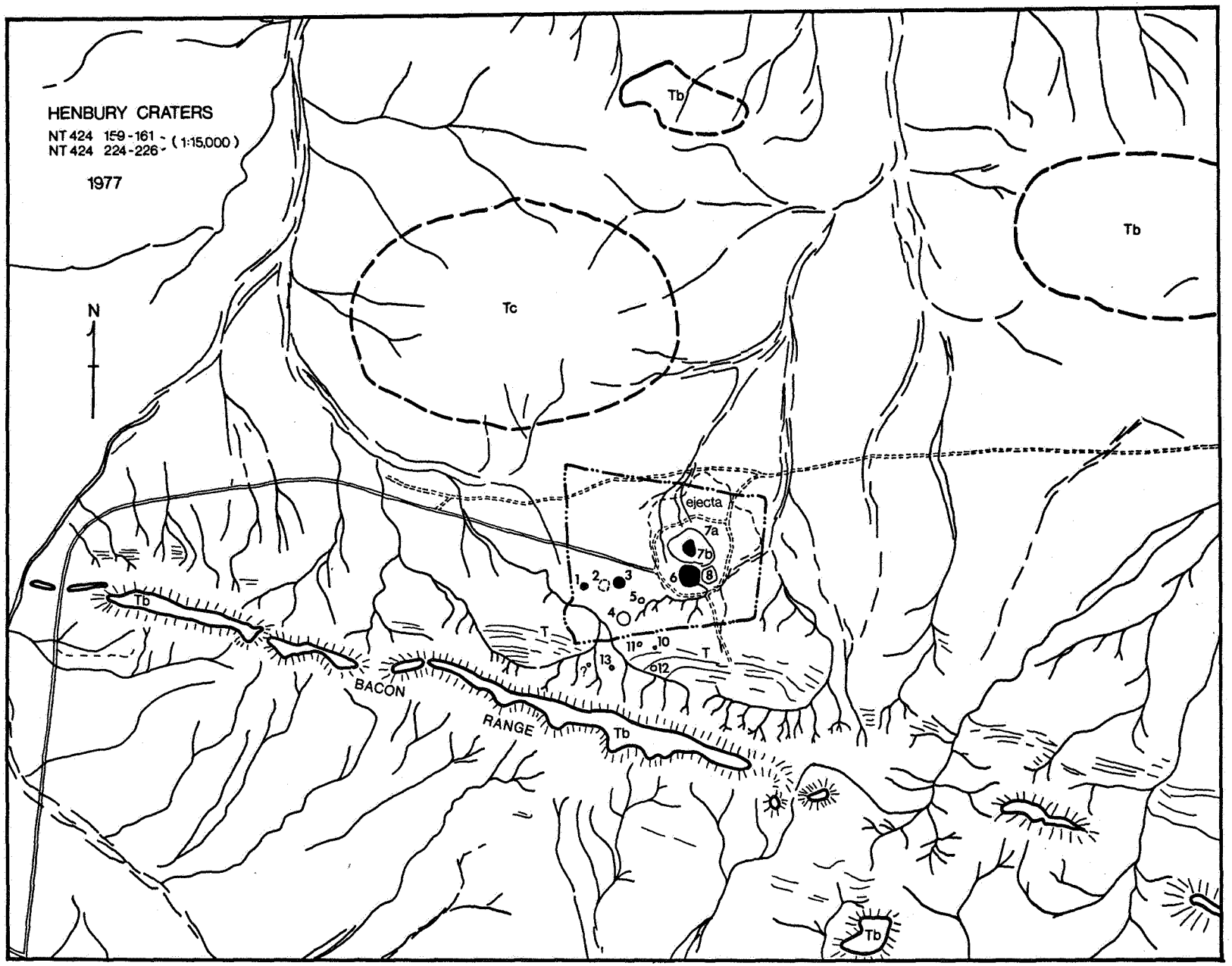

Figure 2. Drainage map of the Henbury Craters region, central Australia.

THE 19 MARCH 1982 ERUPTION AND LAHAR AT MOUNT ST. HELENS: IMPLICATIONS FOR MARTIAN OUTFLOW CHANNELS?

Gary L. Beach
U.S. Geological Survey
Cascades Volcano Observatory
5400 MacArthur Blvd.
Vancouver, Washington 98661

A small explosive eruption of Mount St. Helens on 19 March 1982 set into motion an unusually complex series of geomorphic and hydrologic processes that had not previously been described in the literature. This event was unusual in that a laterally-directed eruption dislodged and mobilized a thick snowpack from the surrounding crater floor and walls, resulting in the formation of a temporary lake. Catastrophic release of this self-impounded lake spawned a series of destructive debris avalanches and debris flows that moved rapidly down the volcano's north flank and into the North Toutle River valley.

Preliminary interpretation of air photos taken on 23 March suggests that the eruption began with a lateral blast from the southern base of the composite lava dome, or from the nearby crater floor. The initial explosion hurled juvenile pumice and lithic blocks from the dome onto and over the the 600 meter high south crater wall. The blast generated a pumice, ice, and lithic block avalanche which cascaded down the crater wall, then separated into two lobes when it impinged on the lava dome below. The avalanche incorporated more juvenile pumice, snow, and talus blocks from the crater floor, and exited the inner crater through a breach formed by the large 18 May 1980 landslide and eruption. The two lobes of the debris avalanche coalesced about 400 meters north of the dome, and travelled at least 6 kilometers to the valley below. The dynamic characteristics of the avalanche suggest that its movement was rapid (tens of meters per second), causing only minor erosion of pre-existing landforms near its margins.

Within minutes of the initial blast, a crescent-shaped lake formed rapidly on the south crater floor, fed by snow and ice melt caused by the eruption. Evidence for this temporary lake includes strandlines of pumice accumulations and mudlines in remaining snow cover. Catastrophic release of the self-impounded lake discharged a flood of water and suspended pumice through outlets east and west of the dome, incising deep gullies in the process. The resulting debris flows, moving over essentially the same course as the earlier debris avalanche, eroded and incorporated debris from the initial avalanche and from underlying 1980 pyroclastic flow deposits. Preliminary analysis suggests that the rapidly-draining lake then fed a second, smaller debris flow before relative calm returned to the crater.

Catastrophic release of volatiles mobilized by volcanic activity has been discussed as a possible mechanism to explain a class of outflow channels on Mars. The 19 March 1982 eruption of Mount St. Helens provides a unique opportunity to study the deposits and landforms created by such an event; a more detailed field study and examination of Viking photographs of martian outflow channels is currently underway.

DRAINAGE EVOLUTION IN THE DEBRIS AVALANCHE DEPOSITS NEAR MOUNT ST. HELENS, WASHINGTON

Gary L. Beach and Dan Dzurisin, U.S. Geological Survey, Vancouver, WA 98661

The 18 May 1980 eruption of Mount St. Helens was initiated by a massive rockslide-debris avalanche which completely transformed the upper 25 km of the North Fork Toutle River valley. The debris was generated by one of the largest gravitational mass movements (2.3 km^3) ever recorded on Earth (Lucchitta, 1978; Voight and others, 1981). Moving at an average velocity of 35 m/s, the debris avalanche buried approximately 60 km^2 of terrain to an average depth of 45 m with unconsolidated, poorly sorted volcaniclastic material, all within a period of 10 minutes (Voight and others, 1981). Where exposed and unaltered by subsequent lahars and pyroclastic flows, the new terrain surface was characterized predominantly by hummocks, closed depressions, and the absence of an identifiable channel network.

Following emplacement of the debris avalanche, a complex interrelationship of fluvial and mass wasting processes immediately began operating to return the impacted area to an equilibrium status through the removal of material (potential energy) and re-establishment of graded conditions (Schumm, 1977). In an attempt to chronicle the morphologic evolution of this unique environmental setting, a systematic series of interpretative maps of several selected areas is being produced. These maps document the rate and character of active geomorphic processes. The simplified maps shown in Fig. 1 illustrate the dramatic changes that have occurred in one small area during a six month interval.

Initial erosion of the debris avalanche proceeded principally through the development of incipient channels and the secondary mass movement of material downslope, as voids were filled and rafted glacial ice blocks melted. In the summer of 1980, the first channels were formed by surface water discharging onto the debris deposits from groundwater seepage and springs situated along the valley sidewalls. As impounded lakes along the debris avalanche margins filled, overflowed, and breached, channels were rapidly incised until a new temporary base level was reached at a lower elevation within the valley floor. Fig. 1a shows a lake formed in this manner for which there is no surface outlet. When the storage capacity of this lake was eventually exceeded, it breached and set into motion a chain-reaction of surface water movement, channel development, and sediment transport.

Channels and gullies on the debris avalanche during 1980-81 were typically steep-walled, trapezoidal-shaped, 3-50 m deep and 30-120 m wide. These average dimensions have continued to increase, though at a declining rate, since the winter of 1981. The slope angle of channel walls is commonly 30-45°, but may be as steep as 70° (Lehre and others, 1982). Channels have been observed to widen by bank undercutting and failure during high discharge conditions; with slumps, debris slides, and debris falls common (Fig.1b). Bank recession is most rapid where anastamosing braided channels fill the floodplain channel (Fig. 1c). Between September and November 1980 (Fib. 1b and 1c), the established floodplain more than doubled in width in response to runoff generated by the first fall storm events.

The maps in Fig. 1 indicate the rapidity with which a drainage network system can evolve following a major disturbance. The various events that transpired in response to a multiplicity of erosional and depositional processes can be briefly summarized at roughly two month intervals, as follows: (1) the lake filled to capacity and then breached westward at the downslope low saddle point; (2) as the lake drained (rapidly at first and then more slowly), a floodplain was established and an integrated channel network developed; (3) back-wasting of the channel slopes and removal of displaced sediment through suspended and bedload transport accelerated in direct response to surface runoff events; (4) rapid lateral widening of the floodplain resulted in the removal of hummocks and the filling of depressions; and (5) periods of degradation and aggradation frequently alternated as evidenced, in part, by multiple terrace deposits above the active channel floor.

One interesting process observed throughout the debris avalanche area concerns the contributions apparently made by groundwater sapping. In Fig. 1d, a number of springs are shown emanating from the base of a ridge southwest of the active floodplain. The slope above the in-filling pond is experiencing retrograde backwasting as the debris at the base super-saturates, liquifies, loses toe support and thereby contributes to the failure of a debris slab. Groundwater sapping has been observed not only in depression ponds, but also along active channels whenever the groundwater seepage plane is slightly elevated above the surface water level. Recent interest in this process, especially as it relates to the development of channels on Mars, has been expressed by Laity and Saunders (1981), Higgins (1982) and others.

References

1. Higgins, C., 1982. "Drainage Systems Developed by Sapping Earth and Mars." Geology, vol. 10, pp. 147-152.
2. Laity, J., and R. Saunders, 1981. "Sapping Processes and the Development of Theatre-Headed Valleys." Reports of Planetary Geology Program, 1981, NASA TM 84211, pp. 280-282.
3. Lehre, A., B. Collins, and T. Dunne, 1982. "Preliminary Post-Eruptions Sediment Budget for the North Fork Toutle River Drainage, June 1980-May 1981." Proceedings, Mount St. Helens: Effects on Water Resources, pp. 215-224.
4. Lucchitta, B., 1978. "A Large Landslide on Mars." Geological Society of American Bulletin, vol. 89, pp. 1601-1609.
5. Schumm, S., 1977. The Fluvial System. New York: John Wiley and Sons, 338 pp.
6. Voight, B., H. Glicken, R. Janda, and P. Douglass, 1981. "Catastrophic Rockslide Avalanche of May 18." U.S. Geological Survey Prof. Paper 1250. pp. 347-377.

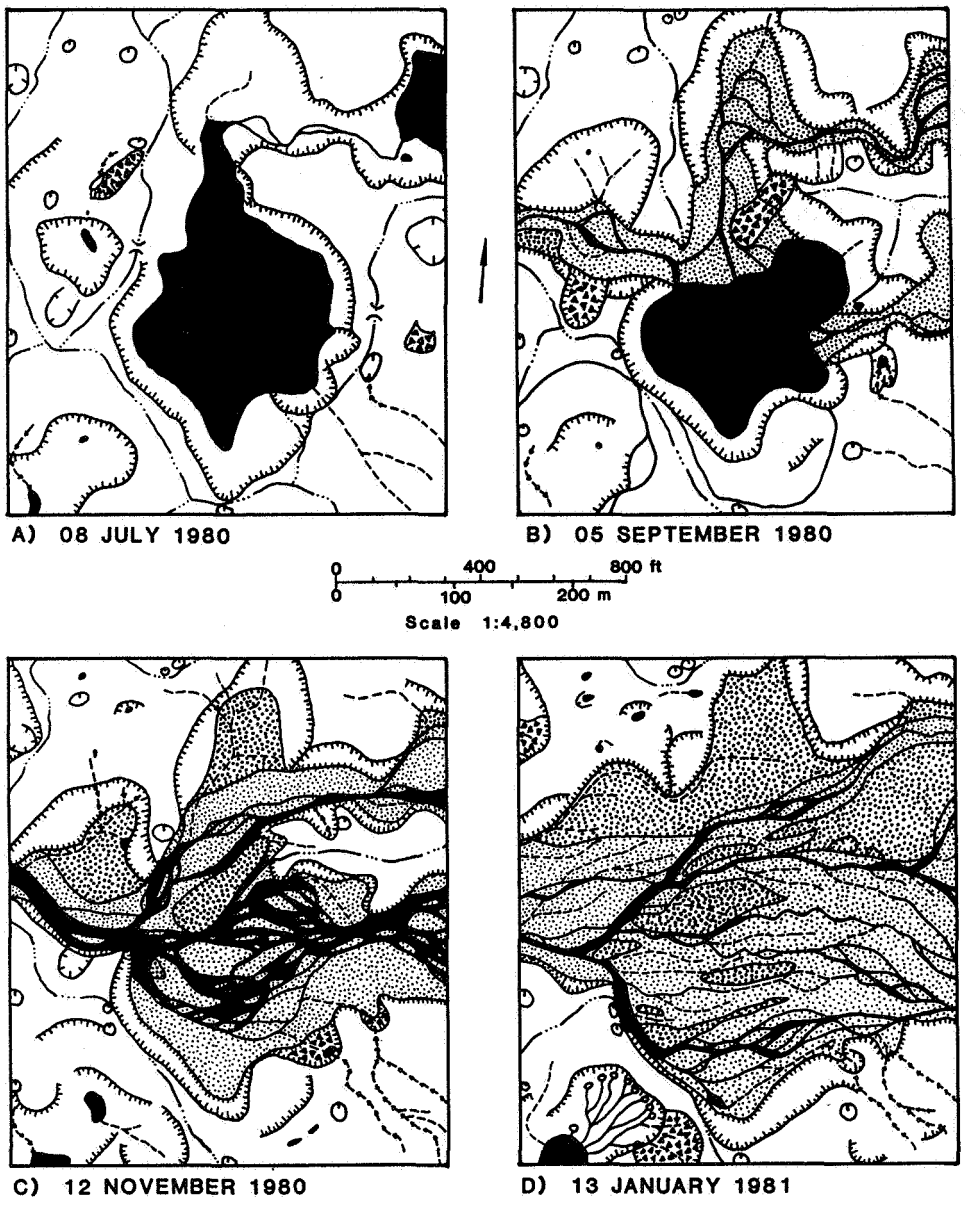

Figure 1. Drainage evolution near the confluence of Maratta Creek and North Fork Toutle River.

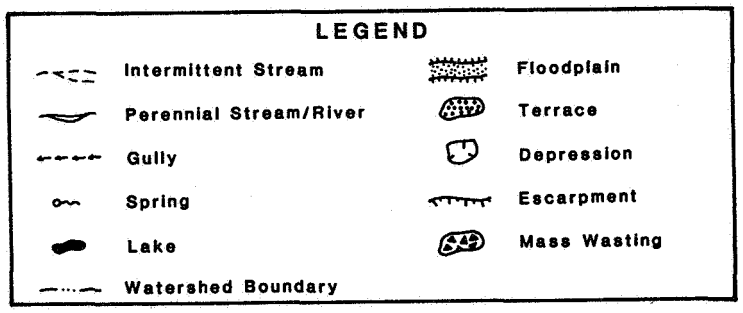

D68

N84 23499

FLUVIAL DRAINAGE SYSTEMS: MARGARITIFER SINUS AND AGYRE (NC, NE) QUADRANGLES, MARS

BOOTHROYD, Jon C., and GRANT, John A., Dept. of Geology, Univ. of Rhode Island, Kingston, RI 02881

Fluvial drainage systems, delinated by mapping on stereo pairs of Viking Orbiter images, have developed in various-sized basins in the Margaritifer Sinus (MC-19) and Agyre (MC-26) Quadrangles, Mars. The Ladon Valles system discussed previously by Boothroyd (1982) and Pieri (1980) is the largest, draining into and through two of the multi-ringed impact basins discussed by Schultz and others (1982) (LA, Figure 1). Smaller fluvial basins to the southeast of the Ladon structural basin appear to have internal drainage. An intermediate-scale fluvial basin containing Himera Vallis (H, Figure 1), extends along a north-south axis at 22°W and opens northward toward outflow channels south of Margaritifer Chaos.

Stereo-pair mapping has been extended further to the east, in MC-19 NE, SE, and MC-26 NE, to investigate sources of outflow to the Ares Vallis system. The direction of flow in the channel at the northeast quadrant of the Ladon Basin (N, Figure 1) is unresolved at present because of the poor quality of images available to form stereo pairs.

However, an easterly drainage basin boundary running north-south along longitude 9°W, and extending westward at latitude 32-35°S, encloses a series of longitudinal drainage systems, the morphology of which were discussed by Pieri (1980) and Baker (1982). Both the Parana Valles-Loire Vallis system (P, L, Figure 1) and the Samara Valles system (S, Figure 1) appear to drain in a northwesterly direction. The Samara flows to the Himera drainage basin, and the Parana-Loire to the northeast Ladon channel area. Internal boundaries between the two large systems have not yet been established.

If these two large systems are through going as suggested, and a northeast flow direction for the Ladon channels is established; then a substantial source area for early Ares outflow will have been identified.

REFERENCES

Baker, V.R., 1982, The channels of Mars: Austin, TX., University of Texas Press, 198 p.

Boothroyd, J.C., 1982, Ancient fluvial drainage systems: Margaritifer Sinus area, Mars: Reports of the Planetary Geology Program, 1982, NASA Tech. Memo 85127, p. 209-212.

Pieri, D.C., 1980, Geomorphology of martian valleys: p. 1-160, in Advances in Planetary Geology, NASA Tech. Memo. TM 81979, 326 p.

Schultz, P.H., Schultz, R.A., and Rogers, J., 1982, The structure and evolution of ancient impact basins on Mars: Jour. Geophys. Res., v. 87, No. B12, p. 9803-9820.

Figure 1. Viking Orbiter mosaic of part of the Margaritifer Sinus (MC-19) and Agyre (MC-26) Quandrangles showing selected drainage basin boundaries. See text for details (Mosaic 211-5821).

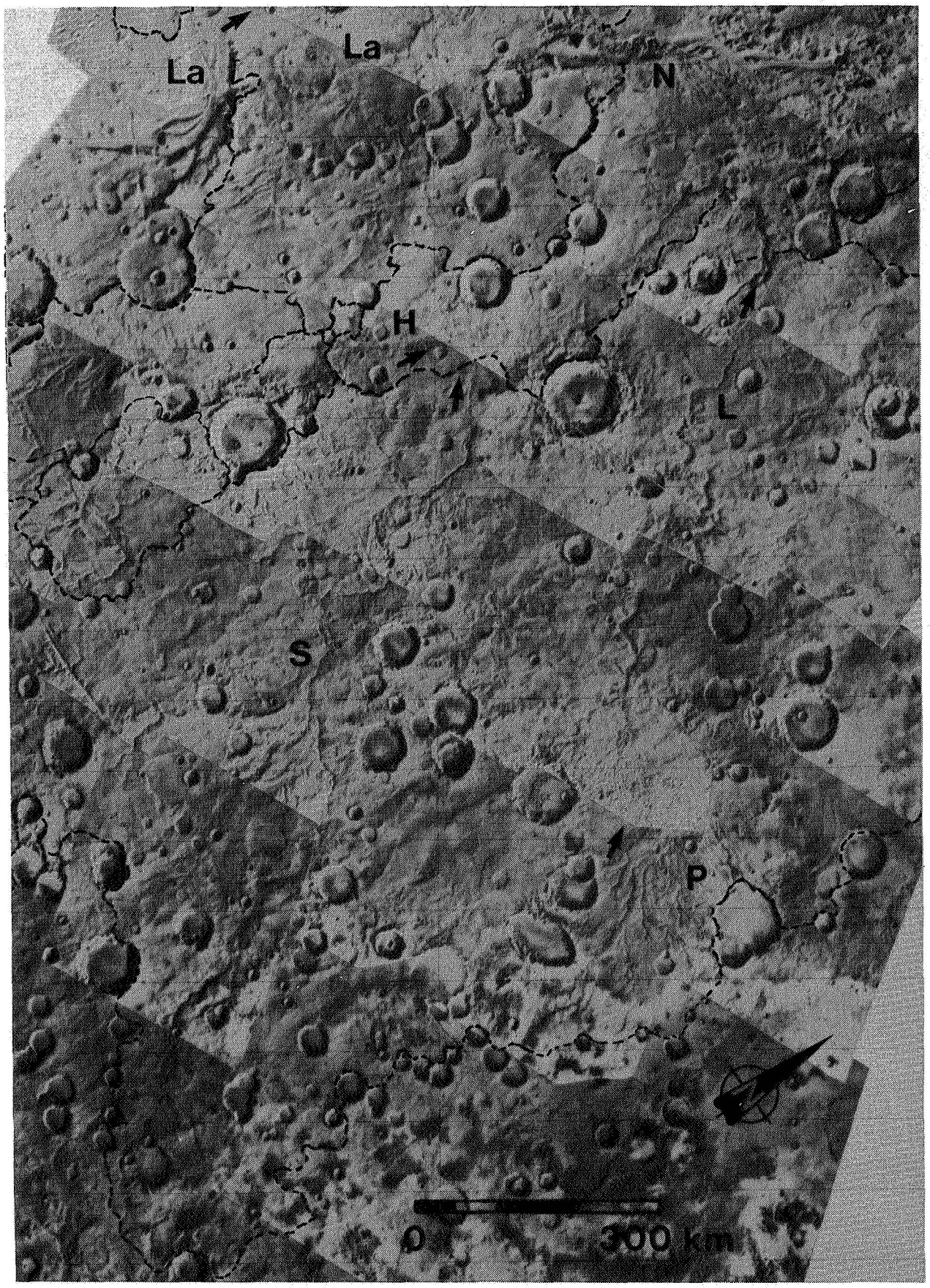
La
La
N
H
L
S
P
0
300 km

N84 23500

D69

FREEZING OF MARTIAN STREAMS UNDER DIFFERENT CLIMATIC CONDITIONS.

Michael H. Carr, U.S. Geological Survey, Menlo Park, CA

The valley networks of Mars are widely believed to have formed at a time when climatic conditions on the planet were significantly different from those that currently prevail. This view arises from the following observations: (1) the valleys form integrated branching networks which suggests fluid drainage, and water is the most plausible fluid, (2) the present atmosphere contains only minute amounts of water, (3) the networks appear to be more akin to terrestrial valleys that are eroded by streams of modest discharges than features that form by catastrophic floods, and (4) small streams of water will rapidly freeze under present climatic conditions. This study examines what can be inferred about climatic conditions at the time of formation of the valleys on the assumption that they were cut by running water.

The problem of valley formation can be divided into two parts: (1) initiation of flow at the surface, and (2) sustaining the flow long enough to perform the erosion required. Only the second part of the problem is discussed here. How flow might be initiated under different climatic conditions will be examined at a future date. The freezing of a stream can be considered as a three-stage process (figure 1). In the first stage the stream cools to the freezing temperature. Second, ice accumulates within the stream but fails to form a continuous cover because of turbulence. Third, a continuous ice cover forms. The rate at which streams on Mars cool, freeze, and pass through each stage was calculated for a variety of climatic conditions that would result from thickening of the CO_2 atmosphere.

Normally as a stream freezes the discharge in the trunk channel falls because freezing of the tributaries cuts off the water supply. However, if flow is sustained, such as from a spring, partial damming of the stream by ice causes repeated diversion of the flow out of the stream channel and over the adjacent terrain to form ice sheets or icings. A spring fed stream on Mars might therefore consist of a long-lived segment in which the stream is cooling down to where sufficient ice accumulates to form a continuous cover, and a relatively short lived segment where formation of a continuous ice cover soon leads to creation of an icing. The time taken for such a stream to accumulate enough ice to form a cover and the time taken for it to freeze solid once the cover formed were calculated. The distance the water travels from its source to where an icing would form is also calculated for various slopes and initial stream temperatures by means of empirical hydraulic relations appropriately modified for Mars.

For uncovered streams calculation of cooling and freezing rates is relatively simple. Heat gained by incident radiation and frictional head loss is offset by re-radiated energy, conductive losses to both the

walls and the atmosphere, evaporative losses, cooling and freezing. For ice covered streams the surface temperature of the ice was determined from the heat balance at the surface. The freezing rate was then computed by balancing the heat gained by the stream by friction and penetration of radiation through the ice against heat losses by conduction into the walls and through the ice. The ice thickness was increased incrementally and the calculations repeated to derive a growth rate. Details of the method are given in Carr (in press). The technique used was similar to that used by Wallace and Sagan (1979) except that conduction to the atmosphere and ground and frictional heat were taken into account, visible and infrared radiation were treated separately, empirically derived adsorption coefficients were used for the ice, and ground and atmospheric temperatures were changed for the different atmospheric pressures, according to models of Pollack et al. (1979) and Cess et al. (1979).

Figure 2 shows times taken for streams 1 m deep and 30 cm deep to freeze solid assuming that the initial temperature of the stream was 273°K. Figure 3 shows the distances travelled by water in a stream before flow is arrested by formation of a continuous ice cover and the consequent creation of an icing. The results indicate that the cooling and freezing of a stream on Mars is not strongly dependent on atmospheric pressure, particularly if wind is significant. Indeed, if a stream 1-2 m deep and 5°K above freezing can be initiated it can travel for distances comparable to the length of many of the observed valley networks, even under present climatic conditions. Thus clues concerning former climatic conditions are more likely to be found in the mechanisms of stream initiation than in the means of sustaining the flow.

REFERENCES.

Carr, M.H., 1984, The stability of streams and lakes on Mars: Icarus (in press).

Cess, W.G., Ramanathan, V., and Owen, T., 1980, The martian paleoclimate and enhanced atmospheric carbon dioxide. Icarus, 41, 159-165.

Pollack, J.B., 1979, Climate change on the terrestrial planets. Icarus, 37, 479-553.

Wallace, D., and Sagan, C., 1979, Evaporation of ice in planetary atmospheres: Ice covered rivers on Mars. Icarus, 39, 385-400.

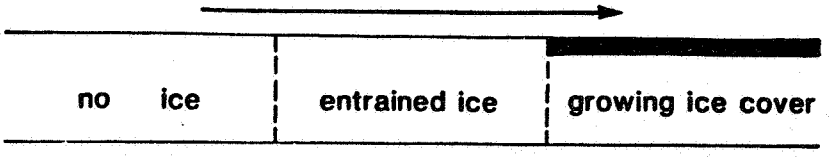

Fig. 1. Three stages in the cooling and freezing of a stream.

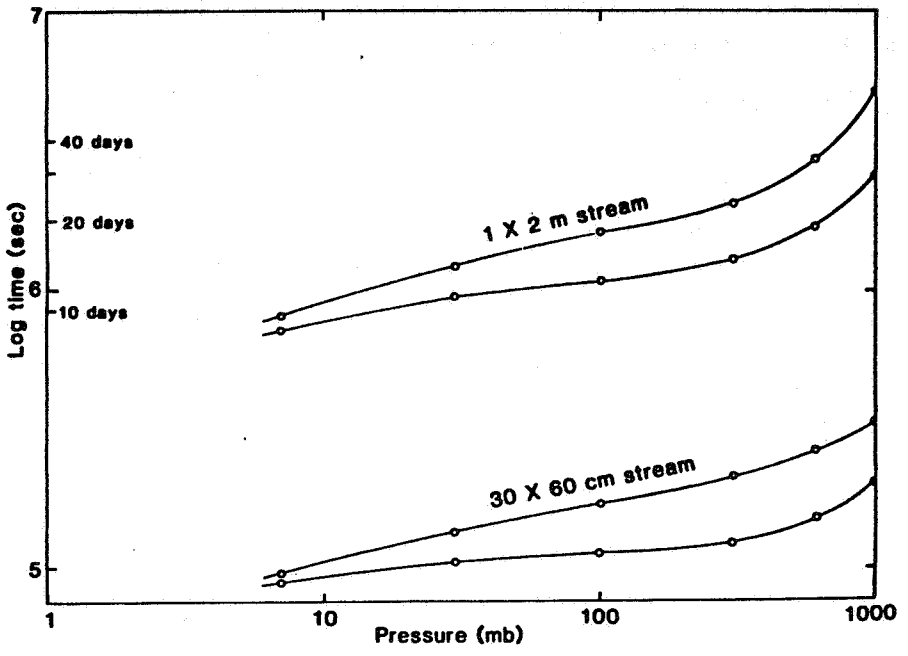

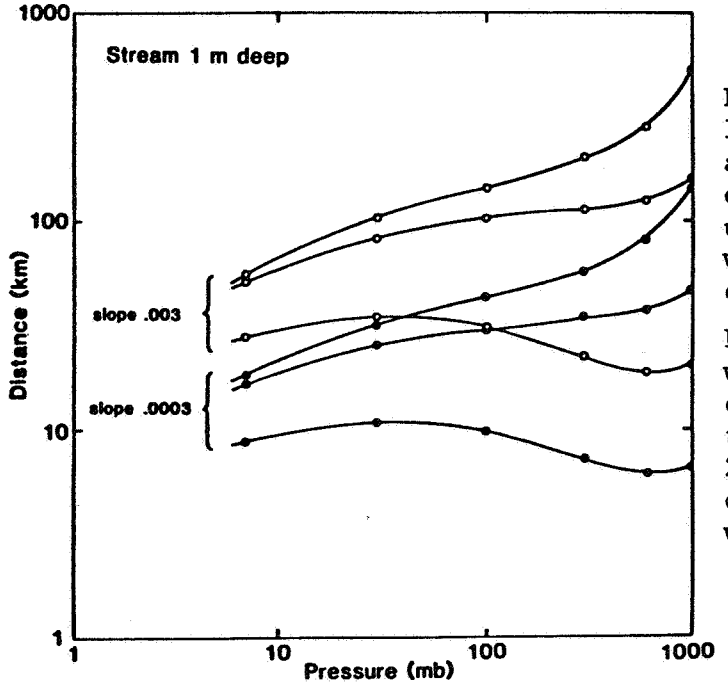

Fig. 2. Times taken to freeze 1 m and 30 cm deep streams assuming an initial temperature of 273°K. In each case the upper curve is for a frictional wind speed of 1 cm/sec, lower curve for 100 cm/sec.

Fig. 3. Distances travelled by water before a continuous ice cover forms assuming the stream temperature was initially at 278°K. The three curves for each slope are for different wind speeds.

D70

N84 23501

DARK STREAKS ON TALUS SLOPES, MARS

H. M. Ferguson and B. K. Lucchitta, U.S. Geological Survey, Flagstaff, Arizona 86001

High-resolution pictures of talus slopes on Mars show small, dark streaks that characteristically widen downward (Fig.1). These streaks are different from the thin and even streaks of various albedos that stream from cliffs on talus slopes, but gradations between the two streak types occur and not all streaks can be classified with confidence. In order to study the nature and origin of the small, widening, dark streaks, we surveyed all Viking pictures with a resolution of less than 100 m/pixel. To date we have located several hundred streaks, but only few are of high enough resolution to be confidently identified as widening downwards. We measured the approximate dimensions of the streaks, noted their shapes, numbers, position, and spacing on slopes, plotted them on a topographic map [1], and studied their relation to topography, geologic units, and regions of distinct thermal inertia and albedo. We also noted the season at which images containing streaks were acquired and the direction of illumination. Albedo measurements are in progress. Several streaks can be seen stereoscopically, but none are observed on color images.

The streaks are very small and can be detected only on images of very high resolution (less than 50 m/pixel). All emanate from point sources, and trend downslope. Some are diverted by obstacles in their paths. A few extend across valley floors to a maximum distance of about 100 m. The streaks have oblong, oval, or fan shapes. They are generally about 50 m wide (ranging from about 20 to 250 m) and about 1,000 m long (ranging from 200 to 2,500 m). They occur either singly or in clusters that are spaced regularly or irregularly on steep slopes. As many as about 30 have been detected inside some craters of about 15 km diameter. Most are seen on the illuminated side of craters, but, where high sun angles permit, they also appear on the shadowed side; apparently they are not controlled by direction of illumination or exposure.

Albedos vary from medium dark to very dark. Medium-dark streaks measured inside a crater are about 10% to 15% darker than adjacent talus (P. A. Davis, oral communication); very dark streaks, therefore, have more pronounced albedo contrasts. Because medium-dark streaks appear more diffuse than very dark streaks, which have sharply delineated boundaries, medium-dark streaks are best explained as degraded very dark streaks. The degradation mechanism is not known, but could have been blanketing by light-colored wind deposits.

All small dark streaks are found on scarps with smooth, steep slopes best interpreted as talus slopes; most are on the inside walls of craters. They occur dominantly in the equatorial area (±15° lat.) except for streaks on the aureole of Olympus Mons (lat 28° N.). Within the equatorial area the streaks occur in clusters in the Mangala Vallis and Arabia areas; questionable ones occur in Amazonis Planitia and north of Hebes Chasma. Even though gigantic talus slopes exist in the Valles Marineris, none of the small streaks have been detected on very high resolution images in that area.

The streaks appear to be restricted neither to specific elevations nor specific geologic units on the geologic map of Mars [2]: They occur at elevations ranging from 0 to 10 km above the Martian datum plane, and in regions underlain by ancient highland materials, plateau materials, and possible volcanic materials, such as a caldera in Amazonis Planitia (lat 8° N., long 141°) and on the aureole mountains of Olympus Mons. However, they do appear to correlate with certain types of surficial materials: all streaks

occur in areas of high albedo and low thermal inertia on the pertinent published maps [1, 3], which suggests the occurrence in surface layers of fine grain size. Many images with streaks were acquired during the extended mission in late northern spring to early summer (L_s 80 to L_s 130), and during evening illumination (from the west).

In the past, only the streaks on the aureole of Olympus Mons have been studied. Morris [4] interpreted them as talus streaming from dark rock outcrops. Tanaka [5] envisioned fresh talus shed across older talus blanketed by lighter, wind-blown dust. We disagree with the interpretations that this type of streak represents merely talus shed from rocks. Talus from dark layers forms thin streaks or is V-shaped, the V pointing toward the valley floor. Talus from isolated outcrops also forms uniformly thin streaks. By contrast, the dark streaks here discussed emanate from point sources and fan out downward. A particularly dark and wide streak near Mangala Vallis (lat 11° S., long 157°) was analyzed in detail for volumetric considerations. It widens to 250 m, 500 m below its point source, and extends another 500 m down slope at 250-m width. If this streak consisted of dark material only 10 cm thick, it would contain nearly 20,000 m^3 of material. In order to supply this amount of material, an outcrop 10 m^2 in plan would have to have been 200 m high before collapse. Such a spire is unrealistic as a source outcrop on a smooth talus slope where no other cliffs are observed. Furthermore, in order to effectively blanket an underlying rough talus slope, this dark streak is probably thicker than 10 cm; such a thickness would imply that the source outcrop was of even greater height. Thus the material forming this streak was most likely not derived from a single outcrop, but must have had a contribution from elsewhere. Other streaks with less extreme dimensions also fan out downwards, implying similar source relations. Fan-shaped debris aprons on Earth occur below chutes, where debris is fed from above and funneled through, or below tributary valleys with large intake areas. Similarily, the fan-shaped streaks on Mars require an additional supply; this supply appears to have been fed to the talus slope from a source area behind the scarp walls.

Several observations suggest that the material forming the dark streaks once flowed: it is fed through a point source, trends downhill, is diverted around obstacles, and extends locally onto valley floors. These considerations eliminate an eolian agent. Remaining possibilities for streak origin are lava or fluidized debris. Lava is an unlikely candidate because none of the streaks extend far across adjacent floors or form sizable pools at the bottom of slopes. Fluidized debris could have been wet or dry, but dry debris emerging from a point source in the wall is difficult to envision; the debris was more likely wet and flowed from the source like a spring. The lack of pooling of debris on the floor and the limited length of the streaks suggests that the postulated liquid evaporated rapidly, and that the flow was an event of short duration. The lack of collapse structures or sapping features on the wall above the streaks also suggests that the flowing debris was small in volume and flow time brief.

That the debris may have been wet is further indicated by the occurrence of streaks mainly in the equatorial belt, where temperatures may rise to above freezing (maximum diurnal temperatures to 290° K during the primary mission according to Kieffer et al., [6]. The restriction of the streaks to areas of high albedo and low thermal inertia also supports our hypothesis that the debris may have been wet: the presence of fine debris blankets at the surface may have prevented desiccation of the ground [7]; without blankets, desiccation occurs in equatorial areas during present-day atmospheric conditions [8].

The age of the streaks cannot be established firmly by counting superposed craters because of the small size of the streaks and their occurrence on steep scarps where craters are not retained. The crispness of very dark streaks suggests that they are young. Temperatures for the latitude and season at which the pictures were taken reached no higher than 270° K during the primary mission [6]; this maximum precludes fluidization by liquid water, but permits fluidization by brines. Our observations thus do not preclude the possibility that the dark streaks are formed by liquids seeping from the walls today. On the other hand, the streaks observed may be stains resulting from salt deposits after liquids evaporated, such as tufa deposits, sinter, or manganese stains in arid regions on Earth. The causes of low albedo of the streaks or stains is a question that has not yet been explored.

In summary, the observation of small dark streaks on talus slopes on Mars is compatible with an interpretation of their origin as eruptions of small masses of wet debris in places where steep walls intersect aquifers or where seasonal equatorial warming permits the local melting of ground ice.

References

[1] U. S. Geological Survey, U. S. Geol. Survey Misc. Inv. Map, I-961, scale 1:25,000,000, 1976. [2] Scott, D. H. and Carr, M. H., U. S. Geological Survey Misc. Inv. Map I-1083, scale 1:25,000,000, 1978. [3] Palluconi, F. D., Bull. Am. Astron. Soc. 11, p. 575, 1979. Reprinted in Carr, M. H., p. 20, Yale University Press, New Haven, 232 p., 1982. [4] Morris, E. C., J. Geophys. Res., 87, B2, 1164-1178, 1982. [5] Tanaka, K. L., Univ. of Calif. at Santa Barbara, Ph.D. diss, 264 p., 1983. [6] Kieffer, H. H., Martin, T. Z., Peterfreund, A. R., Jakosky, B. M., Miner, E. D., and Palluconi, F. D., J. Geophys. Res., 82, 28, 4249-4271, 1977. [7] Smoluchowski, R., Science, 150, 1348-1350, 1968. [8] Farmer, C. B., and Doms, P. E., J. Geophys. Res., 84, B6, 2881-2888, 1979.

Fig. 1. Small dark streaks on crater rim in Arabia, lat 9° N., long 321°, Viking Orbiter 1 image 713A57.

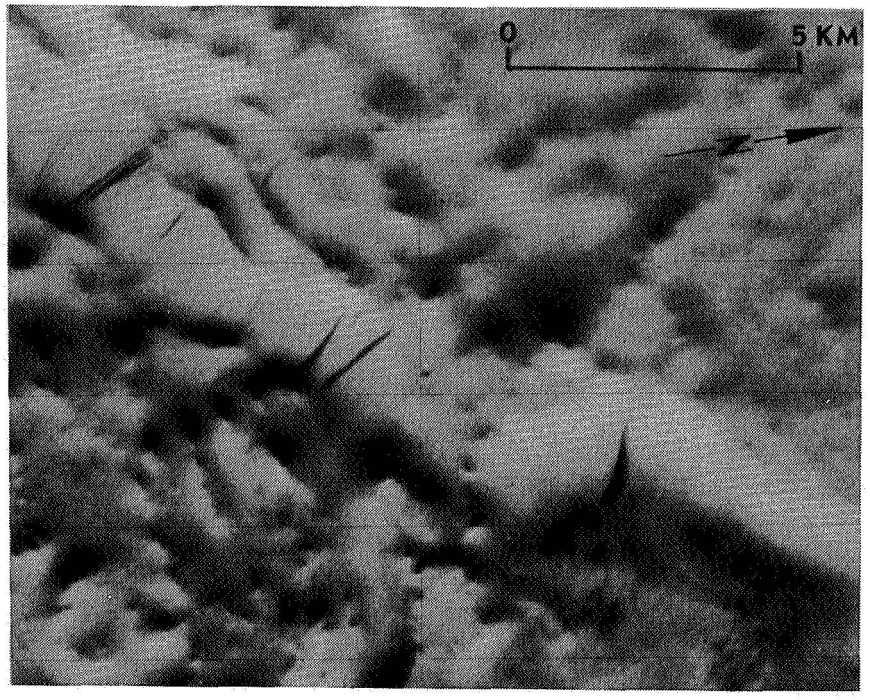

Quantitative and Experimental Modelling of Sapping Networks.

Alan D. Howard and Craig Kochel, Department of Environmental Sciences, University of Virginia, Charlottesville, VA 22903.

Development of drainage networks by erosion by emergent groundwater (sapping) is being modelled by a combination of laboratory experiments and theoretical modelling. Results of preliminary analog expermiments in a sapping box are being reported in Kochel et al. (1984). Miniature drainage networks formed in fine-grained sediments (e.g. Figure 1) share many morphologic characterisics of Martian and terrestrial networks suspected to be formed by sapping processes. These similarities include low dimensionless drainage density, theater-headed valley terminations, broad, flat-bottomed valley floors, and stubby tributaries. A larger and better instrumented sapping box has been constructed to further explore the processes of sapping and the morphology of resulting networks. The experiments to be conducted in the sapping box will investigate the roles of several factors in controlling network morphology, including: 1) variations in flow rates; 2) effects of surface morphology; 3) effects of varying cohesion; 3) structural influences, such as layering and fracturing; and 4) sapping development through ground ice melting.

The mechanics of sapping of fine-grained sediments have been investigated in experiments in a two-dimensional sapping chamber (Fig. 2) and through development of a theoretical model. Results of extensive tests on sapping erosion of fine-grained, cohesionless sediment (Howard and McLane, 1983; Kochel et al., 1984) have been analysed with a theoretical model of the mechanics of sapping erosion and transport. Figure 3 illustrates a cohesionless particle lying on the surface of a sedimentary deposit and subjected to gravity (F_g), fluid drag due to surface water flow (F_w), and fluid drag due to emergent groundwater seepage (F_s). If it is assumed that 1) all forces act through the particle center, 2) surface fluid lift forces are negligible, 3) the surface fluid drag is proportional to the particle surface area and the shear stress, 4) the seepage force is proportional to the particle volume and the hydraulic gradient, and 5) that the hydraulic gradient, I, is given by (Howard and McLane, 1981):

$$I = \mathrm{Sin}(\theta)/\mathrm{Cos}(\psi+\theta),$$

then the balance of torques at the initiation of movement is given by:

$$T + C_1\, d\, \mathrm{Sin}(\theta)\, \{1 + \mathrm{Tan}(\theta+\psi)\, \mathrm{Tan}(\alpha)\} - C_2\, d\, \mathrm{Sin}\,(\alpha-\theta)/\mathrm{Cos}(\alpha) = 0$$

where T is the shear stress exerted by the surface flow, d is the particle diameter, and C_1 and C_2 are constants. The capacity of the fluid to transport sediment is related to the degree by which the applied forces exceed the threshold of motion. The rate of sediment transport, q_s, at and below the sapping face is assumed

to be a power function of the value (R) of the left-hand side of the above equation:

$$q_s = K R^m$$

The rate of erosion of the slope equals the downslope rate of change of q_s. Analysis of the flow tank experiments suggests a value of about 2.5 for the exponent m, which is in agreement with published transport relationships for cohesionless sediment transport. Local values of the surface fluid stress were estimated from the discharge and surface gradient using an assumed Manning's n of about 0.015, which is consistent with measurements made of flow resistance in shallow flows over smooth slopes. Discharges and seepage angles were calculated using finite-element flow simulation. The successive changes occuring during the experimental sapping erosion runs are being modelled numerically by calculating local surface erosional rates using the above equations with the flow net being recalculated as erosion progresses. Figure 4 shows a preliminary version of these simulations. The numbers indicate the elapsed time, in seconds, since initiation of sapping erosion due to groundwater flow from the left. The solid lines indicate the observed slope configurations (note the angle-of-repose slopes above the sapping face and the fluvial transport slopes below the sapping face) and the dotted lines are the predicted surface positions at the indicated times. The successive divergence from the true surface configuration indicates that adjustments will be necessary to the model parameterization. We are presently refining the model to increase its accuracy in predicting the experimental results. Eventually we plan to generalize the model to three dimensions to predict the drainage network characterisics that will result from groundwater erosion, using our sapping tank experiments for model verification and calibration.

REFERENCES

Kochel, R. C., Howard, A. D., and McLane, C., 1984, Channel networks developed by groundwater sapping in fine-grained sediments: Analogs to some Martian Valleys: 1983 Geomorphology Symposium, George Allen and Unwin, Boston, in press.

Howard, A. D. and McLane, C., 1981, Groundwater sapping in sediments: Theory and experiments: NASA Tech. Mem. 84211, 283-85.

Howard, A. D. and Mclane, C., 1983, Groundwater sapping studies: NASA Tech. Mem. 85127.

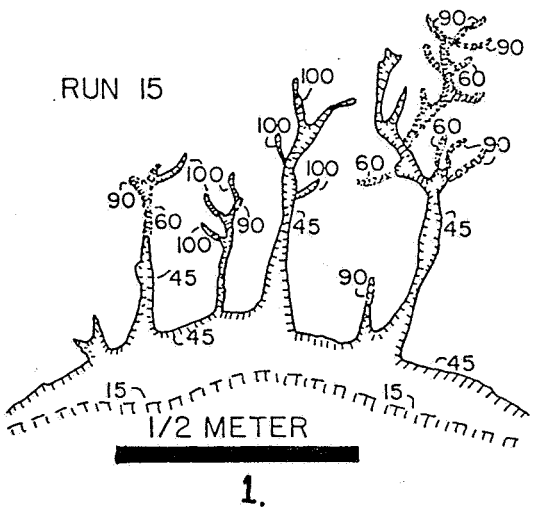
RUN 15
90
90
100
100
60
60
90
100
100
60
90
90
60
45
45
100
90
45
45
45
15
15
1/2 METER

1.

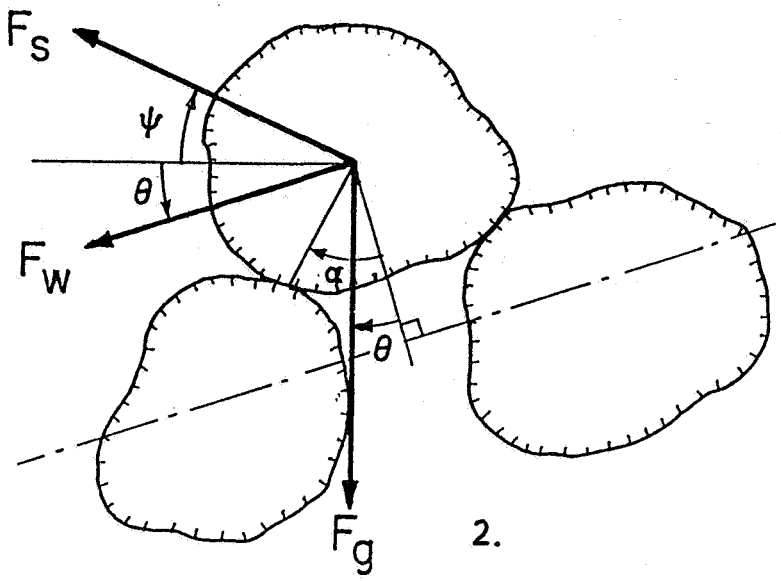
F_s
ψ
θ
F_w
α
θ
F_g

2.

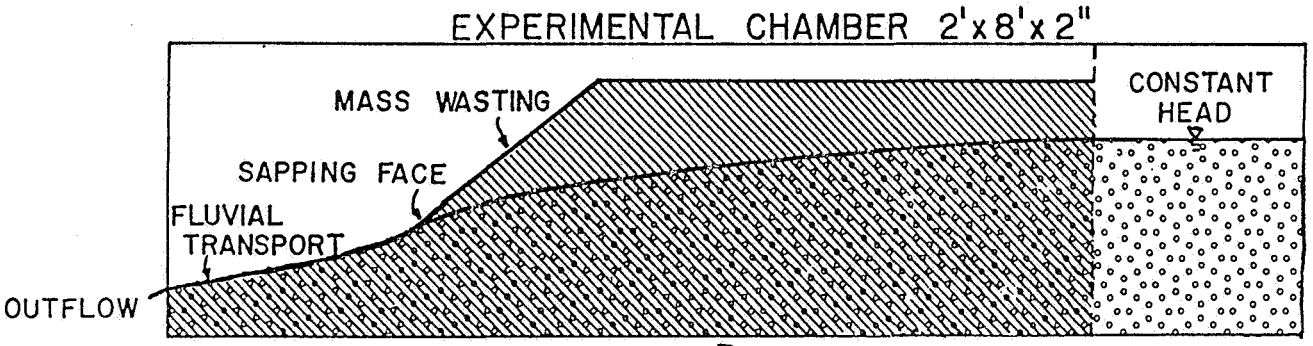
EXPERIMENTAL CHAMBER 2'x8'x2"
MASS WASTING
CONSTANT HEAD
SAPPING FACE
FLUVIAL TRANSPORT
OUTFLOW

3.

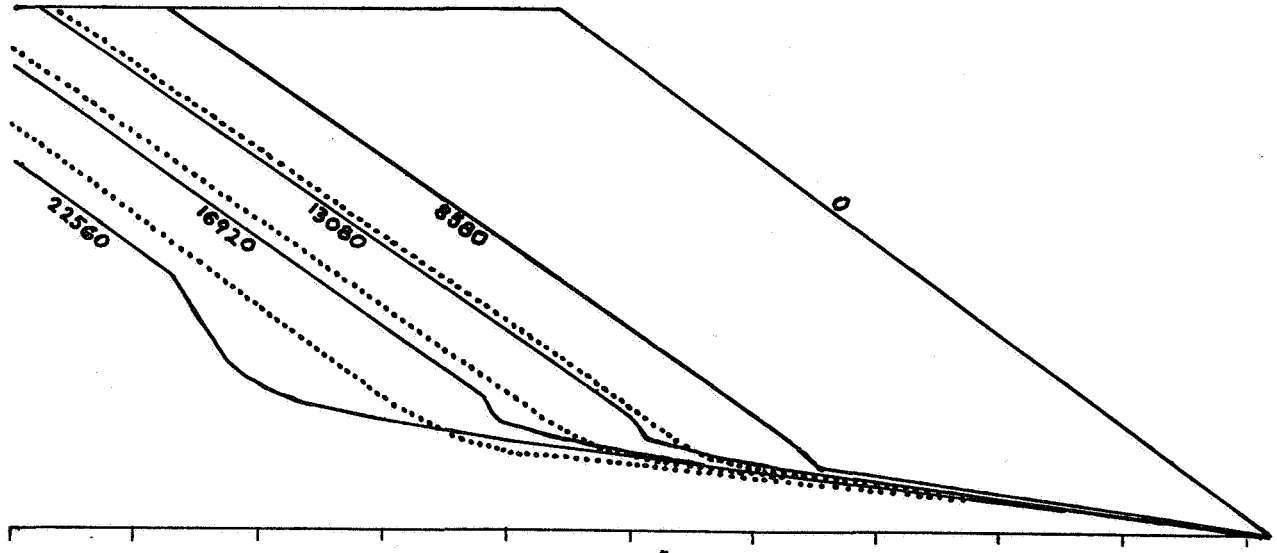
22560
16920
13080
8580
0

4.

D72

N84 23503

Planetary Geomorphology Field Studies: Washington and Alaska

Michael C. Malin, Department of Geology, Arizona State University, Tempe, AZ 85287

As noted in a companion abstract, field studies of terrestrial landforms and the processes that shape them have provided new directions to study of planetary features. Investigations discussed in this abstract address principally mudflow phenomena and drainage development.

At the Valley of 10,000 Smokes (Katmai, AK) and Mount St. Helens, WA, studies of the development of erosional landforms (in particular, drainage) on 'fresh, new' surfaces has permitted analysis of the result of competition between geomorphic processes. Of specific interest is the development of stream pattern as a function of the competition between perennial seepage overland flow (from glacial or groundwater sources), ephemeral overland flow (from pluvial or seasonal melt sources), and ephemeral/perennial groundwater sapping, as a function of time since initial resurfacing, material properties, and seasonal/annual environmental conditions.

Washington

At Mount St. Helens, drainage developed in the pyroclastic plains north of the mountain in three stages. First, short duration enhancement of runoff from perennial sources of water (principally glaciers) caused by thermal effects of volcanic eruptions established an extremely sparse network of drainage channels, narrow and deeply cut into the relatively soft pyroclastic materials. This system closely mimiced the location of pre-eruption drainages (even though over a landscape covered by as much as 100 m of material), suggesting that perennial seepage runoff was the principal force that determined earlier drainage development. At this time, ephemeral runoff from rainfall formed extremely shallow, very long, parallel rilles (mostly by mobilization of surficial pumice), and sapping processes were confined to the upper soil (primarily in the 'blast deposit' formed during the 18 May 1980 eruption). The second stage occurred after the major pyroclastic events had ceased, when thermal events were localized within the crater by dome growth and dome-related ash events. These events dramatically emphasized ephemeral runoff, and combined with rainfall and seasonal runoff from snowmelt, led to an increase of drainage density and the development of a broader range of network type. Highest order streams were still dominantly channels formed by perennial runoff, but networks developed many lower-order tributaries through ephemeral flow. Sapping occurred in areas where water movement within the pyroclastic plains caused local saturation, or where such water reached the surface along compositional planes and under some hydrostatic head. Finally, both forms of drainages have now become well entrenched in the pyroclastic material, and the processes are now competing for the remainder of the drainage surface area. Bedrock springs, similar to those common on the low hills that surround the volcano and that were active shortly after the 18 May eruption, are now found on the northern slopes of the volcano. These are creating new channels much like those

formed earlier by glacial meltwater runoff, and represent yet another form of drainage development on the plains.

Alaska

In the Valley of 10,000 Smokes, events similar to those that occurred at Mount St. Helens have led to results in some ways similar, and in other ways dissimilar to those just described. Again, perennial runoff of glacial meltwater, enhanced by the thermal effects of tephra, rapidly established streams in locations similar to their pre-eruption sites (i.e., the Lethe and Knife rivers). Rapid and continued incision of these streams was limited by the induration of the welded portion of the ash flow within the Valley (the downward propagating 'wave' of stream incision met the upward propagating 'wave' of hardening tuff). Sapping appears to have played a more limited role in the evolution of drainage in the Valley, perhaps owing to the differences in induration of the various airfall and ash flow deposits, the declivity of the terrain, and the nature of groundwater supplies and their recharge cycle.

These studies suggest that martian valley formation may be much more complicated than earlier surmised based on our work on the Colorado Plateau (1). In particular, we are currently developing criteria by which the various contributions of these competing processes may be deciphered. These criteria include statistical analyses of network pattern parameters, small-scale morphologic characteristics of channel and valley walls and floors, and topographic analysis of longitudinal and transverse profiles. These criteria are concurrently being applied to martian valley networks, in particular those in the Margaritifer Sinus region.

References

1) Laity, J. L. and M. C. Malin (1984) Geo. Soc. Am. Bull. (in press).

D73

N84 23504

A REGRESSION MODEL FOR THE TEMPORAL DEVELOPMENT OF SOIL PIPES AND ASSOCIATED GULLIES IN THE ALLUVIAL-FILL VALLEY OF THE RIO PUERCO, CENTRAL NEW MEXICO

Christopher D. Condit and Wolfgang E. Elston; Department of Geology, University of New Mexico, Albuquerque, NM 87131

On Mars, the association of gullied escarpments and chaotic terrain is evidence for failure and scarp retreat of poorly consolidated materials. Some martian gullies have no surface outlets and may have drained through subterranean channels. Similar features, though on a much smaller scale, can be seen in alluvium along terrestrial river banks in semiarid regions, such as the Rio Puerco Valley of central New Mexico. Many of the escarpments along the Rio Puerco are developing through formation of collapse gullies, which drain through soil pipes (Fig. 1). Gully development can be monitored on aerial photographs taken in 1935, 1962, and 1980. A regression model has been developed to quantify gully evolution over a known time span.

Soil pipes and their associated collapse gullies make recognizable signatures on the air photos. The areal extend of this signature can be normalized to the scarp length of each pipe-gully system, which makes comparisons between systems possible. The term Y = area/length, when combined with the difference in years (X) between repetitive photos of a given scarp, generates a data base for regression analysis of change through time. The best least-squares regression model for 42 scarps from the Rio Puerco in central New Mexico results in the equation $Y=0.43X^{0.83}$. The derivative of this equation, $dy/dx=0.36X^{-0.17}$, indicates that pipe-gully systems in this area grow at a decreasing rate. Quantitative application of this model to the Rio Puerco supports the suggestion that the alluvial fill was incised over the last 100 years. The success of this simple model offers the possibility of dating alluvial surfaces within a particular climatic zone and of predicting the extent of future development of a pipe-gully system.

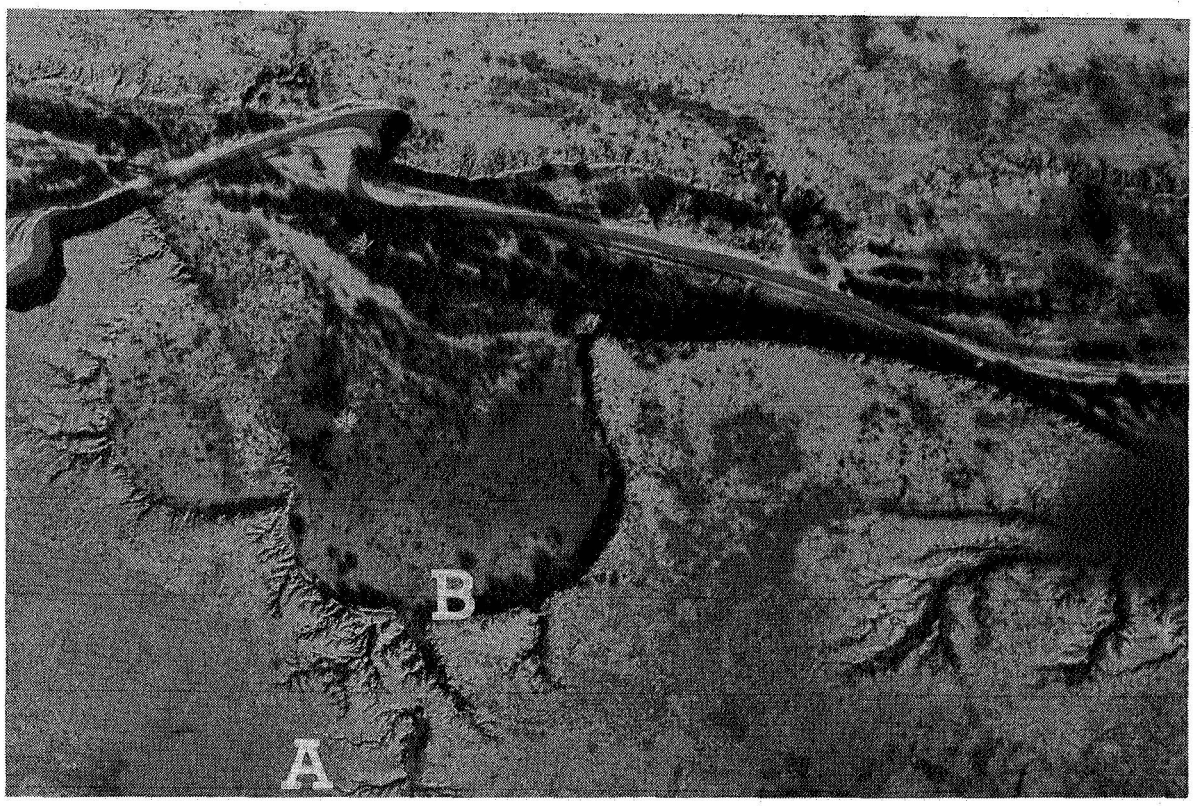

Figure 1. Gully system in alluvial escarpments along the Rio Puerco, New Mexico. A - gully without surface outlet draining into a soil pipe. B - gully and escarpment controlled by a fence, not a tectonic lineament.

D74 N84 23505

EXPERIMENTS EXAMINING THE SHAPES OF ISOLATED BARS IN COMPARISON WITH THOSE OCCURRING IN BRAIDED RIVERS

Komar, Paul D., School of Oceanography, Oregon State University, Corvallis, Oregon

Sand bars and islands within braided rivers have characteristic rhomboid or diamond shapes, often becoming very complex in form as the density of islands increases [see, for example, Krigstrom (1962), Collinson (1970), Rust (1972) and Cant (1978)]. Similar forms are observed in the martian outflow channels where the islands occur in groups (Trevena and Picard, 1978). This contrasts with the more isolated martian islands which have airfoil shapes, as do isolated streamlined islands in rivers and in the Channeled Scabland. These observations indicate that the bar and island forms are controlled by the density of the islands, with increasing island interaction and flow modification as the density increases. As a continuation of my previous flume experiments on the shapes of isolated islands (Komar, in press), I have begun a new series of experiments to investigate the modifications produced by a progressive increase in island density, finally leading to a true braided system.

My previous experiments were largely with "cohesive" islands composed of sand and clay, the objective being to focus mainly on the erosive landforms such as those observed in the martian channels. The present experiments, however, are employing pure sand where deposition plays a more important role. This series of experiments began with an isolated sand island to see how it is modified by the flow in the absence of other nearby islands. The initially-circular island, extending above the water surface, quickly eroded on its upstream side, the eroded sand depositing in the island lee to fill in the wake, thereby forming an overall streamlined shape. Initially there was a lee V-wave, also observed in my previous experiments, which modified the downstream point of the depositional zone, but once the island had eroded down, leaving a submerged sand bar, this V-wave disappeared so that the deposit formed a single downstream point. The bar flattend out sufficiently that no hydraulic jump occurred over its top such as those observed in the previous experiments with submerged

cohesive islands. In its final form the main body of the bar had a near-ideal airfoil shape, the closest agreement found in any of my experiments. The main difference from the airfoil form was the presence of a linear shoal extending downstream from the island's pointed lee, just as observed on many streamlined islands and bars in active rivers. The upstream side was well rounded, not being diamond shaped as observed for islands within braided rivers.

This experiment with a single sand island was followed by runs where the flume contains several islands arranged into patterns just as found in a braided system, but with the islands given initially rounded shapes. Again the islands were rapidly modified by the flow, but it was apparent that the dense pattern of islands was in turn controlling the flow, forcing it into a series of channels characteristic of braided rivers. The islands also developed diamond shapes.

Thus far these experiments have been only qualitative, the purpose being to assess whether more detailed analyses are warranted. My intention now is to conduct a more thorough series of experiments with a range of island densities, documenting the effects on the water flow, the patterns of sand exchange between islands, as well as the modifications and final shapes of the islands.

REFERENCES

Cant, D.J. (1978) Bedforms and bar types in the South Saskatchewan River: Jour. Sedimentary Petrology, v. 48, p. 1321-1330.

Collinson, J.D. (1970) Bedforms of the Tana River, Norway: Geografiska Annaler, v. 52A, p. 31-56.

Komar, P.D. (in press) The shapes of streamlined islands on earth and Mars: Experiments and analyses of the minimum-drag form: Geology.

Krigstrom, A. (1962) Geomorphological studies of sandur plains and their braided rivers in Iceland: Geografiska Annaler, v. 44, p. 328-346.

Rust, B.R. (1972) Structure and process in a braided river: Sedimentology, v. 18, p. 221-245.

Trevena, A.S., and M.D. Picard (1978) Morphometric comparison of braided martian channels and some braided terrestrial features: Icarus, v. 35, p. 385-394.

D75

N84 23506

THE EROSION OF STREAMLINED ISLANDS, LONGITUDINAL GROOVES AND SCOUR MARKS: IMPLICATIONS TO THE ORIGIN OF THE MARTIAN OUTFLOW CHANNELS

Komar, Paul D., School of Oceanography, Oregon State University, Corvallis, Oregon 97331

The martian outflow channels have sparked considerable interest since their discovery and a wide variety of imaginative hypotheses to account for their origin: catastrophic water floods (Baker and Milton, 1974; Baker, 1978, 1982), structural control (Schumm, 1974), lava flows (Schonfield, 1976; Cutts et al., 1978), wind erosion (Cutts and Blasius, 1981), debris flows (Nummedal and Prior, 1981), and glacial erosion (Lucchitta et al., 1981). This diversity of proposed origins for these large channels results from the differing interpretations given to the landforms associated with the outflow channels. In an attempt to help limit the possible mechanisms of channel erosion, I have undertaken more detailed studies of three of the channel features; the streamlined islands, longitudinal grooves and scour marks.

My analyses of the streamlined islands have been completed and the results presented as two journal papers (Komar, in press; in review). This examination involved a comparison of the martian streamlined islands with various streamlined landforms on earth including those found in the Channeled Scabland (Baker, 1978; Baker and Kochel, 1978), in large rivers, glacial drumlins and desert yardangs. The comparisons included statistical analyses of the landform lengths versus widths and positions of maximum width, and an examination of the degree of shape agreement with the geometric lemniscate which was in turn demonstrated to correspond closely with true airfoil shapes (Joukowski Sections). The analyses showed that the shapes of the martian islands correspond closely to the streamlined islands in rivers and the Channeled Scabland. Drumlins on the other hand tend to be more elliptical and their dimensions show a much smaller correlation than for the water-formed islands. In addition, erosional rock "islands" formed by glaciers are very much different in shape, generally being pointed at both ends with the predominant point

forming on its upflow side. Yardangs have a wide range of length to width ratios with very large values occurring (Ward, in review). All of these shape analyses support a water-erosion hypothesis for the martian streamlined islands and hence for the outflow channels. It is also of interest that the water-formed streamlined islands on average have length to width ratios of 3 to 4, and a reanalysis of the drag on airfoils shows that this shape minimizes the flow drag. This further implies that the fluid which eroded the martian channels must have been fully turbulent.

The focus of my study has now turned to the origin of the parallel, longitudinal grooves observed in the outflow channels. Thompson (1979) provides the only previous examination of the mechanism of formation. His instability analyses suggest a high viscosity for the flows, in the range of debris flows rather than water. His analysis, however, assumes a basal slip velocity and makes other simplifying assumptions so that the results are questionable when applied to the flow of water. My attention instead has focused primarily on actual observations of secondary flows in rivers which could form longitudinal bed features. Secondary helical flows in rivers were first noted independently by Stearns and Moller in 1883 as the cause of the depression of the maximum velocity of the river away from the water's surface and for the occurrence of parallel lines of floating debris on the river. These helical secondary currents combine with the main river flow to produce rows of spiral circulation of the water as it travels along the channel. Studies by Vanoni (1946) and Chiu and McSparran (1966) have demonstrated the importance of helical flow to the control of sediment transport and deposition in rivers and flumes. The number of helical "cells" present in a river cross-section may vary from two to perhaps a dozen or more, the number increasing as the width to depth proportions of the river increase. Their occurrence in terrestrial rivers suggests a possible role in the formation of the martian grooves, and the dependence of the helical flow on the depth may provide a key to evaluations of the depth of the martian flows from the observed groove spacings. This possibility is now under investigation.

REFERENCES

Baker, V.R. (1978) A preliminary assessment of the fluid erosional processes that shaped the martian outflow channels: Proc. Lunar and Planetary Sci. Conf., 9th, p. 3205-3223.

Baker, V.R. (1982) The Channels of Mars: Univ. of Texas Press, Austin, 198 pp.

Baker, V.R., and R.C. Kochel (1978) Morphometry of streamlined forms in terrestrial and martian channels: Proc. Lunar and Planetary Sci. Conf., 9th, p. 3193-3203.

Baker, V.R., and D.J. Milton (1974) Erosion by catastrophic floods on Mars and earth: Icarus, v. 23, p. 27-41.

Chiu, C.L., and J.E. McSparran (1966) Effect of secondary flow on sediment transport: Proc. Amer. Soc. Civil Engrs., v. 92, HY5, p. 57-70.

Cutts, J.A., and K.R. Blasius (1981) Origin of martian outflow channels: The eolian hypothesis: Jour. Geophys. Res., v. 86, p. 5075-5102.

Cutts, J.A., W.J. Roberts, and K.R. Blasius (1978) Martian channels formed by lava erosion: Proc. Lunar and Planetary Sci. Conf., 9th, p. 209.

Komar, P.D. (in press) The shapes of streamlined islands on earth and Mars: Experiments and analyses of the minimum-drag form: Geology.

Komar, P.D. (in review) The lemniscate loop — Comparisons with the shapes of streamlined landforms: Jour. of Geology.

Lucchitta, B.K., D.M. Anderson and H. Shoji (1981) Did ice streams carve martian outflow channels?: Nature, v. 290, p. 759-763.

Nummedal, D., and D.B. Prior (1981) Generation of martian chaos and channels by debris flows: Icarus, v. 45, p. 77-86.

Schonfeld, E. (1976) On the origin of the martian channels: EOS, v. 57, p. 1749.

Schumm, S. (1974) Structural origin of large martian channels: Icarus, v. 22, p. 371-378.

Thompson, D.E. (1979) Origin of longitudinal grooving in Tiu Vallis, Mars: Isolation of responsible fluid-types: Geophys. Res. Letters, v. 6, p. 735-738.

Vanoni, V.A. (1946) Transportation of suspended sediment by water: Trans. Amer. Soc. Civil Engrs., v. 111, p. 67-133.

Ward, A.W. (in review) A theoretical, scale-modelling, and field study of yardangs: Geol. Society Amer. Bulletin.

Chapter 8

PERIGLACIAL AND PERMAFROST PROCESSES

D76

SMALL-SCALE POLYGONS ON MARS

Baerbel K. Lucchitta, U.S. Geological Survey, Flagstaff, Arizona

Polygonal-fracture patterns on the martian surface were discovered on Viking Orbiter images. The polygons are 2-20 km in diameter, much larger than those of known patterned ground on Earth [1, 2]. New observations show, however, that polygons exist on Mars that have diameters similar to those of ice-wedge polygons on Earth (generally a few meters to more than 100 m, [3]): Evans and Rossbacher [4] noticed networks of polygons outlined by ridges in the smooth plains material of Lunae Planum (lat 17°N, long 56°W), and Brook [5] discovered light-colored polygonal networks on a layered tableland (lat 23°N, long 35°W) near the Viking 1 Lander Site.

Another area underlain by small-scale polygonal ground [6] occurs on a platform in Deuteronilus Mensae, near lat 47°N, long 346°W. An example is shown in figure 1. The polygons measure 50-300 m in diameter, but smaller ones may also exist locally; faint networks can be detected down to the limit of resolution of the pictures. The interiors of these polygons are dark, similar to the polygons observed by Brook [5]. The polygons occur mostly on level ground but are also found on the sloping rim of a crater (8 km diam.), where the light-toned network can be clearly identified as linear depressions or cracks. Fractures parallel to the slope are emphasized, similar to what is observed on some terrestrial polygons [3]. No upturned margins are visible; it appears that most of the polygons are flat or high centered. In some cases the patterned ground dissolves into a field of dark spots or low hummocks on a lighter-toned background.

Terrestrial patterned ground may be sorted or unsorted [3]. Most large polygons on the Earth are unsorted; they may be more than 100 m in diameter, have cracks as much as 30 m deep, and occur in well-sorted fines, sand, gravel, or poorly sorted glacial deposits [3]. Patterns may be dominated by orthogonal intersections (random or oriented orthogonal systems) or by triradial 120° intersections (nonorthogonal system) [7]. Apparent influence on the shape of the polygons on Mars by subparallel linear structures resulted in a network pattern most compatible with the random-orthogonal class.

Unsorted polygons can be formed by desiccation, thermal contraction, or phase changes [7, 3]. An origin of the martian polygons by contraction of cooling volcanic materials is implausible because polygons occur on impact crater rims superposed on the patterned plains.

An origin by desiccation presents some difficulties. On the Earth, desiccation polygons are commonly small, whereas the polygons on Mars are large. However, the common occurrence of desiccation polygons on the Earth in thin layers of mud predisposes cracks to be limited to shallow depths and polygons to small sizes. By contrast, desiccation on Mars may have affected materials to considerable depth, the desiccation being caused by seasonal or secular climatic cycles. Since thick layers may thus have been affected by desiccation on Mars, the polygons might have grown commensurately larger than those on the Earth.

Recent seasonal desiccation to the depths required to form polygons 50-300 m in diameter is unlikely at the latitude of Deuteronilus Mensae, where the newly discovered patterned ground is situated, because water there is in equilibrium with the atmosphere year round and may remain in the ground below about 1 m depth [8]. During astronomic cycles of 10^5-10^6 years, however,

resulting in a temporary high obliquity of Mars' rotational axis, the ground might have possibly warmed to sufficient depth for large-scale desiccation. However, Helfenstein [9] calculated that these climatic cycles have large effects near the poles but only negligible effects near lat 45°, and so fractured ground near this latitude would probably not be affected much by secular climatic cycles.

An origin of the martian polygons as thermal-contraction cracks in ice-rich ground appears to be compatible with the observations. The seasonal temperature change in the area discussed is substantial. The mean diurnal temperature ranges from -50°C in the summer to -110°C in the winter during a martian year, a drop of 60°C [10]. The amount of this drop is more than adequate to initiate thermal contraction in ice-rich ground. That ice exists in the ground in the area is suggested by the local disintegration of the polygonal network into fields of hummocks. This disintegration is similar to the collapse of ice-rich ground on the Earth, where polygons disintegrate into fields of baydjarakhs.

Another question is whether the fractures on Mars are filled by ice wedges or sand wedges. The climate on Mars is extremely dry; only very few to about 30 precipitable microns of water exist at this latitude [11]. Wind-driven material, however, is ubiquitous and would readily fill cracks. The lighter tone of the polygonal network is compatible with infilling by drift: sand wedges, therefore, are plausible. On the other hand, as seen at the Viking 2 Lander site, waterfrost is precipitated in winter on Mars [12], and may be redistributed by the wind. Crystals may grow in cracks. Overall, the fractures may be filled by a combination of dirt and ice.

It is difficult to ascertain whether the polygons are forming today or are relics from the past. The crispness of some cracks suggests a recent origin. On the other hand the absence of upturned edges (indicating actively forming ice wedges), the locally disintegrating ground, and a few possible superposed rayed craters indicate that the polygons are not forming at the present.

REFERENCES

[1] Black, R. F., 1976, Periglacial features indicative of permafrost: Ice and soil wedges: Quaternary Research, v. 6, p. 3-26.

[2] Black, R. F., 1978, Comparison of some permafrost features on Earth and Mars: Some cautions and restrictions, in Proceedings of the Second Colloquium on Planetary Water and Polar Processes, Hanover, N. H., 16-18 Oct. 1978, p. 127-130: Hanover, N. H., U.S. Army, Cold Regions Research and Engineering Laboratory.

[3] Washburn, A. L., 1980, Geocryology: A survey of periglacial processes and environments: New York, John Wiley and Sons, 406 p.

[4] Evans, N. and Rossbacher, L. A., 1980, The last picture show: Small-scale patterned ground in Lunae Planum, in Reports of Planetary Geology Program, 1980, p. 376-378: U.S. National Aeronautics and Space Administration Technical Memorandum 82385.

[5] Brook, G. A., 1982, Ice-wedge polygons, baydjarakhs, and alases in Lunae Planum and Chryse Planitia, Mars, in Reports of Planetary Geology Program, 1982, p. 265-267: U.S. National Aeronautics and Space Administration Technical Memorandum 85127.

[6] Lucchitta, B. K., 1983, Permafrost on Mars: Polygonally fractured ground, in Proceedings, 4th International Conference on Permafrost, Fairbanks, Alaska, 18-22 July, 1983. In press.
[7] Lachenbruch, A. H., 1962, Mechanics of thermal contraction cracks and ice-wedge polygons in permafrost: Geological Society of America Special Paper 70, p. 69.
[8] Farmer, C. B. and Doms, P. E., 1979, Global seasonal variation of water vapor on Mars and the implications for permafrost: Journal of Geophysical Research, v. 84, no. B6, p. 2881-2888.
[9] Helfenstein, P., 1980, Martian fractured terrain: Possible consequences of ice-heaving, in Reports of Planetary Geology, 1980, p. 373-375: U.S. National Aeronautics and Space Administration Technical Memorandum 82385.
[10] Kieffer, H. H., Martin, T. Z., Peterfreund, A. R., Jakosky, B. M., Miner, E. D., and Palluconi, F. D., 1977, Thermal and albedo mapping of Mars during the Viking primary mission: Journal of Geophysical Research, v. 82, no. 28, p. 4249-4271.
[11] Jakosky, B. M., and Farmer, C. B., 1982, The seasonal and global behavior of water vapor in the Mars atmosphere: Complete global results of the Viking atmospheric water detector experiment: Journal of Geophysical Research, v. 87, no. B4, p. 2999-3019.
[12] Wall, S. D., 1981, Analysis of condensates formed at the Viking 2 Lander site: The first winter: Icarus, v. 47, no. 2, p. 173-183.

FIGURE 1 (a) - Polygonally fractured ground in Deuteronilus Mensae, Mars. Polygons occur on flat terrain and on slopes of an ancient impact crater rim. Illumination is from bottom. Center of picture is at lat 46.7°N, long 346.1°W. Viking Orbiter frame 458B67. Orientation and scale same as in (b).
(b) - Sketch map of polygons shown in (a). Polygons are about 50-300 m in diameter. Stippled areas denote impact craters and their ejecta, dashed lines crater rim crests of large subdued craters.

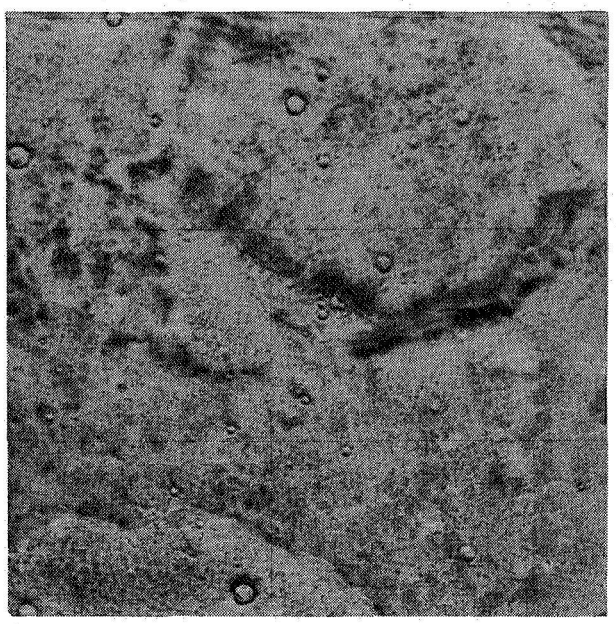

a

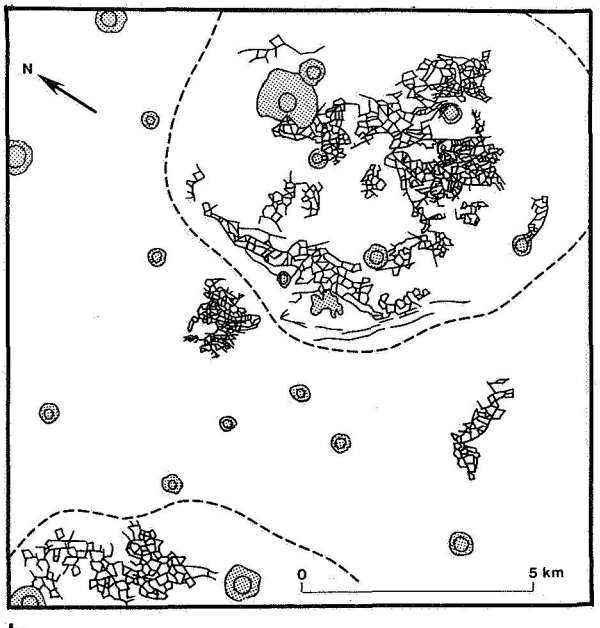

b

D77

N84 23508

PERMAFROST ON MARS: DISTRIBUTION, FORMATION, AND GEOLOGICAL ROLE

Dag Nummedal, Department of Geology, Louisiana State University, Baton Rouge, LA 70803.

The morphology of channels, valleys, chaotic and fretted terrains and many smaller features on Mars is consistent with the hypothesis that localized deterioration of thick layers of ice-rich permafrost has been a dominant geologic process on the Martian surface. Such ground ice deterioration has given rise to large-scale mass movement, including sliding, slumping and sediment gravity flowage, perhaps also catastrophic floods. In contrast to Earth, such mass movement processes on Mars lack effective competition from erosion by surface runoff. Therefore, Martian features due to mass movement have grown to reach immense size without being greatly modified by secondary erosional processes.

The Viking Mission to Mars in 1976 provided adequate measurements of the relevant physical parameters to constrain models for Martian permafrost.

The mean annual surface temperature on Mars is everywhere below 273 K. Thus, permafrost is global. The lower boundary of the permafrost layer is controlled by the geothermal heat flux. Fanale (1976) determined the present rate of heat production on Mars by assuming that, in bulk, the planet had the same ^{40}K, ^{232}Th, ^{238}U, and ^{235}U concentrations as chondrites. Based on this he found a near-surface heat flux of 29.3 ergs/cm^2/s. Assuming perfect temperature equilibrium with the atmosphere, Fanale's model showed that the 273 K isotherm would be encountered at a depth of 1 km at the equator, at 2 km at 40° latitude and at greater depths at higher latitudes. These numbers probably give the maximum thickness of the global permafrost. Toksoz and Hsui (1978) calculated a heat flux of 35 ergs/cm^2/s. This higher value would correspond to a steeper temperature gradient and somewhat thinner permafrost zone than the one calculated by Fanale (1976). Rossbacker and Judson (1981) have computed the permafrost distribution based on this revised heat flux value.

The global permafrost distribution discussed in the preceding paragraph is based on the currently observed Martian climate. The Martian temperature regime, however, is variable. The depth penetration of the thermal wave corresponding to these temperature variations depends on the wave frequency. The daily thermal wave probably affects only the upper few centimeters, the annual changes the upper 1-10 m. These fluctuations produce a layer which is subject to alternating ice formation and desiccation on an annual basis. In mid-latitudes this layer is from 10 cm to 1 m thick, in the equatorial zone it extends down to 10 m (Farmer and Doms, 1979). Temperature changes on time scales of 10^5-10^6 years should penetrate to depths of a few hundred meters to 1 km. Temperature changes over geologic time scales of billions to years may affect the entire regolith (Table 1).

Prior to the Mariner 9 mission in 1971-1972 Mars was considered a planet greatly impoverished in water. Morphological evidence for flowing water in the form of large channels, discovered by Mariner 9 (McCauley et al. 1972), completely changed that perception. As stated by

Pollack (1979), "Water is the only plausible, cosmically abundant substance that meets all the morphological constraints imposed by the many channels on Mars." Water is probably present in frozen interstitial form in the permafrost zone, some is tied up in the polar caps, and some is tied up in hydrated minerals or adsorbed onto clay particles in the regolith.

The temperatures on Mars suggest thick global permafrost. Models for planetary evolution indicate abundant water. Consequently, a most reasonable conclusion is that the Martian regolith contain large amounts of ice-rich permafrost. In all probability, additional water is available in the liquid phase in pore spaces beneath the ice-rich zone.

The presence of thick global permafrost underlain by a high-pressured zone of liquid water is consistent with the two principal models proposed for the origin of the large Mars outflow channels (for details see: Mars Channel Working Group, 1983). Carr (1979) suggested that venting of subsurface water reservoirs through fracture of the ground ice seal might be a mechanism for the release of vast floods. Carr's (1979) proposal calls for a regional system of confined aquifers. These were created by the progressive downward freezing of ground ice during a period of cooling climate. Liquid water between this freezing front and the base of the porous regolith would gradually increase in pressure. In region downslope of high potential head differences the artesian pressure could have exceeded the lithostatic pressure, fractured the ground ice seal, and caused water to rush to the surface at enormous discharge rates.

Nummedal (1978, 1983) called for liquefaction of subsurface unconsolidated materials to explain the Chryse channels and associated chaos. Liquefaction in unfrozen terrain is normally limited to very fine-grained materials where internal pore water pressure can reach the vertical confining pressure without substantial fluid leakage. In permafrost terrain, however, an ice-rich cap may provide the necessary seal such that even gravels may become liquefied (Finn et al. 1978). In fact, Carr's (1979) proposed system of confined aquifers is likely first to reach an internal pressure adequate for liquefaction of unconsolidated materials before the artesian pressure can rupture the overlying seal. Once such a highly sensitive subpermafrost layer was formed, a seismic shock (internal or impact) could have triggered the liquefaction, with consequent collapse and fluid release.

It is now generally recognized that ice-rich permafrost is responsible for the abundant "cold-region" morphologic features seen in Viking images (Lucchitta, 1981). This study indicates that some of the large-scale Mars outflow channels also derive from the failure of a permafrost seal. This seal probably overlies water-saturated unconsolidated material subject to liquefaction in response to impacts or internal seismic events.

TABLE 1 Climatic changes on Mars: Factors, Time Scales, and Depths of Penetration of the Associated Thermal Wave

Time scale	Cause	Penetration Depth of Thermal Wave
Daily	Planetary Rotation	cm
Year	Orbital revolution	1-10 m
10^5-10^6 years	Obliquity and eccentricity variations	
1-4 x 10^9 years	Polar wandering Greenhouse effect Solar luminosity	km

REFERENCES

Carr, M. H., 1979, Journal of Geophysical Research, v. 84, p. 2995-3007.
Fanale, F. P., 1976, Icarus, v. 28, p. 179-202.
Farmer, C. B., and Doms, P. E., 1979, Journal of Geophysical Research, v. 84, p. 2881-2888.
Finn, W. D. L., Yong, R. N., and Lee, K. W., 1978, Journal of Geotechnical Engineering Division, American Association of Civil Engineers, v. 104, p. 1243-1255.
Lucchitta, B. K., 1981, Icarus, v. 45, p. 264-303.
Mars Channel Working Group, 1983, Geol. Soc. Am. Bull., v. 94, p. 1035-1054.
McCauley, J. F. et al., 1972, Icarus, v. 17, p. 289-327.
Nummedal, D., 1978, NASA Technical Memorandum 79729, p. 257-259.
Nummedal, D., 1983, Proc. 4th Internal. Conf. Permafrost (in press).
Pollack, J. B., 1979, Icarus, v. 37, p. 479-553.
Rossbacker, L. A., and Judson, S., 1981, Icarus, v. 45, p. 39-59.
Toksoz, M. N., and Hsui, A. T., 1978, Icarus, v. 34, p. 537-547.

D78

N84 23509

GLACIAL AND PERIGLACIAL LANDFORMS IN DENMARK: SCANDINAVIAN ANALOGS FOR MARTIAN FEATUTES

Lisa A. Rossbacher, Dept. of Geology, Whittier College, Whittier, California 90608 (spring 1984: Dept. of Physical Geography, Univ. of Uppsala, Box 554, S-751 22 Uppsala, Sweden)

The geomorphology of Denmark is dominated by glacial deposits, including both end moraines and ground moraines. Many of these features have morphologies similar to features observed on Mars.

A characteristic landscape complex in Denmark is a series of irregular mounds or parallel curvilinear ridges that outline the former ice margin. Many of these resemble curvilinear features on Mars, and the Danish landforms occur at a similar scale (Rossbacher and Judson, 1981; Rossbacher, in press). Some of the prominent moraine ridges in Denmark stand 50-100 m above the surrounding topography and can be traced for several km. Where the ice margin oscillated, parallel-hill moraine landscapes developed. The highest point in the country (173 m) is atop a moraine that probably reflects a long still-stand of the Scandinavian ice sheet during the Weichsel (Würm) maximum (Schou, 1949; Embleton and King, 1968, p. 351; Nielsen, 1979; Krüger, 1983). Pre-World War II aerial photographs taken by the Royal Danish Flying Corps show that these high-standing end moraines used to cover more of Denmark's landscape; many Pleistocene moraines have been mined for fill or removed for crop cultivation (Schou, 1949). Some of the conditions of emplacement for these landforms can be inferred from their morphology. Similar configurations often characterize margins of modern ice caps that terminate in areas of low relief (Krüger and Humlum, 1981). Subglacial topography also controls the ice flow; relief in the substratum of more than one-tenth the ice thickness can divert ice flow to create lobes that deposit curvilinear end moraines (Krüger, 1981).

Another distinctive landform in Denmark is the hummocky moraine landscape found in parts of Sjælland (Schou, 1949; Rasmussen, 1968). Although their size is smaller, these areas resemble the hummocky terrain associated with some of the curvilinear features in the northern plains of Mars (Rossbacher, 1983, in press). The hummocky Danish terrain is probably caused by the melting of masses of dead ice left during glacial retreat. Similar landscapes have been observed developing during retreat of smaller

ice caps in Scandinavian mountains and in Greenland (Schou, 1949).

This study of terrestrial analogs in Denmark is continuing and will include field work, literature searches, and inspection of historical aerial photographs. This project will also include analogs in other parts of Scandinavia. Subjects for future study include the Salpausselkä moraines, which extend for more than 300 km across southern Finland (Embleton and King, 1968, p. 344; Punkari, 1982), ice-cored moraines that are currently forming in northern Norway and Sweden (Østrem, 1964), and some large periglacial dune complexes in Sweden (Sundborg, 1955; Seppälä, 1970, 1971). This work should provide a group of possible terrestrial analogs for Martian features from a region that has not been considered closely before.

REFERENCES CITED

Embleton, C., and C.A.M. King, 1968, Glacial and periglacial geomorphology: New York, St. Martin's Press, 608 p.

Krüger, J., 1983, Glacial morphology and deposits in Denmark, in Glacial deposits in North-west Europe, ed. by J. Ehlers: Rotterdam, A.A. Balkema, p. 181-191.

Krüger, J., and O. Humlum, 1981, The proglacial area of Myrdalsjökull with particular reference to Slettjökul and Höfdabrekkuljökull, in General report on the Danish geomorphological expedition to Iceland, 1977: Folia Geographica Danica, v. 15, 58 p.

Nielsen, A.V., 1979, Landskabets tilbivelse, p. 251-344, in Danmarks natur, v. 1, Landskabernes opståen: København, Politikens Forlag, 448 p.

Punkari, M., 1982, Glacial geomorphology and dynamics in the eastern parts of the Baltic Shield interpreted using Landsat imagery: The Photogrammetric Journal of Finland, v. 9, p. 77-93.

Rasmussen, H.W., 1968, Danmarks geologi: København, Gjellerup, 176 p.

Rossbacher, L.A., 1983, Geomorphic studies of Mars: Princeton, NJ, Princeton University (Ph.D. dissertation), 242 p.

Rossbacher, L.A., in press, Ground ice models for the distribution and evolution of curvilinear landforms on Mars: Proceedings, 14th Binghamton Geomorphology

Symposium (September 1983, Buffalo, New York).

Rossbacher, L.A., and S. Judson, 1981, Ground ice on Mars: Inventory, distribution, and resulting landforms: Icarus, v. 45, p. 39-59.

Schou, A., 1949, Atlas of Denmark: København, The Royal Danish Geographical Society, 130 p.

Seppälä, M., 1970, Location, morphology, and orientation of inland dunes in northern Sweden: Geografiska Annaler, v. 54A, p. 85-104.

Seppälä, M., 1971, Evolution of eolian relief of the Kaamasjoki-Kiellajoki river basin in Finnish Lapland: Fennia, v. 104, p. 1-88.

Sundborg, Å., 1955, Meteorological and climatological conditions for the genesis of aeolian sediments: Geografiska Annaler, v. 37, p. 94-111.

Østrem, G., 1964, Ice-cored moraines: Geografiska Annaler, v. 46, p. 282-337.

CURVILINEAR GROUND ON MARS: THE SEARCH FOR TERRESTRIAL ANALOGS

Lisa A. Rossbacher, Dept. of Geology, Whittier College, Whittier, California 90608 (spring 1984: Dept. of Physical Geography, Univ. of Uppsala, Box 554, S-751 22 Uppsala, Sweden)

Curvilinear features on Mars have dimensions ranging from 0.5 to 18.6 km in length and 0.2 to 2.0 km in width; these landforms can occur as curving ridges and troughs, rimless arcuate depressions, or features with no apparent relief. The Martian curvilinear ground has a relatively consistent relationship to both regional and local geomorphology. These landforms are one of a suite of features that occur near the base of the regional slope that marks the transition from the cratered uplands to the northern plains. The curvilinear features occur primarily on one of four photogeologic map units identified on the northern plains.

Based on morphologic similarities, numerous terrestrial analogs have been proposed for these Martian features. These include gilgai, backwasting scarps, solifluction lobes, ice-cored ridges, and glacial moraines. Process models for the origin of the curvilinear ground suggest that its formation probably involved several processes, including scarp retreat by backwasting. In part, this occurs through sublimation of ice from the substrate which allows particles to be removed by wind or mass movement. Evidence based on climatic, geological, and geochemical data supports the conclusion that at least some of the curvilinear features were created by the activity of interstitial or segregated water ice. The probable significance of water ice in this region of the planet suggests that ice might also have been active in the formation of other large-scale geomorphic features on Mars.

D86 N84 23511

WEATHERED STONY METEORITES FROM VICTORIA LAND, ANTARCTICA, AS POSSIBLE GUIDES TO ROCK WEATHERING ON MARS

J. L. Gooding, Planetary Materials Branch, NASA/Johnson Space Center, Houston, TX 77058 USA.

Introduction. Parallel studies of Martian geomorphic features and their analogs on Earth continue to be fruitful in deciphering the geologic history of Mars. In the context of rock weathering, the Earth-analog approach is admirably served by the study of meteorites recovered from ice sheets in Antarctica (1). Among those meteorites are a variety of mafic and ultramafic igneous rocks, breccias, and clast-laden impact melt-rocks that should be expected to resemble the lithologies exposed at the Martian surface, either as lava flows or as crater ejecta. In fact, some evidence exists to support the notion that members of the shergottite-nakhlite-chassignite (SNC) suite of meteorites are literally samples of Mars that were ejected by major impact events (2,3). To date, two SNC-group members have been identified among meteorites recovered from Victoria Land, Antarctica. Because Antarctic meteorites have been exposed to a low-temperature weathering environment for times on the order of 10^4-10^6 yr (1), they have recorded weathering features that might develop only on geologic timescales and, consequently, may contain information not obtainable in the timescales of laboratory experiments intended to simulate Martian weathering. Accordingly, direct petrological study of weathered Antarctic meteorites should be an indispensable part of the total effort to understand rock weathering on Mars.

Mars-Analogous Features of Antarctic Meteorites. The weathering environment of Victoria Land possesses several Mars-like attributes. For example, the Allan Hills (ALH) and Elephant Moraine (EET) areas, which have yielded many meteorites, are characterized by maximum daily air temperatures of $\sim$260 K in austral summer and typical wind speeds of 5-10 m/sec with gusts to > 30 m/sec. Precipitation of atmospheric water is probably limited to a few centimeters of snow per year and, in fact, the ice fields most likely show net loss of water through sublimation and wind erosion by dust-sized ice particles (4). Some Antarctic stony meteorites display incipient wind sculpturing and evidence for mass loss by spalling. The most conspicuous results of chemical weathering are spots and zones of reddish-brown, hydrous Fe-oxide "rust" and surface or near-surface deposits of salts (5). Rust forms by alteration of FeS and primary Fe-oxide minerals (and, especially, from Ni-Fe metal in chondrites), probably accelerated in many cases by films of liquid water developed on the hygroscopic mineral lawrencite, $FeCl_2$. Rust is characteristically rich in S and Cl (5) and salts are dominated by hydrous Mg-carbonates and Mg-sulfates (6). Both rust and salts commonly occur in fractures and undoubtedly contribute to crack growth and disintegration of the rocks.

Study Plan and Preliminary Results. The following achondritic meteorites are currently being studied as analogs of weathered Martian rocks: ALHA77256 (diogenite), EETA79001 (shergottite), EETA79002, 79004, and 79005 (eucrites). In addition, the non-Antarctic diogenite Johnstown, and rust samples from the non-Antarctic octahedrites Canyon Diablo and Cranbourne, and various terrestrial minerals are being used as reference test materials. Weathering features are being documented petrographically by optical and scanning electron microscopy and weathering products are being further characterized by x-ray diffractometry, electron microprobe analysis, and differential scanning calorimetry.

Four of the five Antarctic meteorites being studied contain rust and EETA79005 further possesses a conspicuous, dark weathering rind on one side. Secondary minerals (rust and salts) occur both on the surfaces and interiors of some of the samples and textural evidence indicates that such secondary mineralization has contributed to physical weathering (by salt riving) of the rocks. Several different rust morphologies occur and emphasis is being placed on identifying the phase compositions of the various rust occurrences. One SNC-group meteorite, EETA79001, is the most popular candidate for a rock possibly ejected from Mars by impact cratering (3) but is also comparatively free of terrestrially-formed rust. Nonetheless, its weathering features are being carefully studied and particular attention is being paid to possible evidence for "pre-terrestrial weathering". Indeed, a thorough understanding of terrestrial weathering features of the meteorites is a prerequisite for identifying possible "Martian weathering" features (if such features exist) that might be postulated to occur in some SNC meteorites.

Implications for Martian Geology. Enrichment of Antarctic meteorite rust in S and Cl is qualitatively consistent with observed properties of Martian surface fines and the abundance of Mg-sulfates among Antarctic meteorite salts parallels the currently favored inference that Mg-sulfates are the principal carriers of S in Martian fines (7). Phase identification of rusts and salts should lend clues to possible identities of hydrous phases that may be important parts of the volatile/regolith system and the total volatile inventory on Mars. Macroscopic and microscopic weathering textures of meteorites might yield morphological criteria, based on features accentuated by weathering, for recognizing and classifying major rock types observed in Viking lander (and future) imagery of the Martian surface. Most importantly, should some SNC-group meteorites prove to be of Martian origin, any relict weathering features that may be preserved in them will become immediately and directly important in understanding volatile/rock interactions as a critical portion of Martian geologic history.

References: (1) W. A. Cassidy and L. A. Rancitelli (1982) Amer. Sci., 70, 156. (2) C. A. Wood and L. D. Ashwal (1981) Proc. Lunar Planet. Sci. 12B, 1359. (3) D. D. Bogard and P. Johnson (1983) Science, 221, 651. (4) J. O. Annexstad, personal communication, 1983. (5) J. L. Gooding (1981) Proc. Lunar Planet. Sci. 12B, 1105. (6) U. B. Marvin (1980) Antarctic J. of U. S., XV (5), 54. (7) B. C. Clark and D. C. Van Hart (1981) Icarus, 45, 370.

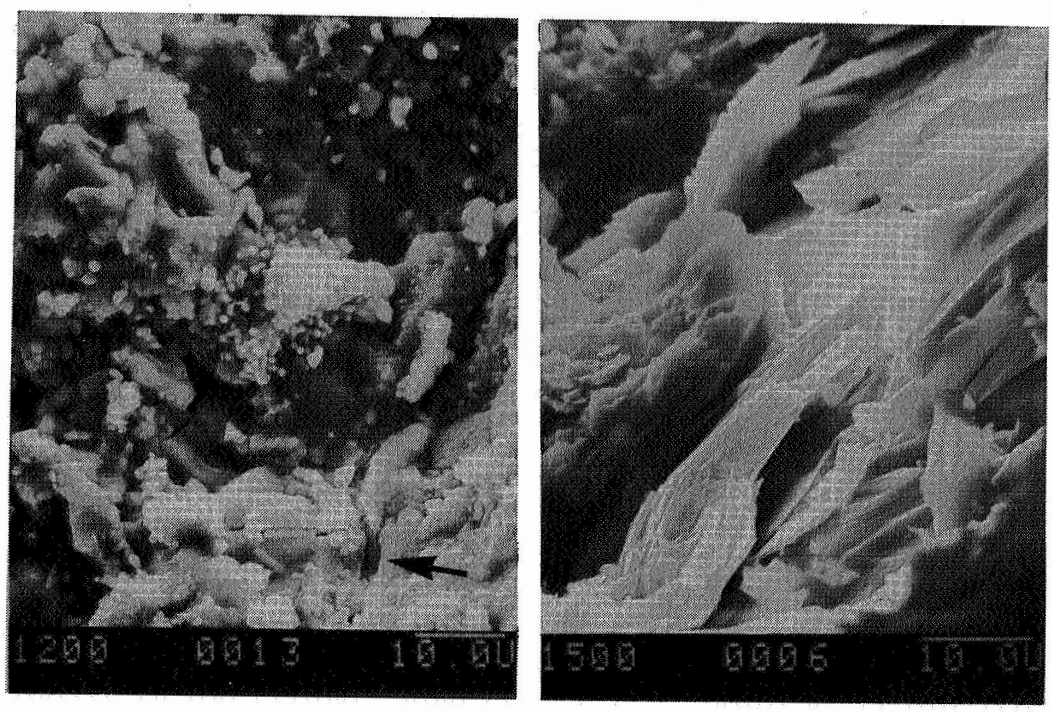

(a) (b)

Fig. 1. Morphologies of rust on Antarctic stony meteorites revealed by scanning electron microscopy (scale bars = 10 μm). (a) fractured mamillary and botryoidal growths on surface of brecciated eucrite EETA79004. Note secondary mineral deposit in fracture (arrow). (b) bladed, fibrous growth on "weathering rind" surface of brecciated eucrite EETA79005. In both (a) and (b), spalling of rust would produce free particles in the silt-sized range that is characteristic of surface fines at both Viking landing sites on Mars.

D81

SALTS IN THE DRY VALLEYS OF ANTARCTICA

E.K. Gibson, Jr., SN4/NASA JSC, Houston, TX 77058
B.J. Presley, Dept. of Oceanography, Texas A&M Univ., College Station, TX
J. Hatfield, Dept. of Geology, Utah St. Univ., Logan, UT

The Dry Valleys of Antarctica are examples of polar deserts which are rare geological features on the Earth. Such deserts typically have high salinities associated with their closed-basin waters and on many surficial materials throughout them (Figs. 1,2). Within the Dry Valleys of Antarctica there are numerous saline water bodies which range in surface area from a few 100 m to a few km . These closed-basins have compositions which range from enrichments in Na and Cl to those enriched in Ca, Mg, and Cl. The few fresh water bodies generally are temporal and small in area and are relatively enriched in Na^+, SO_4^{2-} , and HCO_3^- (Harris, 1981). All of the waters associated with the Dry Valley lakes are typically depleted in oxygen-18 and deuterium (Stuiver et al., 1976; Matsubaya et al., 1979). Soluble salts common in the surface materials are typically calcite, thenardite, halite, and gypsum (Nishiyama, 1979).

In common with soils from other arid parts of the world, soluble salt concentrations are characteristic of Dry Valley soils (Fig. 3). The origins of the water-soluble ions forming the salts is controversial; proposed origins include chemical weathering of rocks, hydrothermal fluids, marine aerosols, and the evaporation of water from marine incursions (Gibson et al., 1983). Ratios of Na^+/Cl^-, Mg^{2+}/SO_4^{2-}, Na^+/SO_4^{2-}, and CL^-/SO_4^{2-} , which are uniform regardless of site location and similar to those of sea water suggest that Na^+, SO_4^{2-}, and CL^- are of marine origin. Pastor and Bockheim (pers. written comm., 1980) concluded, however, that the less abundant ions Ca^{2+}, Mg^{2+}, and K^+ were derived mainly from rock weathering because ratios of Mg^{2+}/Ca^{2+}, Mg^{2+}/K^+, and Ca^{2+}/K^+ resemble those for the lithosphere.

In order to examine the possible sources for the salts observed in association with the soils in the Dry Valleys, we have measured the chloride and bromide concentrations of the water leachates from 58 soils and core samples. To our knowledge, there are no previously reported bromide analysis of Antarctic soils. It is well known that the bromide and chloride have similar geochemical affinities, but bromide undergoes chemical fractionation from the chloride during evaporation of brines. For example, as NaCl precipitates from a brine, bromide is concentrated in the residual liquor. Thus, during an early-stage evaporite sequence, the precipitate is enriched in chloride and the residual solution enriched in bromide. If the sources of the salts within the Dry Valleys were related to a seawater history, it is believed that the salts within the soils would be enriched in chlorine, because seawater is rarely evaporated to the extreme needed to precipitate bromide-bearing phases.

The Cl/Br ratio for seawater is 289 and ratios measured for most of the 58 soils studied (greater than 85% of the soils studied) was larger than the seawater ratio (ratios typically were greater than 1000 and ranged up to 50,000). The enrichment in Cl relative to Br is strong evidence that the

salts present within the soils were derived from seawater during ordinary evaporation processes, and not from the deposition of Cl and Br from aerosols or from rock weathering as has often been suggested. Aerosols derived from seawaters would result in the deposition of halides in the expected sea water ratio of 289. The salts within the valley soils were for the most part derived from evaporation of sea waters which had invaded the valley networks during earlier times. The only evidence for deposition by aerosols was found in the top 1 cm at the soil pit on Prospect Mesa in Wright Valley. This ancient top cm of soil showed a Cl/Br ratio of 223 but immediately below (2-4cm depth) the ratio increased to greater than 25,000.

The chemical composition of the brines associated with the Dry Valley ponds (especially Don Juan Pond, Figs. 2,3) is controlled by phase relations in the aqueous system $CaCl_2$-NaCl, for which the important solid phases are antarcticite, halite, hydrohalite, and ice (Harris, 1981). Evaporation — which forces the precipitation of antarcticite and halite — and dilution by ground waters control the chemistry of the ponds during the austral summers. The chemistry of the ponds are restricted by the depressed winter temperatures of -50 to -60°C. Groundwater brines are less saline, but otherwise similar in composition to the brines in the ponds (Harris, 1981). During the austral summers, the ground water temperatures are near the mean annual air temperature of -17 to -18°C. During the summer, the concentrations of species in the solutions are such that, at these temperatures, the ground water is at or near equilibrium with ice. It is clear that an understanding of the behavior of brines, evaporation processes, along with the movement of ground waters will play an important role in our development of regolith models for processes operating on the Martian surface.

References:

Gibson, E.K. et al. (1983) Proc. Lunar and Planet. Sci. Conf. 13th, J. Geophys. Res. 88, Suppl. A912-A928.

Harris, H.J.H. (1981) Ph.D. Dissertation, U. of Illinois, Urbana, IL.

Matsubaya, O. et al. (1979) Geochim. Cosmochim. Acta 43, 7-25.

Nishiyama, T. (1979) Proc. Seminar III on DVDP, 1978, T. Nagada (ed.) Natl. Inst. Polar Res., Tokyo, 136-147.

Stuiver, M. et al. (1976) Nature 261, 547-550.

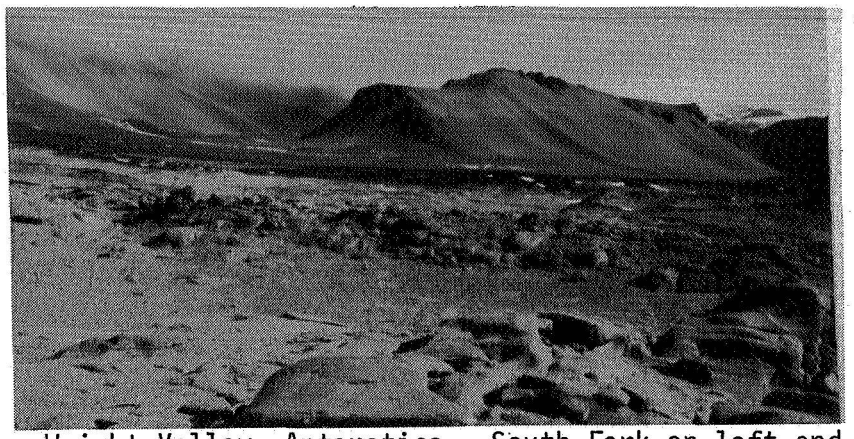

Fig. 1. Wright Valley, Antarctica. South Fork on left and North Fork on right. View is to west from south shore Lake Vanda

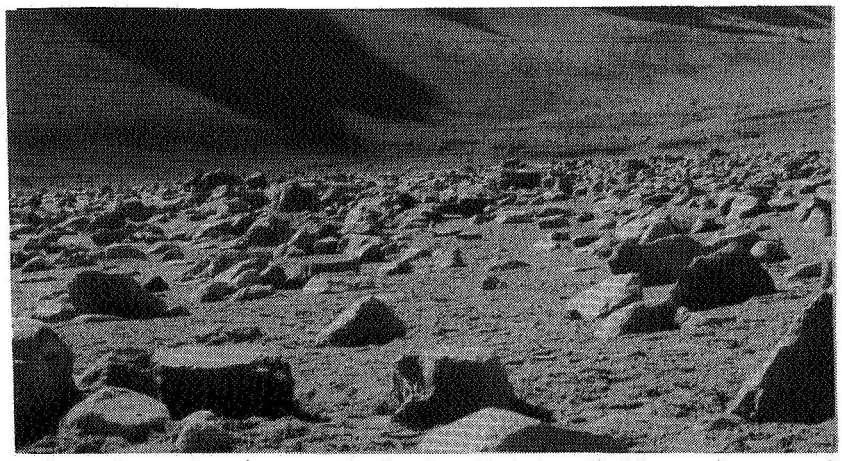

Fig. 2. Don Juan Pond, South Fork, Wright Valley, Antarctica. View is northeast across upper flanks of pond. Salt deposits occur between debris boulders on floor of pond.

Fig. 3. Salt deposits in Don Juan Pond. Large crystals across center of photo are Antarcticite ($CaCl_2 \cdot 6H_2O$). Scale in center is 2" square.

Chapter 9

GEOMORPHOLOGY

D82

MULTIPROCESS EVOLUTION OF LANDFORMS IN THE KHARGA REGION, EGYPT--APPLICATIONS TO MARS

C. S. Breed, J. F. McCauley, and M. J. Grolier, U.S. Geological Survey, Flagstaff, AZ 86001

In order to understand better the polygenetic evolution of landforms on the martian surface, field studies were conducted in and around the Kharga Depression, Egypt [1]. The Kharga region, on the eastern edge of Egypt's Western Desert, has been subject to erosion under mostly hyperarid climatic conditions, punctuated by brief pluvial episodes of lesser aridity, since early Pleistocene time. The region contains numerous landforms analogous to features on the martian surface: yardangs carved in layered surficial deposits and in bedrock, invasive dune trains, wind-modified channels and interfluves, and depressions bounded by steep scarps (figs. 1, 2). Like many of the topographic depressions on Mars, the Kharga Depression has been invaded by crescentic dunes. In Egypt, stratigraphic relations between dunes, yardangs, mass-wasting debris, and wind-eroded flash-flood deposits record shifts in the relative effectiveness of wind, water, and mass-wasting processes as a function of climate change.

The "semi-playa" deposits [2] on the floor of the Kharga Depression (fig. 3a) consist partly of sediments transported by running water from springs or precipitation and partly of windblown debris that accumulated in shallow lakes during pluvial episodes. Rates of deflation of these layered deposits can be established by stratigraphic relations and datable artifacts in localities such as Gala Hill [3], an exhumed sandstone yardang several hundred meters long (similar to the ridges shown in figure 3b). Gala Hill is mantled by remnants of wind-eroded lake beds lying 80 m above deposits of equivalent age on the surrounding deflated plains. The semi-playa deposits on the floor of the Kharga Depression are eroded to fleets of aligned "mud yardangs", whose history may be analogous to that of wind-eroded layered deposits on chasma floors in the Coprates region, Mars (fig. 2b) [4].

The fretted cliffs that bound the Kharga Depression to the north and east (fig. 1) are dissected by dry stream valleys enlarged and modified by mass wasting, sapping, and wind erosion. Traces of gullies on cliffs below the thick caprock of the adjacent Limestone Plateau indicate artesian outflow of groundwater there under less arid conditions. Dated spring deposits [5] and evidence of cliff-sapping occur at the contact of the caprock with the underlying shales and sandstones. The artesian sapping of the cliffs that bound the Kharga Depression provides a model for the mechanism of scarp retreat along the plateau/plains boundary on Mars and also suggests a mechanism for formation of scarps on Io [6].

The crystalline limestone caprock north and east of Kharga has been eroded by wind into one of the largest arrays of bedrock yardangs on Earth [7]. The imprint of wind erosion on the plateau has nearly obliterated evidence of former streamcourses and traces of a relict karst topography [5] of probable pre-Pleistocene age. Along the base of the plateau scarps, interfluves between dry, sand-choked valleys have been wind-streamlined to elongate, kilometer-size sandstone yardangs and have lost much or all of their fluvial character (figs. 1, 3b). The orientations of hills between washes, now dry, that once flowed into the depression from the east scarp, in courses normal to the prevailing wind direction (fig. 1b), bear little or no relation

to the valley networks that carved them; these interfluves are now eroded to narrow ridges aligned parallel to the wind but normal to the direction of former streamflow (fig. 1b). Such remodeling by wind of water-laid deposits, stream valleys, and interfluve slopes in Egypt has implications for the interpretation of landforms on the surface of Mars (fig. 2), where much longer periods of hyperaridity and associated wind erosion and deposition have undoubtedly also modified the shape characteristics of fluvial channels, valley networks, and associated deposits.

References

[1] Whitney, M. I., Breed, C. S., McCauley, J. F., and Grolier, M. J., Yardangs of the Kharga region, Egypt: Annals of the Egyptian Geological Survey (in preparation).

[2] Embabi, N. S., The semi-playa deposits of Kharga Depression, the Western Desert, Egypt: Bulletin de la Société de Géographie d' Egypte, v XLI-XLII, p. 7-87, 1972.

[3] Haynes, C. V., Gala Hill, a late Holocene climatic record of deflation and agricultural aggradation in the Kharga Depression, Egypt (in preparation).

[4] McCauley, J. F., Geologic map of the Coprates quadrangle of Mars: U.S. Geological Survey Atlas of Mars, 1:5,000,000 geologic series, I-897 (MC-18), 1978.

[5] Haynes, C. V., Quaternary geochronology of the Western Desert: Proc., 1st Thematic Conf. on Remote Sensing of Arid and Semi-Arid Lands (Cairo), ERIM, p. 297-311, 1982.

[6] McCauley, J. F., Smith, B. A., and Soderblom, L. A., Erosional scarps on Io: Nature, v. 280, no. 5725, p. 736-738, 1979.

[7] Grolier, M. J., Yardangs of the Western Desert, in El-Baz et al., Journey to the Gilf Kebir and Uweinat, Southwest Egypt, 1978: Geographical Journal, v. 146, pt. 1, p. 86-87, 1980.

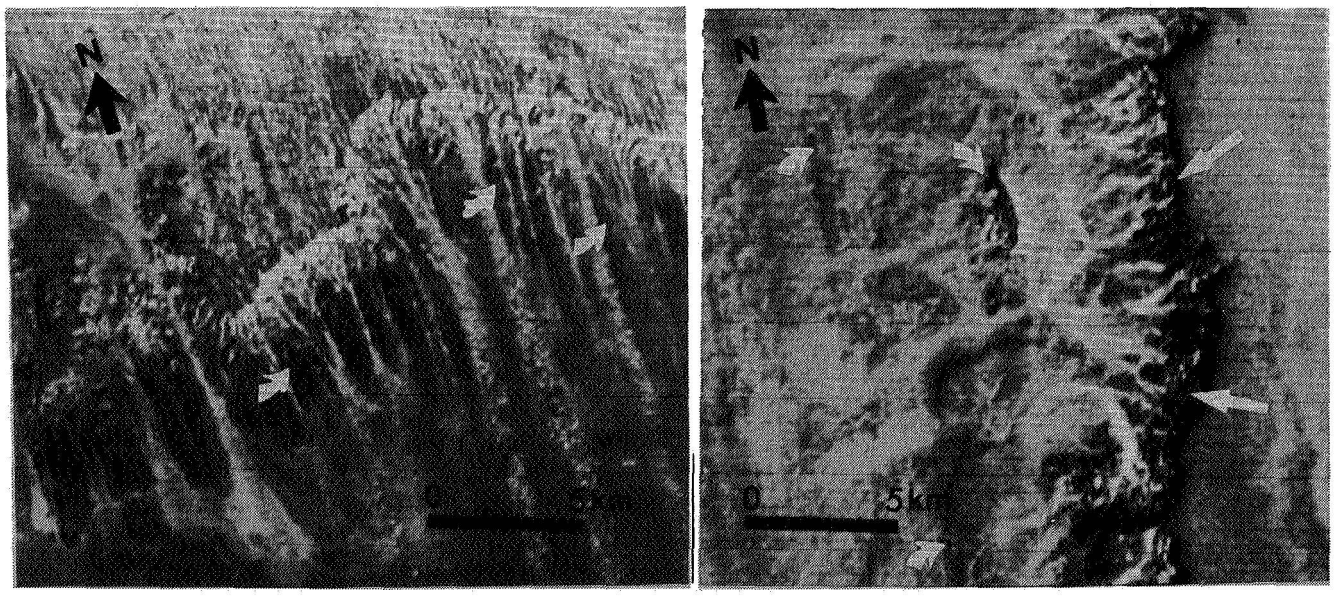

Figure 1. Landsat images of the 300-m-high scarps that bound the north (a) and east (b) sides of Kharga Depression. Interfluves (curved arrows) along the lower slopes of the scarps are eroded by the strong north wind to kilometer-scale sandstone yardangs. Along the east scarp (b) these hills are aligned normal to drainage lines (straight arrows) that issue from the base of the caprock.

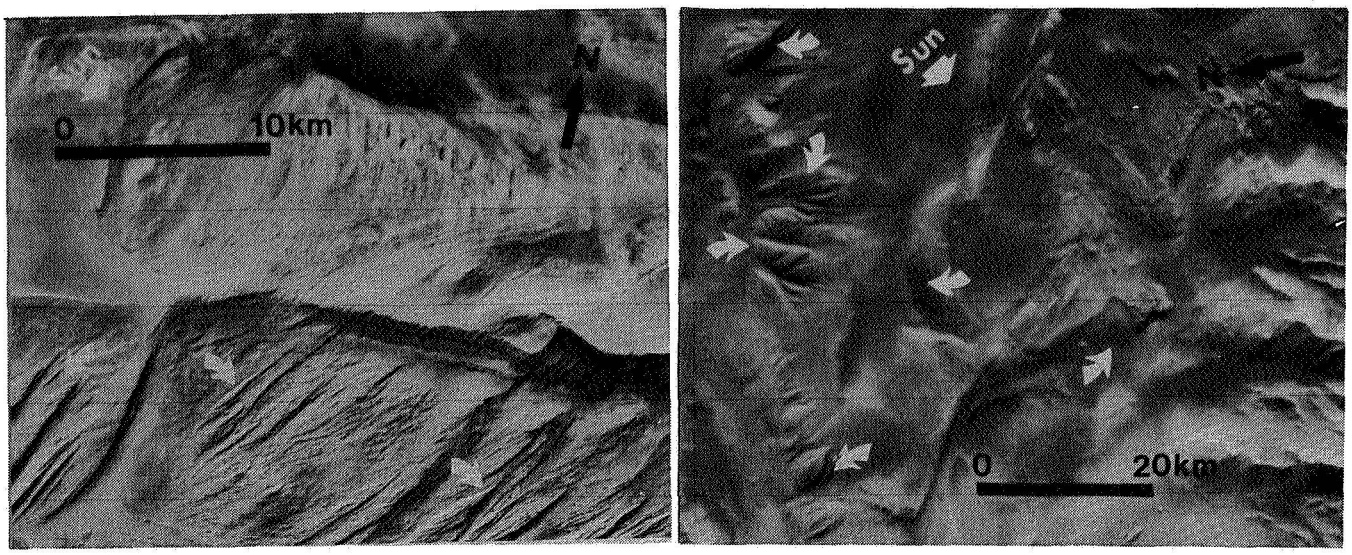

Figure 2. Remodeling by wind has carved yardangs (arrows) on scarp slopes (a) and on former interfluves and surficial deposits on chasma floors (b) in the Coprates region, Mars.

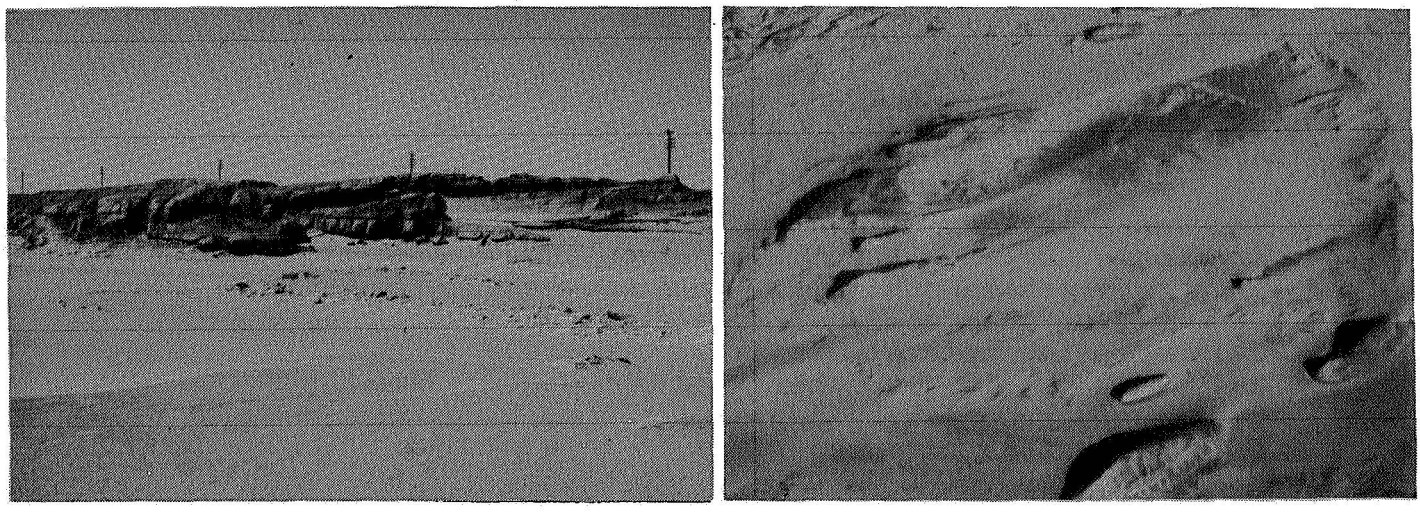

Figure 3. a) Decameter-scale yardangs carved in semi-playa deposits on the floor of the Kharga Depression; b) aerial view of kilometer-scale sandstone yardangs and eroded surficial deposits in the Kharga Depression.

D83

N84 23514

INVERSION OF TOPOGRAPHY IN MARTIAN HIGHLANDS TERRAINS

R. A. De Hon, Department of Geosciences, Northeast Louisiana University, Monroe, LA 71209.

Mars displays a diverse physiography which reflects a complex history of surficial processes. Layered deposits and erosional landforms attest to a more varied set of geologic agents than the impact and volcanic processes that dominate other planetary bodies without atmospheres. One unique feature on Mars is the presence of "ring furrows" which are apparently produced by inversion of topography at the rims of partially buried craters.

Ring furrows are flat-floored trenches, circular in plan view, forming rings 7 to 50 km in diameter. The moat is on the order of 0.5 km deep and 2 to 10 km wide, and it surrounds a flat topped circular mesa or plateau that is 5 to 40 km across. The central plateau is at the same elevation or lower than the surrounding plain outside the ring. A typical example of a ring furrow is found in the Syrtis Major Quadrangle (MC-13SW, Viking Orbiter frame 373S72) at 3-5°N; 308-310°W (Fig. 1-1).

Ring furrows typically occur in the highlands associated with cratered plateau materials. The cratered plateau materials are interpreted as ancient lava flows (1) overlying older cratered terrains. The thickness of the flows is quite variable but averages 800 m (2). Most of the rings are in or near regions of younger surface modification by channel dissection or on the edge of chaotic terrain (Fig. 1-2). The outer wall of many of the rings is breeched by valley drainage (Fig. 1-2) or open to lower surfaces (Fig. 1-1).

The occurrence of several variations of seemingly similar landforms suggests that ring furrows are simply one form in a progression of forms. In some regions, circular segments of channels and arcuate channel patterns delineate incompletely isolated circular plateaus (Fig. 1-4 and Ref. 3). In other areas, isolated, smooth topped plateaus surrounded by degraded plains (Fig. 1-5) appear to represent an advanced stage of development.

The circular nature and size range of ring furrows tend to suggest that these features are related to craters partially buried by younger lava flows. The rings have

been formed by preferential removal of the exposed crater rims. Ground ice decay, sapping, or fluvial erosion removed the less resistant, porous material of crater rims while leaving the more resistant volcanic flow material. Differential erosion has thus led to a reversal of topography in which the original positive relief of the rim is reduced to a negative relief feature.

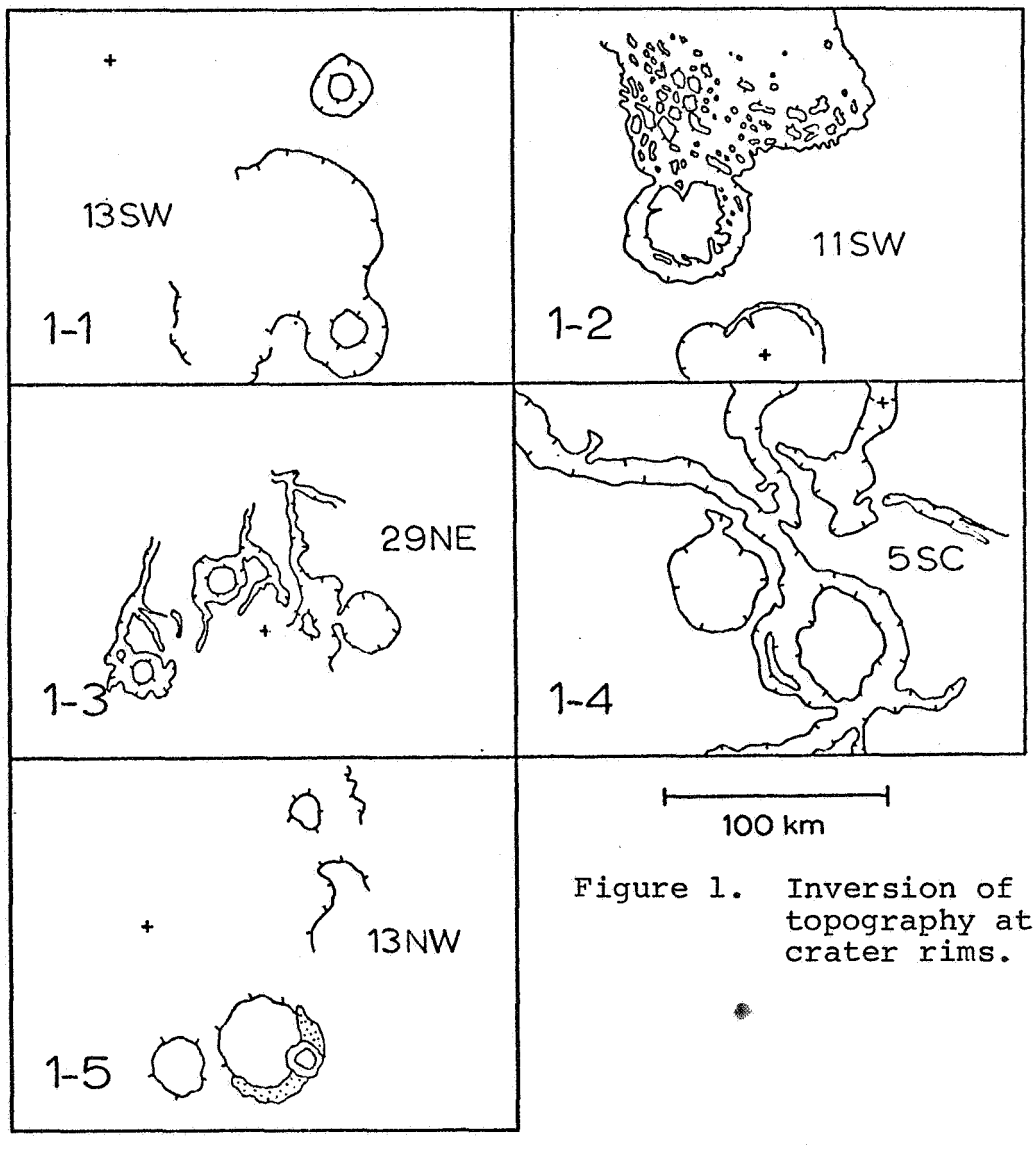

Figure 1. Inversion of topography at crater rims.

References
(1) Scott D. H. and Carr M. H. 1978. U.S. Geol. Surv., Misc. Geol. Inv. Map I-1083.
(2) De Hon R. A. 1982. NASA Tech Mem. 85127, 129-131.
(3) Baker V. B. 1982. NASA Tech Mem. 85127, 206-208.

D84

N84 23515

THE CORFU LANDSLIDE: ANALOG TO GIANT LANDSLIDES ON MARS

Scott W. Lewis and Victor R. Baker, Department of Geosciences, University of Arizona, Tucson, Arizona 85721

As an analog to the great landslides of the Valles Marineris, Mars, we have made a detailed study of the Corfu Landslide in south-central Washington. This prehistoric slide is located on the northern flank of the Saddle Mountains, southwest of Othello, Washington. The slide covers a 13 km^2 area centered on section 11 of T.15N., R.27E., Willamette Meridian, adjacent to the Corfu townsite. Approximately 1 km^3 of material is involved in sliding that was probably initiated by Missoula flooding through the Channeled Scabland.

The geology of the Saddle Mountains has been studied by various workers, who have shown that the Saddle Mountains is an asymmetrical anticline which varies in character along its length. However, none of these previous studies have dealt with the detailed geology of the Corfu Landslide. Moreover, many other large landslides associated with anticlinal ridges occur in the region, but none have been studied in detail. A detailed analysis is necessary to understand the association of the structures with the landslides, as well as to add information to the geologic history of the Yakima Folds.

The detailed analysis of the Corfu Landslide required geologic mapping at a large scale. This mapping revealed many important aspects about the evolution of the landslide. The slide is best described as compound-complex. At least 24 separate landslide pulses occurred between about 6000 and 12,000 years before present. This is demonstrated by stratigraphic relationships between the slide material and overlying deposits of diagnostic volcanic ash falls from Cascade volcanoes. Selective erosion of some, but not all of the slide deposits indicates that at least one and possibly as many as three catastrophic floods occurred between periods of landsliding.

Each of the individual slides appears to have been structurally controlled. The sliding surface in almost every case occurs along the same stratigraphic horizon: the Mabton interbed between the Saddle Mountains Basalt above, and the Wanapum Basalt below. A previously unmapped thrust fault is present along the top of many of the slides and seems to have provided a break from which the rocks could slide away. The direction of movement was to the north in all cases. However, the style of sliding was variable. Some were apparently quite rapid, while others may have been very slow.

It is concluded that there were four primary factors involved in the initiation of the Corfu landsliding: 1) A slip surface was present at the right orientation; 2) Glacial flooding undercut the slope; 3) Wetter climatic conditions prevailed during that time period; and 4) Some seismic vibrations, known to occur locally, probably acted as a trigger. These factors show that special conditions were required in conjunction to produce landsliding. Studies in progress of the Valles Marineris suggest that the same factors probably contributed to landsliding there.

Planetary Geomorphology Field Studies: Iceland and Antarctica

Michael C. Malin, Department of Geology, Arizona State University, Tempe, AZ 85287

Field studies of terrestrial landforms and the processes that shape them have provided new directions to study of planetary features. These studies, conducted in Alaska, California, Utah, Washington and Iceland (under NASA sponsorship), and in Antarctica (under NSF sponsorship), have investigated physical and chemical weathering mechanisms and rates, eolian processes, mudflow phenomena, drainage development, and catastrophic fluvial and volcanic phenomena. In this abstract, research in Iceland and Antarctica is discussed. In a companion abstract, research in Alaska, California, and Washington is discussed.

Iceland

Continuing investigations in Iceland fall in three main catagories: 1) catastrophic floods of the Jökulsá á Fjöllum, 2) lahars associated with explosive volcanic eruptions of Askja caldera, and 3) rates of eolian abrasion in cold, volcanic deserts.

The largest river in Iceland, the Jökulsá á Fjöllum, has been subjected to repeated but irregularly timed floods of enormous magnitude. An especially large flood some 2500 years ago created Ásbyrgi, a 100 m high cataract, and Vesturdalur, a scabland/canyonland region similar in scale to the scablands in Washington state, though not as areally extensive (1,2,3). The magnitude of this flood, estimated by hydraulic equations (Chezy and Manning) exceeded 400,000 cubic meters per second (cms)(2). Based on channel, cataract, and plunge pool geometry, a similar estimate (~350,000 cms) was obtained (4). Bed-load caliber and deposit location and geometry can be used to estimate velocities of flow and duration of 'maximum' discharge. Preliminary estimates of these values are 10 m/sec and ~40 hours. Current mapping and granulometric analyses are aimed at determing the distribution in time and space of the flood effects. The development and use of these techniques, and their calibration against known, historic floods is aimed at application to potential observations of the Mars Geoscience/Climatology Orbiter.

Lahars generated by explosive historic and pre-historic eruptions of Askja Caldera have surface morphologies and distribution characteristics difficult to distinguish in aerial photography from basaltic lava flows. This results in part from incorporation into the lahars of coarse basaltic debris, that, owing to the physical properties of the mudflows, 'floats' at the surface, and in part from the inundation of the entire area by fine basaltic tephra (silt- to sand-sized ash), greatly subduing primary morphology and covering much of the surface roughness characteristics of real lava flows. Continuing analyses of these flows, and similar studies at Mount St. Helens and Lassen Peak, are permitting criteria to be established that separate different types of flows, specify their physical properties (in particular their water content), and allow lithologic and environmental factors governing their appearance to be

separated. Landforms on Mars, in particular those associated with several of the large Tharsis and Elysium volcanoes, and especially associated with debris movements within canyons, chaotic terrain, fretted terrain, and channeled terrain, are under similar analysis.

Eolian abrasion is considered one of the most important processes on Mars (5). Laboratory and wind tunnel studies have provided great insight into martian applications (5), but have lacked significant field verification. This study is aimed at verification through micro-analysis of in situ abrasion of known standard materials. Preliminary results have been report elsewhere (6). A detailed analysis of the initial results of the short term experiment has been prepared and submitted for publication (7). These observations have led to two new models for application to Mars. A technique for estimating long-term changes in atmospheric pressure (climatic change) from the distribution of surface debris has been developed. This model assumes that the martian surface reaches equilibrium between net deposition and net transport on a time-scale short relative to climate change and the introduction of new wind-transportable material. If this model is correct, then the limited abrasion of martian surface materials noted by many investigators (e.g., 5,8) results from limitations in the supply of abrading material and in the capability of the surface to allow transportation rather than from burial, impact of soft materials, or the absense of strong, debris-transporting winds.

Antarctica

The ice-free valleys of Antarctica, in particular those in South Victoria Land, have much is common with the surface of Mars. These valleys have been the site of several comparative studies, exploiting biological (e.g., 9,10), geological (e.g., 11,12), and environmental similarities. A National Science Foundation project to determine the present rates of physical and chemical weathering, and to examine landform evolution in the harsh Antarctic environment was initiated during the 1982-1983 austral summer season. In part this project builds on experience in Iceland outlined above. Using similar techniques, abrasion processes in a region of extreme cold (<-75C) and high winds (> 250 km/hr) are under study. Mass movements, in particular apparently slow movements of unconsolidated material, are also being studied. Preliminary results suggest little contemporary activity. Rather, abrasion and mass movements seem to date from periods of past glacial retreats, when liquid water was more abundant and available to participate in re-working fines (as a source for abrading material) and to saturate the ground (thus facilitating slope creep and drbris flows).

In addition to providing independent support for the application of the Iceland findings to consideration of the martian erosional system, the Antarctic observations also provide analogies to other martian phenomena. For example, a family of sand dunes in Victoria Valley (13-15) are stabilized by the incorporation of snow as beds. The dune crests appear to migrate slowly westward under summer easterly winds, but to reverse their direction during the winter. The location of the dunes

in the easternmost portion of the valley suggest a net eastward migration, but parts of the dunes seem to complete the seasonal cycle with a slight net westward displacement (< 1 m/yr). However, the majority of the dune mass is unmoving under present climatological conditions. These dunes are direct analogs to the martian north polar dunes (which appear to display similar behavior), and possibly, to the polar layered terrain. Studies of these dunes will help determine the minimum volatile 'cement' needed to hold dunes fixed, the nature of volatile migration within such dunes, and the climatological dependence of these phenomena. Another study in Antarctica addresses the formation of pits in massive rocks. This is a continuing problem in studies stones in the Viking lander images, and the Antarctic research may provide clues to the nature of such pitting processes, their rates of attack, and controlling factors.

These field studies provide a means of calibrating many diverse and competing processes under known conditions, and allow for informed, though speculative, extrapolation to alien environments. Much of the work is geared towards field observable factors that may be addressed through future planetary missions, in particular geoscience orbiters, rovers and sample returns. These studies also permit specific questions to be developed as geological objectives for such future missions to Mars and the other terrestrial planets.

References

1) Thorarinsson, S. (1950) Náttúrufraedingurinn 20, 113-133.
2) Thómasson, H. (1973) Náttúrufraedingurinn 43, 12-34.
3) Saemundsson, K. (1973) Náttúrufraedingurinn 43, 52-60.
4) Malin, M. C. and D. B. Eppler (1981) NASA Tech. Mem. 84211, 272-273.
5) Greeley, R. and others (1982) J. Geophys. Res. 87, 10009-10024.
6) Malin, M. C. and D. B. Eppler (1981) NASA Tech. Mem. 84211, 247-248.
7) Malin, M. C. and D. B. Eppler (1984) Geo. Soc. Am. Bull. (submitted)
8) Arvidson, R. E., and others (1979) Nature 278, 533-535.
9) Horowitz, N. H. and others (1972) Science 176, 242.
10) Friedmann, E. I. (1982) Science 215, 1045-1053.
11) Morris, E. C., T. A. Mutch, and H. E. Holt (1972) U. S. Geol. Survey Interagency Report: Astrogeology 52, 156 p.
12) Gibson, E. K., and others (1983) J. Geophys. Res. 88, 912-928.
13) Calkin, P. E. and R. H. Rutford (1974) Geograph. Rev. 64, 189-216.
14) Lindsay, J. F. (1973) Geo. Soc. Am. Bull. 84, 1799-1806.
15) Selby, M. J., and others (1974) N. Z. J. Geol. Geophys. 17, 543-562.

D86 N84 23517

SCARP DEVELOPMENT IN THE VALLES MARINERIS

P. C. Patton, Department of Earth and Environmental Sciences, Wesleyan University, Middletown, CT 06457

The scarps along the margins of the Valles Marineris display a complex assemblage of forms that have been related to a variety of mass wasting and sapping processes. Mass wasting forms include catastrophic landslides similar to large rock avalanches recognized on earth (Lucchitta, 1978a) to small scale slumps and retrogressive slides, talus cones (Sharp, 1973; Blasius and others, 1977; Lucchitta, 1978b) and small enclosed pits of probable subsidence origin (Baskerville, 1982; Steiner and others, 1982). In many instances modification of the scarps has resulted in the development of spur and gully topography (Lucchitta, 1978b). Sapping features include the branching theatre-headed valleys prominent in Ius Chasma and smaller unbranched features throughout the Valles Marineris (Laity and Saunders, 1981; Kochel and Capar, 1982). Many of the slope forms are associated with tectonic features with some forms preferentially developed along structural features while other slope forms appear to be modified by later structural elements. Examples of the former include the theatre-headed valleys (Kochel and Capar, 1982) while examples of the latter are the fault scarps that terminate the spur and gully topography (Blasius and others, 1977). The lack of craters on the floor of the Valles Marineris is significant and indicates that resurfacing of the floor has been an ongoing process throughout the evolution of the canyon system. The bulk of the sediment has probably been derived from the adjacent slopes, although the rates and processes of sediment transport have probably varied through time. The investigation of the slope forms within the Valles Marineris is of value in determining both past and present surficial processes acting on the martian landscape as well as the relative importance of structure and lithology on martian landform development.

For example, detailed studies of the spur and gully topography have demonstrated that within a given chasma, such as Candor Chasma, an evolutionary sequence of scarp forms can be observed (Patton, 1981, 1982) which reflects increasing regolith storage on the scarps with time. The general pattern of scarp evolution also suggests that dry mass wasting processes are the most significant in creating the spur and gully topography. However, when the spur and gully topography is analyzed on a regional basis throughout the Valles Marineris, the variations in morphology observed over small areas are obscured by the greater regional variability. This is partly the result of resolution of the scarp morphology which varies throughout the system but also the result of differences in scarp lithology and the relative importance of processes other than dry mass wasting in controlling slope form.

Because the Valles Marineris transects three geologic provinces distinct in terms of the age of surficial material and in the thickness of stratigraphic units (Scott and Carr, 1978; DeHon, 1982) it is likely that there should be recognizable differences in the scarps developed on these materials throughout the chasmata. In addition, regardless of the tectonic model one accepts for the Tharsis region (Wise and others, 1979; Plescia and Saunders, 1982; Solomon and Head, 1982) it is clear that the region has had a complex structural history with deformation varying in time and space. Furthermore, the combined evidence suggests that the structural evolution of the Tharsis region and therefore the Valles Marineris spanned a long time period of martian history (Plescia and Saunders, 1982). Therefore one should not expect the tectonically created scarps in the Valles Marineris to be equivalent in age.

In order to evaluate the regional variation in scarp form and the influence of time and structure on scarp development geomorphic mapping and morphometric analysis of geologically distinct regions of Valles Marineris is being undertaken. Areas being analyzed include 1) Noctis Labyrinthus where it cross cuts the Syria Planum flow unit 2 (Scott and Tanaka, 1981) as this graben system is apparently related to the latest period of tectonic activity in the Tharsis region (Plescia and Saunders, 1982); 2) the eastern end of Ius at the transition between the cratered plains and the ridged plains of the Sinai Planum (McCauley, 1978); 3) Candor Chasma within the ridged plains; and 4) the eastern end of the Valles Marineris that cuts the cratered plateau material. These scarp segments display variations in the degree of development of spur and gully topography, the number and density of apparent sapping features and the frequency of large scale landslides which reflect the age, geology and processes of slope development throughout the Valles Marineris. This regional analysis should provide more information on the geologic evolution of the Valles Marineris as well as new insight into the relative importance of different processes in the development of the scarp forms.

References Cited

Baskerville, C.A., 1982, Collapse: a mechanism for martian scarp retreat: Reports of Planetary Geology Program-1982, TM 85127, p. 244-252.

Blasius, K.R., Cutts, J.A., Guest, J.E., and Masursky, H., 1977, Geology of Valles Marineris: first analysis of imaging from the Viking orbiter primary mission: Jour. of Geophys. Research, v. 82, p. 4067-4091.

DeHon, R.A., 1982, Martian volcanic materials; preliminary thickness estimates in the eastern Tharsis region: Jour. Geophys. Research, v. 87, p. 9821-9828.

Kochel, R.C., and Capar, A.P., 1982, Structural control of sapping valley networks along Valles Marineris, Mars: Reports of Planetary Geology Programs - 1982, N.A.S.A. TM 85127, p. 295-297.
Laity, J.E., and Saunders, R.S., 1981, Sapping processes and the development of theatre-headed valleys: Reports of Planetary geology Program-1981, N.A.S.A. TM 84211, p. 280-182.
Lucchitta, B.K., 1978a, A large landslide on Mars: Geol. Soc. Am. Bull. v. 89, p. 1601-1609.
Lucchitta, B.K., 1978b, Morphology of chasma wall, Mars: U.S. Geol. Survey Journal of Research, v. 6, n. 5, p. 651-662.
McCauley, J.F., 1978, Geologic map of the Coprates Quadrangle of Mars: U.S. Geological Survey Map I-897 (MC-18).
Patton, P.C., 1981, Evolution of the spur and gully topography on the Valles Marineris wall scarps: Reports of Planetary Geology Program-1981, N.A.S.A. TM 84211, p. 324-325.
Patton, P.C., 1982, Quantitative morphology of the Valles Marineris scarps: Reports of Planetary Geology Program-1982, TM 85127, p. 242-243.
Plescia, J.B., and Saunders, P.S., 1982, Tectonic history of the Tharsis region: Jour. Geophys. Research, v. 87, p. 9775-9791.
Scott, D.H., and Carr, M.H., 1978, Geologic map of Mars: U.S. Geological Survey, Map I-1083.
Scott, D.H., and Tanaka, K.L., 1981, Map showing lava flows in the northeast part of the Phoenicas Lacus quadrangle of Mars: U.S. Geological Survey Map I-1277 (MC-17 NE).
Sharp, R.P., 1973, Mars: troughed terrain: Jour. Geophy. Research v. 78, p. 4063.
Solomon, S.C., and Head, J.W., 1982, Evolution of the Tharsis province of Mars: the importance of heterogenous lithospheric thickness and volcanic construction: Jour. Geophys. Research, v. 87, p. 9755-9774.
Steiner, J., Sodden, C., and Weiss, D., 1982, Aligned subsidence depressions in the vicinity of certain martian valleys: Reports of Planetary Geology Program, N.A.S.A. TM 85127, p. 298-299.
Wise, P.U., Golombek, M.P., and McGill, G.E., 1979, Tharsis province of Mars: Geologic sequence, geometry, and a deformational mechanism: Icarus, v. 38, p. 456-472.

GEOMORPHIC CLUES TO THE MARTIAN VOLATILE INVENTORY: II. LANDSLIDES

David Pieri, Jet Propulsion Laboratory, Pasadena, CA
Ann Kirkpatrick*, University of Colorado, Boulder, CO
*NASA Summer Intern

In an attempt to better understand the history, distribution and amount of volatiles in the martian subsurface, as well as related implications for the paleo-climate of Mars, we are looking at the interrelationships between four major classes of landforms: (1) valley networks, (2) outflow channels, (3) flow-ejecta blankets, and (4) landslides. In this context, we have begun detailed mapping of well-expressed individual landslides to assess geomorphic constraints on candidate physical models for their emplacement, with a goal of inferring quantitatively the degree of participation of volatiles in the landslide formation process.

From terrestrial experience, landslide failures typically occur in three modes: falls and topples, slides (rotational and translational) and flows (Varnes, 1958, 1978), and any slide may involve one or more modes. Falls and topples occur in highly fractured rock along a discontinuity parallel to cliff faces, leaving steep free faces and talus at the base, with water playing a weathering role (Brunsden, 1979). Rotational slides occur in thick, homogeneous, cohesive materials (e.g., clays), with a steep U-shaped head scarp with slump blocks tilted back, undistorted failed mass, tension cracks at the foot, and bulging at the toe (Brunsden, 1979; Rib and Liang, 1978). Translational slides have discontinuities which occur parallel to slope surfaces (e.g., bedding planes, bedrock-slope debris interface), are associated with a high water table, may develop into avalanches if slopes are steep enough and water abundant (e.g., mudslides), and consist of an upper supply area, a central neck with shear surfaces, and a bulbous lobated toe with radial and transverse cracks (Brunsden, 1979). Flows involve loose debris, weak weathered rock, may begin as heavily laden streams following existing drainageways where material is picked up in long neck areas and deposited downslope as long narrow lobes with coarser lateral levees (Varnes, 1978), with deposits generally smoother than those of slides and with radial flow lines usually present (Rib and Liang. 1979). Complex slides, which begin as large rockfalls or slides, disintegrate, and cover large areas, and seem to travel farther than predicted by the enegy generated during their fall, have been intensely studied (e.g., Shreve, 1966, 1968; Kent, 1966; Hsu, 1975; Melosh, 1983) but remain poorly understood. Almost all varieties of large scale morphologies described in terrestrial landslide experience can be found in martian landslides as seen in the rich Viking data set (Luccitta, 1978, 1979).

Eight landslide locales were selected in Valles Marineris for preliminary geomorphological mapping. We aimed for a representative sample, however, many areas of Valles Marineris are not covered by high resolution imaging. In the mapped slides, four main suites of morphological features were identified. In four order outward from the head scarp they are:

(1) Large ridges in head area, transverse to movement direction, probably slump blocks or pieces of wall that fell or toppled, possibly backward rotated,

(2) Smaller ridges, convex toward distal edge of slides, many with lobate pattern, some possibly step-like scarps rather than ridges,

(3) Thin, sheet-like debris cover, forms discrete fan-shaped lobe with edge scarps unconfined,

(4) Low transverse, continuous ridges (possibly folds) found at distal edge of slides where debris appears to have encountered obstructions (e.g., opposing canyon walls), but not all confined slides exhibit this feature.

Any one landslide may possess all or some of these features, any slides in Tithonium and Ius Chasmas (western Valles Marineris) are usually more complex and show more variety than Coprates, Capri, and Gangis Chasmas (eastern Valles Marineris). These differences may be related to the topographical and structural differences between the two areas: western Vallis Marineris has greater relief (3-7 km) with gullied and ridged canyon walls and more shallow graben-like structures on the adjacent plateau surfaces while its eastern counterpart has fewer graben, canyon wall relief is lower (1-2 km), and there is less gully and ridge topography. Slides in the east typically lack head scarps, large slump blocks and sheet-like debris lobes predominate, and there are typically smaller in area and volume. We have begun to pose physical models of landslide emplacement which will eventually utilize preliminary qualitative and quantitative observations of ours and others (e.g., Luccitta, 1978, 1979) as boundary conditions.

We hope that in the future we can compare estimates of subsurface lithologic character and volatile content inferred from quantitative modeling of both rampart ejecta and landslide emplacement processes to the distribution and morphologic style of both nearby valley networks and outflow channels.

Brundson, D., 1979, Mass movements, in Embleton, C. and Thornes, J. B., Process Geomorphology, Halsted Press.

Hsu, K. J., 1975, Catastrophic debris streams (sturtzstroms) generated by rockfalls, Geol. Soc. Am. Bull. 86, pp. 129-140.

Kent, P. E., 1966, The transport mechanism in catastrophic rock falls, Jour. Geol. 74, pp. 79-83.

Luccitta, B. K., 1978, A large landslide on Mars, Geol. Soc. Am. Bull. 89, pp. 1601-1609.

Luccitta, B. K., 1979, Landslides in Vallis Marineris, Mars, J. Geophys. Res. 84, pp. 8097-8114.

Melosh, H. J., 1983, Acoustic fluidization, Amer. Sci. 74, pp. 158-165.

Rib, H. T. and Ta Liang, 1978, Recognition and identification, in Landslides Analysis and Control, pp. 34-80, Natl. Acad. Sci. Res. Coun. Spec. Rept. #176.

Shreve, R., 1966, Sherman landslide, Alaska, Science 154, pp. 1639-1643.

Shreve, R., 1968, Leakage and fluidization in air-layer lubricated avalanches, Geol. Soc. Am. Bull. 79, pp. 653-658.

Varnes, D. J., 1978, Slope movement types and process, pp. 11-33, in Landslides: Analysis and Control, Natl. Acad. Sci., Natl. Res. Council Special Report #176.

D88

N84 23519

TEMPORAL AND SPATIAL DISTRIBUTION OF EXHUMED TOPOGRAPHY

Dallas D. Rhodes, Dept. of Geology, Whittier College, Whittier, California 90608 (spring 1984: Dept. of Physical Geography, Univ. of Uppsala, Box 554, S-751 22 Uppsala, Sweden)

The conditions required for exhumation and the spatial distribution of the exhumed features are related. The exhumation of topographic forms occurs because there is a change in environment or base level, caused by either tectonic or eustatic conditions, that causes the location of the buried features to undergo net erosion. In a general sense, climate and geomorphic processes are latitudinally distributed, and climate change tends to shift the climatic belts latitudinally (Büdel, 1968). Perhaps the greatest chance for exhumation, or burial, of a landscape by terrestrial processes exists near the boundaries of the climatic belts. These locations are likely because the most severe denudation occurs where drastic climatic change leads to disequilibrium between geomorphic features and processes, resulting in accelerated erosion.

The vast majority of the sampled exhumed landforms are located in the northern hemisphere within Büdel's zone of extra-tropical valley formation. As a result of Pleistocene climatic change, the boundaries of this zone must have shifted northward to their present positions since the last glacial maximum. During the Pleistocene, these middle latitudes were subjected to a number of climatic changes.

Examples of resurrected landforms in the southern hemisphere and from tropical areas are notably few in number. It is possible that this sample of exhumed features is biased in that the geomorphology of the southern hemisphere and the tropical regions has not been as extensively studied as has that of the northern middle latitudes (Thomas, 1974).

In the southern hemisphere, there is, however, comparatively little land area within Büdel's zone of extra-tropical valley formation, which contains most of the examples of exhumed topography in the northern hemisphere.

The only examples of resurrected landforms that occur within Büdel's tropical zone are located near the boundary of this zone, where climate may have changed during the Pleistocene. In the interior of the tropical zone, climate has not varied markedly since the end of the Pleistocene and essentially the same processes active today may have been at work for several million years (Büdel, 1968).

Given this long period of tropical conditions, the intense, deep chemical weathering characteristic of such climates may have softened the undermass of buried landforms and thereby destroyed the contrast in erosional resistance necessary for exhumation.

Correlations between particular tectonic conditions and the locations of exhumed landforms are tenuous. In general, it is possible to say that exhumed features do not occur in currently active orogenic belts. Furthermore, epiorogenic uplift should promote exhumation due to lowered base levels and, consequently, increased erosion. Similarly, past periods of lowered sea level may have been times of exhumation. However, climatic variation may either temper or enhance any of these conditions (Melhorn and Edgar, 1975).

Virtually all of the resurrected features exposed today have been exhumed during the late Tertiary, although the landforms themselves vary in age from Precambrian to Pleistocene. Landscapes have probably been created and buried during all periods of Earth history, but some studies have suggested that there have been distinct periods of erosion during which landscape formation was widespread (Gorelov et al., 1970; King, 1967; Martin, 1966, 1968; Melhorn and Edgar, 1975; Sloss, 1963).

Melhorn and Edgar (1975) reviewed these earlier studies and combined this work with Sloss and Speed's (1974) model of plate-spreading-rate-controlled sedimentation. Melhorn and Edgar tentatively concluded that since the Jurassic, the period for which there is any information on spreading rates, four long periods of world-wide erosion have occurred. These periods were long enough for extensive erosion surfaces of low relief to form. However, they also recognized that regional differences in climate, lithology, or base level could influence the rate and manner of denudation.

The ages of exhumed landforms sampled in this study are not equally distributed through geologic time. Most of the exhumed features were created during either the Precambrian or the Tertiary, periods which have been commonly cited as episodes of significant landform development. Few examples of resurrected topography date from the Paleozoic or Mesozoic erosional episodes. The paucity of exhumed landforms of these ages may be a vestige of the sampling, or the features may actually be rare dating from those times.

REFERENCES CITED

Büdel, J., 1968. Geomorphology--principles. In: Fairbridge, R.W. (Editor), The Encyclopedia of Geomorphology. Reinhold Book Company, New York, pp. 416-422.

Gorelov, S.K., Drenev, N.V., Meschcheryakov, Yu.A., Tikanov, N.A., and Fridland, V.M., 1970. Planation surfaces of the U.S.S.R. (translated from Russian). Geomorphology (English edition), 1:18-29.

King, L.C., 1967. The Morphology of the Earth (2nd edition). Hafner Publishing Company, New York, 766 pp.

Martin, R., 1966. Paleogeomorphology and its application to exploration for oil and gas (with examples from western Canada). American Association of Petroleum Geologists Bulletin, 50: 2277-3211.

Martin, R., 1968. Paleogeomorphology. In: Fairbridge, R.W. (Editor), The Encyclopedia of Geomorphology. Reinhold Book Company, New York, pp. 804-812.

Melhorn, W.N., and Edgar, D.E., 1975. The case for episodic, continental-scale erosion surfaces. In: Melhorn, W.N., and Flemal, R.C. (Editors), Theories of Landform Development. Publications in Geomorphology, Binghamton, New York, pp. 243-276.

Sloss, L.L., 1963, Sequences in the cratonic interior of North America. Geological Society of America Bulletin, 74: 93-114.

Sloss, L.L., and Speed, R.C., 1974. Relationships of cratonic and continental margin episodes. In: Dickinson, W.R. (Editor), Tectonics and Sedimentation. Society of Economic Paleontologists and Mineralogists Special Publication, 22: 98-119.

Thomas, M.F., 1974. Tropical Geomorphology. John Wiley and Sons, Inc., New York, 332 pp.

D89

A TECTONIC GEOMORPHOLOGICAL CLASSIFICATION OF THE WALLS OF VALLES MARINERIS

John R. Spencer, Lunar and Planetary Lab., University of Arizona, Tucson, AZ 85721

This study has attempted to develop a geomorphic classification scheme for the canyon walls of Valles Marineris analagous to that devised by Bull (1977) to evaluate the relative tectonic activity of terrestrial mountain fronts. In this way it was hoped that the relative intensity of tectonism in various parts of the Valles Marineris system could be systematically mapped, providing useful information about the origin of the system as a whole.

The Coprates NW guadrangle was chosen for detailed study, as it is the region of the canyons that has the most complete mapping and photographic coverage. Sources of data included the U.S.G.S. 1:2 million photomosaic, shaded-relief map, and topographic map for the MC-18 NW sub-quad. The detailed mapping was mostly performed using Viking 1 imagery from orbits 910 thru 929, supplemented by pictures taken during orbits 57, 59, 62 thru 66, 79, and 91. All this imagery has a resolution of 50 80 metres per pixel, with a variety of illumination angles and some stereo coverage. Low-resolution stereo coverage from Viking 1 orbits 608, 645, and 682, and very high resolution swaths taken on orbits 737, 738, 776, and 815 were also valuable.

As is the case with terrestrial mountain fronts, the morphology of the base of the front provided the most useful indicators of the degree of tectonic activity. A well developed fault scarp at the wall base indicates a tectonically active region, and an irregular, embayed, wall suggests an inactive area. More accurately, wall morphology records the relative importance of tectonic and erosional processes, and in using morphology to map rates of tectonism it must be assumed that wall degredation rates are roughly comparable in different parts of the canyon system. As the erosional process that is degrading the canyon walls is unknown this may not be a good assumption. Four major classes of wall were established, as described below:

Class 1 Class 1 walls have a distinct linear scarp, presumably a fault scarp, at their base. Such scarps, which were recognised by Blasius et al. (1977), indicate a relatively tectonically active canyon wall.

Class 2 Here there is no fault scarp, but the wall base is still very linear and well-defined, being marked by an abrupt break-in-slope rather than a discrete scarp. These walls are interpreted as being tectonic scarps in which the most recent fault scarp has been destroyed or buried by erosion.

Class 3 These walls have bases that are linear on a large scale (> 20km) but have either no well-defined base, or a base that is sinuous on a small scale. More extensive erosion since the most recent faulting than in class 2 walls is inferred, some retreat of the wall

having occurred to destroy the small-scale linearity of the base.
Class 4 These walls have an irregular base even at large scales. Such walls probably result from extensive erosion and retreat of an originally linear tectonic front, though it is also possible that they result from a non-tectonic process producing walls with initially irregular morphology. The coalescing pits of Tithonia Catena may represent an early stage of such a non-tectonic process.

In many cases the base of the original canyon wall is invisible, being buried by intra-canyon sediments or landslide debris. In these cases a wall class using the above scheme cannot be assigned. Intra-canyon sediments were identified in this study using stereo imagery and the topographic map wherever possible, supplemented by the monoscopic data. Such sediments are very extensive, as has been noted by previous workers (e.g. Blasius et. al. 1977). On the south side of the East Candor Chasma they attain a thickness of 5 km, burying the southern canyon wall up to half its height, and their presence there may account for some of the morphological differences between the north and south walls of East Candor that were noted by Patton (1982).

The accompanying map summarizes the results of this study in greatly simplified form. The 4 classes of wall are shown, as are regions where a class cannot be assigned owing to the presence of intra-canyon sediments, landslides, or landslide debris. Apparent fault scarps that occur on the canyon floor rather than at the wall base are also shown, though the numerous graben present on the plateau surrounding the canyons have been omitted.

The most striking feature is the concentration of active tectonic features within Ius Chasma, and to a lesser extent in Tithonium Chasma, and along the north walls of Coprates and East Candor. These canyons are also the most linear of the Valles Marineris system, and, in the case of Ius and Coprates, the most easily explained as simple (if extremely large) graben produced largely by extensional faulting. Tithonium and East Candor have blunt terminations that argue against an origin as simple graben.

The irregular Hebes, Ophir, and Melas Chasmas have walls that are dominantly of class 3 and 4, implying an origin largely by processes other than faulting, or extensive erosion since the most recent faulting episode. Hebes, however, has some quite fresh tectonic features at its east end, which is surprising considering its closed-depression, ungrabenlike shape. These apparent tectonic features take the form of large arcuate inward-facing scarps in the floor of Hebes, running parallel to the canyon rim, that show an intriguing resemblance to ring-faults associated with volcanic caldera collapse elsewere on Mars and on Earth. The possibility the Hebes Chasma contained a volcanic source for the layered deposits currently present within the canyon was suggested by Peterson (1981), and the presence of the arcuate scarps invites speculation that Hebes might be a single enormous volcanic caldera of unique type. Such a hypothesis would help solve the otherwise embarassing problem of what happened to the material formerly occupying the canyon (it was erupted), but the gross similarity of Hebes and the other canyons, most of which are

clearly not volcanic in origin, argues against the caldera idea. The problem may not be resolvable with current data.

References

Blasius, Cutts, Guest and Masursky , 1977, Geology of the Valles Marineris: First Analysis of Imaging from the Viking 1 Orbiter Primary Mission, J.G.R. 82, 4067-4091

Bull and McFadden, 1977, Tectonic Geomorphology North and South of the Garlock Fault, California, in Doehring, ed., Geomorphology in Arid Regions, Publications in Geomorphology, Binghamton, N.Y., 115-136.

Patton, 1982, Quantitative Morphology of the Valles Marineris Scarps (abstract), Reports of the Planetary Geology Program 1982, NASA Tech. Memo. 85127, 242-243.

Peterson, 1981, A Secondary Origin for the Central Plateau of Hebes Chasma, Proc. Lun. Planet. Sci. Conf. 12B, 1459-1471.

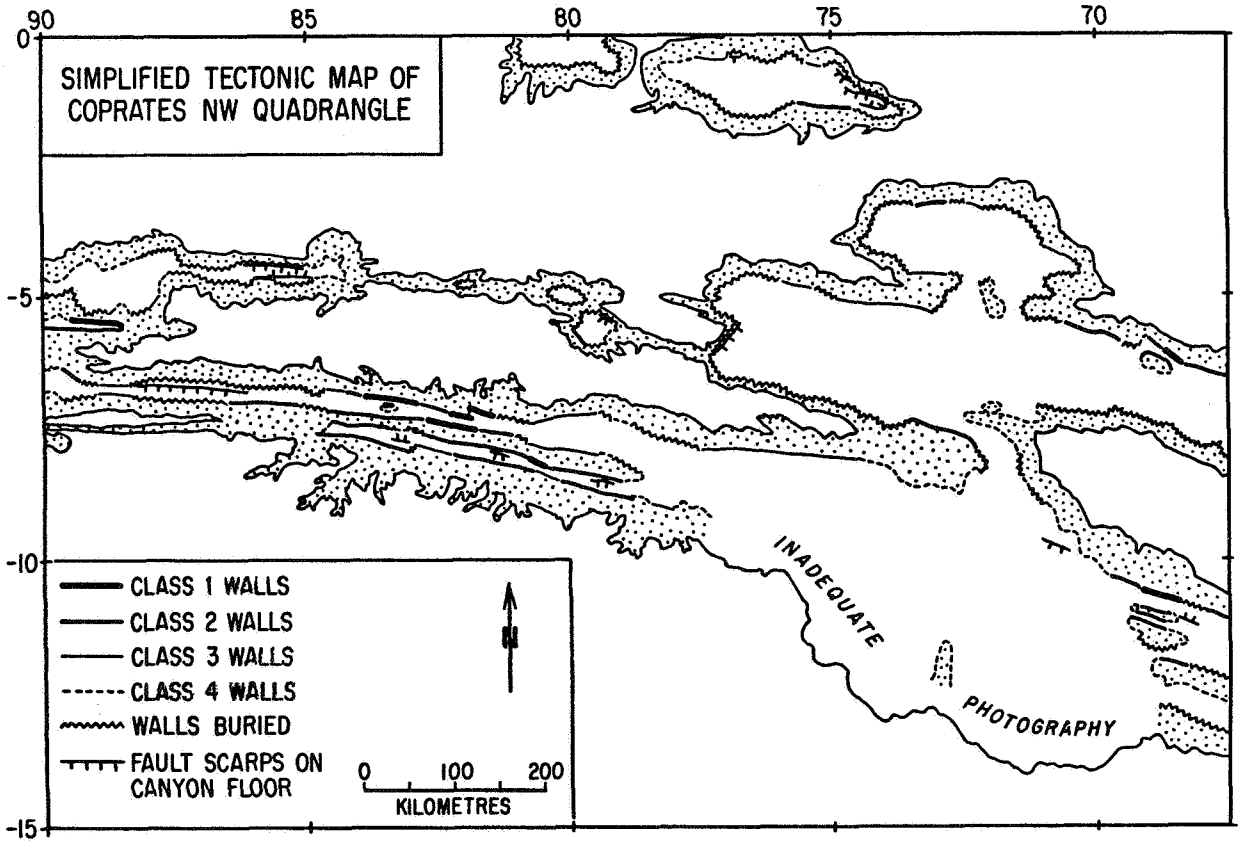

Chapter 10

REMOTE SENSING AND REGOLITH STUDIES

THE OPPOSITION EFFECT

Bruce Hapke
Department of Geology and Planetary Science
University of Pittsburgh
Pittsburgh, PA 15260

The problem of radiative transfer in a medium of large, randomly-spaced particles is considered in the case where the particles are close together. The extinction of a layer of thickness z containing n particles per unit volume with cross-section σ is given by $\exp [\ln(1-F)\ n\ \sigma\ z/F]$, where F is the fractional volume occupied by solid particles. When $F \ll 1$ this reduces to the commonly used form $\exp(-n\sigma z)$. The opposition effect is reconsidered in light of this result, and a new analytic expression is derived which is more rigorous than ones which have been previously available. The amplitude of the OE is controlled by 2 factors: the ratio of single-to-multiple-scattering and the ratio of surface-to-volume-scattering from a single particle. The angular width of the OE is dependent on 3 factors: the porosity 1-F, the particle size distribution, and the manner in which n changes from close-packed at depth to zero at the mean surface. The new model explains a number of heretofore-puzzling observations, including those by Oetking (1966), and fits astronomical data well. The very narrow OE of the Uranian satellites (Brown & Cruikshank, 1983) can be understood if the density of scatterers near the optical surface decreases from close-packed to zero over a distance of the order of 30 times their mean size.

D91 N84 23522

SURFACE COMPOSITIONS IN THE ARISTARCHUS REGION: IMPLICATIONS FOR REGIONAL STRATIGRAPHY

B.R. Hawke, P.G. Lucey, and T.B. McCord, Planetary Geosciences Div., Hawaii Inst. of Geophysics, Univ. of Hawaii, Honolulu, HI; C.M. Pieters and J.W. Head, Dept. of Geological Sciences, Brown Univ., Providence, RI.

Introduction: The Aristarchus Plateau is one of the most geologically complex regions of the Moon and exhibits a number of spectral and geochemical anomalies. The plateau is an elevated crustal block blanketed by varying thicknesses of dark mantling material of probable pyroclastic origin and dissected by large sinuous rilles. Aristarchus crater straddles the plateau/mare boundary. Although this region has been the subject of numerous geological and remote-sensing investigations[1-6], significant questions concerning the composition, origin, and evolution of the observed geologic units remain. The purpose of this study was to use a variety of visible and near-infrared spectral data to investigate the composition and distribution of surface material in the Aristarchus region. It was anticipated that the results would have important implications for 1) the composition and stratigraphy of the lunar crust, 2) the nature of Imbrium ejecta and pre-Imbrium material, 3) the stratigraphy of the Aristarchus target site, 4) the impact cratering process, and 5) the composition of the dark mantling material.

Method: An early step in the project was the production of multispectral ratio images (.40/.56μm and .95/.56μm) and a variety of spectral unit maps. The techniques used in the preparation of the products as well as the preliminary interpretations have been previously discussed[7]. Near-infrared reflectance spectra (.6-2.5μm) for the Aristachus region were obtained using the 2.2m UH telescope at the Mauna Kea Observatory. Most spectra were obtained during periods of exceptional "seeing" (.5 arcsec) at Mauna Kea and are of very high quality. The spectra were reduced and analyzed following the procedure described by McCord et al.[8]. The spectra most important for the understanding of the Aristarchus region are presented in Figure 1.

Results: The spectra obtained for the central peak, southern floor, southwestern wall, eastern wall, and northwestern wall of Aristachus crater share generally similar spectral characteristics. These spectra exhibit shallow continuum slopes, relatively strong feldspar bands, pyroxene bands stronger than those typically seen in the spectra of fresh highland features, and pyroxene band centers near 1μm suggesting the dominance of Ca-rich clinopyroxene. These characteristics indicate that Aristarchus crater material has a feldspar-rich highland composition, with an unusual pyroxene assemblage dominated by clinopyroxene. These spectra can be divided into two classes. The southwest and northwest wall spectra have stronger pyroxene and feldspar bands and somewhat steeper continuum slopes than the floor, peak, and east wall spectra. This may be indicative of either compositional or grain size differences. These differences may be attributable to minor variations in the highland composition of the target site or to differing amounts of impact melt in the various portions of the

crater interior. It seems likely that the Th high centered on the crater is associated with one or both of the compositions identified in the crater interior.

The spectrum of Aristarchus A, a bright crater in rugged terrain northwest of Aristarchus, is quite similar to the southwest and northwest wall spectra and indicating that both Aristarchus and Aristarchus A have excavated a regional compositional unit. Aristarchus crater has exposed material similar to that present under at least portions of the dark mantle deposit on the plateau. The spectrum of the south rim of Aristachus is quite distinct from those of other crater units. It has a broad, shallow band centered just beyond one micrometer eliminating typical pyroxene assemblages as its major mafic component. A similar spectrum was obtained for Herodotus X, a mountain on the plateau 200 km from Aristachus. The spectral characteristics of both the Aristarchus south rim and Herodotus X could be explained by the presence of material rich in olivine. We suggest that this material was derived from a deep-seated layer that was exposed by the Aristarchus impact, and which also formed the pre-Imbrian crater of which Herodotus X is part of the rim.

The position of Aristarchus on the plateau/mare boundary raises questions concerning compositional variations in crater ejecta deposits. One spectrum of a dark ejecta deposit on the mare side of the boundary was taken which is very mare-like. The continuum slope is somewhat shallow for fresh mare material, but is identical to a small crater in the mare (Aristarchus C) to the north of the plateau. This suggests mare basalt was included in Aristarchus ejecta at least to the northeast. No other spectrum taken in the crater interior is similar to a mare spectrum indicating little, if any, mare basalt was present in the material which was shock melted to produce the Aristachus impact melt.

The dark mantle blanketing the region has unique spectral characteristics. Its spectrum, "A" in Figure 1, has a very steep continuum slope and a very shallow, broad band centered beyond 1μm. This band may be due to Fe^{2+} absorptions in pyroclastic glass.

References: 1) S. Zisk, et al., 1977, The Moon, 17, 59; 2) H.J. Moore, 1965, U.S. Survey Geol. Inv. Map I-465; 3) E.L. Haines, 1978, Proc. Lunar Planet. Sci. Conf. 9th, 3285; 4) M.I. Etchegaray-Ramirez, et al., 1982, Proc. Lunar Planet. Sci. Conf. 13th, 529; 5) D.W. Davies, et al., 1979, Proc. Lunar Planet Sci. Conf. 10th, 1819; 6) J.E. Guest, 1973, Geol. Soc. Amer. Bull., 84, 2873; 7) P.G. Lucey, et al., 1982, LPSC XIII, 678; 8) T.B. McCord, et al., 1981, JGR, 86, 10883.

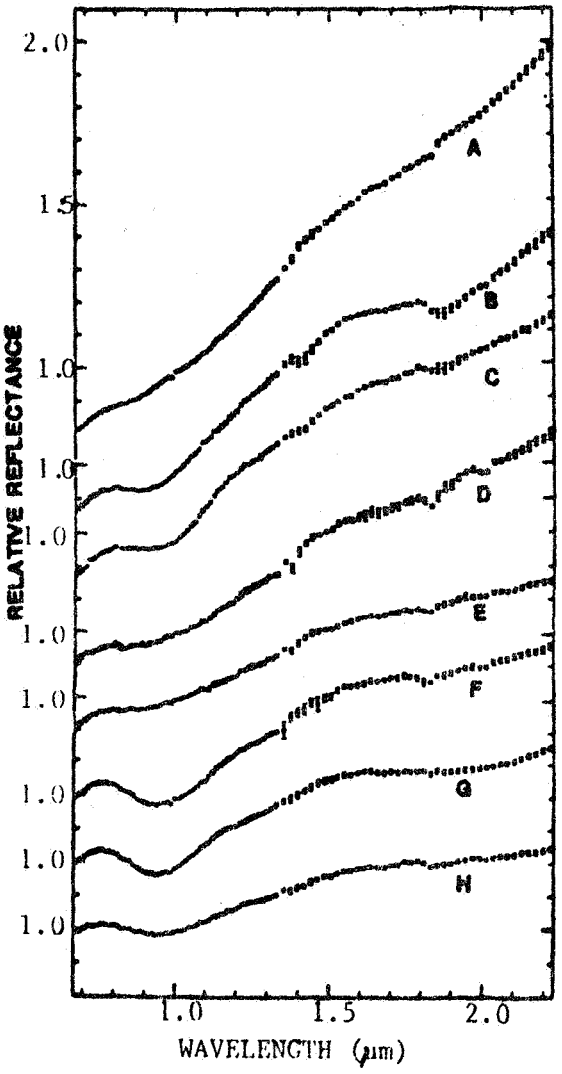

A: PLATEAU PYROCLASTICS
B: HERODOTUS D
C: NORTH RIM DARK DEPOSIT
D: HERODOTUS X
E: SOUTH RIM
F: ARISTARCHUS A
G: SOUTHWEST WALL
H: ARISTARCHUS CENTRAL PEAK

D92

N84 23523

A Case for Olivine on Mars. R. Huguenin, L. Vale, and D. McIntire, Remote Sensing Center - Hasbrouck, UMassachusetts, Amherst 01003.

It was noted in earlier papers that Mars dark area reflectance spectra contain absorption features that point to the possible existence of mafic silicate minerals on the surface (McCord et al, 1977; Huguenin et al, 1977). Regional variations in absorption band positions and strengths suggested that there were regional variations in the rock types of the areas measured. For many of the areas, relative strengths of absorption bands suggested that olivine (and/or mafic glass) may be a dominant phase and that high-calcium pyroxenes may be more abundant than low-calcium pyroxines (Huguenin et al, 1978). A few areas had absorptions that suggested that low-Ca pyroxenes and high-Ca pyroxenes, rather than olivine, may be dominant phases. Analyses were centered in the Coprates and Margaritifer Sinus quadrangles between 0 and 90° W longitude and from 0 to 30°S latitude.

Spectra of new areas from another part of the planet were measured during 1978 and 1980, and they showed general similarities to the earlier spectra (Singer et al, 1979). In a subsequent interpretation of a 1978 spectrum, Singer (1981, 1982) concluded that only pyroxene bands contributed to the absorptions in the new areas. Noting similarities to the earlier spectra, he then extended this interpretation to challenge our proposal that olivine may be a dominant phase on Mars. His interpretation also challenged an earlier interpretation by Adams and McCord (1969) that dark area spectra were similar to laboratory spectra of oxidized olivine basalt.

In this paper we report a new analysis that supports the earlier proposals that olivine may be an important phase on Mars. The analysis is based on the similarity of the laboratory reflectance spectrum of ALHA 77005, a meteorite proposed to be from Mars, and the telescopic spectrum of a dark area north of Hellas on Mars (15°S, 300°W). This is the same spectrum analyzed by Singer (1981, 1982), but the approach and results are different.

The Mars spectrum is shown in Figure 1, which we published in 1979 (Singer et al, 1979). Also shown in Figure 1 is a continuum spectrum (solid line) that, when divided into the Mars spectrum, reveals the absorption feature produced by the surface rocks and soil (Singer et al, 1979). The Mars spectrum with the continuum divided out is shown in Figure 2.

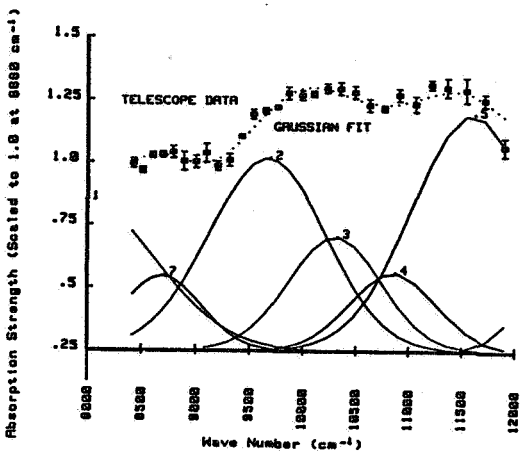

Figure 1

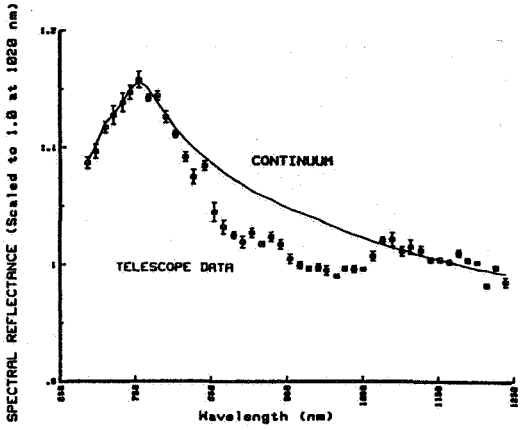

Figure 2

The contimuum is very similar to that of photooxidized magnetite, published by Huguenin (1973a). For the photooxidized magnetite the spectrum characteristics were produced by thin (1-3μm) layers of ferric oxide on the substrate grains. For Mars the continuum may similarly represent an optically thin Fe^{3+}-bearing layer on the surface rocks and/or Fe^{3+} in dust suspended in the atmospheric column above the surface.

The Mars spectrum with the continuum divided out (Figure 2) has been reformatted, with the abscissa ranging from 0.8-1.25μm and linear in energy (rather than wavelength) and the ordinate scale made proportional to absorption strength. A gaussian fit to the Mars spectrum, included in Figure 2, is discussed below.

A reflectance spectrum of ALHA 77005, measured with the same instrument used to measure the Mars spectrum in Figure 1, is shown in Figure 3 (the spectrum was measured and provided to us by L. McFadden). It is presented in the same format as the Mars spectrum in Figure 2.

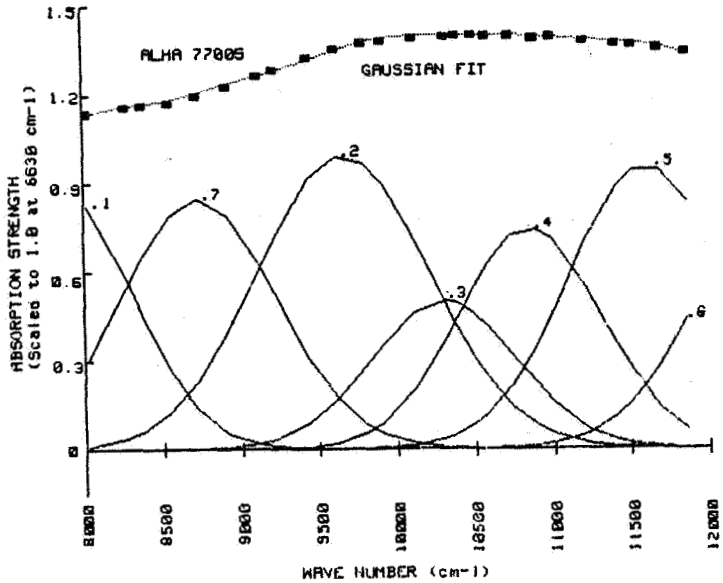

Figure 3

From the mineralogical analysis of ALHA 77005 (McSween et al, 1979; Wood and Ashwal, 1981), absorption band positions and half-widths were determined for the constituent minerals in ALHA 77005. Gaussian fits to laboratory spectra of representative minerals were used to determine half-widths and gross positions for the bands, and the technique of Adams (1975) was employed to refine the band positions. The constituent phases and their corresponding seven absorption bands are listed in Table I. Using these seven bands with their characteristic positions and half-widths, we adjusted individual band strengths to obtain a best fit to the meteorite spectrum. The result is shown in Figure 3.

TABLE I: ALHA 77005 Absorption Bands

Band Designation	Mineral	Wavelength (nm)
1.	Olivine (Fo_{74})	1274 ($7846cm^{-1}$)
2.	Olivine (Fo_{74} + Glass	1036 ($9646cm^{-1}$)
3.	*Augite (Band 1a)	970 ($10300cm^{-1}$)
4.	Pigeonite	921 ($10850cm^{-1}$)
5.	Ferric Oxide + Olivine (Fo_{74})	862 ($11600cm^{-1}$)
6.	*Augite ($Fe^{2+} \rightarrow Fe^{3+}$) charge transfer	789 ($12665cm^{-1}$)
7.	*Augite (Band 1b)	1151 ($8687cm^{-1}$)

*Augite with composition $Wo_{35}En_{50}Fs_{15}$ would be expected to have two Fe^{2+} bands near 1000nm and a charge transfer band near 794nm (Adams, 1975)

Using the *same* seven band positions and appropriate half-widths, we again adjusted absorption strengths to obtain a best fit to the Mars spectrum. The result is shown in Figure 2.

Comparison of the results reveals notable similarity. In Table II the gaussian strengths for the seven bands, normalized to pigeonite (Band 4), are compared for the two fits in Figures 2 and 3.

TABLE II: Relative Gaussian Band Strengths for Mars and ALHA 77005

Mineral Bands	Relative Gaussian Band Strengths	
	Mars	ALHA 77005
Olivine/pigeonite	1.93 } 2.21(Av)	1.16 } 1.26(Av)
Olivine + Glass/pigeonite	2.48 }	1.36 }
Augite (1a) /pigeonite	1.46 } 1.18(Av)	0.67 } .923(Av)
Augite (1b)/pigeonite	0.90 }	1.17 }
Augite (ch.tr.)/pigeonite	1.90	1.47
Ferric Oxide + Olivine/pigeonite	3.07	1.19

First, note the similarity of the augite/pigeonite average band strengths for ALHA 77005 (.923) and Mars (1.18). They are both close (within 8-18%) to 1.0. Note also that the ratio of the charge transfer band to the average electronic transition band strengths for the augite are similar to within 2% for Mars (1.90/1/18 = 1.61) and ALHA 77005 (1.47/.923 = 1.59). Considering that band strengths were adjusted simply to generate a best fit to the spectra and were otherwise unconstrained, these similarities are striking. They suggest that the relative abundances and compositions of pyroxenes in the Mars area may be quite similar to those in ALHA 77005.

Second, note the similarity of the ratios of the strengths of the olivine + glass vs. the olivine bands for ALHA 77005 (1.36/1.16 = 1.17) and the Mars area (2.48/1.93 = 1.28). They are the same to within 9%, even though the average olivine/pigeonite band strengths are a factor of 1.8 higher for the Mars area (2.21) than for ALHA 77005 (1.26). The ratios of these two band strengths (band 2/band 1) for the meteorite and the Mars area are similar to that for the laboratory spectra of olivine of similar composition, and this suggests that olivine dominates over glass in controlling the strength of band 2 in the spectra of both ALHA 77005 and the Mars area. This is consistent with the modal analyses of ALHA 77005, and it supports the proposed existence of possibly abundant olivine in the Mars area. Indeed, olivine is the dominant phase (52%) in ALHA 77005 (Wood and Ashwal, 1981), and for the Mars area the relative olivine band strengths are nearly twice as great as for ALHA 77005.

A third point to note is that the Fe_2O_3 + olivine band near 862nm is of comparable strength to the other two olivine bands in ALHA 77005.

This is observed in laboratory spectra of olivines of comparable composition, and it suggests that Fe_2O_3 may have contributed very little to the strength of this band in ALHA 77005 (which would be consistent with modal analyses of the meteorite). For the Mars area, the Fe_2O_3 + olivine/pigeonite relative band strength is a factor of 2.6 higher than for ALHA 77005. This can be attributed to expected contaminant dust in the surface soils of the Mars area (McCord et al, 1977; Huguenin et al, 1977, 1978; Singer et al, 1979).

The fourth point is the similarity of band positions for ALHA 77005 minerals in Table I with band positions derived from the McCord et al (1977) spectra of Mars areas (Huguenin et al, 1977, 1978). We deduced the presence of olivine and/or glass with a band near 1.05μm, within 2% of the corresponding band position (band 2) in Table I (band 1 was beyond the range of the telescope spectra). We deduced the presence of high-calcium pyroxenes in the Mars areas with band positions varying from region to region, but generally in the range 930-1000nm. The corresponding band position in Table I is in the middle of this range at 970nm (band 3). We deduced the presence of charge transfer bands in the Mars spectra between 600-770nm. A corresponding band again exists in Table I, and it lies only ∿3% longer in wavelength near 789nm. We deduced the presence of low-calcium pyroxenes in the Mars spectra with bands centered between 900 and 930nm. Again such a band exists in Table I near 921nm for pigeonite (band 4). We deduced the presence of Fe^{3+} in the Mars soil with a band near 870nm, and a corresponding band exists in Table I near 862nm (band 5), only ∿1% shorter in wavelength. The only bands listed in Table I that were not deduced from the earlier Mars spectra, viz bands 1 and 7, are beyond the wavelength range of the earlier Mars spectra (300-1100nm). In addition to derived band positions we deduced from band depths in the Mars spectra that opaques occupied less than 10wt% of the surface soils. For ALHA 77005 and the other SNC meteorites proposed to be of candidate Martian origin, opaques were less than 4% of the mass by weight. We also predicted that sulfide may be present, based on correlations between albedo and inferred mafic silicate abundance ratios. Troilite was indeed present at levels up to 4wt% in SNC meteorites.

A fifth point is the agreement between the inferred relative band strengths derived from the earlier Mars spectra (Huguenin et al, 1978) and those derived here for ALHA 77005 and the newer Mars area.

A sixth point of significance is that petrologic models for Martian primitive rock types, derived from the Mars dark area spectra, analyses of Viking XRF data, and mantle thermal models (Smyth et al, 1978) are similar to proposed source rock petrologies for ALHA 77005 and the other candidate Mars meteorites. Our derived parent normative mineralogy for primitive Mars rocks (planetwide average) is shown in Table III.

TABLE III: Normative Mineralogy of Primitive Martian Source Rock (Planetwide Average)

Mineral	Composition	Weight Percent
Olivine	Fa_{44}	37-38%
Diopside	$Wo_{50}En_{28}Fs_{22}$	20-29%
Plagioclase	An_{60}	20-32%
Orthoclase	-	0.6-1.4%
Magnetite	-	4.4-7%
Nephline	-	2.5-5%

It was proposed by McSween et al (1979) that the parent for ALHA 77005 and the other candidate Mars meteorites were probably plagioclase-bearing peridotites, consisting dominantly of olivine with smaller amounts of pyroxene and plagioclase. This is consistent with our model in Table III. Most striking, however, was that plagioclase composition for the meteorite parent was proposed to be An_{50-70}, essentially the same as our derived plagioclase composition of An_{60} in Table III for the Mars parent.

These six points suggest that ALHA 77005 may have a similar mineralogic assemblage to that in the Mars area north of Hellas. The spectrum of this area is similar to spectra of several other areas measured during the earlier oppositions (McCord et al, 1977), and hence ALHA 77005 may be similar to surface rocks in several regions of the planet. The agreement between the mineral assemblage of ALHA 77005 and those derived earlier from the Mars spectra provide good support for our original interpretations, particularly the interpretation that olivine may be an abundant component in some of the surface regions.

Acknowledgement. This research was supported by NASA grants NSF 7405 and NAGW 440.

References. Adams, J.B., in Infrared and Raman Spectra of Lunar and Terrestrial Minerals, Academic Press, NY, 1975, pp 91-115; Adams, J.B. and T.B. McCord, J. Geophys. Res., 74, 4851, 1969; Huguenin, R.L., J. Geophys. Res., 78, 8481, 1973; Huguenin, R.L., Adams, J.B., and McCord, T.B., Lunar Science VIII, 478, 1977; Huguenin, R.L., Head, J.W., and Mc Getchin, T.R., NASA Tech Mem TM79729, 118, 1978; McCord, T.B., Huguenin, R.L., Mink, D., and Pieters, C., Icarus, 31, 25, 1977; McSween, H.Y. et al, Earth Plan. Sci. Letters, 45, 275, 1979; Singer, R.B., Ph.D. Dissertation, MIT, 1981; Singer, R.B., J. Geophys. Res. (in press), 1982; Singer, R.B., McCord, T.B., Clark, R.N., Adams, J.B., and Huguenin, R.L., J. Geophys. Res., 84, 8415, 1979; Smyth, J.R., Huguenin, R.L., and Mc Getchin, T.R., Lunar Plan. Sci IX, 1077, 1978; Wood, C.A. and Ashwal, L.D., Proc. Lunar Planet Sci. 12B, 1359, 1981.

N84 23524

D 93

GALILEAN SATELLITE MULTISPECTRAL DATA BASE PRODUCTION

Principal Investigator: T.V. Johnson (JPL)
Co-Investigators: J.A. Mosher(JPL), L.A. Soderblom(USGS Flagstaff)

We are producing a photometrically and geometrically reduced data base for the Galilean Satellites using Voyager imaging data. The basic data set used is essentially all the useful satellite images returned by Voyager. Each frame has been radiometrically calibrated and many have been projected into cartographic formats. Mosaics of low, medium and high resolution frames are being made for each satellite. These mosaics consist of registered digital images with intensity values scaled through a traceable calibration procedure to normal albedo values. Many of the mosaics are being made in two versions. One version is a albedo version and the second is a maximum discrimination version in which large variations in brightness across the picture are suppressed.

These databases are being used by many groups studying the geochemistry, geology, and surface/atmosphere interactions of the satellites. B. Luchitta (USGS Flagstaff) has distributed photographic copies of the completed digital mosaics to the geologists who are preparing geologic maps of the satellites. T. B. McCord's (U of Hawaii) group is using some of the mosaics to study the color and photometry of the satellites. M. E. Davies is leading an effort to compile an atlas of satellite pictures. This atlas will also contain the computer mosaics.

Future work will include completing the mosaics, geometrically correcting every individual frame, and distributing the data to regional data centers. Below is a table listing the status of the mosaics.

HIGH RESOLUTION MOSAICS (NARROW ANGLE CAMERA)

Object	Picture # Range	# Frames	Status
IO	1639024-1639236	51	Done
Europa	2065139-2065223	12	Not Started
Ganymede	1640422-1640711	51	Done
Ganymede	2063517-2064055	100	Done
Callisto	1642416-1642817	68	Almost Done
Callisto	2061609-2061741	17	Done
Callisto	2061832-2061921	10	Not Started

MEDIUM RESOLUTION MOSAICS (NARROW ANGLE CAMERA)

IO	1637748-1637756	5	Not Started
Callisto	1642121-1642228	20	Done
Callisto	2060621-2060653	9	Not Started

MULTISPECTRAL MOSAICS (NARROW ANGLE CAMERA)

Object	Picture # Range	# Frames	Status
IO	1638209-1638239	16	Done
IO	1638850-1639020	46	Done
Europa	2064910-2065007	20	Not Started
Ganymede	1640132-1640420	85	Done
Ganymede	2063059-2063133	18	Done
Callisto	1641752-1641908	39	Not Started
Callisto	2061330-2061436	18	Not Started

MULTISPECTRAL MOSAICS (WIDE ANGLE CAMERA)

IO	1639216-1639243	12	Done
IO	1637429-1639155	37	Not Started
Europa	2065012-2065233	25	Not Started
Ganymede	1640141-1640557	40	Not Started
Ganymede	2063519-2064042	48	Not Started
Callisto	1641753-1642810	42	Not Started
Callisto	2060627-2061926	33	Not Started

MULTI-IMAGE PHOTOMETRIC SOLUTIONS FOR THE GALILEAN SATELLITES

Alfred S. McEwen and Laurence A. Soderblom, U. S. Geological Survey, Flagstaff, AZ 86001

The commonly used method to determine the limb-darkening of a planet or moon is to fit a solution through many points on a single image. This method requires the assumption that variations in normal albedo (A_n) are random with respect to photometric coordinates. However, systematic variations in brightness are common on planetary bodies: Ganymede has bright poles, Io has dark poles, and most of the Galilean and Saturnian moons show rotational variations, resulting in systematic errors in single-image, limb-darkening fits. Furthermore, different surface materials may have different photometric behaviors.

The method described here utilizes two images of the same region on a planet, acquired in the same wavelength range (λ), within a few degrees of the same phase angle (α), but acquired at different illumination and viewing conditions. The two images are first geometrically registered in simple cylindrical format. A limb-darkening factor is computed for each pixel pair and output as a digital image. Systematic trends with photometric coordinates across this image indicate either a calibration error or inappropriateness of the particular photometric function. This method can be used for any photometric function with a single limb-darkening factor, such as the Minnaert function or the function which combines the Lommel-Seeliger and Lambert functions. suggested by Buratti et al. [1]. By solving for many pairs of images, the limb-darkening factor as a function of α and λ may be determined. A_n is determined by comparing the disk-integrated phase function with the limb-darkening corrected phase function. New global multispectral mosaics of A_n have been produced for Europa, Callisto, and Io.

Two-image limb-darkening solutions have been determined for 1 Voyager image pair on Ganymede, 16 image pairs on Callisto, 44 pairs on Europa, and 19 pairs on Io. Results for Ganymede and Callisto are consistent with lunar-like scattering [2,3]. Scattering on Europa is very uniform as a function of surface materials and wavelength λ, and can be described by the Minnaert K factor as a function of phase angle (α): $K(\alpha) = 0.64 - 0.005\alpha + 0.00066\alpha^2 - 0.000012\alpha^3$, for α from 3° to 30°, with a correlation coefficient of 0.94. Europa's disk-integrated phase function (geometric albedo (p) vs. α), is linear for α 3° to 30° and varies with λ: $p(.59\mu m) = 0.69 - 0.0081\alpha$, $p(.54\mu m) = 0.66 - 0.0070\alpha$, $p(.48\mu m) = 0.55 - 0.0061\alpha$, $p(.41\mu m) = 0.44 - 0.0054\alpha$, $p(.35\mu m) = 0.30 - 0.0046\alpha$, as determined from 34 Voyager images at each λ and normalized by the rotational light curve, with correlation coefficients from -0.93 to -0.97. The systematic variation of slope with λ is consistent with the same $K(\alpha)$ for each λ and increasing p at longer wavelengths.

The limb-darkening of Io varies strongly with λ at low phase angles (α 3° - 15°): $K(\alpha,.59\mu m) = 0.55 + 0.005\alpha$, $K(\alpha,.54\mu m) = 0.53 + 0.005\alpha$, $K(\alpha,.48\mu m) = 0.52 + 0.005\alpha$, $K(\alpha,.41\mu m) = 0.49 + 0.006\alpha$, $K(\alpha,.35\mu m) = 0.44 + 0.009\alpha$. K also varies with surface materials on Io; conspicuous in the K images are higher values for Bactria Regio (45°S., 125°W.) and Nina Patera (40°S., 165°.W). The brown polar materials have a uniform limb-darkening, and the normal albedo systematically darkens with increasing latitude. With increasing phase angle, Io becomes redder and darker, especially the reddest materials such as the

lava flows in the south polar region. Both the blueing towards the limb at low phase angles and the reddening at high phase angles are consistent with the laboratory results for powdered sulfur [4].

References

[1] Buratti, B., and Veverka, J., and Thomas, P., Voyager Photometry of Saturn's Satellites (abs): Reports of Planetary Geology Program, 41-43, 1982.

[2] Hapke, B. W., A theoretical photometric function for the lunar surface: J. Geophysical Research, v. 68, 4571-4586, 1963.

[3] Irvine, W. M., The shadowing effect in diffuse reflectance: J. Geophysical Research, v. 71, 2931-2937, 1966.

[4] Gradie, J., Veverka, J., and Buratti, B., The effects of scattering geometry on the spectrophotometric properties of powdered materials: Proceedings Lunar and Planetary Science XI, 799-815, 1980.

N84 23526

RAPID EXTRACTION OF RELATIVE TOPOGRAPHY FROM VIKING ORBITER IMAGES II. - APPLICATION TO IRREGULAR TOPOGRAPHIC FEATURES

P. A. Davis and L. A. Soderblom, U.S. Geological Survey, Flagstaff, AZ 86001

INTRODUCTION: The number of stereo images of the martian surface is quite small: thus an alternative method to stereo photogrammetry must be devised for topographic extraction. Over the past three years we have developed reliable photoclinometric methods to estimate the topography of craters from Viking Orbiter images [1,2,3]. We have devised two photoclinometric methods to determine crater-form topography [4]. The first method, termed the ratio method or Method I, is the most reliable and precise of the two in that it compensates for changing albedo within the profile by ratioing the respective picture-element (pixel) brightness values along two profile directions that have symmetric topography and albedo. Hence, the multiplicative effect of albedo in the photometric function cancels out, leaving slope as the only unknown. The second method, the flat-field method or Method II, is less reliable because it uses only a single profile on the assumption that albedo along the profile is constant. In this method, the combined effects of solar flux, albedo, and camera sensitivity are replaced by an estimate of the flat-field brightness that is derived from areas within the image where the slope is negligible. Its advantage over Method I is that it does not require any form of topographic symmetry and is therefore useful in calculating the relative heights of such irregular features as individual scarps.

The above methods compensate for the effects of atmospheric scattering by subtraction of a haze value from all brightness values along the designated profiles. This haze value is most accurately obtained from shadows within the image or through calibration on known topography. The above methods also compensate for geometric distortions of the imaged surface, introduced by oblique viewing angles, by applying an iterative matrix transformation to the image coordinate system, utilizing the most recent estimate of each pixel's relative height, which is obtained from the photometric integration [3]. We have found a modified Minnaert photometric function to be applicable to Mars. Solutions obtained by these methods are possible because the user implicitly designates the upslope or downslope directions for the profiles. The most accurate solution for the ratio method is obtained when the two radial profile directions are designated in opposing directions within the maximum scattering plane.

The photoclinometric techniques described above have been tested to our satisfaction [3,4] and are now being used in several crater studies. However, another equally intriguing photoclinometric problem still exists: the extraction of relative topographic data for irregular features such as ejecta blankets, lava flows, graben and ridge scarps, dune forms, and stratified materials such as polar deposits. Topographic data obtained for such features would allow inferences to be made concerning target-material properties of cratered terrain (as well as projectile velocity), rheology of lava flows, geophysical conditions for graben and wrinkle-ridge formation, physical character of stratified deposits, and eolian erosion and deposition.

Howard et al. [5] presented a photoclinometric technique for topographic extraction for the martian polar regions. Their method requires that the surface albedo remain constant within the designated profile, and it does not correct for oblique viewing geometry. It further requires a measure of the flat-field brightness, which necessitates the presence within or near the disignated profile of an area that has negligible slope. Unfortunately, some of the more interesting problems on Mars involve the delineation of stratified deposits; the mere presence of stratified deposits indicates varying albedo, and precludes the use of their technique.

METHOD: In order to derive relative topographic data for irregular features, we have altered the algorithms that we developed for crater-form topography, but we still utilize the basic concepts that allow topographic extraction of terrain of variable albedo. We have devised two additional methods for irregular topography: the first, Method IIa, is a more versatile version of the flat-field method developed for crater-form topography; the second, Method III, utilizes the basic concept of profile symmetry developed for Method I.

Both new methods utilize two profile directions whereby the starting positions of the two profiles can be either the same point or entirely different points, as long as downslope or upslope directions can be designated for the profiles. Method I (the ratio method for crater-form topography) currently uses the same starting position for both radial profiles; Method II [3,4] was previously unidirectional, as in the technique of Howard et al. [5].

Method IIa utilizes two profile directions that can have totally different starting and ending points as long as the total change in elevation within both profiles is the same and the albedo is constant. Method IIa iterates through flat-field brightness values, starting with a seed value, to find the flat-field value that produces the same total change in height for both profiles. Thus Method IIa is quantitatively more constrained than Method II.

Method III is basically designed for features whose topography and albedo, along two profile directions, are roughly symmetric, even though the topography is generally irregular (for example, two sides of a spur). As in Method I, ratioing respective pixel-brightness values of the two profiles will produce a solution for pixel slope that is independent of albedo. In order to insure that the downslope or upslope direction is utilized for both profile directions when a common point is desired for their starting position, the user estimates a local tangent to the rim of the irregular feature at two locations by designation of two points along the rim at the two locations. Method III then calculates the profile directions and the starting point by the perpendicular bisection of the two tangent line segments.

In both methods, after the elevations along the profiles are obtained by integration of the photometric function, a matrix transformation is applied to the image coordinates of each pixel within each profile, utilizing each pixel's integral height, to produce a projection of each profile line onto the surface. Pixel-brightness values are then resampled

along the projected track of each profile to determine a more correct height value for each pixel, and the process is repeated. The iteration process terminates when the integral heights of two consecutive iterations do not change by more than 2 percent of the image resolution. For Method IIa, an additional constraint for convergence is required, in that the integral heights of both profiles must not differ by more than 2 percent of the image resolution.

RESULTS: Both new methods are currently in the development stage, but preliminary test data for grabens and valley scarps in the Tithonia Chasma and Olympus Mons regions [6,7] indicate a precision for both Method IIa and III of 10-20 percent; in some instances, the precision has reached 5 percent. Development of these two methods will continue in order to increase precision to better than 10 percent in all cases.

REFERENCES:

[1] Davis, P.A., Eliason, E.M., and Soderblom, L.A. (1981) Rapid computer determination of relative height profiles of partly-shadowed, bowl-shaped craters on Mars (abs.): Third International Colloquium on Mars, Lunar and Planetary Institute, Houston, Texas, p. 56-58.

[2] Davis, P.A., Soderblom, L.A., and Eliason, E.M. (1982) Rapid extraction of relative topography from Viking Orbiter imagery (abs.): Lunar and Planetary Science XIII, p. 144-145.

[3] Davis, P.A., Soderblom, L.A., and Eliason, E.M. (1982) Rapid estimation of martian topography from Viking Orbiter image photometry (abs.): National Aeronautics and Space Administration Technical Memorandum 85127, Reports of Planetary Geology Programs 1982, p. 331-332.

[4] Davis, P.A., and Soderblom, L.A. Rapid extraction of crater-form topography from monoscopic Viking Orbiter images: submitted to Jour. Geophys. Res.

[5] Howard, A.D., Blasius, K.R., and Cutts, J.A. (1982) Photoclinometric determination of the topography of the martian North Polar cap: Icarus, v. 50, p. 245-258.

[6] U.S.G.S., Topographic orthophoto mosaic of the Tithonium Chasma region of Mars, U.S.G.S. Misc. Inv. Ser. I-1294 (1980).

[7] U.S.G.S., Topographic contour map of Olympus Mons of Mars, U.S.G.S. Misc. Inv. Ser. 19/134 T (1981).

D96 N84 23527

THERMAL INFRARED ANALYSIS OF VOLCANIC SURFACES: MARS AND HAWAII

James R. Zimbelman, *Department of Geology, Arizona State University, Tempe, Arizona 85287*

Thermal infrared measurements of a planetary surface indicate the surface temperatures through the amount of energy they emit. The variation of surface temperatures is governed by the thermal inertia, a measure of how rapidly or slowly the temperature changes throughout the day. Thermal inertia is related to the particle size and porosity of the surface (1,2), which should be related to the geologic history of the surface. Global mapping by the Viking Infrared Thermal Mapper (IRTM) revealed that the Tharsis volcanoes were situated within a vast area of low thermal inertia material, implying very fine particle size or very high porosity, with the volcanoes having the lowest thermal inertias (2,3,4). This work involves the use of high spatial resolution IRTM data to examine the volcanoes in more detail.

Figure 1 shows the longitudinally averaged thermal inertias for a sequence that crossed Ascraeus Mons through the summit caldera, providing profiles of the volcano. Globally mapped thermal inertias display a trend of decreasing values with increasing elevation and this is attributed to three atmospheric effects: 1) decreasing thermal conductivity of particulate materials with decreasing atmospheric pressure (1,2), 2) decreasing atmospheric thermal radiation with increasing elevation (5), and 3) decreasing dust opacity with increasing elevation (5). The sequence used for the data in Figure 1 were collected in a relatively dust-free period; line b in the figure shows the thermal inertia values that result from the other two effects (see ref. 6 for details). The basal shield thermal inertia is considerably larger than that of the surrounding plains with the thermal inertia gradient located on the geologic contact between these units. This contrast may be related to differing lava flow characteristics between the shield lavas and the flood lavas of the plains. Thermal inertia decreases from the base toward the summit but levels off at a value consistent with the surrounding plains when less than half way up the volcano. The zone of this "leveling off" corresponds with the lower limit of the dark collar zone for the Tharsis volcanoes (7) and also with a general change in surface morphology; above this zone morphologies are very sharp and distinct in high resolution photos while below this area the morphology is generally subdued. The highest thermal inertias in the summit area correspond to caldera walls where large blocks or rock outcrop would be more likely. The other Tharsis shield volcanoes have thermal trends similar to that of Ascraeus Mons but the Elysium volcanoes and the highland patera appear to lack the properties contrast with the surrounding units. Future effort will be centered on these older volcanic features.

Lava flow surface textures can produce roughness elements at many scales, including roughness ranging from 10^{-3} to 10 m in scale—the range that contributes to thermal infrared emissions (8). Hawaiian lavas provide a variety of flow types and ages on which to evaluate roughness scales and their potential contribution to thermal emissions. Pahoehoe flows gradually loose surface glassy zones and flow textures (e.g. ropes) through weathering with increasing age but with relatively little changes over distances of a meter or more. Aa flows loose mm-sized glassy spines with increasing age but also the m-scaled chaotic placement of clinkers becomes more subdued as clinkers are worn down or sediments settle among them. Thermal infrared images of the 1823 flow on Kilauea's southwest rift zone show lower thermal inertias near the vent area where shelly pahoehoe is common while individual channelized aa flows with abundant broken pahoehoe slabs are higher thermal inertia. The increase in aa flows to the southeast leads to a general trend of increasing thermal inertias from near vent to distal areas.

Martian shield volcanoes have thermal inertias equal to or higher than their surrounding plains when atmospheric effects are removed from the data. The general increase in thermal inertias away from the summit calderas is consistent with the trend of the Hawaiian 1823 flow

and may be related to changing lava properties away from the summit. The potential contribution of roughness to thermal emissions from volcanic surfaces may aid in the differentiation of flow characteristics but it also will complicate the interpretation of thermal inertias in terms of particle size.

REFERENCES

1) *Kieffer et al., 1973. J. Geophys. Res. 78, 4291-4312.*
2) *Kieffer et al., 1977. J. Geophys. Res. 82, 4249-4291.*
3) *Zimbelman, J.R. and H.H. Kieffer, 1979. J. Geophys. Res. 84, 8239-8251.*
4) *Palluconi, F.D. and H.H. Kieffer, 1981. Icarus 45, 415-426.*
5) *Jakosky, B.M., 1979. J. Geophys. Res. 84, 8252-8262.*
6) *Zimbelman, J.R. and R. Greeley, 1983. Lunar Planet. Sci. XIV, 879-880.*
7) *Lee, S.W., P.C. Thomas, and J. Veverka, 1982. J. Geophys. Res. 87, 10025-10041.*
8) *Winter, D.F., J.A. Bastin, and D.A. Allen, 1972. In Thermal Characteristics of the Moon, J. Lucas, ed., MIT Press, 269-299.*

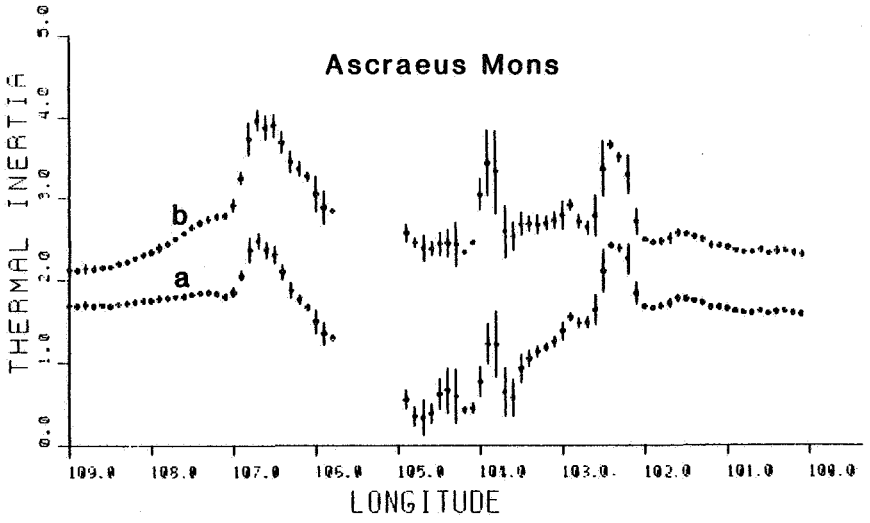

Figure 1. Longitudinally averaged thermal inertias for Ascraeus Mons. Data are from orbit 543 of spacecraft 1, around local midnight, with a spatial resolution of ~11 km^2 (2 by 5.5 km) for each measurement. Data were binned by 0.1° in longitude and the standard deviation determined for each bin. a) Observed thermal inertias (units of 10^{-3} cal cm^{-2} sec$^{-1/2}$ K^{-1}). b) Thermal inertias corrected for elevation-dependent properties of the atmosphere.

D97 N84 23528

PROGRESS REPORT: RADAR BACKSCATTER MODELLING

Gerald G. Schaber, Richard C. Kozak, and Robert L. Gurule; U.S. Geological Survey, Flagstaff, AZ

Death Valley and Northern Arizona Research

A major area of progress has been the modification of software necessary to handle the vast amounts of data and calculations required for correlation of radar cross-section and digital terrain data. The Terrain Analysis software package comprises 21 programs written and modified over the past decade for use in empirical modelling of radar backscatter from natural terrains. Two problems were addressed in the most recent modification: the inefficient and very job specific nature of the program; and the conversion of the system-specific switches in the Fortran code, which was orginally written to operate on the Modcomp II/25. The latter problem was corrected by alteration of I/O statements in the code, thus allowing the Terrain Analysis programs to be run on the much faster DEC PDP VAX 11/750 recently installed at the USGS Flagstaff facility by the Branch of Astrogeology. In August, we completed restructuring of the program to make it more widely usable, more flexible, and easier to read and modify. Restructuring consisted chiefly of breaking the programs down into component subroutines, and creating a main calling program specific to our needs, freeing the rest of the code to be more usable to others. We also added documentation, as the original documentation was very sparse.

Another area of progress involved writing a program to test the Johnson Space Center four-band scatterometer data for spurious signal data, caused by excessive aircraft roll/pitch/drift, electrical surges, or some other system glitches. The raw signal data has been reduced by JSC for about one-half hour of data over both the Death Valley and northern Arizona sites, which cover 14 different surficial deposits of Quaternary-Tertiary age, ranging from a blocky andesite flow to stabilized linear dunes to eroded massive halite deposits. Time-history plots of the scatterometer data have been generated for the northern Arizona scatterometer data, and will be completed shortly for the Death Valley data. A simple statistical program to analyze the scatterometer data is nearly complete, and will plot return radar cross section against parameters such as polarization, incidence angle, and wavelength, as well as providing statistical information. Five pairs of stereo airphotos (1:3000 scale) from the northern Arizona site, each representing a surficial unit, were selected for photogrammetric reduction to two-dimensional profiles, from which the digital data will act as input to the Terrain Analysis programs. Nine Death Valley geologic units have already been topographically reduced to reflect millimeter- to hundred-meter slope lengths; these data will be run through the revised Terrain Analysis programs by the end of September 1983 for the purpose of obtaining spatial frequency information on relief, in addition to slope information.

A catalog of our extensive terrain-roughness statistics and calibrated, four-frequency, multi-polarization scatterometer data is currently being prepared for publication at the request of many members of the radar-geology community. The catalog will support the maintainance of Death Valley as a radar backscatter calibration "super site" for all future airborne and spacecraft (e.g., SIR-B) missions. This document will be submitted in FY 84 for publication as a NASA Special Report. It will also contain simple

correlation graphs and tabulations of a wide variety of radar cross-section and terrain-roughness parameters for use in radar backscatter modelling and/or calibration by the radar-geology community at large.

Radar Penetration Research in Arid Terrains

In conjunction with our ongoing studies on surface radar backscatter modelling, we continue to make significant progress on our analysis of subsurface radar backscatter. This new aspect of the project was spurred by our discovery of significant backscatter from below several meters of sand sheet, dunes and drift sand in the Eastern Sahara of Egypt and Sudan as portrayed on the SIR-A images [1]. The results of our NASA-funded (Planetary Geology Program) radar backscatter research over the years has proven to be invaluable in assessing the radar physics involved in the Sahara subsurface returns.

During our March 1983 expedition into the Eastern Sahara, test pits were dug through sand-covered terrains representing numerous types of SIR-A image-response for the purpose of defining the depth and character of subsurface interfaces responsible for either backscatter or specular response. Blocky sandstone bedrock surfaces at depths of about 1 m were found to be responsible for the brightest SIR-A returns, whereas irregular, very dense, $CaCO_3$-cemented sand interfaces (characterizing an abrupt dielectric discontinuity) at depths of 1 to 1.5 m were responsible for the intermediate grey tone returns. The weakest responses, which delineated the extent of the ancient river valleys described by [1], are caused by smooth surface specular reflection and dissipation of the radar energy at depth within a deep sand fill in the absence of a effective radar interface (dielectric discontinuity).

Our SIR-A discoveries in the Sahara have spurred a considerable interest in re-examining the Seasat L-band radar images for evidence of penetration, especially in deserts of the southwestern United States. A number of previously overlooked indications of penetration in the Seasat data have been reported by several groups (JPL and others). We re-examined the Seasat images of Death Valley for evidence of penetration of the sand sheet and dunes (linear and complex) north of Cottonball Basin. Clear evidence of substantial penetration on these sand deposits was indeed discovered by comparing the Seasat L-band images with in-hand aerial photography, Landsat and X-band radar images. An analysis of these new results is underway and will be published in a formal paper to be submitted during FY 84.

Reference

[1] McCauley, J. F., Schaber, G. G., Breed, C. S., Grolier, M. J., Haynes, C. V., Issawi, Bahay, Elachi, Charles, and Blom, Ron, Subsurface valleys and geoarcheology of the Eastern Sahara revealed by Shuttle Radar: Science 218, 4576, 1004-1020, 1982.

D98 ABS ONLY

N84 23529

PINACATE-GRAN DESIERTO REGION, MEXICO – SIR-A DATA ANALYSIS

P. Christensen, R. Greeley, J. McHone, Y. Asmerom, and S. Barnett, *Department of Geology, Arizona State University, Tempe, AZ 85287*

Northwest Sonora is dominated by the interplay of volcanic, aeolian, and fluvial processes. Radar images (SIR-A) from the shuttle spacecraft Columbia were used to assess the radar "returns" of terrain shaped by these processes. SIR-A data were compared with Seasat data (similar to SIR-A, but obtained at a lower incidence angle) and images from Landsat, Skylab, and aircraft. Field studies and photointerpretation yield the following: 1) sand dunes are poorly imaged by SIR-A, in contrast to Seasat, evidently a consequence of the greater SIR-A incidence angle; star dunes are visible only as small bright spots representing merging "arms" at dune apices which may act as corner reflectors; 2) desert grasses and bushes (~2 m high) have little effect on radar brightness. Only larger trees with woody trunks >0.5 m across are effective radar reflectors; their presence contributes to radar bright zones along some arroyos, 3) radar brightness of lava flows decreases with surface roughness and presence of mantling windblown sediments and weathering products; however, old uplifted (faulted) flows are of equal brightness to fresh, unmantled aa flows, and 4) maar craters display circular patterns of varying radar brightness which represent a combination of geometry, slope, and distribution of surface materials (ejecta, etc.); furthermore, some radar-bright rings in the Pinacates resemble craters on radar but are observed to be playas encircled by trees. These results place constraints on radar interpretation of desert terrains and demonstrate the importance of radar incidence angle in the discrimination of dunes.

RADAR-VISIBLE WIND STREAKS IN THE ALTIPLANO OF BOLIVIA

Ronald Greeley, Philip Christensen, *Department of Geology, Arizona State University, Tempe, AZ 85287,* **and Raul Carrasco,** *Servicio Geologico de Bolivia, La Paz, Bolivia*

In the fall, 1981, the Shuttle Imaging Radar (SIR-A) experiment obtained a 50 km wide radar image across the Andes of Chile and Bolivia. The Altiplano is an interior valley within the Andes and is more than 800 km long, up to 220 km wide, and stands at an elevation of about 3600 m. Bordered by silicic volcanic rocks on the east, and predominantly by folded sedimentary rocks on the west, the valley has been partly filled with lake sediments, volcanoclastics, and glacial materials. Isolated knobs that are erosional remnants of central volcanoes or of folded rocks occur in several areas of the Altiplano. These knobs act as topographic obstructions to the prevailingly westerly winds and result in the formation of wind streaks, some of which are as long as 15 km and are visible on both optical and radar images (Fig. 1). The optically-visible streaks occur in the immediate lee of the knobs, whereas the radar-visible streaks occur in the zone downwind between the knobs. In June, 1983, a field study was conducted in order to: 1) determine the reason(s) for the "offset" between the radar- and optically-visible streaks, 2) assess the physical properties of the surface where the streaks occur, and 3) to obtain concurrent wind velocity profiles for areas inside and outside the radar-visible streak. Wind measurements were made using two portable meteorological towers, each 5 m high and outfitted with 3 anemometers. Concurrent recording of wind velocity for all 6 anemometers enabled the derivation of wind friction speeds (U_*) for the two locations for comparison of the potential for particle movement. Secondary objectives of the field trip included analyses of the radar image for the general volcanic terrain and examination of Culloma Crater, a possible impact structure.

Aerial reconnaissance and field studies showed that the optically-visible streaks consist of a series of small (<100 m wide) barchan and barchanoid dunes, intradune sand sheets, and sand hummocks (large shrub-coppice dunes) up to 15 m across and 5 m high. On Landsat images these features are poorly resolved but combine to form a bright streak. On the radar image, this area also appears brighter than the zone of the radar-dark streak; evidently, the dunes and hummocks serve as radar reflectors. The radar-dark streak consists of a relatively flat, smooth sand sheet which lacks organized aeolian bedforms, other than occasional ripples. Wind velocity profiles show a greater U_* value in the optically-bright streak zone than in the radar-dark streak. We infer that sand forms a sheet throughout the area and that turbulence generated in the wake of the knobs is sufficient to organize the sand into dunes, hummocks, and active sand sheets; winds outside the knob-wake zone are insufficient to organize the sands into large bedforms such as dunes; rather, the sand accumulates as a flat deposit which is a poor radar reflector and hence is dark.

Analyses of the Altiplano streaks and radar visible streaks in other areas (Greeley et al., 1983) demonstrate the potential for the detection of wind-related streaks by radar images of Venus. Terrestrial radar-visible streaks are well within the resolution range of the Venus Radar Mapper; should aeolian processes operate on Venus as predicted (Sagan, 1975 and others) and generate wind streaks associated with topographic features, then their detection and analysis could enable near surface atmosphere circulation patterns to be derived and would contribute to the understanding of general venusian surface processes.

The study was supported by the Planetary Geology Program, NASA, and by Contract 956428 from the Jet Propulsion Laboratory for SIR-A data analyses. We acknowledge with gratitude the cooperation and field support provided by Servicio Geologicio de Bolivia (GEOBOL).

REFERENCES

Greeley, R., Y. Asmerom, S. Barnett, 1983. Radar signatures of wind streaks: Preliminary SIR-A analysis, Lunar Planet. Sci. 14, Houston, 259-260.

Sagan, C., 1975. Windblown dust on Venus, J. Atmos. Sci. 32, 1079-1083.

Figure 1. SIR-A image of part of the Altiplano of Bolivia showing bright zone and radar dark streak associated with volcanic bedrock knobs. Prevailing winds are from the west (left). Area shown is about 20 km by 30 km.

THE CASE FOR AEOLIAN CONTROL OF METER-SCALE SURFACE TEXTURE ON MARS

Richard A. Simpson and G. Leonard Tyler
Center for Radar Astronomy, Stanford, CA 94305

Mars is our best candidate for the study of extraterrestrial aeolian effects. With the possible exception of Venus (Greeley, **EOS, 63,** 1021, 1982) and Titan there appear to be no other bodies in the solar system capable of supporting aeolian features. The origin of Mars surface units and the extent of subsequent cratering play key roles in determining surface texture. At scale sizes of 0.1-10 meters, however, there is a growing body of evidence that wind is the dominant force. In this paper we discuss the evidence (both direct and indirect) which implies that meter-scale surface texture on Mars is controlled by the wind. Since radar is uniquely sensitive to structure on these scales, radio scattering data can provide insight on aeolian activity available from no other source.

Large-Scale Aeolian Formations

Several large-scale dune formations have been identified in Viking images. Of these the dunes comprising the north polar sand sea (Tsoar, **JGR, 84,** 8167, 1979) are the most striking. The quasi-periodic and anisotropic nature of these features suggests that distinctive radar signatures might be expected. Data collected during the Viking Bistatic Radar Experiment (Simpson and Tyler, **Icarus, 46,** 361, 1981) are the only ones available, however, and no such signatures have been found.

Although no resonances or directional scattering effects have been observed, the rms roughness of the dune units measured by radar is higher than for any other unit in the polar region (Fig. 1). Values in the range $4^0 < \sigma < 6^0$ are typical. These compare with $2^0 < \sigma < 3^0$ for the permanent polar cap, the next roughest unit.

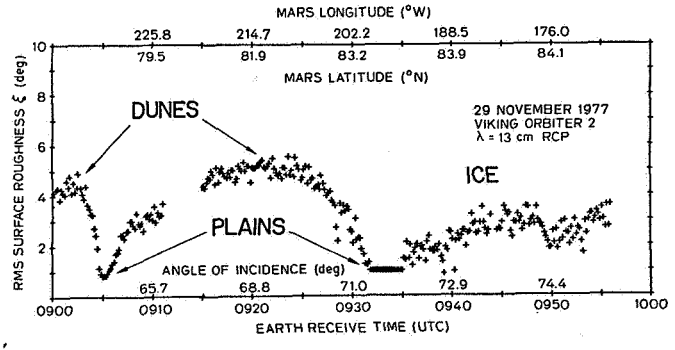

Fig. 1 - Radar roughness measured along a track which crosses three distinct surface units near Mars' north pole. Dune areas are roughest and plains units are smoothest. In the polar region the 50-100 m relief of 500-1000 m wavelength dunes is sufficient to explain the radar observations; no additional small scale roughness is necessary. In the equatorial region, such as at the VL-1 site, there is very little large-scale relief; the radar roughness must be the product of small-scale texture.

Syrtis Major is a martian plain, recently resurfaced by low viscosity basalts (Meyer and Grolier, USGS map I-995, 1977). The basalts themselves appear to be quite smooth (Simpson **et al., Icarus, 49,** 258, 1982), even by mar-

tian standards, exhibiting surface roughness values in the range $1^0 < \sigma < 2^0$ rms. At the center of Syrtis Major Peterfreund (**Icarus, 45,** 447, 1981) has identified a dune area near an ancient caldera (perhaps a source vent for the resurfacing materials). Radar tracks across this dune area show an increase in roughness (Fig. 2), albeit not to the high values seen in the polar region. Other factors may be involved (such as the roughness of the caldera and related structures), but the dune field is large enough to contribute to the increased roughness values itself.

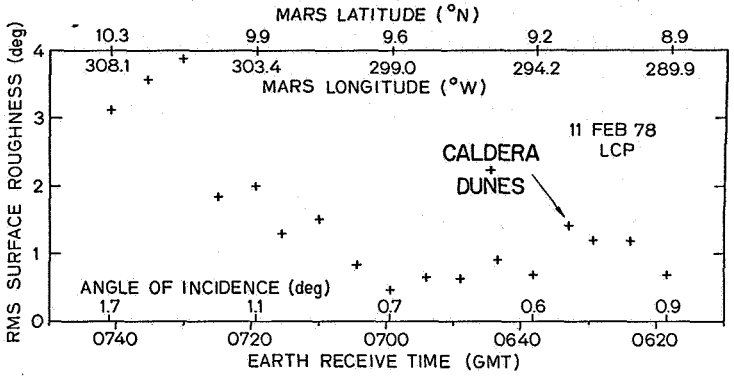

Fig. 2 - Radar roughness across part of Syrtis Major and cratered terrain to the west. Dunes are intermingled with caldera remnants near the center of Syrtis Major; the combination is rougher than the surrounding young volcanic plain.

Lack of Cratering Control at Meter Scales

Dycus (**Publ. Astron. Soc. Pac., 81,** 399, 1969) and Gault and Baldwin (**EOS, 51,** 343, 1970) have calculated that there should be a deficiency of meter-sized and smaller craters on Mars because impacting bodies would be ablated by the present atmosphere. Images returned from the surface (Mutch **et al., Science, 193,** 791, 1976) have been interpreted as confirming this -- and, in fact, indicate that the limiting size is somewhat larger.

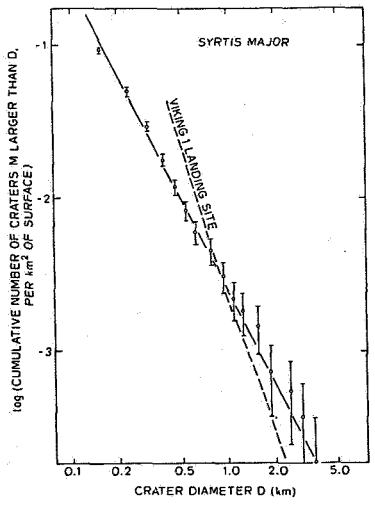

Fig. 3 - Crater density curve for central Syrtis Major. The -2 slope is also found in lunar highlands where it has been related to the absence of wavelength variation in scattering. Very few regions on Mars exhibit any wavelength variation, but Syrtis Major is one of them.

Using medium resolution orbital images from Viking, Simpson **et al.** (**Icarus, 49,** 258, 1982) have obtained cratering statistics (Fig. 3) from Syrtis Major for comparison with radar roughness estimates. The cratering data

are similar in distribution to those found in lunar highlands where the scattering behavior is independent of observing wavelength (Simpson and Tyler, **IEEE Trans., AP-30**, 438, 1982). In Syrtis Major the opposite was found -- that is, Syrtis Major is one of a very few regions on Mars where a wavelength variation **can** be detected. The conclusion is that the cratering which can be observed from orbit (crater diameters of 100 m and more) does not control the surface texture on smaller scales -- the scales important to radio wave scattering. This was the result expected from the ablation hypothesis (above) but this result extends the range of validity to larger diameters.

Aeolian Smoothing of Ancient Cratered Terrain

Approximately half of Mars' surface is covered by what appears to be old cratered crust. In the lunar case cratered highlands are among the roughest surface units studied by radar (Simpson and Tyler, **IEEE Trans., AP-30**, 438, 1982). On Mars, however, the cratered terrain exhibits intermediate values of roughness, with values as low as $\sigma \sim 2.5^0$ rms in some cases (Fig. 4). The evidence for aeolian modification of these ancient cratered surfaces is limited -- dune fields within crater rims, for example (Carr, **The Surface of Mars**, 1982). Wind streaks are common in some areas (Thomas and Veverka, **JGR, 84**, 8131, 1979), but these may be so thin that they are invisible at radio wavelengths and are not likely to be factors in determining meter-scale roughness. The Viking lander images provide additional evidence for local aeolian activity, albeit at only two spots. Since the ancient cratered terrain shows few signs of recent volcanic activity, it is fair to assume that aeolian erosion and deposition have played the major role in modifying the surface on scales of a few meters. Because most of the cratered terrain was presumably rough after the large impact events and now has a more subdued texture, aeolian processes evidently have done more to smooth the surface than roughen it in these areas.

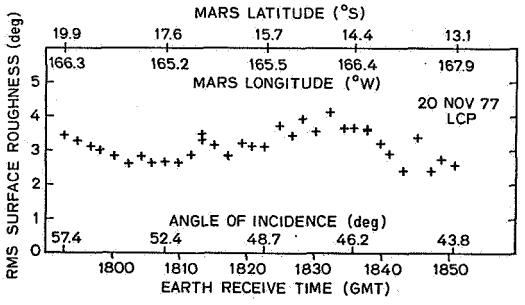

Fig. 4 - Relatively modest values of rms roughness in martian cratered terrain. Comparable surfaces on the moon would be twice as rough on scales of a few meters. We infer that aeolian processes have smoothed the martian cratered terrain at small scales.

Conclusions

The origin of Mars surface units is obviously important in determining their meter-scale roughness. Likewise, cratering must be considered in discussing their evolution over geologic time. But evidence now points toward aeolian erosion and deposition as the dominant processes in modifying surface texture on dimensions of 10 cm to 100 m. Since radio wave scattering is uniquely sensitive to roughness in this scale range, radar offers the potential for global monitoring of aeolian processes on planets like Mars.

D104

N84 23532

IS THERE RADAR EVIDENCE FOR LIQUID WATER ON MARS?

L. E. Roth, Jet Propulsion Laboratory, California Institute of Technology, Pasadena, California 91109.

Let a smooth, homogeneous dielectric be illuminated with microwave radiation. At normal incidence, the strength of the reflected signal is determined by the dielectric constant of the material. The higher the dielectric constant, the stronger the echo, the higher the reflectivity. Detection of liquid water is predicated upon the fact that below $\sim$5 GHz (P, L, S bands) the liquid water has a dielectric constant substantially higher than any known rock ($\varepsilon \simeq 80$ vs. $2 \lesssim \varepsilon \lesssim 15$). Accordingly, free water dispersed in clays/soils would cause the dielectric constant of the host material to increase. For instance, an $\sim$2.5% increase in volumetric water content would raise the dielectric constant of most soils from $\sim$3.5 to $\sim$4.2 (Birchak's mixing formula (1)), accompanied with an increase in reflectivity from $\sim$.09 to $\sim$.12 (Fresnel's formula). Reflectivity changes of this magnitude, higher values deeper into the local summer, have been noted in the Goldstone Mars S-band data (2) (Fig. 1), taken in the general area of Syria Planum ('Solis Lacus radar anomaly' (3,4)). The observed trend, coupled with an extraordinary radar-smoothness of the target led to a suggestion that ground moisture might be present (3,4).

This is an attractive hypothesis since, in addition to the standard requirement that the reflecting surface be smooth in order to minimize dissipation of incident power through diffuse scattering, it rests on one assumption only, viz. that on the penetration-depth scale, the dielectric constant be an isotropic quantity. In other words, the planet's surface should have no vertical structure. This assumption assures that the returned power is not enhanced/diminished by internal reflections and that the Fresnel's formula holds. This allows a straightforward interpretation of reflectivity variations in terms of the variations in dielectric constant.

The difficulty with the assumption of a homogeneous Mars is that, given our present knowledge, it can neither be confirmed nor refuted. The initial interpretations of the lunar reflectivity observations rested also on the assumption of a homogeneous moon (5). However, parallel with the realization that the lunar cross-section was not frequency-independent, alternative interpretations based on two-layer models were proposed (5, 6, 7). We report here some results of modeling exercises based on the early lunar two-layer models. The goal of the exercises was to simulate the behavior of radar reflectivity, at S-band, over Solis Lacus, without manipulating the dielectric constant of the base layer (i. e. without adding 'moisture'). The results are summarized in Figs. 2a and 2b. Fig. 2a. Light line; reflectivity of a configuration consisting of a variable-dielectric-constant substrate (ε ranging between 2.8 and 6.5) covered with a uniform -thickness layer of dust ($\varepsilon = 2.6$). Heavy line: reflectivity of the same configuration after removal of .10 to .15 cm of dust. Fig. 2b. Light line: reflectivity of a configuration consisting of a uniform-dielectric-constant substrate ($\varepsilon = 5.5$) covered with a variable -thickness layer of dust (h ranging between .85 and 1.00 cm). Heavy line: reflectivity of the same configuration after removal of .10 to .15 cm of dust.

It is probably a safe assumption that much, if not all, of the planet's surface is coated with a dust veneer of unknown, perhaps seasonally variable thickness. By slightly varying the thickness of this veneer it is possible to imitate the observed seasonal reflectivity changes to any degree of accuracy. It can also be demonstrated (not shown here) that an increase in the dielectric constant of the base layer due, possibly, to permafrost melting, may result, depending on the dust layer thickness, in a decrease in reflectivity, in contrast to the homogeneous-planet model which would predict a reflectivity increase. Wavelength is a parameter in the layered models. At S-band, the calculated reflectivity is more sensitive to surface layer thickness than at L-band. Simultaneous observations at different wavelengths might separate the surface effects from the subsurface ones.

The following, tentative conclusions can be stated: (a) The homogeneous-planet model has to be approached with caution. 'The use of [Fresnel's formula] for surfaces that deviate significantly from [homogeneous] model is suspect' (8); (b) The layered-planet model has to be approached with the same caution (9). Purely computational results on ideal, planar configurations may have little bearing on reality; (c) Because of the uncertainties associated with both models, this writer's answer to the question posed in the title is a qualified 'not yet'.

More sophisticated, explicit, rather than iterative (10) multi-layer models involving dust, duricrust, mollisol, and permafrost are currently under study. It is anticipated that a paradoxical situation will be reached when each improvement in the model will introduce additional ambiguities into the data interpretation.

References: (1) Wang, J. R., Schmugge, T. J. (1980). IEEE Trans. R. Sens. GE-18, 288-295. (2) Downs, G. S., Reichley, P. E., Green, R., R. (1975). Icarus 26, 273-312. (3)Zisk, S. H., Mouginis-Mark, P. J. (1980). Nature 288, 735-738. (4) Zisk, S. H., Mouginis-Mark, P. J. (1981). LPS XII, 1239-1241. (5) Hagfors, T. (1965). In Hess, W. N., Menzel, D. H., O'Keefe, J. A., Eds. The nature of the lunar surface. The Johns Hopkins Press. (6) Giraud, a. (1965). J. Res. NBS, Ser. D, 1677-1681. (7) Hagfors, T. (1967). Radio Sci. 2, 445-455. (8) Muhleman, D. O., Goldstein, R., Carpenter, R. (1965). IEEE Spectrum, 44-55. (9) Zisk, S. H., Mouginis-Mark, P. J., (1981). In Papers submitted to 3rd Int'l Coll. on Mars, 294-296. (10) Ward, S. H., Jiracek, G. R., Linlor, W. I. (1968). J. Geophys. Res. 73, 1355-1372.

Figures captions:
Fig. 1. Smoothed radar reflectivity over Solis Lacus. Running averages, bins of 7. Shown is one pair of scans along virtually identical latitudes. Light line: 24/9/71, -15.93^{o}. Heavy line: 6/10/73, -15.94^{o}. Latitudes referred to the 6.1 mbar areoid. L_s is sun's areocentric longitude. $L_s=270^{o}$ corresponds to the summer solstice in the S hemisphere.

Fig. 2. Simulated radar reflectivity over Solis Lacus. See text for details.

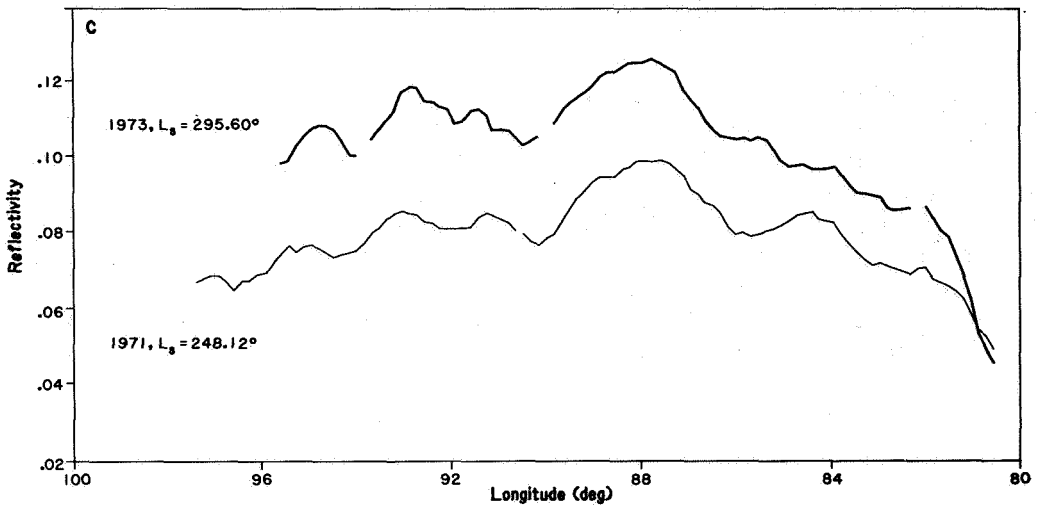
c
1973, L_s = 295.60°
1971, L_s = 248.12°
Reflectivity
.12
.10
.08
.06
.04
.02
100
96
92
88
84
80
Longitude (deg)

Fig. 1

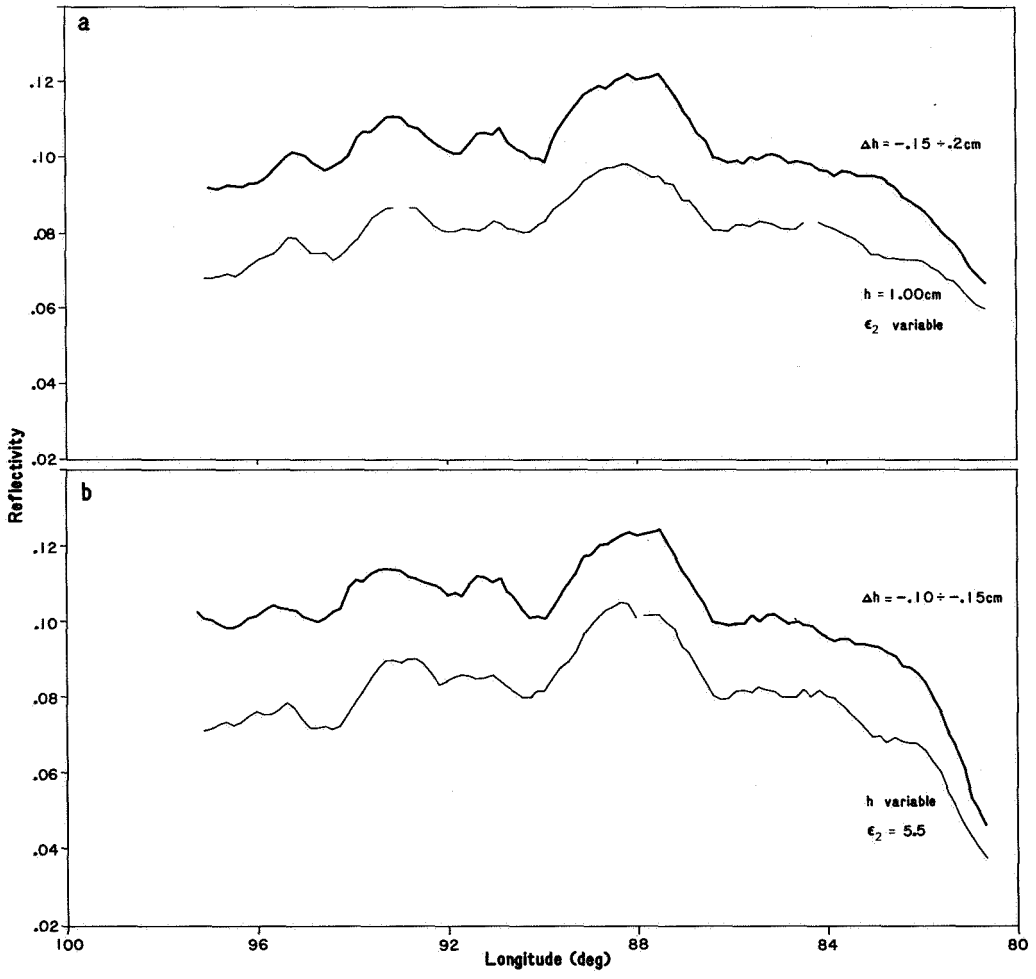
a
Δh = −.15 ÷ .2cm
h = 1.00cm
ϵ_2 variable
b
Δh = −.10 ÷ −.15cm
h variable
ϵ_2 = 5.5
Reflectivity
.12
.10
.08
.06
.04
.02
100
96
92
88
84
80
Longitude (deg)

Fig. 2

HYPSOMETRIC STUDIES OF MARS

Pamela L. Blake[1], Peter J. Mouginis-Mark[1] and Stanley H. Zisk[2]
1. Planetary Geosciences Divn., Hawaii Institute Geophysics, Univ. Hawaii Honolulu, HI 96822; 2. NEROC Haystack Observatory, Westford MA 01886.

Hypsometric analyses of planetary topography have been conducted in the past in order to assess modes of crustal formation and modification[1-3]. This approach can also be applied to more limited areas of a planet's surface[4], where the smaller diversity of terrain types permits a more direct correlation between hypsogram shape and surface geomorphology. We have been using data derived from Earth-based radar measurements[5,6] to explore the utility of this type of regional analysis and to develop criteria for the interpretation of hypsometric data for planets where no visual images are available.

The altitude data used for this analysis were derived from the 12.6 cm radar measurements obtained at JPL's Goldstone Facility during Mars oppositions in the decade 1970-1980. The data set consists of approximately 45,000 elevation measurements covering most of the circumference of the planet in the latitude bands 14.5°-22.0°S, 2.4°-6.9°S, 4.0°-12.6°N and 20.0°-23.0°N. Data resolution is 10-30 km in longitude and 80-120 km in latitude, with the highest number-density of measurements located south of 14°S. In order to standardize the spatial resolution and numerical significance of each height estimate for an area, we have applied an averaging function to these data to give elevation estimates for 2° x 2° latitude/longitude sample bins. Such an averaging technique provides a total of 1060 2° x 2° bins containing data in the southern hemisphere and 332 2° x 2° bins in the northern hemisphere. Approximately 14% of the planet's surface is included in this averaged form of the elevation data.

Close examination of the radar-derived hypsogram for Mars (Figure 1) shows that the unimodal distribution of elevations contains several second order peaks and is skewed toward a modal elevation of about 3.5 km above the 6.1 mb datum. Individual topographic features can be recognized from this hypsogram, but such interpretations are based on the known surface morphology that has been determined from spacecraft images. It is not yet known how, for example, cratered terrain, regional slopes or other morphological features could be identified using the hypsogram if no images were available for "ground-truth". Accordingly, we hope to address some of these issues by studying the hypsogram in greater detail.

If only random processes operate to alter smooth surface units, the shape of the hypsogram can be assumed to be Gaussian around the mean (and modal) elevation. In reality, regional slopes or non-uniform large-scale geological processes (e.g., cratering, canyon formation or constructional volcanism) produce asymmetries in the hypsogram. Thus the shape of the curve (the dispersion of the data in altitude-space, and the skewness, kurtosis and standard deviation of the Gaussian distribution) can be interpreted in terms of surface processes.

Our most recent studies have focused on interpreting the role that large (greater than 50 km diameter) impact craters play in influencing the shape of a hypsogram. In addition to investigating the topography of regions with different numbers of craters with different degrees of preservation,

our effort is also directed toward investigating how a radar system would smooth individual elevation estimates over the size of the radar foot-print for different types of terrain. We believe that the topographic effects of various sizes of craters with different degrees of preservation can be assessed by this method. Using a series of numerical simulations utilizing morphometric data for martian impact craters[7,8] as the primary data input, we are estimating the resultant elevation measurement for the radar system by testing various dispersion patterns for the radar echo from undulating terrains. Once this task has been completed, we intend to investigate the hypsometric properties of sloping surfaces and tectonic features; these criteria will subsequently be applied to the interpretation of other planetary surfaces such as Venus.

References:

1) M. Coradini, M. Fulchignoni and F. Visicchio (1980) The Moon and the Planets 22, 201-210.

2) H. Masursky, E. Eliason, P. G. Ford, G. E. McGill, G. H. Pettengill, G. G. Schaber and G. Schubert (1980) J. Geophys. Res. 85, 8232-8260.

3) M. C. Malin (1981) Rpts. Plan. Geol. Prog. 1981, NASA TM-84211, 369-370.

4) P. J. Mouginis-Mark and S. H. Zisk (1981) Lunar Plan. Sci. XII, 735-737.

5) G. S. Downs, P. E. Reichley and R. R. Green (1975) Icarus 26, 273-312.

6) G. S. Downs, P. J. Mouginis-Mark, S. H. Zisk and T. W. Thompson (1982) J. Geophys. Res. 87, 9747-9754.

7) C. A. Wood, J. W. Head and M. J. Cintala (1978) Proc. Lunar Plan. Sci. Conf. 9th, 3691-3709.

8) R. J. Pike (1980) Proc. Lunar Plan. Sci. Conf. 11th, 2159-2189.

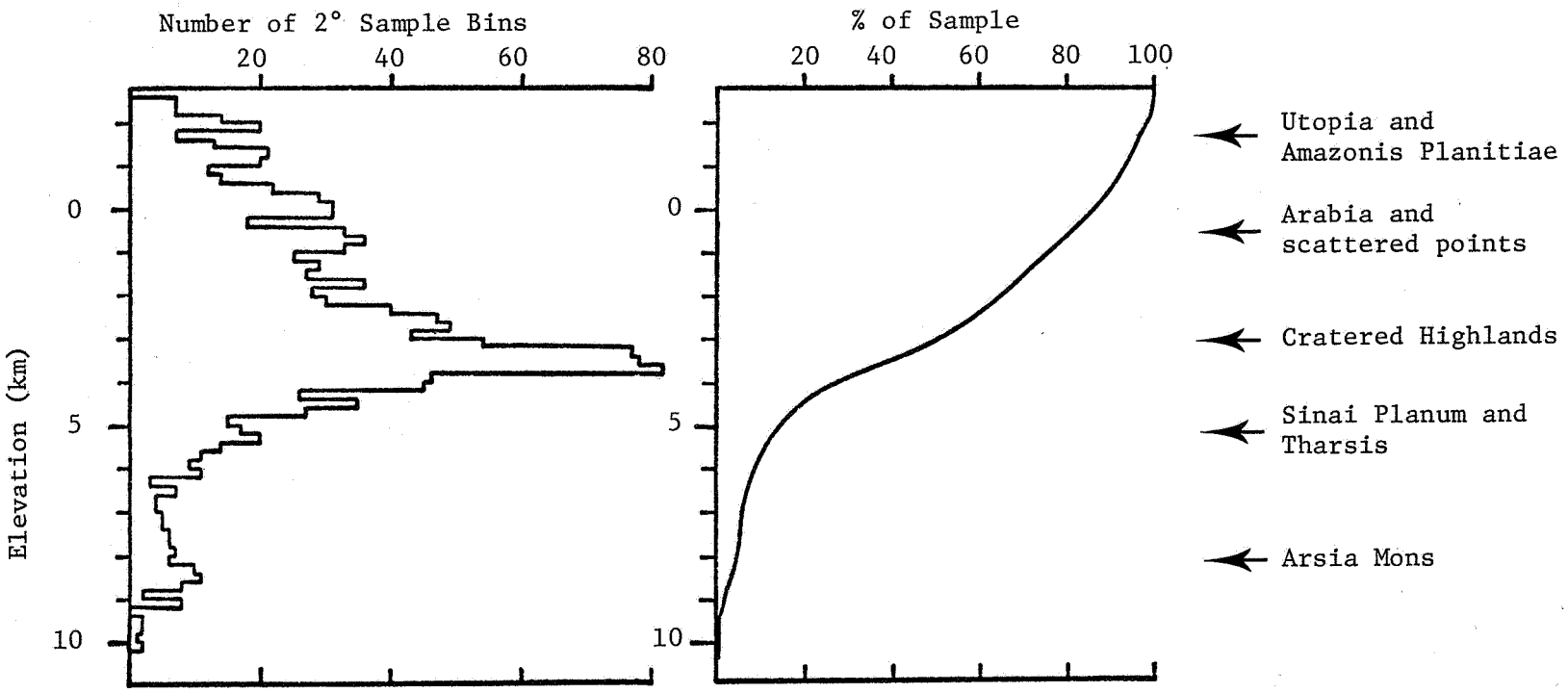

Figure 1: Frequency distribution of elevations on Mars, derived from Earth-based radar measurements of topography. Data are 2° x 2° averages (containing 10 - 50 data points per bin) and are displayed in 200 meter increments. Elevations are referenced to the 6.1 mb pressure surface. The effects of major topographic features on the hypsogram are indicated. Note that due to the incomplete coverage of Mars by the radar system (only about 14% of the surface area of the planet is included in this analysis), these curves should not be interpreted as representative of the whole planet.

D103 N84 23534

CORRECTION AND GEOLOGICAL ANALYSIS OF LUNAR 3.8 CM RADAR DATA

P. E. Clark (Murray State U.) and T. W. Thompson (JPL)

Earth-based radar observations of the moon have been taken at many wavelengths during the last ten years - at 3.8 cm (1), 70 cm (2), and most recently, 7.5 m (3). Radar returns have been collected in both polarized and depolarized form, so that it is possible to derive both topographic and local surface roughness from the data.

Until recently, work with 3.8 cm radar data had consisted of qualitative correlation of photographic and thermal IR data (4) with individual depolarized radar data frames (local surface roughness) at different wavelengths (5,6,7). These studies provided results which demonstrated that the relationship between surface roughness (measured by either thermal emission or radar reflectivity) at different wavelengths can be used as an index of a crater's state of degradation (age). However, systematic studies of craters, or other local terrane features, as well as regional or global studies of major terranes (involving a number of data frames), cannot be done until individual frames are calibrated, geometric distortion is removed, and corrected frames are mosaicked.

At this point, a number of 3.8 cm radar frames have been calibrated, and corrected for geometric distortion. Calibration was accomplished empirically, by histogram fitting, because no instrument background data is available. Then data were corrected for geometric distortion by: 1) redetermining position of individual frames using most accurate recent lunar ephemerides; 2) reprojecting frames into simple cylindrical standard map projection; 3) using most recent catalogue of lunar craters (8) to determine the exact positions of features identifiable on radar frames, and then correcting for apparent distortion (misplacement of features in frames) by resampling using a different bilinear interpolation derived for each of the parallelopideds of the set defined for each frame. A hardcopy set of corrected frames has now been produced. We are presently attempting to produce a mosaic of such corrected frames. The resulting mosaic will be used to show the systematic relationship between photographic thermal IR and radar data at different wavelengths in a region dominated by both mare and highland terrain.

REFERENCES

(1) S. H. Zisk, G. H. Pettengill, G. W. Catuna (1974) The Moon 10, p. 17-50.

(2) T. W. Thompson (1974) The Moon 10, p. 51-85.

(3) T. W. Thompson (1978) Icarus 36, p. 174-188

(4) R. W. Shorthill (1973) The Moon 7, p. 22-45

(5) S. H. Zisk, M. H. Carr, H. Masursky, R. W. Shorthill, T. W. Thompson (1971) Science 173, p. 808-812

(6) T. W. Thompson, H. Masursky, R. W. Shorthill, G. L. Tyler, S. H. Zisk (1974), The Moon 10, p. 87-117.

(7) S. H. Zisk, C. A. Hodges, H. J. Moore, R. W. Shorthill, T. W. Thompson, E. A. Whitaker, D. E. Wilhelms (1977) The Moon 17 p. 59-99

(8) C. A. Wood, C. E. Anderson, D. W. G. Arthur, R. G. Strom, E. A. Whitaker (1979) Catalogue of Lunar Craters, The Lunar and Planetary Laboratory

D104

N84 23535

MAPPING AND GEOLOGICAL ANALYSIS OF MERCURY RADAR DATA

P. E. Clark (Murray State Univ.), M. E. Strobell and G. G. Schaber (USGS),
R. F. Jurgens and G. S. Downs (JPL)

Although many radar profiles and images of the area within 20° of Mercury's equator had been obtained from 1971 to 1981, at both Goldstone and Arecibo radar facilities, surprisingly little geological analysis had been done with these data until recently (1,2,3). Topographic profiles and radar roughness reflectivity images which can be derived from these data will be crucial in completing the geological mapping of Mercury now underway at the U.S. Geological Survey (4,5,6). Earth-based radar observations of Mercury and the other terrestrial planets as well are a potentially very valuable tool in the determination of the physical nature of their surfaces. Processing of available radar data must be completed to establish any systematic relationship between radar reflectivities and roughness, density, dielectric constant, and other related geological parameters. Specific tasks accomplished for these purposes include the following.

(1) Documentation was located and searched to establish the type and quantity of Goldstone 12.5 cm radar observations which were available for Mercury. Data has been collected during approximately 50 observation periods from 1971 to 1981. Each observation period consists of large numbers of collected spectra. About half of the data, collected during 1972 and 1973, have been processed, but without adequate documentation. We chose to begin systematic processing on 1974 data, due to its relatively good documentation and quality.

(2) We attempted to establish a standardized, well-documented procedure for processing and analysis for all Goldstone earth-based observations of Mercury, by starting this effort with the relatively well-documented, high-quality radar observations of 1974. Steps included:

   (a) Preliminary processing - tape conversion and data translation;

   (b) Ephermerides determination - location of area of detection on planet from celestial mechanics considerations, incorporating standard set of ephemeris programs;

   (c) Display of measured reflectivities in delay and frequency coordinates as received by the instrument;

   (d) Mapping and display of reflectivities in planetary coordinates (longitude, latitude);

   (e) Correction - removal of noise and normal scattering function from data;

   (f) Calibration, registration, and combining of individual data runs with overlapping coverage for image enhancement;

   (g) Production of topographic (reflectivity) profiles along doppler equator;

   (h) Removal of twofold ambiguity from reflectivity maps;

   (i) Accurate determination of Mercury's spin axis.

Work on items (a) through (b) has been completed. We are in the process of producing hardcopy of individual data frames processed through Step (e). In regard to Step (f), preliminary work has shown that the signal to noise ratio of data is noticeably enhanced when frames from half of an observation period (approximately 10) are simply averaged together, even without adjusting for the slight shifts in longitude of the subradar point from frame to frame. Further work is being done to calibrate and register series of overlapping frames taken during each observation period. Work has been initiated on developing and revising existing software to create topographic profiles from each observation period of 1974 (Step g), to remove twofold ambiguity from the reflectivity maps, and to determine Mercury's spin axis (and hence exact longitudinal and latitudinal coordinates). On the bases of our preliminary calculations and our ability to match features on derived radar reflectivity maps with known geological features, the spin axis has already been determined surprisingly accurately at the level of the spatial resolution of the Mercury radar data.

(3) In collaboration with colleagues at the U.S. Geological Survey (4,5,6), and on the basis of analysis of available profiles and reflectivity maps, we have made the following determinations:

(a) Correlation between radar and geological features on the 1:5 million Mercury maps, H-6, H-6, and H-8, and on the 1:15 million map are generally quite good. Overlapping portions of Goldstone radar profiles agree well. In addition, we have found good correlation between the one Arecibo radar profile which we managed to obtain, and Goldstone radar profiles of the region (H-8 and west near Caloris).

(b) Systematic elevation and roughness differences between major terranes are quite noticeable on Mercury, though smaller in magnitude than analogous differences on the moon. Extensive mare-like smooth plains units are low in elevation; smooth plains around Caloris Basin are more than 2 km lower than adjacent material. A volcanic origin is inferred for the unit.

(c) Craters, ridges and scarps along the radar track have distinctive signatures. Ridges and scarps reach heights of almost 1 km. Crater depth-to-diameter ratios appear to be much lower on Mercury than on the moon; depth-to-diameter ratios are 1:90 for the fresh basin Mozart (280 km diameter) and the crater Titian (185 km diameter).

(d) Radar profiles of the unimaged region southwest of Caloris basin reveal high areas which may be structural rings, and a low area which may be another basin.

(e) It appears that the extensive surface heating of Mercury may be responsible for the relatively subdued topography of Mercury, due to extensive plastic deformation.

Active collaboration by our interdisciplinary team on the radar geology of Mercury has proved to be quite fruitful and will continue to provide more details on the nature and origin of Mercury's surface, and the relationship between the surfaces of Mercury and the other terrestrial planets.

REFERENCES

(1) S. Zohar and R. M. Goldstem, 1974, 1974, Astron J, 79, pp. 85-91.

(2) R. F. Jurgens, 1980, personal communication, from S. Zohar unpublished report of 1974.

(3) P. E. Clark, 1983, Lunar and Planetary Science XIV, pp. 119.

(4) P. E. Clark, G. G. Schaber, M. E. Strobell, R. F. Jurgens and G. S. Downs, 1983, DPS Abstracts.

(5) M. E. Strobell, P. E. Clark, G. G. Schaber, R. F. Jurgens, 1983, GSA Abstracts.

(6) P. E. Clark, M. E. Strobell, G. G. Schaber, R. F. Jurgens and G. S. Downs, 1983, in preparation.

(7) D. E. Campbell, 1982, personal communication.

MERCURY: TOPOGRAPHIC AND GEOLOGIC DATA FROM EARTH-BASED RADAR OBSERVATIONS

Strobell, M. E., U.S. Geological Survey, Flagstaff, AZ; Clark, P. E., Murray State University, Murray, KY; Schaber, G. G., U.S. Geological Survey, Flagstaff, AZ and Jurgens, R. F. and Downs, G. S., Jet Propulsion Laboratory, Pasadena, CA

Significant new geologic information has been revealed by comparing 1:5 million scale geologic maps of the equatorial zone quadrangles of Mercury (H-6, H-7 and H-8) to Earth-based elevation profiles and surface reflectivity maps of Mercury obtained in the early 1970's at the Arecibo (PR) and Goldstone (CA) radar facilities. These data consist of 23 Goldstone images and profiles of polarized return data at 12.5-cm wavelength [1,2] and one Arecibo profile [3]. Radar data with 150-m vertical accuracy and 10- to 20-km horizontal resolution are available for areas between latitudes 13° N. and 11° S. In general, these data sets show excellent correlation between: (1) relative elevation and roughness differences that are reflected by mapped geologic contacts; (2) mapped ridges and scarps that display distinctive radar signatures; and (3) position and morphology of crater-and-basin topographic elements. Inferences can also be drawn about topographic and geologic terrain beyond the area imaged by Mariner 10 cameras. Overlapping portions of seven radar profiles and images correlate well. The elevation profiles have confirmed that large areas of smooth plains, which resemble lunar mare units, commonly occur in areas of low elevation; their location supports the hypothesis that smooth plains may be of volcanic origin [4]. An extensive area of smooth plains surrounding the 1300-km-diameter Caloris Basin, as seen by radar in the H-6 quadrangle is more than 1 km lower than adjacent cratered plains material. Ridges and scarps along the radar tracks are as much as 900 m high. The large, relatively fresh craters Mozart (280 km diam.) and Titian (120 km diam.) have very low depth-to-diameter ratios of .007 and .008, respectively. The old crater Thokar and an old C_1 crater south of crater Lermontov show ratios of .009. In the unimaged area west of long 190°, elevated and depressed zones identified from radar profiles are probably associated with Caloris ring structures. Elevation differences are about 3 km between the basin rings and inter-ring lows.

References

[1] Zohar, S., and R. M. Goldstein, Astron. J., 79, 85-91, 1974.
[2] Zohar, S., and R. M. Goldstein, unpublished report, The 1972, 1973 probe of Mercury.
[3] Campbell, D. B., written communication, March 7, 1980.
[4] Strom, R. G., N. J. Trask, and J. E. Guest, Tectonism and volcanism on Mercury: J. Geophys. Res., 80(17), 2420-2507, 1975.

Chapter 11

STRUCTURE, TECTONICS AND STRATIGRAPHY

ELYSIUM REGION, MARS: CHARACTERIZATION OF TECTONIC FEATURES.

J. Lynn Hall and Sean C. Solomon, Dept. of Earth and Planetary Sciences, M.I.T., Cambridge, MA 02139; James W. Head, Dept. of Geological Sciences, Brown University, Providence, RI 02912; and Peter J. Mouginis-Mark, Planetary Geosciences Division, Hawaii Institute of Geophysics, University of Hawaii, Honolulu, HI 96882.

Introduction. The Elysium region is the second largest volcanic center on Mars [1,2]. It consists of a broad dome, 2400 by 1700 km, on top of which sit three volcanoes: Elysium Mons, Hecates Tholus and Albor Tholus [2]. The Elysium province has both a topographic rise and a broad positive free-air gravity anomaly [3]. On the basis of crater densities, the surfaces of both the plains and the shields of Elysium are older than their Tharsis counterparts [2,4], with the surfaces of the volcanoes being about 1 b.y. old.

In this paper we identify and characterize the tectonic features of the Elysium region. Identification of features was made using USGS controlled photomosaics (Elysium quadrangle, and portions of Amenthes and Cebrenia quadrangles); Viking Orbiter photographic data were used in individual cases to assist in identification. The positions and orientations of tectonic features can then be used, in conjunction with estimates of the mass of the volcanic load obtained from gravity modelling, to constrain the thickness of the elastic lithosphere in the region.

The principal physiographic features of the Elysium region are shown in Figure 1. These features can be grouped into five categories:

(1) Elysium Mons concentric fractures. An extensive set of concentric graben almost entirely encircles Elysium Mons at distances of approximately 100 to 450 km from the central caldera. The two most distant fractures cut across the shield of Albor Tholus, the southernmost shield of the group, and disappear into the volcanic plains that surround the shield. Some of the fractures are quite fresh in appearance, while others appear to have been mantled by subsequent volcanic or aeolian activity. Differences in appearance of the graben cannot be completely attributed to differences in ages of the fractures, but may also be due to the asymmetric geometry of the mantling material. The presence of concentric fractures indicates that there has been failure of the elastic lithosphere under the load imposed by the Elysium Mons shield [5], and their locations can be used to constrain the thickness of the lithosphere at the time of fracturing [6,7]. The absence of concentric fractures around the other two shields is inconclusive, since both Hecates Tholus and Albor Tholus are surrounded by relatively young lava plains originating at or near Elysium Mons [8]. Any early episodes of fracturing would likely have been obscured by these later flows.

(2) Narrow linear depressions. Most of these features have a NW-SE trend. The majority of these features are interpreted as being fractures, and tectonic in origin.

(3) Wide depressions. These also have a predominantly NW-SE trend. Although some of these features may be exclusively fluvial or erosional in origin, others, particularly the concentric depressions SE of Elysium Mons, are almost certainly tectonic in origin. If formation of graben was followed by volcanic activity (as was the case in Elysium, where fractures are in places partly covered by younger lava flows), erosional processes could have modified the graben to produce the features observed.

(4) Sinuous depressions. These are found throughout Elysium, most notably in the Elysium Fossae region NW of Elysium Mons. Many of these features originate in the wide linear depressions [9], which suggests some tectonic control of the volcanic history. These features closely resemble lunar sinuous rilles [9] and are thought to be the result of erosional processes [10].

(5) Ridges. There is a system of ridges on the eastern edge of Elysium Planitia, generally concentric to the center of the topographic rise. These ridges, which lie in the terrain between the Elysium and Tharsis regions, resemble in appearance both lunar mare ridges and the ridges of the east Tharsis system. Ridges such as these are taken to be evidence of horizontal compression of near-surface material [5,11,12].

Conclusions. The linear features trending NW-SE through the Elysium region indicate a regional stress field with least compressive stress oriented NE-SW. These features may be the result of large-scale lithospheric loading over Elysium Planitia, similar to that which led to radial fracturing in Tharsis [5,13,14]. The failure features around Elysium Mons are most prominent in locations where the local stress field adds constructively to the regional field. Future work will be directed towards determining the relative contribution to the regional stress field of large-scale loading in the Elysium and Tharsis provinces.

References: [1] M.H. Carr (1973) JGR, 78, 4049. [2] M.C. Malin (1977) BGSA, 88, 908. [3] W.L. Sjogren (1979) Science, 203, 1006. [4] J.B. Plescia and R.S. Saunders (1979) PLPSC10, 2841. [5] S.C. Solomon and J.W. Head (1982) JGR, 87, 9755. [6] S.C. Solomon et al. (1979) NASA TM 80339, 60. [7] R.P. Comer et al. (1979) PLPSC10, 2441. [8] S.H. Brown (1980), unpublished. [9] M.H. Carr (1981) The Surface of Mars, Yale. [10] P.J. Mouginis-Mark and S.H. Brown (1981) LPSXII, 729. [11] S.C. Solomon and J.W. Head (1979) JGR, 84, 1667. [12] S.C. Solomon and J.W. Head (1980) RGSP, 18, 107. [13] R.J. Willemann and D.L. Turcotte (1982) JGR, 87, 9793. [14] W.B. Banerdt et al. (1982) JGR, 87, 9723.

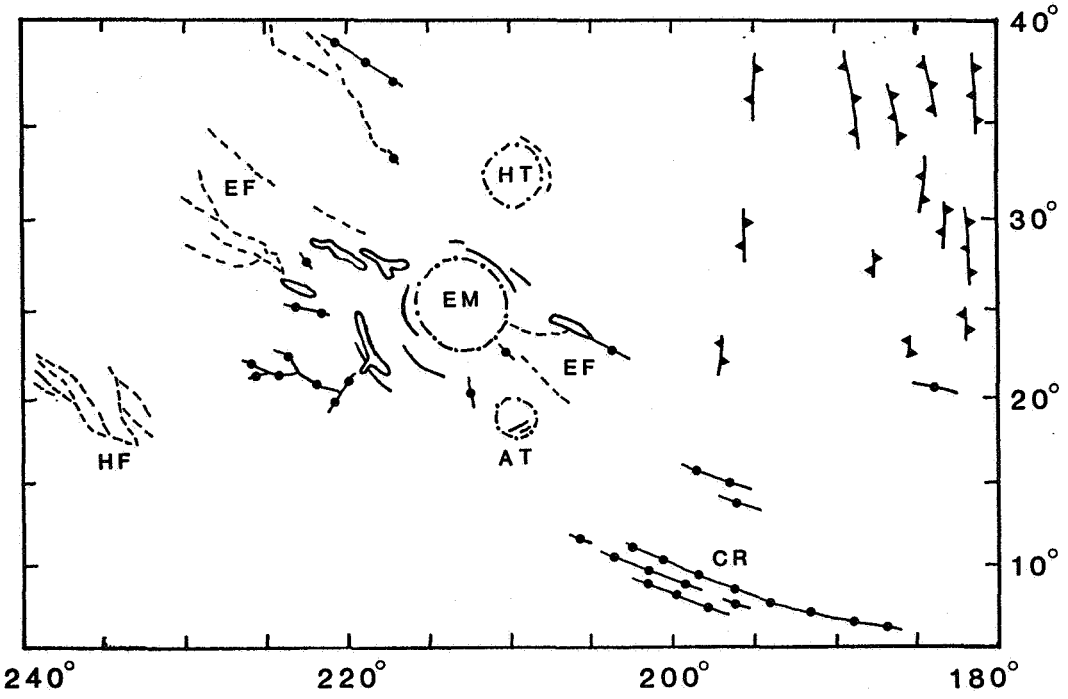

Fig. 1. Physiographic features of the Elysium region. EM = Elysium Mons; AT = Albor Tholus; HT = Hecates Tholus; HF = Hephaestus Fossae; EF = Elysium Fossae; CR = Cerberus Rupes. Solid line indicates EM concentric fractures; beaded line = narrow depression; closed line = wide depression; dashed line = sinuous depression; dotted line = edge of volcanic shield; notched line = ridge. Some detail has been lost in reduction. Prepared on base map I-1321, using USGS photomosaics and VO photographs.

D107

ANCIENT VOLCANO-TECTONIC STRUCTURES OF THE OLYMPUS MONS REGION, MARS

Elliot C. Morris, U.S. Geological Survey, Flagstaff, Arizona 86001

Two old volcano-tectonic collapse structures are exposed north and northeast of the huge shield volcano, Olympus Mons. They are semicircular and were probably low shield volcanoes similar to Alba Patera, but whose central portions have subsided or collapsed. They form the basement upon which younger volcanic materials of Alba Patera and Olympus Mons have been emplaced.

The oldest structure, Acheron Fossae (fig. 1) is over 700 km across and is north of Olympus Mons. It has a surface of considerable relief broken by graben and extensive en echelon and parallel fractures and faults with varied displacements [1]. Acheron Fossae is the most densely cratered in the Olympus Mons region (4,000-5,500 craters >1 km/10^6 km^2); most craters postdate the fracturing. The structure must have formed very early in martian time.

The second structure is Halex Fossae* (fig. 2), northeast of Olympus Mons [2,3]. Where exposed, it is cut by a series of arcuate grabens that become closer spaced toward its center. The radii of the fractures indicate that the structure may be at least 250 km across and centered beneath the Olympus Plains. Lava flows appear to have issued from some of the arcuate fractures and to have flowed radially away from the center of Halex Fossae. North of Halex Fossae, material of the same age as Halex Fossae overlaps Acheron Fossae. The density of craters on the Halex Fossae material (3,200-4,400 > 1 km/10^6 km^2) indicates an old age for its formation but one younger than that of Acheron Fossae. These two ancient volcanic-tectonic structures are evidence that the Olympus Mons region has been the locus of major volcanism over much of martian history.

References

[1] Morris, E. C., and Howard, K. A., 1981, Geologic map of the Diacria quadrangle of Mars, 1:5,000,000, U.S.G.S. Geologic Series Map I-1286.

[2] Schaber, G. G., Horstman, K. C., and Dial, A. L., Jr., 1978, Lava flow materials in the Tharsis region of Mars, Proc. Lunar Plant. Sci. Conf. 9th, p. 3433-3458.

[3] Moore, H. J., and Hodges, C. A., 1980, Some martian volcanic centers with small edifices, NASA Technical Memorandum 82386, p. 266-268.

*Halex Fossae is a provisional name applied to the concentric fractures centered on 27.5° N and 126.5° W. This name has not yet been adopted by the International Astronomical Union.

Figure 1. Acheron Fossae north of Olympus Mons (centered at 38° N., 135° W.). The western and northern margins are buried by young plains material (ps), and its eastern edge covered by Alba Patera flows (ap). The central area is a shallow basin mantled by eolian material (afm) and the southern half is buried by the aureole deposits of Olympus Mons (oa). Fields of small volcanic domes and cones (vu) occur along the western and northern margins and a linear volcano (vu) 180 km long trends northeast. Faulting has been most intense in its eastern part and has been the center for eruption of young lava flows (op) that have buried parts of its eastern margin. Distance across picture about 900 km.

Figure 2. Halex Fossae northeast of Olympus Mons (centered at 27.5° N., 126° W.). The structure is partly buried by Alba Patera flows (ap), Olympus Plains flows (op), and aureole deposits (oa) of Olympus Mons. Several small volcanic cones (vu) $\cong$ 2 km across are present in the floor. The probable center of the structure is indicated by X. Arrows indicate direction of flow. Flow fronts are accentuated by heavy lines. Distance across picture about 260 km.

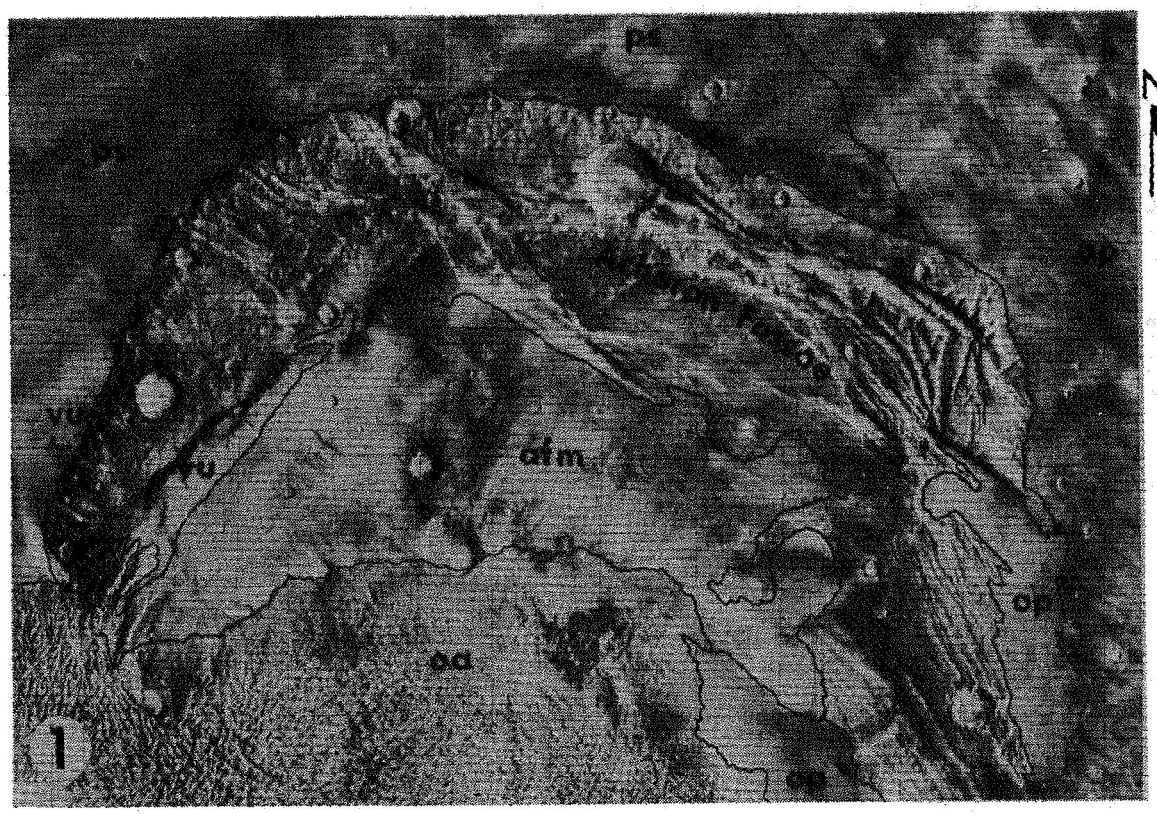
pá
vu
vu
átm
oa
op
op
1

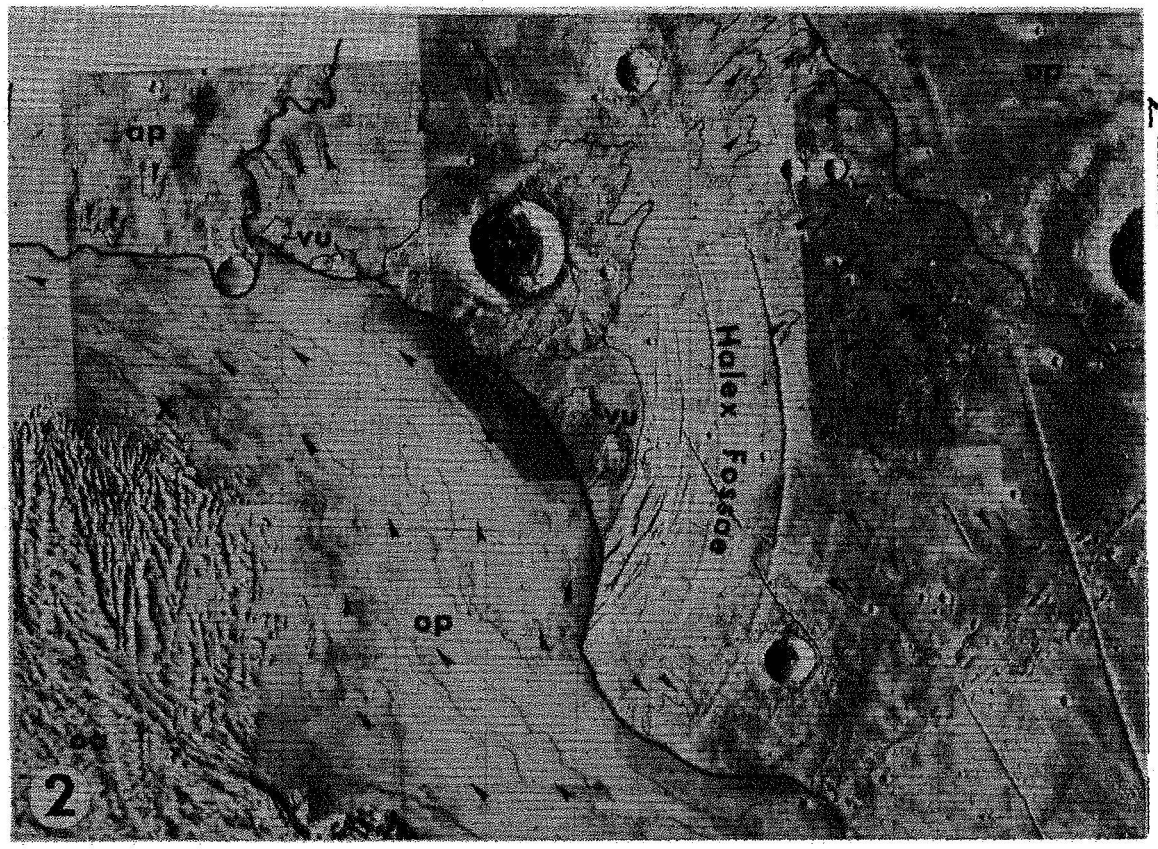
op
op
vu
vu
Holex Fossae
op
oa
2

Dp8 N84 23539

MARS PALEOSTRATIGRAPHY

David H. Scott, U.S. Geological Survey, Flagstaff, AZ 86001

The relative time of emplacement of some major rock units on Mars was recognized to some degree from geologic mapping using Mariner Images. Correlation charts showing the map units and their position in sequence, however, displayed little discrimination in their vertical range of occurrence, as shown, for example, on the 1:25 million scale geologic map of Mars [1]. A more detailed time-stratigraphy is currently being developed as Viking geologic mapping of the planet progresses.

As in many places on Earth, ancient rocks on Mars are structurally deformed and probably metamorphosed by a variety of processes. They appear as prominent peaks, mountains, and highland complexes that are relatively resistant to erosion. Their old age (Noachian System) is substantiated by stratigraphic relations and supported by crater counts. Rugged groups of mountains along the southern end of Claritas Fossae are believed to be among the oldest rocks on Mars. Other ancient occurrences form the rim of Acheron Fossae and also project as prominent ridges and mountains above the plateaus of Tempe Terra and Lunae Planum.

The youngest martian materials (Amazonian System), aside from thin ephemeral eolian deposits, consist of lava and pyroclastic flows around and in the vicinity of Tharsis Montes, and of vast dune fields in the polar regions.

Between these old and young end members lie the majority of rock units, which form the southern highlands and northern lowland plains; they consist of a varied and widespread assemblage of volcanic materials, impact breccias, channel and floodplain deposits, and layered deposits of alluvial, eolian, or volcanic origin. These rocks belong largely to the Hesperian System and have an intermediate stratigraphic position somewhat similar to that of the Imbrian and Erastothenian Systems on the Moon; the youngest and oldest martian rocks correspond with the lunar Copernican and pre-Imbrian ages, respectively.

The geologic time scale of Figure 1 reflects our present concept of correlations between time-stratigraphic systems on Earth, Moon, and Mars. Although materials and events on the Mars column are indicated by arrows as discrete points in time, most extend over relatively long periods.

References

[1] Scott, D.H., and Carr, M.H., 1978, Geologic map of Mars: U.S. Geol. Survey Misc. Inv. Map I-1083.

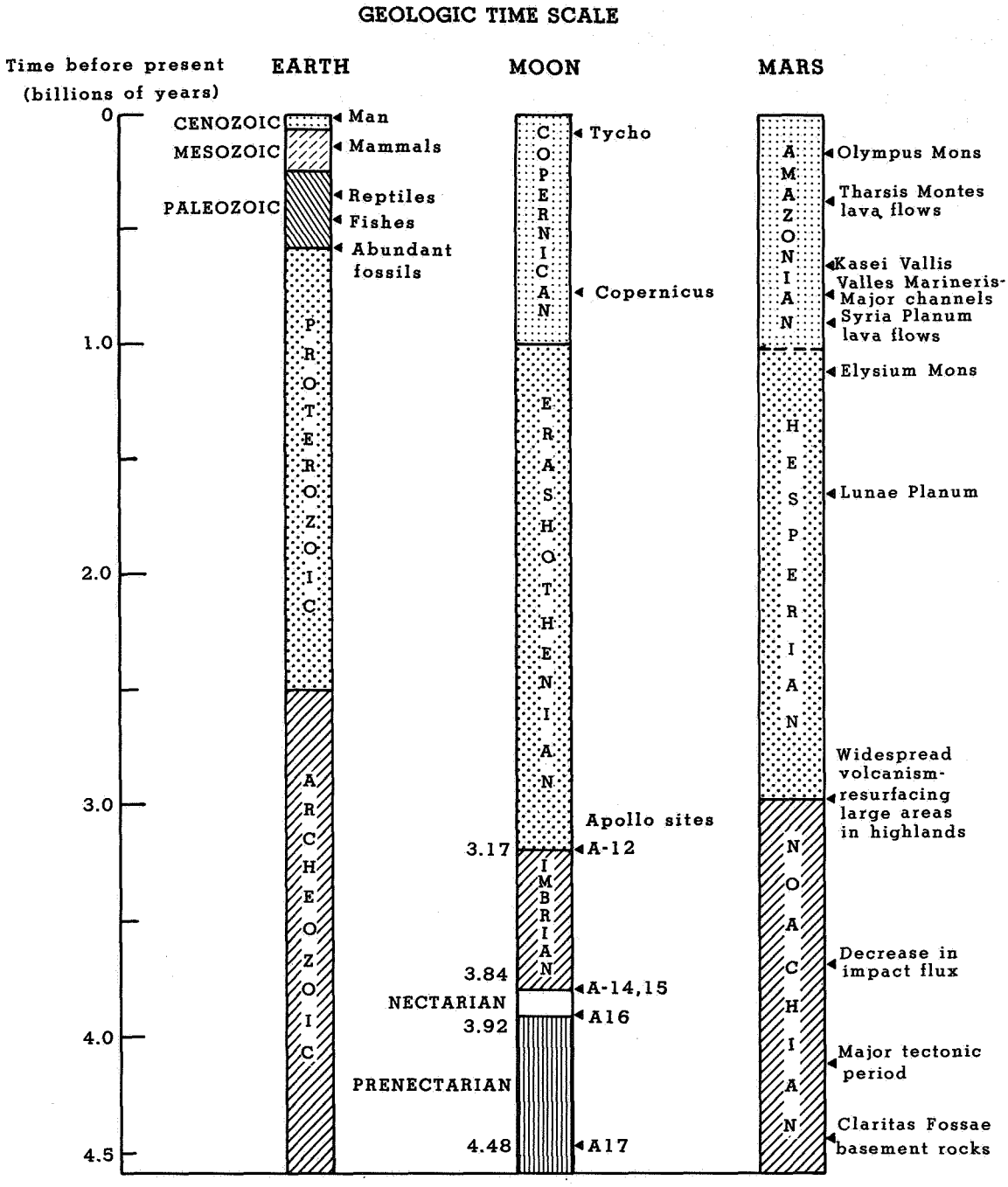

Figure 1. Hypothetical correlation between time-stratigraphic systems on Earth, Moon, and Mars

D109

N84 23540

VALLES MARINERIS LAYERED DEPOSITS: IMPLICATIONS OF ORIGIN

David H. Scott and Nanci E. Witbeck, U.S. Geological Survey, Flagstaff, AZ 86001

Layered deposits within Valles Marineris and its associated system of canyons (Fig. 1) have been considered to consist of two different rock types: (1) thick, competent, cliff-forming, light and dark bedded material in canyon walls, and (2) relatively thin, alternating series of light and dark layered material, both horizontal and inclined, that form rounded hills and large flat-topped mesas rising above the canyon floors [1]. The dissimilarity in appearance between canyon wall and floor materials, as well as their contrasting patterns of erosion, has been considered strong evidence that their modes of origin were different [2].

Most workers agree that the wall rocks are volcanic flows probably derived from Tharsis Montes and other volcanic sources in the region [1,3]. However, several hypotheses have been advanced to account for the softer-appearing, finely stratified floor deposits. Chief among them was the proposal by McCauley [1] that the floor deposits were waterlaid sediments that accumulated in large lakes within the canyons; their deposition was followed by episodes of catastrophic draining from place to place in the canyon systems. Materials eroded from canyon walls and eolian material were the source of the sediments. McCauley stated that no other process could explain the horizontal attitude and lateral continuity of individual beds, especially as there were no obvious volcanic sources on chasma floors.

On the other hand, Peterson [4], in her studies of the central plateau of Hebes Chasma, found it difficult to ascribe such processes to Hebes Chasma, which is an enclosed basin. Also, the plateau in Hebes, as well as layered plateaus within some other canyons of Valles Marineris, is at about the same elevation as the plains surrounding the Valles Marineris canyon system [5]. These conditions would imply sedimentary infilling of a vast lake to its brim, followed by removal of water and re-excavation of the basin. Peterson [4] proposed a pyroclastic theory of origin: the infilling of the chasma during its formation by ash-flow tuffs from sources beneath the floor or within the Tharsis region. According to this hypothesis, infilling of the chasma was followed by continued collapse of the chasma walls and eventual isolation of the central plateau.

In early investigations of Valles Marineris from Viking pictures, Malin [6] had also considered improbable the filling of large martian canyons nearly to their brims. Malin suggested that the mesas within the canyon were simply isolated remnants of the adjacent plateau material. Moreover, Blasius and others [2] showed that some layered light and dark materials on the canyon floor could be traced into the main walls of the canyons, indicating that not all layered material was emplaced after canyon formation. Table 1 summarizes some of our own and earlier workers' observations, evidence, and assumptions regarding the various origins of canyon floor layered deposits. These summaries favor either (1) accumulations of clastic sediments in former large bodies of water or (2) *in situ* remnants of adjacent plateaus, now separated from their parent bodies.

Based on our present geologic mapping of Valles Marineris using Viking Images, we favor the concept that the larger and thicker accumulations of

layered deposits occurring in Hebes, Ophir, Candor, and Melas Chasmata are part of the original canyon wall materials. In places they may have been dissociated from the walls by faulting. Their surfaces are deeply dissected and scoured into smooth streamlined shapes characteristic of erosion by flowing water. Evidence of water erosion occur in various places throughout the canyons, and we do not dispute the former presence of large bodies of water. They probably did not, however, survive long enough to become receptacles for thick accumulations of sedimentary material.

References

[1] McCauley, J.F., 1978, Geologic map of the Coprates quadrangle of Mars: U.S. Geol. Survey Misc. Inv. Map I-897.

[2] Blasius, K.R., Cutts, J.A., Guest, J.E., and Masursky, H., 1977, Geology of the Valles Marineris: First Analysis of imaging from the Viking 1 Orbiter Primary Mission: Jour. Geophys Res. v. 82, no. 28, p. 4067-4091.

[3] Scott, D. H., and Carr, M. H., 1978, Geologic map of Mars: U.S. Geol. Survey Misc. Inv. Map I-1083.

[4] Peterson, C., 1981, A secondary origin for the central plateau of Hebes Chasma: Proc. Lunar Planet. Sci. Conf. 12th, p. 1459-1471.

[5] Wu, S.S.C., Schafer, F. J., and Jordan, R., 1980, Topographic mapping of Mars: 1:2 million contour map series (abstract). In Reports of Planetary Geology Program, 1980, NASA TM 82385, p. 458-461.

[6] Malin, M.C., 1976, Nature and origin of intercrater plains on Mars: Part 3 of Ph.D. thesis, California Inst. of Tech., Pasadena, 176 p.

[7] Lucchitta, B.K., 1982, Lakes or playas in Valles Marineris (abstract). In Reports of Planetary Geology Program 1982, NASA TM 85127, p. 233-234.

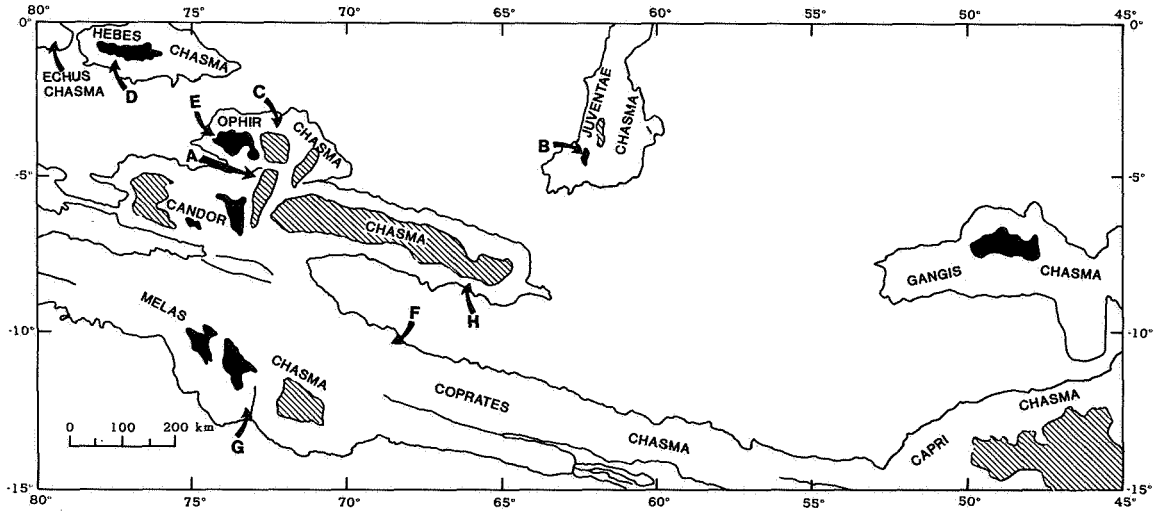

Figure 1. Index map showing locations of generally acknowledged layered deposits (solid black) and possible layered deposits (lines) in Valles Marineris. Letters refer to approximate locations of Viking images illustrating examples in Table 1.

TABLE 1

Evidence Supporting Possible Origins of Canyon Layered Deposits

Secondary Deposits (Lake Beds)	Primary Material (Canyon Wall Equivalent)
1. Distinct difference in erosional style between canyon walls and interior plateaus, i.e., spur-and-gully versus fine rilles (A. Viking Image 66A28)	1. Spur-and-gully develops where canyon walls undisturbed by slides, and retreat by slow mass-wasting produces gentle slopes; thus erosion of interior plateaus may be occurring too fast to form spur-and-gully topography
2. Cyclic bedding seen on slopes of interior plateau but not commonly seen in canyon walls (B. Viking Image 907A05)	2. Layers best developed in lower softer parts of canyon walls but mostly covered by talus and landslides; layers observed where flood drainage and erosion have been severe, exposing lower wall section (C. Viking Image 914A10)
3. Large terrestrial basins fill by subsidence of basin floor in response to depositional load of infilling sediments, build up thick deposits in relatively shallow water	3. Interior plateaus in Hebes and possibly in Gangis (Blasius and others 1977), close to elevation of surrounding canyon rim; hard to explain filling to brim, then re-excavation of "moat" several km deep (D. Viking Image 645A60)
4. Overlap of highly eroded interior remnants of the plateau by the layered materials indicates layered materials postdate plateau rocks [7]	4. Layered deposits can be traced to canyon wall at: (a) west end of Ophir Chasma (E. Viking Image 917A09); (b) north wall of Coprates Chasma (F. Viking Image 80A02, 912A17); (c) base of wall spur, south Melas Chasma (G. Viking Image 91A05); (d) dark layer observed near base of wall in east Candor Chasma, similar dark layer near base of interior deposit (H. Viking Images 80A05, 80A07)
5. Landslides well-developed in canyon walls, interior plateaus do not form landslides; eolian erosion commonly associated with interior deposits, not common in canyon walls, indicates differences in cohesion of materials (Lucchitta, 1982, Transcript of oral presentation at PGPI)	5. Differences in height and slope steepness between canyon walls and interior plateaus may account for erosional differences

D110

COMPRESSIONAL FEATURES IN THE THARSIS REGION OF MARS: I. GEOGRAPHIC EXTENT OF DEFORMATION

Thomas R. Watters and Ted A. Maxwell, National Air and Space Museum, Smithsonian Institution, Washington, D.C. 20560

Studies of the stratigraphy of southwest Coprates have led to further constraints on both the geographic extent and the relative age of the major compressional ridge forming events in the Tharsis region of Mars. Southwestern Coprates is characterized by curvilinear ridges that are regularly spaced, suggestive of harmonic folding (Saunders and Gregory, 1980; Watters and Maxwell, 1982). The western edge of the ridged plains unit of Coprates is marked by volcanic flow fronts. Some of these flows are present in the inter-ridge plains where ridges are partially to completely obscured by flow lobes. In an enhanced Viking Orbiter image, a ridge can be seen completely surrounded by a flow with only a small portion of the ridge crest still exposed (Fig. 1). Comparison of partially buried ridges on the western edge of the ridged plains unit to those in central Coprates suggests that flooding of the inter-ridge plains does not exceed a few hundred meters. The morphological relationship between the flow units to the west and the ridged plains indicates that the deformational events in this region predates the emplacement of the younger units.

Using topographic profiles attained from radar altimetry data by Roth et al. (1980) a cross-section of the area was constructed (Fig. 2). The cross-section shows the thickening volcanic sequence of the Syria Planum flow units (AHsp) to the west (1800-2400 cumulative crater density, number of craters larger than 1 km diameter/10^6km; Scott, 1981). These units are underlain by the ridged plains units (Hprg; Scott and Carr, 1978; 5000-12000 cumulative crater density range; Wise et al., 1979) that are probably emplaced on a thick regolith inter-mixed with pyroclastic units. The regolith lies on the ancient heavily cratered Terra Material (HNht; Scott, 1981). The presence of embayed and buried ridges in southwest Coprates and the complete absence of compressional ridges on the stratigraphically younger Syria Planum flow units indicates that the deformation event that generated the ridges occurred after the emplacement of the ridged plains units and did not extend beyond the emplacement of the Syria Planum flows. This basic stratigraphy is repeated north of Coprates in the northwest Lunae Palus region. Here ridges are present less than 20 km from the contact between the ridged plains units and the Alba Patera flow unit (AHap; 2400-3200 crater density range; Scott et al., 1981). As in southwest Coprates, no ridges occur on the stratigraphically younger units to the west.

Evidence of compressional deformation in Tharsis is found as close as 1100 km and as distant as 5100 km from the regional topographic center (near northern Syria Planum, corresponding to the highest point in the Tharsis region, excluding the major volcanoes). A histogram plot of frequency (heavy line) and cummulative length (thin line) of ridge segments versus distance from the regional topographic center (7°S, 103° W) indicate peaks at 2600 and 2500 km respectively (Fig. 3). These points reflect ridge densities in central Coprates and Lunae Palus and may be interpreted as representing the areas of peak compressional

deformation in the Tharsis region. Although it is possible to assess the outermost extent of Tharsis compressional deformation, the inner extent cannot be determined because, as is the case of SW Coprates, ridges have been buried by volcanic flows. The partially buried ridges of western Coprates represent the innermost observable extent of compression. However, the sharp decrease in cummulative ridge lengths between this area and NW Lunae Palus, which has a similar stratigraphy, may reflect the extent to which the ridged plains units have been buried by more recent volcanic flows or obscured by other resurfacing processes. In addition, the complementary region (corresponding to central Coprates and Lunae Palus) of peak compressional deformation at approximately 2500 km west of the topographic center is buried by the recent flows of the major Tharsis volcanoes. These stratigraphic observations suggest that the observed compressional features may represent only a fraction of the total compression that occurred in the Tharsis region.

References

Roth, E.L., Downs, G.S., Saunders, R.S., and Shubert, G., 1980, Radar Altimetry of South Tharsis, Mars: Icarus, v. 42, p. 287-316.

Saunders, R.S. and Gregory, T.E., 1980, Tectonic implications of Martian ridged plains (abs.): Reports of Planetary Geology Programs, NASA Tech. Mem. 82385, p. 93-94.

Scott, D.H. and Carr, M.H., 1978, Geologic Map of Mars: Misc. Invest. Map I-803. U.S. Geol. Survey.

Scott, D.H., 1981, Map showing lava flow in the southeast part of the Phoenicis Lacus quadrangle of Mars: Misc. Invest. Map I-1274, U.S. Geol. Survey.

Scott, D.H., Schaber, G.G., Horstman, K.C., and Dial, A.L., Jr., 1981, Map showing lava flows in the northeast quadrangle of Mars: Misc. Map I-1267, U.S. Geol. Survey.

Watters, T.R. and Maxwell, T.A., 1982, Strain estimates for the ridged plains of Mars: Evidence of compression in the Coprates quadrangle (abs.): Reports of Planetary Geology Programs, NASA Tech. Mem. 85127, p. 279-281.

Watters, T.R. and Maxwell, T.A., 1983, Cross-cutting relations and relative ages of ridges and faults in the Tharsis region of Mars: Icarus, v. 56 (in press).

Wise, D.U., Golombek, M.P., and McGill, G.E., 1979, Tharsis province of Mars: Geologic sequence, geometry, and a deformation mechanism: Icarus, v. 38, p. 458-472.

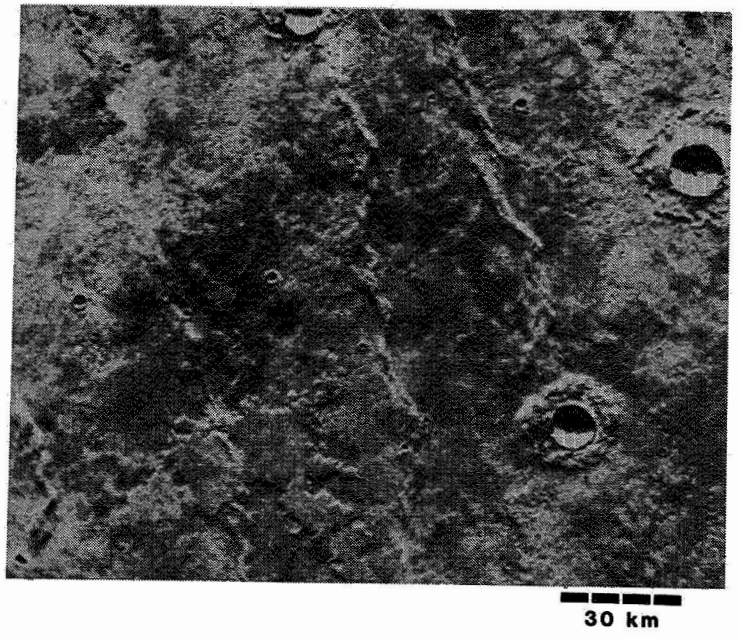

FIGURE 1

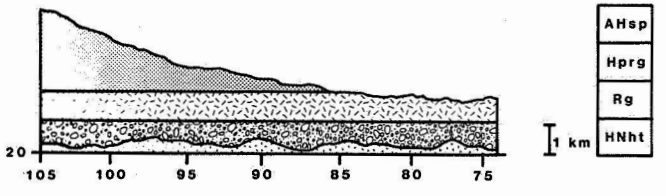

FIGURE 2

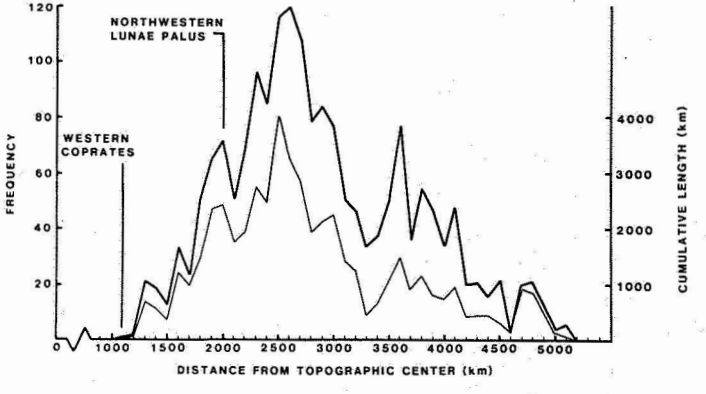

FIGURE 3

D111 N84 23542

COMPRESSIONAL FEATURES IN THE THARSIS REGION OF MARS: II. ORIENTATIONS AND TIMING OF DEFORMATION.

Thomas R. Watters and Ted A. Maxwell, National Air and Space Museum, Smithsonian Institution, Washington, D.C. 20560.

The Tharsis ridge system appears to form a great circle around the major volcanoes. The roughly circumferential orientation of these ridges could be interpreted as the formation of a ridge system in response to a single stress field with a center near Pavonis Mons. Wise et al. (1979) plotted the perpendiculars to strikes of ridges on the eastern flanks of Tharsis as great circles on the upper hemisphere of an equal area net. Based on 66 intersections of the great circles, they observed that the ridge system was not concentric to a single point but to a broadly elliptical area whose long axis was subparallel to the volcanic line formed by Olympus and Pavonis Mons.

In order to further test for circular symmetry and possible other influences on ridge orientations, normals to vector means of ridge orientations were calculated using over 1850 digitized ridge segments sampled in 10 degree boxes (Fig. 1). Orientations of individual ridge segments were weighted by their lengths, and the magnitudes of normals to vectors means were weighted by cummulative length of the ridge segments. As illustrated in Figure 1, cummulative length is represented by line lengths, and double width lines represent 4 times the vector magnitude of single thickness lines. Normals to vector means with magnitudes less than 100 km are not shown. Assuming a single fold origin for ridges, the resulting plot shows compressive stress trajectories for the ridges in the Tharsis region. The averaged compressive stress orientation around Tharsis confirm the suggestion by Wise et al. (1979) that the ridge system is not concentric to any single point. In general, ridge orientations in southern Tharsis indicates a stress center in a broad area near Syria Planum. Orientations in northern Tharsis indicate stress centers in a zone between Olympus and Ascraeus Mons. Overall, this data indicates a zone of stress centers that trend roughly parallel to a line north of Olympus Mons, through Pavonis Mons to Syria Planum. In contrast to the findings of Wise et al. (1979), the zone indicated here extends north of Olympus Mons rather than south.

Models for the origin of the stress responsible for the tectonic features in the Tharsis region must be sensitive to the relative timing of the tectonic events. Those models invoking loading of the lithosphere by the Tharsis volcanic pile (Solomon and Head, 1982; Willemann and Turcotte, 1982) suggest that the compressional ridges formed as a long term viscoeleastic response of the ridged plains units to this load and that compressional deformation was late in the tectonic history of the region.

In an effort to assign a relative age to the compressional ridge forming events, Watters and Maxwell (1983), examined ridge-fault crosscutting relationships on the ridged plains units in the Tharsis region. They concluded that the major compressional ridge forming events were roughly coincident with, and in some cases prior to the period of extension that generated the faulting of the ridged plains of Coprates, Lunae Palus, Tempe, and Memnonia regions, and the rifting of Valles Marineris. The presence of partially buried ridges in southwest Coprates

and the absence of observable compressional deformation on any stratigraphically younger unit west of the ridged plains units of Coprates or Lunae Palus suggport these findings and suggest that ridge formation occurred during an isolated period in the tectonic history of Tharsis (between 5000-12000 cummulative crater density). Further, the regional stress trajectories predicted by a flexural loading model do not fit the observed locations or the principal compressive stress orientations of the ridges (compare Fig. 1 with Fig. 3c in Banerdt et al., 1982).

A model involving one or more isostatically compensated uplifts of the crust followed by relaxation generating a period or periods of regional compression is favored here and in the work of Watters and Maxwell (1983). Uplift with a net volumetric expansion of the crust as a result of partial melting coupled with solidification of low pressure, low density mineral assemblages (Finnerty and Phillips, 1981) could generate such tectonic activity. The observed zone of compressional stress centers (Fig. 1) may represent the non-symmetric relaxation of the uplifted crust along a northwest trending axis or several uplift-relaxation cycles along the same axis. Regional stress trajectories predicted by isostatic models agree well with the observed principal stress orientations. Deviations between the observed and predicted stresses are greatest within approximately 1700 km of the topographic center. Banerdt et al. (1982) suggested that the evolution of the Tharsis region progressed from isostatically-compensated uplift to flexural loading. If this is the case, then the findings presented here suggest that the ridges formed during the isostatic stage and not during the period dominated by flexural loading.

References

Banerdt, W.B., Phillips, R.J., Sleep, N.H., and Saunders, R.S., 1982, Thick shell tectonics on one-plate planets: Applications to Mars: J. Geophys. Res., v.87, p. 9723-9733.

Finnerty, A.A. and Phillips, R.J., 1981, A petrologic model for an isostatically compensated Tharsis region of Mars (abs.): Papers presented to the Third International Colloquium on Mars, p. 77-79, Lunar and Planetary Institute, Houston, Texas.

Solomon, S.C. and Head, J.W., 1982, Evolution of the Tharsis province of Mars: The importance of heterogeneous lithospheric thickness and volcanic construction: J. Geophys. Res., v. 87, p. 9755-9774.

Watters, T.R. and Maxwell, T.A., 1983, Cross-cutting relations and relative ages of ridges and faults in the Tharsis region of Mars: Icarus, v. 56 (in press).

Willemann, R.J. and Turcotte, D.L., 1982, The role of lithospheric stress in the support of the Tharsis rise: J. Geophys. Res., v. 87, p. 9793-9801.

Wise, D.U., Golombek, M.P., and McGill, G.E., 1979, Tharsis province of Mars: Geologic sequence, geometry, and a deformation mechanism: Icarus, v. 38, p. 458-472.

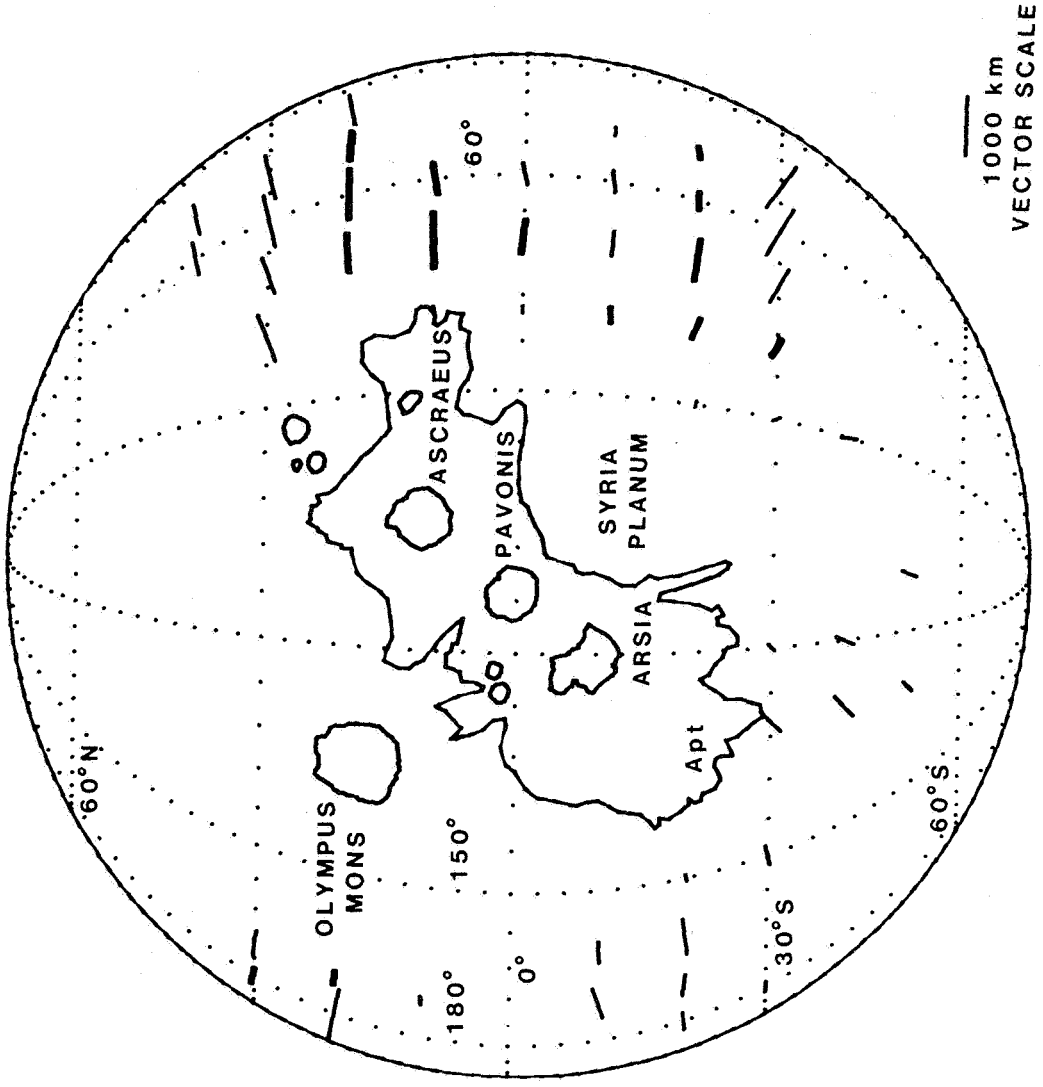
1000 km
VECTOR SCALE
60°
ASCRAEUS
PAVONIS
SYRIA
PLANUM
ARSIA
Apt
OLYMPUS
MONS
60°N
150°
180°
0°
30°S
60°S

FIGURE 1

D112

INTERPRETATION OF PLANETARY STRESS SYSTEMS: DETERMINATION OF TECTONIC OVERPRINTING IN NORTHWEST WYOMING

Wise, Donald U., and Allison, M. Lee, Dept. of Geology & Geography and Remote Sensing Center, Univ. of Mass., Amherst, Mass. 01003

Structural and tectonic interpretations of planetary surfaces rely strongly on visual determination of regional structural grain. This grain can be very complex and confusing, and sorting out of discrete trends in time and space is of utmost importance. This study is a test of some of these techniques applied to a "well known" area having several discrete structural grains.

In the Bighorn Basin region of Wyoming, a largely overlooked N10E structural grain has been verified with detailed structural analysis and indicates a significant change in stress orientation at the end of the Laramide orogeny.

The Bighorn Basin region and its surrounding ranges contain a hierarchy of Laramide structural grains different from the typical pattern of much of the rest of the Wyoming Province. A bimodal size distribution of major and minor structures of "first order" and "second order" respectively (Thom, 1955) is well recognized in the region. The "minor" structures best known as the "basin anticlines", tend to have structural relief of about a thousand meters, whereas the "major" structures, like the Beartooth and Bighorn Ranges, have structural relief as well as map dimensions approaching an order of magnitude larger. The minor structures of the Bighorn Basin tend to be oriented sub-parallel to the NW grain of the basin axis and to be asymmetric, with steep limbs of anticlinal structures on the sides away from the basin axis. The major ranges also include NW trending elements in their structural grain but are much more irregular in their local and in their overall grain. This is particularly true of the eastern portion of the Beartooth Range, whose front trends N10E, partially closing the end of the Bighorn Basin. The N-S grain seems particularly strongly developed in the northern Bighorn Basin region (Fig. 1), where the Dead Indian Monocline continues the trend of the Beartooth front. The N-S grain is also evident in the Oregon Basin area, the western portion of the Little Sheep Mountain area, and in the major faults bounding parts of the Pryor Mountains (Fig. 1 & 2).

The large-scale pattern of the Precambrian rocks is that of broad, open folds with axes striking about N10E and plunging about 30° to the south (Wise, 1957, 1958; and Foose, Wise and Garbarini, 1961). The trends and time sequence of the minor structures are similar to those of the larger structure: NW-trending folds and thrusts were overprinted and disrupted by structures influenced by younger trends of Beartooth frontal structures (Wise, 1983) (Fig. 2). It is interesting to note that the main N10E Beartooth frontal trend continues south as the Dead Indian Monocline, the dips of which steepen sharply in the middle and upper Mesozoic levels, presumably the effect of a deeply buried basement lip marking the edge of the less uplifted segments.

The Tensleep Fault is a Precambrian fracture (Palmquist, 1967) reactivated by Laramide forces (Allison, 1983). Detailed paleostress analysis along the Tensleep Fault clearly shows two phases of deformation. Stylolites, slickensides, faults, fold axes, plumose structures, and joints show a strong NE-SW compression (Figs. 3 & 4) which produced a NW-trending grain. A late Laramide (?) WNW-directed compression is indicated by other sets of joints and plumose structures with associated NNE-SSW extension shown by gypsum veins and fibers (Figs. 3 & 4). This resulted in features with a trend similar to

the Beartooth Front. Fold axis orientations were partly controlled by the upthrown block on the north side of the Tensleep Fault.

The Tensleep Fault could have been preferentially reactivated with regards to basement fractures of other orientations due to its favorable 30° angle to the NE-SW compression. Left oblique slip would be expected as a result. The later WNW compression should have produced a minor component of right slips and may account for the clockwise rotation of gypsum fibers in veins along the fault (Fig. 4).

The dichotomy between major and minor structures and the possible reorientation directions of Laramide compression are not new ideas. However, the late stage stresses are usually thought to have been N-S compression perpendicular to features like the Owl Creek Mountains. The data presented above suggest that the main Bighorn Basin NW-SE trend was well established at least in the northern part of the basin before its disruption by WNW compression with the rise of the eastern Beartooth Block and deformation across the Tensleep Fault.

Whatever its cause, the younger NNW compression uplifted and overthrust the eastern Beartooth Front/Dead Indian Monocline to produce its N10E strike. Associated structures probably modified the deeper portions of Oregon Basin to produce the N-S elements in that structural grain. Depending on the magnitude of frontal displacement, this interpretation would leave the former floor of the Bighorn Basin uplifted on top of the Beartooth Block possibly modified as the Cooke City Sag (Figs. 1 & 2).

A time sequence of such structures of varied orientation carries with it the implication of a complex and evolving basement anisotropy which must be taken into account in any arguments about mechanics. In addition, earlier Laramide structures, dismembered and uplifted onto the ranges, can be examined both as samples of structural styles less accessible for study in the deeper basins as well as clues to structures left behind or beneath the overthrust range fronts. Even in well studied regions significant structural grains have been overlooked. This emphasizes again the care required in deciphering the history of any planetary surface.

References

Allison, M. Lee, 1983, Deformation styles along the Tensleep Fault, Bighorn Basin, Wyoming, Wyo. Geol. Assoc. Guidebook, in press.

Foose, R.M., Wise, D.U., and Garbarini, G., 1961, Structural geology of the Beartooth Mountain Block, Montana and Wyoming, Bull. Geol. Soc. Am., v72, p1147-1172.

Palmquist, John C., 1967, Structural analysis of the Horn area, Bighorn Mountains, Wyoming, Bull. Geol. Soc. Am., v78, p283-298,

Thom, W.T. Jr., 1955, Wedge uplifts and tectonic significance, Geol. Soc. Am. Spec. Paper 62, p369-376.

Wise, D.U., 1957, Tectonics and tectonic heredity in the southern Beartooth Mountains, Wyoming, PhD thesis, Princeton Univ., 187p.

_____, 1958, The relationship of Precambrian and Laramide structures in the southern Beartooth Mountains, Wyoming, 9th Ann. Fieldtrip Guidebook, Billings Geol. Soc., p24-30.

_____, 1983, Overprinting of Laramide structural grains in the Clarks Fork Canyon area and eastern Beartooth Mountain of Wyoming, Wyo. Geol. Assoc. Guidebook, in press.

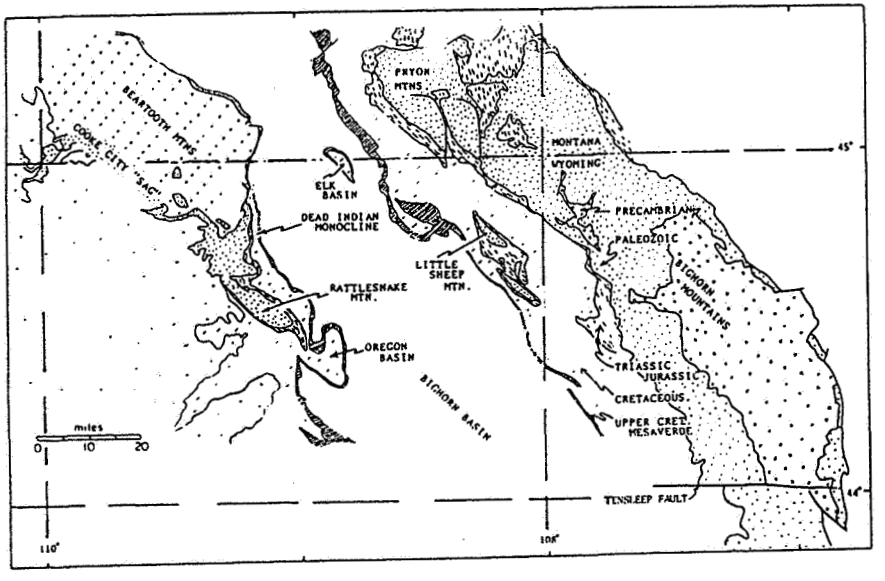

Fig. 1. Structural index to northern Bighorn Basin region. The regional NW-SE grain is evident as is a N-S grain associated with the east front of the Beartooth Range, Dead Indian Monocline, portions of Oregon Basin, the western parts of Little Sheep Mountain, and some faults of the Pryor Mountains.

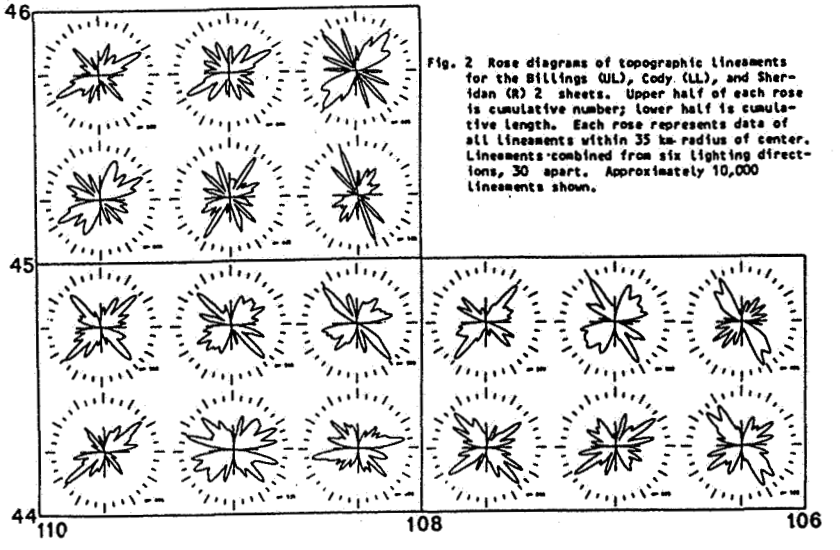

Fig. 2 Rose diagrams of topographic lineaments for the Billings (UL), Cody (LL), and Sheridan (R) 2 sheets. Upper half of each rose is cumulative number; lower half is cumulative length. Each rose represents data of all lineaments within 35 km radius of center. Lineaments combined from six lighting directions, 30 apart. Approximately 10,000 lineaments shown.

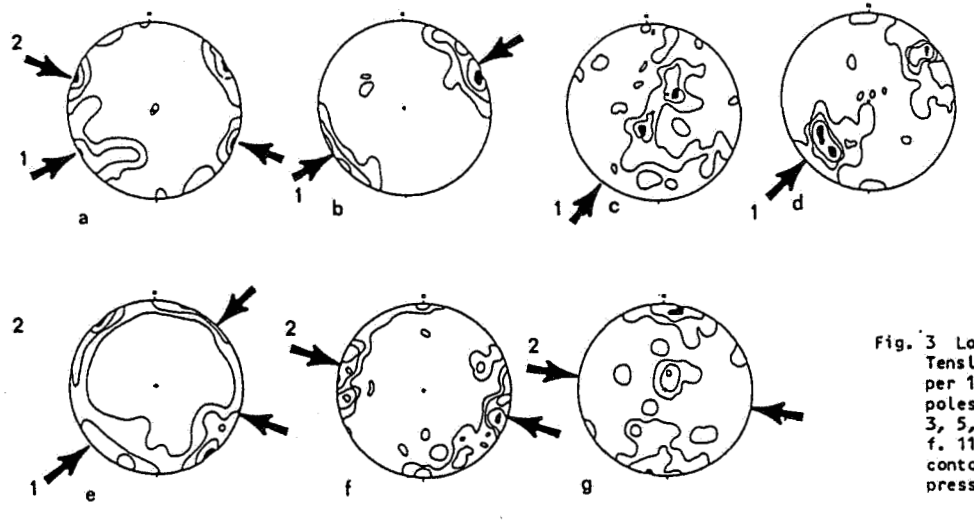

Fig. 3 Lower hemisphere equal area projections of structures along the Tensleep Fault. a. 347 plume stems on joint faces, contours 1, 5, 10% per 1% area. b. 118 stylolite teeth, contours 1, 5, 10, 15%. c. 204 poles to faults, contours 1, 3, 5%. d. 137 slickensides, contours 1, 3, 5, 7%. e. 5070 poles to extension joints, contours 1, 2, 3, 4%. f. 119 fold axes, contours 1, 3, 5, 7%. g. 75 poles to gypsum veins, contours 1, 5, 10%. Arrows give inferred direction of maximum compression for phases 1 and 2.

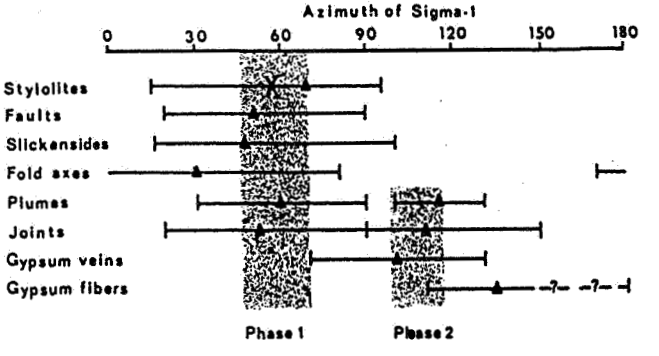

Fig. 4. Ranges of inferred maximum compression (sigma-1) for each feature in the Tensleep Fault area. Triangles are peak values, X is a vector mean. Shaded areas show ranges of two compressive phases.

Chapter 12

GEOLOGICAL MAPPING, CARTOGRAPHY AND GEODESY

D113

THE GALILEAN SATELLITE GEOLOGICAL MAPPING PROGRAM, 1983.

B. K. Lucchitta, U.S. Geological Survey, Flagstaff, Arizona 86001

The Galilean Satellite Geological Mapping Program was established to illuminate detailed geologic relations on the four large satellites of Jupiter. The program involves about 40 investigators from various universities, research institutes, and government offices in the United States, England, Germany, and Italy. A total of 24 researchers have been assigned to map 10 quadrangles on Ganymede, 15 to map 6 quadrangles on Io, and 3 to map 2 quadrangles on Europa. All maps are at a scale of 1:5 million except for three of the Io maps, where high-resolution pictures permitted compilation of selected areas at larger scales.

During 1983, base materials were produced as planned and the following were sent to the mappers: Europa Je3 and Je4; Io Ji2, Ji3, Ji4, Ji2a, Ji2b, and Ji2c; and Ganymede Jg3, Jg7, Jg8, and Jg9. Additionally, final brown-line cronaflexes were distributed for Europa Je3 and Je4. Ozalids of all completed quadrangle bases were made available to all mappers of respective satellites, as were color images prepared by the Jet Propulsion Laboratory in Pasadena, CA, and by the U.S.G.S. Image Processing Facility in Flagstaff, AZ. Two geologic maps of high-resolution areas on Io have been completed and were submitted for review. Two meetings were convened: one in Reston, VA, in January 1983, in conjunction with the Planetary Geology Principal Investigators Meeting, to discuss progress of the program in general; and another in Flagstaff, AZ, in September 1983, to discuss specific mapping problems on Io and Europa.

Problems on Io pertain mostly to the absence of identifiable datum planes across the planet, and to the probable young age of the units. Superposition relations can be established only on a local basis. Flow units and plateau or plains units will be mapped by their surface expression and placed into an approximate overall age sequence. Local age sequences within flow or plains units may be given numerical symbols that express their sequence, but these numerical identifiers will not necessarily correlate across the entire map. Mountain materials, on previous maps considered to be old, emerged as locally younger than plains or plateau materials. Units that have changed between the two spacecraft encounters and thin deposits will be portrayed by insert maps or overlays.

Europa consists of few material units. Subdivisions may have to be based on different structural styles or density of fracture patterns. These subdivisions may be outlined as structural provinces and identified by symbols; insert maps will portray the different lineation sets.

Individual structural sets on the grooved terrain of Ganymede will be outlined by structural symbols and other symbols will be added within the set boundaries to indicate trend and density of grooves. Smooth terrain units will be mapped separately. Crater-floor materials may be categorized by the presence of flat floors, peaks, or pits, or by domes containing central depressions. More specific problems will be discussed at a meeting scheduled at the Lunar and Planetary Institute in March, 1984.

D114

RELATIONSHIPS AND TECTONICS OF THE Jg-7 QUADRANGLE OF GANYMEDE

Marvin F. Glotfelty
Department of Geology
Northern Az. Univ.
Flagstaff, AZ.

Charles W. Barnes
Professor of Geology
Northern AZ. Univ.
Flagstaff, AZ.

Units and Symbology

Craters within the Ganymede Jg-7 quadrangle were divided into seven mappable units. The units represent: 1) irregular or elongate craters, 2) craters with dark ejecta, 3) palimpsests, 4) secondary craters, 5) and craters of young, mature, and old age (mapped as C3, C2, and C1, respectively). Symbols used for crater floors include: 1) flat floors, 2) floors with pits, 3) floors with a central dome or peak, 4) and floors with a central dome and pit.

Grooved terrains were divided into five mappable units. Three units of light grooved material represent small, medium, and large grooves, which are arbitrarily divided. The other two units of grooved terrain represent dark grooved material, and reticulate grooves.

Two units of ungrooved dark terrain and two units of ungrooved light terrain were defined. In Galileo Regio, two units were defined representing large furrowed grooves, and smaller grooves which are orthogonal to the furrowed grooves. Large sinuous scarps which resemble high angle faults are represented by a heavy line with dots.

Boundary Relationships

The groove sets in the southern half of Jg-7 exhibit complex cross-cutting relationships and are most often bounded by a large prominent solitary groove and scarp. The furrowed grooves in the north half of the map area occur as gently arcuate ridges, and trend in two orientations. The dominant set trends NNE, and cuts the minor set, which trends NW. Both sets of furrowed grooves are in most cases cut by smaller secondary grooves, but cross-cutting relations become vague in some areas. These grooves are generally orthogonal to, and superimposed upon the larger furrowed grooves. The boundary between the lighter grooved terrain to the south, and Galileo Regio to the north is an abrupt scarp of considerable relief, with the greater elevation to the north. Craters are most abundant in Galileo Regio, and in all but a few cases, crosscut all other features. There are cases, however, where all of the groove types cut ejecta blankets, rims, and floors of craters. The furrowed grooves and secondary grooves in Galileo Regio are in abrupt contact with surrounding ungrooved materials. This contact is delineated by a sharp change in relief, rather than a difference in albedo or surface texture. The groove sets in the southern terrain bound ungrooved materials either very abruptly across a prominent solitary groove, or very gradationally, in which case boundary lines are arbitrary.

Sequence of Events

A five stage sequence of events has occurred in the Jg-7 quadrangle of Ganymede. The first, and oldest stage was the formation or deposition of the smooth dark areas and hummocky terrains with Galileo Regio. The age of these units is evidenced by crater flux, as well as by crosscutting relations. The high crater density in this terrain suggests that the creation of the terrain dates from the heavy terminal bombardment phase of solar system evolution that ended about 5 b.y.a. (Shoemaker and Wolfe, 1981).

In the second stage, the large furrowed grooves in Galileo Regio formed. This occurred either as a single event in time, with the NNE-trending grooves forming dominantly over the NW-trending grooves, or as two events, the NNE-trending grooves forming after those trending northwest, and cutting them. Soon after or penecontemporaneous with the formation of the large furrowed grooves was the formation of smaller secondary grooves.

The end of the second stage represents the time at which the boundary between the two geological provinces of Jg-7 was delineated. A very large unconformity exists here; this suggests that a substantial period of time may have elapsed between the second and third stages.

The third stage began with the formation of large sinuous escarpments which bounded and cut into the northern dark terrain. These sinuous scarps are similar to those formed by high-angle faulting, and in almost all cases there is a larger change in elevation across them.

In the fourth stage, blocks of older, darker material faulted or rifted off in polygonal "islands." Groove sets in the southern half of the map area are in some locations observed to be composed of small grooves symmetrically oriented about a prominent central groove. This suggests a rifting mechanism, which may also be responsible for the displacement of blocks of dark terrain away from Galileo Regio.

Stage five, which probably occurred at the same time as stage four, is represented by the formation of groove sets in the southern light-colored terrain of Jg-7. Dark and light groove sets formed by the same, or similar processes. Where groove sets grade into smooth materials, the intensity of processes which formed the grooves geometrically decreased.

Crater formation, although of variable flux, was a continuous process from pre-stage one to present. Furrowed grooves in Galileo Regio show less fading due to viscous relaxational flow than old craters, and thus were probably actively forming at least from stage two until the time of mature (C2) craters.

Genetic Mechanisms

The model proposed by Fink (1983) which proposes crustal thinning and ductile necking as a mechanism for groove formation is consistent with observations made in this study. The formation of grooves must be limited to processes which will vertically propagate fractures. All types of grooves of Jg-7 (i.e., furrowed grooves, secondary grooves, and groove sets in light terrain) are observed to cut ejecta blankets, rims, and floors of craters in some locations.

Craters superimpose grooves almost everywhere, so where grooves do cut them, a syn-impact or post-impact genesis is probable. The relatively thin ejecta blanket may have draped over preexisting grooves, but the appearance of grooves on the rim and floor of craters necessitates syn-impact of post-impact formation, or propagation of the grooves from depth.

These grooves must be very high angle features, because the craters cut by a single groove show no extensional or compressional deformation. Because grooves which cut craters are few, they are probably the products of reactivation or propagation of the structural setting which initially formed the grooves.

References Cited

Fink, J.H., 1983, A mechanical analysis of extensional instability on Ganymede: N.A.S.A. Tech. Mem. 65342.

Shoemaker, E.M., and Wolfe, R. F., 1981, Cratering time scales for the Galilean satellites, in Satellites of Jupiter (D. Morrison, ed.): University of Arizona Press, Tucson.

P115
ABS.
ONLY

GEOLOGIC MAPPING OF IO QUADRANGLE JI3

Elbert A. King, Dept. Geosciences, Univ. Houston, Texas

ABSTRACT - A photogeologic map of Io Quadrangle Ji3 is being compiled from interpretation of images of Io obtained by Voyager I and Voyager II in collaboration with C. Wood and R. S. U. Smith. All relevant images have been obtained and evaluated. A preliminary map version has been completed by mapping on individual images and this version is now being compiled on the quadrangle map base recently received from the USGS, Flagstaff, Arizona. It is anticipated that the mappers will meet within the next weeks or months to compare preliminary map versions, discuss discrepancies, resolve problems and to arrive at the final map version which will be inked on the USGS base map and submitted to the USGS for criticism, review and eventual publication together with an interpretive text.

D116

Je3 QUADRANGLE, EUROPA: PRELIMINARY GEOLOGIC DESIGNATIONS

David Pieri, Jet Propulsion Laboratory, Pasadena, CA 91109
Konrad Hiller, DFVLR, Munich, FRG

We have arrived at preliminary assignments of terrain units, classification of lineaments, and have delineated impact craters as well as depressions which are candidate impact craters for our geological map of the Je3 quadrangle of Europa. In addition, we have designated several structural provinces as delineated by lineament style. Two of the outstanding mapping problems which remain are (1) the deciphering of detailed lineament formation sequences, and (2) the classification of lineament materials.

a. TERRAIN UNITS:

We have delineated four major terrain units in the Je3 quadrangle. These are: (i) dark pitted material (mpd), (ii) dark lineated plains (pld), (iii) bright lineated plains (pbl), (iv) dark spots (sd).

We will discuss them in turn:

mpd -- This unit is equivalent to the dark mottled terrain of Lucchitta and Soderblom (1982). These regions are characterized by somewhat lower albedo than surrounding bright plains units and by ubiquitous mottled appearance due to small-scale (<100 km^2) albedo variations and by the occurrence of small depressions throughout the unit. Lineaments do not appear to transect this unit intact. Where major arcuate lineaments enter the mpd unit, they usually disappear. In some cases, however, the bright medial lineament stripe does appear intact into the mpd unit. It is unclear at this stage of mapping whether the large arcuate lineaments emerge again at the distal border of the mpd terrain. In addition, this unit is characterized by the occurrence of numerous thin flexi. As Luccitta and Soderblom (1982) point out, the occurrence of flexi preferentially in this unit may well be due to the high phase angle at which much of this unit is illuminated.

pld -- These are the dark gray plains units of Lucchitta and Soderblom (1982). We feel more comfortable with an albedo/morphological designation rather than a colorimetric one. The mld unit is characterized by a 10 to 15% lower albedo as compared to brighter surrounding units and are characteristically transected by discernable lineaments, the relatively small (typically <10^4 km^2 in area) and appear distinctly in two major areas where high resolution coverage is available.

pbl -- These units are equivalent to the bright plains unit of Lucchitta and Soderblom (1982). They are characterized by the highest regional albedo of any unit on the planet.

sd -- This unit corresponds to the "brown spots" of Lucchitta and Soderblom (1982). There are major occurrences of this type of terrain

surrounded by bright plains units. In some cases, series of brown spots seem to exist as extensions of dark lineaments as they transcend boundaries between bright plains and dark pitted terrain.

b. STRUCTURAL PROVINCES. We have delineated five types of transcendent structural provinces, primarily, but not exclusively, expressed within the bright plains units: (i) a - lineated plains with arcuate lineations, (ii) con - lineated plains with conchoidal lineations, (iii) com - lineated plains with comminuting lineations, (iv) p - lineated plains with polygonal lineations, (v) r - lineated plains with ridges.

(a) -- This province includes most of the great arcuate lineaments on Europa. It appears mainly within apparently smooth bright plains, although bright medial ridges within the arcuate lineaments may possess relief. It is adjacent to and may embay mld occurrences.

(con) -- This province is located near the anti-jovian point on Europa and is characterized by broad wedge-shaped conchoidal lineaments and the plains units which contain it appear smooth.

(com) -- This province is characterized by an abundance of micro-lineaments which subdivide the terrain and give it a comminuted or crushed appearance. It is also smooth and contains the anti-jovian point on Europa.

(p) -- This province contains ubiquitous straight lineaments which join in a polygonal pattern. It appears smooth.

(r) -- This province consists of flexi or cycloid ridges ubiquitously emplaced in bright plains units and to a much lesser extent in dark pitted material. As has been mentioned, it is possible (and perhaps likely) that these ridges occur in all units but are well expressed only at high phase angles.

c. LINEAMENTS. We have delineated several different lineament types basically using the scheme of Pieri (1981):

i. arcuate lineaments (Pieri Type 3) -- These are the broad circum-Europa lineaments which are prominent even on low resolution images of Europa. They are typically 5 to 10 km wide and possess a medial white stripe. They appear to be among the freshest of the lineaments, although if the Pieri Type 1 lineaments are regrouped into this family, the group would probably be considered to span a wider range of degradation states.

ii. conchoidal lineaments (Pieri Type 2) -- These lineaments consist of short wedge-shaped to curved markings producing a curved-to-polygonal lineament set which occurs near the anti-jovian point. These lineaments can be broad (10-20 km wide) and exhibit structure within the marking that can be transverse to the lineament trend.

iii. comminuting lineaments (Pieri Type 5) -- These are among the smallest of the lineaments. They occur at and around the anti-jovian point as seen in the high resolution mosaic. They give an appearance of intense fracturing to the point of increasing the albedo of the affected area.

iv. polygonal lineaments (Pieri Type 4) -- This type of lineament occurs unbiquitously in several areas and consists of straight segments, very thin without a white medial and, subdividing smooth high-albedo zones and typically crossing arcuate lineaments at very high angles.

v. ridges (Pieri Type 6) -- These lineaments are thin positive arcuate topographic features which appear at very high phase angles and may be ubiquitous to all terrains on Europa.

vi. bands -- These are broad faint markings distinguished by the lack of a white medial stripe and the presence of dark spots within the lineament. They are rare with only two definite occurrences. They are equivalent to the "gray bands" of Lucchitta and Soderblom (1982).

d. DEPRESSIONS: IMPACT CRATERS AND IMPACT CRATER-CANDIDATES

We have delineated two groups of depressions on Europa, those which can be identified as impact craters and those which cannot.

1. impact craters -- These have been identified by several authors (Smith et al., 1979 and Lucchitta and Soderblom, 1982). There are about a half-dozen of these features showing clear rims and in several cases, ejecta deposits. Two kinds of ejecta are recognized: bright ejecta surrounding a dark crater rim and dark ejecta surrounding a bright crater. Dark ejecta occurs around a prominent crater located in the mld unit while bright ejecta occurs around several prominent craters in the mpd terrain.

2. impact crater candidates and irregular depressions -- There is another class of quasi-circular depressions which exist on several types of terrain and are particularly well-expressed at high phase angles near the terminator. These may or may not be remnant impact craters. Away from the terminator these pits may be expressed as small dark spots, but this assertion is speculative at this time.

Luccitta, B. K. and L. A. Soderblom, 1982, Geology of Europa in Satellites of Jupiter, pp. 521-555, Morrison, ed., The University of Arizona Press, Tucson, 972 pgs.

Pieri, D. C., 1981, Lineament and polygon patterns on Europa, Nature, 289, pp. 17-21.

Smith, B. A. and the Voyager Imaging Team, 1979, The Galilean satellites and Jupiter: Voyager 2 imaging science results, Science 206, pp. 927-950.

D117

GEOLOGIC MAPPING, MARS: PROGRESS AND HIGHLIGHTS

David H. Scott, U.S. Geological Survey, Flagstaff, Arizona 86001

Geologic mapping of Mars from Viking images has been completed in the north polar and western regions of Mars. This work has been tied along common borders with the mapping currently in progress in the eastern equatorial region by Greeley and Guest. Among the more significant results previously reported are studies of the paleostratigraphy of Tharsis lava flows [1] and of the time of occurrence of water flooding in Kasei channel relative to Tharsis volcanism [2], the recognition of probable ignimbrite fields covering some 2 million km^2 between plains and highlands west of Tharsis Montes [3], the discovery of groups of volcanoes scattered in a broad arc across the southern highlands [4], and the identification of river-meander relics throughout large areas of the northern lowlands [5]. Some of the developments of the mapping to date include the following:

1. Plains units in the northern lowland region of Mars show subtle differences in morphology and are laterally gradational in places. In some areas they cannot be distinguished by physical appearance alone nor are they separated by discrete boundaries. In such areas arbitrary "statistical contacts" are drawn primarily on the basis of crater-count data. A computer program has been designed to plot curves for crater size-frequency distributions for selected crater diameters. These curves can be plotted rapidly and allow better quantitative judgements to be made for placing boundaries between map units.

2. A problem encountered in all planetary geologic mapping is the nomenclature used to describe material units. Adjectives commonly employed to describe the varied surfaces include: smooth, hummocky, rough, fractured, hilly, dark, etc. As more and more units are recognized, these terms become increasingly difficult to follow and the geologic picture is blurred by terminology. Although the use of such terms is still necessary in the mapping of Mars, our geologic knowledge has progressed to the extent that group, formation, and member names can be applied to many rock units. Consequently the explanation accompanying the Viking geologic map of Mars will more nearly resemble those of terrestrial geologic maps and will be more comprehensible to most geologists.

3. In conjunction with the geologic mapping of Mars, gravity data acquired by the Viking orbiters is being studied to determine the presence, type, and magnitude of anomalies associated with surface features having a wide variety of size ranges. The studies are similar to some of those made for lunar gravity anomalies. They will allow models to be made of craters, volcanoes, and canyons involving such variable parameters as density, topography, and subsurface structure. Results should provide information on the size and relative age of features compared to their gravity response and their possible isostatic adjustment.

4. The Viking geologic mapping of Mars has disclosed several localities where particular combinations of rock units having a wide range of ages and lithologies are exposed in close proximity. These areas offer optimum opportunities for any future missions to Mars designed to obtain surface samples from a variety of rocks close to the target site. Some of the more favorable sites include the following:

1. Olympus Mons basal scarp and adjacent terrain (MC-9SW). Specific location: 14°N., 131.5°W or 18°N., 128.5°W. The sample suite includes (1) talus from scarp face; (2) post-scarp lava flows from Olympus Mons; (3) lava flows from fissures in plains that overlap Olympus Mons flows. The rock

types/ages are # (1) talus, highland fractured basement (very old), or lava/pyroclastic material forming aureole (old); (2) Olympus flows, basaltic lavas (very young); (3) plains flows, basaltic lavas (among youngest flows on Mars). Factors affecting accessibility are relatively flat topography; elevation about 2-3 km above datum.

2. Kasei Vallis floodplain - Tharsis Montes lava flows (MC-10NW). Specific location: 20°N., 77.5°W. (Several other locations occur in same area.) The sample suite includes (1) pre-channel basement; (2) channel-floodplain material; (3) lava flows from Ascraeus Mons. The rock types/ages are (1) breccias or volcanic materials forming lower rock sequence of Lunae Planum (old); (2) floodplain and eolian deposits (young to very young); (3) basaltic lava flows, post-channel (very young). Factors affecting accessibility are relatively flat site but criss-crossed in places by wind-eroded joint sets; elevation ~2-3 km.

3. Claritas Fossae highlands - Syria volcanic flows (MC-17SE). Specific location: peripheral to highland basement outcrop centered near 28.5°S., 101°W. Sample suite: (1) highly fractured highland rocks, little or no resurfacing; (2) lava flows of Syria Planum. The rock types/ages are: (1) basement, ancient crustal rocks that underlie all others in region; (2) basaltic lava flows (intermediate to young age). Factors affecting accessibility are relatively flat site around base of highland outcrop but highly faulted and fissured in places.

4. Mangala Vallis distributary - ash-flow tuff(?) (MC-16NE). Specific location - 7.5°S., 156°W. Sample suite: (1) alluvial channel and eolian deposits; (2) highland cratered terrain; (3) ash-flow tuffs (postulated). The rock types/ages are: (1) river and wind deposits, probably intermixed (very young-young); (2) pre-channel floor material and/or cratered highland blocks from channel walls (very old); (3) material resembling nonwelded ash flows, part of an extensive deposit covering about 2×10^6 km^2 (very young). Factors affecting accessibility are flat site around mouth of distributary channel; area to be investigated for all units within radius of about 20-30 km; elevation 1-2 km.

5. Highland-lowland boundary and ash-flows(?) (MC-16NW). Specific location: 11°S., 173°W. Sample suite: (1) densely cratered highland material; (2) lava plains (ridged), lowland material; (3) ash-flow tuffs(?) The rock types/ages are (1) breccias or lava flows (very old); (2) basaltic lava flows (mare type?); (3) felsic pyroclastic rocks. Factors affecting accessibility are flat area and relatively smooth lava plains; elsewhere, rolling to rough terrain; elevation ~1 km or less.

6. Fractured highlands, Olympus Mons aureole (MC-9-SW). Specific location: 12°N., 125.5°W. Sample suite: (1) basal aureole of Olympus Mons; (2) fractured highlands; (3) plains lava flows. The rock types/ages are (1) pyroclastic material or lava flows of possible felsic composition (intermediate age); (2) breccias or lava flows (old age); (3) basaltic lava flows (very young age). Factors affecting accessibility are flat lava plains between outcrops of aureole and highland materials; elevation ~3-4 km.

7. North polar region - Borealis Chasma (MC-1A). Specific location: near 82°N., 55°W. Sample suite: (1) polar perennial ice cap; (2) layered deposits; (3) patterned plains (polygonal). The rock types/ages are (1) water ice (very young?); (2) cyclic eolian beds (very young); (3) lava flows (old). Factors affecting accessibility are flat to rugged topography; elevation ~1 km.

References

[1] Scott, D.H., and Tanaka, K.L., 1980, Mars: Paleostratigraphic restoration of buried surfaces in Tharsis Montes: Icarus 45, p. 304-319.

[2] Scott D.H., 1981, A Viking solution to a Mariner stratigraphic problem: Reports of Plantetary Geology Program, NASA Tech. Memo. 84211, p. 411-413.

[3] Scott, D.H., and Tanaka, K.L., 1982, Ignimbrites of Amazonis Planitia region of Mars: Jour. Geophys. Res., v. 87, no. B2, p. 1179-1190.

[4] Scott, D.H., 1982, Volcanoes and volcanic provinces: Martian western hemisphere: Jour. Geophys Res., v. 87, B12, p. 9839-9851.

[5] Scott, D.H., 1983, Meander relics: Direct evidence of extensive flooding on Mars: Conference on Planetary Volatiles, LPI Technical Report 83-01, p. 157-165.

D118

Viking High-Resolution Studies of Mars

Harold Masursky, D. H. Scott, E. C. Morris, M. E. Strobell, and A. L. Dial, Jr.; U.S. Geological Survey, Flagstaff, Arizona

Several Mars areas are being studied as potential future rover and sample-return sites in order to define loci where complex geologic relations occur in restricted areas. Preliminary results were presented of the Memnonia area, the southeastern scarp of Olympus Mons, the Mangala Valles, and the Kasei Valles at a meeting of the Solar System Exploration Committee at Snowmass, Colorado, in August. This committee has accepted, as the highest priority future large mission, a Mars Sample Return with rover. Three additional sites, at Lunae Planum, Candor Mensa, and Chasma Boreale were not discussed at the Snowmass meeting, but their status is reviewed here.

In the Memnonia region, ancient heavily cratered terrain, cratered plains of intermediate age, and an uncratered very young and heavily wind grooved unit are juxtaposed. This last unit may consist of poorly consolidated young volcanic rocks. This terrain may account for the peculiar radar-scattering characteristics indicating extremely rough terrain reported by [1,2]. A 1:500,000 scale controlled photomosaic is available of the area, and provides the base for a preliminary geologic map (Fig. 1) [3]. Topographic and more detailed geologic maps will be completed in 1984.

The southeastern part of the Olympus Mons area contains volcanic flow units of probable basaltic composition that are of three ages. The oldest rocks are exposed in the cliffs of the scarp. Younger flows cascade over the scarp and flow out onto surrounding plains. The youngest flows emerge from fissures to the north, overlap the older flows, and cover the plains units. Planimetric and topographic maps of the area are available, and a preliminary geologic map has been compiled [4]. An additional controlled photomosaic and a more detailed geologic map will be compiled that will incorporate a strip of very high resolution photos taken on the next-to-last day of the Viking mission. These photos show distinct elongate lava flows.

The Mangala Valles contain ancient cratered terrain, cratered plains of intermediate age, channel deposits, and young volcanic deposits that overlie the channel deposits. All units are highly modified by eolian erosion and deposition. We have not yet located a single site that contains all four geologic units in juxtaposition. Uncontrolled photomosaics of high-resolution Viking photographs have been compiled of the area, and a geologic sketch map has been drawn. Controlled photomosaics, topographic maps, and detailed geologic maps will be made.

In the Kasei Valles site, ancient cratered terrain, intermediate-age cratered plains, channel deposits, and young volcanic deposits occur. The critical outcrops are spread over a considerable area. Two 1:500,000 scale photomosaics are currently available and a geologic sketch map has been completed [3]. Additional photomosaics and a detailed geologic map will be made.

Although the Lunae Planum area west of the Chryse Basin has many well-developed stream channels, it does not seem to have young volcanic deposits that overlie these channels and their deposits. For this reason it would be difficult to date the channel episodes from returned samples. A 1:5

million scale shaded-relief map of the Lunae Planum area is available and 1:500,000 scale maps will be made this coming year. The most favorable geologic area will be studied in detail to define the largest variety of units.

In the Candor Mensa area, layered deposits underlie the mesa and adjacent areas but are not an obvious part of the steep wall of Candor Chasma. There still is uncertainty as to whether the layered deposits are unconformably deposited within the canyon or are part of the normal canyon sequence. These layered deposits may contain soil horizons that were formed during several fluvial episodes. It may be possible to date radiometrically the returned samples from the underlying and overlying volcanic rocks and from these, to date the fluvial episodes of these horizons. Six controlled photomosaics of the general region are completed and two geologic sketch maps showing alternative geologic relations were prepared for earlier rover traverse studies [2]. Contour maps and detailed geologic maps of the mesa, which lies within one quadrangle, will be made. Also, D. H. Scott and N. E. Witbeck are compiling a regional geologic map of the entire Valles Marineris canyon region, and B. K. Lucchitta and H. M. Ferguson will map the areal block of six controlled photomosaics.

Preliminary studies have also been made of the southern end of Chasma Boreale near the edge of the permanent north polar ice deposits. Ice, layered terrain, and eolian sand dunes and sheets are well developed in a small area. Detailed planimetric, topographic, and geologic maps will be made of this area.

References

[1] Simpson, R. A., Tyler, G. L., and Campbell, D. B., Arecibo radar observations of martian surface characteristics near the equator: Icarus 33, 102-115, 1978a.

[2] Simpson, R. A., Tyler, G. L., and Campbell, D. B., Arecibo radar observations of Mars surface characteristics in the Northern Hemisphere: Icarus 36, 153-173, 1978b.

[3] Scott, D. H., and Tanaka, K. L., Ignimbrites of Amazonis Planitia Region of Mars: J. Geophys. Res. 87, 1179-1190, 1982.

[4] Morris, E. C., Geologic map of Olympus Mons: Rept. Planet. Geol., NASA Tech. Mem. 85127, 134-135, 1982.

[5] Masursky, Harold, Dial, A. L., Strobell, M. E., Schaber, G. G., and Carr, M. H., Detailed reports of the Mars sample returns, 715-23, Mars Science Working Group, Mars Sample Return Study Effort: NASA, JPL, Cal. Inst. Tech., unpublished report, 1980.

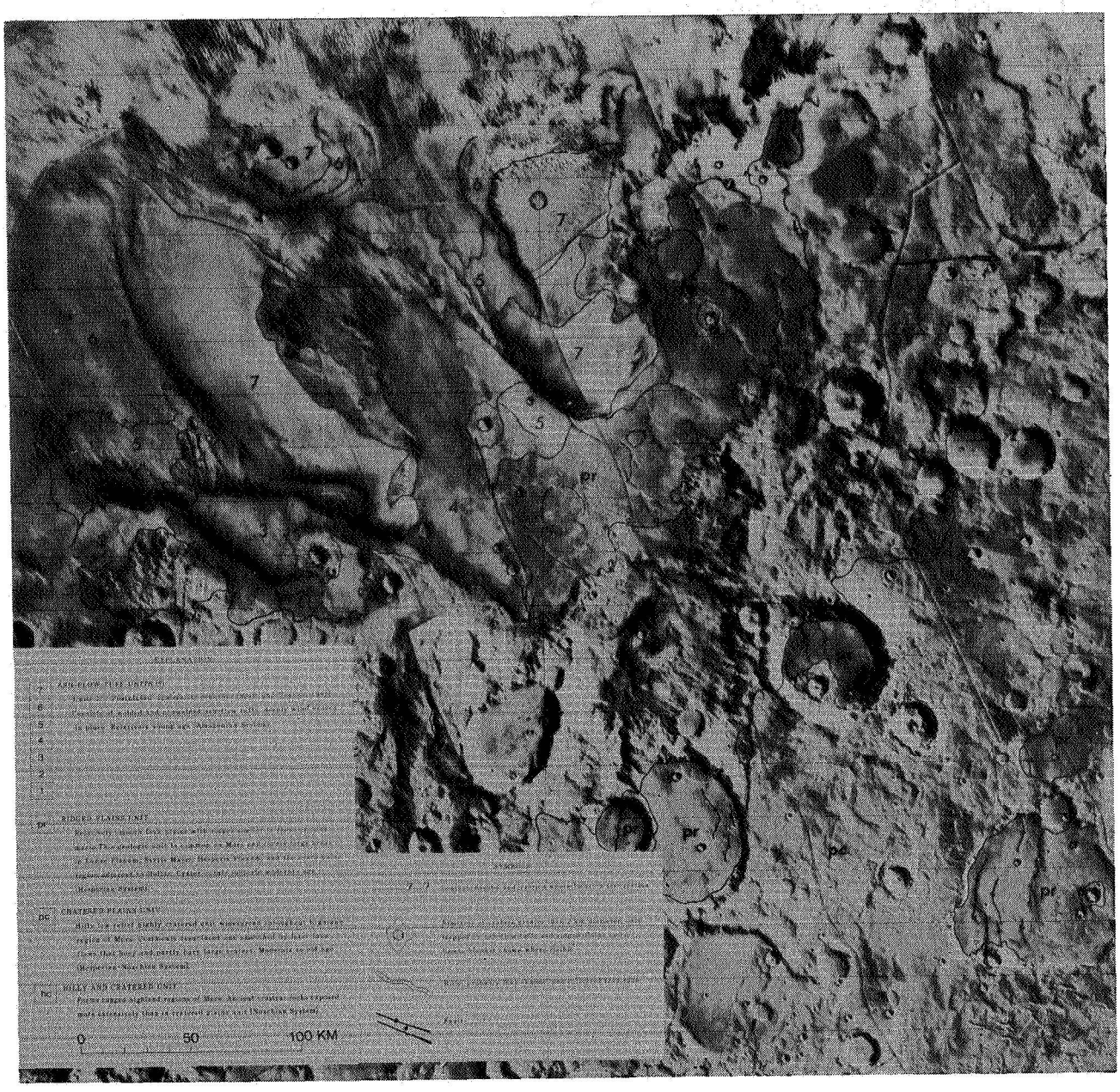
0
50
100 KM

D119

GEOLOGIC MAPPING IN THE CYDONIA REGION OF MARS

WITBECK, N. E., U.S. Geological Survey, Flagstaff, Arizona 86001 and Underwood, J. R., Jr., Kansas State University, Manhattan, Kansas

The Cydonia region on Mars, which includes the approximate area bounded by lat 30°-50° N. and long 0°-30° W. (Fig. 1a), lies along the east margin of Acidalia Planitia, the largest area of low albedo in the martian northern hemisphere. Two major physiographic provinces occur in this region: a high-standing, heavily cratered plateau to the south and low-lying, lightly cratered plains to the north.

Several mappable geologic units have been defined in the Cydonia region. Unit characteristics are summarized in Table 1. The surface of the plateau, interpreted as composed of the oldest units in the area on the basis of the abundance of large impact craters (Fig. 1b), marks the northern extent of the ancient southern highlands. Knobby terrain material that may be plateau remnants occurs throughout the lower plains region, suggesting that the plateau once extended over much of the region.

Most of the plains units appear to have formed after the retreat of the plateau; they represent a complex history of depositional and erosional events that created varied landforms. The two most unusual landforms seen on the plains in this region are the polygonal fracture pattern and the small (<1 km) cratered domes.

Patterned (fractured) terrain has been the subject of controversy since its discovery during the early stages of the Viking Mission. Proposed mechanisms include: permafrost activity [1,2], desiccation of water-saturated sediments [3], contraction of cooling lavas [3,4], and tectonic deformation [5]. None of the proposed mechanisms offers an adequate explanation, and it may be that the troughs were formed by more than one process. The origin of the small cratered domes in the Cydonia region has also been the subject of controversy. Both volcanic and nonvolcanic origins have been suggested for these landforms; however, we favor the volcanic hypothesis. (For further discussion see Witbeck and Underwood [6].)

The decipherable geologic history of the Cydonia region begins with the emplacement of the old, heavily cratered plateau material. This deposition was followed by erosion and scarp retreat that left only remnants of the plateau throughout the plains. The topographically lower plains were then resurfaced with volcanic, eolian, and possibly alluvial materials. Some of the material eroded from the plateau may have been redeposited in the plains region. The fracture pattern may have developed at about the same time. Next, volcanic activity formed many small cratered domes, i.e., cinder cones or pseudocraters, throughout the region. Volcanic activity declined after the extrusion of the lava flows in the northwestern part of the region, which produced young mottled plains material.

References

[1] Carr, M. H., and G. G. Schaber, Martian permafrost features, J. Geophys. Res., 82, 4039-4054, 1977.

[2] Helfenstein, P., Martian fractured terrain: Possible consequences of ice-heaving (abs.), Reports of Planetary Geology Program, NASA Tech. Memo 82385, 373-375, 1980.

[3] Morris, E. C., and J. R. Underwood, Jr., Polygonal fractures of the martian plains (abs.), Reports of Planetary Geology Program, NASA Tech. Memo. 79729, 97-99, 1978.

[4] Masursky, H., and N. L. Crabill, Search for the Viking 2 landing site, Science, 194, 62-68, 1976

[5] Pechmann, J. C., The origin of polygonal troughs on the northern plains of Mars, Icarus, 42, 185-210, 1980.

[6] Witbeck, N. E., and J. R. Underwood, Jr., Lava flow material on the mottled plains in Mare Acidalium quadrangle (MC-4), Mars (abs.), Reports of Planetary Geology Program, NASA Tech. Memo. 85127, 137-139, 1982.

[7] Scott, D. H., and M. H. Carr, Geology map of Mars, U.S. Geol. Survey Misc. Inv. Map I-1083, 1978.

[8] Scott, D. H., and K. L. Tanaka, Mars: Paleostratigraphic restoration of buried surfaces in Tharsis Montes, Icarus, 45, 304-319, 1981.

[9] Guest, J. E., P. S. Butterworth, and R. Greeley, Geologic observations in the Cydonia region from Viking, J. Geophys. Res. 82, 4111-4120, 1977.

a.)

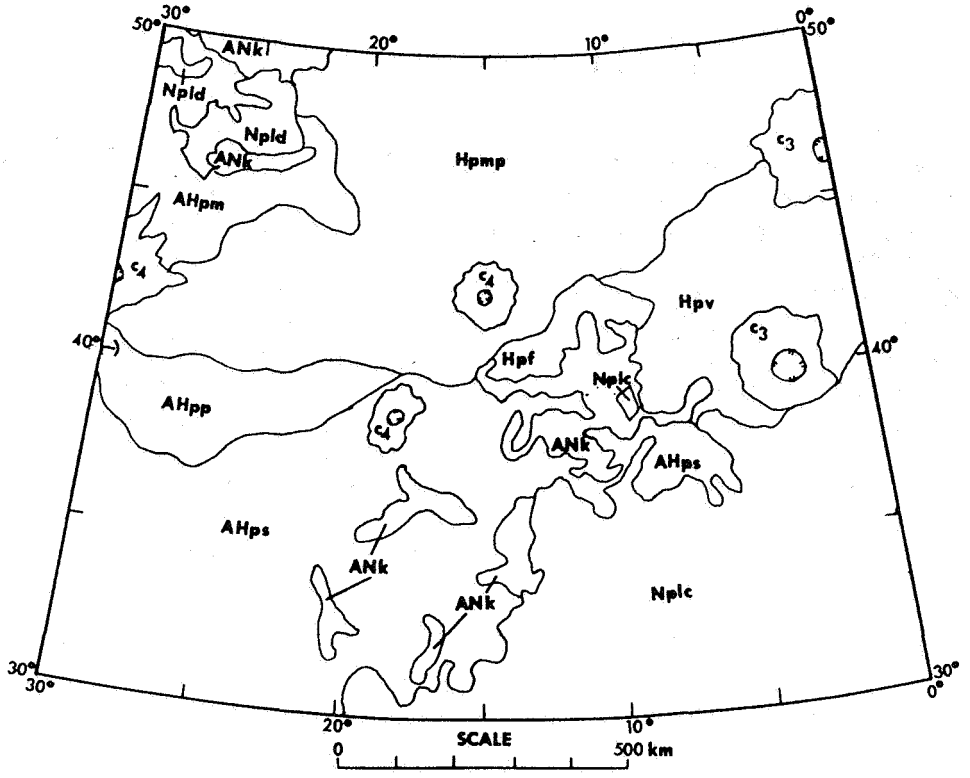

b.)

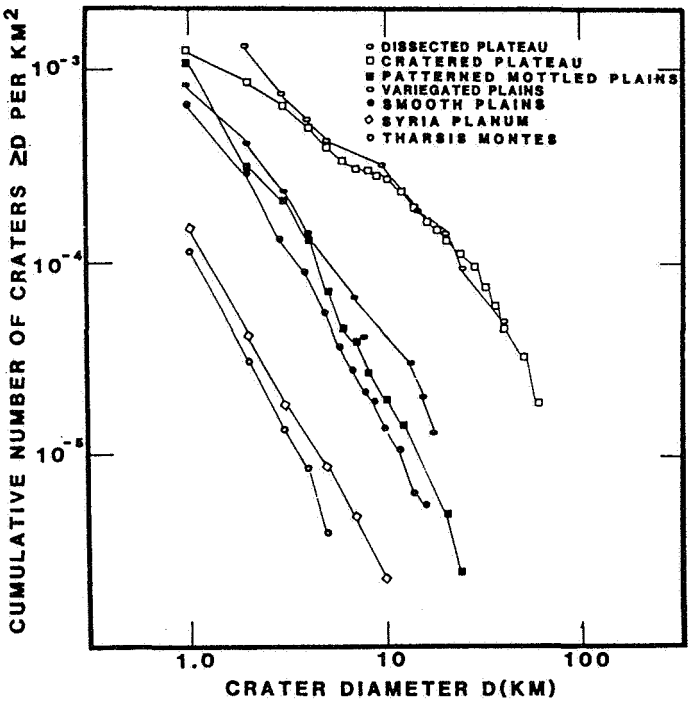

Figure 1. a.) Geologic sketch map of the Cydonia region of Mars. Unit symbols and names are listed in Table 1. Units are classified by systems established by Scott and Carr [7]. C_4 refers to well preserved crater material, C_3 refers to slightly degraded crater material. b.) Crater size-frequency distributions for selected units. Syria Planum and Tharsis Montes curves from Scott and Tanaka [8] are shown for comparison.

Table 1

Plains Units

AHpm	YOUNG MOTTLED PLAINS MATERIAL - Low albedo; relatively smooth dark plains material; several lobate escarpments and small (<1 km) cratered domes; escarpment commonly marks boundary with dissected plateau material; (Viking image 35A41). Interpretation: Young volcanic flows
AHpp	PATTERNED PLAINS MATERIAL - Intermediate albedo; smooth plains cut by troughs several hundred meters wide, <5 km long; gradational boundary with other plains units; (Viking image 597A05). Interpretation: Eolian and possible volcanic material; fractures may be result of permafrost, volcanism, desiccation, or tectonic activity
AHps	SMOOTH PLAINS MATERIAL - Varied albedo; smooth, relatively featureless plains material; large circular features outlined by knobs; cratered domes common near 39° N., 12°; gradational boundary with plains units; escarpment marks boundary with plateau; (Viking image 558A07). Interpretation: Eolian and possible volcanic material blanketing older, cratered surface
Hpv	VARIEGATED PLAINS MATERIAL - Varied albedo; smooth featureless plains; scattered cratered domes; streamlined remnants near boundary with cratered plateau unit; escarpment marks boundary with lower fractured plains unit; (Viking image 36A44). Interpretation: Volcanic, eolian, and alluvial plains
Hpf	FRACTURED PLAINS MATERIAL - Intermediate albedo; smooth plains cut by troughs up to 2 km wide, 20 km long, 5-10 km apart; wider troughs have flat floors; cratered domes common; gradational boundary with patterned mottled plains; escarpment marks boundary with higher variegated plains; (Viking image 32A36). Interpretation: Old unit underlying plateau materials exposed by scarp retreat [9], resurfaced by young volcanic material; fractures result of tectonism, volcanism, permafrost, or desiccation
Hpmp	PATTERNED MOTTLED PLAINS MATERIAL - Low albedo plains with high-albedo crater ejecta; intercrater region cut by troughs <1 km wide, <10 km long; cratered domes common; gradational boundary with other plains units; (Viking image 32A18). Interpretation: Volcanic plains; ejecta blankets result of impact excavating material of high albedo; troughs are volcanic, tectonic, permafrost, or desiccation features

Plateau Units

ANk	KNOBBY TERRAIN MATERIAL - Irregular hills or knobs, locally forming circular pattern; some have summit craters; (Viking image 70A09). Interpretation: Erosional remnants of higher surface; crater rims of buried surface; locally may be volcanic cones
Npld	DISSECTED PLATEAU MATERIAL - Intermediate to high albedo; smooth surface cut by numerous fractures; large, circular outlines common; escarpment commonly marks plateau-plains boundary; (Viking image 670B16). Interpretation: Outlier or remnant of cratered plateau; circular features are old craters; subsequently disrupted by faulting
Nplc	CRATERED PLATEAU MATERIAL - Intermediate albedo; heavily cratered; rough intercrater surface; escarpment commonly marks boundary with lower plains; (Viking image 561A07). Interpretation: Ancient crustal deposits partly resurfaced by volcanic and eolian material

D120

VOYAGER CARTOGRAPHY

R. M. Batson, U.S.Geological Survey, Flagstaff, AZ 86001

The Jovian and Saturnian satellites are being mapped at several scales from Voyager 1 and 2 data. Details of the Galilean satellite mapping program were given by Batson and others [1]. The Saturnian satellite mapping plan and other details of methods used in Voyager cartography were described by Batson and others [2,3].

Airbrush mapping at 1:5,000,000 is well under way. Two maps of Europa (Je-3 and Je-4) are complete and in press, as are three (Ji-2, -3, and -4) of Io and five (Jg-3, -4, -7, -8, -9) of Ganymede. Three Ganymede 1:5,000,000 scale quadrangles (Jg-10, -12, and -13) are in compilation.

More than 300 Voyager images of the Jovian and Saturnian satellites have been radiometrically processed in preparation for cartographic processing, and more than 100 of these have been geometrically transformed to map projections for base mosaic compilations. Film and magnetic tape copies of these images have been distributed to the Regional Planetary Image Facilities.

References

[1] Batson, R. M., Bridges, P. M., Inge, J. L., Isbell, C. E., Masursky, Harold, Strobell, M. E., and Tyner, R. L., Mapping the Galilean Satellites of Jupiter with Voyager data: Photogrammetric Engineering and Remote Sensing, 46, 10, 1303-1312, 1980.

[2] Batson, R. M., Bridges, P. M., and Mullins, K. F., Voyager cartography: in Reports of the Planetary Geology Progeam, NASA TM 84211, 484-485, 1981.

[3] Batson, R. M., Bridges, P. M., Inge, J. L., Lee, E. M., Masursky, Harold, Mullins, K. F., Skiff, B. A., and Strobell, M. E., Voyager 1 and 2 Atlas of six Saturnian satellites: NASA Spec. Pub. (in press).

D12
ABS
ONLY

1:2,000,000 SCALE CONTROLLED PHOTOMOSAICS OF MARS

R. M. Batson and R. L. Tyner, U. S. Geological Survey, Flagstaff, AZ 86001

Compilation of a series of 140 controlled photomosaics of Mars at a scale of 1:2,000,000 is in progress. To date, 107 mosaics have been published, seven are in press, and 27 are in compilation. Several of the mosaics compiled early in the series have been revised by including higher quality images than were available at the time of the original compilation, resulting in publication of more than 140 map sheets.

REVISIONS OF 1:5,000,000 SCALE MARS MAPS

R. M. Batson and P. M. Bridges, U. S. Geological Survey, Flagstaff, AZ 86001

The 1:5,000,000 shaded relief maps of Mars originally compiled from Mariner 9 pictures are being upgraded by adding details visible on Viking Orbiter images. This work is done by modifying the original airbrush drawings; no attempt is made to reposition features according to the latest control nets.

MC-2, -3, -4, -5, -17, -18, -18, and -20 have been revised and published. MC-7, -10, -11, -16, and -23 have been revised and are in press, and MC-6 and -12 are in compilation.

D123
ABS.
0404

MARS SPECIAL-SCALE MAPS: THE 1:500,000 SERIES

R. M. Batson, U. S. Geological Survey, Flagstaff, AZ 86001

Controlled photomosaics of areas of special scientific interest on Mars are being compiled with high-resolution Viking Orbiter pictures at a scale of 1:500,000 on a Mars Transverse Mercator (MTM) system. Areas selected for mapping are based on recommendations by the Planetary Cartography Working Group, which has recommended compilation of six quadrangles in the Valles Marineris region, 18 quadrangles in the Lunae Palus region, and 12 quadrangles in the Alba Patera region. The six Valles Marineris quadrangles are complete and in press, as are two of the Lunae Palus quadrangles. All of the other quads are in various stages of compilation.

D124
ABS
ONLY

MARS COLOR ALBEDO MAPPING

R. M. BATSON, U. S. Geological Survey, Flagstaff, AZ 86001

Viking Orbiter pictures of Mars taken from near apoapsis with small phase angles are being used to compile a visual albedo map of Mars in three colors. Four products are planned: 1) a preliminary 1:15,000,000 airbrush map of a large area between the fiftieth parallels, made with pictures taken through the red filter, and at an Ls of 52 through 87 degrees; 2) a controlled computer mosaic of the equatorial zone consisting of pictures taken through three color filters during Viking 1 orbital revolutions 614 through 699; 3) a final airbrush map of the entire planet compiled at the 1:15,000,000 scale, made with pictures taken through the red or clear filters, and 4) a controlled computer mosaic of the best available color pictures that show as much of the planet as possible.

The first product is in press [1,2]. Color images taken during revolutions 583 through 699 have been processed and projected [3]. Controlled color mosaics for revolutions 586 and 614 are complete, and those for revolutions 583, 593, 609, 663, 666, 669, 672, 681, 684, and 687 are in progress.

References

[1] Batson, R. M., and Davis, Susan L., Albedo map of Mars: in Reports of the Planetary Geology Program, 1982, NASA TM 85127, 1982, 359.

[2] U.S.G.S., Shaded relief and surface markings of Mars, western region (sheet 1) and eastern region (sheet 2), U. S. 1Geol. Survey Misc. Inv. ser. Map I-1535, in press.

[3] Batson, R. M., Hall, D. G., and Jordan, JoAnne, Color pictures of Mars: in Reports of the Planetary Geology Program, 1978-1979, NASA TM 80339, 1979, 439.

D125
ABS
ONLY

ATLAS OF MARS

R. M. Batson, U. S. Geological Survey, Flagstaff AZ 86001

A hard-cover atlas of reduced-scale versions of all Mars cartographic products will be published upon completion of the revisions of the 1:5,000,000 maps, the 1:2,000,000 photomosaics, and the Mars color albedo mapping tasks. This atlas will supercede the existing Atlas of Mars prepared by Batson and others [1]. Although full-scale efforts in preparation of the atlas will not begin until all of the products to be included are essentially complete, preliminary experiments with formats and map presentation style are in progress. This work includes making composite images of comparatively low resolution digital color mosaics and high resolution shaded relief and/or photomosaics, and the definition of scales and formats for the presentation of the maps. In addition to these experiments, a new small-scale index map of Mars has been prepared, showing relief and albedo at resolution suitable for page-size publication.

Reference

[1] Batson, R. M., Bridges, P. M., and Inge, J. L., Atlas of Mars: the 1:5,000,000 map series: NASA SP 438, 146, 1979.

D126

THE CONTROL NETWORKS OF THE SATELLITES OF JUPITER AND SATURN

Davies, Merton E., The Rand Corporation, Santa Monica, California 90406

Geodetic control networks are being computed photogrammetrically for the large satellites of Jupiter and many of the satellites of Saturn using pictures from the Voyager 1 and 2 encounters. Control points have been identified on the satellites and their coordinates computed by single-block analytical triangulations. The status of the control nets is summarized in the following table:

Satellites	Points	Pictures	Measurements	Normal Equations	Overdetermminations	σ(μm)
Jupiter						
Io	640	246	10926	2018	5.41	11.28
Europa	181	120	3804	722	5.27	11.88
Ganymede	1669	295	17212	4223	4.08	21.37
Callisto	624	255	10220	2013	5.08	15.97
Saturn						
Mimas	110	32	1356	316	4.29	13.04
Enceladus	71	22	1052	208	5.06	10.87
Tethys	110	27	924	301	3.07	12.15
Dione	126	28	1322	336	3.93	13.94
Rhea	352	84	3814	956	3.99	11.16
Iapetus	62	80	1858	364	5.10	12.26

Coordinates for the control points on the Galilean satellites have been reported in Davies and Katayama, 1981. The mean radii as measured by the triangulations are Io, 1815 km; Europa, 1569 km; Ganymede, 2631 km; and Callisto, 2400 km. The longitude systems of Europa, Ganymede, and Callisto are defined by craters on their surfaces; because of the extensive volcanism on Io, no feature has been chosen for this purpose on Io.

Davies, 1983, reported that the shape of Io was ellipsoidal with principal axes a = 1820 ± 3 km, b = 1812 ± 3 km, and c = 1812 ± 3 km. The major axis a falls at Io longitude 330° ± 10°.

The surfaces of the Saturnian satellites Mimas and Enceladus are ellipsoidal. For Mimas the best fit axes are a = 200 km, b = 196 km, and c = 194 km; for Enceladus the axes are a = 256 km, b = 250 km, and c = 248 km (see Davies and Katayama, 1982). The mean radii of the other Saturnian satellites are Tethys, 524 km; Dione, 559 km; Rhea, 764 km; and Iapetus, 724 km. In the computation of the control nets it is important that the pictures and points completely encircle the body; with flyby missions this is sometimes difficult to achieve because of the great difference in resolution between pictures taken early and late in the flyby. Sometimes pictures from a second flyby help fill gaps; thus the control nets of Tethys, Dione, and Rhea contain pictures from both Voyager 1 and 2 encourters and do encircle the satellites. The control net of Mimas contains pictures taken by Voyager 1 and does encircle the satellite, whereas the control of Enceladus contains pictures taken by Voyager 2 and does not encircle the satellite. The control net of Iapetus contains two regions, one from pictures taken by Voyager 1 and another from pictures taken by Voyager 2. The regions do not overlap and it has not been possible to tie them photogrammetrically. The control networks of most of these satellites have been published.

References

Davies, M. E., and F. Y. Katayama, "Coordinates of Features on the Galilean Satellites," *J. Geophys. Res.*, Vol. 86, A10, September 30, 1981. pp. 8635-8657.

Davies, M. E., and F. Y. Katayama, "The Control Networks of Mimas and Enceladus," *Icarus*, Vol. 53, No. 2, February 1983.

Davies, M. E., and F. Y. Katayama, "The Control Networks of Tethys and Dione," EOS, June 14, 1983, to be published in *J. Geophys. Res.*

Davies, M. E., and F. Y. Katayama, "The Control Networks of Rhea," to be published in *Icarus*.

Davies, M. E., "The Shape of Io," Abstracts of the *Natural Satellites*, IAU Colloquim 77, July 5-9, 1983, p. 14.

Davies, M. E., "The Control Networks of Iapetus," to be published in the *Bulletin of the American Astronomical Society*, Vol. 15, No. 3, 1983.

D127 NBS ONLY

THE CONTROL NETWORK OF MARS: SEPTEMBER 1983

Davies, Merton E., The Rand Corporation, Santa Monica, California 90406

Strips of Viking mapping pictures are being added to the planetwide control network of Mars. These high resolution strips run from the Viking 1 lander site east to Airy-0, north along the 0° meridian to 60° latitude, southwest through the Viking 1 lander site to the equator, and west along the equator to 180° longitude. Everywhere along these strips, old points are incorporated in the measurements thus assuring that the strips and planetwide net make up a single large data set. The control points are much denser in the areas covered by the strips than in those regions not covered by strips and as they are usually associated with smaller craters their coordinates will be more accurate. Within the strips the standard error of the coordinates of the control points is estimated to be less than 3 km and the error in longitude of a few points near Airy-0 is less than 40 m.

The horizontal coordinates of the control points on Mars have been updated with a single-block planetwide analytical triangulation computed in September 1982. Coordinates of the points will be published later this year. The computation contained 47524 measurements of 6853 points on 1811 pictures. These comprised 1054 Mariner 9 and 757 Viking frames. The overdetermination factor was 2.48 and 19139 normal equations were solved. The standard error of measurement was 18.06 μm. The longitude of the Viking 1 lander site was 47.°962 and the latitude 22.°480. The latitude of Airy-0 was -5.°152. A report has been written and accepted for publication in the *Journal of Geophysical Research*.

References

Davies, M. E. and F. Y. Katayama, "The 1982 Control Network of Mars," EOS, June 7, 1983, to be published in *Journal of Geophysical Research*.

D128

TOPOGRAPHIC MAPPING OF MARS: 1:2 MILLION SERIES

Sherman S. C. Wu and Francis J. Schafer, U. S. Geological Survey, Flagstaff, Arizona 86001

After completion of 13 of the 80 quads of the Mars 1:2 million series contour maps, compilation was halted due to topographic disagreement between the compiled maps and Earth-based radar elevation observations. The Mars mapping task is entirely dependent on the planet-wide control network. The current Mars control net is derived from about 800 Viking orbital photographs within two belts, equatorial and polar, covering about 70% of the martian surface [1]. This net will produce about 5,000 ground-control points, 70% of which will have the same locations as those produced from Davies' primary Mars control net [2]. The purpose of selecting these 3,500 identical points is to tie the new control net to Davies' horizontal positions and to improve Davies' elevations. Primary controls for the new net are: 1) camera parameters from the SEDR (Supplementary Experiment Data Record), 2) about 1,000 ground-control points from Earth-based radar observations, and 3) 400 points from occultation measurements from both Mariner 9 (250 points) and Viking (150 points) missions. In the adjustment, heavy constraints are assigned to the elevations of the radar and the occultation points.

Completion of the Mars planet-wide control network will enable the more accurate compilation of the Mars 1:2 million series maps, and will provide data for completing revision of the Mars global topographic map (1:15,000,000). The data from the new net will also be used to: 1) improve the horizontal locations of occultation points of both the Mariner 9 and Viking Missions [3,4]; 2) calibrate locations of Earth-based radar profiles [5]; 3) adjust the internal consistency of camera positions and orientations in the SEDR; and 4) tie to the control net the detailed local topographic maps at 1:500,000 scale compiled for science studies of possible future landing sites. In fact, the adjustment for internal consistency of the cameras is the only means by which the Viking orbital photographs can be used to establish stereo models on the analytical plotter for photogrammetric compilation [6].

The Mars control network is processed through a block adjustment of analytical aerotriangulation using the U. S. Geological Survey's GIANT (General Integral Analytical Triangulation) program. The computer program has been implemented on the VAX computer in Flagstaff. The processing of the Mars control network will be completed by the end of fiscal year 1983.

References

[1] Wu, Sherman S. C., and Schafer, Francis J., Planetwide control network of Mars, NASA Tech. Memo. 85127, 367-369, 1982.

[2] Davies, M. E., Katayama, F.Y., and Roth, J. A., Control net of Mars, The Rand Corp. R-2039-NASA, 91 p, 1979.

[3] Kliore, A., Cain, D. L., Fjeldbo, G., and Seidel, B. L., Mariner 9 S-band martian occultation experiment: Initial results on the atmosphere and topography of Mars, Science, vol. 175, 313-317, 1972.

[4] Lindal, G. F., Hotz, H. B., Sweetnam, D. N., Shippony, Z., Brenkle, J. P., Hartsell, G. V., and Spear, R. T., Viking radio occultation measurements of the atmosphere and topography of Mars: Data acquired during 1 martian year of tracking, J. Geophys. Res. vol. 84, B14, 8443-8456, 1979.

[5] Downs, G. S., Reichley, P. E., and Green, P. R., Radar measurements of martian topography and surface properties, Icarus, vol. 26, no. 3, 273-312, 1975.

[6] Wu, Sherman S. C., Elassal, A. A., Jordan, R., and Schafer, F. J., Photogrammetric application of Viking orbital photography, Planet. Space Sci. vol. 30, no. 1, 45-55, 1982.

D129

TOPOGRAPHY OF MARS DERIVED FROM HIGH-RESOLUTION IMAGES

Sherman S. C. Wu and Brian A. Skiff, U. S. Geological Survey, Flagstaff, Arizona 86001

High-resolution Viking Orbiter images of Mars are being used to compile topographic maps of features of special geologic interest and of areas that are the subject of future mission planning. Maps are compiled at the largest scales that can be supported by available images. Completed maps of this type include those of Arsia Mons, Olympus Mons [1], Canyonland [2], a few maps covering the polar caps [3], and several maps of volcanic features and impact craters. A detailed contour map of Candor Chasma is being compiled to support possible future rover missions. Detailed topographic maps of the regions of the two polar caps are being compiled to support climate studies.

Digital elevation data are collected simultaneously with compilation of high-resolution contour maps on the analytical plotter. These data can be merged with image data for the production of orthophoto mosaics, shaded relief maps, and perspective views including synthetic stereo [4,5,6]. These techniques were applied to the Olympus Mons map [7], using digital elevation data together with Viking Orbiter photograph 646A28 to make oblique perspective views. Figure 1 consists of monoscopic views of Olympus Mons viewed from due east (a), due west (b), and stereoscopic views from due north (c), and from the southeast (d). These images are valuable tools for geologic interpretation. In fact, with this technique, digital terrain data of Olympus Mons have been processed for a film by the Jet Propulsion Laboratory for "touring" Olympus Mons.

References

[1] Wu, S. S. C., Garcia, P. A., Jordan, Raymond, and Schafer, F. J., Topographic map of Olympus Mons, Third Intl. Colloquium on Mars, LPI Contribution 442, 287-289, 1981.

[2] U. S. Geological Survey, Topographic orthographic mosaic of the Tithonium Chasma region of Mars, I-1294 map, 1980.

[3] Masursky, Harold, Dial, A. L., and Strobell, M. H., Polar ice inventory--A progress report, NASA Tech. Memo. 81776, 399-401, 1980.

[4] Batson, R. M., Edwards, Kathleen, and Eliason, E. M., Synthetic stereo and LANDSAT pictures, Photogrammetric Engineering and Remote Sensing, v. 42, no. 10, 1279-1284, 1976.

[5] Batson, R. M., Hall, D. G., and Edwards, Kathleen, An orthophoto mosaic of Tithonium Chasma, NASA Tech. Memo. 80339, 415, 1979.

[6] Batson, R. M., Edwards, Kathleen, and Skiff, B. A., Orthophoto mosaics and three dimensional transformations of Viking Orbiter pictures, NASA Tech. Memo. 84211, 493-495, 1981.

[7] Wu, S. S. C., Garcia, P. A., Jordan, Raymond, Schafer, F. J., and Skiff, B. A., Topography of the shield volcano, Olympus Mons on Mars, Nature, (in press).

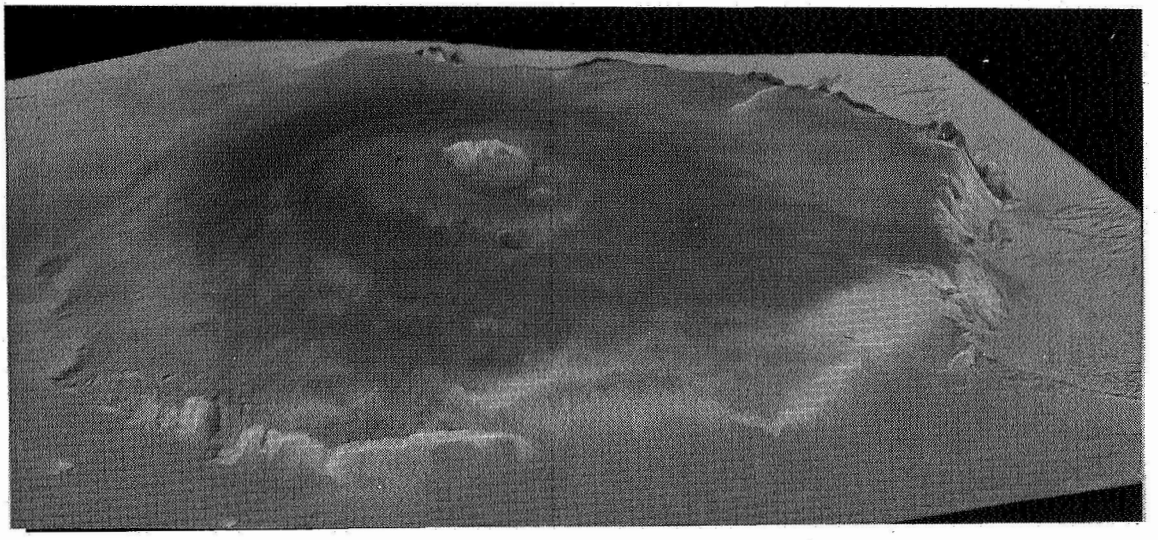

Fig. 1a - Viewing from the east

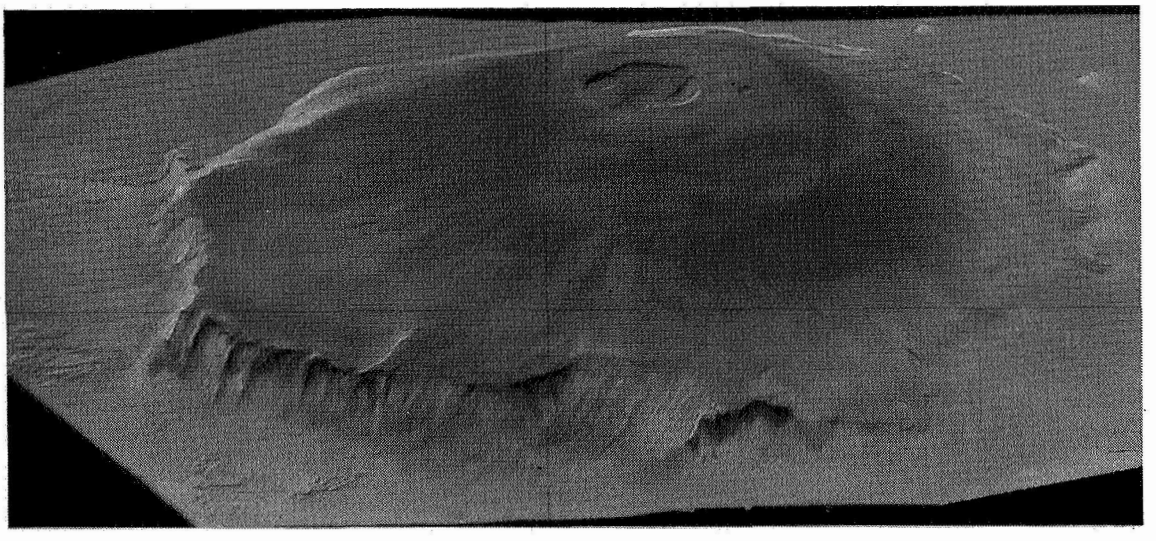

Fig 1b - Viewing from the west

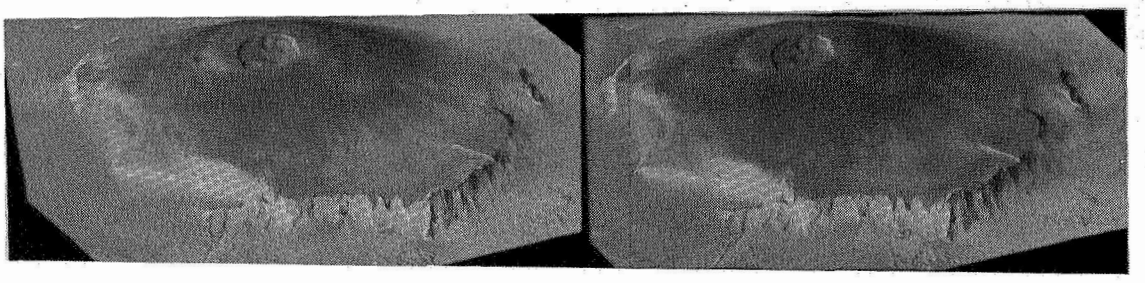

Fig. 1c - Viewing from the north

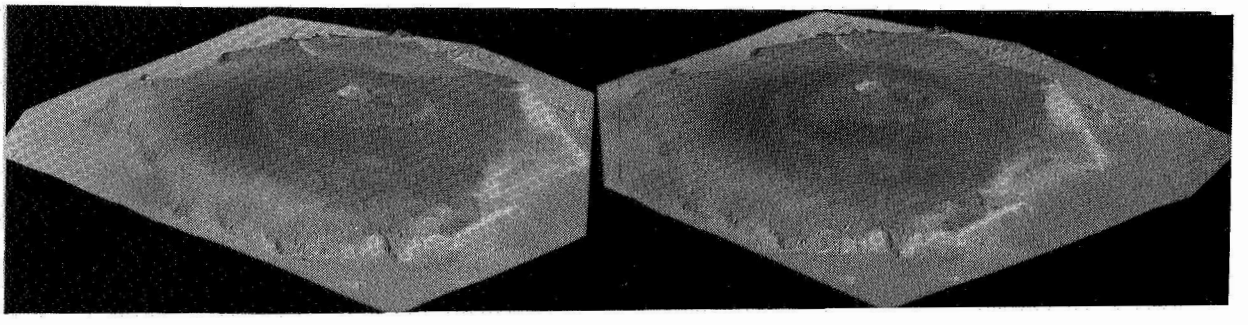

Fig. 1d - Viewing from the southeast

Figure 1 - Perspective views of Olympus Mons. Pictures were generated by three-dimensional transformation of digital image processing of Viking Orbiter photograph 646A28. The transformation was controlled by digital elevation data collected at the time of compilation of the map. Viewing angle is 25° from the horizon. A 5X vertical exaggeration has been applied. Figures a and b are monoscopic views from due east and due west, respectively; c and d are stereoscopic views from due north and from the southeast. Both stereo pairs have 5° separation in azimuth between the left and the right pictures.

D130

PLANETARY ELEVATION REFERENCE SYSTEMS

Sherman S. C. Wu, U. S. Geological Survey, Flagstaff, Arizona 86001

Because none of the known planets in the Solar System, other than Earth, have large bodies of water, it is not possible to use a sea-level reference for their topographic datums. One of the alternative methods is to define a datum on the basis of a planet's gravity field. By using Mariner 9 radio-tracking data, the topographic datum of Mars was defined by its gravity field [1,2] described in terms of fourth-order and fourth-degree spherical harmonics combined with a 6.1-millibar pressure surface with a mean radius of 3,382.9 km [3-6]. All Mars maps of various scales have been compiled using the topographic datum defined by the gravity field of Mars.

Based on Lunar Orbiter IV tracking data and laser ranging data, a new topographic datum of the Moon has been defined using the lunar gravity field [7], described in terms of spherical harmonics of fifth-order and fifth-degree and with sixth-order sectorial terms [8,6,9]. The mean radius used to define the datum is 1738 km. Based on this newly defined topographic datum, a new global topographic map of the Moon is under compilation.

A question has arisen in the mapping community as to whether it is worthwhile, for purposes of mapping the planets, to use a complex gravity surface as opposed to using a triaxial figure or even simply a spheroidal figure, as is the case for terrestrial mapping. Because the purpose of planetary mapping is to provide topographic information for planetary scientific studies and for the support of planetary mission planning and operations, I consider the use of gravity potential the most appropriate method for elevation reference. For example, it is of vital importance to such studies to know the directions of slopes on planetary surfaces, especially if a landing mission is proposed. In order to test the use of gravity fields for defining topographic datums of planetary bodies, I have devised the following method to compare the topographic datum defined by tri-axiality and that defined by gravity.

Topographic datums defined by tri-axiality are computed by:

$$R_p = 1/\left[\frac{1}{R_e^2} \cos^2 \psi + \frac{1}{C^2} \sin^2 \psi \right]^{1/2}$$

Where R_e is the radius along the equator of the planet and is determined by,

$$R_e = 1/\left[\frac{\cos^2 (\lambda-\lambda_0)}{A^2} + \frac{\sin^2 (\lambda-\lambda_0)}{B^2} \right]^{1/2}$$

λ_0 is the longitude of intersection intersected by the longer axis A of the major axes and ψ is the geocentric latitude which is converted from geodetic latitude ϕ as:

$$\psi = \tan^{-1} [(1-e^2) \tan \phi] = \tan^{-1} [\frac{C^2}{R_e^2} \tan \phi]$$

A and B are the semi-major axes and C is the semi-minor axis of the planet.

From the gravity derivations, A, B, and C of both Mars and the Moon have been computed [6] as, respectively, A=3,394.6 km, B=3,393.3 km, C=3,376.3 km and A=1,738.299 km, B=1,738.182 km, C=1,737.649 km. The topographic datums of Mars and the Moon were then computed from their tri-axiality, using the above three equations, for 5° increments in both longitude and latitude. Differences between the topographic datums defined by gravity and tri-axility were obtained by subtracting the datums defined by tri-axiality from those defined by gravity. As shown in fig. 1, the difference between these two systems ranges from +435 m to -592 m for Mars; for the Moon it ranges from +331 m to -212 m. These two ranges represent one contour interval on each of the 1 km interval global map of Mars and the 500 m interval global map of the Moon. Therefore, topographic datums of Mars and the Moon should continue to be defined by their gravity fields.

References

[1] Jordan, J. F., and Lorrell, J., Mariner 9: An instrument of dynamical science: Icarus, 25, 1, 146-165, 1975.

[2] Lorell, J. Anderson, J. D., and Shapiro, I. I., Celestial mechanics experiment for Mariner Mars 1971: Icarus, 12, 1, 78-81, 1970.

[3] Wu, S. S. C., Topographic mapping of Mars, U. S. Geological Survey Interagency Report: Astrogeology 63, 193 p, 1975.

[4] Wu, S. S. C., Mars synthetic topographic mapping: Icarus 33, 3, 417-440, 1978.

[5] Wu, S. S. C., Photogrammetric portrayal of Mars topography, J. Geophys. Res., Second Mars Colloquium Spec. Pub. 84, B14, 7955-7959, 1979.

[6] Wu, S. S. C., A method of defining topographic datums of planetary bodies: Ann. Geophys., 37, 1, 147-160, 1981a.

[7] Ferrari, A. J., Sinclair, W. S., Sjogren, W. L., Williams, J. G., and Yorder, C. F., Geophysical parameters of the Earth-Moon system: J. Geophys. Res., 85, B7, 3939-3951, 1980.

[8] Wu, S. S. C., Topographic mapping of the Moon: NASA Tech. Memo. 80339, 429-431, 1979b.

[9] Wu, S. S. C., New global topographic mapping of the Moon: Proc. Lunar Planet. Sci. Conf. 12th. 1217-1218, 1981b.

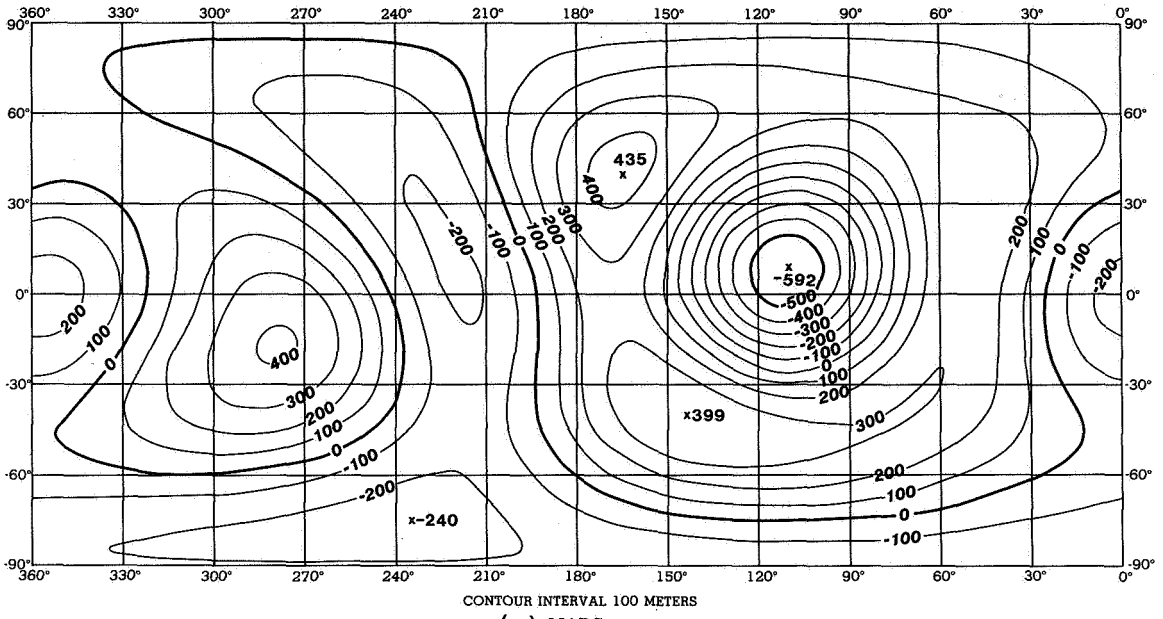

(a) MARS

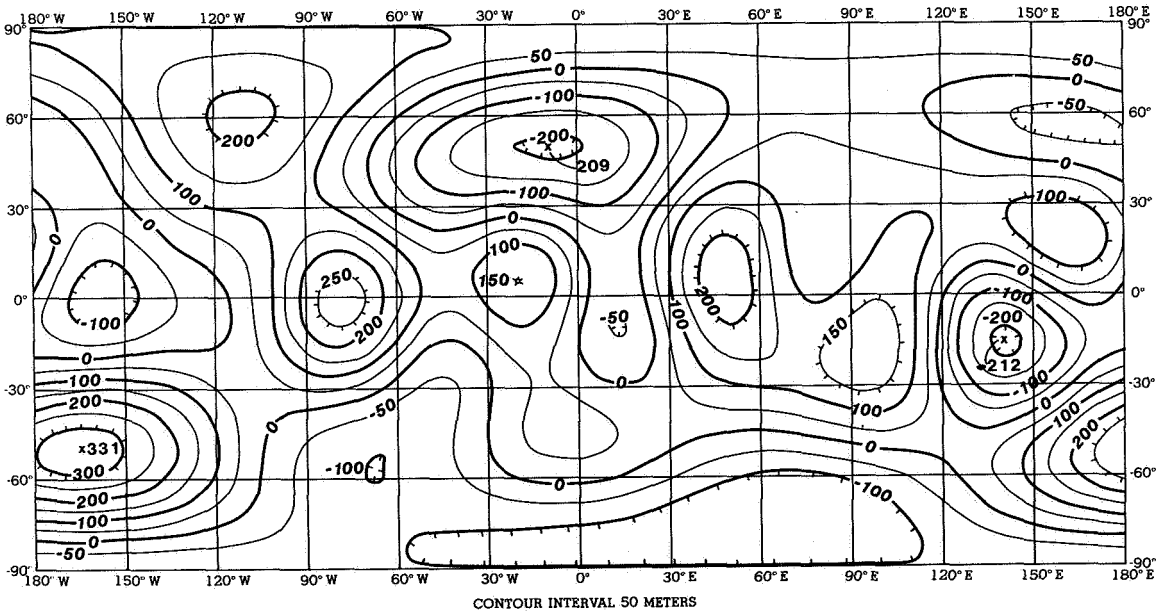

(b) MOON

Figure 1 - Contour maps of differences between topographic datums defined by gravity field and tri-axiality. Differences are computed by subtracting the topographic datum of tri-axiality from the datum based on gravity field. Maximum difference between these two systems ranges from +435 m to -592 m for Mars (a) and ranges from +331 m to -212 m for the Moon (b).

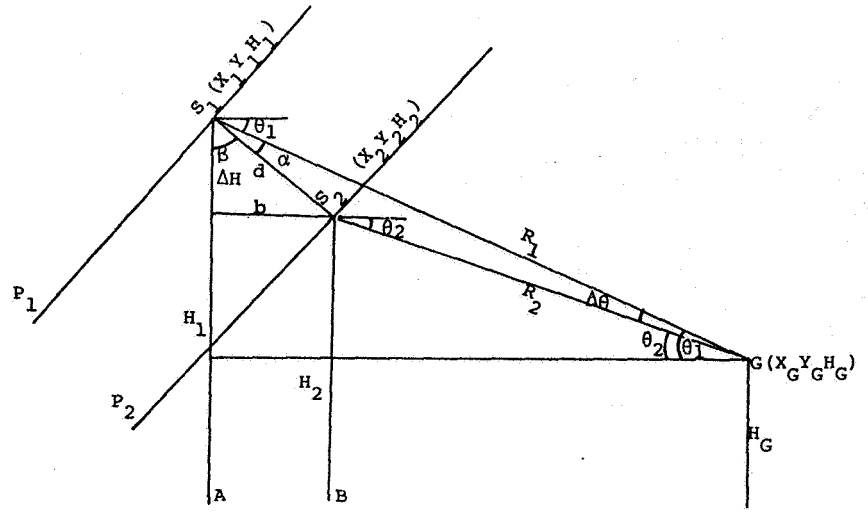

(a) Special case: Vertical planes of both radar looks are coincident.

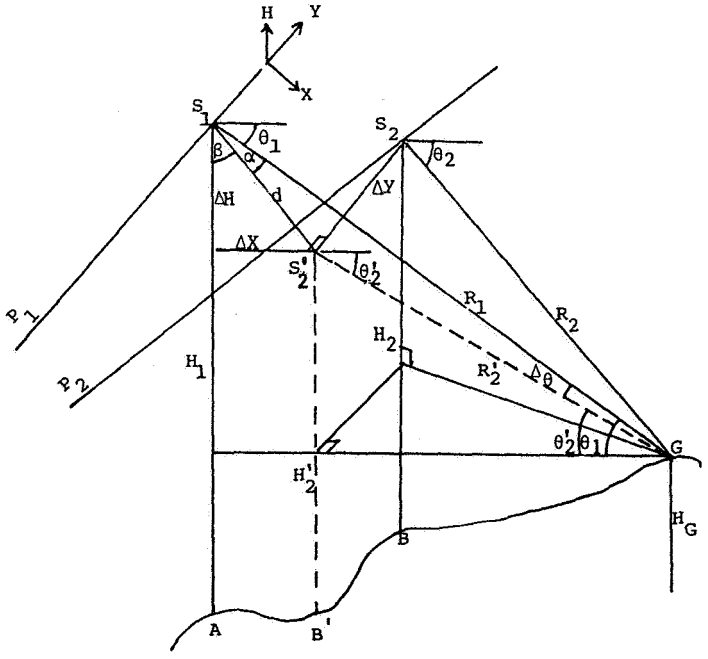

(b) General Case: Vertical planes of both radar looks are not coincident.

Figure 1 - Solution of radar-layover problem. (S_1 and S_2 are two stations along radar paths P_1 and P_2, from which ground point G is measured and recorded. θ_1, θ_2, and R_1, R_2 are depression angles and ranges, respectively, of radar stations S_1 and S_2.)

D131

RADARGRAMMETRY FOR THE VENUS RADAR MAPPER

Sherman S.C. Wu, U.S. Geological Survey, Flagstaff, AZ 86001

For the Venus Radar Mapper (VRM) mission, the Photogrammetry Section of the Branch of Astrogeology, U. S. Geological Survey, at Flagstaff, AZ, has been continuing to conduct research and development in mapping, using side-looking radar images. The studies of stereo radar-mapping problems have advanced to a point where derivation of topography and resolution of the radar-layover redundancy can be mathematically solved simultaneously. The problem of radar-layover geometry has been previously defined and the general concept of the solution reported [1]. Research has progressed to a point where a practical geometric solution has been achieved. The solution involves two equations, (1) and (2), each of which represents a sphere (or a circle), and relates the radar station and radar range to a ground point in each of a pair of overlapped radar images [2], supplemented by a specific projection and rotation.

As shown in Fig. 1a, S_1 and S_2 are radar stations in, respectively, radar paths P_1 and P_2; R_1 and R_2 are ranges of ground point G measured normally to the radar paths, respectively, from S_1 and S_2. Equations (1) and (2) represent two spheres but equations (4) and (5) represent only 2 circles when H_G, the elevation of ground point G, is determined in terms of flight heights, ranges and depression angles as in equations (3), (6), and (7).

$$(X_G - X_1)^2 + (Y_G - Y_1)^2 + (H_G - H_1)^2 = R_1^2 \tag{1}$$

$$(X_G - X_2)^2 + (Y_G - Y_2)^2 + (H_G - H_2)^2 = R_2^2 \tag{2}$$

$$H_G - H_1 = R_1 \sin \theta_1 \qquad H_G - H_2 = R_2 \sin \theta_2 \tag{3}$$

$$(X_G - X_1)^2 + (Y_G - Y_1)^2 = R_1^2 - R_1^2 \sin^2 \theta_1 = (R_1 \cos \theta_1)^2 \tag{4}$$

$$(X_G - X_2)^2 + (Y_G - Y_2)^2 = R_2^2 - R_2^2 \sin^2 \theta_2 = (R_2 \cos \theta_2)^2 \tag{5}$$

Where, $\theta_1 = 90^0 - (\alpha + \beta)$, (6)

$$\alpha = \cos^{-1} \left[\frac{R_1^2 + d^2 - R_2^2}{2R_1 d}\right]$$

$$\beta = \cos^{-1} \frac{\Delta H}{d} = \sin^{-1} \frac{b}{d}$$

$$d = (\Delta H^2 + b^2)^{1/2}$$

$$\Delta H = H_1 - H_2$$

$$b = [(X_1 - X_2)^2 + (Y_1 - Y_2)^2]^{1/2}$$

$$\theta_2 = \theta_1 - \Delta\theta \qquad (7)$$

$$\Delta\theta = \cos^{-1}\left[\frac{R_1^2 + R_2^2 - d^2}{2R_1 R_2}\right]$$

By solving simultaneous equations (4) and (5), i.e., by determining ground coordinates X_G and Y_G of a ground point, and combining with the elevation H_G, which is obtained by taking the average of the two equations in (3), the plotter computer will command the plate stage holders to displace radar images as though the images were taken by conventional aerial photography, so that the stereo model can be retained for photogrammetric measurements.

In the general case, the two vertical planes of the two radar look directions do not coincide, as shown in fig. 1b. Then the solution to the radar-layover problem is, first, to project the plane S_2BG normally onto plane S_1AG, so that the vertical plane S_2BG is in the vertical plane S_1AG, becoming plane $S_1AB'GS_2'$.

$$R_2' = (R_2^2 - \Delta Y^2)^{1/2} \qquad (8)$$

If the model coordinate system is rotated to the P_1S_1 system, then $Y_2' = Y_2 - \Delta Y$, $H_2' = H_2$, and $b = \Delta X = X_2 - X_1$. The rest of the parameters are determined by using the same procedures as are used in the special case (coplanearity of S_1, S_2 and G).

Based on this solution of the radar geometry, the next step is to implement these algorithms on the analytical plotters in order to handle map compilation using radar images. This step will be followed by an error analysis which will determine the range of radar observation geometries that can be used to determine topography reliably for given uncertainties of spacecraft location.

References

[1] Wu, S. S. C., The solution of the layover problem of side-looking radar images: NASA Tech. Memo. 85127, 370-372, 1982.

[2] Wu, S. S. C., Geometric corrections of side-looking radar images: Tech. Papers of ASP 49th Annual Meeting, 354-364, 1983.

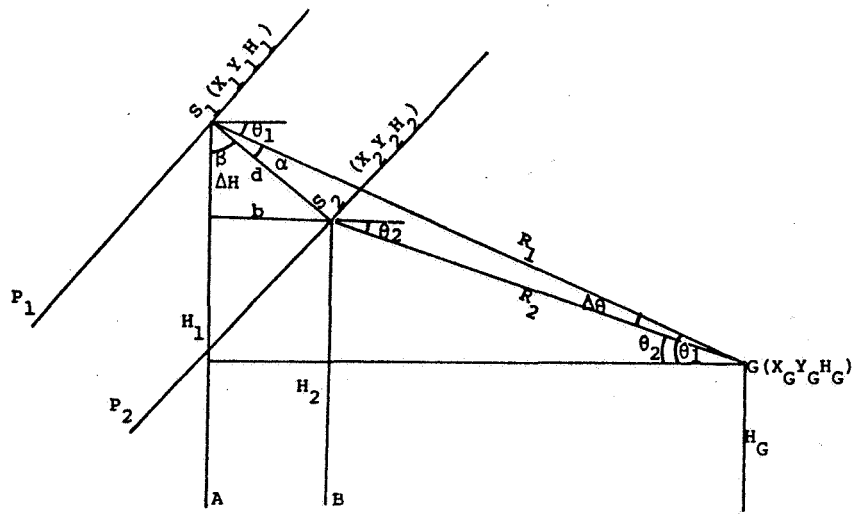

(a) Special case: Vertical planes of both radar looks are coincident.

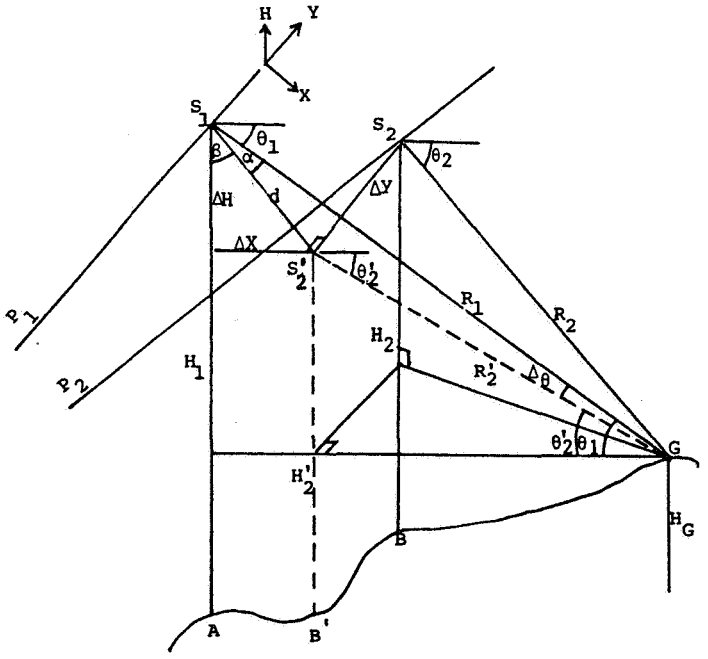

(b) General Case: Vertical planes of both radar looks are not coincident.

Figure 1 - Solution of radar-layover problem. (S_1 and S_2 are two stations along radar paths P_1 and P_2, from which ground point G is measured and recorded. θ_1, θ_2, and R_1, R_2 are depression angles and ranges, respectively, of radar stations S_1 and S_2.)

Chapter 13

SPECIAL PROGRAMS

D132

PLANETARY NOMENCLATURE

Masursky, Harold, Strobell, M. E., and Beer, K. E.; U.S. Geological Survey, Flagstaff, Arizona

Activity level is now very high in planetary nomenclature as the full flood of new planimetric, topographic, and geologic maps flows through the system. We have now named more than 3600 features on planetary bodies. At the last meeting of the International Astronomical Union we named 241 new features on Mars and outer planet satellites, five new small satellites of Jupiter and Saturn and four new gaps in Saturn's rings (Fig. 1), and 66 additional features on Venus (Fig. 2).

In the past 12 months we have processed and applied more than 100 new names to features on about 80 maps and have introduced two new names for geomorphic features: "facula" (plural, "faculae") for bright spots and "lapsus" (plural, "lapsūs") for landslides. Specific assignments include the following newly named features: 34 that appear on 28 Mars maps, 19 features on three Io maps, 34 features on four Ganymede maps, and 14 features on two Europa maps. In FY 84 we expect to process and complete the martian nomenclature on about 10 new revised maps of Mars at 1:5 million scale, 20 1:2 million scale mosaic maps, and at least 12 and possibly as many as 28 1:500,000 scale maps. Eleven more maps of Ganymede, scale 1:5 million, will be processed for nomenclature. Planetwide maps of Io and Europa at a scale of 1:15 million also will be processed.

Geologists using these base maps for their studies are becoming much more active in the nomenclature process. As is true in terrestrial geographic and geologic nomenclature, even very small or large features with little topographic expression can be named; in planetary nomenclature, this phase is adjudicated by the I.A.U. The name of the feature can then be used by geologists for nearby geologic or stratigraphic formations or structures. During the last few weeks we have received requests for names for 33 craters on Mercury and 30 features, largely paterae, on Io. As other high-resolution planetary maps are compiled by geologic mappers, we probably will receive additional requests.

The Mars nomenclature has been reviewed thoroughly during the preparation of the name plate for the new 1:15 million-scale map (shaded relief and albedo versions). All features named on maps at 1:2 million scale and smaller are shown on the 1:15 million scale maps; named features on very large scale landing-site maps (1:1 million and larger) cannot be shown. In addition to these maps, work will be completed on a comprehensive gazetteer that will give latitude, longitude, map numbers, and a brief description of every named planetary feature, listed in three different ways. This document probably will be printed as a NASA Special Publication.

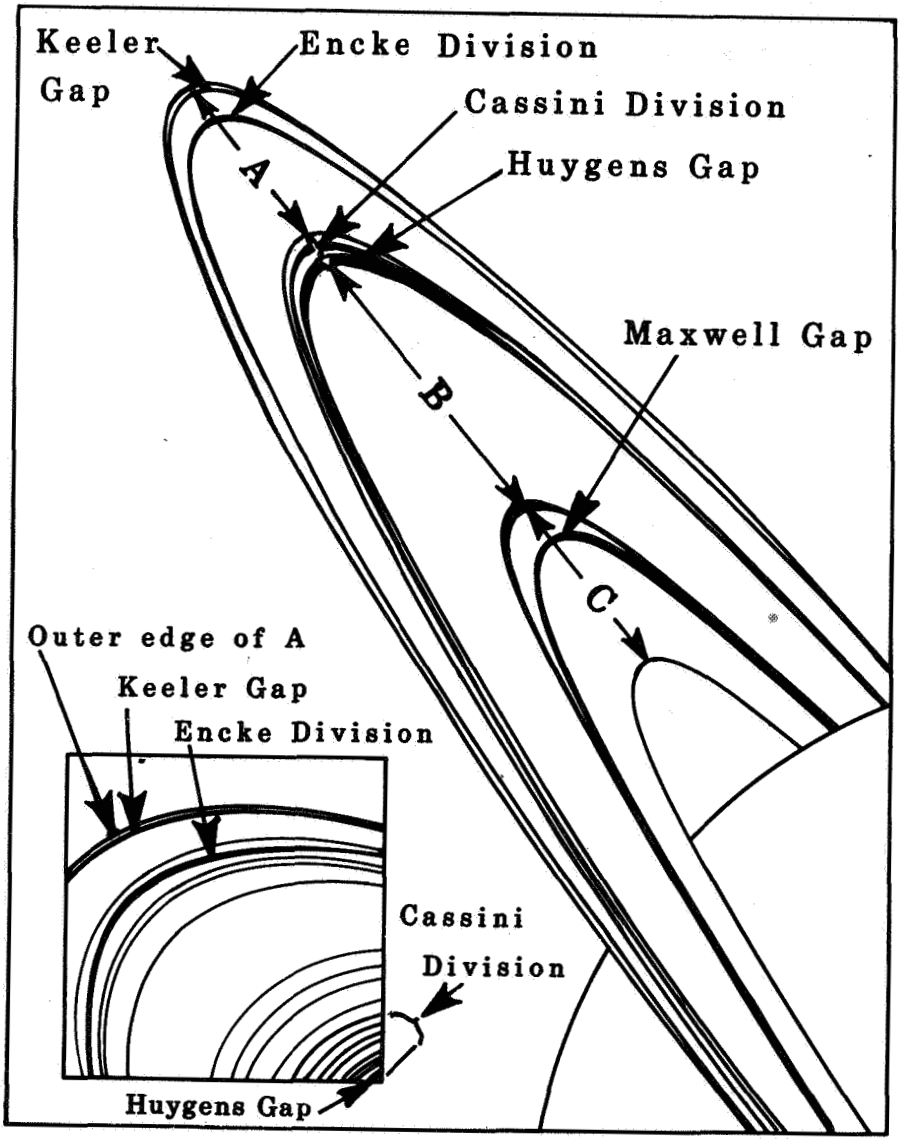

Figure 1 shows the corrected new nomenclature for the Saturn ring gaps.

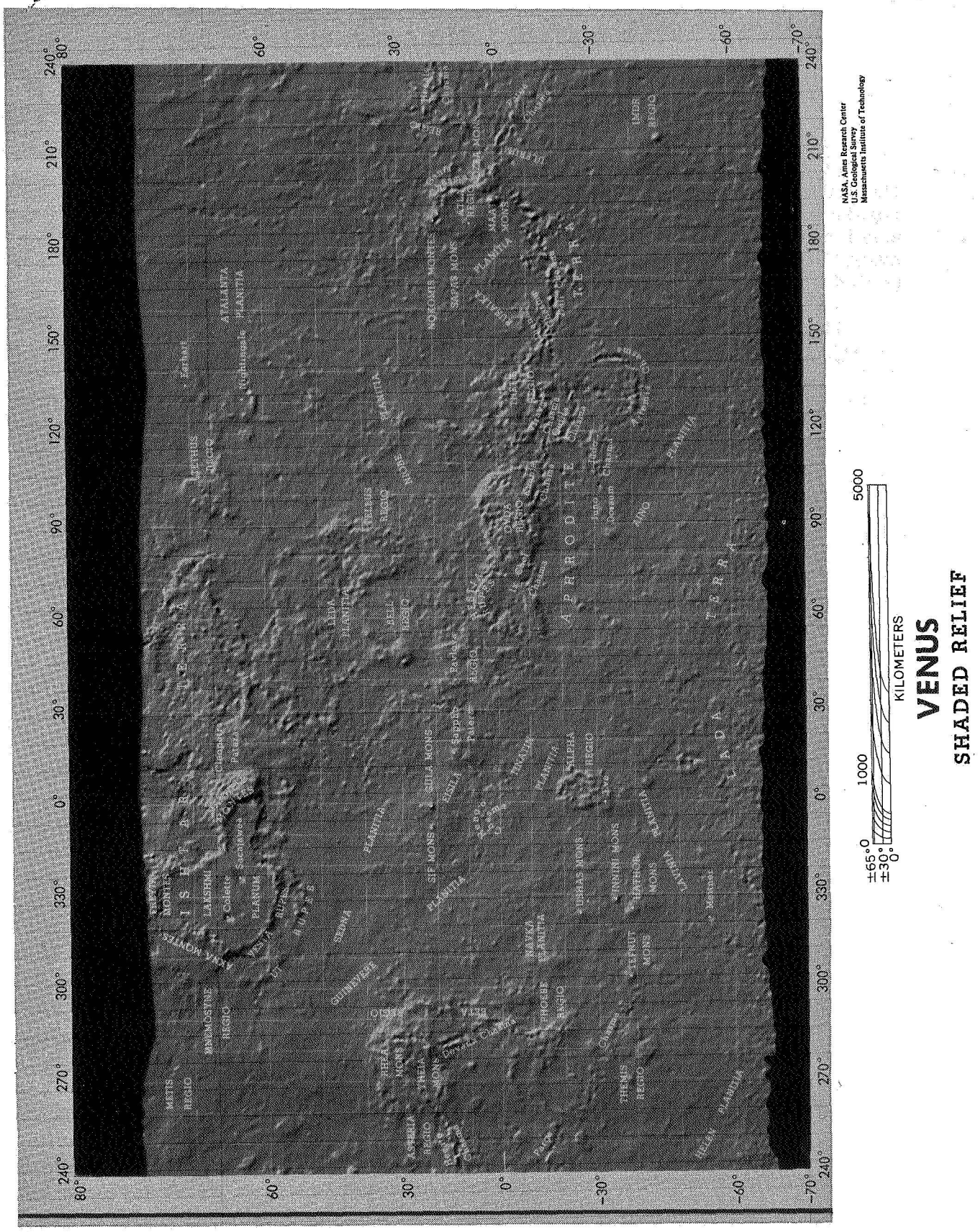

Figure 2 shows the current version of the Venus altimeter map with complete nomenclature.

D133

CONCLUSION OF THE VIKING LANDER IMAGING INVESTIGATION

Stephen D. Wall, Jet Propulsion Laboratory

Contact was lost with the Mutch Memorial Station (MMS), formerly the Viking I lander, in late 1982. Despite considerable efforts to regain communications, the lander remained silent, and the end of the mission was declared in the spring of 1983. A total of 2498 camera events (images, rescans, etc.) were taken by the MMS cameras over a period of almost 8 earth years.

All imaging data from the lander have completed standard processing by IPL. EDR tapes and photoproducts and TDR photoproducts will be distributed to Regional Planetary Imaging Facilities (RPIFs) this year. A summary of all surface changes observed over the 8-year period is in preparation (Arvidson et al., "Three Mars Years: Mutch Memorial Station Imaging Observations," Science, in press). Images of the surface are also being used to infer atmospheric optical depth by extracting surface and sky radiance and fitting these observations to a computer model, leaving the optical depth as a free parameter. The previous record of directly measured optical depths will thus be extended to cover the entire Viking mission duration for lander 1.

The final lander EDR catalogue will be published in early 1984. It will include all previously uncatalogued images from both the MMS and Viking II lander and will conclude the series of catalogues of the Viking lander Imaging Investigation. The catalogue will include a reproduction of each camera event along with numerous sorted listings to aid investigators in finding images, and a complete explanation of the data set and how to use it. In addition, the RPIF image retrieval system (BIRP) will be updated to include all Viking lander imagery.

This work is supported by the NASA Mars Data Analysis Program and by the Viking Project.

AUTHOR INDEX

1. Report No.	2. Government Accession No.	3. Recipient's Catalog No.
NASA TM-86246		

4. Title and Subtitle	5. Report Date
Reports of Planetary Geology Program - 1983	April 1984
	6. Performing Organization Code: EL

7. Author(s)	8. Performing Organization Report No.
Compiled by Henry E. Holt	
	10. Work Unit No.
9. Performing Organization Name and Address: Planetary Geology Program, Office of Space Science and Applications, Solar System Exploration Division, Washington, DC 20546	11. Contract or Grant No.
	13. Type of Report and Period Covered: Technical Memorandum
12. Sponsoring Agency Name and Address: National Aeronautics and Space Administration, Washington, DC 20546	14. Sponsoring Agency Code

15. Supplementary Notes

16. Abstract

This is a compilation of abstracts of reports from Principal Investigators of NASA's Planetary Geology Program, Office of Space Science and Applications.

The purpose is to provide a document which succinctly summarizes work conducted in this program. Each report reflects significant accomplishments within the area of the author's funded grant or contract.

No attempt has been made to introduce editorial or stylistic uniformity; on the contrary, the style of each report is that of the Principal Investigator and may best portray his research.

17. Key Words (Suggested by Author(s))	18. Distribution Statement
Planetary Geology Solar System Evolution Planetary Geologic Processes	Unclassified - Unlimited Subject Category 91

19. Security Classif. (of this report)	20. Security Classif. (of this page)	21. No. of Pages	22. Price
Unclassified	Unclassified	376	A17

For sale by the National Technical Information Service, Springfield, Virginia 22161

NASA-Langley, 1984